

Cumhuriyet Science Journal
Faculty of Science Cumhuriyet University 58140
Sivas-TURKEY
Phone: +90(346)2191010-1522
Fax: +90(346)2191186
e-mail: csj@cumhuriyet.edu.tr
<http://dergipark.gov.tr/csj>

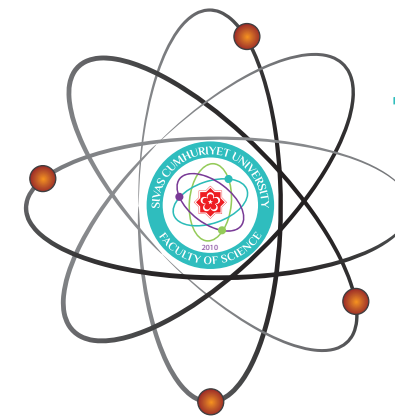
Cumhuriyet Science Journal Vol: 42 No: 2 Year: 2021



Sivas Cumhuriyet University

ISSN : 2587-2680
e-ISSN : 2587-246X

Cumhuriyet
Science
Journal



Volume: 42

Number: 2

Year: 2021



ISSN: 2587-2680
e-ISSN: 2587-246X
Period: Quarterly
Founded: 2002
Publisher: Sivas Cumhuriyet
University

Cumhuriyet Science Journal (CSJ)

Journal Previous Name: Cumhuriyet Üniversitesi Fen-Edebiyat Fakültesi Fen Bilimleri Dergisi

Old ISSN: 1300-1949

Owner on behalf of the Sivas Cumhuriyet University, Faculty of Science

Prof. Dr. İdris ZORLUTUNA (Sivas Cumhuriyet University)

Editor in Chief

Prof. Dr. İdris ZORLUTUNA (Sivas Cumhuriyet University)

Managing Editor

Assoc. Prof. Dr. Adil ELİK (Sivas Cumhuriyet University)

Editors

Prof. Dr. Baki KESKİN

bkeskin@cumhuriyet.edu.tr

Subjects: Mathematics and Statistics

Institution: Sivas Cumhuriyet University

Assoc. Prof. Dr. Adil ELİK

elik@cumhuriyet.edu.tr

Subjects: Chemistry and Chemical Engineering,
Environmental Sciences, Basic Sciences (General)

Institution: Sivas Cumhuriyet University

Prof. Dr. Nilüfer TOPSAKAL

ntopsakal@cumhuriyet.edu.tr

Subjects: Applied Mathematics

Institution: Sivas Cumhuriyet University

Prof. Dr. Serkan AKKOYUN

sakkoyun@cumhuriyet.edu.tr

Subjects: Physics and Physical Engineering

Institution: Sivas Cumhuriyet University

Prof. Dr. Hülya KURŞUN

hkursun@cumhuriyet.edu.tr

Subjects: Earth Sciences

Institution: Sivas Cumhuriyet University

Prof. Dr. Halil İbrahim ULUSOY

hiulusoy@cumhuriyet.edu.tr

Subjects: Chemistry, Analytical Chemistry, Drug Analysis, Pharmacy

Institution: Sivas Cumhuriyet University

Assoc. Prof. Dr. Nail ALTUNAY

naltunay@cumhuriyet.edu.tr

Subjects: Bioanalytical Chemistry, Chemometric Analysis

Institution: Sivas Cumhuriyet University

Section Editors

Prof. Dr. Natalia BONDARENKO

bondarenkonp@info.sgu.ru

Subjects: Applied Mathematics and Physics

Institution: Samara University

Prof. Dr. Muhammet BEKÇİ

mbekci@cumhuriyet.edu.tr

Subjects: Statistics

Institution: Sivas Cumhuriyet University

Prof. Dr. Marcello LOCATELLI

marcello.locatelli@unich.it

Subjects: Analytical Chemistry

Institution: University "G. d'Annunzio" of Chieti-Pescara

Prof. Dr. Konstantin P. KATIN

kpkatin@yandex.ru

Subjects: Theoretical Chemistry, Computational design of nanostructures, nanodevices and nanotechnologies

Institution: National Research Nuclear University

Assoc. Prof. Dr. Duran KARAKAŞ

dkarakas@cumhuriyet.edu.tr

Subjects: Inorganic Chemistry, Theoretical Chemistry

Institution: Sivas Cumhuriyet University

Assoc. Prof. Dr. Yaşar ÇAKMAK

ycakmak@cumhuriyet.edu.tr

Subjects: Applied Mathematics

Institution: Sivas Cumhuriyet University

Assoc. Prof. Dr. Sevgi DURNA DAŞTAN

sdurna@cumhuriyet.edu.tr

Subjects: Molecular Biology

Institution: Sivas Cumhuriyet University

Assist. Prof. Dr. Didem ALTUN

didemaltun@cumhuriyet.edu.tr

Subjects: Engineering sciences

Institution: Sivas Cumhuriyet University

Abstracted&Indexing

ULAKBİM TR-Dizin

Index Copernicus (ICI Journals Master List)

Clarivate Analytics Zoological Record

Crossref

Directory of Open Access Journals (DOAJ)

WorldCat

Akademik Dizin

Arastirmax Bilimsel Yayın İndeksi

Bielefeld Academic Search Engine (BASE)

Directory of Research Journal Indexing (DRJI)

Google Scholar

Research Gate

Idealonline

Editorial Board

Prof. Dr. Sezai ELAGÖZ (ASELSAN)
Prof. Dr. Mustafa SOYLAK (Erciyes University)
Prof. Dr. Chuan Fu Yang (Nanjing University of Science and Technology)
Prof. Dr. Münevver SÖKMEN (KGTU)
Prof. Dr. Hüseyin MERDAN (TOBB ETU)
Prof. Dr. Mehmet AKKURT (Erciyes University)
Prof. Dr. Mustafa KAVUTÇU (Gazi University)
Prof. Dr. Francois VOS (The University of Queensland)
Prof. Dr. Abuzar KABIR (International Forensic Research Institute)
Prof. Dr. Mustafa TÜZEN (GOP University)
Prof. Dr. Songül KAYA MERDAN (METU)
Prof. Dr. Jose Javier Valiente-Dobon (INFN-LNL, Padova University)
Prof. Dr. Yeşim SAĞ AÇIKEL (Hacettepe University)
Prof. Dr. Mehmet ŞİMŞİR (Sivas Cumhuriyet University)
Prof. Dr. Atalay SÖKMEN (KGTU)
Prof. Dr. Ricardo I. JELDRES (Universidad de Antofagasta)
Prof. Dr. Mustafa YILDIRIM (Sivas Cumhuriyet University)
Prof. Dr. Ali DELİCEOĞLU (Erciyes University)
Prof. Dr. Tuncay BAYRAM (Karadeniz Technical University)
Prof. Dr. Gökhan KOÇAK (Erciyes University)
Prof. Dr. Nadjet Laouet (Freres Mentouri Constantine-1 University)
Assoc. Prof. Dr. Savaş KAYA (Sivas Cumhuriyet University)

Layout Editors:

Assist. Prof. Dr. Merve Esra TÜRKAY
Lecturer Aykut HASBEK

Copyeditors:

Research Assistant Özgür İNCE
Research Assistant Doğa Can SERTBAŞ
Research Assistant Dr. Hacı Ahmet KARADAŞ

Proofreader:

Assist. Prof. Dr. Yener ÜNAL
Lecturer Aykut HASBEK

Publication Type. Peer Reviewed Journal

Cite Type: Cumhuriyet Sci. J.

Contact Information

Faculty of Science Cumhuriyet University
58140 Sivas- TURKEY
Phone: +90(346)2191010-1522
Fax: +90(346)2191186
e-mail: csj@cumhuriyet.edu.tr
<http://dergipark.gov.tr/csj>

CONTENTS

PAGES

Süleyman İLHAN, Çisil ÇAMLI PULAT <i>Biogenic silver nanoparticles synthesized from Piper longum fruit extract inhibit HIF-1α/VEGF mediated angiogenesis in prostate cancer cells</i>	236 - 244
Yusuf TEMEL <i>The in vitro effect of 5-FU and Tamoxifen Chemotherapeutics on penthose phosphate pathway enzymes</i>	245 - 251
Çisil ÇAMLI PULAT <i>In vitro cytotoxic activity of Tarantula cubensis alcoholic extract on different human cell lines</i>	252 - 259
Fuat ÖZYONAR, Mehmet KOBYA, Ülker Aşlı GÜLER <i>Investigation of the adsorption of Astrazon Blue FGRL dye in synthetic wastewater using waste mine clay</i>	260 - 268
Hasan Basri KARAYEL <i>Effects of natural boron mineral on the essential oil ratio and components in medicinal sage (Salvia officinalis L.)</i>	269 - 275
Yasin ŞENOL, Ayşegül DOĞAN, Mustafa ÇELEBİER <i>Ultrafiltration-Based extraction of Ibuprofen from human plasma samples and HPLC analysis: developing an innovative bioanalytical analysis method</i>	276 - 284
İbrahim NARİN, Abdullah Taner BİŞGİN, Mustafa TÜZEN, Mustafa UÇAN, Durali MENDİL, Mustafa SOYLAK <i>Determination and evaluation of Cu, Mn, Zn, Cd, Pb and Ni contents in wild-grown edible mushroom species from Cappadocia, Turkey</i>	285 - 291
İnci KAYGUSUZ, Mustafa TÜZEN <i>Flame atomic absorption spectrometric determination of multi element in apricot and soil samples after wet and microwave digestion method</i>	292 - 298
İdil KARACA AÇARI <i>Determination of the chemical structure of diet biscuits with modern enstrumental techniques</i>	299 - 309
Hamdi MIHÇIÖKUR <i>Environmental risk assessment of commonly used anti-cancer drugs</i>	310 - 320
Tülay YILDIRIM <i>Remarks on the group of units of a corner ring</i>	321 - 326
M. Tamer SENEL, Bengü ÇINA <i>Existence of nonoscillatory solutions of second-order neutral differential equations</i>	327 - 332
Özlem TEKİN <i>Quasi ideals of nearness semirings</i>	333 - 338
Jiarul HOQUE, Shyamapada MODAK <i>Algebra of frontier points via semi-kernels</i>	339 - 345
Şükran UYGUN <i>The relations between bi-periodic jacobsthal and bi-periodic jacobsthal lucas sequence</i>	346 - 357
Abdurrahman BAYTAR, Deniz SUNAR ÇERÇİ, Salim ÇERÇİ <i>Simulation study for 3D dynamic characteristics of voltage losses in PEM fuel cell</i>	358 - 363
Hülya KURU MUTLU <i>Analysis and calculations of decentration amount and prism in eyeglass lenses</i>	364 - 371
Erdem UZUN <i>Numerical solutions of the randall-wilkins and one trap one recombination models for first order kinetic</i>	372 - 379

Mustafa Kemal BAHAR <i>Velocity-dependent potential effects on two interacting electrons in Cornell quantum dot planted in plasma medium.....</i>	380 - 388
Melek GÖKBULUT <i>Examination of ^{99m}Tc-mdp radioactivity after injection according to time and distance.....</i>	389 - 396
Öznur BAĞ, Saffet NEZİR <i>Investigation of physical and structural properties of cs doped y1ba2cu3o7 superconductors.....</i>	397 - 402
Pınar BAŞER <i>Effect of pressure, temperature, and magnetic field on the binding energy of the electron-hole system in III-V group semiconductors.....</i>	403 - 412
Gokcen ALTUN <i>A study on Freeman-Tukey test statistic under the symmetry model for square contingency tables.....</i>	413 - 421
İbrahim ABDULLAHİ <i>The Nakagami-Weibull distribution in modeling real-life data.....</i>	422 - 433
Sinan SARAÇLI, Olcay ULUCAN <i>Examination of effects of radiation awareness on protection from radiation via structural equation modeling.....</i>	434 - 440
Sayiter YILDIZ, Can Bülent KARAKUŞ <i>Estimation of organic matter dependent on different variables in drinking water network using artificial neural network and multiple regression methods.....</i>	441 - 451
İpek ÇELEN-ERDEM, Gülsüm ÜRPER, Derya KÖSEOĞLU, İsmail KOYUNCU, İzzet ÖZTÜRK <i>Optimization of operational parameters at laboratory scale membrane bioreactor for treatment of high-strength opium alkaloid wastewater: The effect of pretreatment.....</i>	452 - 464
Asuman Işıl ÇARHOĞLU <i>Investigation of behavior of cooling tower structure under external loads.....</i>	465 - 475
Ufuk PARALI <i>Computational analysis of optical trapping of transparent and reflecting micron-sized spherical particles.....</i>	476 - 492
Emine CAN GÜVEN <i>Optimization of process parameters in coagulation of landfill leachate by Al₂(SO₄)₃ and PACl.....</i>	493 - 501
Tanju TEKER, Mustafa ÖZASLAN <i>Investigation of deformation and element diffusion in joint interface of mild carbon steel and HCrWCI welded by friction welding.....</i>	502 - 507
Muzaffer ASLAN, Zeynep ALÇİN <i>Detection of epileptic seizures from EEG signals with Hilbert Huang Transformation.....</i>	508 - 514



Biogenic silver nanoparticles synthesized from *Piper longum* fruit extract inhibit HIF-1 α /VEGF mediated angiogenesis in prostate cancer cells

Süleyman İLHAN^{1,*} , Çisil ÇAMLI PULAT²

¹ Manisa Celal Bayar University, Faculty of Science and Letters, Department of Biology, Manisa / TURKEY

² Manisa Celal Bayar University, Applied Science Research Center, Manisa / TURKEY

Abstract

In the present study, biogenic silver nanoparticles (PL-AgNPs) were synthesized by using *Piper longum* (PL) dried fruit extract and investigated the effect of PL-AgNPs on angiogenesis and signal transduction pathway of hypoxia-inducible factor alpha (HIF-1 α)/vascular endothelial growth factor (VEGF) on human prostate cancer cells. The prepared PL-AgNPs were characterized by ultraviolet-visible (UV-vis) spectroscopy, scanning electron microscopy (SEM), energy-dispersive X-ray spectroscopy (EDX) and dynamic light scattering (DLS) analysis. Potential cytotoxic and anti-angiogenic effects of PL-AgNPs were evaluated on PC-3 and DU-145 prostate cancer cells. Cytotoxicity was evaluated by MTT assay. The anti-angiogenic effect was investigated via a cell migration assay. Protein and mRNA levels of key angiogenesis related molecules such as VEGF and HIF-1 α were evaluated via ELISA and qRT-PCR assays. UV-vis spectroscopy showed an absorbance peak at 450 nm confirming the PL-AgNPs synthesis. Various characterization techniques revealed that the average size of synthesized PL-AgNPs was below 100 nm. The cytotoxic effect was elevated in a concentration-dependent manner ($p < 0.05$). The biosynthesized PL-AgNPs inhibited cell migration and reduced the levels of both protein and mRNA levels of VEGF and HIF-1 α in prostate cancer cells ($p < 0.05$). Results revealed that the PL extract with AgNO₃ nanoparticles may be a potential candidate for developing novel anticancer and antiangiogenic compounds for prostate cancer.

Article info

History:

Received: 21.11.2020

Accepted: 27.05.2021

Keywords:

Silver nanoparticles,
Prostate cancer,
VEGF,
HIF-1 α ,
Piper longum.

1. Introduction

Prostate cancer is a common malignancy among elderly men [1]. Although there are several treatment strategies including chemotherapy and radiotherapy, mortality is still high. Angiogenesis is one of the key processes for tumor development. Therefore, inhibition of angiogenesis is accepted as a hopeful treatment strategy for prostate cancer. Vascular endothelial cell growth factor (VEGF) is the most potent angiogenic promoter that induces vascular growth [2]. The levels of VEGF are modulated by hypoxia-inducible factor alpha (HIF-1 α) which is expressed under the hypoxic microenvironment of the tumor [3]. Therefore, VEGF and HIF-1 α have become important targets of anti-tumor angiogenesis.

Currently, natural compounds are promising alternative sources for novel drug production. Among the natural compounds, plant extracts show high efficiency and easy availability [4]. *Piper longum*

(PL) belongs to the Piperaceae family. It is widely used as a spice and for traditional medicine mainly in Asia [5]. Piperlongumine and piperine have been identified as the major bioactive secondary metabolites of PL [6]. Antitumor, antioxidant and antibacterial effects of PL extracts and its alkaloid component piperine were investigated in several studies [7–10]. It was shown that PL has antioxidant activity against the free radical inducers, anti-inflammatory activity, and it is used for several types of infections as well as respiratory system diseases [7, 11, 12]. Anticancer activity of PL extracts was also shown on various cancer cells [8–10, 13]. The anti-metastatic effect of piperine was shown on C57BL/6 mice [14]. It was also demonstrated that piperine can increase the cytotoxic effect of anti-cancer drugs for resistant cell lines like A-549/DDP and MCF-7/DOX [15]. The effect of piperonaline as a piperine derivate

*Corresponding author. e-mail address: suleyman.ilhan@cbu.edu.tr

was examined on PC-3 prostate cancer cells. The results demonstrated that piperonaline has an apoptotic effect on PC-3 cell lines [16]. As demonstrated, PL holds great anticancer potential as a natural compound.

Nanotechnology is the world's fastest-growing manufacturing sector, with a never-ending quest for new nanomaterials and manufacturing methods. Because of their peculiar properties and possible applications in catalysis, photonics, optoelectronics, biological tagging, and pharmaceutical applications, metal nanoparticles have attracted a lot of interest in recent years. Using nanoparticles as a novel approach for improving antioxidant, anticancer and antimicrobial activities of natural compounds became the new promising source recently [18]. There are many in vitro studies showing different approaches for the synthesis of nanoparticles and the enhancing effect of these nanoparticles [19, 20]. However, exploration of the plant systems as the potential nano factories has heightened interest in the biological synthesis of nanoparticles. Further, the cytotoxic effect of PL leaf extract with silver nanoparticles was studied on Hep-2 cell lines and it was shown that the nanoparticles have a significant cytotoxic effect on the laryngeal carcinoma cells indicating that PL nanoparticles show potential for cancer cell cytotoxicity [8]. The present study was aimed at the synthesis of silver nanoparticles (PL-AgNPs) using *Piper longum* (PL) dried fruit extract and evaluation of their effect on hypoxia-inducible factor alpha (HIF-1 α)/vascular endothelial growth factor (VEGF) signal transduction pathway on human PC-3 and DU-145 prostate cancer cells.

2. Materials and Methods

2.1. Extraction of PL fruit

The plant material was obtained from a local market and identified at Ege University, Department of Botany. Dried powder (5 g) was extracted in absolute ethanol (EtOH) (50 mL) at room temperature, extracted for 60 min by ultra-sonication, and stored at room temperature (0.1 g/mL). The concentration of EtOH was <0.1 % in all experiments and had no effect on cells.

2.2. Biosynthesis of PL-AgNPs

The biosynthesis of PL-AgNPs was carried out by mixing 34 mg of AgNO₃ (10 mM) with 45 mL of H₂O (18 M Ω) and 5 mL PL ethanolic extract. Then, the obtained solution was incubated at 90°C in a laboratory-grade microwave (25 min, at 300 W) (CEM, Mars 6, USA). The reduction of Ag⁺ to AgNPs is observed by the light greenish-brown color of the

mixture. After synthesis, large particles were removed by filtering the samples through a 2.5 mm filter paper (Whatman No 5). The biosynthesis PL-AgNPs was centrifuged (4 °C, 5000xg,) for 10 min. To discard plant extract residues, the solution was washed with double distilled water.

2.3. Spectrophotometric characterization of PL-AgNPs

To prevent unwanted additional photochemical reactions, all the reduction processes were carried out in the dark. The color of the solution changed to brownish-yellow which was observed by the naked eye. Then, to confirm the results, the so-called change was measured by UV-visible spectroscopy. The PL-AgNPs solution was centrifuged at 12000xg for 15 min at RT. After the centrifugation step, the solution was washed with distilled water. Then, the obtained PL-AgNPs were collected in deionized water for other characterization steps.

2.4. SEM-EDX and DLS analyses

AgNO₃ nanoparticles in PL extract were identified via Scanning Electron Microscope (SEM) and followed by Energy Dispersive X-ray Spectroscopy (EDX) analysis. A small drop of the sample was used on SEM stub and allowed to dry. After Au-Pd coating, SEM images were acquired with a secondary electron (SE) detector (Zeiss Gemini 500, Germany). EDX analysis was done to verify the elemental silver via EDAX, APEX™ Software for EDX. The PL-AgNPs were additionally analyzed by DLS which determines the size of colloidal scattering via the radiance of a molecule suspension having Brownian motion.

2.5. Cell culture

PC-3 (ATCC, CRL-1435) and DU-145 (ATCC, HTB-81) cells were purchased from ATCC. Both prostate cancer cells were maintained in RPMI 1640 medium including L-glutamine (1%), FBS (10%), and penicillin-streptomycin solution (1%) (Sigma) and incubated at CO₂ incubator (37°C with 5% CO₂) during the experiments.

2.6. MTT assay

The viable cells were counted via trypan blue dye with Countess cell counter (Countess, Thermo Fisher Scientific, Massachusetts, USA) and were seeded at 1 \times 10⁵ cells/well. For attachment of cells, the plates were maintained for 24 h and then, treated with different extract concentrations (10-100 μ g/mL) of PL ethanolic extract or PL-AgNPs solutions. After 24, 48 and 72 h incubations with the extract solutions, 20 μ L (10% of the final volume) of MTT solution (Sigma) was pipetted to each well. After incubation for 4 h with

MTT solution, cells were emptied and filled with 200 μL dimethyl sulfoxide (DMSO). Measurement of color change was carried out at 570 nm with the 690 nm reference wavelength by an ELISA reader (TECAN, Männedorf, Switzerland). The IC_{50} values of the extracts were calculated via Biosoft CalcuSyn 2.1 software (Biosoft, Cambridge, UK).

2.7. Cell migration assay

For assessing cell migration, the scratch assay protocol of Liang et al. (2007) was carried out. Briefly, 10^5 cells/well were incubated for 24 h to obtain confluent monolayer cells. Then, a 200 μL pipette tip was used to scratch the plate. Cells were exposed to the IC_{50} concentrations of PL-AgNPs (IC_{50} value of PC-3 cells was 73.41 $\mu\text{g}/\text{mL}$ and 38.53 $\mu\text{g}/\text{mL}$ for DU-145). Closure of the scratched areas was measured for 24, 48 and 72 h. Wells were monitored with an inverted microscope and photographed by Axiovision software (Zeiss, Germany).

2.8. Measurement of VEGF and HIF-1 α levels

Both VEGF and HIF-1 α protein levels were quantitated via ELISA assay (Biovision, VEGF cat# K5363, HIF-1 α cat#: E4285). Briefly, cell lysates were obtained by using lysis buffer, then 50 μL cell lysates were transferred into antibody-coated 96 well plates. Then, streptavidin-HRP solution (50 μL) and 10 μL antibody (VEGF or HIF-1 α) were added to each well. Then the sealing membrane was sealed and plates were incubated 60 minutes at 37 $^{\circ}\text{C}$. After two washing steps with washing buffer, seconder antibodies were added to all wells and incubated at 37 $^{\circ}\text{C}$ for 1 h. Colorimetric reading was performed by ELISA reader at 450 nm (with 650 nm reference wavelength). Concentrations of both VEGF and HIF-1 α were calculated from the standard curves. The minimum detection limit of HIF-1 α was 1 pg/mL and VEGF was 20 ng/L.

2.9. Quantitative real time PCR (qRT-PCR)

The levels of VEGF and HIF-1 α mRNAs were quantified via qRT-PCR analysis. For the RNA extraction Trizol agent (Qiagen, USA) was used. First, cells were incubated with 1 mL Trizol for 5 min at RT. Obtained suspension was centrifuged at 12000xg for 20 min (at 4 $^{\circ}\text{C}$). After centrifugation, the supernatant was discarded and mixed with 1 mL isopropanol. Then, the suspension was incubated at 4 $^{\circ}\text{C}$ for 1 h, and centrifugated at 12,000 g for 10 min for precipitation. The supernatant was removed and precipitants were dissolved in 20 μL ultra-pure water. The obtained RNAs were checked for integrity and quality via agarose gel electrophoresis. cDNA was obtained from extracted total RNAs via using a commercial kit (Quantitect reverse transcription kit, Qiagen, USA).

The PCR was conducted in a mixture that was containing SYBR Green Master Mix (12.5 μL), H_2O (10.5 μL , DNAase-RNase free) 1 μL of primer stock (20 μM), and 1 μL cDNA for each primer (Qiagen, USA). The reaction was carried out using the Light Cycler 480 instrument (10 min. at 95 $^{\circ}\text{C}$, 15 s. at 95 $^{\circ}\text{C}$, 1 min. 60 $^{\circ}\text{C}$, 40 cycles) (Roche Applied Science, Germany).

Glyceraldehyde-3-phosphate dehydrogenase (GAPDH) was used as a positive control. The primers of targeted genes were as follows: VEGF, forward 5'-GCACCCATGGCAGAAGG-3' and reverse 5'-CTCGATTGGATGGCAGTAGCT-3', HIF-1 α forward 5'-GATGTGGTTGTATTTCGTG-3' and reverse 5'-ATCTCCTGCTTCTTTAGTC-3', GAPDH forward 5'-TGAAGGTCGGAGTCAACGGATTGGT-3' and reverse 5'-CATGTGGGCCATGAGGTCCACCAC-3' (Microsynth, Germany).

2.10. Statistical analysis

Data was analyzed via GraphPad Prism software (USA). Two-way ANOVA followed by *Dunnnett's t-test* was done to demonstrate significant differences between different treatments. * $p < 0.05$ values were accepted as significant.

3. Results

3.1. Confirmation of PL-AgNP formation via UV-vis spectroscopy

First, the PL-AgNPs were characterized via the color change of the solution to brownish-yellow within 3 min after AgNO_3 s were added. Then, the optical properties of PL-AgNPs were evaluated via UV-vis spectrophotometer. A peak occurring at 450 nm in the UV-Vis spectrum was characteristic for AgNPs and confirmed the formation of PL-AgNPs (Figure 1).

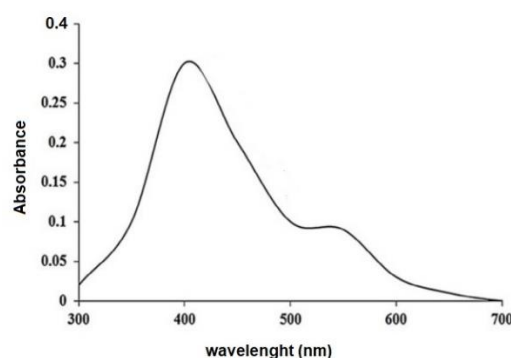
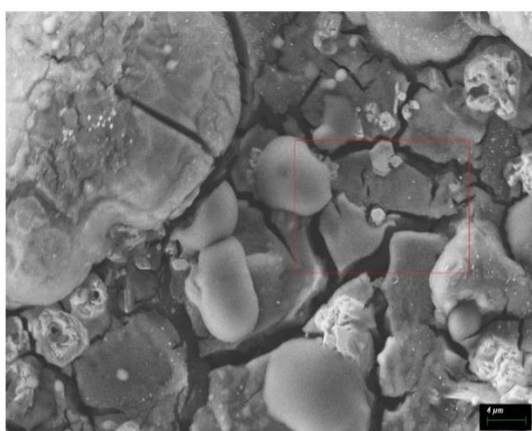


Figure 1. UV-visible spectrum recorded as a function of the reaction time of 1 mM AgNO_3 solution with PL ethanolic extract.

3.2. SEM-EDX analysis

The synthesized nanoparticles were scanned with SEM (Figure 2a). PL-AgNPs were also confirmed by using Energy Dispersive X-ray Spectroscopy (EDX) analysis. SEM image was recorded in 6mm working distance (WD) with 5000 magnification. SE detector was used with 10kV electron high tension (EHT) in order to obtain the image. EDX data was acquired via EDAX, APEX™ Software and Ag La signals were detected. An absorption peak at 3 keV verified the elemental silvers in the nanoparticles. The EDX peaks corresponding to carbon, oxygen and sulfur indicated that AgNPs were properly capped by plant extract (Figure 2b).

a



b

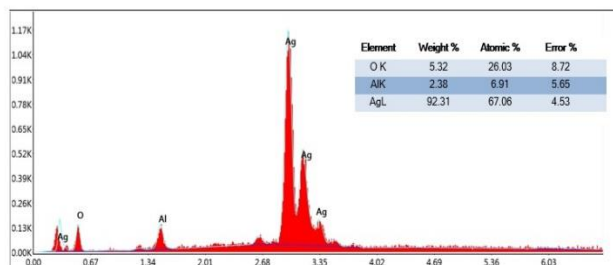


Figure 2. a) SEM image of PL extract with AgNO₃ nanoparticles. (b) The area within the red square was used for SEM-EDX analysis and Ag signals were detected.

3.3. Dynamic light scattering (DLS) analysis

The impact of AgNPs was affected by the shape, particle size and size distribution as well as the composition. DLS analysis revealed that the mean diameters of PL-AgNPs in optimum conditions were

approximately 11 nm (Std E: 5.5). Figure 3 shows the size distribution pattern of the suspension of PL-AgNPs.

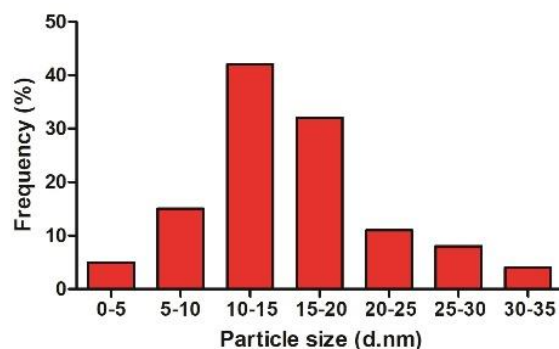


Figure 3. Dynamic light scattering of AgNO₃ nanoparticles.

3.4. Effects of PL ethanolic extract and PL-AgNPs on the viability of PC-3 and DU-145 cells

The effects of both PL ethanolic extract and PL-AgNPs on cell viability were evaluated by MTT assay. While the PL ethanolic extract showed a very little cytotoxic effect on the prostate cancer cells at all tested concentrations, the extract with AgNO₃ nanoparticles decreased the viability of both cancer cells dramatically at the same concentrations (Figures 4. and 5.) ($p < 0.05$). The effect of PL-AgNPs was concentration-dependent but not time-dependent in both prostate cancer cells. The most effective time point for PL-AgNPs was determined as 48 h for both cell lines. As shown in Figure 4, there were 18% and 30% reduction in the viability of PC-3 cells exposed to 80 and 100 $\mu\text{g/mL}$ of PL ethanolic extract, respectively, as compared to the control group at 48 h ($p < 0.05$), while there were 49% and 94% reduction in PC-3 cell viability exposed to 80 and 100 $\mu\text{g/mL}$ of PL-AgNPs, respectively, at 48 h ($p < 0.05$). In DU-145 cells, similar results were obtained (Figure 5). There were 10% and 14% reduction in the viability of DU-145 cells exposed to 80 and 100 $\mu\text{g/mL}$ of PL ethanolic extract respectively, as compared to the control group at 48 h ($p < 0.05$), while there were 97% and 98% reduction in DU-145 viability exposed to 80 and 100 $\mu\text{g/mL}$ of PL-AgNPs, respectively, at 48 h ($p < 0.05$). From the cell viability data, the calculated IC₅₀ value of PC-3 cells was 73.41 $\mu\text{g/mL}$ and 38.53 $\mu\text{g/mL}$ for DU-145 cells which were treated with PL-AgNPs.

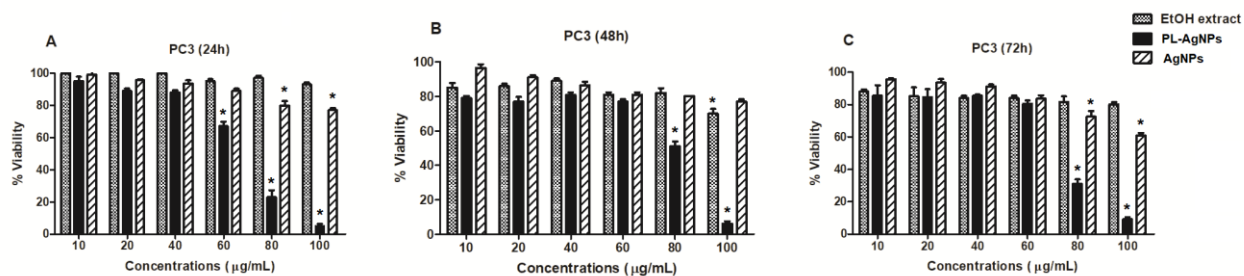


Figure 4. (A-C) Comparative effect of AgNPs, PL ethanolic extract and PL-AgNPs on PC-3 cell viability (*P<0.05, as compared to untreated controls).

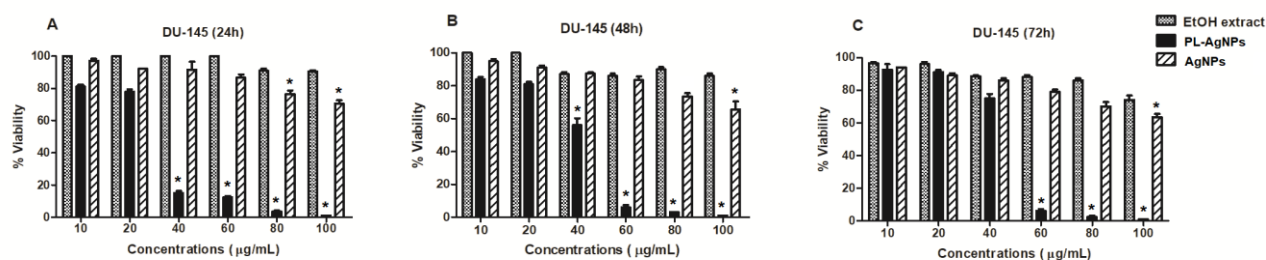


Figure 5. (A-C) Comparative effect of AgNPs, PL ethanolic extract and PL-AgNPs on DU-145 cell viability (*P<0.05, as compared to untreated controls).

3.5. Effect of PL-AgNPs on cell migration

Next, in vitro scratch assay was performed to evaluate the effect of PL-AgNPs on human prostate cancer cell motility. Treatment of both cells by PL-AgNPs resulted in a significant decrease in the cell motility (Figure 6.) suggesting the potential anti-angiogenic effects of the synthesized PL-AgNPs. When obtained data is compared with the control group, it is observed that PL-AgNPs has a considerably high wound healing effect at 48 and 72 h.

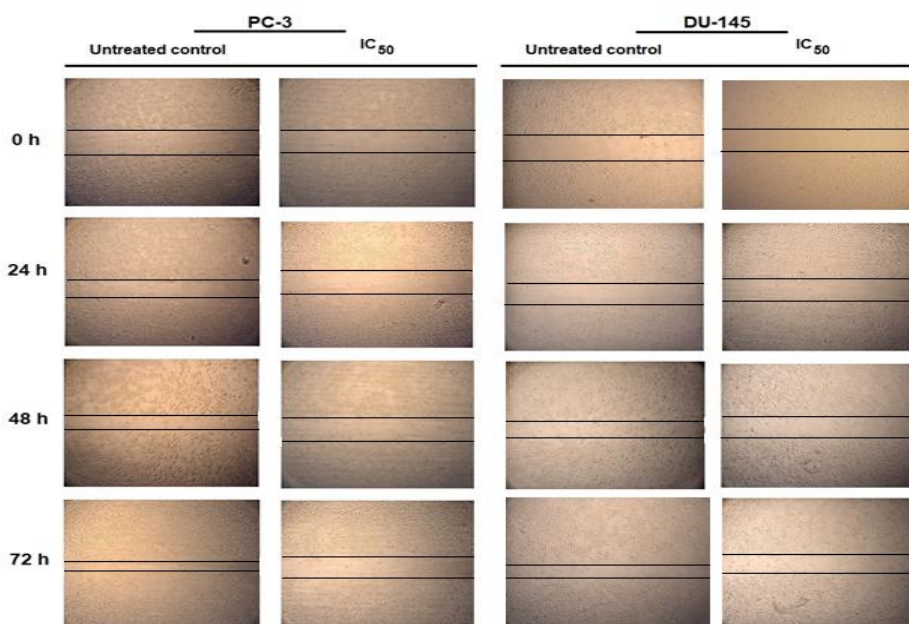


Figure 6. Effect of PL-AgNPs on the migration of PC-3 and DU-145 cells at 24, 48 and 72 h. The lines define the area lacking cells.

3.6. Evaluation of VEGF and HIF-1 α protein and mRNA levels

The VEGF and HIF-1 α protein levels by PL-AgNPs treatment were evaluated via ELISA assay. The levels

of both VEGF and HIF-1 α proteins were inhibited in a concentration dependent manner at 48 h in both prostate cancer cells ($p < 0.05$) (Figure 7.).

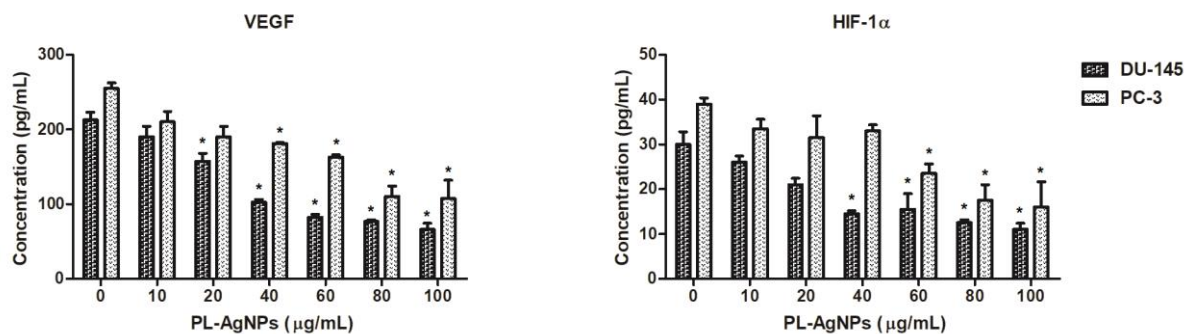


Figure 7. Levels of VEGF and HIF-1 α proteins by increasing concentrations of PL-AgNPs at 48 h in PC-3 and DU-145 cells (* $p < 0.05$).

qRT-PCR was confirmed the inhibition of VEGF and HIF-1 α in both prostate cancer cells. The levels of VEGF and HIF-1 α mRNAs were reduced by 2.8- and 3.2- fold in PC-3 prostate cancer cells treated with 73.41 $\mu\text{g/mL}$ PL-AgNPs at 48 h ($p < 0.05$) (Figure 8.), while in DU-145 cells, VEGF and HIF-1 α levels were decreased by 2.4- and 2.8- fold exposed to 38.53 $\mu\text{g/mL}$ PL-AgNPs at 48 h ($p < 0.05$).

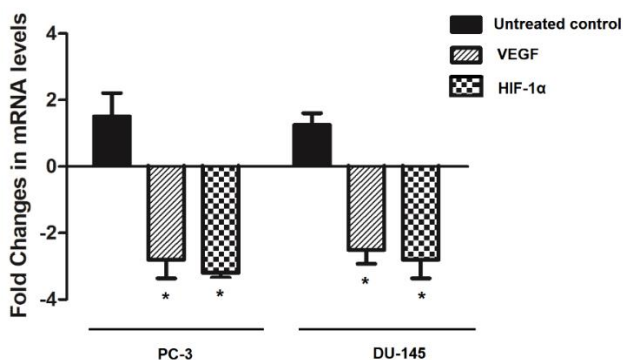


Figure 8. Inhibition of VEGF and HIF-1 α mRNA levels in PC-3 and DU-145 cells by PL-AgNPs at 48 h ($p < 0.05$).

4. Discussion

As a rapidly growing area, nanotechnology provided different insights to many other disciplines. Nanoparticles became the new promising source for biomedical studies with many different applications [21]. Synthesis of nanoparticles with the biosynthesis

approach via using different organisms like yeast and bacteria have been studied closely [22–24]. On the other hand, using plant extracts with nanoparticles provided a new area since it also offers an enhancing effect of the plant extracts on cancer cells as an alternative treatment source. In this study, microwave-assisted and rapid phytosynthesis AgNPs using PL dried fruit extract are reported. In microwave heating, the nucleation process accelerates because of controlled high temperatures when the nanoparticles are initially formed. Thus, it is accepted as a very promising single step and easy approach for nanoparticle synthesis. Compared to the conventional methods, microwave heating provides higher degrees of crystallinity and more importantly small size nanoparticles.

It has been clearly shown that the green synthesis of nanoparticles having nontoxic properties by using plant extracts is a prevalent strategy and also provides natural capping agents. Results here showed the change in dark brown color indicating the generation of PL-AgNPs, which was further verified by spectroscopy. The UV spectra of the synthesized silver nanoparticles show the blue shift of the absorption band by increasing PL-AgNPs concentration. These results indicate that the PL-AgNPs were successfully developed from the extract solution, indicating that the Ag^+ has been reduced to Ag^0 . Secondary metabolites and other constituents such as proteins of the extract affect the reducing potential of nanoparticle formation

[25]. These metabolites broaden the plasmon band as they can be read at the same spectrophotometric wavelengths. SPR of Ag can be read at 450 nm. Mie theory claims that nanoparticles display a single SPR band. If the diversity of the particle shapes expands, the number of peaks also increases [26]. The size and morphology of PL-AgNPs have been also evaluated by SEM and EDX analysis. Then Ag signals were detected via APEX™ Software. The EDX signals confirmed the abundance of silver elements in the synthesized PL-AgNPs. The size of the tested PL-AgNPs was approximately 19-125 nm.

Effects of PL on several diseases have been reported [7]. Especially studies on anti-cancer activity attract attention [16, 27]. Synthesis of silver nanoparticles using PL leaf extract has been reported many times in the literature. Jacob et al. investigated its cytotoxic effect on human larynx epithelioma cancer (HEp-2) cell lines and the IC₅₀ value was calculated as 31.25 µg/mL at 24 h [8]. In another study, AgNPs using PL leaf extract were found to be cytotoxic against HeLa cervical cancer cell line. IC₅₀ values were 221.4, 35.6, 17.8, 12.9 and 8.8 µg/mL after 24 h treatment for hexane, chloroform, ethyl acetate, methanol and aqueous extracts, respectively. Different from the literature, in this study, the effect of PL dried fruit extract on PC-3 and DU-145 cells was investigated and compared with the existence of AgNO₃ nanoparticles. The IC₅₀ values were 73.41 µg/mL and 38.53 µg/mL in PC-3 and DU-145 cells at 48 h, respectively, which were higher than the PL leaf extract nanoparticles. Since it has been known that PL extract is cytotoxic on prostate cancer cells, the concentrations were kept low (10-100 µg/mL) to identify the enhancing effect of AgNO₃ nanoparticles. It was shown that while PL extract was not effective on these low concentrations, the presence of AgNO₃ nanoparticles along with PL extract increased the effect of cytotoxicity.

Angiogenesis, the generating of new vessels, has a vital role in tumor growth, metastasis, and invasion. Thus, it became an important target for cancer therapy [28]. PL-AgNPs inhibited cell migration of prostate cancer cells and decreased the levels of some key molecules having vital roles in angiogenic regulation. Vascular endothelial growth factors (VEGFs) are the main players in the angiogenesis of tumors [29, 30]. The primary stimulator of angiogenesis is hypoxia which induces hypoxia-inducible factors (HIFs) activating VEGF transcription. HIF-1 α is the key molecule that responds to hypoxia and is expressed highly in more than 70% of human cancers [31]. By exposure to PL AgNPs, the expression levels of VEGF and HIF-1 α were decreased in prostate cancer cells. Inhibition of cell migration and reduction of the most potent

angiogenic regulator molecules may explain one of the most important mechanisms of the antitumor effects of PL AgNPs.

This is the first study demonstrating the microwave assisted synthesis and characterization of AgNPs from PL dried fruit extract. The characteristics of the biosynthesized PL-AgNPs were measured by different methods. Combining AgNO₃ nanoparticles with PL dried fruit extract remarkably increased the effect of the ethanolic extract on prostate cancer cells. Moreover, inhibition of cell migration and reduction of the key angiogenic molecules may represent one of the most important mechanisms of its antitumor effect. These results showed that combining PL extract with AgNO₃ nanoparticles could be a potential candidate as a novel anticancer nanomedicine approach for prostate cancer.

Acknowledgments

The authors wish to thank Serdar Gültekin for helping with the preparation of silver nanoparticles. The experiments in this paper were partially performed at Manisa Celal Bayar University (Turkey)- Applied Science and Research Center (DEFAM).

Conflict of Interest

The authors stated that did not have conflict of interests.

References

- [1] Bray F., Ferlay J., Soerjomataram I., Siegel R.L., Torre L.A., Jemal A., Global cancer statistics 2018: GLOBOCAN estimates of incidence and mortality worldwide for 36 cancers in 185 countries, CA. *Cancer J. Clin.*, 68(6) (2018) 394–424
- [2] Paduch R., The role of lymphangiogenesis and angiogenesis in tumor metastasis, *Cell. Oncol.*, 39(5) (2016) 397-410
- [3] Ahn G.O., Seita J., Hong B.J., Kim Y.E., Bok S., Lee C.J., et al., Transcriptional activation of hypoxia-inducible factor-1 (HIF-1) in myeloid cells promotes angiogenesis through VEGF and S100A8, *Proc. Natl. Acad. Sci. U. S. A.*, 11(7) (2014) 2698-2703.
- [4] Cragg G.M., Newman D.J., Natural products: A continuing source of novel drug leads, *Biochim. Biophys. Acta - Gen. Subj.*, 1830(6) (2013) 3670-3695.

- [5] Ahmad N., Fazal H., Abbasi B.H., Farooq S., Ali M., Khan M.A., Biological role of Piper nigrum L. (Black pepper): A review, *Asian Pac. J. Trop. Biomed.*, 2012(1) (2012) 1945–1953
- [6] Liu H.-L., Luo R., Chen X.-Q., Ba Y.-Y., Zheng L., Guo W.-W., et al., Identification and simultaneous quantification of five alkaloids in Piper longum L. by HPLC–ESI-MSn and UFLC–ESI-MS/MS and their application to Piper nigrum L., *Food Chem.*, 177 (2015) 191–196
- [7] Kumar S., Kamboj J., Suman, Sharma S., Overview for Various Aspects of the Health Benefits of Piper Longum Linn. Fruit, *J. Acupunct. Meridian Stud.*, 4(2) (2011) 134–140
- [8] Justin Packia Jacob S., Finub J.S., Narayanan A., Synthesis of silver nanoparticles using Piper longum leaf extracts and its cytotoxic activity against Hep-2 cell line, *Colloids Surfaces B Biointerfaces*, 91(1) (2012) 212–214.
- [9] Sunila E.S., Kuttan G., Immunomodulatory and antitumor activity of Piper longum Linn. and piperine, *J. Ethnopharmacol.*, 90(2-3) (2004) 339-346.
- [10] Sruthi D., John Zachariah T., In vitro antioxidant activity and cytotoxicity of sequential extracts from selected black pepper (Piper nigrum L.) varieties and Piper species, *Int. Food Res. J.*, 24(1) (2017) 75-85.
- [11] Kumar S., Arya P., Mukherjee C., Singh B.K., Singh N., Parmar V.S., et al., Novel Aromatic Ester from Piper longum and Its Analogues Inhibit Expression of Cell Adhesion Molecules on Endothelial Cells †, *Biochemistry*, 44(48) (2005) 15944–15952.
- [12] Natarajan K.S., Narasimhan M., Shanmugasundaram K.R., Shanmugasundaram E.R.B., Antioxidant activity of a salt–spice–herbal mixture against free radical induction, *J. Ethnopharmacol.*, 105 (2006) 76–83.
- [13] Priya N., Kumari S., Research Article Antiviral Activities and Cytotoxicity Assay of Seed Extracts of Piper longum and Piper nigrum on Human Cell Lines, *Int. J. Pharm. Sci. Rev. Res.*, 44 (2017) 197–202
- [14] Pradeep C.R., Kuttan G., Effect of piperine on the inhibition of lung metastasis induced B16F-10 melanoma cells in mice., *Clin. Exp. Metastasis*, 19 (2002) 703–708.
- [15] Li S., Lei Y., Jia Y., Li N., Wink M., Ma Y., Piperine, a piperidine alkaloid from Piper nigrum re-sensitizes P-gp, MRP1 and BCRP dependent multidrug resistant cancer cells, *Phytomedicine*, 19(1) (2011) 83–87.
- [16] Lee W., Kim K.-Y., Yu S.-N., Kim S.-H., Chun S.-S., Ji J.-H., et al., Pipernonaline from Piper longum Linn. induces ROS-mediated apoptosis in human prostate cancer PC-3 cells, *Biochem. Biophys. Res. Commun.*, 430(1) (2013) 406–412.
- [17] Bezerra D.P., Pessoa C., Moraes M.O. de, Alencar N.M.N. de, Mesquita R.O., Lima M.W., et al., In vivo growth inhibition of sarcoma 180 by piperlonguminine, an alkaloid amide from the Piper species, *J. Appl. Toxicol.*, 28 (2008) 599–607
- [18] Patra J.K., Das G., Fraceto L.F., Campos E.V.R., Rodriguez-Torres M. del P., Acosta-Torres L.S., et al., Nano based drug delivery systems: recent developments and future prospects, *J. Nanobiotechnology*, 16 (2018) 1-33.
- [19] Chandran S.P., Chaudhary M., Pasricha R., Ahmad A., Sastry M., Synthesis of Gold Nanotriangles and Silver Nanoparticles Using Aloe vera Plant Extract, *Biotechnol. Prog.*, 22 (2006) 577–583
- [20] Sathishkumar M., Sneha K., Won S.W., Cho C.-W., Kim S., Yun Y.-S., Cinnamon zeylanicum bark extract and powder mediated green synthesis of nano-crystalline silver particles and its bactericidal activity, *Colloids Surfaces B Biointerfaces*, 73 (2009) 332–338.
- [21] McNamara K., Tofail S.A.M., Nanoparticles in biomedical applications, *Adv. Phys. X*, 2 (2017) 54–88
- [22] Siddiqi K.S., Husen A., Rao R.A.K., A review on biosynthesis of silver nanoparticles and their biocidal properties, *J. Nanobiotechnology*, 16(1) (2018) 14.
- [23] Saifuddin N., Wong C.W., Yasumira A.A.N., Rapid Biosynthesis of Silver Nanoparticles Using Culture Supernatant of Bacteria with Microwave Irradiation, *E-Journal Chem.*, 6 (2009) 61–70.
- [24] Kowshik M., Ashtaputre S., Kharrazi S., Vogel W., Urban J., Kulkarni S.K., et al., Extracellular synthesis of silver nanoparticles by a silver-tolerant yeast strain MKY3, *Nanotechnology*, 14 (2003) 95–100.
- [25] Marslin G., Siram K., Maqbool Q., Selvakesavan R., Kruszka D., Kachlicki P., et al., Secondary Metabolites in the Green Synthesis of Metallic Nanoparticles, *Materials (Basel)*, 11(6) (2018) 1-

25.

- [26] Rajesh R.W., Jaya L.R., Niranjan K.S., Vijay D.M., Sahebrao B.K., Phytosynthesis of Silver Nanoparticle Using *Gliricidia sepium* (Jacq.), *Curr. Nanosci.*, 5(1) (2009) 112-117.
- [27] Golovine K. V., Makhov P.B., Teper E., Kutikov A., Canter D., Uzzo R.G., et al., Piperlongumine induces rapid depletion of the androgen receptor in human prostate cancer cells, *Prostate*, 73 (2013) 23–30.
- [28] Shin J.-M., Jeong Y.-J., Cho H.-J., Park K.-K., Chung I.-K., Lee I.-K., et al., Melittin Suppresses HIF-1 α /VEGF Expression through Inhibition of ERK and mTOR/p70S6K Pathway in Human Cervical Carcinoma Cells, *PLoS One*, 8(7) (2013) e69380
- [29] Hosseini H., Rajabibazl M., Ebrahimizadeh W., Dehbidi G.R., Inhibiting angiogenesis with human single-chain variable fragment antibody targeting VEGF, *Microvasc. Res.*, 97 (2015) 13–18.
- [30] Ferrara N., Gerber H.-P., LeCouter J., The biology of VEGF and its receptors, *Nat. Med.*, 9 (2003) 669–676
- [31] Semenza G.L., Targeting HIF-1 for cancer therapy, *Nat. Rev. Cancer*, 3 (2003) 721–732.

The in vitro effect of 5-FU and Tamoxifen Chemotherapeutics on pentose phosphate pathway enzymes

Yusuf TEMEL^{1,*} 

¹Bingöl University, Solhan Vocational School of Health Services, Bingöl / TURKEY

Abstract

The pentose phosphate pathway is the metabolic pathway where NADPH, the reducing force in metabolism, and ribose 5-phosphate, the building block of DNA and RNA, are produced. In this study, the in vitro effects of 5-fluorouracil and Tamoxifen chemotherapeutic agents on glucose 6-phosphate dehydrogenase (G6PD) and 6-phosphogluconate dehydrogenase (6PGD), which are key enzymes of the pentose phosphate pathway, were investigated. In the first stage of the study, G6PD and 6PGD enzymes were purified from rat erythrocytes using 2', 5'-ADP Sepharose-4B affinity chromatography. The control of enzyme activities was determined spectrophotometrically at 340 nm wavelength according to the Beutler method. Then, the in vitro effects of 5-FU and Tamoxifen agents, which are widely used in chemotherapy, on enzyme activities were investigated. The results of the study showed that 5-FU increased the activity of both G6PD and 6PGD enzymes in the concentration range of 0.19-1.9 mM and Tamoxifen in the concentration range of 26-260 μ M.

Article info

History:

Received: 06.10.2020

Accepted: 27.05.2021

Keywords:

G6PD,
6PGD,
Enzyme Rat
erythrocyte,
5-FU,
Tamoxifen.

1. Introduction

Cancer is a group of diseases that involve abnormal cell growth and the potential for these abnormal cells to spread or invade other parts of the body. More than 100 species are known to affect humans today [1]. Chemotherapeutics inhibit the growth and proliferation of the tumor and other rapidly growing cells [2]. However, chemotherapeutics can damage organs such as the liver and kidneys during the treatment process, cause inhibition of various metabolic enzymes, prolong the treatment process and negatively affect the patient's well-being [3–7]. The fluoropyrimidine 5-fluorouracil (5-FU) and its prodrug Capecitabine are widely used chemotherapeutic agent in the treatment of gastrointestinal, breast, head and neck cancers. 5-FU is first converted to fluorodeoxyuridine monophosphate in the cell, which binds to the thymidylate synthase (TS) enzyme together with 5,10-methylene 5,10-methylenetetrahydrofolate and forms a triple complex. This complex causes inhibition of the TS enzyme. TS is required for DNA replication and repair, so TS inhibition causes DNA damage [8–11]. In treatments with 5FU, a wide variety of side effects such as diarrhea, dehydration, abdominal pain, nausea, stomatitis and hand-foot syndrome are seen and causes toxicities of different intensities [12]. Tamoxifen, a triphenylethylene derivative, is a non-steroidal antiestrogen especially used in the treatment of female

breast cancer. Tamoxifen also has a potential role in other malignancies such as pancreatic carcinoma and in the treatment of benign breast cancer [13,14].

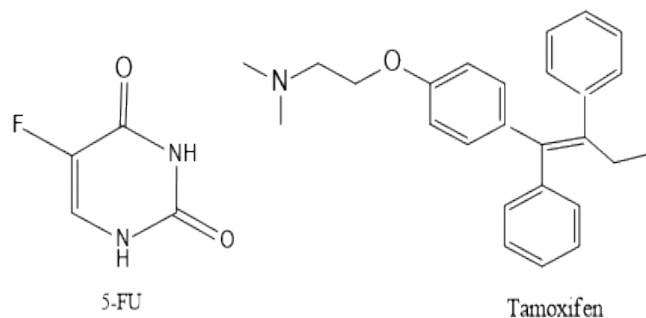


Figure 1. Chemical structures of 5-FU and Tamoxifen chemotherapeutic agents.

Glucose-6-phosphate dehydrogenase (EC 1.1.1.49; G6PD) is the regulatory enzyme catalyzing the initial and irreversible reaction of the pentose phosphate pathway (PPP) [15,16]. 6-phosphogluconate dehydrogenase (EC 1.1.1.44; 6PGD) catalyzes the conversion of 6-phosphogluconate to ribose-5-phosphate isomerase in the third and irreversible step of the oxidative pentose phosphate pathway and produces NADPH [17,18]. NADPHs produced by both glucose-6-phosphate dehydrogenase and 6-phosphogluconate dehydrogenase in PPP are

*Corresponding author. e-mail address: ytemel@bingol.edu.tr
<http://dergipark.gov.tr/csj> ©2021 Faculty of Science, Sivas Cumhuriyet University

particularly involved in the biosynthesis of cholesterol and fatty acids. NADPHs supplies electrons to the glutathione and thioredoxin systems, which are two major intracellular antioxidant systems. These two antioxidant systems take on the task of reducing hydrogen peroxide and oxygen radicals formed in the cell or resulting from the metabolism of xenobiotics and protecting hemoglobin and other red blood cell proteins in a reduced state. Since erythrocytes lack mitochondria, the G6PD and 6PGD enzymes are their only source of NADPH, so their defense against oxidative damage. They also provides intracellular redox balance [19–22].

Clinical studies show that the pentose phosphate pathway is associated with various human diseases such as cancer, cardiovascular diseases, alzheimer and metabolic disorders [20,23,24]. Most of the pentoses in the DNA structure are met through the pentose phosphate pathway. For this reason, the pentose phosphate pathway is needed in abnormally proliferating cells such as cancer cells. Abnormal activation of the 6PGD enzyme occurs in different types of cancer. It stimulates biosynthesis events such as glycolysis and fatty acid synthesis to keep cancer cells alive. In addition, activation of the 6PGD enzyme provides resistance of cancer cells to chemotherapeutics. Inhibition of the 6PGD enzyme sensitizes tumor cells in response to cytotoxic drugs [23].

In this study, it was aimed to investigate the *in vitro* effects of 5FU and Tamoxifen agents, which are widely used in chemotherapy, on G6PD and 6PGD enzymes, which are the regulatory enzymes of the pentose phosphate pathway.

2. Materials and Methods

2.1. Chemicals

NADP⁺, glucose 6-phosphate, 6-Phosphogluconolactone and 2',5'-ADP Sepharose-4B were provide from Sigma Chem. Co. The others were provided from either Sigma-Aldrich (St. Louis, MO, USA) or Merck (Kenilworth, NJ,USA).

2.2. Preparation of hemolysate

The fresh rat blood was centrifuged at 2500 g for 15 min. The plasma and leukocyte layer were carefully separated and precipitated erythrocytes were obtained. The obtained erythrocytes were washed with isotonic (0.16 M KCl) saline solution. The erythrocytes were hemolyzed with 5 volume of cold-water. Finally, hemolysis erythrocytes were centrifuged at 10000 g for 30 minutes and supernatant was taken for analysis. All processes carried out at +4 °C [15]. The study was

carried out after approval of the experimental procedures by the Bingöl University Animal Experiments Local Ethics Committee (BUHADEK: 4.10.2018-2018 / 08-08 / 02).

2.3. 2',5'-ADP sepharose-4B affinity chromatography

The previously prepared hemolysate was loaded into the 2', 5'ADP -sepharose affinity column prepared with 2g gel for 10 mL volume. And column balanced with 50 mM KH₂PO₄, 1 mM EDTA, 1 mM DTT at pH 7.3. The column was washed with the same buffer after equilibration. The washing process was continued until the absorbance change at 280 nm of the fractions taken from the column was 0.05. Flow rate was set to 20 mL / h during column equilibration and washing. The G6PD enzyme was eluted column with 80 mM KH₂PO₄, 10 mM EDTA, 80 mM KCl, and 0.5 mM NADP⁺ at pH 7.3. The 6PGD enzyme was eluted column with 80 mM KH₂PO₄, 10 mM EDTA, 80 mM KCl, and 5 mM NADP⁺ at pH 7.3. Enzyme activities were checked in all fractions and active fractions were taken. All operations were carried out at +4 °C [25].

2.4. Activity determination

The G6PD and 6PGD enzyme activity was measured spectrophotometrically (Shimadzu Spectrophoto meter UV-1800 at 25 °C) according to Beutler method at 340 nm. This method is based on the principle that NADPHs in the reaction medium absorb light at 340 nm. In reactions catalyzed by both G6PD and 6PGD enzymes, NADP⁺ reacts as a co-substrate and converts to NADPH. This increase is followed spectrophotometrically and the amount of absorption per minute is found and converted into enzyme unit [26].

2.5. *In vitro* evaluation the effect of chemotherapeutics

The chemotherapeutics were added to the reaction medium at different concentrations (5-FU; 0, 0.19, 0.38, 0.74, 1.14, 1.90 mM and tamoxifen; 0, 26, 52, 104, 156, 260 µM on G6PD enzyme and 5-FU; 0, 0.19, 0.38, 0.74, 1.14, 1.90 mM and tamoxifen; 0, 26, 52, 104, 156, 208 µM on 6PGD enzyme respectively), to examine the effect of the 5-FU and tamoxifen chemotherapeutics on the G6PD and 6PGD enzyme activities. After the chemotherapeutics were added to the reaction medium at the concentrations determined above, % activity versus chemotherapeutic concentration graphics were prepared.

3. Results and Discussion

In the present study, it was investigated the *in vitro* effect of 5-FU and tamoxifen chemotherapeutics on G6PD and 6PGD are the key enzymes of the pentose phosphate pathway purified from rat erythrocytes. In the first stage of our study, G6PD and 6PGD enzymes were purified from rat erythrocyte tissues by 2', 5' ADP sepharose-4B affinity chromatography. The G6PD enzyme was obtained to have a specific activity of 13.7 EU/mg protein with a yield of 67.7% and 1556 of purification fold and the 6PGD enzyme was obtained to have a specific activity of 1.37 EU/mg protein with a yield of 61,5% and 244 of purification fold. The enzyme activities were determined spectrophotometrically at 340 nm. In the stage of this study, the chemotherapeutics were added to the reaction medium at different concentrations (5-FU; 0-1.90 mM and tamoxifen; 0-260 mM on G6PD and 5-FU; 0-1.90 mM and tamoxifen; 0-208 μ M on 6PGD enzymes respectively), to examine the effect of the 5-FU and tamoxifen chemotherapeutics on the G6PD and 6PGD enzyme activities. The chemotherapeutics concentrations versus % activity graphs were prepared. The results of this study showed that 5-FU chemotherapeutics agent increased G6PD enzyme activity in the concentration range 0-1.90 mM (Figure 2).

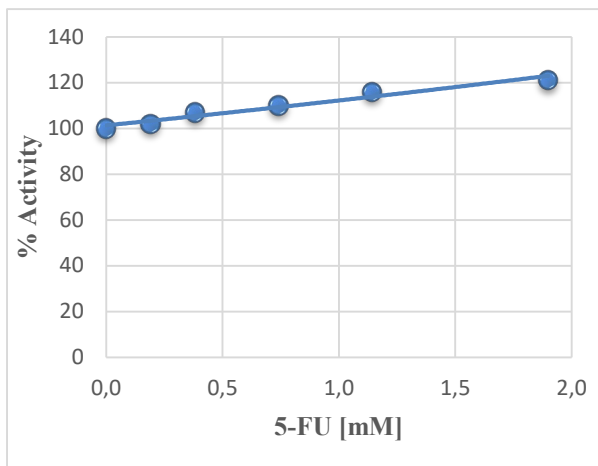


Figure 2. *in vitro* effect of 5-FU chemotherapeutic on G6PD enzyme activity

At the same time, it was determined that tamoxifen chemotherapeutic agent increased G6PD enzyme activity in the concentration range of 0-260 μ M (Figure 3).

When the effects of these chemotherapeutics on 6PGD enzyme activity were examined, it was determined that 5-FU chemotherapeutic agent increased the enzyme

activity in the concentration range of 0-1.90 mM, similarly (Figure 4), tamoxifen chemotherapeutic agent increased the enzyme activity in the 0-208 μ M concentration range (Figure 5).

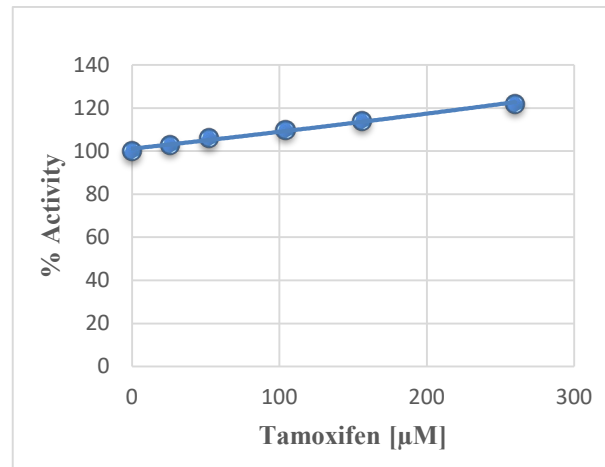


Figure 3. *in vitro* effect of tamoxifen chemotherapeutic on G6PD enzyme activity

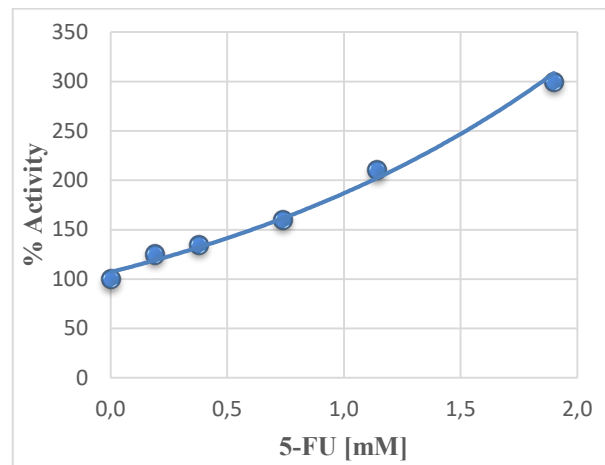


Figure 4. *in vitro* effect of 5-FU chemotherapeutic on 6PGD enzyme activity

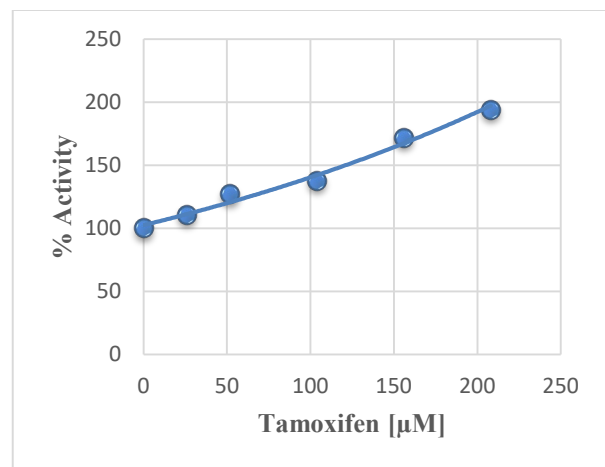


Figure 5. *in vitro* effect of tamoxifen chemotherapeutic on 6PGD enzyme activity

Cancer formation is directly associated with mutations in DNA structure and disorders in cellular metabolic pathways. Therefore, enzymes that play a role in DNA, replication and cell growth and at the crossroads of metabolic pathways are an important target in chemotherapy [26]. The pentose phosphate pathway is a promising target for chemotherapy, as it provides two substrates that cancer cells need to divide and proliferate, ribose 5-phosphate and NADPH, and also buffer ROS damage [27,28]. Also, activation of PPP leads to many effects such as promoting malignant transformation in the cell, increasing tumor progression, protecting cells from apoptosis, disrupting tumor metastasis and angiogenesis [27]. G6PD and 6PGD enzymes are regulatory enzymes that catalyze the first and third stage reactions of the oxidative phase of the pentose phosphate pathway [25,29]. Investigation on G6PD and 6PGD enzymes show that these enzymes are associated with cancer, various metabolic disorders and cardiovascular diseases [4,5,30,31]. It has been reported in previous studies that 6PGD enzyme activity is upregulated in many cancers, including colorectal cancers, cervical intraepithelial neoplasia, thyroid tumors and lung cancers [18].

Clinical research over the past century has shown that tumor growth can be effectively treated with surgery, chemotherapy and radiotherapy. Chemotherapy strategies, used alone or in combination with surgery and radiotherapy, can significantly affect tumor growth and even improve patient healing [26]. Although cancer cells harbor mutated genes and mutated proteins that affect cell division, tumor and normal cells share the same DNA and major metabolic pathways.

For such reasons, conventional chemotherapeutic compounds that attack DNA replication or cell division in a cancer cell can also attack a normally dividing cell, causing serious side effects such as bone marrow, enzyme, kidney, liver and gastrointestinal toxicity [5,27,28]. Current research aims to prevent this toxicity exhibited by chemotherapeutics by detecting specific differences between tumor and normal tissues [27]. 5-FU is a chemotherapeutic agent used in the treatment of gastrointestinal, breast head and neck cancers. 5-FU is converted into fluorodeoxyuridine monophosphate in the cell and acts by causing the inhibition of the thymidylate synthase enzyme. However, 5-FU can cause toxic side effects such as severe hematological, mucosal and digestive system disorders [29]. Tamoxifen, a non-steroidal antiestrogen, is a chemotherapeutic agent used in the treatment of female breast cancer [13]. Previous studies reveal that tamoxifen has a general disruptive effect on cognition

in breast cancer patients and may cause ocular toxicity [14,30].

The effects of some drugs, antibiotics, heavy metals and some organic compounds on G6PD and 6PGD enzyme activities have been investigated in the studies conducted so far. In these studies, it was determined that drugs such as netilmicin sulfate, cefepime, amikacin, isepamycin, chloramphenicol, ceftazidim, teicoplanin, ampicillin, ofloxacin, levofloxacin, cefotaxime, penicillin, gentamicin sulfate, ciprofloxacin were determined to inhibit human and rat tissue G6PD and 6PGD enzyme [15,26,31–36]. In the study by Gümüştekin et al., the effects of nicotine and vitamin E on glucose 6-phosphate dehydrogenase (G-6PD) activity in rat muscle, heart, lungs, testes, kidney, stomach, brain and liver tissues were investigated *in vivo* and *in vitro*. The results of this study showed that nicotine inhibited the G6PD activity in the lungs, testicle, kidney, stomach and brain tissues. Vitamin E administration, on the other hand, regulated the G6PD activity, which was inhibited by nicotine administration in various rat tissues both *in vivo* and *in vitro* [37]. Temel et al. investigated the *in vivo* and *in vitro* effects of astaxanthin, which is natural antioxidants, and aluminum ions on G6PD and 6PGD enzyme activities. It has been reported that aluminum ions inhibits enzyme activities both *in vivo* and *in vitro*, whereas astaxanthin reduces this inhibitory effect [38]. Bayramoglu et al. reported that cadmium ions inhibited G6PD and 6PGD enzymes, while astaxanthin reduced this effect [39]. Bayindir et al., new oxindoles were synthesized as analogues of the natural product 3,3'-bis (indolyl) oxindole by the reaction of 4,7-dihydro-1H-indole and isatine. These synthesized oxyindole compounds inhibited G6PD and 6PGD enzyme activities *in vitro* [25]. In a recent study, the effects of 5-FU and tamoxifen chemotherapeutics on glutathione S-transferase (GST) enzyme activity, which is an important enzyme of glutathione and detoxification metabolism, purified from human erythrocytes by affinity chromatography was investigated. The results of this study showed that both 5-FU and tamoxifen increase the GST enzyme activity. The results of this study are similar to the results of our study [6]. In a different study, it was determined that 5-FU coumarin derivatives showed a potent and totally selective inhibitory action against the target CA IX/XII enzyme activities [40]. Emile et al. reported that tamoxifen administration increased rat liver xenobiotic enzyme activities in a dose-dependent manner [41]. Jahani *et al.* investigated the effect of L-arginine and 5-fluorouracil (5-FU) combination therapy on cell viability, apoptosis and nitric oxide (NO) production on BT-20 and MCF-7 cell lines. In this study, the

effects of 5-FU chemotherapeutic agent on cellular energy metabolism were analyzed by lactate production and glucose-6-phosphate dehydrogenase (G6PD) activity analysis. Study results show that G6PD activity is significantly reduced by L-arginine or 5-FU alone and in combination in MCF-7. Jahani *et al.* suggested that 5-FU chemotherapy could inhibit the G6PD enzyme by increasing nitric oxide and ROS levels *in vivo* [12].

In the literature, there are no studies showing the *in vitro* effects of 5-FU and tamoxifen chemotherapeutics on G6PD and 6PGD enzymes. The results of the presented study show that both 5-FU and tamoxifen increase G6PD and 6PGD enzyme activities and have no inhibitory effect on these enzyme activities. Our results are different from previous *in vivo* studies. It is thought that the reason for this difference is the absence of free radicals and reactive oxygen species *in vitro* environment that can cause inhibition of enzymes. On the other hand, the mechanism of action of G6PD and 6PGD enzymes is the production of NAPH through the transfer of electrons in substrates such as G6P and 6PGA to the NADP⁺ coenzyme. Since both 5-FU and tamoxifen chemotherapeutics contain electron-rich groups in their structures, they may have reduced NADP⁺ to NADPH by acting as a lewis base or as a hydride donor. It was also determined that these ligands increase the activity of the 6PGD enzyme more than the activity of the G6PD enzyme. It is thought that the reason for this is that the active sites of enzymes are different from each other. As mentioned earlier, activation of the pentose phosphate pathway can cause healthy growth of normal cells, while tumor cells develop resistance to chemotherapy. Therefore, more research should be done to reveal the effect of the pentose phosphate pathway in preventing the resistance of cancer cells to 5-FU and tamoxifen chemotherapeutic agents.

4. Conclusion

In the present study, the G6PD and 6PGD enzyme was purified from rat erythrocyte tissues using 2', 5'-ADP Sepharose-4B affinity chromatography. Then, the effect of 5-FU and tamoxifen chemotherapeutics on the purified enzyme was investigated. As a result of this study, it has been found that 5-FU and tamoxifen chemotherapeutics increase the G6PD and 6PGD enzyme activities.

Conflicts of Interest

The authors state that there is no conflict of interests.

References

- [1] Kasala E.R., Bodduluru L.N., Madana R.M., Athira K. V., Gogoi R., Barua C.C., Chemopreventive and therapeutic potential of chrysin in cancer: Mechanistic perspectives, *Toxicol. Lett.*, 233 (2015) 214–225.
- [2] Buerge I.J., Buser H.R., Poiger T., Müller M.D. Occurrence and fate of the cytostatic drugs cyclophosphamide and ifosfamide in wastewater and surface waters, *Environ. Sci. Technol.*, 40 (2006) 7242–7250.
- [3] Kandemir F.M., Kucukler S., Caglayan C., Gur C., Batil A.A., Gülçin İ. Therapeutic effects of silymarin and naringin on methotrexate-induced nephrotoxicity in rats: Biochemical evaluation of anti-inflammatory, antiapoptotic, and autophagic properties, *J. Food Biochem.*, 41 (2017) e12398.
- [4] Temel Y., Kucukler S., Yıldırım S., Caglayan C., Kandemir F.M. Protective effect of chrysin on cyclophosphamide-induced hepatotoxicity and nephrotoxicity via the inhibition of oxidative stress, inflammation, and apoptosis, *Naunyn. Schmiedebergs. Arch. Pharmacol.*, 393 (2020) 325–337.
- [5] Caglayan C., Temel Y., Kandemir F.M., Yildirim S., Kucukler S., Naringin protects against cyclophosphamide-induced hepatotoxicity and nephrotoxicity through modulation of oxidative stress, inflammation, apoptosis, autophagy, and DNA damage, *Environ. Sci. Pollut. Res.*, 25(21) (2018) 20968-20984.
- [6] Aybek H., Temel Y., Ahmed B.M., Ağca C.A., Çiftci M. Deciphering of The Effect of Chemotherapeutic Agents on Human Glutathione S-Transferase Enzyme and MCF-7 Cell Line, *Protein Pept. Lett.*, 27 (2020) 1–7.
- [7] Karaman M., Temel, Y., Bayindir S. Inhibition effect of rhodanines containing benzene moieties on pentose phosphate pathway enzymes and molecular docking, *J. Mol. Struct.*, 1220 (2020) 128700.
- [8] Maxwell P.J., Longley D.B., Latif T., Boyer J. Allen W., Lynch M., McDermott U., Paul Harkin, D. Allegra C.J., Johnston P.G. Identification of 5-fluorouracil-inducible target genes using cDNA microarray profiling, *Cancer Res.*, 63 (2003) 4602–4606.
- [9] Glazer R.I., Lloyd L.S. Association of cell lethality with incorporation of 5-fluorouracil and

- 5-fluorouridine into nuclear RNA in human colon carcinoma cells in culture, *Mol. Pharmacol.*, 21 (1982) 468–473.
- [10] Cohen P., Rosemeyer M.A. Glucose-6-phosphate dehydrogenase from human erythrocytes, *Methods Enzymol.*, 41 (1975) 208–214.
- [11] Pullarkat S.T., Lenz H.J. Thymidylate synthase gene polymorphism determines response and toxicity of 5-FU chemotherapy, *Pharmacogenomics J.*, 1 (2001) 65–70.
- [12] Jahani M., Azadbakht M., Norooznezhad F., Mansouri K. L-arginine alters the effect of 5-fluorouracil on breast cancer cells in favor of apoptosis, *Biomed. Pharmacother.*, 88 (2017) 114–123.
- [13] Buckley M.M.T., Goa K.L., Tamoxifen: A Reappraisal of its Pharmacodynamic and Pharmacokinetic Properties, and Therapeutic Use, *Drugs*, 37 (1989) 451–490.
- [14] Novick A.M., Scott A.T., Neill Epperson C., Schneck C.D., Neuropsychiatric effects of tamoxifen: Challenges and opportunities, *Front. Neuroendocrinol.*, 59 (2020) 100869.
- [15] Özmen İ., Çiftçi M., Küfrevioğlu Ö.İ., Çürük M.A., Investigation of glucose 6-phosphate dehydrogenase (G6PD) kinetics for normal and G6PD-deficient persons and the effects of some drugs, *J. Enzyme Inhib. Med. Chem.*, 19 (2004) 45–50.
- [16] Temel Y., Kocuyigit U.M., Purification of glucose-6-phosphate dehydrogenase from rat (*Rattus norvegicus*) erythrocytes and inhibition effects of some metal ions on enzyme activity, *J Biochem Mol Toxicol.*, (2017).
- [17] Adem S., Ciftci M., Purification of rat kidney glucose 6-phosphate dehydrogenase, 6-phosphogluconate dehydrogenase, and glutathione reductase enzymes using 2',5'-ADP Sepharose 4B affinity in a single chromatography step, *Protein Expr. Purif.*, 81 (2012) 1–4.
- [18] Yang X., Peng X., Huang J., Inhibiting 6-phosphogluconate dehydrogenase selectively targets breast cancer through AMPK activation, *Clin. Transl. Oncol.*, 20 (2018) 1145–1152.
- [19] Özaslan M.S., Balcı N., Demir Y., Gürbüz M., Küfrevioğlu Ö.İ., Inhibition effects of some antidepressant drugs on pentose phosphate pathway enzymes, *Environ. Toxicol. Pharmacol.*, 72 (2019).
- [20] Patra K.C., Hay N., The pentose phosphate pathway and cancer, *Trends Biochem. Sci.*, 39 (2014) 347–354.
- [21] Temel Y., Taysi M.Ş., The Effect of Mercury Chloride and Boric Acid on Rat Erythrocyte Enzymes, *Biol. Trace Elem. Res.*, (2018) 177–182.
- [22] Temel Y., Koçuyigit U.M., Taysi M.S., Gökalp F., Gürdere M.B., Budak Y., Ceylan M., Gülçin I., Çiftçi M., Purification of glutathione S-transferase enzyme from quail liver tissue and inhibition effects of (3aR,4S,7R,7aS)-2-(4-(E)-3-(aryl)acryloyl)phenyl)-3a,4,7,7a-tetrahydro-1H-4,7-methanoisindole-1,3(2H)-dione derivatives on the enzyme activity, *J. Biochem. Mol. Toxicol.*, 32(3) (2018) e22034.
- [23] Chen H., Wu D., Bao L., Yin T., Lei D., Yu J., Tong X., 6PGD inhibition sensitizes hepatocellular carcinoma to chemotherapy via AMPK activation and metabolic reprogramming, *Biomed. Pharmacother.*, 111 (2019) 1353–1358.
- [24] Temel Y., Küfrevioğlu Ö.İ., Çiftçi M., Investigation of the effects of purification and characterization of turkey (*Meleagris gallopavo*) liver mitochondrial thioredoxin reductase enzyme and some metal ions on enzyme activity, *Turkish J. Chem.*, 41 (2017) 1603-1635.
- [25] Bayindir S., Ayna A., Temel Y., Çiftçi M., The synthesis of new oxindoles as analogs of natural product 3,3'-bis(indolyl)oxindole and in vitro evaluation of the enzyme activity of G6PD and 6PGD, *Turkish J. Chem.*, 42 (2018) 1706-1751.
- [26] Beydemir S., Gülçin I., Küfrevioğlu O.İ., Çiftçi M., Glucose 6-phosphate dehydrogenase: in vitro and in vivo effects of dantrolene sodium., *Pol. J. Pharmacol.*, 55 (2003) 787–792.
- [27] Shewach D.S., Kuchta R.D., Introduction to cancer chemotherapeutics, *Chem. Rev.*, 109 (2009) 2859–2861.
- [28] Kern J.C., Kehrer J.P., Acrolein-induced cell death: A caspase-influenced decision between apoptosis and oncosis/necrosis, *Chem. Biol. Interact.*, 139 (2002) 79–95.
- [29] Gamelin B.E., Gue V., Delva R., Lortholary A., Genevieve F., Larra F., Ifrah N., Robert J., Correlation between Uracil and Dihydrouracil Plasma Ratio, Fluorouracil (5-FU) Pharmacokinetic Parameters and Tolerance with Advanced Colorectal C, *J Clin Oncol.*, 17(4) (1999) 1105–1110.

- [30] Ashford A.R., Donev I., Tiwari R.P., Garrett T.J., Reversible ocular toxicity related to tamoxifen therapy, *Cancer*, 61 (1988) 33–35.
- [31] Akkemik E., Budak H., Ciftci M., Effects of some drugs on human erythrocyte glucose 6-phosphate dehydrogenase : an in vitro study, *J Enzyme Inhib Med Chem.*, 25(6) (2010) 871–875.
- [32] Akkoyun H.T. Bengu A.S., Uluçan A., Bayramoğlu Akkoyun M., Ekin S., Temel Y., Çiftçi M. Effect Of Astaxanthin On Rat Brains Against Oxidative Stress Induced By Cadmium:Biochemical, *Histopathological Evaluation, J. Inst. Sci. Technol.*, 8 (2018) 33–39.
- [33] Özmen I., Küfrevioğlu Ö.I., Effects of antiemetic drugs on glucose 6-phosphate dehydrogenase and some antioxidant enzymes, *Pharmacol. Res.*, 50 (2004) 499–504.
- [34] Temel Y., Ayna A., Hamdi Shafeeq I., Ciftci M., In vitro effects of some antibiotics on glucose-6-phosphate dehydrogenase from rat (*Rattus norvegicus*) erythrocyte , *Drug Chem. Toxicol.*, 43(2) (2018) 219-223.
- [35] Adem S., Ciftci M., Purification of rat kidney glucose 6-phosphate dehydrogenase, 6-phosphogluconate dehydrogenase, and glutathione reductase enzymes using 2',5'-ADP Sepharose 4B affinity in a single chromatography step, *Protein Expr. Purif.*, 81 (2012) 1–4.
- [36] Mykkanen H. M., Ganther H. E., Effect of mercury on erythrocytes glutathione reductase activity: in vivo and in vitro studies., *J. Clin. Invest.*, 48 (1969) 1957–1966.
- [37] Gumustekin K., Ciftci M., Coban A., Altikat S., Aktas O., Gul M., Timur H., Dane S., Effects of nicotine and vitamin E on glucose 6-phosphate dehydrogenase activity in some rat tissues in vivo and in vitro, *J. Enzyme Inhib. Med. Chem.*, 20 (2005) 497–502.
- [38] Temel Y., Bengü A.Ş., Akkoyun H.T., Akkoyun M., Ciftci M., Effect of astaxanthin and aluminum chloride on erythrocyte G6PD and 6PGD enzyme activities in vivo and on erythrocyte G6PD in vitro in rats, *J. Biochem. Mol. Toxicol.*, (2017).
- [39] Bayramoğlu Akkoyun M., Bengü A.Ş., Temel Y., Akkoyun H.T., Ekin S., Ciftci M., The effect of astaxanthin and cadmium on rat erythrocyte G6PD, 6PGD, GR, and TrxR enzymes activities in vivo and on rat erythrocyte 6PGD enzyme activity in vitro, *J. Biochem. Mol. Toxicol.*, 32 (2018) 1–5.
- [40] Petreni A., Bonardi A., Lomelino C., Osman S.M., AlOthman Z.A., Eldehna W.M., El-Haggag R., McKenna R., Nocentini A., Supuran C.T., Inclusion of a 5-fluorouracil moiety in nitrogenous bases derivatives as human carbonic anhydrase IX and XII inhibitors produced a targeted action against MDA-MB-231 and T47D breast cancer cells, *Eur. J. Med. Chem.*, 190 (2020) 112112.
- [41] Nuwaysir E.F., Dragan Y.P., Jefcoate C.R., Jordan,V.C., Pitot H.C., Effects of Tamoxifen Administration on the Expression of Xenobiotic Metabolizing Enzymes in Rat Liver, *Cancer Res.*, 55 (1995) 1780–1786.



In vitro cytotoxic activity of *Tarantula cubensis* alcoholic extract on different human cell lines

Çisil ÇAMLI PULAT^{1, *}

¹Manisa Celal Bayar University, Applied Science Research Center (DEFAM), Manisa / TURKEY

Abstract

Spider venoms are known to have great potential for their antimicrobial, antifungal, and antitumor activities due to their rich peptide content. *Tarantula cubensis* alcoholic extract Theranekron[®] is a homeopathic remedy and it is frequently used in veterinary treatments. Specifically, the anti-inflammatory, antitumor and wound healing effects of Theranekron[®] provide a wide range of use in animal treatments. More importantly, it can reduce the growth rate of canine mammary tumors. This effect shows that Theranekron[®] can be a potential candidate for cancer treatment. In this study, the cytotoxic effect of Theranekron[®] was evaluated in four different human cancer cell lines and one non-cancerous human cell line. It was aimed to provide a foundation for further studies by conducting an *in vitro* screening for the cytotoxic effect of Theranekron[®]. Results showed that Theranekron[®] has a high cytotoxic effect on human breast cancer cell lines. On the other hand, the rate of cytotoxicity was found to be relatively lower on human small cell lung cancer, glioblastoma and human prostate cancer cell lines as compared to breast cancer cells. These results indicated that *T. cubensis* alcoholic extract might be utilized as an anticancer bio-therapeutic and should be further examined for its potential.

Article info

History:
Received: 12.01.2021
Accepted: 15.06.2021

Keywords:
Theranekron[®],
Venom,
Cytotoxicity,
Cancer.

1. Introduction

Venoms are described as poisonous secretions of animals and they contain a variety of chemicals, enzymes and distinctive bioactive peptides [1]. In general, venoms cause severe damage to cells and organs. However, they also hold great potential for novel pharmacological approaches and as medicine enhancements because of the bioactive peptides and chemicals [1,2]. Peptides that are obtained from various venoms are already being investigated as pain killers, against diabetes, cardiovascular diseases and cancer [3,4]. Spider venoms are rich in different peptides. In several studies, it was demonstrated that these peptides have antimicrobial, antifungal, cytolytic and antitumor activities [1,5].

Cancer is a global health problem [6], and it is crucial to find novel potential targets for cancer therapeutics. Cytotoxic effects of several venoms on cancer cells were investigated and provided promising results [4,7]. Theranekron[®] is the alcoholic extract of *Tarantula cubensis*. It is a homeopathic solution abstained from *T. cubensis* being processed and diluted in 60% alcohol [8]. *T. cubensis* belongs to the Theraphosidae family and its venom known to contain a variety of enzymes

[9]. Theranekron[®] is used as a veterinary remedy for the treatment of several indications as a commercial extract. It is used mostly for its anti-inflammatory effect. It is also reported to be effective on lesions, endometriosis and decrease the growth rate of canine tumors in veterinary clinical studies [10-12].

There is a number of maladies that Theranekron[®] was used for treatment on different animal groups. One of the most common applications is related to its wound healing effect. In one of these studies, 20×20 mm of full thickness wound composed on 7 months bulls and then treated with 6 mL Theranekron[®] subcutaneously. The results demonstrated that, the application of Theranekron[®] can quicken the epithelialization of the wounds [13]. In another study, the wound healing effect of Theranekron[®] was observed on rats with open wounds. Similarly, it was shown that Theranekron[®] was found to be stimulating on epithelialization of the wounds and fastens the wound healing [14]. *T. cubensis* alcoholic extract was shown to be effective for the treatment of oral lesions caused by Bluetongue disease in Holstein cattle. During an outbreak in Iran, Theranekron[®] was used in a controlled clinical trial, and it was found to be a potential application against the foot-and-mouth disease (FMD) of cattle. Finally,

*Corresponding author. e-mail address: cisil.camli@cbu.edu.tr

its effect was also observed against papillomatosis, which can be a widespread problem in cattle [15–17]. Along with these effects, it was shown that Theranekron® could be used for neutralizing the damaging impacts of aflatoxins [18]. Another beneficial use of Theranekron® was its peripheral nerve healing effects caused by nerve injury on rats. It was demonstrated that alcoholic extract of *T. cubensis* reduced the axon and myelin damage, which could be linked to its modifying effects on pro-inflammatory cytokines like TNF- α , IL-1 and IL-6 [19].

Along with many other applications, although the antitumor effect was demonstrated in clinical veterinary studies, the anticancer effect of Theranekron® on different cancer cell lines was not fully investigated. Only a few studies demonstrated that it holds a great potential [9,20], but expanded *in vitro* studies specifically on human cancer cell lines are still needed. The aim of this study is to investigate the cytotoxic effect of Theranekron® on different cancer and non-cancerous cell lines in order to provide a foundation for further studies.

2. Materials and Methods

2.1. Chemicals and reagents

Theranekron® (alcoholic extract of *T. cubensis*) purchased by Richter Pharma AG (Wels, Austria), was obtained from the local veterinary clinic with the permission of the veterinary physician. As described from Richter Pharma AG, it is prepared by processing the whole spider and diluted in alcohol. It is commercially sold in 50 mL bottles, each mL contains 1 mg alcoholic extract (1:100) from *T. cubensis* in an alcoholic solution. Other chemicals and reagents used for this study are given within the related sections.

2.2 Cell lines and cell culture conditions

For this study, five different cell lines consist of four different cancer, and one non-cancerous cell line were used to evaluate the cytotoxic effect of Theranekron®. Cell lines and culture conditions were summarized in Table 1.

Table 1. List of Cells and Cell Culture Conditions. ATCC, American Type Culture Collection; MEM, Eagle's Minimum Essential Medium; RPMI-1640, Roswell Park Memorial Institute medium 1640; FBS, fetal bovine serum

Cell line	Source	Medium	FBS (%)	L -glutamine (%)	penicillin-streptomycin
Human embryonic kidney cell line, HEK-293	ATCC CRL-1573	MEM	10	1	1
Multidrug resistant variant of the human small cell lung cancer cell line, H69AR	ATCC CRL-11351	RPMI-1640	20	1	1
Glioblastoma cell line, T98G	ATCC CRL-1690	MEM	10	1	1
Human prostate cancer cell line, PC3	ATCC CRL-1435	RPMI-1640	10	1	1
Human breast cancer cell line, MCF-7	ATCC HTB-22	RPMI-1640	10	1	1

All the cell lines were grown as monolayers in 75 cm² polystyrene flasks (Corning Life Sciences, UK), and maintained at 37°C in a humidified atmosphere with 5 % CO₂. Cell morphologies and growth rates of all the cell lines were monitored daily under the inverted microscope (Zeiss Primovert, Germany) and the cells were passaged when reached 90 % confluence.

2.3 MTT cell viability assay

Trypan blue dye exclusion test was used to determine cell viability and the cell numbers for all the cell lines. Countess Automated Cell Counter (Countess, Thermo

Fisher Scientific, Massachusetts, USA) was used for measuring the cell viability and cell numbers.

The cytotoxic effect of Theranekron® was evaluated via 3 - (4 , 5 - dimethylthiazol - 2 - yl) - 2 , 5 - diphenyltetrazolium bromide (MTT) assay [21]. Cells were seeded at 1×10⁴ cells/well, in a final volume of 200 μ L, in 96-well flat-bottomed plates. After 24h incubation, cells were treated with increasing concentrations (10-100 μ g/mL) of Theranekron®. Plates were then incubated at 37°C in a 5% CO₂ incubator for 24, 48 and 72 h.

At the end of the incubation, 20 μL (10% of the final volume) of MTT was added to each well. Plates were then incubated for 4 h at 37°C. Then, the medium was removed, and the formed formazan crystals were dissolved in 100 μL of dimethyl sulfoxide (DMSO). The absorbance of each well was measured at 570 nm against a reference wavelength at 690 nm using a microplate reader (TECAN PRO200, Männedorf, Switzerland). IC_{50} values were calculated from the mean of the triplicate experiments.

2.4 Statistical Analysis

Cytotoxicity experiments were carried out in triplicates, and GraphPad Prism 5.0 software (GraphPad Software, San Diego, USA) was used for data analysis. For significant values, a one-way analysis of variance test (ANOVA) followed by Dunnett's t-test. Statistically significant data were those with a p-value ≤ 0.05 . IC_{50} values were calculated via Biosoft CalcuSyn 2.1 software (Ferguson, MO, USA).

3. Results and Discussion

In this study, first the effect of Theranekron[®] on human embryonic kidney HEK-293 cells was determined. For this aim, HEK-293 cells were treated with the increasing concentrations (10-100 $\mu\text{g}/\text{mL}$) of

Theranekron[®] for 24, 48 and 72 h, and then MTT cell viability assay was performed. It was found that the Theranekron[®] treatment decreased the cell viability of HEK-293 cells specifically at 72h (Figure 1, 2). The IC_{50} value of Theranekron[®] was found as 88.3 $\mu\text{g}/\text{mL}$ at 72h for HEK-293 cell line. Acquired results in this study were consistent with two other studies that showed the cell viability levels of HEK-293 cell line treated with Theranekron[®] [9], [20].

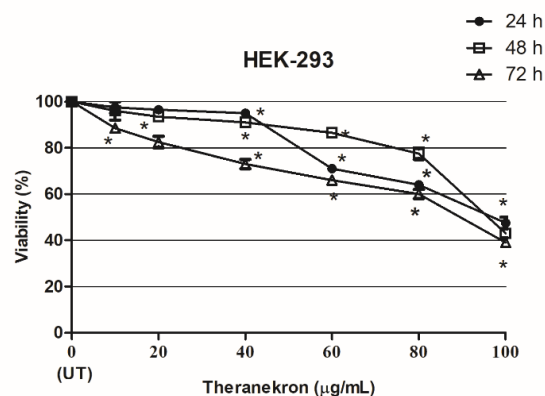


Figure 1. Time and concentration dependent effect of Theranekron[®] on human embryonic kidney HEK-293 cells (* $P < 0.05$ compared to the untreated control, UT: Untreated control)

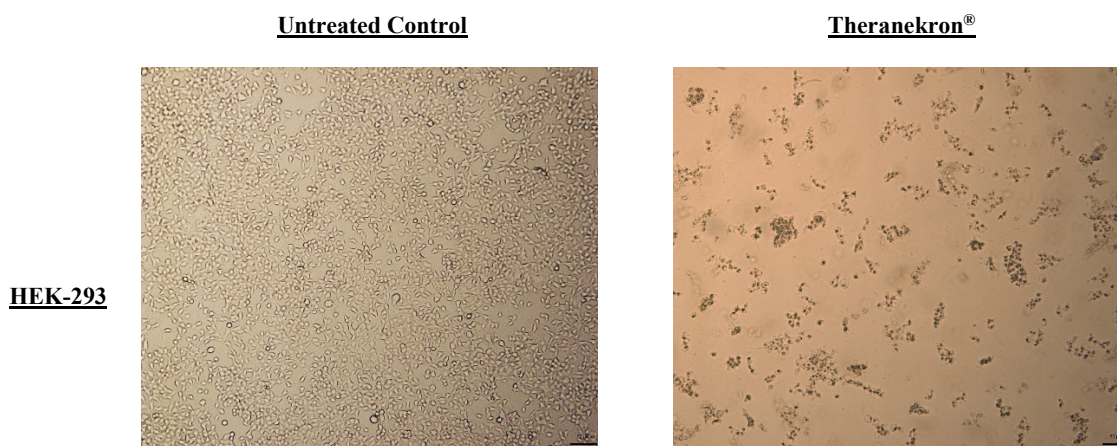


Figure 2. Images of HEK-293 cells treated with Theranekron[®] with the IC_{50} value of 88.3 $\mu\text{g}/\text{mL}$ for 72h. Reduced viability and aberrant adhesion morphology were observed on treated cells as compared to the untreated control group (Magnification 10X).

For the cancer cell lines, the effect of Theranekron[®] was evaluated on glioblastoma cell line T98G, human small cell lung cancer cell line H69AR, human prostate cancer cell line PC-3 and human breast cancer cell line MCF-7 with the increasing concentrations (10-100 $\mu\text{g}/\text{mL}$) of Theranekron[®] for 24, 48 and 72 h. Obtained MTT cell viability assay results indicated that Theranekron[®] is highly cytotoxic for breast cancer cell

line MCF-7 in a time- and concentration-dependent manner ($p \leq 0.05$). Its effect can be clearly observed after 48h (Figure 3, 4). The IC_{50} value of Theranekron[®] was found as 94.7 $\mu\text{g}/\text{mL}$ at 72h for MCF-7 cells.

While Theranekron[®] was found to be highly cytotoxic for breast cancer cell line MCF-7, its effect was found to be relatively lower for human small cell lung cancer

H69AR, glioblastoma T98G and human prostate cancer PC3 cell lines. IC₅₀ values were calculated as 278 µg/mL for H69AR, 295 µg/mL for PC3 and 118.9 µg/mL for T98G cell lines at 72h. As a difference,

decreased cell viability was observed after 24h for these three cell lines while it was observed after 48h for MCF-7 (Figure 3, 4).

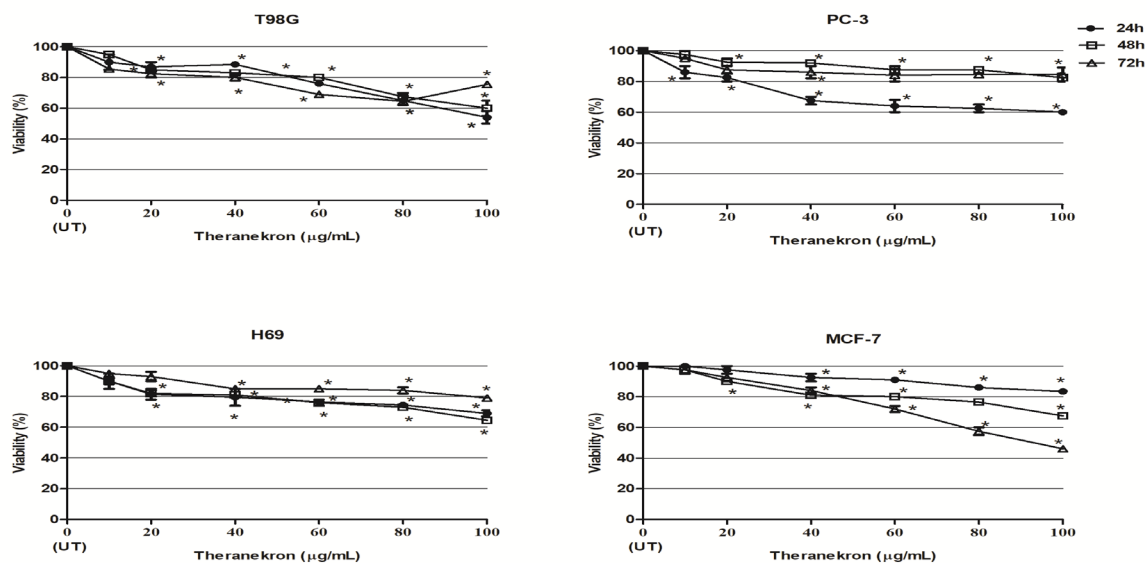


Figure 3. Time and concentration dependent effect of Theranekron® on glioblastoma T98G, human prostate cancer PC3, human small cell lung cancer H69AR and breast cancer cell line MCF-7 (*P < 0.05 compared to the untreated control, UT: Untreated control)

Spider venoms are known to have an anticancer perspective, via tempering the cell cycle, several cell death mechanisms, ion channels and receptors [22]. *T. cubensis* alcoholic extract, commercially named Theranekron®, is commonly used as a veterinary remedy [23]. It is known to have several therapeutic effects such as anti-inflammatory, antitumor and wound healing. These therapeutic effects make Theranekron® hold great potential for treatment [24–26]. More importantly, it is known to have a strong antitumor activity on canine mammary tumors. It was shown that *T. cubensis* extract supports the inhibition of tumor growth, thickening of tumor capsules and demarcation of the surrounding tissue. It was also demonstrated that it has an anti-inflammatory effect on lymph nodes [11]. In light of these, cytotoxic activity screening of Theranekron® is crucial to comprehend its activity and potential for also human cancers. The apoptotic activity of Theranekron® was investigated only in few other studies. In one study, it was shown that the *T. cubensis* alcoholic extract caused DNA fragmentation and remarkable cell death in MCF-7 and HN5 cell lines as a result of over activation of apoptosis [9]. It was explained that Theranekron® was affected the adhesion of the cells while decreasing the proliferation levels of the MCF-7 and HN5 cells. In another study, it was determined that alcoholic extract of *T. cubensis* induces apoptosis on MCF-7 cell line as

a result of increased tumor necrosis factor- α (TNF- α) and transforming growth factor- β (TGF- β) levels. Both of these factors are crucial for the proliferation, survival and cell death levels of the cells [20].

It was shown that although *T. cubensis* alcoholic extract has a cytotoxic effect on HEK-293, it is considerably more toxic for cancer cells, specifically for MCF-7 cells. Similar results were also shown in another study stating that although Theranekron® found to be slightly cytotoxic to HEK-293, its effect was higher on breast cancer cell line MCF-7 and human head and neck cancer cell line HN5 [9]. This phenomenon is explained as a result of the hyperactivation of apoptosis on these cell lines. To explain the reason for the different levels of cytotoxicity between the normal and cancer cells, it was stated that the rapid metabolism rate of the cancer cells causes increased vulnerability against the extract. When Theranekron® was tested on canine mammary tumors, immunohistochemical staining of these tumors revealed that Bcl-2 and Ki-67 expression levels were significantly affected after the Theranekron® treatment [27]. Bcl-2 expression levels are crucial for apoptosis regulation, specifically for human breast cancer [28]. Bcl-2 expression is known to be increased in human mammary tumors as well as in canine mammary tumors [29].

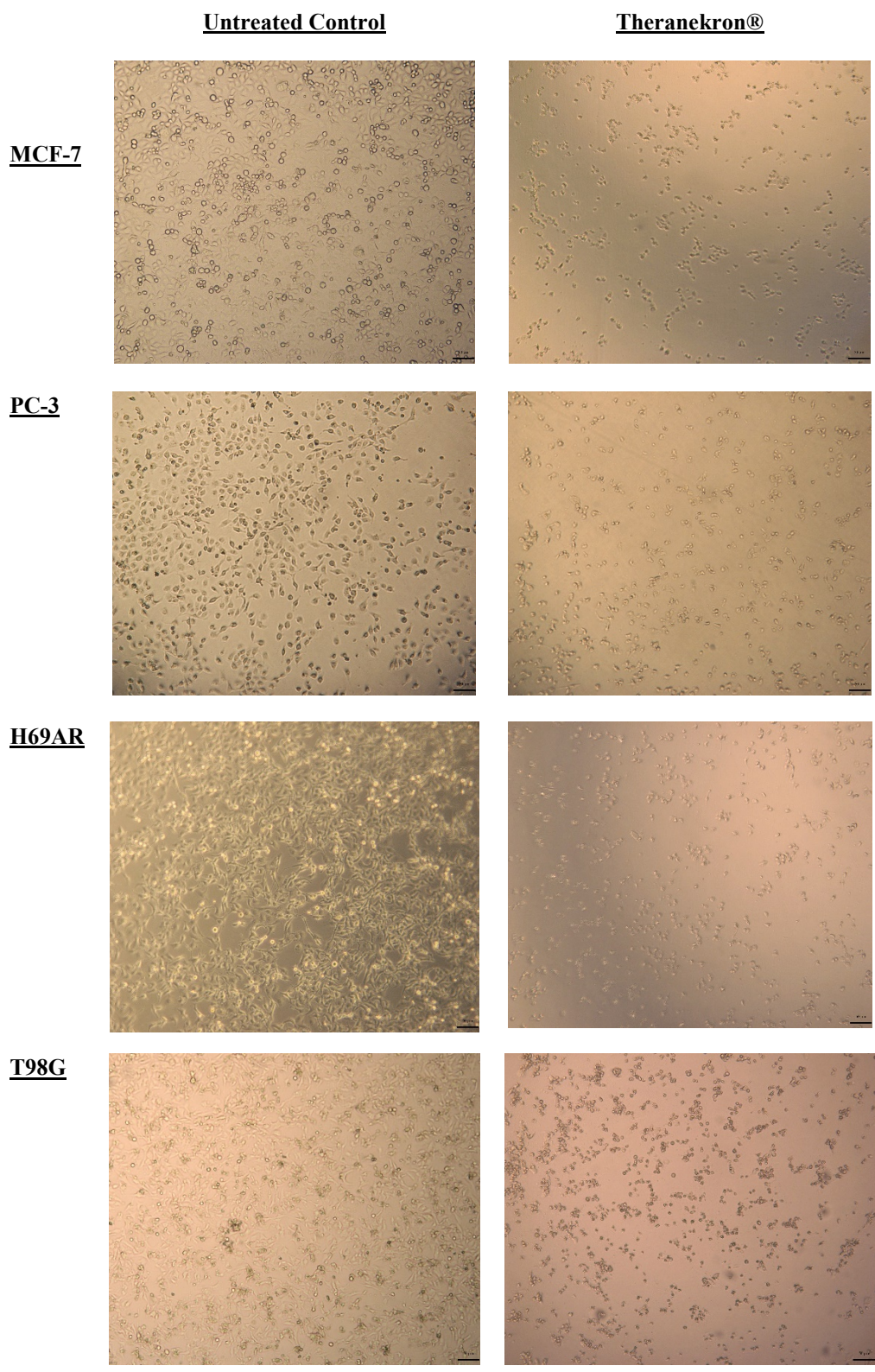


Figure 4. Images of cancer cell lines treated with Theranechron® with IC₅₀ values of each cell line for 72h. Reduced viability and cell number were observed highly on MCF-7 cells compared to other cell lines. While reduced viability was observed on all treated cells as compared to the untreated control groups (Magnification 10X).

For the canine tumors, it was found that Bcl-2 expression was significantly decreased in the Theranekron® treated tissues [27]. Considering the similarities between canine and human mammary tumors [29], the effect of Theranekron® on MCF-7 cells can be considered as expected.

When the comparison was made among the cancer cell lines, it was found that Theranekron® was more effective to MCF-7 cells, followed by T98G and finally H69AR and PC-3 cells. Since it was already demonstrated that *T. cubensis* alcoholic extract was effective on canine mammary adenocarcinomas [11] and was shown to have potential against endometriosis in a rat model [25], it can be hypothesized that Theranekron® has higher potential against estrogen-dysregulation related diseases. Endometriosis is known to be an estrogen-dependent disease [30,31] and MCF-7 cell line is also known as an estrogen receptor positive cell line [32]. Thus, higher levels of cytotoxicity of Theranekron® on MCF-7 cell line can be explained with this relation. Among the other screened human cancer cell lines, the IC₅₀ value of T98G cell line was 118.9 µg/mL at 72h for *T. cubensis* alcoholic extract. When looked at the commonalities, there are number of studies that explains that tamoxifen (estrogen receptor modulator used against ER positive breast cancers) can constrain the proliferation of malignant ER(-) glioma cells, and reports the expression and function of ER-related receptors in T98G cell line along with other cell lines [33,34]. On the other hand, the cytotoxicity levels were found relatively low for H69AR and PC-3 cells. Considering the complex molecular mechanisms of different cancer cell lines, further studies might be more enlightening on the effect of *T. cubensis* alcoholic extract on other cancer cells as well.

4. Conclusion

In this report, the cytotoxic effect of alcoholic extract of *T. cubensis* obtained from the local veterinary clinic was evaluated in five different cell lines. One non-cancerous human cell line and four different human cancer cell lines were used for *in vitro* screening for the cytotoxic effect of Theranekron® with the increasing concentrations (10-100 µg/mL). It was aimed to offer a basis for further studies on the anticancer effect of *T. cubensis* alcoholic extract.

Results showed that Theranekron® decreased the cell viability of non-cancerous cell line HEK-293 with an IC₅₀ value of 88.3 µg/mL at 72h. Among the cancer cell lines, the highest cytotoxic effect of *T. cubensis* extract was observed on human breast cancer cell line MCF-7.

The IC₅₀ value of Theranekron® was calculated as 94.7 µg/mL at 72h in MCF-7 cells. Its cytotoxic effect was apparent after 48h of treatment. However, the cytotoxicity rate of Theranekron® was noted relatively lower on the glioblastoma cell line T98G, human small cell lung cancer H69AR, and human prostate cancer cell line PC-3 measured up to MCF-7 cell line. Among these 3 cell lines, the highest effect was observed on T98G with the IC₅₀ value of 118.9 µg/mL at 72h. It is followed by H69AR and finally PC-3 cell lines with the IC₅₀ values of 278 µg/ml and 295 µg/mL respectively.

In conclusion, the anticancer effect of *T. cubensis* venom has a great prospect not only in canine tumors but also in human cancer cell lines. It can be also promising for other cancer cell lines, however, its effect should be further studied. Based on this conclusion, it can be suggested that by describing the molecular mechanisms and further understanding of the composition of *T. cubensis* extract, it can be considered as a novel bio-therapeutic for cancer in the future.

Acknowledgment

The experiments in this paper were partially performed at Manisa Celal Bayar University (Turkey) - Applied Science and Research Center (DEFAM).

Theranekron® D6 solution used for the experiments was accessed courtesy of Veterinary Physician Bora Benli.

Conflicts of interest

The author(s) declare that they have no conflict of interest.

References

- [1] King G. F., Venoms as a platform for human drugs: Translating toxins into therapeutics, *Expert Opin. Biol. Ther.*, 11(11) (2011) 1469–1484.
- [2] Oldrati V., Arrell M., Violette A., Perret F., Sprüngli X., Wolfender J. L., Stöcklin R., Advances in venomics, *Mol. Biosyst.*, 12(12) (2016) 3530-3543.
- [3] Lewis R.J., Garcia M.L., Therapeutic potential of venom peptides, *Nat. Rev. Drug Discov.*, 2(10) (2003) 790-802
- [4] İlhan S., Çiçek K., Tok C.V., Atmaca H., Profiling of apoptosis-associated proteins in human prostate cancer cells in response to *Montivipera bulgardaghica albizona* venom by protein array, *Toxin Rev.*, (2020) 1–8.
- [5] Saez N. J., Senff, S., Jensen, J. E., Er, S.Y., Herzig, V., Rash, L.D., King, G.F., Spider-Venom Peptides as Therapeutics, *Toxins (Basel)*, 2(12) (2010) 2851–2871.
- [6] Comprehensive Cancer Information - National Cancer Institute, Available at: <https://www.cancer.gov/>. Retrieved Dec. 09, 2020.
- [7] Pennington M. W., Czerwinski A., Norton R.S., Peptide therapeutics from venom: Current status and potential, *Bioorganic Med. Chem.*, 26(10) (2018) 2738–2758.
- [8] RichterPharma, Theranekron D6. Available at: https://www.richter-pharma.at/product-theranekron-d6_301.htm. https://www.richter-pharma.at/product-theranekron-d6_301.htm. Retrieved Dec. 09, 2020.
- [9] Ghasemi-Dizgah A., Nami B., Amirmozafari N., *Tarantula cubensis* venom (Theranekron®) selectively destroys human cancer cells via activating caspase-3-mediated apoptosis, *Acta Medica Int.*, 4(1) (2017) 74-80.
- [10] Kaçar C., Zonturlu A.K., Oral H., Yıldız S., Arı U.Ç., İneklerde erken puerperal dönemde theranekron uygulamalarının uterus involusyonu ve vaginal akıntı üzerine etkisi, *Kafkas Üniversitesi Vet. Fak. Derg.*, 13(1) (2007) 11–15.
- [11] Gültiken N., Rifat Vural M., The effect of *Tarantula cubensis* extract applied in pre and postoperative period of canine mammary tumours, *J. Istanbul Vet. Sci.*, 2(2) (2007) 13–23.
- [12] Koch H., Stein M., Conservative and surgical treatment of panaritium (bovine interdigital necrobacillosis) of cattle in combination with Theranekron (spider venom preparation), *Prakt. Tierarzt*, 61 (1980) 116–119.
- [13] Sardari K., Kakhki E. G., Mohri M., Evaluation of wound contraction and epithelialization after subcutaneous administration of Theranekron® in cows, *Comp. Clin. Path.*, 16(3) (2007) 197–200.
- [14] Gül Satar N.Y., Cangül I.T., Topal A., Kurt H., Ipek V., Önel G.I., The effects of *Tarantula cubensis* venom on open wound healing in rats, *J. Wound Care*, 26(2) (2017) 66–71.
- [15] Albay K., Şahinduran Ş., Kale M., Karakurum Ç. M., Sezer, K., Influence of *Tarantula cubensis* Extract on the Treatment of the Oral Lesions in Cattle with Bluetongue Disease, *Kafkas Univ. Vet.Fak.Derg.*, 16(4) (2021) 593–596.
- [16] Lotfollahzadeh S., Alizadeh M.R., Mohri M., Mokhber Dezfouli M.R., The therapeutic effect of *Tarantula cubensis* extract (Theranekron®) in foot-and-mouth disease in cattle: A randomised trial in an endemic setting, *Homeopathy*, 101(3) (2012) 159–164.
- [17] Paksoy Z., Güleşçi N., Kandemir F.M., Dinçel G.Ç., Effectiveness of levamisole and *Tarantula cubensis* extract in the treatment of teat Papillomatosis of cows, *Indian J. Anim. Res.*, 49(5) (2015) 704–708.
- [18] Karabacak M., Eraslan G., Kanbur M., Sarica Z.S., Effects of *Tarantula cubensis* D6 on aflatoxin-induced injury in biochemical parameters in rats, *Homeopathy*, 104(3) (2015) 205–210.
- [19] Kızılay Z., Aktaş S., Kahraman Çetin N., Kılıç M.A., Öztürk H., Effect of *Tarantula cubensis* extract (Theranekron) on peripheral nerve healing in an experimental sciatic nerve injury model in rats, *Turk. Neurosurg.*, 29(5) (2019) 743–749.
- [20] Er A., Çorum O., Çorum D.D., Hitit M., Dönmez H., Güzeloğlu A., Alcoholic extract of *Tarantula cubensis* induces apoptosis in MCF-7 cell line, *Biomed. Res.*, 28(8) (2017) 3660–3665.
- [21] Atmaca H., İlhan S., Batır M. B., Pulat Çamlı Ç., Güner A., Bektaş H., Novel benzimidazole derivatives: Synthesis, in vitro cytotoxicity, apoptosis and cell cycle studies, *Chem. Biol. Interact.*, 327 (2020) 109163.
- [22] de Souza-Fagundes E. M., Cota B. B., Almeida F. D. M., Anticancer Potential of Spider Venom, in Spider Venoms, *Toxinology*, (2016), 293–311.
- [23] Gürbulak K., Akçay, A., Gümüşsoy, K.S., Sist,

- B., Steiner, S., Abay, M., Canoğlu, E., Bekyürek, T., Investigation of the efficacy of *Tarantula cubensis* extract (Theranekron D6) in the treatment of subclinical and clinical mastitis in dairy cows, *Turkish J. Vet. Anim. Sci.*, 38 (2014) 712–718.
- [24] İçen H., Sekin S., Şimsek A., Kochan A., Tunik S., The efficacy of *Tarantula cubensis* extract (Theranekron) in treatment of canine oral papillomatosis, *Asian J. Anim. Vet. Adv.*, 6(7) (2011) 744–749.
- [25] Dolapçioğlu K., Doğruer G., Özsoy Ş., Ergun Y., Çiftçi Ş., Soylu Karapınar O., Aslan E., Theranekron for treatment of endometriosis in a rat model compared with medroxyprogesterone acetate and leuprolide acetate, *Eur. J. Obstet. Gynecol. Reprod. Biol.*, 170(1) (2013) 206–210.
- [26] Oryan A., Moshiri A., Raayat A.R., Novel application of Theranekron® enhanced the structural and functional performance of the tenotomized tendon in rabbits, *Cells Tiss. Org.*, 196(5) (2012) 442–455.
- [27] Gültiken N., Güvenç, T., Kaya, D., Ağaoglu, A.R., Ay, S.S., Küçükaslan, I., Emre, B., Findık, M., Schäfer-Somi, S., Aslan, S., *Tarantula cubensis* extract alters the degree of apoptosis and mitosis in canine mammary adenocarcinomas, *J. Vet. Sci.*, 16(2) (2015) 213–219.
- [28] Kumar R., Vadlamudi R.K., Adam L., Apoptosis in mammary gland and cancer, *Endocr.-Relat. Cancer*, 7(4) (2000) 257–269.
- [29] Kumaraguruparan R., Prathiba D., Nagini S., Of humans and canines: Immunohistochemical analysis of PCNA, Bcl-2, p53, cytokeratin and ER in mammary tumours, *Res. Vet. Sci.*, 81(2) (2006) 218–224.
- [30] Rižner T. L., Estrogen metabolism and action in endometriosis, *Mol. Cell. Endocrinol.*, 307(1-2) (2009) 8-18.
- [31] Chantalat E., Valera, M. C., Vaysse, C., Noirrit, E., Rusidze, M., Weyl, A., Vergriete, K., Buscail, E., Lluell, P., Fontaine, C., Arnal, J. F., Lenfant, F., Estrogen receptors and endometriosis, *Int. J. Mol. Sci.*, 21(8) (2020) 21082815.
- [32] Brooks M. C., Locke E.R., Soule H.D., Estrogen Receptor in a Human Cell Line (MCF-7) from Breast, *J. Biol. Chem.*, 248(10) (1973) 6251–6253.
- [33] Gandhari M. K., Frazier C.R., Hartenstein J. S., Cloix J.F., Bernier M., Wainer I.W., Identification and characterization of estrogen receptor-related receptor alpha and gamma in human glioma and astrocytoma cells, *Mol. Cell. Endocrinol.*, 315(1–2) (2010) 314–318.
- [34] Hui A.M., Zhang, W., Chen, W., Xi, D., Purow, B., Friedman, G.C., Fine, H.A., Agents with selective estrogen receptor (ER) modulator activity induce apoptosis in vitro and in vivo in ER-negative glioma cells, *Cancer Res.*, 64(24) (2004) 9115–9123.

Investigation of the adsorption of Astrazon Blue FGRL dye in synthetic wastewater using waste mine clay

Fuat ÖZYONAR¹ , Mehmet KOBYA^{2,3} , Ülker Aslı GÜLER^{1,*} 

¹Sivas Cumhuriyet University, Department of Environmental Engineering, Sivas/TURKEY

²Gebze Technical University, Department of Environmental Engineering, Gebze/TURKEY

³Kyrgyz-Turkish Manas University, Department of Environmental Engineering, Bishkek/ KYRGYZSTAN

Abstract

In this investigation is aimed at the removal of Astrazon Blue FGRL (AB FGRL) (basic dye) from an aqueous solution using waste clay (MC) obtained from the gold mine area. The natural clay was characterized and identified using X-ray diffraction (XRD) analysis. Then, the contact time, adsorbent dosage, pH, initial dye concentration and temperature experiments were carried out in a batch system. The removal efficiency was found to be 97% at pH 7, 80 min, 30°C, 4 g/L MC dosage, 50 mg/L initial dye concentration. The adsorption data are applied to the Langmuir, Freundlich, and Temkin isotherm models. The maximum capacity of waste mine clay (MC) was found to be 191.75 mg/g. The pseudo-second-order kinetic models and Elovich kinetic model were used to examine the adsorption process of Astrazon Blue FGRL. The results of kinetic experiments were defined by the pseudo-second-order model point out a chemisorption reaction. The adsorption thermodynamics were investigated using parameters such as enthalpy change (ΔH°), Gibbs free energy change (ΔG°) as well as entropy change (ΔS°). These calculations reveal that sorption of Astrozon Blue FGRL is endothermic, spontaneous and enthalpy driven. This work provides guidance for using of waste clay materials for applications in the adsorption removal of dye from aqueous solution.

Article info

History:

Received: 02.12.2020

Accepted: 03.04.2021

Keywords:

Waste clay,
Astrazon Blue FGRL,
Adsorption isotherms,
Kinetics,
Thermodynamic.

1. Introduction

The textile industry has used large amounts of water and chemicals in various processing stages for instance sizing, washing, decolorant, mercerizing, coloring, printing, and finishing [1]. The wastewater generated from the textile industries contains different types of dyes that are very low biodegradable due to complex structures and high molecular weight [2]. The cationic textile dyes are basic dyes which are synthetic pigments and are widely used in the textile industry. These dyes belonging to the cationic basic dye group are water-soluble. The basic dyes have often used in several processes for example acrylic, nylon, silk, and wool coloring [3]. The performance of the coloring process is often poor, causing large amounts of dye to escape from the wastewater. Dumping into the water bodies from no treatment of dye-bearing wastewaters has posed a danger to human health, aquatic living, and water quality, thus becomes vital importance [4]. Discharge of wastewater containing dyes into natural receiving environments such as streams and rivers have a great influence on the photosynthetic activity in aquatic organisms and exhibit a low biodegradability

[5]. It also damages the aesthetic structure of the environment and causes health problems for people such as skin irritation, cancer, mutation, allergic dermatitis [6]. The treatment obligation of dye wastewater, relevant industries need to treat wastewater containing dyes before discharging them into a body of water.

Many treatment techniques for example chemical coagulation [1], biodegradation [7], membrane separation [8], electrocoagulation [9], Fenton process [10], ozone oxidation [11], electrochemical degradation [12], ultrasonic degradation [13], photocatalytic oxidation [14], and adsorption techniques [15] have been applied for the removal of textile wastewater. Adsorption is a prime wastewater treatment method for dyes removal due to its simplicity of design, non-generation of toxic materials, low cost and high efficiency [16]. Generally, activated carbon is the most common adsorbent that commonly utilized for treatment of wide range of water pollutants [17]. However, its initial cost, rapid saturation and difficult in regeneration make it less attractive as an adsorbent. [18, 19]. Therefore, in recent years, studies have

*Corresponding author. e-mail address: asli.atay@cumhuriyet.edu.tr
<http://dergipark.gov.tr/csj> ©2021 Faculty of Science, Sivas Cumhuriyet University

focused on the development of cost effective and environment friendly adsorbents. Various low-cost adsorbents have been proposed by numerous researchers, containing natural materials, waste materials, and biosorbents, from agriculture and industry processes [4, 6, 20-22]. The sorbents are used in other studies are clay materials (kaolinite, bentonite), siliceous materials (alunite, silica beads, perlite), zeolites, agricultural waste (corn cob, pulp, nutshells, rice husk, almond shell, coconut shell), products of the industrial waste (red sludge, compost industry waste, blast furnace sludge, and fly ash), biosorbents (chitosan, biomass, peat) and others (cyclodextrin, starch, chitosan). These materials can be used as adsorbents for removing cationic, anionic, and reactive dyes from aqueous solutions. The utilization of natural clays as alternative adsorbents for the removal of dyes from wastewater offers several advantages such as low-cost, high adsorption properties, porosity, availability, thermal stability, large potential for ion exchange, plenty in most landmasses worldwide and nontoxicity [23]. The strong adsorption capabilities of clay minerals are related to the negative charge in the structure of grain silicate minerals. This negative charge can be neutralized by adsorption of positively charged cations such as dyes. [24].

The aim of this study is to provide dye removal from wastewater and to investigate the reusability of wastes by using waste material. In addition, the reuse of waste materials is an environmentally friendly approach. For this purpose, the use of waste mine clay (MC) from the gold mine area as an effective adsorbent for the treatment of Astrazon Blue FGRL (basic dye) from an aqueous solution was evaluated. Adsorption experiments were applied under various operational parameters such as contact time, adsorbent dosage, solution pH, initial dye concentration and temperature. Adsorption kinetic data were verified with the so-called pseudo-second-order kinetic model and Elovich equation model. Equilibrium data were calculated using the Langmuir, Freundlich, and Temkin isotherm models. Also, the adsorption thermodynamics were calculated.

2. Materials and Methods

2.1. Waste clay and dye characterization

Waste mine clay (MC) was collected from a gold mine area in Sivas, Turkey, and XRD spectrum is as follows (Figure 1). The MC was crushed and dried followed by in a hot air oven at 80 °C for 48 h before use.

Astrazon Blue FGRL used for the study was supplied from Dystar, Turkey. This dye contains two main dyes,

including C.I. Basic Blue 159 and C.I. Basic Blue 3. The ratio of the two dyes is 5:1 (w/w), respectively, and the structures of two dye components are presented in Figure 1 [25]. The basic dye is mostly used as acrylic painting in the industry [26]. This dye has not intensely toxic, nonetheless could cause short-term rapid or difficult breathing when inhaled [26].

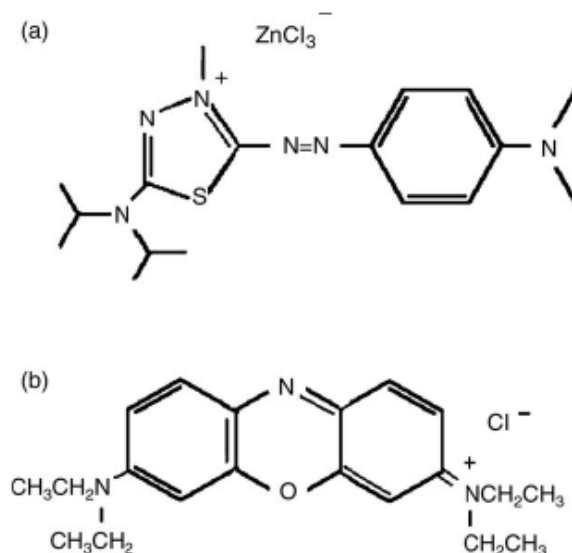


Figure 1. Chemical structure of AB FGRL ((a) C.I. Basic Blue 159 and (b) C.I. Basic Blue 3).

2.2. Adsorption experiments

All batch adsorption tests were completed in 100 mL Erlenmeyer and 50 mL solution volume in a shaker unit with a thermostat at 300 rpm. Influences of contact time, adsorbent dosage, solution pH, initial dye concentration and temperature were studied. In this study, samples were taken over time to measure the dye concentration residual in the aqueous solution. The influence of varying contact time (5-80 min) was studied at 100 ppm Astrazon Blue FGRL dye concentrations, adsorbent dosage (0.5-1-2 g/L), pH 7.0 and 30 °C. The influence of MC dosage on removal of Astrazon Blue FGRL dye was tested by varying adsorbent dosage from 0.5 to 10 g/L in initial dye concentration (100-200-400-600 and 800 mg/L) at pH 7.0 and 30 °C for contact time 1440 min. The influence pH was studied different pH values as 5, 7, 9 and 12 at MC dosage 4 g/L for different contact time (5-10-15-20-30-40-60-80 min). The initial pH of the dye aqueous solution was adjusted using HCl and NaOH solutions. The influence of different initial dye concentrations (50-100-200-400-600-800 mg/L) was carried out by in for contact time 80 min at pH 7.0 and 30 °C. Thermodynamic adsorption experiments were performed in a shaker water bath (GFL model 1086) at 30, 40 and 60 °C. At the end of the experiment, solid-liquid separation was made by centrifugation at 4000

rpm for 20 min. Thus, the final dye concentration in the supernatant was determined. The amount of dye (q_e , mg/g) adsorbed on the adsorbent at equilibrium was calculated as follows (Eq. 1):

$$q_e = \frac{(C_o - C_e)V}{m_s} \quad (1)$$

where C_o and C_e are dye concentrations in solution at the initial time and equilibrium, respectively (mg/L); V , is the volume of the dye solution (L); m_s , is the mass of the adsorbent or MC (g). The removal efficiency (R_e ,%) of Astrazon Blue FGRL by the adsorbent was calculated as follows (Eq. 2):

$$R_e = \frac{(C_o - C_t)}{C_o} \times 100 \quad (2)$$

2.3. Analytical methods

The concentration of the Astrazon Blue FGRL solution was determined using a UV/vis spectrophotometer (Merck, Pharo 300 Model, German) with a detecting wavelength at 576 nm. The pH of the dye solution was measured with a pH meter (WTW Inolab Multi 9310 IDS) using a combined glass electrode. All chemical reagents used are of analytical grade and are prepared in Millipore Milli-Q deionized water. All experiments were done twice and the experimental error was less than 1%.

2.4. Kinetic modeling, isotherm and thermodynamic parameters

The pseudo-second-order adsorption kinetic rate equation is given as (Eq. 3) [27]:

$$\frac{t}{q_t} = \frac{1}{k_2 q_e^2} + \frac{1}{q_e} (t) \quad (3)$$

The plot of t/q_t and t should give a linear relationship from which q_e and k_2 can be determined from the slope and intercept of the plot, respectively. This equation is the initial adsorption rate (h) (Eq. 4);

$$h = k_2 q_e^2 \quad (4)$$

The Elovich model equation is commonly expressed as (Eq. 5) [28]:

$$q_t = \frac{1}{\beta} \ln(\alpha\beta) + \frac{1}{\beta} \ln(t) \quad (5)$$

where: α is the initial adsorption rate ($\text{mg}\cdot\text{g}^{-1}\cdot\text{min}^{-1}$), β is the desorption constant ($\text{g}\cdot\text{mg}^{-1}$) during any one experiment.

The equilibrium data were analysed using Langmuir, Freundlich and Temkin isotherm models (Eq. 6, 7 and 8) [29,30].

Langmuir isotherm:

$$q_e = \frac{Q_o b C_e}{1 + b C_e} \quad (6)$$

where Q_o (mg/g) is the maximum adsorption capacity and b (L/mg) is the Langmuir constant.

Freundlich isotherm:

$$q_e = k_F C_e^{1/n} \quad (7)$$

where k_F (L/g) is the adsorption diffusion coefficient and represents the quantity of adsorbed dye on the adsorbent surface per unit equilibrium concentration, the other Freundlich constant $1/n$ represents the adsorption intensity or surface heterogeneity.

Temkin isotherm:

$$q_e = \frac{RT}{bt} \ln K_T + \frac{RT}{bt} \ln C_e \quad (8)$$

where K_T (L/g) is the isotherm constant, bt (kJ/mol) is the constant relating to sorption energy, R is $8.314 \text{ kJ mol}^{-1}\text{K}^{-1}$, and T temperature (K). According to the Temkin isotherm model, the adsorbate interacts with each other and the sorption energy in the layers decreases linearly with the coating of the adsorbate. By plotting q_e versus $\ln C_e$, a straight line is obtained by which K_T and bt can be measured.

Thermodynamic parameters such as changes in Gibbs free energy ΔG° (kJ mol^{-1}), as well as enthalpy ΔH° (kJ mol^{-1}) and entropy ΔS° ($\text{J mol}^{-1}\text{K}^{-1}$) were determined by using the following equation (Eq. 9 and 10) [31].

$$\ln K_C = \frac{\Delta S^\circ}{R} - \frac{\Delta H^\circ}{RT} \quad (9)$$

$$\Delta G^\circ = \Delta H^\circ - T\Delta S^\circ \quad (10)$$

where R is gas constant ($8.314 \text{ kJ mol}^{-1}\text{K}^{-1}$) and T is reaction temperature (K).

3. Results and Discussion

3.1. Characterization of waste clay by XRD

The spectroscopic analysis performed by the X-ray diffractometer of the waste clay used is represented in Figure 2.

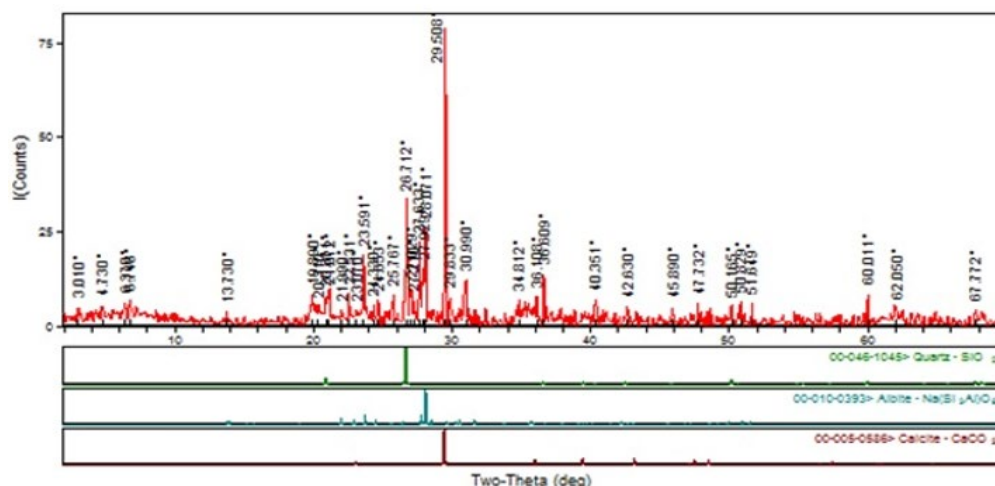


Figure 2. XRD spectrum of waste clay

From Figure 2, many diffraction peak at 2θ range 20° - 30° can be observed. These results indicate the presence of Quartz, Albite and Calcite in the structure of waste clay.

3.2. Influence of contact time and MC dosage on the adsorption process and adsorption kinetics

Figure 3 represents the influence of contact time and MC dosage on the Astrazon Blue FGRL adsorption. According to Figure 3(a), the adsorption capacity slows down at longer contact times and it reaches equilibrium. In general, at the start of the experiment, the adsorption is rapid and during this phase the quantity of dye adsorbed is high. During the stationary phase, although the contact time increases the amounts of dye adsorbed by the clay are small. This can be

explained during the first phase by the increased binding of dye molecules on the clay surface studied while the stationary phase is explained by the saturation of the binding sites [32, 33].

The adsorption capacity decreased when the MC dosage was increased. In this case, the high surface area and/or adsorption active sites available for adsorption of Astrazon Blue FGRL dye molecules may occur [23]. This, in turn, is thought to increase the efficiency and capacity of Astrazon Blue FGRL. Further increase in MC dosage above 4 g/L did not show any further improvement in Astrazon Blue FGRL dye removal. Therefore, optimum MC dosage was chosen to be 4g/L for studies the influence of pH and initial dye concentration.

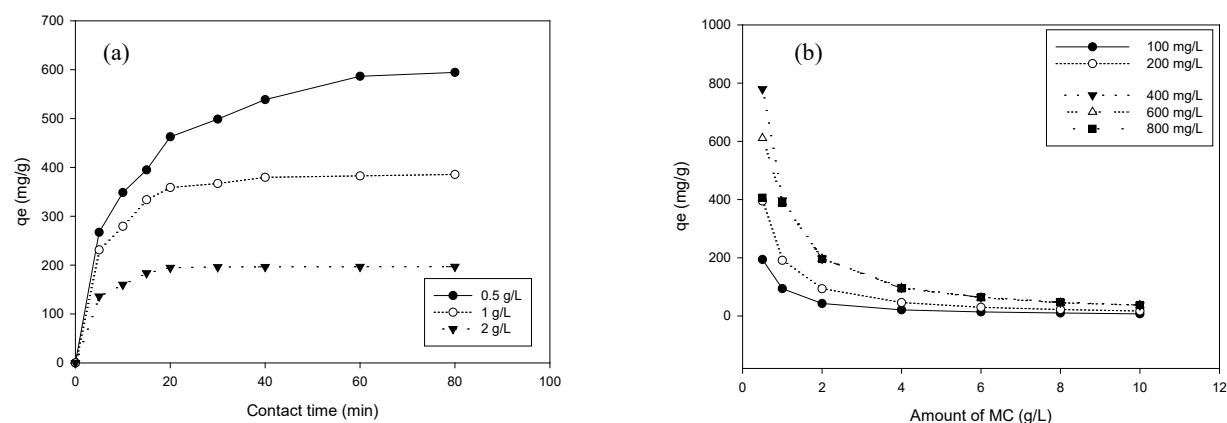


Figure 3. Influence of contact time (a) ($m_s=0.5$ - 1 - 2 g/L, $C_o=400$ mg/L, $t=5$ - 10 - 15 - 20 - 30 - 40 - 60 - 80 min, $T=30$ °C, $pH=7$) and adsorbent dosage (b) ($m_s=0.5$ - 1 - 2 - 4 - 6 - 8 - 10 g/L, $C_o=100$ - 200 - 400 - 600 - 800 mg/L, $t=1440$ min, $T=30$ °C, $pH=7$) and on the adsorption process

The adsorption kinetic model constants and r^2 values are given in Table 1. Correlation coefficients of the pseudo second-order kinetic model is relatively greater than that of the Elovich kinetic model and the $q_{e,teo}$ values fitted well compliance with the $q_{e,exp}$ values, in this case, the rate-determining step can be surface

adsorption. Based on the assumption of the pseudo-second-order model it can be concluded that the adsorption of Astrazon Blue FGRL onto MC was chemisorption involving exchange or sharing of electrons between adsorbent and adsorbate [19, 24, 34, 35].

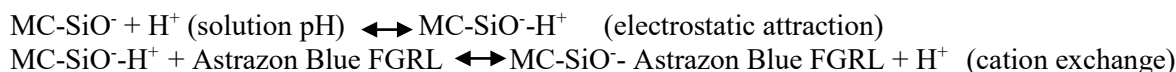
Table 1. The kinetic models of the Astrazon Blue FGRL adsorption in the different MC dosages

The Pseudo second-order kinetic						The Elovich kinetic		
m_s (g/L)	$q_{e,exp}$ (mg/g)	k_2 (g/mg.min)	$q_{e,teo}$ (mg/g)	h (mg/g.min)	r^2	α (mg/g min)	β (g/mg)	r^2
0.5	614.376	2.51×10^{-4}	632.91	100.54	0.988	1.683	8.02×10^{-3}	0.985
1.0	385.609	1.02×10^{-3}	398.41	161.91	0.998	1.932	17.71×10^{-3}	0.858
2.0	196.854	3.96×10^{-3}	200.80	159.67	0.999	2.132	46.63×10^{-3}	0.738

3.2. Influence of initial solution pH on the adsorption process

Solution pH plays an important role in the sorption process. It appears to interrupt the solution chemistry of dyes and functional groups of the adsorbents. Adsorption capacity of dye depends on pH of the solution [36]. The influence of the solution pH on the Astrazon Blue FGRL adsorption was studied at initial pH values of 5–12. The adsorption capacity of Astrazon Blue FGRL was high at pH 5, 7 and 9 values (Figure 4). It was observed from Figure 4 that the

increasing in solution pH from 5 to 12 the adsorption capacity, q_e (mg/g) decreases from 97.96 mg/g to 90.11 mg/g for equilibrium time 30 min. Hence there was a significant change in adsorption capacity at especially pH 12. The adsorption capacity depends on the relationship of dye molecules with the surface of the adsorbent. The high adsorption capacity of the Astrazon Blue FGRL at acidic and neutral pH could be based on the cation exchange and H-bonding interactions among that can be occurred between H atom available on the MC surface and N atom in the Astrazon Blue FGRL dye structure.



These results indicate that pH values were a limiting factor in high dye removal, pH control is necessary. The adsorption capacity of Astrazon Blue FGRL increased until 30 min contact time and at longer contact times, the adsorption rate reached equilibrium. Therefore, pH 7 was determined to be the best solution pH for the further applications.

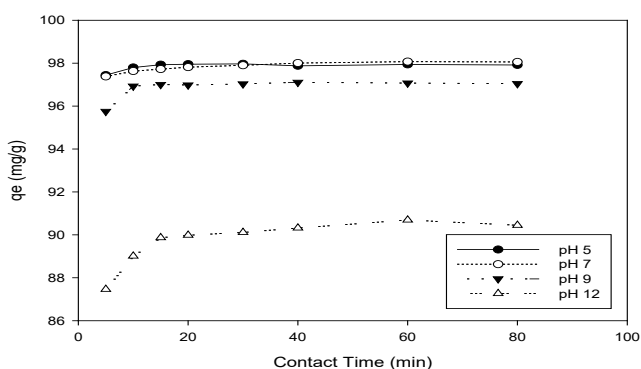


Figure 4. Influence of solution pH on adsorption process ($C_0=400$ mg/L, $m_s=4$ g/L, $t=5-10-15-20-30-40-60-80$ min, $T=30^\circ\text{C}$).

3.3. Influence of initial dye concentration on the adsorption process

The influence on the adsorption capacity of the initial Astrazon Blue FGRL concentration is demonstrated in Figure 5. The adsorbed dye amount increased when the concentration Astrazon Blue FGRL (to 147.9 mg/g from 12.18 mg/g) was increased.

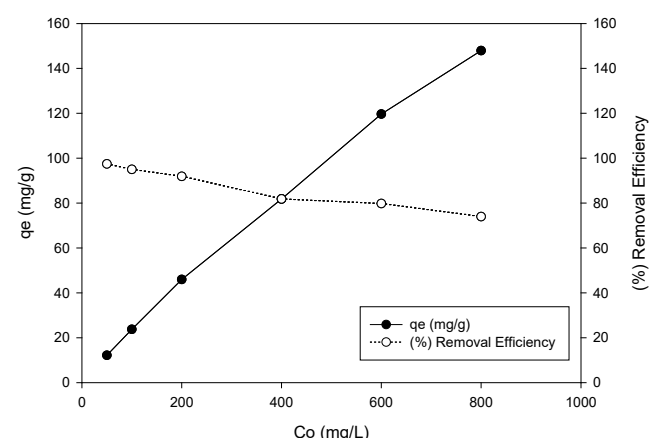


Figure 5. Influence of the initial dye concentration on adsorption process ($C_0=50-100-200-400-600-800$ mg/L, $m_s=4$ g/L, $t=80$ min, $pH=7$, $T=30^\circ\text{C}$).

The increases with the increasing of the initial dye concentration, this can be explained by the good diffusion of the dye molecules towards to specific surface of clay studied [32]. The initial concentration was considered to play an important role in providing the necessary driving force to overcome the force to mass transfer of Astrazon Blue FGRL between aqueous solution and solid phases [37]. It was found that the interaction between the adsorbate and the adsorbent also increases with the increase in the initial concentration. Similar output has been reported in the adsorption of congo red dye using cabbage waste powder [19]. Therefore, it can be concluded that a higher initial concentration increases the adsorption

uptake of Astrazon Blue FGRL. The removal efficiency was reduced with the increase in Astrazon Blue FGRL concentration (to 73% from 97%).

3.4. Adsorption isotherms

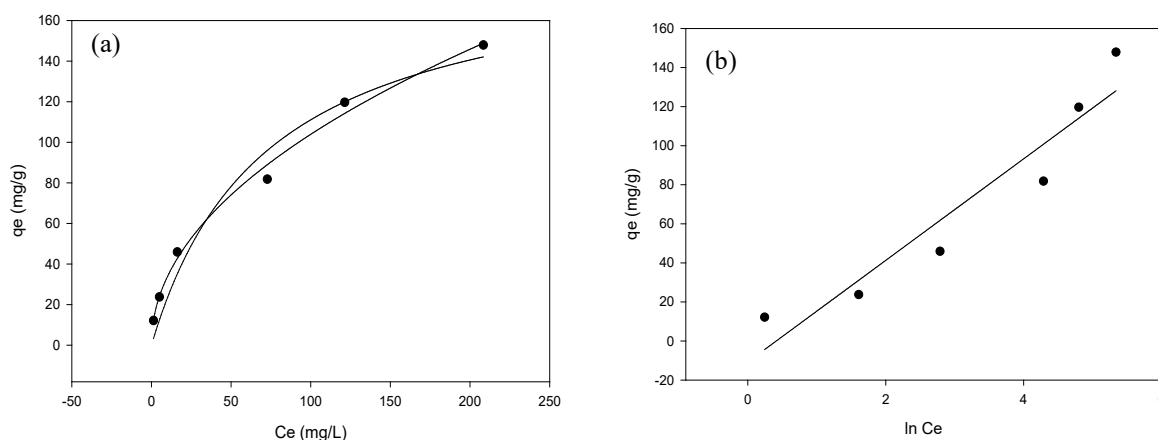


Figure 6. Langmuir, Freundlich (a) and Temkin (b) isotherm plots for Astrazon Blue FGRL adsorption

Table 2. Langmuir, Freundlich and Temkin isotherm model parameters for adsorption of Astrazon Blue FGRL dye on the MC

Langmuir Isotherm Model	MC	Freundlich Isotherm Model	MC	Temkin Isotherm Model	MC
Q_0 (mg/g)	191.75	k_F (L/g)	10.9281	K_T	0.66
b (L/mg)	0.0138	$1/n$	0.4890	bt	96.90
r^2	0.981	r^2	0.997	r^2	0.953

According to data indicates in Table 2, Langmuir and Freundlich models are applicable and the removal efficiencies varies in the same direction according to the two models as well as the adsorption of Astrazon Blue FGRL by MC used (all $r^2 > 0.980$). It can be thought that adsorption occurs on homogeneous and heterogeneous surfaces of the adsorbent. In this case; the effect of physical and chemical adsorption can be combined [38]. The high value of the Freundlich constant (k_F ; 10.9281 L/g) is associated with the high clay capacity for Astrazon Blue FGRL dye removal. The Q_0 value of MC was determined as 191.75 mg/g. A comparison of Q_0 values of Astrazon Blue FGRL onto various adsorbents are reported in Table 3. The results were also fitted by the Temkin model (Table 2), which suggested a reduction in the heat of adsorption along with coverage due to adsorbent-adsorbate interactions. As a result, adsorption of Astrazon Blue FGRL dye could be characterized by a uniform distribution of binding energies up to maximum value [39].

Different isotherm models were employed to study the Astrazon Blue FGRL dye adsorption by MC. The adsorption plots and isotherm parameters are presented in Figure 6 and Table 2.

Table 3. The Q_0 values obtained for adsorption of Astrazon Blue FGRL on different adsorbents

Adsorbent	Q_0 (mg/g)	Reference
MC	191.75	This study
Apricot stone activated carbon	181.5	[25]
Sepiolite	155.5	[25]
Fly ash	128.2	[25]
Macroalga <i>C. lentillifera</i>	94.3	[40]
Macroalga <i>C. lentillifera</i>	49.26	[25]
Macroalga <i>C. lentillifera</i>	38.9 ± 3.4	[40]

3.5. Influence of temperature on the adsorption process and adsorption thermodynamic

The temperature is another driving force in the adsorption of Astrazon Blue FGRL dye. Temperature is known to influence the viscosity of the solution as well as controlling the rate of diffusion of the dye molecules over the external boundary layer and in the internal pores of the adsorbent [19]. The influence on the adsorption capacity of the temperature, and

adsorption thermodynamic plot are given in Figure 7. As seen in Figure 7, while the temperature was increased, the adsorption capacity increased. This is because at elevated temperatures, the kinetic energy of Astrazon Blue FGRL dye molecules increase which in

turn increases the collision rate of the dye and MC. However, temperatures there is also a possibility of the inner pores of MC opening up increasing the adsorption sites hence high adsorption rate [19].

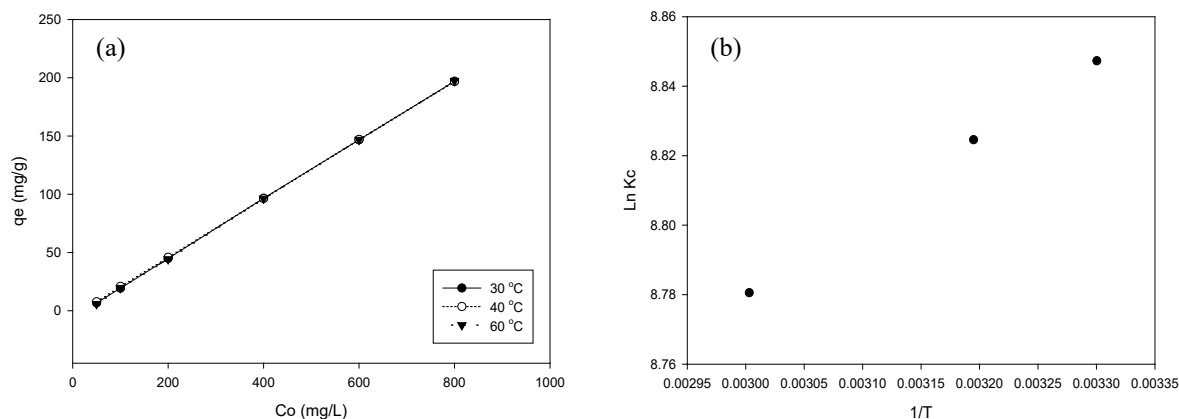


Figure 7. Influence of temperature on adsorption process (a) ($C_o=50-100-200-400-600-800$ mg/L, $m_s=4$ g/L, $t=80$ min, $pH=7$) and thermodynamic plot (b)

Therefore, the temperature parameter played an important role in removing Astrazon Blue FGRL from the aqueous solution. According to the thermodynamic parameters, the positive value of ΔH° indicates that the adsorption process is endothermic (Table 4). The positive values of entropy (ΔS°), show that randomness increased (adsorbate/adsorbent) during the adsorption process. Negative ΔG° values indicate that adsorption is thermodynamically spontaneous and feasible. Adsorption of congo red on cabbabe waste powder showed similar trend [19].

Table 4. Thermodynamic parameters obtained for Astrazon Blue FGRL dye adsorption

	Astrazon Blue FGRL dye
ΔH° (kJ/mol)	1.871
ΔS° (kJ/mol.K)	67.38
ΔG° (kJ/mol)	
303 K	-22.28
313 K	-22.96
333 K	-24.32

Conclusion

In this study, the waste clay in the gold mine region was used as an effective adsorbent for the removal of Astrazon Blue FGRL dye from aqueous solution. The amounts of adsorbed dye were calculated as a function of various parameters such as the contact time effect

between clay and dye molecules, the adsorbent dosage effect, the pH of the solution, the effect of the initial dye solution concentration and solution temperature. Percent removal of Astrazon Blue FGRL dye increased with increase in contact time, temperature, dosage but dropped when pH were increased. The MC showed good sorption performance for the uptake of Astrazon Blue FGRL in various pH and concentrations. The results of the study showed that the Langmuir and Freundlich isotherms are applicable to the study of the adsorption of Astrazon Blue FGRL dye using the MC. The values of Q_o for Astrazon Blue FGRL dye at optimum conditions were 191.75 mg/g. According to the literature; the maximum adsorption capacity (Q_o) of MC for removal of Astrazon Blue FGRL dye was higher than many other adsorbents. Kinetic data were expressed by a pseudo-second-order model that demonstrates that Astrazon Blue FGRL uptake occurs by the chemisorption process. The intraparticle diffusion model confirms that the rate-determining step of adsorption is unlikely to be mass transfer diffusion. The ΔG° and ΔS° values obtained from thermodynamic studies showed that the adsorption process occurred spontaneously, and the feasibility and randomness increased. This study shows that MC is low-cost adsorbent, which have been successfully used for the adsorption of dye from aqueous solution on laboratory scale.

Conflicts of interest

The authors state that there is no conflict of interests.

References

- [1] Verma A.K., Dash R.R., Bhunia P., A review on chemical coagulation/flocculation technologies for removal of colour from textile wastewaters, *J. Environ. Manage.*, 93 (2012) 154-168.
- [2] O'Neill C., Hawkes F.R., Hawkes D.L., Lourenco N.D., Pinheiro H.M., Delee W., Colour in textile effluents—sources, measurement, discharge consents and simulation: a review, *J. Chem. Technol. Biotechnol.*, 74 (1999) 1009-1018.
- [3] Ince N.H., Tezcanli G., Treatability of textile dyebath effluents by advanced oxidation: preparation for reuse, *Water Sci. Technol.*, 40 (1999) 183-190.
- [4] Bharathi K.S., Ramesh S.T., Removal of dyes using agricultural waste as low-cost adsorbents: a review, *Appl. Water Sci.*, 3 (2013) 773-790.
- [5] Xu X.R., Li H.B., Wang W.H., Gu J.D., Decolorization of dyes and textile wastewater by potassium permanganate, *Chemosphere*, 59 (2005) 893-898.
- [6] Salleh M.A.M., Mahmoud D.K., Karim W.A.W.A., Idris A., Cationic and anionic dye adsorption by agricultural solid wastes: A comprehensive review, *Desalination*, 280 (2011) 1-13.
- [7] Baban A., Yediler A., Avaz G., Hostede S.S., Biological and oxidative treatment of cotton textile dye-bath effluents by fixed and fluidized bed reactors, *Bioresource Technol.*, 101 (2010) 1147-1152.
- [8] Zahrim A.Y., Tizaoui C., Hilal N., Coagulation with polymers for nanofiltration pre-treatment of highly concentrated dyes: A review, *Desalination*, 266 (2011) 1-16.
- [9] Khandegar V., Saroha A.K., Electrocoagulation for the treatment of textile industry effluent—a review, *J. Environ. Manage.*, 128 (2013) 949-963.
- [10] Bouafia-Chergui S., Oturan N., Khalaf H., Oturan M.A., A photo-Fenton treatment of a mixture of three cationic dyes, *Procedia Eng.*, 33 (2012) 181-187.
- [11] Baek M.H., Ijagbemi C.O., Kim D.S., Spectroscopic studies on the oxidative decomposition of Malachite Green using ozone, *J. Environ. Sci. Health A.*, 45 (2010) 630-636.
- [12] Martinez-Huitle C.A., Brillas E., Decontamination of wastewaters containing synthetic organic dyes by electrochemical methods: A general review, *Appl. Catal. B.*, 87 (2009) 105-145.
- [13] Eren Z., Ince N.H., Acar F.N., Degradation of textile dyes, dyebaths and dyeing wastewater by homogeneous and heterogeneous sonophotolysis, *J. Adv. Oxid. Technol.*, 13 (2010) 206-211.
- [14] Gozmen B., Turabik M., Hesenov A., Photocatalytic degradation of Basic Red 46 and Basic Yellow 28 in single and binary mixture by UV/TiO₂/periodate system, *J. Hazard. Mater.*, 164 (2009) 1487-1495.
- [15] Hazzaa R., Hussein M., Adsorption of cationic dye from aqueous solution onto activated carbon prepared from olive stones, *Environ. Technol. Innov.*, 4 (2015) 36-51.
- [16] Abdulhameed A.S., Mohammad A.T., Jawad A.H., Application of response surface methodology for enhanced synthesis of chitosan tripolyphosphate/TiO₂ nanocomposite and adsorption of reactive orange 16 dye, *J. Clean. Prod.*, 232 (2019) 43-56.
- [17] Bhatnagar A., Hogland W., Marques M., Sillanpaa M., An overview of the modification methods of activated carbon for its water treatment applications, *Chem. Eng. J.*, 219 (2013) 499-511.
- [18] Novais R.M., Carvalheiras J., Tobaldi D.M., Seabra M.P., Pullar R.C., Labrincha J.A., Synthesis of porous biomass fly ash-based geopolymer spheres for efficient removal of methylene blue from wastewaters, *J. Clean. Prod.*, 207 (2019) 350-362.
- [19] Wekoye J.N., Wanyonyi W.C., Wangila P.T., Tonui M.K., Kinetic and equilibrium studies of Congo red dye adsorption on cabbage waste powder, *Environ. Chem. and Ecotoxicol.*, 2 (2020) 24-31.
- [20] Adeyemo A.A., Adeouye I.O., Bello O.S., Adsorption of dyes using different types of clay: a review, *Appl Water Sci.*, 7 (2017) 543-568.
- [21] Sharma P., Kaur H., Sharma M., Sahore V., A review on applicability of naturally available adsorbents for the removal of hazardous dyes from aqueous waste, *Environ. Monit. Assess.*, 183 (2011) 151-195.
- [22] Foo K.Y., Hameed B.H., An overview of dye removal via activated carbon adsorption process, *Desalin. Water Treat.*, 19 (2010) 255-274.
- [23] Jawada A. H., Abdulhameed A.S., Mesoporous Iraqi red kaolin clay as an efficient adsorbent for

- methylene blue dye: Adsorption kinetic, isotherm and mechanism study, *Surf. Interface.*, 18 (2020) 100422.
- [24] Kausar A., Iqbal M., Javeda A., Aftab K., Nazli Z.H., Bhatti H.N., Nouren S., Dyes adsorption using clay and modified clay, *A review J. Mol. Liq.*, 256 (2018) 395–407.
- [25] Karagozoglu B., Tasdemir M., Demirbas E., Kobya M., The adsorption of basic dye (Astrazon Blue FGRL) from aqueous solutions onto sepiolite, fly ash and apricot shell activated carbon: Kinetic and equilibrium studies, *J. Hazard. Mater.*, 147 (2007) 297-306.
- [26] Sulak M.T., Demirbas E., Kobya M., Removal of Astrazon yellow 7GL from aqueous solutions by adsorption onto wheat bran, *Bioresource Technol.*, 98 (2007) 2590-2598.
- [27] Chien S.H., Clayton W.R., Application of elovich equation to the kinetics of phosphate release and sorption in soils, *Soil Sci. Soc. Am. J.*, 44 (1980) 265-268.
- [28] Khan T.A., Khan E.A., Shahjahan, Removal of basic dyes from aqueous solution by adsorption onto binary iron-manganese oxide coated kaolinite, Non-linear isotherm and kinetics modeling, *Appl. Clay Sci.*, 107 (2015) 70-77.
- [29] Naeimi S., Faghihian H., Modification and magnetization of MOF (HKUST⁻¹) for removal of Sr²⁺ from aqueous solutions. Equilibrium, kinetic and thermodynamic modeling studies., *Sep. Sci. Technol.*, 52 (18) (2017) 2899-2908.
- [30] Cottet L., Almeida C.A.P., Naidek N., Viante M.F., Lopes M.C., Debacher N.A., Adsorption characteristics of montmorillonite clay modified with iron oxide with respect to methylene blue in aqueous media, *Appl. Clay Sci.*, 95 (2014) 25-31.
- [31] Salvestrini S., Leone V., Iovino P., Canzano S., Capasso S., Considerations about the correct evaluation of sorption thermodynamic parameters from equilibrium isotherms, *J. Chem. Thermodyn.*, 68 (2014) 310–316.
- [32] Es-sahbany H., Hsissou R., El Hachimi M.L., Allaoui M., Nkhili S., Elyoubi M.S., Investigation of the adsorption of heavy metals (Cu, Co, Ni and Pb) in treatment synthetic wastewater using natural clay as a potential adsorbent (Sale-Morocco), *Mater Today Proc.*, 2021 in press.
- [33] Mnasri-Ghnimi S., Frini-Srasra N., Removal of heavy metals from aqueous solutions by adsorption using single and mixed pillared clays, *Appl. Clay Sci.*, 179 (2019) 105151.
- [34] Zhou Q., Gao Q., Luo W., Yan C., Ji Z., Duan P., One-step synthesis of aminofunctionalized attapulgite clay nanoparticles adsorbent by hydrothermal carbonization of chitosan for removal of methylene blue from wastewater, *Colloid. Surf. A Physicochem. Eng. Asp.*, 470 (2015) 248–257.
- [35] Ahmad R., Mirza A., Synthesis of guar gum/bentonite a novel bionanocomposite: isotherms, kinetics and thermodynamic studies for the removal of Pb (II) and crystal violet dye, *J. Mol. Liq.*, 249 (2018) 805-814.
- [36] Kausar A., Bhatti H.N., Adsorptive removal of uranium from wastewater: a review, *J. Chem. Soc. Pak.*, 35 (2013) 1041-1052.
- [37] Chen Z., Wang T., Jin X., Chen Z., Megharaj M., Naidu R., Multifunctional kaolinite-supported nanoscale zero-valent iron used for the adsorption and degradation of crystal violet in aqueous solution, *J. Colloid Interf. Sci.*, 398 (2013) 59-66.
- [38] Ozcan A.S., Gok O., Ozcan A., Adsorption of lead(II) ions onto 8-hydroxy quinoline immobilized bentonite, *J. Hazard. Mater.*, 161 (2009) 499-509.
- [39] Khataee A.R., Vafaei F., Jannatkah M., Biosorption of three textile dyes from contaminated water by filamentous green algal *Spirogyra sp.*: kinetic, isotherm and thermodynamic studies, *Int. Biodeter. Biodegr.*, 83 (2013) 33-40.
- [40] Marungrueng K., Pavasant P., High performance biosorbent (*Caulerpa lentillifera*) for basic dye removal, *Bioresource Technol.*, 98 (2007) 1567-1572.



Effects of natural boron mineral on the essential oil ratio and components in medicinal sage (*Salvia officinalis* L.)

Hasan Basri KARAYEL^{1,*}

¹Dumlupınar University, Gediz Vocational School, Department of Medicinal and Aromatic Plants, Kütahya / TURKEY

Abstract

The effects of different boron doses (boron-free, pure boron, diluted in 1/2 and 1/8 ratios) on the ratio and quality of essential oil in medicinal sage (*Salvia officinalis* L.) during the years 2016 and 2017 were investigated. Field trials were conducted with the randomized block design in triplicates. The essential oil of *S. officinalis* L. was obtained by gas chromatography/mass spectrometry (GC-MS) with flame ionization detection (FID). The required measurement could not be taken at the pure dose application because the plants were damaged. In the analysis carried out on dry leaf, the main components of essential oil were found as follows: α -thujone 32.99%; 1,8-cineol 17.41% for the boron-free dose; viridiflorol 24.25%, manool 15.28% for the 1/2 boron dose, and lastly, α -thujone 32.31%, camphor 14.23% for the 1/8 boron dose. Some boron doses had a positive effect on the essential oil yield and essential oil components. In this study, different compounds were obtained with different boron dose applications. The dose to be recommended is the 1/8 boron dose since it has the minimum toxic effect on the plants and a positive effect on the essential oil yield and quality as general.

Article info

History:

Received: 01.11.2020

Accepted: 17.04.2021

Keywords:

Boron,
Medicinal sage,
Natural fertilizer,
Salvia,
Viridiflorol.

1. Introduction

The *Salvia* genus, which is commonly called sage, has approximately 900 species, which are naturally distributed in the world. Turkey is very rich in different types of sage and 89 *Salvia* species are naturally found in Turkey 46 of which are endemic [1]. Despite the development of medical science in the 20th century, the use of plants in traditional medicine has not lost its importance. Developed countries have focused more on herbal products. Natural remedies constitute a large part of drugs used in treatment. Natural source drugs constitute 60% of the total drug quantity in developed countries and 4% in developing countries [2]. The refractive indices of essential oils, which are lighter than water and optically active, are generally high. The interest in aromatherapy, which is considered a new field of medicine recently, has expanded the alternative uses of essential oils [3]. Essential oils that are considered medically valuable include α , β -thujone, 1,8-cineol, camphor and borneol. The essential oils of some sage species also reportedly contain thymol and carvacrol [4]. Essential oils have different uses. In addition to the use of essential oils in the perfume, food, medicine and cosmetics industries, their use in aromatherapy and agricultural production has increased the demand for essential oils. Recently,

essential oils have been used in agricultural research, animal husbandry and beekeeping [5]. Plants need fundamental macro and micronutrients for their normal development in their growth period. The nutrient stress, whether it may cause deficiency or toxicity, influences the development of the plant and may cause losses of yield and quality in agricultural plants [6]. The deficiency and toxicity range of boron is remarkably narrow. Fertilization may be the solution of the deficiency problem, while a set of procedures can be utilized to ameliorate soil boron toxicity. However, these approaches are costly and time-consuming, and they do not have permanent effects most of the time. Plant species and also the genotypes within species are highly different in terms of their boron requirements. So, a sort of soil boron which is accepted deficient for one crop may exhibit toxic effects on another [6]. In the agricultural sector, boron is used as fertilizers, insecticides and herbicides [7]. In a study on essential oil percentages, it was found that ecology and soil structure were affected by the development of the plant and the amount of essential oil [8]. A shortage of boron supply may lead to a set of biochemical, physiological and anatomic changes. Boron deficiency reduces male fertility by decreasing

*Corresponding author. e-mail address: kbasri23@hotmail.com

microsporogenesis, germination, and elongation of the pollen tube [9]. Boron is the only element which cannot be taken up from the soil as an ion. In conditions of sufficient supply, this element is transported by passive diffusion, and during this process, no protein catalysis and energy consumption are required. Passive diffusion was considered as the only mechanism of transport since the cell is extremely permeable to boron, characteristic patterns of flux along the transpiration stream, and accumulation in the tips of the leaves [10 -11].

This study is a type of comparison of essential oil composition of *S. officinalis* L. species which grow in the Central Aegean Region and also an evaluation of essential oils. Accordingly, it was aimed to compare the essential oils of *S. officinalis* L. species according to different boron doses and to determine the effect of boron doses on essential oil ratio and essential oil components. It is also aimed to increase the product range and contribute to the pharmaceutical and food sector for the people of the region.

2. Materials and Methods

2.1. Study site and experimental material

This study was conducted in the application area of the Dumlupinar University (74.74°E, 29.24°N; altitude 804 m asl) during the years 2016–2017. Seed germination lasted 20–25 days. The rooted seedlings began to be transferred to the farm in April 2016. Soil analysis of the trial area in Kutahya is given in Table 1.

2.2. Preparation of boron extracts

The powdered boron mineral was weighed in 20 g and then shaken in 100 ml pure water. Subsequently, it was homogenized for five minutes for precipitation. Then, the homogenate boron was centrifuged at 3500 rpm for five minutes. The residue was weighed as 0.0260 g from a mixture of 100 ml water and 20 g powdered boron. The supernatant was stored in a refrigerator. This extract was then used either in absolute form or diluted with pure water at ratios of 1/2 and 1/8 (Table 2) [12].

Table 1: Pre-sowing chemical analysis of experimental soil

Soil variables	Values	Status
Potassium (K ₂ O; kg ha ⁻¹)	20.01	Medium
Phosphorus (P ₂ O ₅ ; kg ha ⁻¹)	6.23	Medium
Lime (%)	4.03	Limy
Organic matter (%)	0.78	Very Little
Total salts (%)	0.003	Salt-free
pH	7.14	Neutral
Saturation (%)	53.3	Clay and Loam

Table 2: Chemical analysis of pure boron mineral

Nutrient/element	Ca	K	Mg	Na	Fe	Mn	Zn	Cu	Ni	Cd	Cr	Co
Units	mg kg ⁻¹	mg kg ⁻¹	mg kg ⁻¹	mg kg ⁻¹	mg kg ⁻¹	mg kg ⁻¹	mg kg ⁻¹	µg kg ⁻¹	µg kg ⁻¹	µg kg ⁻¹	µg kg ⁻¹	µg kg ⁻¹
Values	108.9	19.66	33.22	58.68	0.680	0.042	0.10	<10	<10	<10	0.034	<10

Ca: calcium, K: potassium, Mg: magnesium, Na: sodium, Fe: iron, Mn: manganese, Zn: zinc, Cu: copper, Ni: nickel, Cd: cadmium, Cr: chromium, Co: cobalt

2.3. Experimental details

In the experiment, four different boron doses [boron-free, pure boron (80 L ha⁻¹), and boron diluted in 1/2 and 1/8 ratios] were applied to the medicinal sage plant. After the plant reached 20 cm in length, the prepared boron mineral was supplied in all treatments; it was administered as 80 liters ha⁻¹ after 1 month. In both years, experiment was conducted with a randomized complete block design in triplicates. The dimensions of each planting area were 40 cm × 30 cm. A total of 72 plants were planted by 24 plants per plot. There were 3 rows of plants in each plot, and each plot had an area of 1.6 m × 3 m. The plants were watered according to their water needs. New ones were planted in place of the dried plants, and there were 72 plants in each plot. Experiment was irrigated considering rainfall, air temperature, and humidity in the soil to save plants from moisture stress. No other additives or fertilizer were applied to the plant neither before nor during the planting session except for boron mineral. The weeds were observed and they were cleared manually.

2.4. Data recorded

Observations and measurements were made on leaf samples obtained from 9 plants labeled in 72 healthy plants in each plot. Since the first year was the plantation year and the plant growth was too low, no measurement could be taken and no doses were applied. In the second year, two harvests were made, and the beginning of flowering was preferred as the harvest time. After the second week, the plants were watered once a week.

2.5. Isolation of essential oil

The samples were diluted 1:100 with hexane for analysis. At the beginning of the trial essential oil analysis, 20 g of dry material was weighed and taken in a 500 ml flask. The samples were diluted with 1% hexane and injected into gas Chromatography in 1 µl with 40:1 split ratios. Agilent 7890 A Capillary columns (HP Innova x Capillary: 60.0 m × 0.25 mm × 0.25 µm) were used to separate the components. The scan range (m/z) for the mass detector was 35-450 atomic mass units, and the electron bombardment ionization energy was 70 eV. The data of the WILEY and OIL ADAMS libraries were taken as a basis in the diagnosis of the components of the essential oil. The data from the FID detector were used for the essential oil component ratios [13].

2.6. Determination of essential oil composition by GC-MS

The samples were diluted with 1% hexane and injected with 40:1 split ratio to gas chromatography (Agilent 7890 A). Capillary columns were used to separate the components. The column was split into two fractions at a ratio of 1:1 using a splitter to the FID and MS detector (Agilent 5975 °C). In the analysis, helium was used as the carrier gas at a flow rate of 0.8 ml min⁻¹. The scan range (m/z) for the mass detector was 35–450 atomic mass units, and the electron bombardment ionization energy was 70 eV. The data of the FID detector were used for determining essential oil component ratios [14].

2.7. Statistical analysis

Two harvests for aerial parts of plants at flowering periods were made on 28.05.2017 and 02.09.2017 in the second year. Statistical analysis of the data obtained in the experiment was performed using the JUMP package program according to the random blocks experiment pattern. The significance levels of the investigated features were determined by random blocks experimental model and by variance analysis. The differences between meaningful applications are grouped according to the calculated LSD value (Table 3).

3. Results and Discussion

Different boron doses (0, Pure dose, 1/2 boron dose, 1/8 boron dose) were applied to the type of medical sage (*Salvia officinalis* L.) examined in this study. While natural boron mineral applied without extraction has a toxic effect on the plant causing the plant to dry out, extracted pure boron doses also has the same effect on the plant. However, no complete drying or death occurred in the plant in 1/2 and 1/8 boron dose applications. According to analysis of variance, the effects of applications on yield and essential oil parameters were found statistically significant (Table 3). The medical sage species started flowering by the date of 20 May 2017, and till the end of the month, it arrived at the harvest period by completing 50% flowering. Considering the flowering dates of the plant based on the doses, it was determined that the boron-free dose reached the first and complete flowering dates earlier than the other doses. The plants under the treatment of the 1/8 boron dose started flowering earlier, while those lower than 1/2 dose started later. In this context, in our study, the boron-free dose and the 1/8 boron dose provided more than 1.5% essential oil contents (Table 3). The lowest essential oil ratio was 0.67% in the 1/2 boron dose application, while the highest one was 2.05% in the boron-free dose

application (Table 3). According to the GC-FID/MS analyses on the boron doses (boron free dose, 1/2 boron dose, 1/8 boron dose), the essential oils of medical sage contained respectively 17, 16, 25 different components.

The ratios of the total essential oil components in dry leaf for the boron-free dose, 1/2 boron dose and 1/8 boron dose were respectively 97.78%, 98.94% and 99.07% (Table 3). Among these components, (boron free dose, 1/2 boron dose, 1/8 boron dose) especially α -thujone, camphor, 1,8-sineol, manool and

viridiflorol were compounds found at high ratios (Figure 1). Viridiflorol, which was one of the main components obtained in the 1/2 boron dose application, was found as 24.25% and higher than the values obtained in all other dose applications. Natural factors may have a positive or negative effect on essential oils. The viridiflorol component has *in vitro* anti-inflammatory, antioxidant, anti-tuberculosis effects [15]. If the viridiflorol component is required pharmacologically, the 1/2 boron dose is recommended.

Table 3. Effect of different doses of boron mineral on essential oil components (%) obtained from the leaves of *S. officinalis* L.

Essential oil components (%)	RI	RT	Boron-free	1/2 of pure boron mineral	1/8 of pure boron mineral
Cis-salvene	944	8.90	0.72±0.029b	-	0.82±0.016a
α -pinene	977	11.42	4.40±0.101b	2.31 ±0.197c	5.53±0.013a
Camphene	1026	13.13	4.65±0.178b	3.72±0.099c	6.82±0.02a
β -pinene	1068	14.85	3.30±0.068c	3.82±0.017a	3.52±0.013b
1,8-cineol	1171	19.39	17.41±0.625a	9.2±0.223b	2.33±0.013c
α -thujone	1383	28.23	32.99±0.467a	4.23±0.085c	32.31±0.026b
β -thujone	1400	28.87	6.35±0.219b	0.44±0.012c	7.74±0.019a
Camphor	1477	31.54	10.22±0.424b	8.89±0.024c	14.23±0.021a
Bornyl-acetate	1477	33.39	2.32±0.146c	4.80±0.024a	2.94±0.030b
β -caryophyllene	1552	34.00	1.62±0.225b	5.24±0.039a	1.62±0.028b
α -humulene	1623	36.23	4.30±0.187a	4.08±0.026b	2.07±0.025c
Borneol	1646	36.92	1.74±0.030c	5.17±0.024a	4.25±0.023b
Humulene epoxide II	1994	46.40	0.29±0.039c	2.75±0.028a	0.65±0.013b
Viridiflorol	2026	47.20	3.17±0.109c	24.25±0.037a	4.83±0.017b
Manool	2589	64.87	0.77±0.049c	15.28±0.057a	4.18±0.022b
Limonene	1160	18.89	1.36±0.115b	0.94±0.014c	1.92±0.014a
Tricyclene	958	10.92	-	-	0.31±0.023a
Myrcene	1123	17.24	-	-	1.04±0.021a
α -terpinene	1141	18.03	-	-	0.30±0.019a
Cis- β -ocimene	1192	20.36	-	-	0.34±0.045a
γ -terpinene	1204	20.89	-	-	0.37±0.011a
P-cymene	1230	21.99	-	-	0.72±0.019a
Terpinolene	1241	22.46	-	-	0.26±0.016a
Caryophyllene oxide	1939	45.01	-	3.82±0.042a	0.25±0.025b
β -myrcene	1123	16.2	2.17±0.071a	-	-
Linalool	1490	31.97	-	-	0.26±0.023a
Total (%)			97.78	98.94	99.07
Essential oil rate (%)			2.05a	0.67c	1.54b

Means±standard deviation with different letters are significantly different from each other $p \leq 0.01$
The value of the compounds with no value is zero

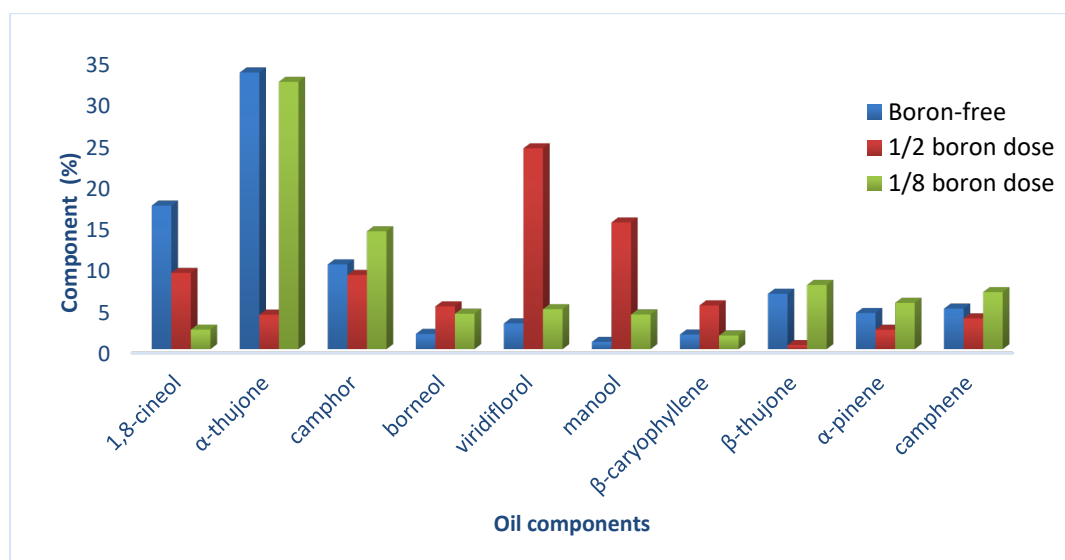


Figure 1. Changes in significant components of essential oil obtained from the leaves of *Salvia officinalis* L. species according to (%)

Since natural boron mineral which was used in this study is rich in Ca, it had a positive effect on *Salvia officinalis* L. species as expected (Table 2). Consequently, it is obvious that Ca along with other elements, is a crucial nutrient for *Salvia species*. The cis-salvene component was a common essential oil component in boron-free and 1/8 dose applications, but no cis-salvene component was obtained in the 1/2 dose application. While the β-myrcene component was found in the boron-free application, this component was not obtained in the 1/2 and 1/8 dose applications (Table 3). The highest number of components were obtained as a result of the 1/8 dose application with 25 components. Moreover, the compounds “linalool, tricyclene, myrcene, α-terpinene, cis-β-ocimene, γ-terpinene, p-cymene, terpinolene, and caryophyllene oxide” were obtained only in the 1/8 dose application. As the boron dose was diluted as in the essential oil ratio, the essential oil components increased, and different components were obtained (Table 3). Viridiflorol, which was one of the main components obtained in the 1/2 boron dose application, was found as 24.25% and higher than the values obtained in all applications (Table 3). Consequently, it was projected in this study that boron doses may be assessed as a priority in medical sage species breeding with drug-leaf yield and essential oil quality. The essential oil of medical sage is mainly composed of monoterpenes consisting of bicyclic, monocyclic and acyclic carbon frames. However, it was reported that thujones may be toxic on both brain and liver cells in humans, and especially α-thujone is more toxic in comparison to β-thujone [16 -17]. The essential oil component ranges in *S. officinalis* L. which is known as a rich source of essential oil with prevalent usage in folk medicine were

found as follows: α-thujone (21.43%–40.10%), β-thujone (2.06%–7.41%), camphor (11.31%–37.67%), 1,8-cineol (4.47%–9.17%), camphene (1.89%–7.04%), viridiflorol (2.14%–5.56%), β-caryophyllene (1.06%–5.59%). It was reported that some populations had chemotypes of the camphor type, while some others had those of the thujone type [18]. The effect of different water and nitrogen applications on some yield parameters and antioxidant activity on sage (*Salvia officinalis* L. var.) was investigated in a study. The highest essential oil ratio was obtained from the S3 water dose as 2.07%. The main component in the essential oils recovered by both experiments were α+β thujone showing a large variation. Considering the N fertilization combined with the S2 irrigation had positive effect on the characteristics measured [19]. Some researchers studied the effects of boron fertilization on chemical composition, of *Arnica montana* L. and *A. chamissonis* L. It was determined that essential oil contents ranged between 0.174% and 0.200%, between 0.158% and 0.188%, respectively [20]. In another study, the main components of the essential oil of *S. officinalis* L. found as follows: cis-thujone (19.8%–42.5%), manool (3.6%–15.1%), viridiflorol (3.1%–12.8%), 1,8-cineol (2.8%–13.8%), camphor (1.4%–22.1%), borneol (0.9%–4.8%) whereas it was reported that some populations had chemo-types of the camphor type, while some others had those of the thujone type [21]. These findings coincide with the results in this study. In terms of the boron doses and essential oil components in our study, this situation indicates that some medical sage plants contains different chemo-types. For example, high camphor at the 1/8 boron dose and low α-thujone at the 1/2 boron dose were significant chemo-types (Table 3).

Therefore, studies in this field and specifically on this species, particularly focusing on the use of natural boron mineral, would be necessary and invaluable.

4. Conclusions

The following inferences were made based on the results obtained from this study. In terms of essential oil yield, the most effective dose was the 1/8 boron dose. In general, to obtain different essential oil ratios and different essential oil components in a plant, either different parts of the plant are used, or a genotype-environment study is necessary. On the other hand, with this study, it was determined that we could obtain some important components with the 1/2 and 1/8 boron doses without needing studies conducted at different locations (Table 3). In this context, in our study, the 1/8 boron dose provided more than 1.5% essential oil contents (Table 3). The dose to be recommended is the 1/8 boron dose since it has the minimum toxic effect on the plants and a positive effect on the essential oil yield and quality as general.

Conflicts of Interest

No conflict of interest

References

- [1] Ipek A., Effects of nitrogen fertilization on herb yield and some characteristics of sage (*Salvia Officinalis*) lines, Ph.D. thesis, Ankara University, Institute of Science and Technology, (2007).
- [2] Jain S., Shrivastava S., Nayak S. and Sumbhate S., Phcog mag: plant review, recent trends in Curcuma longa, *Linn. Pharm Rev.*, 1 (2007) 119–128.
- [3] Kılıc A., Essential oil production methods, *Bartın Faculty For J.*, 10 (2008) 37-45.
- [4] Zeybek U., Zeybek N., Pharmaceutical botany [closed seed plants (angiospermae) systematics and important substances], Ege University, Faculty of Pharmacy Publications, (3) (2002).
- [5] Baser K.H.C., Ozek T., Yıldız B., Bahcecioglu Z., Tumen G., Composition of the essential oil of *Nepeta fissa* CA Meyer., *Journal of Essential Oil Research*, 12 (2000) 27-28.
- [6] Brdar-Jokanovic M., Boron toxicity and deficiency in agricultural plants, *Int J Mol Sci.*, 21 (2020) 1424.
- [7] Yenmez N., The importance of boron minerals for Turkey as a strategic mineral., *Istanbul University, Faculty of Letters, Department of Geography. J Geography.*, 19 (2009) 59–94.
- [8] Karık U., Some yield and quality characteristics of anatolian sage (*Salvia fruticosa* Mill.) populations in Aegean and Western mediterranean flora, *J. Tekirdag Agriculture Faculty*, 12 (2015) 32–42.
- [9] Cheng C., Rerkasem B., Effects of boron on pollen viability in wheat, *Plant and Soil Vol.*, 155 (1993) 313-315.
- [10] Nable R.O., Resistance to boron toxicity amongst several barley and wheat cultivars: a preliminary examination of the resistance mechanism, *Plant Soil.*, 112 (1988) 45-52.
- [11] Marschner H., Mineral nutrition of higher plants. 2nd ed., New York: Academic Press, (1995) 85-131.
- [12] Karayel H.B., The Effects of walnut leaf extracts and juglone on vegetative and generative growth of muskmelon, Ph.D.Thesis, Dumlupinar University Graduate School of Natural and Applied Sciences Graduate Program in Biology, (2006).
- [13] Tabanca N., Demirci B., Ozek T., Kirimer N., Baser K.H.C., Bedir E., Ikhlas A.K., David E.W., Gas chromatographic–massspectrometric analysis of essential oils from *Pimpinella* species gathered from Central and Northern Turkey, *J Chromat A.*, 1117 (2006) 194–205.
- [14] Ozek T., Tabanca N., Demirci F., David E., Wedgea D.E., Husnu C.B., Enantiomeric distribution of some linalool containing essential oils and their biological activities, *Records Nat Prod.*, 4 (2010) 180–192.
- [15] Trevizan L.N.F., Nascimento K.F.D., Santos J.A., Kassuya C.A.L., Cardoso C.A.L., Vieira M.D.C., Moreira F.M.F., Croda J., Formagio A.S.N., Viridiflrolun antiinflamatuvar, antioksidan and anti-Mycobacterium tuberculosis activity: The main structure of *Allophylus edulis* (A.S.-Hil., A. Juss. Cambess.) Radlk., *J. Ethnopharmacol*, Nov., 4.192 (2016) 510-515.
- [16] Hold K.M., Sirisoma N.S., Ikeda T., Narahashi T., Casida J.E., α -Thujone (the active component of absinthe): γ -Aminobutyric acid type A receptor modulation and metabolic detoxification, *Natl Acad Sci USA.*, 97 (2000) 3826–3831.
- [17] Baydar H., Tuglu U., Agronomic and technological properties of B-clones developed by

- clonal selection of common sage (*Salvia officinalis* L.), *J Nat Appl Sci.*, 23 (2019) 452-456.
- [18] Raina A.P., Negi K.S., Dutta M., Variability in essential oil composition of sage (*Salvia officinalis* L.) grown under North Western Himalayan Region of India, *J Med Plant Res.*, 7 (2013) 683–688.
- [19] Sonmez C., Bayram E., The influence of different water and nitrogen applications on some yield parameters and antioxidant activity in sage (*Salvia officinalis* L.), *Turk. J. Field Crops.*, 22(1) (2017) 96-103.
- [20] Sugier D., Sugier P., Kowalski R., Kolodziej B., Olesinska K., Foliar boron fertilization as factor affecting the essential oil content and yield of oil components from flower heads of *Arnica montana* L. and *Arnica chamissonis* L. cultivated for industry, *Ind Crops Prod.*, 109 (2017) 587-597.
- [21] Verma R.S., Padalia R.C., and Chauhan A., Harvesting season and plant part dependent variations in the essential oil composition of *Salvia officinalis* L. grown in northern India, *J. Herbal Med.*, 5 (2015) 165–171.



Ultrafiltration-Based extraction of Ibuprofen from human plasma samples and HPLC analysis: developing an innovative bioanalytical analysis method

Yasin SENOL¹ , Aysegul DOGAN^{1,*} , Mustafa ÇELEBİER¹

¹Hacettepe University, Faculty of Pharmacy, Department of Analytical Chemistry, Ankara/ TURKEY

Abstract

Some commercially available scientific products for ultrafiltration are readily available and have been used for a long time, especially in environmental sciences, life sciences and analysis of active ingredients from plants. Recent studies of metabolomics discuss the advantage and disadvantage of ultrafiltration versus protein precipitation and solid phase extraction. However, ultrafiltration techniques are rarely used in pharmaceutical analysis, even though they have advantages over solid phase extraction, such as easy to apply and no buffer preparations. The aim of this study is to develop a simple and innovative analysis technique for IBU determination from human plasma samples by ultrafiltration-based extraction in a pharmaceutical analysis. The prepared samples were analyzed using HPLC system equipped with C18 Column (100 x 4.6 mm, 3.5 μ m). The flow rate was set to 1.0 mL min⁻¹ while using isocratic elution with the mobile phase of [acetonitrile: phosphate buffer (pH 3.0, 15 mM) (56:44 v/v)] solution. Injection volume was 20 μ L and UV detection was performed at 220 nm wavelength. The developed method was validated according to FDA Bioanalytical Guidelines and found accurate, precise, sensitive, selective and efficient with the high recovery values samples.

Article info

History:

Received:12.12.2020

Accepted:17.04.2021

Keywords:

Ibuprofen,
Ultrafiltration,
HPLC bioanalytical
analysis,
Sample preparation.

1. Introduction

Nonsteroidal anti-inflammatory drugs (NSAIDs) are known with their analgesic, anti-inflammatory and antipyretic properties [1]. NSAIDs are effective within the acute treatment of pain, as well as headache, dysmenorrhea and surgical pain [2]. The effect of NSAIDs in cancer treatment or prevention are attracting attention recently [3-7]. In a significant study conducted, it was shown that ibuprofen (IBU) is effectively used for the treatment of chronic cancer pain and provides a rise in physiological state in conjunction with a decrease within the use of narcotics in the treatment [8]. Although NSAIDs have restricted use because of their emerging side effects, they have been studied for an extended time within the pharmacological treatment of cancer pain [9-12]. Pharmacodynamic and pharmacokinetic interactions associated with the employment of NSAIDs are still under investigation [2-4]. Although it has a bright profile in terms of safety and efficacy, Ibuprofen also has potential side effects such as acute renal dysfunction, allergic reactions, gastrointestinal

bleeding, and inhibition of platelet aggregation. [13]. In the light of all this data, it can be concluded that the pharmacokinetic and pharmacodynamic profiles of NSAIDs will be the subject of research for a long time.

Ibuprofen is referred as a 2 arylpropionic acid (2-APA) category non-steroidal anti-inflammatory (NSAID) drug [14]. Its chemical structure is shown in Figure 1. The solubility and dissolution rate of their enantiomers and their racemate are highly dependent on the temperature and pH of the solvent [14, 15]. Ibuprofen is often used for the treatment of rheumatoid arthritis, osteoarthritis, pain, and fever. According to its pharmaceutical formulation, ibuprofen is absorbed from the gastrointestinal tract (GI) in about 1-2 hours [14]. Absorption is rapid and complete when given orally. The drug is highly concentrated to plasma albumin [16].

*Corresponding author. e-mail address: ayseguld@hacettepe.edu.tr
<http://dergipark.gov.tr/csj> ©2021 Faculty of Science, Sivas Cumhuriyet University

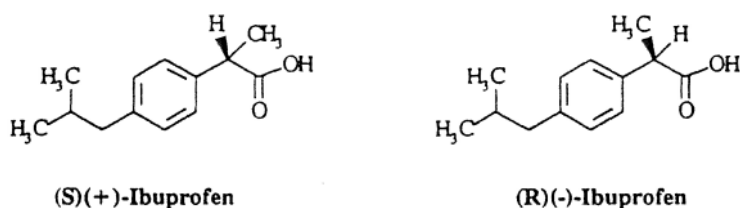


Figure 1. Chemical structure of the R (-) and S (-) enantiomers of ibuprofen [3].

Of all the biofluids (blood, urine, saliva, sweat), whole blood is the richest in information as well as the most complex sample matrix. Blood contains ~ 55% aqueous fraction (plasma) and ~ 45% solids. Although blood is the primary sample in most clinical chemistry-based research, it is first converted into plasma or serum due to the lack of current sample preparation technology that can directly process whole blood [17].

There is an analytical method in the literature based on high performance liquid chromatography (HPLC) linked to a micro-extraction packed sorbent (MEPS) and photodiode array (PDA) detector to simultaneously measure multiple nonsteroidal anti-inflammatory drugs (NSAIDs) and fluoroquinolones (FLQs). It is emphasized that this method may be a suitable tool to simultaneously detect a possible drug association in human biological samples [18].

Ultrafiltration is a selective separation process where membranes with 1-100 nm pore size are used for extracting macromolecules such as proteins. There are many factors influencing this technique like solute size, membrane pore size, the aim of the separation, and instrumental configurations. This technique is used in many areas like pharmaceutical analyses in micromolar quantity and wastewater treatment plants in micromolar quantity. These membranes also found applications in food and biotechnology. However, ultrafiltration techniques have not been used very often in pharmaceutical analysis, even though they are more advantageous over solid phase extraction, such as easy to apply and no buffer preparations [19]. The aim of this study is to develop and validate a simple and innovative analysis technique for IBU determination from human plasma samples by ultrafiltration-based extraction in a pharmaceutical analysis.

2. Materials and Methods

2.1. Apparatus

LC system Shimadzu HPLC was utilized for the analysis. Cold trap (-105 °C) equipped CentriVap centrifugal vacuum concentrator was purchased from Labconco, USA. Hermle Z 233 M-2 (Hermle, Germany) centrifugator and Ika Vortex Genius (Germany) were used in sample preparation. Microcon® centrifuge filters (500 µL, <3 kD) for ultrafiltration were purchased from EMD Millipore (Darmstadt, Germany).

2.2. Chemicals

IBU standard solution was obtained from Gen Ilac's INTRAFEN (100 mg mL⁻¹) preparation. Naproxen sodium (NS, purity > 98%) internal standard solution (was obtained from Sigma-Aldrich (St Louis, USA). Acetonitrile and methanol of analytical grade and potassium phosphate dibasic were purchased from Merck (Darmstadt, Germany). All solutions were prepared using ultra pure water produced with the Barnstead Nanopure™ (Thermo Scientific).

2.3. Preparing mobile phase buffer of HPLC analysis

2.61 g of potassium dihydrogenphosphate (KH₂PO₄) was dissolved in 1000 mL water to prepare 15.0 mM phosphate buffer and the pH set to 3.0 using o-phosphoric acid.

2.4. Chromatographic conditions

Waters XSELECT HSS C18 column (100 x 4.6 mm, 3.5 µm) was used for separation. The flow rate was set to 1.0 mL min⁻¹ in isocratic elution mode using acetonitrile: phosphate buffer (pH 3.0, 15 mM) (56:44 v/v) as the mobile phase. 20 µL of injection volume was set and the analysis were recorded 220 nm wavelength.

2.5. Ultrafiltration procedure

The following steps were applied for sample preparation with ultrafiltration process:

- 1) Plasma samples (250 µL) were added into eppendorf tubes (1.5 mL) with methanol (1000 µL) to precipitate the proteins.
 - 2) Tubes of first stage vortexed for 30 seconds and then centrifuged at 15,000 rpm for 10 minutes.
 - 3) 500 µL of supernatants were put into ultrafiltration centrifuge tubes and centrifuged at 15,000 rpm for 1 hour.
 - 4) 250 µL of the filtrate under the filter was taken into eppendorf tubes (1.5 mL) and centrifuged in vacuum at 24 ° C for 24 hours.
 - 5) 250 µL of mobile phase was added to each tube and the tubes were vortexed for 30 seconds and the supernatants transferred to HPLC bottles.
- The ultrafiltration procedure is presented in Figure 2.

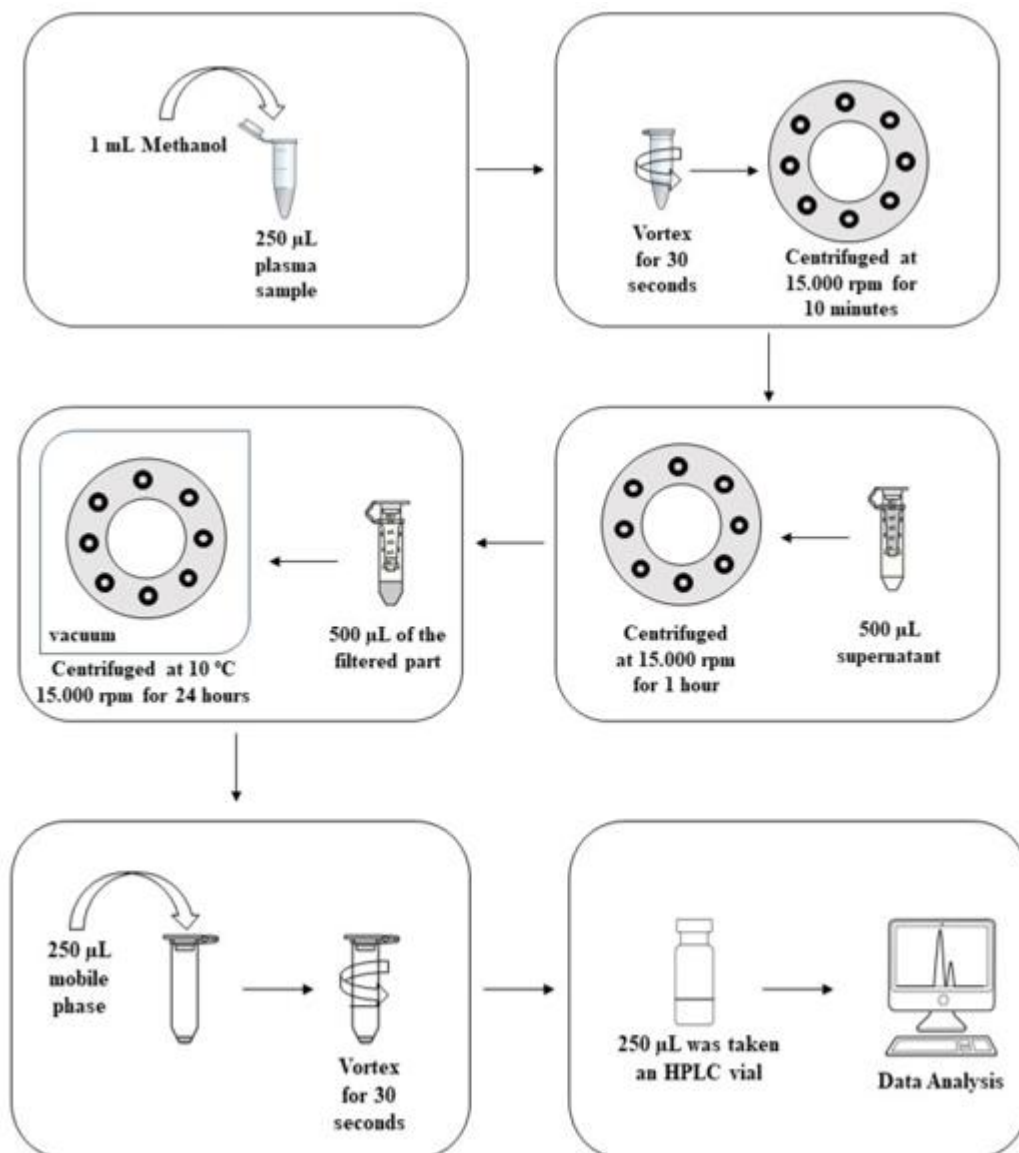


Figure 2. Schematic presentation of ultrafiltration procedure

2.6. Standard stock solutions

IBU (2000 µg mL⁻¹) standard stock solutions and NS (1000 µg mL⁻¹) were prepared in Milli-Q water. Both of these standard solutions were kept in 4°C during the analysis and freshly prepared twice in a week. Appropriate dilution was applied by using

micropipettes to prepare calibration standards and sample solutions.

2.7. Calibration curve construction

Calibration curve solutions were prepared with ultrafiltration procedure using spiked plasma samples.

IBU standard stock solution was diluted to 2, 20 and 160 $\mu\text{g mL}^{-1}$. NS standard stock solution was diluted to 25 $\mu\text{g mL}^{-1}$. These solutions were put into the HPLC vials containing extracted blank plasma samples to prepare the standard solutions including 0.25, 0.5, 1.0, 2.0, 4.0, 16.0, 32.0, 64.0 $\mu\text{g mL}^{-1}$ IBU and 4 $\mu\text{g mL}^{-1}$ NS as an internal standard. The final volume was added upto 250 μL by the mobile phase. The injected plasma standards peak areas of IBU to NS ratios were used in construction of calibration curve against concentration.

2.8. Recovery studies

Samples were prepared triplicate in concentrations of 4.0, 16.0 and 64.0 $\mu\text{g mL}^{-1}$ IBU and 4 $\mu\text{g mL}^{-1}$ NS as internal standard in plasma. The mobile phase was added to fill the final volume to 250 μL after the ultrafiltration procedure. The triple-replicate peak area ratio results for this group were compared on each concentration level.

2.9. Preparation of IBU spiked plasma samples

Plasma samples containing 20.00 $\mu\text{g mL}^{-1}$ IBU and 4 $\mu\text{g mL}^{-1}$ NS were subjected to ultrafiltration. The

spiked samples (n=6) were analyzed by the calibration equation and the results were statistically evaluated by MS Excel.

2.10. Analytical method validation

Validation of the developed method was performed based on the FDA guidelines in terms of sensitivity, precision, trueness and selectivity [20].

3. Results and Discussion

3.1. Method optimization

According to previous studies and some experiments [18, 21-23], it was agreed to use acetonitrile-potassium phosphate buffer (pH: 3.0) and its mixture (56:44, v/v) as the mobile phase. A C18 column [Waters XSELECT HSS C18 (100 x 4.6 mm, 3.5 μm), PN: 186004767 SN: 01113431413401] was used for analysis. The water-soluble plasma interference was found to be quickly decomposed by dead volume, and then IBU was separated from the baseline under specified experimental conditions.

Table 1. System suitability parameters of IBU for the proposed method (n = 6)

	Found	Requirements
Injection repeatability (RSD of IBU _t)	0.9 %	< 1%
Capacity factor (k')	4.73	> 2
Efficiency (N)	7851	> 2000
Tailing Factor	1.06	< 2
Resolution	4.75	> 1.5

Mobile phase optimisation ended up with acetonitrile: potassium phosphate buffer (pH 3.0, 15 mM) (56:44, v/v). It was observed that run time of the analysis was less than 10.0 minutes. Chromatograms of calibration standards, blank, added sample and standard solutions are given in Figure 3. The calibration standards prepared in the mobile phase and stored at ambient temperature (24 - 28 °C). These solutions were then injected 24 hours later to check the stability.

There was no difference observed between the peak areas compared to previous injections. This process was applied three times for 20.0 $\mu\text{g mL}^{-1}$ IBU calibration standard. The system compatibility and injection stability of the developed HPLC method thus proved. The system suitability of method meets the requirements and the prepared solutions can be injected within 24 hours when they are kept in the automatic sampler (Table 1).

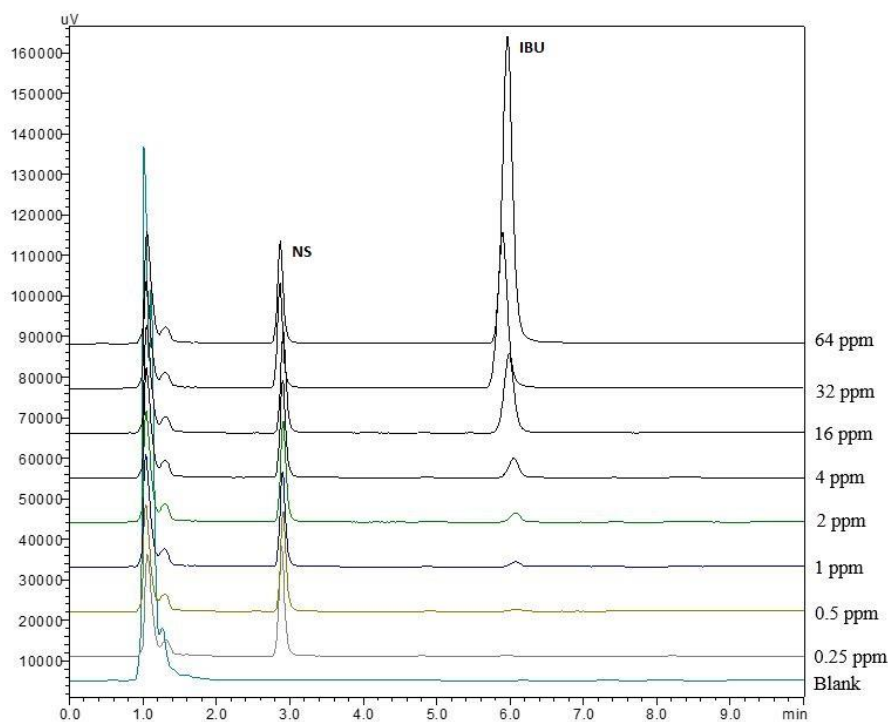


Figure 3. Chromatograms of calibration samples (0.25 – 64.0 $\mu\text{g mL}^{-1}$ IBU). Experimental conditions: mobile phase: acetonitrile: potassium phosphate buffer (pH 3.0, 15 mM) (56:44 v/v), flow rate: 1 mL min^{-1} ; injection volume: 20 mL, detection wavelength: 220 nm, NS: 2.5 $\mu\text{g mL}^{-1}$

3.2. Method validation

3.2.1. Linearity and sensitivity of the developed method

The linearity of the analysis is a measure of the acquisition of test results directly proportional to the analyte concentration in the sample [19]. The calibration curve was constructed between 0.25 and 64.0 $\mu\text{g mL}^{-1}$ where

the method was linear. Sensitivity values of the developed method were calculated from the following equations.[24].

The linearity and sensitivity findings of the established technique are summarized in Table 2.

LOQ (Limit of Quantification) and LOD (Limit of Detection) values of PCA were calculated due to the following equations (Table 4).

$$\text{LOD} = (3.3 \times \text{standard deviation of the response})/\text{slope of the calibration curve} \quad (1)$$

$$\text{LOQ} = (10 \times \text{standard deviation of the response})/\text{slope of the calibration curve} \quad (2)$$

Table 2. Linearity and sensitivity of the developed method (n=6)

Regression equation	$y = 0.0851x + 0.0125$
Standard error of intercept	0.0393
Standard error of slope	0.0204
Regression coefficient (R^2)	0.9993
Range ($\mu\text{g mL}^{-1}$)	0.25 - 64
Number of data points	8
LOD ($\mu\text{g mL}^{-1}$)*	0.15
LOQ ($\mu\text{g mL}^{-1}$)*	0.25

* LOQ: Limit of quantification, LOD: Limit of detection

3.2.2. Trueness and precision of the developed method

Three different IBU concentrations in the linear range were analyzed on three consecutive days (inter-day studies) and three times on the same day (intra-studies) (Table 3). Duplicate injections were performed. **Trueness** of the method is explained by the relative error (RE) values, while precision was stated with

relative standard deviation values (RSD). The RE values in the intra-day and inter-day studies were between 3.61 and 6.07, respectively. The relative standard deviations of the intra-day and inter-day studies were between 2.54 and 9.98, respectively. The findings showed that the analysis method developed was accurate and precise (RSD<15%)

Table 3. Precision and trueness of the proposed method (n = 6)

Added ($\mu\text{g mL}^{-1}$)	Intra- day			Inter- day		
	Found ($\mu\text{g mL}^{-1}$)	Precision (RSD %)	Trueness (Bias %)	Found ($\mu\text{g mL}^{-1}$)	Precision (RSD %)	Trueness (Bias %)
4.00	3.87 ± 0.210	6.83	-3.07	4.08 ± 0.13	2.54	2.05
16.00	15.84 ± 0.353	4.72	- 0.99	16.97 ± 0.31	3.39	6.07
64.00	64.08 ± 0.572	3.07	0.13	64.30 ± 0.58	3.10	0.47

Found: Mean \pm standard error ($\bar{X} \pm \text{SE}$), RSD % Relative standard deviation, Bias %: [(Found-Added)/Added] x 100

3.2.3. Selectivity of the developed method

The selectivity of the analysis is the ability of to the system to recognize a specific compound within the analyzed matrices. Therefore, the blank, plasma-spiked IBU and standard IBU chromatograms were compared. (Figure 4). IBU and NS were separated at retention times of 5.90 and 2.81 minutes, respectively without any interference from matrix components.

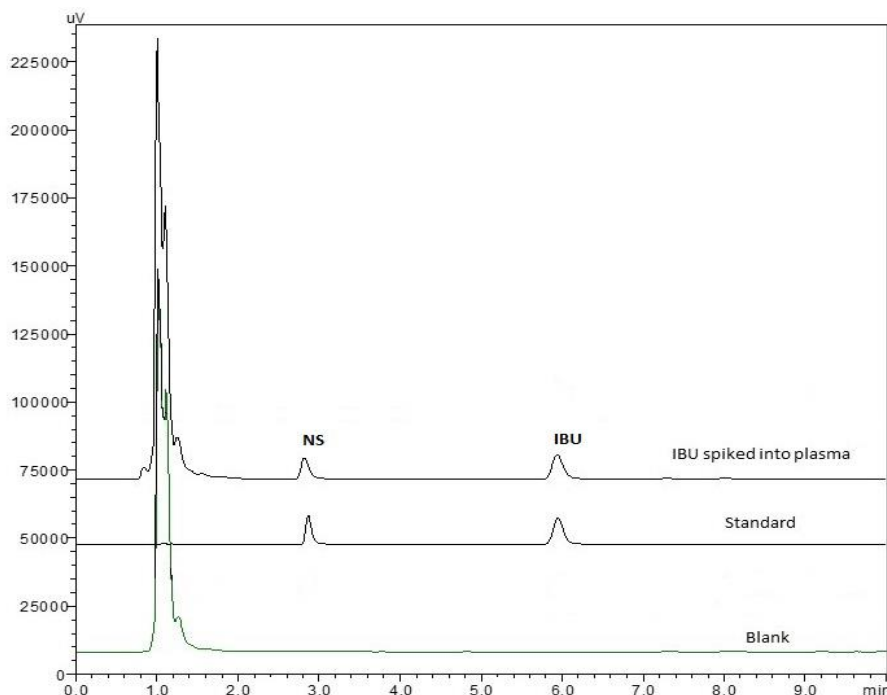


Figure 4. Chromatograms of blank plasma sample, standard sample and spiked in plasma under indicated experimental conditions (IBU:20 $\mu\text{g mL}^{-1}$ and NS:2.5 $\mu\text{g mL}^{-1}$)

3.2.4. Recovery of the developed method

For 4.0, 16.0 and 64.0 $\mu\text{g mL}^{-1}$ concentrations of plasma samples, as defined in the experimental section, the recovery of the established analytical method was investigated. The developed method was applied to three different concentration levels in the linearity range for six times. For IBU, the recoveries from plasma samples of 4.0, 16.0 and 64.0 $\mu\text{g / mL}$ in concentration, respectively, were 100.05% (SD: 0.10), 102.01% (SD: 0.57) and 100.19% (SD: 2.00) (SD: Standard deviation, n = 6). The results show that the developed method for IBU analysis using

ultrafiltration-based extraction sample preparation step from human plasma samples is accurate.

3.2.5 Robustness

The effects of small and deliberate changes in the chromatographic conditions of the analysis from optimized conditions were tested with the robustness test. The changed parameters were flow rate, buffer concentration and acetonitrile ratio of the mobile phase (Table 4). Due to robustness tests for synthetic tablet analysis 20 $\mu\text{g/mL}$ of IBU were calculated from found concentrations and it was examined that there was no difference statistically proven between them ($p > 0.05$).

Table 4. Results of robustness findings (IBU: 10 $\mu\text{g mL}^{-1}$, NS: 10 $\mu\text{g mL}^{-1}$, n=3)

Parameters	Found	RSD %	t calculated
Optimum conditions	19.06 \pm 0.06	0.52	-
Flow rate 0.95 mL min^{-1}	19.05 \pm 0.04	0.33	0.72
Flow rate 1.05 mL min^{-1}	19.10 \pm 0.01	0.13	0.59
Buffer concentration 13 mM	18.78 \pm 0.05	0.43	0.04
Buffer concentration 16 mM	18.93 \pm 0.02	0.17	0.16
Acetonitrile ratio 54%	19.40 \pm 0.04	0.38	0.02
Acetonitrile ratio 58%	19.28 \pm 0.07	0.61	0.11

The results were compared with the results obtained under optimum conditions ($p > 0.05$, t_{table} : 4.30)

3.3. Analysis of spiked plasma samples

The results from the analysis of 20.0 $\mu\text{g mL}^{-1}$ IBU spiked plasma samples with the developed HPLC method were evaluated using the regression equation from the calibration curve. The results (Table 5) proposed that ultrafiltration-based extraction can be successfully used for IBU analysis in human plasma samples with the developed HPLC method. It should be noted that the proposed extraction technique dilutes the sample concentration up to 5x, so the plasma concentration of the analyzed compound should be below the linear range.

Table 5. Determination of IBU from spiked plasma samples

Added amount ($\mu\text{g mL}^{-1}$)	Found amount ($\mu\text{g mL}^{-1}$)
20.00	19.41
	19.30
	19.48
	19.12
	19.33
	19.40
\bar{X}	19.34 \pm 0.14
SD	0.12
RSD (%)	0.64

\bar{X} : Mean \pm Standard error; SD: Standard Deviation; RSD: Relative Standard Deviation

3.4. Advantages and disadvantages of Ultrafiltration-Based extraction

The results of this study show that ultrafiltration-based extraction can be successfully applied to determine IBU from human plasma samples. The application of ultrafiltration-based extraction can be an effective alternative. However, the costs of the filters used in this technique should be considered for high sample amounts. In our analysis, we injected more than one hundred and twenty samples altogether and the column backpressure was stable around 102 bar. This can be stated that interference in the supernatant after protein precipitation can damage the next generation HPLC columns after several dozen injections. Column life can be an extra cost for analysis when protein precipitation alone is used. The ultrafiltration-based extraction proposed in this study not only preserves column life, but also prevents peaks from parasites in the matrix components. Solid phase extraction also requires commercial filters and can be used in pharmaceutical analysis. The advantage of ultrafiltration versus solid phase extraction is that it is simpler to apply and does not require additional buffers to be prepared. In addition, depending on the capacity of the centrifuge, more than a hundred samples can be prepared in the same order, which is almost impossible for solid phase extraction or takes too long and effort compared to ultrafiltration-based extraction. Liquid-

liquid extraction is another way to analyze drugs from human plasma samples. The problem for liquid-liquid extraction is that water-soluble pharmaceuticals are difficult to separate from plasma samples with organic solvents, or the recoveries are relatively low and require some extra procedures. In this case, the method presented in this study can be modified to identify water- and fat-soluble active pharmaceutical ingredients, including NSAIDs, in human plasma samples in further studies.

4. Conclusion

One of the main components of pharmaceutical science is pharmaceutical analysis. Studies such as pharmaceutical quality control, dissolution tests, pharmacokinetic studies and drug interaction studies are also based on analytical analysis. Because of its simplicity behind its precision, HPLC is still one of the most flexible techniques compared to electrochemistry, capillary electrophoresis and UV-Spectroscopy. Although LC-MS / MS is a valuable technique for pharmacokinetic studies with better sensitivity and selectivity advantages, HPLC equipped with UV detector is a simple, fast and cost-effective alternative. However, the HPLC-UV technique cannot be directly adapted to pharmacokinetic studies as it requires pre-cleaning procedures to prevent unwanted interference from matrix components as a result of plasma samples. For biological samples, commercial solid-phase extraction and liquid-liquid extraction equipments offer valuable alternatives to pre-cleaning procedures.

At this point, the reason why extraction based on ultrafiltration is seldom used in pharmaceutical research. In the study presented, IBU was extracted via commercial centrifugal filters from plasma samples and satisfactory results were observed. A large variety of active pharmaceutical ingredients can be adapted to the methodology proposed in this study.

Conflicts of interest

The authors state that they did not have any conflict of interests

References

- [1] Crofford L.J., Use of NSAIDs in Treating Patients with Arthritis, *Arthritis Res. Ther.*, 15 (S3) (2013) S2.
- [2] Simon L.S., Nonsteroidal Anti-inflammatory Drugs and Their Risk: A Story Still in Development, *Arthritis Res. Ther.*, 15 (S3) (2013) S1.
- [3] Cha Y.I., DuBois R.N., NSAIDs and Cancer Prevention: Targets Downstream of COX-2, *Annu. Rev. Med.*, 58 (2007) 239-252.
- [4] Tinsley H.N., Grizzle W.E., Abadi A., Keeton A., Zhu B., Xi Y., Piazza G.A., New NSAID Targets and Derivatives for Colorectal Cancer Chemoprevention, *Recent Results Cancer Res.*, 191 (2013), 105-120.
- [5] Wang D., DuBois R.N., The Role of Anti-inflammatory Drugs in Colorectal Cancer, *Annu. Rev. of Med.*, 64 (2013) 131-144.
- [6] Gurpinar E., Grizzle W.E., Piazza G.A., NSAIDs Inhibit Tumorigenesis, But How?, *Clin. Cancer Res.*, 20(5) (2014) 1104-1113.
- [7] Tsioulis G.J., Go M.F., Rigas B., NSAIDs and Colorectal Cancer Control: Promise and Challenges, *Curr. Pharmacol. Rep.*, 1(5) (2015) 295-301.
- [8] Stambaugh Jr J.E., Drew J., The Combination of Ibuprofen and Oxycodone/Acetaminophen in the Management of Chronic Cancer Pain, *Clin. Pharmacol. Ther.*, 44(6) (1988) 665-669.
- [9] Portenoy, R.K., Lesage P., Management of cancer pain, *Lancet*, 353(9165) (1999) 1695-1700.
- [10] Derry S., Wiffen P.J., Moore R., McNicol E.D., Bell R.F., Carr D.B., McIntyre M., Wee B., Oral Nonsteroidal Anti-Inflammatory Drugs (Nsaids) for Cancer Pain in Adults, *Cochrane Database of Syst. Rev.*, 7 (2017)
- [11] Carr D.B., Goudas L.C., Balk E.M., Bloch R., Ioannidis J.P., Lau J., Evidence Report on the Treatment of Pain in Cancer Patients, *J. Natl. Cancer Inst. Monogr.*, 32 (2004) 23-31.
- [12] Abdulla A., Adams N., Bone M., Elliott A.M., Gaffin J., Jones D., Knaggs R., Martin D., Sampson L., Schofield P., British Geriatric Society, Guidance on the Management of Pain in Older People, *Age Ageing*, 42 (S1) (2013) 1-57.
- [13] Kamsvåg, T., Hedén L., Essen L. V. Ljungman G., Ibuprofen in Needle Procedures in Children with Cancer—A Feasibility and Pilot study, *Acta Paediatr.*, 110 (2) (2020) 704-710.
- [14] Rainsford, K., Ibuprofen: Pharmacology, Efficacy and Safety, *Inflammopharmacology*, 17(6) (2009) 275-342.
- [15] Leising G., Resel R., Stelzer F., Tasch S., Lanziner A., Hantich G., Physical Aspects of Dexibuprofen and Racemic Ibuprofen, *J. Clin. Pharmacol.*, 36(12) (1996) 3S-6S.

- [16] Davies N.M., Clinical Pharmacokinetics of Ibuprofen, *Clin. Pharmacokinet*, 34(2) (1998) 101-154.
- [17] Locatelli M., Tartaglia A., D'Ambrosio F., Ramundo P., Ulusoy H.I., Furton K.G., Kabir A., Biofluid Sampler: A New Gateway for Mail-in-Analysis of Whole Blood Samples, *J. Chromatogr. B.*, 1143 (2020) 122055.
- [18] D'Angelo V., Tessari F., Bellagamba G., De Luca E., Cifelli R., Celia C., Primavera R., Di Francesco M., Paolino D., Di Marzio L., Locatelli M., Microextraction by Packed Sorbent and HPLC-PDA Quantification of Multiple Anti-Inflammatory Drugs and Fluoroquinolones in Human Plasma and Urine, *J. Enzyme Inhib. Med. Chem.*, 31(Sup3) (2016) 110-116.
- [19] Çelebier M., Nenni M., Altınöz S., Ultrafiltration-Based Extraction and HPLC Analysis of Naproxen Sodium in Human Plasma Samples: An Innovative Approach to Pharmaceutical Analysis, *Pharm. Chem. J.*, 50(4) (2016) 275-279.
- [20] FDA, Guidance for Industry: Bioanalytical Method Validation. 2018.
- [21] Tartaglia A., Kabir A., D'Ambrosio F., Ramundo P., Ulusoy S., Ulusoy H.I., Merone G.M., Savini F., D'Ovidio C., Grazia U., Furton K.G., Locatelli M., Fast Off-line FPSE-HPLC-PDA Determination of Six NSAIDs in Saliva Samples, *J. Chromatogr. B.*, 1144 (2020) 122082.
- [22] Locatelli M., Tartaglia A., Ulusoy H. I., Ulusoy S., Savini F., Rossi S., Santavenere F., Merone G. M., Bassotti E., D'Ovidio C., Rosato E., Furton K. G., Kabir A., Fabric-Phase Sorptive Membrane Array As a Noninvasive In Vivo Sampling Device For Human Exposure To Different Compounds, *Anal. Chem.*, 93(4) (2021) 1957-1961.
- [23] Karaca E., Ulusoy S, Morgül Ü., Ulusoy H., Development of Analytical Method for Sensitive Determination of Streptozotocin Based on Solid Phase Extraction, *Cumhuriyet Sci. J.*, 41(4) (2020) 826-831.
- [24] Bonfilio R., Cazedey E. C. L., de Araújo M. B., Salgado H. R. N., Analytical Validation of Quantitative High-Performance Liquid Chromatographic Methods in Pharmaceutical Analysis: A Practical Approach, *Crit. Rev. Anal. Chem.*, 42 (1) (2012) 87-100.



Determination and evaluation of Cu, Mn, Zn, Cd, Pb and Ni contents in wild-grown edible mushroom species from Cappadocia, Turkey

İbrahim NARİN¹ , Abdullah Taner BİŞGİN² , Mustafa TÜZEN^{3,*} , Mustafa UÇAN² ,
Durali MENDİL³ , Mustafa SOYLAK⁴ 

¹Erciyes University, Faculty of Pharmacy, 38039 Kayseri / TURKEY

²Niğde Ömer Halisdemir University, Faculty of Science and Arts, Department of Chemistry, 51240 Niğde / TURKEY

³Tokat Gaziosmanpaşa University, Faculty of Science and Arts, Department of Chemistry, 60250 Tokat / TURKEY

⁴Erciyes University, Faculty of Science and Arts, Department of Chemistry, 38039 Kayseri / TURKEY

Abstract

The aim of this study was to determine the Cu, Mn, Zn, Cd, Pb and Ni concentrations in sixteen different wild-grown edible mushroom species grown in Niğde and Nevşehir. In the sample preparation step, the samples were dried, ground and sieved by 200 meshed sieve, consecutively. The extractions of metals were conducted by acid mineralization using concentrated nitric acid and hydrogen peroxide in microwave digestion unit. The determinations of metals were performed by flame atomic absorption spectrometry. Among the mushroom samples that were analyzed, Cu, Mn, Zn, Cd, Pb, and Ni concentrations were determined in the range of 6.7-1353, 4.7-109, 44.8-406, 0.14-6.4, 4.28-25.6 and 1.7-11.0 mg/kg, respectively. The accuracy and precision of the proposed method for metal determinations were validated by using the NIST SRM 1573a Tomato Leaves certified standard material. The obtained results were evaluated in terms of human health and compared with each other and previously reported values in the literature. In addition, the habitats of the mushroom samples were identified.

Article info

History:

Received: 11.11.2020

Accepted: 29.04.2021

Keywords:

Cappadocia,
Heavy metals,
Microwave digestion,
Mushrooms,
Atomic absorption
spectrometry.

1. Introduction

In the world, food production and consumption are increasing due to population growth. Increased population, growing industrialization, developments in technology, new industrial factories and their activities bring a lot of advantages and adversely affect to environment and also inhabitants. As a result of these activities considerable amount of trace metal can be released to environment. So, environment has been polluted mostly in terms of heavy metals. The majority of heavy metals (Cd, Ni, Pb, etc.) have toxic effects on living organisms [1]. On the other hand, some of these metals (Cu, Mn, Zn, etc.) are essential for human health [2]. Heavy metals are introduced to the human body via inhalation, the food chain, drinking water and skin contact and accumulate in vital organs (the brain, liver, bones and kidneys) [3]. Accumulated heavy metals can lead to diseases and cancers [4].

Trace metal pollution in the world is the biggest problem and also inevitable for environment and inhabitants. Heavy metals are found naturally in the earth and become concentrated with increasing anthropogenic and industrial activities [5]. Concentrated heavy metals can be accumulated by some plants [6,7] and animal species [8,9]. When the mushrooms are compared in the plant family, they can accumulate a considerable amount of heavy metal such as Zn, Cu and Pb [10,11]. Wild-grown edible mushrooms are a dietetic food and have high nutritional value, low calories and pharmacological characteristics. Therefore, mushrooms are highly preferred by people as a natural nutrient [12,13]. For these reasons, the determination and evaluation of heavy metal levels in wild-grown edible mushrooms are very important.

Great efforts have been made to determine the trace metal levels of wild-grown edible mushrooms by using flame atomic absorption spectrometry [14], graphite

furnace atomic absorption spectrometry [15], inductively coupled plasma mass spectrometry [16,17] and inductively coupled plasma optic emission spectrometry [18,19] after application of different digestion methods such as wet digestion [20], dry ashing [21] and microwave digestion procedures [22]. The wet digestion and dry ashing methods are complicated and more time-consuming than the microwave digestion method without having any advantages. The obtained results in the literature from standard reference material analysis show that the microwave digestion method provided the best quantitative recovery among these digestion methods [23].

In this study, evaluation of the heavy metal pollution level in Cappadocia was performed. The trace metal levels of wild-grown edible mushroom species in Cappadocia, Turkey were determined by using flame atomic absorption spectrometry. Mushroom samples were digested by a microwave digestion unit. In addition, the metal contents of mushroom species were compared with previously reported results in the literature.

2. Materials and Methods

2.1. Apparatus

A Perkin Elmer AAnalyst 700 (Waltham, Massachusetts, ABD) flame atomic absorption

spectrometer was used for the determination of the heavy metal levels in mushroom species. Milestone Ethos D (Milestone, Sorisole, Italy) microwave digestion unit was used for the digestion process. The Milli-Q Millipore ultrapure distilled water system (Darmstadt, Germany, resistivity of 18.2 M Ω -cm) was used throughout the experiments.

2.2. Reagents and solutions

The chemicals and acid solutions used in the experiments were of analytical grade and obtained from Merck (Darmstadt, Germany) and Sigma-Aldrich (St. Louis, MO). Ultrapure distilled water was used for all dilutions, preparation of solutions and washing processes. Glassware and plastic equipment were washed with a 10% HNO₃ (Merck) solution, rinsed with ultrapure water and dried in an oven before use throughout the experiments. In atomic absorption measurements, standard metal solutions for the calibration graph were prepared daily by dilution of 1000 μ g/mL stock metal solutions from Merck and Sigma. NIST SRM 1573a Tomato Leaves were used as a certified reference material to check the accuracy of the method.

2.3. Collecting site and sampling

Nevşehir and Niğde are small cities which are located in the touristic Cappadocia region of Turkey. Domestic and foreign visitors come to the area throughout the year.

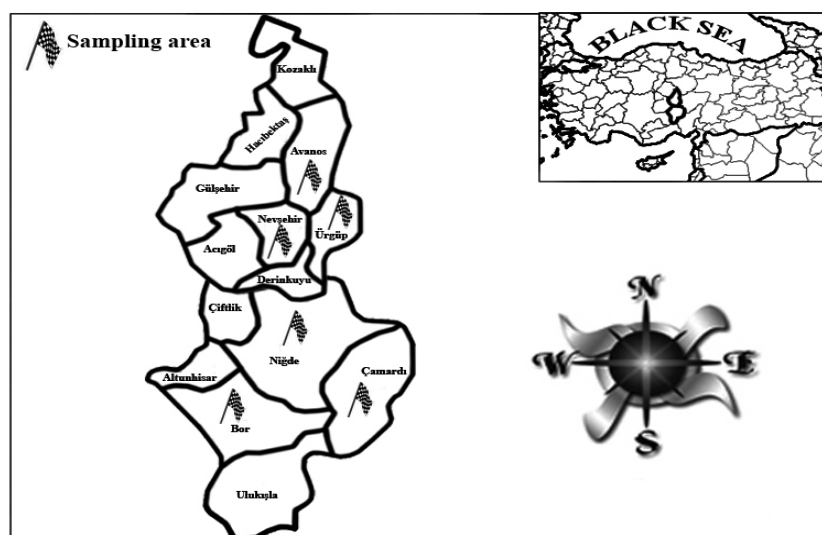


Figure 1. Map of the study area

A total of 187 living fresh samples from 16 different species of mushrooms (*Agaricus campestris*, *Agrocybe aegerita*, *Agrocybe dura*, *Armillaria mellea*, *Boletus edulis*, *Boletus luteus*, *Coprinus comatus*, *Lactarius piperatus*, *Lactarius salmonicolor*, *Lactarius volemus*,

Marasmius oreades, *Panellus stipticus*, *Piptoporus betulinus*, *Pleurotus ostreatus*, *Rhizopogon luteolus*, *Russula delica*) were collected from different sites of Cappadocia (Nevşehir 38° 42' North, 34° 50' East and Niğde 37° 57' North, 34° 40' East). The locations of

the collected mushroom samples are given in Figure 1. In addition, 10 ± 2 g mushroom samples were collected from each species and sampling study was performed during March-April 2015. The collected mushroom samples were stored in polyethylene bags.

2.4. Preparation of mushroom samples

The collected fresh mushroom samples were kept for 48 hours in an oven at 80 °C for the drying process. Dry mushroom samples were homogenized in a porcelain agate homogenizer. Samples were stored in polyethylene bags after being sieved through a 200

mesh sieve. The samples were kept in these bags at room temperature until the digestion process.

2.5. Digestion process

The digestion procedure was performed by using a microwave digestion unit [24]. 1.0 ± 0.1 g. of each dry mushroom sample, 6 mL of concentrated (65%) HNO_3 and 2 mL of (30%) H_2O_2 solution were added in the teflon reaction vessel of the microwave digestion system and diluted to 10 mL of final volume with ultrapure distilled water after applying the digestion process.

Table 1 Digestion conditions for Milestone Ethos D microwave digestion unit

Digestion Step	Time, (Min)	Power, (W)
1	2	250
2	2	0
3	6	250
4	5	400
5	8	550
Ventilation	8	0

Table 2 Obtained and certified metal levels of NIST SRM 1573a Tomato Leaves, N=4

Element	Certified value ($\mu\text{g/g}$) ^a	Obtained value ($\mu\text{g/g}$) ^a	Recovery (%) ^a
Cu	4.7	4.60 ± 0.28	98 ± 2
Zn	30.9	29.7 ± 1.5	96 ± 3
Mn	246	238 ± 15	97 ± 1
Cd	1.52	1.52 ± 0.10	100 ± 1
Ni	1.59	1.55 ± 0.10	97 ± 3

^aMean \pm Standard deviation

The analyses of blank samples and standard reference material were performed at the same conditions. The digestion conditions of the microwave unit and analysis results of the certified reference material are given in Tables 1 and 2, respectively.

3. Results and Discussion

As shown in Table 2, the results obtained from certified reference material analyses were in good agreement

with the certified levels. The recovery values of the investigated metal ions were quantitative ($>95\%$). The relative standard deviations were less than 10% for the investigated metals. The families of wild-grown mushroom species were identified and given in Table 3 with their habitats. The results obtained from the analysis are given in Tables 4 and 5. They were compared with each other and also with previously reported results in the literature.

Table 3 Habitats of the edible mushroom species

Mushroom species	Habitat
<i>Agaricus campestris</i>	Among grass
<i>Agrocybe aegerita</i>	In forests
<i>Agrocybe dura</i>	Roadside or in meadows
<i>Armillaria mellea</i>	In dense clusters on or around tree trunks
<i>Boletus edulis</i>	In pine forests
<i>Boletus luteus</i>	In broad-leaved woods
<i>Coprinus comatus</i>	In meadows
<i>Lactarius piperatus</i>	On ground or native trees
<i>Lactarius salmonicolor</i>	Under trees
<i>Lactarius volemus</i>	In pine forests
<i>Marasmius oreades</i>	Often forming rings in the short grass of pasture or lawns
<i>Panellus stipticus</i>	On dead wood
<i>Piptoporus betulinus</i>	On wood or trees
<i>Pleurotus ostreatus</i>	On wood or trees
<i>Rhizopogon luteolus</i>	In soil
<i>Russula delica</i>	In coniferous and mixed woodland

The Cu concentrations in the mushroom samples were found in the range of 58-1353 and 6.7-250 mg/kg for Niğde and Nevşehir, respectively. The Cu contents of mushroom samples in Niğde were higher than the mushroom samples of Nevşehir. When the copper concentrations were compared with other studies, the copper levels of the mushroom samples were slightly higher than previously reported studies [25]. Only *Agaricus campestris* had a considerably high concentration of copper (1353 mg/kg). In a previous study, copper concentrations in wild-grown edible mushrooms were found to be between 100 and 300 mg/kg, which were not considered a health risk [26].

The Mn levels of the mushroom samples were between 7.9 and 109 mg/kg for Niğde, 4.7 and 55.6 mg/kg for Nevşehir. The Mn concentrations of the mushroom samples grown in Niğde city were relatively higher than the mushroom samples of Nevşehir. The manganese levels of the analyzed mushrooms, when compared with other studies, showed that the results were in agreement with previous studies [27,28]. The reported manganese concentrations for edible mushrooms were between 13.5 and 113 mg/kg on dry weight basis [29].

The Zn contents in mushroom samples were determined to be between 44.8 to 406 mg/kg and 49.2 to 147 mg/kg for Niğde and Nevşehir, respectively. The Zn levels of the mushroom samples were almost equal. Only one species of mushroom which was *Agaricus campestris* had a high concentration of zinc. The zinc contents of the analyzed mushroom samples, when compared to other studies, showed that the zinc

levels were consistent with previously reported studies [30,31]. The determined Zn levels in edible mushroom samples ranged from 35.8 to 410 mg/kg in a previously reported study [32].

The Cd contents of mushroom samples were determined to be between 0.14 and 2.01 mg/kg on a dry weight basis for Niğde. The Cd levels of Nevşehir mushrooms were determined to be between 1.2 and 6.4 mg/kg. Levels in Nevşehir mushroom samples were higher than the mushroom samples of Niğde. The cadmium levels of mushrooms in Niğde were lower than those previously reported in the literature [33] while the Cd concentrations of the mushroom samples grown in Nevşehir were higher than previous studies [34]. According to Maximum Levels of Contaminants in Foods (GB2762-2005) and Hygienic Standard for Edible Fungi (GB7096-2003), the safe limit was 0.2 mg/kg for Cd. High levels of cadmium in analyzed mushroom species may be sourced from fertilizer.

The minimum and maximum Pb levels in mushroom samples were found as 4.3-25.6 mg/kg and 7.9-22.2 mg/kg for Niğde and Nevşehir, respectively. The Pb concentrations in edible mushrooms grown in both cities were the same and there was no significant difference in terms of Pb concentration. When the lead contents of mushrooms were compared with other studies, lead levels were higher than previously reported in the literature [35]. In another previous study Pb levels were determined between 0.1 to 40 mg/kg [36]. According to reported values, the Pb concentrations of the mushroom samples were found at

lower levels. High levels of lead in analyzed mushroom samples can be sourced from traffic.

The Ni concentrations of mushroom samples were determined in the range of 2.8 and 11.0 mg/kg for Niğde and 1.7 and 10.5 mg/kg for Nevşehir, respectively. The Ni concentrations in mushroom

samples from both cities were approximately the same. The nickel concentrations of the analyzed mushroom samples were lower than in a previous study [37]. In previously reported studies, nickel concentrations were determined to be between 8.2-21.6 mg/kg and 0.4-15.9 mg/kg [38].

Table 4 Trace metal contents (mg/kg) of mushroom species from Niğde, N=4

Sample Name	Cu ^a	Mn ^a	Zn ^a	Cd ^a	Pb ^a	Ni ^a
<i>Agaricus campestris</i>	1353±32	50.0±3.7	406±33	0.83±0.05	25.6±1.1	10.3±0.7
<i>Agrocybe aegerita</i>	137±10	10.7±0.8	76.5±5.9	0.74±0.03	6.9±0.3	*BDL
<i>Armillaria mellea</i>	154±9	81.3±6.0	50.3±5.5	0.53±0.03	20.8±1.3	4.2±0.3
<i>Boletus edulis</i>	425±29	109.0±8.0	211±18	0.44±0.02	22.1±1.7	11.0±0.8
<i>Coprinus comatus</i>	214±8	7.9±0.4	95.4±7.4	2.01±0.05	4.3±0.2	4.2±0.3
<i>Lactarius piperatus</i>	161±11	25.2±1.9	90.6±8.2	1.28±0.03	4.3±0.4	6.2±0.4
<i>Lactarius volemus</i>	258±15	67.9±5.3	93.1±7.9	0.85±0.06	11.9±0.8	6.2±0.5
<i>Panellus stipticus</i>	374±10	67.1±5.6	59.0±4.6	1.48±0.05	9.7±0.7	9.6±0.6
<i>Pleurotus ostreatus</i>	58±4	16.8±1.2	44.8±4.1	0.24±0.02	4.3±0.3	4.2±0.3
<i>Rhizopogon luteolus</i>	159±9	8.2±0.7	49.9±3.0	0.14±0.01	6.8±0.4	2.8±0.2
<i>Russula delica</i>	592±43	71.9±7.7	172±14	0.98±0.04	14.4±1.6	7.6±0.6
Detection limit	0.08	0.07	0.31	0.05	0.58	0.63

*BDL: Below detection limit

^aMean±standard deviation

Table 5 Trace metal contents (mg/kg) of mushroom species from Nevşehir, N=4

Sample Name	Cu ^a	Mn ^a	Zn ^a	Cd ^a	Pb ^a	Ni ^a
<i>Agrocybe aegerita</i>	250.0±23.0	55.6±6.4	147±15	4.6±1.0	22.2±2.5	7.8±2.4
<i>Agaricus campestris</i>	103.0±16.0	36.8±3.6	119±7	2.5±0.5	14.9±0.9	5.2±0.8
<i>Agrocybe dura</i>	21.2±1.5	11.3±1.3	79.1±2.5	1.5±0.5	10.6±0.2	3.7±1.4
<i>Armillaria mellea</i>	42.2±2.8	9.9±0.9	87.4±8.1	6.4±0.5	12.8±0.8	5.2±1.0
<i>Boletus luteus</i>	34.4±2.8	12.4±1.1	91.5±8.7	2.8±0.5	11.1±0.3	4.8±1.6
<i>Coprinus comatus</i>	90.3±7.1	21.2±3.7	89.4±7.8	1.8±0.3	13.1±1.1	5.5±0.9
<i>Lactarius volemus</i>	64.3±2.0	8.2±2.1	94.3±4.7	1.7±0.6	12.4±1.4	4.2±0.8
<i>Lactarius salmonicolor</i>	6.7±1.1	10.5±2.6	82.7±6.0	1.2±0.3	7.9±0.9	1.7±0.6
<i>Marasmius oreades</i>	49.5±1.7	28.1±2.4	56.4±5.7	3.0±0.5	13.0±1.1	2.1±0.8
<i>Piptoporus betulinus</i>	32.6±2.5	4.7±1.1	49.2±10.5	1.3±0.4	10.3±1.0	10.5±0.2
<i>Rhizopogon luteolus</i>	26.7±0.9	14.0±2.8	88.4±3.5	3.3±0.5	12.0±0.5	1.9±0.3
<i>Russula delica</i>	31.3±3.2	14.1±2.0	95.2±6.3	3.6±0.5	10.6±0.3	2.8±0.3
Detection limit	0.08	0.07	0.31	0.05	0.58	0.63

*BDL: Below detection limit

^aMean±standard deviation

4. Conclusions

Among the six metals, Cd, Pb and Ni are potentially hazardous. These heavy metals in wild-grown edible mushrooms may enter the human body via food chain and seriously damage human health. Therefore, it is necessary to periodically evaluate the metal contents and health risks of these mushrooms. Heavy metal pollution in wild-grown edible mushrooms from Cappadocia Region of Turkey has become a serious problem. The essential element concentrations (Mn, Cu, and Zn) in the mushrooms were determined to be at typical levels. However, the concentrations of toxic metals (Cd, Pb) in nearly all of the mushroom samples

exceeded safe limits. The wild edible mushrooms in the study area have been contaminated with heavy metals so that they pose a threat to human health. Among the toxic heavy metals, Pb and Cd were accumulated by the mushrooms. Pb and Cd in wild edible mushrooms may pose a higher health risk than Ni. Intakes of Pb and Cd by consuming wild edible mushrooms from the study area may cause serious health problems.

Acknowledgements

The authors would like to thanks to Dr. Ibrahim Turkecul for identification of mushroom species. The authors would like to thank Demirhan Cıtaç and Şahin

Duran for their help in experimental studies. This study was supported by Niğde University Scientific Project Unit, project number FEB 2012/23.

Conflict of interest

The authors declare that they have no conflict of interests.

References

- [1] Habila M., Unsal Y. E., Alothman Z. A., Shabaka A., Tuzen M., Soylak M., Speciation of Chromium in Natural Waters, Tea, and Soil with Membrane Filtration Flame Atomic Absorption Spectrometry, *Anal. Lett.*, 48 (2015) 2258–2271.
- [2] Kara D., Fisher A., Hill S., Extraction of trace elements by ultrasound-assisted emulsification from edible oils producing detergentless microemulsions, *Food Chem.*, 188 (2015) 143-148.
- [3] Squadrone S., Brizio P., Chiaravalle E., Abete M. C., Sperm whales (*Physeter macrocephalus*), found stranded along the Adriatic coast (Southern Italy, Mediterranean Sea), as bioindicators of essential and non-essential trace elements in the environment, *Ecol. Indic.*, 58 (2015) 418-425.
- [4] Reddy U. A., Prabhakar P. V., Rao G. S., Rao P. R., Sandeep K., Rahman M. F., Kumari S.I., Grover P., Khan H.A., Mahboob M., Biomarkers of oxidative stress in rat for assessing toxicological effects of heavy metal pollution in river water, *Environ. Sci. Pollut. R.*, 22 (2015) 13453-13463.
- [5] Tuzen M., Soylak M., Evaluation of trace element contents in canned foods marketed from Turkey. *Food Chem.*, (2007) 102 1089-1095.
- [6] Yan W., Mahmood Q., Peng D., Fu W., Chen T., Wang Y., Li S., Chen J., Liu D., The spatial distribution pattern of heavy metals and risk assessment of moso bamboo forest soil around lead–zinc mine in Southeastern China, *Soil Till. Res.*, 153 (2015) 120-130.
- [7] Chavez E., He Z. L., Stoffella P. J., Mylavarapu R. S., Li Y. C., Moyano B., Baligar V. C., Concentration of cadmium in cacao beans and its relationship with soil cadmium in southern Ecuador, *Sci. Total Environ.*, 533 (2015) 205-214.
- [8] Komoroske L. M., Lewison R. L., Seminoff J. A., Deustchman D. D., Deheyn D. D., Trace metals in an urbanized estuarine sea turtle food web in San Diego Bay, CA, *Sci. Total Environ.*, 417-418 (2012) 108-116.
- [9] Pareja-Carrera J., Mateo R., Rodríguez-Estival J., Lead (Pb) in sheep exposed to mining pollution: Implications for animal and human health, *Ecotox. Environ. Safe.*, 108 (2014) 210-216.
- [10] Kalač P., Svoboda L., A review of trace element concentrations in edible mushrooms, *Food Chem.*, 69 (2000) 273-281.
- [11] Svoboda L., Chrastný V., Levels of eight trace elements in edible mushrooms from a rural area, *Food Addit. Contam.*, 25(1) (2008) 51-58.
- [12] García M. Á., Alonso J., Melgar M. J., Lead in edible mushrooms Levels and bioaccumulation factors, *J. Hazard. Mater.*, 167 (2009) 777-783.
- [13] Isildak O., Turkekul I., Elmastas M., Aboul-Enein H. Y., Bioaccumulation of Trace Metals in Some Wild-Grown Edible Mushrooms, *Anal. Lett.*, 40 (2007) 1099-1116.
- [14] J. Ji, J. Dai, W. Zhang, H. Xu, Factors affecting the uptake of lead and copper in five wild mushroom species from Chengdu, China, *Food Addit. Contam.*, 26(9) (2009) 1249-1255.
- [15] Chen X., Zhou H., Qiu G., Analysis of Several Heavy Metals in Wild Edible Mushrooms from Regions of China, *B. Environ. Contam. Tox.*, 83 (2009) 280-285.
- [16] Karadeniz Ö., Yaprak G., ¹³⁷Cs, ⁴⁰K, alkali–alkaline earth element and heavy metal concentrations in wild mushrooms from Turkey, *J. Radioanal. Nucl. Chem.*, 285 (2010) 611–619.
- [17] Benbrahim M., Denaix L., Thomas A. L., Balet J., Carnus J. M., Metal concentrations in edible mushrooms following municipal sludge application on forest land, *Environ. Pollut.*, 144 (2006) 847-854.
- [18] Cocchi L., Vescovi L., Petrini L. E., Petrini O., Heavy metals in edible mushrooms in Italy, *Food Chem.*, 98 (2006) 277-284.
- [19] Kula İ., Solak M. H., Uğurlu M., Işıloğlu M., Arslan Y., Determination of Mercury, Cadmium, Lead, Zinc, Selenium and Iron by ICP-OES in Mushroom Samples from Around Thermal Power Plant in Muğla, Turkey, *B. Environ. Contam. Tox.*, 87 (2011) 276–281.
- [20] Ouzouni P.K., Petridis D, Koller W.D., Riganakos K.A., Nutritional value and metal content of wild edible mushrooms collected from West

- Macedonia and Epirus, Greece, *Food Chem.*, 115 (2009) 1575-1580.
- [21] Svoboda L., Zimmermannová K., Kalač P., Concentrations of mercury, cadmium, lead and copper in fruiting bodies of edible mushrooms in an emission area of a copper smelter and a mercury smelter, *Sci. Total Environ.*, 246 (2000) 61-67.
- [22] Çayır A., Coşkun M., Coşkun M., The Heavy Metal Content of Wild Edible Mushroom Samples Collected in Canakkale Province, Turkey, *Biol. Trace. Elem. Res.*, 134 (2010) 212-219.
- [23] Tüzen M., Determination of trace metals in soil, mushroom and plant samples by atomic absorption spectrometry, *Microchem. J.*, 74 (2003) 289-297.
- [24] Turkecul I., Elmastas M., Tüzen M., Determination of iron, copper, manganese, zinc, lead, and cadmium in mushroom samples from Tokat, Turkey, *Food Chem.*, 84 (2004) 389-392.
- [25] Alonso J., García M. A., Pérez-López M., Melgar M. J., The Concentrations and Bioconcentration Factors of Copper and Zinc in Edible Mushrooms, *Arch. Environ. Contam. Toxicol.*, 44 (2003) 180-188.
- [26] Liu B., Huang Q., Cai H., Guo X., Wang T., Gui M., Study of heavy metal concentrations in wild edible mushrooms in Yunnan Province, China, *Food Chem.*, 188 (2015) 294-300.
- [27] Sesli E., Tuzen M., Soylak M., Evaluation of trace metal contents of some wild edible mushrooms from Black sea region, Turkey, *J. Hazard. Mater.*, 160 (2008) 462-467.
- [28] Yamaç M., Yıldız D., Sarıkürkcü C., Çelikkollu M., Solak M. H., Trace metals in some edible mushrooms from the Central Anatolia, Turkey, *Food Chem.*, 103 (2007) 263-267.
- [29] Zhu F., Qu L., Fan W., Qiao M., Hao H., Wang X., Assessment of heavy metals in some wild edible mushrooms collected from Yunnan Province, China, *Environ. Monit. Assess.*, 179(1-4) (2011) 191-199.
- [30] Tüzen M., Turkecul I., Hasdemir E., Mendil D., Sarı H., Atomic Absorption Spectrometric Determination of Trace Metal Contents of Mushroom Samples from Tokat, Turkey, *Anal. Lett.*, 36(7) (2003) 1401-1410.
- [31] Soylak M., Saraçoğlu S., Tüzen M., Mendil D., Determination of trace metals in mushroom samples from Kayseri, Turkey, *Food Chem.*, 92 (2005) 649-652.
- [32] Mykhailo M. V., Copper, zinc, and cadmium in various fractions of soil and fungi in a Swedish forest, *J. Environ. Sci. Heal. A*, 48(8) (2013) 980-987.
- [33] Meghalatha R., Ashok C., Nataraja S., Krishnappa, M. Studies on chemical composition and proximate analysis of wild mushrooms. *World J. Pharmaceutical Sci.* 2 (2014) 357-363.
- [34] Tuzen M., Sesli E., Soylak M., Trace element levels of mushroom species from East Black Sea region of Turkey, *Food Control*, 18 (2007) 806-810.
- [35] Ouzouni P. K., Veltsistas P. G., Palelogos E. K., Riganakos K. A., Determination of metal content in wild edible mushroom species from regions of Greece, *J. Food Compos. Anal.*, 20 (2007) 480-486.
- [36] Sesli E., Tüzen M., Levels of trace elements in the fruiting bodies of macrofungi growing in the East Black Sea region of Turkey, *Food Chem.*, 65(4) (1999) 453-460.
- [37] Isildak Ö., Turkecul I., Elmastas M., Tuzen M., Analysis of trace metals in some wild-grown edible mushrooms from the middle Black Sea region, Turkey, *Food Chem.*, 86 (2004) 547-552.
- [38] Mendil D., Uluözlü Ö. D., Tüzen M., Hasdemir E., Sarı H., Trace metal levels in mushroom samples from Ordu, Turkey, *Food Chem.*, 91(3) (2005) 463-467.



Flame atomic absorption spectrometric determination of multi element in apricot and soil samples after wet and microwave digestion method

İnci KAYGUSUZ¹ , Mustafa TÜZEN^{1, *} 

¹Tokat Gaziosmanpaşa University, Faculty of Science and Arts, Chemistry Department, 60250 Tokat, TURKEY

Abstract

Iron, copper, zinc, manganese, nickel, cobalt, lead, cadmium and chromium in various apricot and soil samples were determined by atomic absorption spectrometry in this study. Microwave digestion method and wet ashing method efficiency were compared for digestion of the samples. Recovery values were nearly found quantitative. The analysis results were evaluated. The accuracy of the digestion procedures was confirmed by analyzing Montana Soil and Apple Leaves certified reference materials. There are no important differences between digestion methods. The results were compared with literature values. Relative standard deviations were found below 10 %. Heavy metal levels in analyzed samples were not found toxic limits.

Article info

History:

Received: 16.11.2020

Accepted: 30.04.2021

Keywords:

Heavy metal,
Microwave digestion,
Wet Ashing
Apricot,
Soil, Atomic
absorption
spectrometry.

1. Introduction

The most important environmental pollution is sourced from heavy metals. Food contamination is now accepted as an indisputable fact all over the world. Toxic elements found naturally in foodstuffs are not generally harmful to human health [1]. Chemical contamination can be of natural, environmental and technological origin. Since food contamination is difficult to prevent and control, the consequences appear in a long time and can be even more effective in terms of health [2, 3]. Apricot is a product that is consumed throughout the year in the form of fresh, dried and fruit juice. Apricot has positive effects on human health through organic and inorganic substances contains [4]. Heavy metals are passed to apricot from soil and its irrigation water. The other source of heavy metals is traffic [5].

Iron, copper, zinc, manganese and cobalt are known essential heavy metals, but nickel, lead, cadmium and chromium are toxic element for human, animal and environmental health. Essential elements can be also harmful effects when their high consumption [6]. So, it is very important for accurate and sensitive determination of heavy metal levels in food, soil and environmental samples. Digestion procedure is very important step before determination of heavy metals in solid matrix. Various digestion procedures such as dry

ashing, wet ashing and microwave digestion are used for this aim. Dry ashing and wet ashing procedures are slow and time consumption but microwave digestion method is fast, clean and environmentally friendly [7, 8].

Various instrumental detection system such as inductively couple plasma mass spectrometry (ICP-MS), inductively couple plasma optic emission spectrometry (ICP-OES), energy dispersive x-ray fluorescence spectrometry and atomic absorption spectrometry (AAS) have been used for the determination of traces heavy metal ions in food and environmental samples [9-12]. Atomic absorption spectrometry is the main instrument for the determination of heavy metals in food, soil and environmental samples because of its simplicity, low cost and sensitivity [13, 14]. According to our literature survey, multi element levels were not determined in apricot and soil samples collected from Malatya, Turkey after different digestion methods. It is aimed to determine the levels of traces heavy metals in apricot and soil samples and to evaluate them in terms of environment and human health. In this study the performance of wet ashing and microwave digestion methods were compared by using real apricot and soil samples. The accuracy of the digestion procedures was confirmed by analyzing Montana Soil and Apple Leaves certified reference materials.

*Corresponding author. e-mail address: mustafa.tuzen@gop.edu.tr

2. Materials and Methods

2.1. Reagents

Analytical reagent grade chemicals were used in this study. Double distilled deionized water (Milli-Q Millipore (Bedford, MA, USA) 18.2 M Ω cm⁻¹) was used for the dilutions of all solutions. All plastic and glassware were soaked with HNO₃ (10 %) and then rinsed with deionized water before use. 1000 mg L⁻¹ stock solutions of the elements were prepared their salts purchased from Merck company (Darmstadt, Germany). Working solutions of elements were prepared daily from stock solution by using dilution procedure. NIST SRM 1515 Apple Leaves and NIST

SRM 2711 Montana Soil certified reference materials were used to check the accuracy of the method.

2.2. Apparatus

Perkin Elmer AAnalyst 700 model deuterium background corrected atomic absorption spectrometry (Norwalk, CT, USA) was used for the measurement of elements. Flame atomization was performed in air-acetylene environment. Working conditions of element in FAAS were given in Table 1. Hollow cathode lamps were used. Milestone Ethos D model (Soriso-Bg, Italy) closed system microwave oven (maximum temperature 300 °C, maximum pressure 1450 psi) was used to dissolve standard reference materials and apricot samples.

Table 1. Working conditions of element in FAAS

Element	Acetylene (L/min)	Air (L/min)	Wavelengths (nm)	Slit wave (nm)
Fe	2.0	17.0	248.3	0.2
Cu	2.0	17.0	324.8	0.7
Zn	2.0	17.0	213.9	0.7
Mn	2.0	17.0	279.5	0.2
Cd	2.0	17.0	326.1	0.2
Ni	2.0	17.0	341.5	0.2
Co	2.0	17.0	345.4	0.2
Cr	2.0	17.0	357.9	0.7
Pb	2.0	17.0	283.3	0.7

2.3. Sampling

In this study, apricot and soil samples collected from various regions of Malatya city, Turkey were used. The samples were dried in an oven at 105 °C and ground into powder. The samples were then packaged and stored.

2.4. Digestion procedures

2.4.1. Microwave digestion

Apricot samples (0.5 g) and standard reference material (NIST SRM 1515 Apple Leaves) (0.25 g) were taken into microwave container and 6 mL of 65% HNO₃ and 2 mL of 37 % HCl were added. Soil samples (0.5 g) and NIST SRM 2711 Montana Soil (0.1 g) were taken into the microwave container and 6 mL of 37 % HCl, 2 mL of 65% HNO₃, 0.5 mL of 40% HF were added. The samples were digested in microwave system. The following program was used in the digestion process; 4 min, 250 W; 7 min, 400 W; 10 min, 550 W; ventilation: 10 min. The samples

dissolved in the microwave system then particles filtered through the blue band filter paper. Then it was completed to 10 mL with distilled deionized water. A blank digest was also prepared.

2.4.2. Wet digestion

1 g of apricot samples and 0.2 g of NIST SRM 1515 Apple Leaves were taken into a conical flask and 6 mL of 65% HNO₃ and 2 ml of 37% HCl were added. Soil samples (0.5 g) and NIST SRM 2711 Montana Soil (0.1 g) were taken into a conical flask and 6 mL of 37 % HCl, 2 mL of 65% HNO₃ were added. The samples were put on the hot plate and heated 30 min in 150 °C until dryness. This process was repeated two times. The samples were cooled and filtered by using blue band filter paper. The final volume was completed to 10 mL with deionized water. A blank digest was also prepared as the same way.

3. Results and Discussion

Analytical characteristics such as correlation coefficient, linear range, regression equation and RSD values of trace elements in FAAS were given in Table

2. RSD values were found below 10 %. The comparison of the microwave and wet ashing digestion performance of trace elements by using NIST SRM 1515 Apple Leaves and NIST SRM 2711 Montana Soil were given in Table 3 and Table 4, respectively.

Table 2. Analytical characteristics

Element	Correlation coefficient	Linear range (mg L ⁻¹)	Regression equation	RSD, %
Co	0.9999	0.25-5.0	A=0.0383C+0.0013	5.5
Pb	0.9999	0.5-10.0	A=0.0048C+0.0005	4.5
Ni	0.9996	0.25-5.0	A=0.0219C+0.00002	3.9
Cu	0.9999	0.25-5.0	A=0.02667C-0.0006	6.4
Fe	0.9996	0.25-5.0	A=0.0202C+0.0036	5.9
Cd	0.9995	0.02-2.0	A=0.1405C+0.0076	7.2
Cr	0.9998	0.50-10.0	A = 0.0245C+ 0.0011	8.5
Mn	0.9995	0.10-3.0	A = 0.081C+ 0.0029	9.0
Zn	0.9996	0.02-1.0	A = 0.2831C+ 0.0041	10

A: Absorbance, C: Concentration, RSD: Relative standard deviation

Table 3. Comparison of the digestion performance of trace elements using NIST SRM 1515 Apple Leaves, N=4

Element	Certified value (µg/g)	Method	Observed value (µg/g)	Recovery (%)
Co	(0.09) ^a	Microwave digestion	BDL	-
		Wet ashing	BDL	-
Pb	0.47	Microwave digestion	0.48±0.03	102
		Wet ashing	0.45±0.03	96
Ni	0.91	Microwave digestion	0.90±0.05	99
		Wet ashing	0.86±0.08	95
Cu	5.64	Microwave digestion	5.55±0.10	98
		Wet ashing	5.36±0.30	95
Fe	(83)	Microwave digestion	80.7±2.5	97
		Wet ashing	78.9±4.7	95
Cd	0.013	Microwave digestion	BDL	-
		Wet ashing	BDL	-
Cr	(0.3)	Microwave digestion	0.31±0.03	103
		Wet ashing	0.28±0.03	93
Mn	54	Microwave digestion	53.1±3.1	98
		Wet ashing	51.8±4.2	96
Zn	12.5	Microwave digestion	12.2±0.9	98
		Wet ashing	11.9±0.8	95

^anot certified, BDL: Below detection limit

Table 4. Comparison of the digestion performance of trace elements using NIST SRM 2711 Montana Soil, N=4

Element	Certified value ($\mu\text{g/g}$)	Method	Observed value ($\mu\text{g/g}$)	Recovery (%)
Co	(10) ^a	Microwave digestion	9.8±0.4	98
		Wet ashing	9.5±0.7	95
Pb	1162	Microwave digestion	1127±30	97
		Wet ashing	1103±75	95
Ni	20.6	Microwave digestion	20.1±1.5	98
		Wet ashing	19.6±1.7	95
Cu	114	Microwave digestion	110±5	96
		Wet ashing	108±8	95
Fe	28900	Microwave digestion	28033±250	97
		Wet ashing	27455±530	95
Cd	41.7	Microwave digestion	41.4±2.6	99
		Wet ashing	40.1±3.1	96
Cr	(47)	Microwave digestion	45.4±1.9	97
		Wet ashing	45.1±2.7	96
Mn	638	Microwave digestion	625±20	98
		Wet ashing	606±45	95
Zn	350.4	Microwave digestion	352±23	101
		Wet ashing	336±30	96

^anot certified

The recovery of trace element in NIST SRM 1515 Apple Leaves were found in the range of 93-95 % for wet ashing, 97-103 % for microwave digestion. The recovery of trace element in NIST SRM 2711 Montana Soil were found in the range of 95-96 % for wet ashing, 96-101 % for microwave digestion, respectively. Recovery values were nearly quantitative for analyzed iron, copper, zinc, manganese, nickel, cobalt, lead, cadmium and chromium ions. The results were close to each other for wet and microwave digestion methods. Microwave digestion method has been applied in real samples because the recoveries in microwave is higher, the analysis time is shorter and the risk of contamination is less. HF was not used in wet ashing method because of its can be damage to glassware. HF is important for solubilization of silicates in soil samples. But, the recovery values were found quantitative without HF.

Optimized method was applied to real apricot and soil samples collected from different region of Malatya city, Turkey. Soil samples were collected from near and far from traffic areas. The results are given in Table 5. Trace element contents of analyzed soil samples collected near the traffic areas were found higher than other samples. The highest and lowest values of the samples were found in iron and cadmium. Lead, chromium and cadmium concentrations in some apricot samples were found below detection limit of FAAS. Cadmium levels were also found below detection limit in some soil samples. Heavy metal levels in analyzed samples were in agreement with literature values [15-22]. The maximum iron, lead and cadmium levels permitted for food samples is 15 mg kg⁻¹, 0.1 mg kg⁻¹ and 0.05 mg kg⁻¹, respectively according to Turkish Food Codex [23]. Heavy metal levels in analyzed samples were not found toxic limits.

Table 5. Trace element contents of apricot and soil samples collected from Malatya, Turkey ($\mu\text{g/g}$), N=3

Sample	Pb	Cd	Fe	Cu	Zn	Cr	Ni	Co	Mn
Apricot 1	BDL	BDL	8.93±0.50	3.97±0.10	3.38±0.14	BDL	4.05±0.10	1.52±0.10	0.67±0.05
Apricot 2	BDL	BDL	5.91±0.32	2.50±0.15	0.58±0.03	BDL	7.07±0.27	2.92±0.20	0.81±0.06
Apricot 3	BDL	0.33±0.01	14.6±1.1	3.23±0.20	1.47±0.12	BDL	4.48±0.15	2.57±0.11	1.10±0.10
Apricot 4	BDL	BDL	8.94±0.30	3.73±0.12	2.36±0.16	BDL	2.33±0.12	1.87±0.13	1.25±0.11
Region 1 (near traffic) Soil	24.6±1.5	0.49±0.02	4340±50	54.6±2.3	162±20	39.7±2.5	56.6±3.8	12.9±1.1	179±7
Region 1 (far traffic) Soil	21.2±1.1	0.67±0.03	4192±25	37.8±2.7	26.2±1.7	37.5±1.5	44.3±3.1	14.2±0.9	199±10
Region 2 (near traffic) Soil	24.5±1.3	0.84±0.05	5799±30	39.7±2.1	23.5±1.9	38.5±2.4	52.1±2.8	12.8±0.8	233±16
Region 2 (far traffic) Soil	27.8±1.5	0.67±0.04	6266±55	51.9±1.9	27.8±2.2	55.8±3.6	62.2±4.8	16.3±1.2	309±21
Region 3 (near traffic) Soil	17.9±0.9	BDL	17377±76	16.7±0.8	29.0±2.1	56.8±2.8	57.3±3.5	29.7±1.9	671±32
Region 3 (far traffic) Soil	17.9±0.8	BDL	13410±80	17.2±0.9	20.3±1.5	50.7±2.7	49.4±2.6	24.0±1.4	580±27

BDL: Below detection limit

4. Conclusions

The performance of wet ashing and microwave digestion methods were compared for the digestion of apricot and soil samples collected different regions according to near and far traffic area from Malatya, Turkey. Recovery values were tested by using certified reference materials. There are no important differences between digestion methods. RSD values in microwave digestion method were found lower than wet ashing method. Trace element contents of soil samples collected near the traffic areas were found higher than other samples. Microwave digestion method has been used in real apricot and soil samples because of its higher recoveries and shorter digestion time. Microwave digestion has also some advantages with respect to the risk of contamination, reduce to some volatile species and environmental protection. Food samples collected from industrial and traffic areas should be more analyzed with respect to toxic heavy metals. Contaminated food samples should not be consumption in all time.

Acknowledgements

The authors would like to thanks Dr. Demirhan Cıttak and Dr. Ozgur Dogan Uluoğlu for their help in experimental studies. The authors would like to Tokat Gaziosmanpaşa University for master thesis of İnci Kaygusuz.

Conflict of interest

The authors declare that they have no conflict of interests

References

- [1] El-Kady, A.A., Abdel-Wahhab, M.A., Occurrence of trace metals in foodstuffs and their health impact, *Trends in Food Science & Technology*, 75 (2018) 36-45.
- [2] Dar, M.I. Green, I.D., Khan, F.A., Trace metal contamination: Transfer and fate in food chains of terrestrial invertebrates, *Food Webs*, 20 (2019) e00116.
- [3] Gallo, M., Ferrara, L., Calogero, A., Montesano, D., Navigli, D., Relationships between food and diseases: What to know to ensure food safety, *Food Research International*, 137 (2020) 109414.
- [4] Munzuroglu, O., Karatas, F., Geckil, H., The vitamin and selenium contents of apricot fruit of different varieties cultivated in different geographical regions, *Food Chemistry*, 83 (2003) 205-212.
- [5] Davarynejad, G. H., Vatandoost, S., Soltész, M., Nyéki, J., Szabó, Z., Nagy, P.T., Hazardous element content and consumption risk of 9 apricot cultivars, *International Journal of Horticultural Science*, 16 (4) (2010) 61–65.
- [6] Briffa, J., Sinagra, E., Blundell, R., Heavy metal pollution in the environment and their toxicological effects on humans, *Heliyon*, 6 (2020) e04691.
- [7] Chavez E., He Z. L., Stoffella P. J., Mylavarapu R. S., Li Y. C., Moyano B., Baligar V. C., Concentration of cadmium in cacao beans and its relationship with soil cadmium in southern Ecuador, *Sci. Total Environ.*, 533 (2015) 205-214.
- [8] Tuzen M., Soylak M., Evaluation of trace element contents in canned foods marketed from Turkey. *Food Chem.*, 102 (2007) 1089-1095.
- [9] Suo, L., Dong, X., Gao, X., Xu, J., Huang, Z., Ye, J., Lua, X., Silica-coated magnetic graphene oxide nanocomposite based magnetic solid phase extraction of trace amounts of heavy metals in water samples prior to determination by inductively coupled plasma mass spectrometry, *Microchemical Journal*, 149 (2019) 104039.
- [10] Altundag, H., & Tuzen, M. (2011). Comparison of dry, wet and microwave digestion methods for the multi element determination in some dried fruit samples by ICP-OES. *Food and Chemical Toxicology*, 49 (2011) 2800-2807.
- [11] de Almeida, O.N., Luzardo, F.H.M., Amorim, F.A.C., Velasco, F.G., González, L.N., Use of fiberglass support in the application of dried-spot technique with dispersion liquid-liquid microextraction for the determination of Co, Cr, Cu, Ni and Pb by Energy Dispersive X-Ray Fluorescence Spectrometry, *Spectrochimica Acta Part B*, 150 (2018) 92–98.
- [12] Zhao, X., Song, N., Zhou, W. & Jia, Q., Preconcentration procedures for the determination of chromium using atomic spectrometric techniques: A review. *Cent. Eur. J. Chem.*, 10 (2012) 927-937.
- [13] Mykhailo M. V., Copper, zinc, and cadmium in various fractions of soil and fungi in a Swedish forest, *J. Environ. Sci. Heal. A*, 48(8) (2013) 980-987.
- [14] Squadrone S., Brizio P., Chiaravalle E., Abete M. C., Sperm whales (*Physeter macrocephalus*), found stranded along the Adriatic coast (Southern Italy, Mediterranean Sea), as bioindicators of essential and non-essential trace elements in the environment, *Ecol. Indic.*, 58 (2015) 418-425.
- [15] Gaw, S.K., Wilkins, A.L., Kim, N.D., Palmer, G.T., Robinson, P., Trace element and ΣDDT concentrations in horticultural soils from The Tasman, Waikato and Auckland Regions of New Zealand, *Science of The Total Environment*, 355 (2006) 31-47.
- [16] Al-Bachir, M., Sarhil, A., Al-Haddad, Th., Trace elements measurement in apricot (*Prunus Armeniaca*L.) seeds by neutron activation analysis, *Journal of Biotechnology and Biomedical Science*, 1(3) (2018) 1-10.
- [17] Saracoglu S., Tuzen M., Soylak M., Evaluation of trace element contents of dried apricot samples from Turkey, *J. Hazard. Mater.*, 167 (2009) 647-652.
- [18] Mehari T.F., Greene, L., Duncan, A.L., Fakayode, S.O., Trace and macro elements concentrations in selected fresh fruits, vegetables, herbs, and processed foods in North Carolina, USA. *J. Environ. Prot.*, 6 (2015) 573-583.
- [19] Gergely A., Papp N., Banyai E.S., Hegedus A., Rabai M. et al., Assessment and examination of mineral elements in apricot (*Prunus armeniaca* L.) cultivars: A special attention to selenium and other essential elements, *Eur. Chem. Bull.*, 3(8) (2014) 760-762.
- [20] Zhanbin, L., Qinling, Z., Peng, L., Distribution characteristics of available trace elements in soil from a reclaimed land in a mining area of north

- Shaanxi, China, *International Soil and Water Conservation Research*, 1 (2013) 65-75.
- [21] Yang, H., Wang, F., Yu, J., Huang, K., Zhang, H., Fu, Z., An improved weighted index for the assessment of heavy metal pollution in soils in Zhejiang, China, *Environmental Research*, 192 (2021) 110246.
- [22] Yuan, X., Xue, N., Han, Z., A meta-analysis of heavy metals pollution in farmland and urban soils in China over the past 20 years, *Journal of Environmental Sciences*, 101 (2021) 217-226.
- [23] Anonymous Regulation of setting maximum levels for certain contaminants in foodstuffs, *Official Gazette*, Iss: 24908 (2002).

Determination of the chemical structure of diet biscuits with modern instrumental techniques

İdil KARACA AÇARI^{1,*} 

¹Bioengineering Department, Faculty of Engineering and Natural Sciences, Malatya Turgut Ozal University, 44210, Malatya / TURKEY

Abstract

There are too many deficiencies in the studies in terms of diet biscuit in the literature. This study aims to fill this gap in the literature. The % moisture content, structural content verification, thermal stability, degradation properties and % ash content of diet biscuit samples, structural characterizations, surface micromorphology and detailed structural analysis were determined with fast, precise, new instrumental techniques. Thermal degradation of the lemon-fiber diet biscuit sample started at 250 °C in four stages and completed at 585 °C. There is three-stage thermal degradation in wholemeal diet biscuit samples, starting at 229 °C and completed at 580 °C. There are 46.06% C, 1.60% N, 0.12% S and 6.68% H in lemon-fiber diet biscuits, and 45.51% C, 2.39% N, 0.15% S and 7.05% H in whole-wheat diet biscuits. Ca, K, Mg, Na, Zn element contents in diet biscuit samples were determined by AAS technique. In the diet biscuit samples, K was determined as the element with the highest amount and the element with the least amount was Zn. As a result, the work is comprehensive and original. It is believed that the study will fill an important gap in the literature and will be a useful resource for researchers.

Article info

History:

Received:08.12.2020
Accepted:02.05.2021

Keywords:

Instrumental techniques,
Diet biscuit,
Structural characterization,
Thermal analysis,
Morphologies analysis.

1. Introduction

Bakery products are the most popular processed foods in the world [1]. Biscuits, included in the bakery products class, represent the most popular snack category in all population groups around the world. The reason why biscuits are made from simple, inexpensive, easily available raw materials, very acceptable taste, availability in different flavors and long shelf life are the reasons that make them the most consumed bakery products all over the world [2, 3]. The name biscuit originated in France for the first time, as a result of baking a type of bread twice in order to provide better protection [4]. A popular food eaten by both children and adults, biscuits typically contain ingredients (fat and sugar) that make them unhealthy. The traditional method of making biscuit dough is to use semi-solid fat at room temperature [5]. Briefly, biscuits are high-energy, easily digestible foods based mostly on wheat flour, oil and sugar [6, 7]. The high calorie content of the biscuits disrupts the balanced diet of the consumer. Therefore, recently, in line with the attempts to improve nutritional profiles, fat, sugars and energy levels have been reduced [8]. Therefore, dietary forms have been developed and presented to

consumers. The diet (light) product consists of low-fat, artificial sweeteners and fiber-added products used instead of sugar. Dietary product consumption habit started in the 1960s [9]. Dietary product usage is very common nowadays. Today, health problems related to nutrition such as obesity, diabetes, hypertension, hypercholesterolemia and gastrointestinal problems are increasing. This increase brought the awareness that people should pay more attention to their diet. In the studies, the reasons for individuals to prefer dietary products were investigated. These are slimming, feeling healthier, eating a balanced and healthy diet, low-calorie foods are healthier than other foods, low-calorie foods prevent weight gain, and low-calorie foods taste good [10]. With the increasing use of dietary products, various diet products have started to be produced. Diet biscuits are widely consumed among diet products. The chemical structure contents of the dietary biscuit samples (lemon-fiber and wholemeal) selected within the scope of the study were determined by instrumental techniques. Structural characterizations of dietary biscuit samples were checked with Fourier transform infrared spectroscopy

*Corresponding author. e-mail address: idal.karaca@ozal.edu.tr
<http://dergipark.gov.tr/csji> ©2021 Faculty of Science, Sivas Cumhuriyet University

(FTIR), atomic absorption spectrometry (AAS), elemental analysis techniques, surface morphology and structures with scanning electron microscope (SEM) / energy dispersive X-ray spectroscopy (EDX) techniques, and also thermal properties with differential thermal analysis (DTA) and thermogravimetric analysis (TGA) techniques.

2. Materials and Methods

2.1. Materials

In this study, lemon-fiber and wholemeal diet biscuit samples of brand A were used. In the diet biscuit samples selected for this study were determined respectively general analytical properties, structural characterizations, surface morphology and structure determinations and thermal properties by appropriate techniques.

2.1. Preparation of samples

Biscuits are highly hygroscopic and quickly absorb moisture when exposed to the atmosphere [11, 12]. For this reason, the preparation of the sample was carried out very quickly by grinding in a porcelain mortar. The powdered diet biscuit samples were stored in a dry airtight glass jar until analysis.

2.2. Determination of % moisture content

Moisture content in diet biscuit samples was determined by gravimetric method based on drying process in Ecocell branded oven at 105 °C [13,14]. The weighing values of the samples were taken at certain time intervals. The weighing process was continued until the difference between the two weightings was 0.5% [15]. The % moisture content in diet biscuit samples was calculated according to the formula below.

$$\% \text{ Moisture} = (W_1 - W_2) / W_1 - W \times 100$$

Based on the formula given, the sample weight before drying is shown as W_1 , the dried sample W_2 and the tared sample container W which is dried and brought to constant weight. Experiments were performed in triplicate.

2.3. Thermal properties and % ash content

Thermal analysis includes methods based on the measurement of the change in physical properties as a function of temperature by heating the samples in a controlled manner. Analyzes were performed with Shimadzu system 50 model thermogravimetric analysis (TGA), Shimadzu system 50 model differential thermal analysis (DTA) devices. Ash content of diet biscuit samples was determined by thermogravimetric analysis, which is one of the thermal analysis methods, instead of traditional dry burning ash determination method [13].

2.4. Structural characterization

Chemical structure characterization was determined by Fourier transform infrared spectroscopy (FTIR) analysis, elemental analysis and atomic absorption spectrometry (AAS) techniques. LECO brand CHNS-932 model device was used in elemental analysis and Perkin Elmer AAnalyst AAS device was used for determination of mineral content. The change in the chemical bond structures of the dietary biscuit samples was investigated by Thermo Matson 1100 brand Fourier transform infrared spectroscopy (FTIR) analysis using the attenuated total reflection (ATR) technique in the 4000-400 cm^{-1} wavelength range.

2.5. Surface morphology-structure determination

Micromorphological properties of diet biscuit samples were determined with Leo EVO 40 model scanning electron microscope (SEM) at different magnifications. Structural determination was performed with "Quantax" brand energy dispersive X-ray spectroscopy (EDX) device with Bruker 125 eV detector.

2.6. Statistical analysis

Statistical analysis for % moisture and % ash of the samples was performed using GraphPad Prism. Results are presented as mean \pm SD, unless otherwise stated, and statistical significance was accepted as $p < 0.05$.

3. Results and Discussion

3.1. % Moisture content of diet biscuit samples

Moisture contents which are the general analytical properties of dietary biscuit samples are given in figures 1. When we look at figure 1 for moisture content, we see that this value is 2.85 ± 0.06 for lemon-fiber diet biscuit, and 2.77 ± 0.09 for wholemeal diet biscuit. There is no statistically significant difference between the % moisture values of the diet biscuit samples.

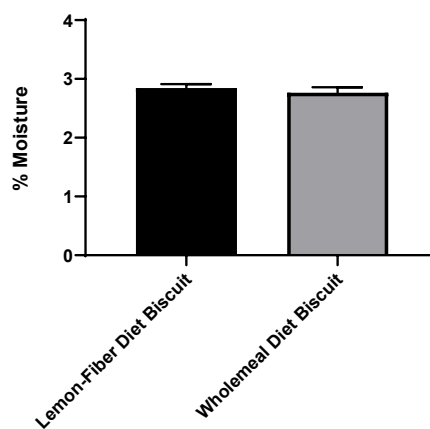


Figure 1. % Moisture Content in Diet Biscuit Samples.

There is no study similar to our study for dietary biscuit types in the literature. For this reason % moisture contents were discussed according to the existing biscuit studies in the literature not by comparing them with diet biscuit varieties. Nakov et al. determined the moisture in the biscuits containing different amounts of inulin between 2.5-2.94% [7]. Moisture ranges are compatible with our moisture ranges. Adeola et al. determined the moisture ratio between 6.30-7.90% in biscuits made of banana, pigeon pea and sweet potato flour at different rates [16]. In this study the moisture content is quite high compared to the diet biscuits we used in the study. Low moisture content of diet biscuits is known. Low moisture content in biscuits extends their shelf life. Ullah et al. made biscuits by adding different amounts of alfalfa seed flour to refined wheat flour. They observed that the amount of the moisture content in biscuits changed from 3.57% to 3.26%, respectively [17]. Their moisture content is higher than the diet biscuits we used in the study. This is an expected situation. Kumar et al. made biscuits containing seaweed in different proportions. They gave moisture ratios of these biscuits by comparing them with normal biscuits. They determined the moisture as $4.19 \pm 0.07\%$ in the normal biscuit sample. They determined the moisture content of the biscuit samples containing 1%, 5% and 10% seaweed as $4.08 \pm 0.12\%$, $3.97 \pm 0.1\%$, 4.03 ± 0.16 , respectively [18]. In this study, we see once again that the moisture content of normal biscuits is higher than that of diet biscuits. Agu et al. made biscuits containing different proportions of wheat flour and boiled and unripe banana flour. They determined the moisture content of these biscuit samples as $1.84 \pm 0.17\%$, $2.01 \pm 0.11\%$ and $2.55 \pm 0.28\%$ [19]. When compared to the diet biscuits we use, we see that the moisture content is low. As a result, biscuits have different moisture values due to the different additives they contain. As a result, we can say that diet biscuits contain lower moisture than other biscuits. Because diet biscuits contain fiber and bran. The water was retained by the fiber and bran [20].

3.2. Determination of thermal properties and % ash content of diet biscuit samples

Thermal properties of dietary biscuit samples were determined by TGA and DTA analyzes. Thermal analysis of dietary biscuit samples is used to verify the structural content of samples, to determine their thermal stability and degradation properties, as well as to offer an important and sensitive alternative to the determination of classical moisture and ash content by gravimetric method. The results of the TGA analysis performed within the scope of the study are given in figure 2. In these analyzes, wholemeal diet biscuits and lemon-fiber diet biscuits gave slightly different

thermograms. 3 different mass loss can be seen in the TGA thermogram of a wholemeal diet biscuit sample given in figure 2 (A). The first mass loss seen between 65 °C and 120°C is due to the moisture in the biscuit structure [21]. This mass loss resulting from the removal of structural moisture is approximately 2.05%. The second mass loss is seen between 180 °C and 400 °C and is caused by the degradation of the carbohydrate structures and starch in the biscuit structure [21]. This mass loss was determined to be approximately 59.27%. The final mass loss is due to thermal decomposition of difficult degraded structures such as bran structure. It is approximately between 400 °C and 500 °C and is around 30.39% [22]. According to TGA analysis results, the amount of ash at 600 °C was determined to be $7.47 \pm 0.04\%$ for a wholemeal diet biscuit. There are four different mass losses in the lemon-fiber diet biscuit structure. The first mass loss occurs between 75 °C and 120 °C, about 1.65% and is due to the removal of structural moisture. The second mass loss is due to the degradation of aromatic compounds added to the diet biscuit structure. It is seen between 140 °C and 240 °C and is approximately 10%. The third mass loss, approximately 55.42%, is due to the degradation of the capillary components, carbohydrate and starch, and is between 240-400 °C. The final mass loss between 400 °C and 580 °C is due to the thermal decomposition of hard-graded components and is approximately 25.22%. The amount of ash at 600 °C for lemon-fiber diet biscuit is $6.51 \pm 0.03\%$. There is a statistically significant difference between lemon-fiber biscuit ash ratio and wholemeal biscuit ash ratio ($p < 0.05$). The wholemeal biscuit ash ratio is due to the excessive bran content it contains. The bran biscuit ash ratio is due to the excessive bran content it contains. Ash contents were discussed according to the existing biscuit studies in the literature not by comparing them with diet biscuit varieties. Majzoobi et al. determined the ash content in the biscuit samples containing palm syrup and palm liquid sugar in the range of $5.30 \pm 0.51 - 25.3 \pm 0.3\%$ and $0.60 \pm 0.03 - 27.1 \pm 0.2\%$, respectively [23]. Increasing excess of ash content compared to the ash content of diet biscuit samples is due to the additives of palm syrup and palm liquid sugar in their structure. Adeola et al. determined the ash ratio in the range of 0.9-2.40% in biscuits made of banana, pigeon pea and sweet potato flour at different rates [16]. Ullah et al. made biscuits by adding different amounts of alfalfa seed flour to refined wheat flour. They observed that the amount of ash in biscuits changed from 1.37% to 1.92%, respectively [17]. Ash content is in accordance with our results, and their moisture content is higher than the diet biscuits we used in the study. Kumar et al. made biscuits containing seaweed in different

proportions. They gave moisture and ash ratios of these biscuits by comparing them with normal biscuits. They determined the amount of ash in normal biscuits as $1.28 \pm 0.01\%$. In other biscuit samples, they determined the amount of ash as $1.37 \pm 0.02\%$, $1.68 \pm 0.00\%$ and $2.23 \pm 0.03\%$ respectively [18]. The amount of ash is less than the wholemeal diet biscuit

we used in the study. Agu et al. made biscuits containing different proportions of wheat flour and boiled and unripe banana flour [19]. They determined the ash amount as $2.94 \pm 0.16\%$, $3.16 \pm 0.03\%$, $3.68 \pm 0.18\%$, respectively. As a result, we can say that the fiber and bran content of the diet biscuit samples is higher and therefore the ash content is higher.

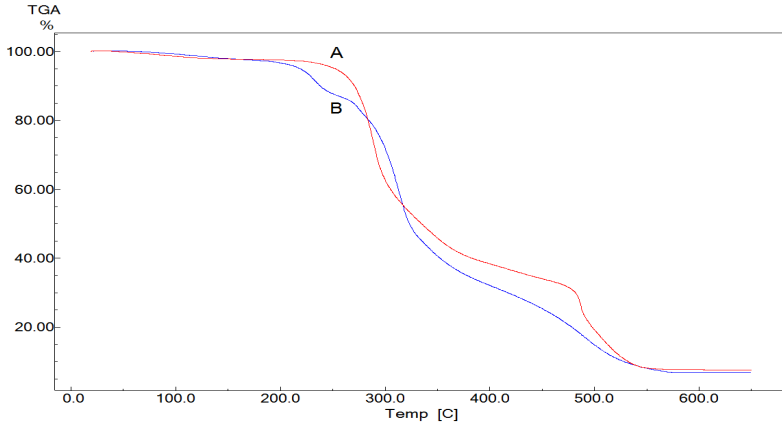


Figure 2. TGA Thermograms of Diet Biscuit Samples (wholemeal diet biscuit (A) and lemon-fiber diet biscuit (B)).

In Figure 3, DTA thermograms of diet biscuit samples are given. These thermograms have been seen to be compatible with TGA thermograms. Thermal decomposition in wholemeal diet biscuit starts at approximately 229 °C and is completed at approximately 580 °C with a three-stage thermal

decomposition [24]. Lemon-fiber diet biscuit structure shows a thermal degradation structure that starts at 250 °C and ends at 585 °C. This structure degrades in four stages and has a different thermogram than the wholemeal diet biscuit structure.

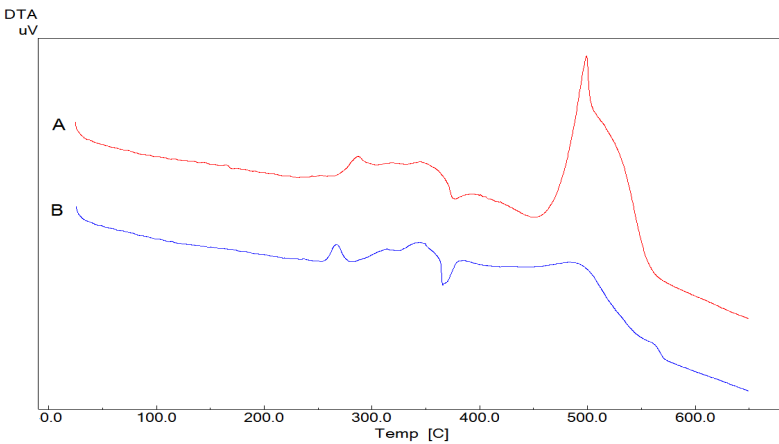


Figure 3. DTA Thermograms of Diet Biscuit Samples (wholemeal diet biscuit (A) and lemon-fiber form biscuit (B)).

3.3. Structural characterization of diet biscuit samples with elemental analysis, FTIR and AAS techniques

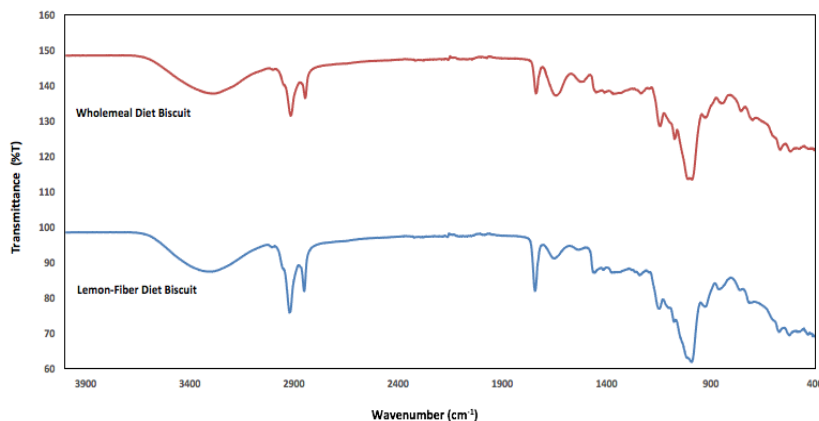
In this part of the study, diet biscuit samples were examined structurally and information about their chemical structures was obtained. Significant element percentages in diet biscuit samples were determined with the results of elemental analysis. The results are given in table 1. According to this, it was determined that 46.06% C, 1.60% N, 0.12% S and 6.68% H in lemon-fiber diet biscuit structures. Wholemeal diet

biscuit structures contain elements in the ratios of 45.51% C, 2.39% N, 0.15% S and 7.05% H. When these values are compared with the elemental analysis results of classical biscuit structures in the literature, it is seen that the N and S elemental content is high [25]. This situation is diet biscuits contain more bran and bran protein than normal biscuits. Especially N and S elements in protein structure directly contribute to the biscuit structure.

Table 1. Percentages of Elements Determined in Diet Biscuit Samples.

Sample Name	Element Percentages
Lemon-fiber diet biscuit	46.06% C, 1.60% N, 0.12% S and 6.68% H
Wholemeal diet biscuit	45.51% C, 2.39% N, 0.15% S and 7.05% H

FTIR analysis was used to illuminate the chemical structure of the diet biscuit samples and the FTIR spectra obtained are given in figure 4. FTIR spectra provide useful structural information that can help identify samples enriched with specific functional food ingredients [18].

**Figure 4.** FTIR spectrum results of diet biscuit samples.

On the FTIR spectra of the diet biscuit samples given in figure 4, the 3 main peak structures are clearly seen. The peaks in these structures are caused by carbohydrate, protein and structural fat molecules and are clearly visible. Especially due to the carbohydrate molecules, we see peaks of free OH groups in the range of 3000-3600 cm^{-1} . These peaks are caused by both structural moisture and surface hydroxyls. In addition, a wide and severe peak in the range of about 1000-1100 cm^{-1} due to carbohydrate structures is caused by etheric stretching vibration. C-O stretching vibrations stand out as a thin peak around 1200 cm^{-1} . Due to protein structures, FTIR spectra contain amide 1 and amide 2 peaks [26, 27]. Peaks in protein structure; 1650 cm^{-1} amide 1 peak is the amide 2 peak that comes around 1548 cm^{-1} . These specifically show carbonyl stretching vibrations in protein structures. Again, due to the protein structure peptide bonds, C-N stretching vibrations were detected at 1440 cm^{-1} . At low wave numbers, especially at 825-650 cm^{-1} , aliphatic C-H vibrations, aliphatic CH stretch vibrations in the range of 2850-2950 cm^{-1} and C-C stretch vibrations at 1380 cm^{-1} are seen due to both protein structures and carbohydrate structures. A very small C = O stretching

vibration is observed in diet biscuit structure especially at 1730 cm^{-1} . This peak is proof that the amount of fat in the diet biscuit structure is very low. This peak is generally seen in classical biscuits as prominent and severe. This situation is due to the fat molecules in the structure. However, it is almost non-existent in the diet biscuit structure. When FTIR spectra in Figure 3 are compared with each other, an ester carbonyl stretch vibration around 1820 cm^{-1} is seen in the lemon fiber diet biscuit structure. This is due to the aromatic ester flavors in the biscuit structure.

Analysis of Ca, K, Mg, Na, Zn elements in dietary biscuit samples was performed by flame atomic absorption spectrometry (FAAS) technique. Samples were digested primarily by wet digestion method. According to this method, after adding 5 mL (HCl-HNO₃, 3:1 v / v) to the 0.5 g samples, 2 mL ethanol (99.8 %) was added to the mixture. The resulting mixture was then filtered through whatman 42 filter paper [28]. Calibration graph was drawn for each given element for Ca, K, Mg, Na, Zn analyzes in the samples obtained.

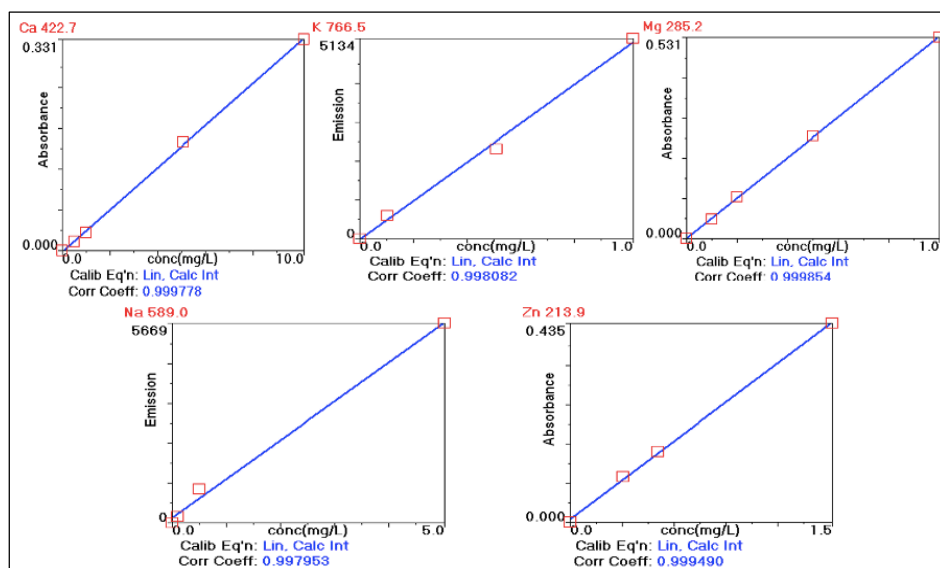


Figure 5. Calibration graph for Ca, K, Mg, Na, Zn elements

Table 2. Analytical working ranges, correlation coefficients and wavelengths of Ca, K, Mg, Na and Zn elements.

Element	Analytical working range (mg/L)	Correlation coefficient (R ²)	Wavelength (nm)
Ca	0-10.0	0.9998	422.7
K	0-1.0	0.9981	766.5
Mg	0-1.0	0.9999	285.2
Na	0-5.0	0.9980	589.0
Zn	0-1.5	0.9995	213.9

The graphics are given in figure 5. Information about the analytical working ranges, correlation coefficients and wavelengths of Ca, K, Mg, Na and Zn elements is given in table 2. Elemental analyzes in the prepared samples were determined in triplicate by flame atomic absorption spectroscopy. Results are given in Table 3.

3.4. Surface Morphology-Structure Analysis of Diet Biscuit Samples with SEM / EDX technique

Diet biscuit samples have a different structure than other biscuits and cookies due to the bran structure they contain and with low fat content [29, 30]. Basically, it displays more harder and rigid morphology.

Table 3. Analytical results of Ca, K, Mg, Na, Zn elements in diet biscuits samples (metal concentrations as, mg/100 g).

Sample Name	Ca	K	Mg	Na	Zn
Lemon-fiber diet biscuit	24.89±0.15	100.2±0.42	25.16±0.01	46.92±0.40	0.505±0.01
Wholemeal diet biscuit	31.01±0.32	170.3±2.97	42.22±0.01	55.73±0.11	0.813±0.01

SEM analyzes were performed to examine the micro morphological and surface structure of the apparently hard-structured diet biscuit samples and the results are given in Figure 6 and Figure 7.

A very fractal but monolithic structure is seen in the lemon-fiber diet biscuit structure given in figure 6. An uninterrupted and cavitated SEM surface image is seen. Due to starch structures, spherical structures are seen in places. However, the microstructure shows irregular and small porosity.

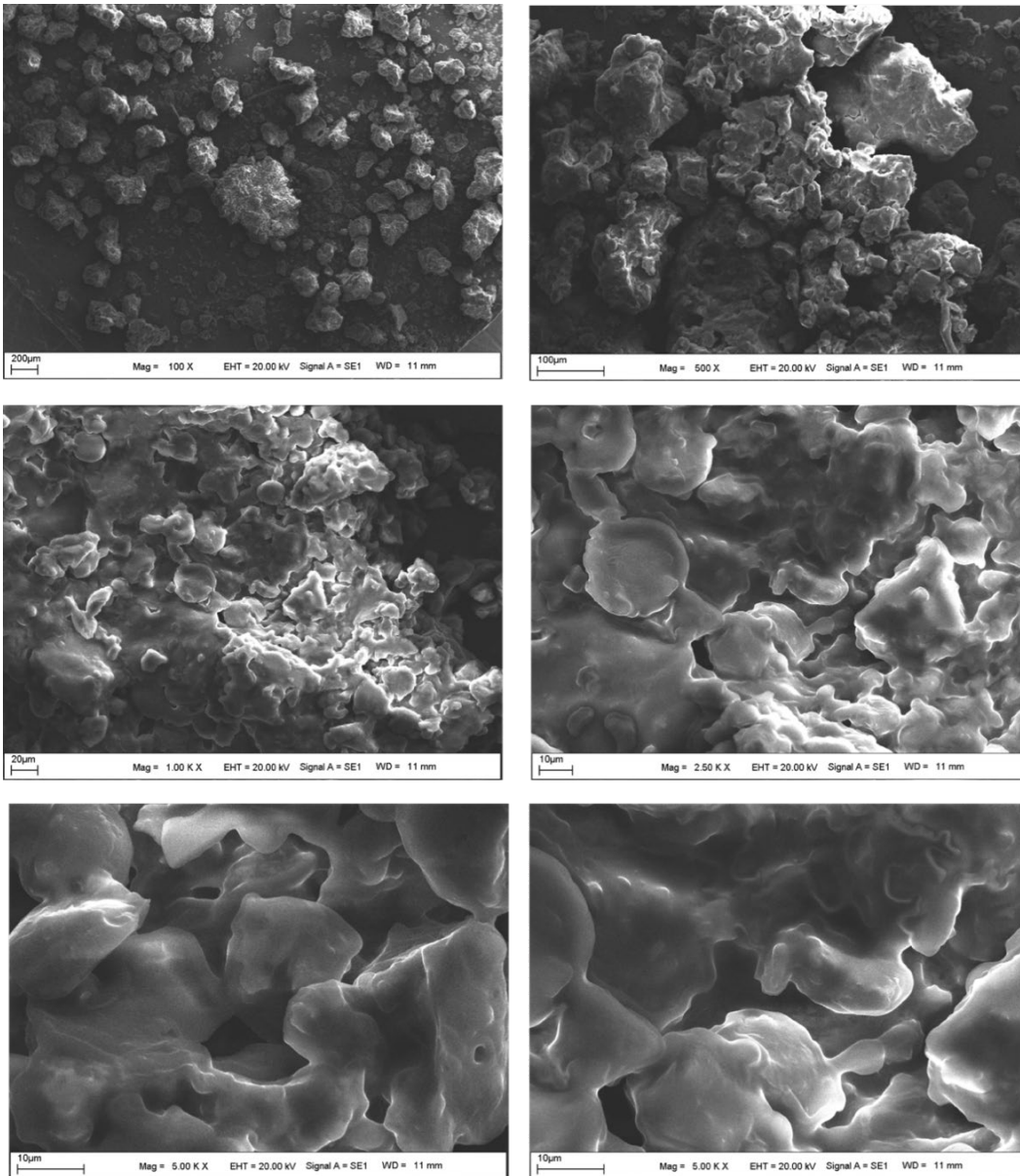


Figure 6. SEM Images of Lemon-Fiber Diet Biscuit Sample at Different Magnifications.

A high cavital structure is seen in the wholemeal biscuit structure in figure 7. In places, bran fibers are visible and starch structures are frequently encountered. In particular, the porosity was seen to be greater. Although the biscuit structure exhibits a monolithic structure, it contains fractal and granular parts in places. The evaluation of the starch spherical structures of the lemon-fiber diet and wholemeal diet

biscuit samples given in Figure 6 and Figure 7 is given in detail in figure 8. In the SEM images of the lemon-fiber diet biscuit sample given in figure 8 (A) and (B) the more prominent spherical structures are clearer and distinct. However, it is seen that the starch structures in the structure of wholemeal diet biscuit in figures (C) and (D) are better adhered to the main surface and structurally fused.

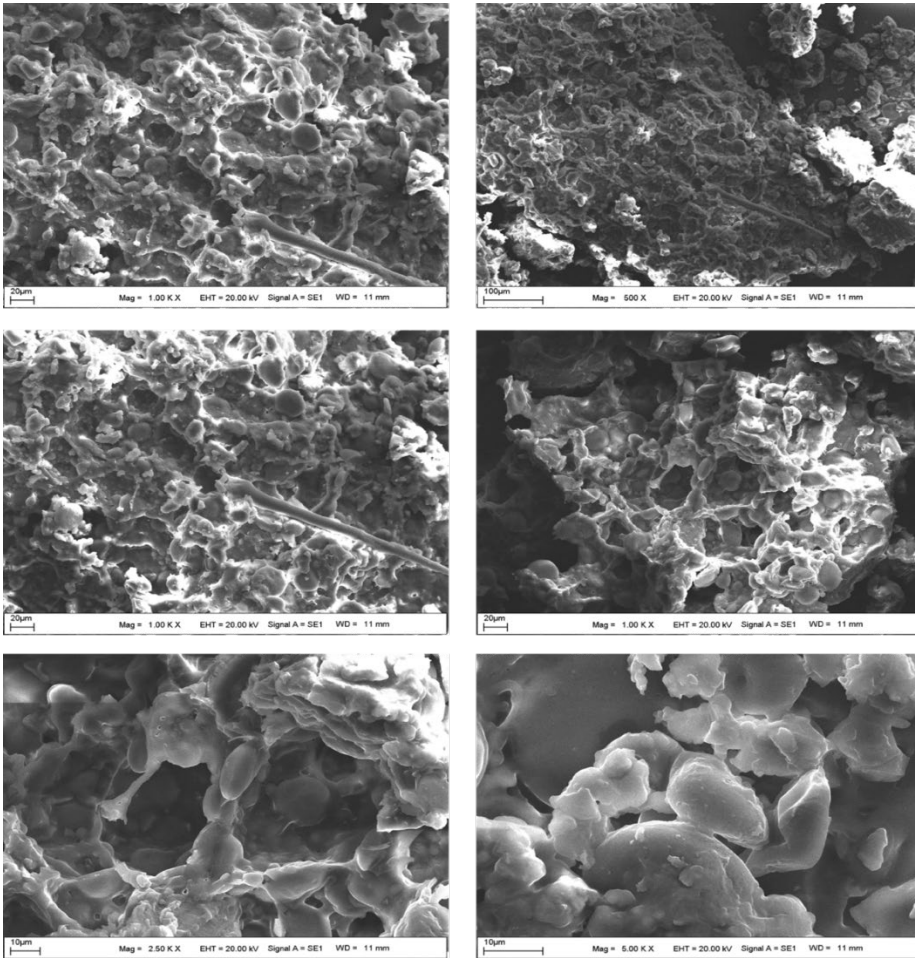


Figure 7. SEM Images of Wholemeal Diet Biscuit Sample at Different Magnifications.

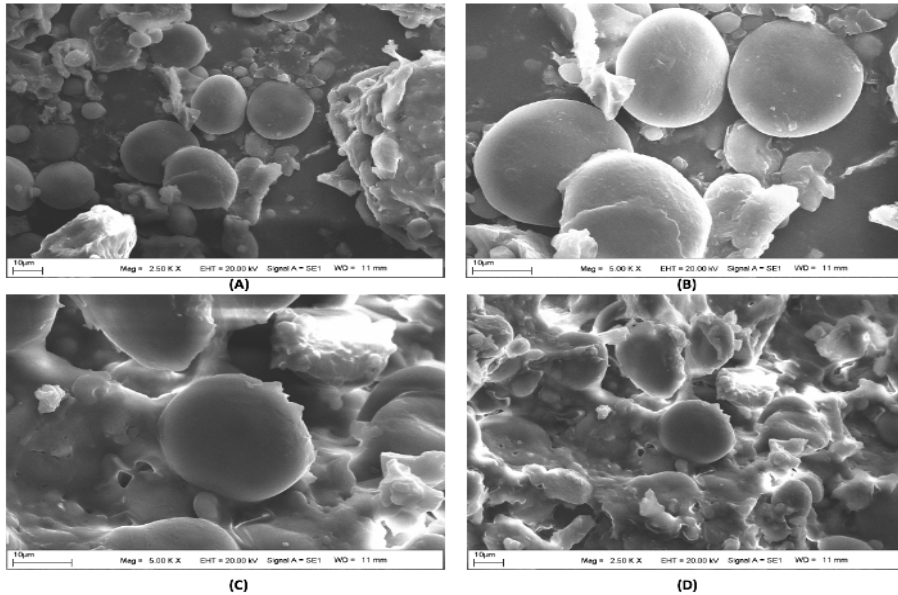


Figure 8. SEM Images of Starch Structures in Diet Biscuit Samples at Different Magnifications.

EDX spectra of diet biscuit samples were taken for a detailed surface analysis. The results of these analyzes are given comparatively in figure 9. When we look at the surface analysis results of this diet biscuit, although

the peak intensities are different, we see the surface peaks of Ca, K, Mg, Na elements as well as P and Cl elements.

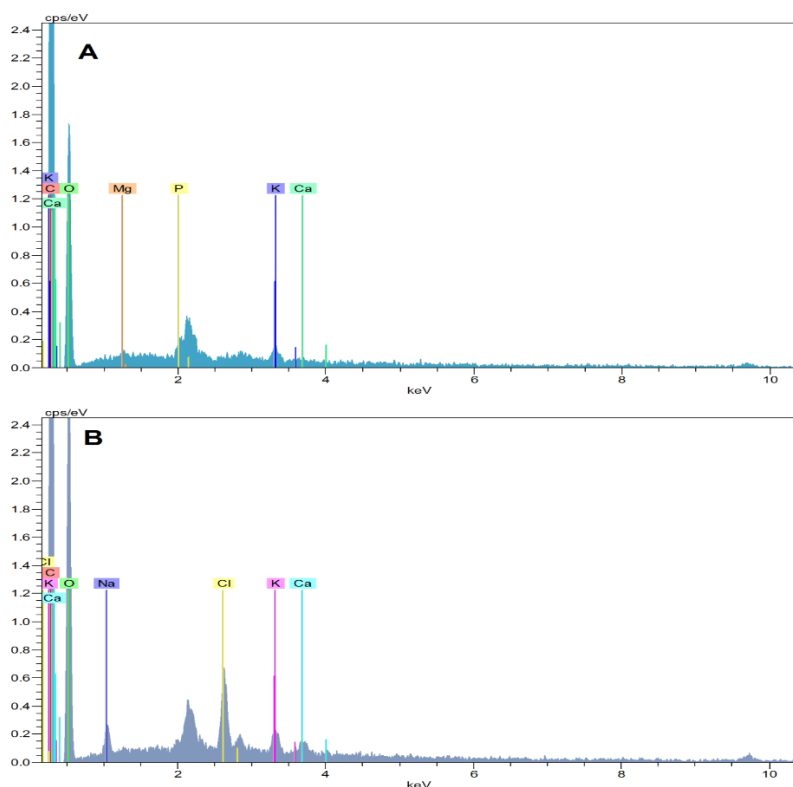


Figure 9. EDX Spectra for Lemon-Fiber diet biscuit (A) and wholemeal diet biscuit (B) samples

4. Conclusion

The moisture content of the diet biscuit samples used in the study was determined as $2.85 \pm 0.06\%$ in the lemon-fiber diet biscuit sample and $2.77 \pm 0.09\%$ in the diet biscuit sample with whole wheat. Accordingly, four different mass losses are observed in the lemon-fiber diet biscuit samples. First mass loss ($75-120^\circ\text{C}$) from removal of structural moisture, second mass loss ($140-240^\circ\text{C}$) from decay of flavoring aromatic compounds, third mass loss ($240-400^\circ\text{C}$) from structural carbohydrate and starch degradation, fourth mass loss ($400-580^\circ\text{C}$) is due to the fiber in the structure. There are three different mass losses in the example of wholemeal diet biscuit. The first ($65-120^\circ\text{C}$) is the moisture in the structure, the second ($180-400^\circ\text{C}$) is the structural carbohydrate and starch, and the third ($400-500^\circ\text{C}$) is the degradation of the bran structures. Ash contents of diet biscuit samples were determined by TGA analysis. Ash contents were determined as $6.51 \pm 0.18\%$ in the lemon-fiber diet biscuit sample, and $7.47 \pm 0.04\%$ in wholemeal diet biscuit. Thermal degradation of the lemon-fiber diet biscuit sample started at 250°C in four stages and was completed at 585°C . It was observed that there was a three-stage thermal degradation in wholemeal diet biscuit samples started at 229°C and completed at 580°C . 46.06% C, 1.60% N, 0.12% S and 6.68% H

elements were observed in the samples of lemon-fiber diet biscuit. 45.51% C, 2.39% N, 0.15% S and 7.05% H elements were observed in the sample of wholemeal diet biscuit. In FTIR spectra, three main peaks originating from carbohydrate, protein and fat structure are clearly observed. In the lemon-fiber diet biscuit sample, there is an ester carbonyl stretch vibration around 1820 cm^{-1} , unlike the whole wheat diet biscuit, due to the aromatic esters that give the lemon flavor. When we look at the AAS results, we see different amounts of Ca, K, Mg, Na, Zn elements in both diet biscuit sample contents. Since a structural characterization has been carried out for the first time in dietary biscuit samples with this study, the elements determined by the AAS technique are in harmony with the biscuit samples previously made [31]. When the micromorphologies of the surface are examined with SEM, a very fractal, monolithic structure is seen in the lemon-fiber diet biscuit sample. Wholemeal diet biscuit sample exhibits a high cavital structure. Spherical starch structures are present in both biscuit samples. Surface analyzes are detailed with EDX spectra. In the EDX spectrum, we see the peaks of Ca, K, Mg, Na elements as well as P and Cl elements with different intensities on the dietary biscuit sample surfaces. We can explain both structural and superficial content differences of diet biscuit samples as follows. We know that flour containing wheat flour and wheat

bran are used in the production of snacks such as biscuits etc. snacks. Contrary to expectations, flour contents are extremely complex and the composition can vary. It has different ingredient contents in bakery products (biscuits, etc.). Different ingredient contents vary greatly depending on the genetic potential of the selected wheat, growing conditions and climate. Especially the main source of mineral content in flour is soil. The amount of mineral matter obtained from the soil depends largely on the soil type, rainfall, the type and amount of fertilizer applied and environmental conditions [32]. In addition; The prominence of the P peak is due to phytic acid molecules in the structure of wholemeal [33]. Cl is caused by NaCl added to biscuit samples for aroma and preservative purposes [34]. As a result, the study showed us that the moisture, ash content, chemical structure properties, surface morphology-structure properties and thermal properties of the diet biscuit samples are different from the classical biscuit structures. The study is the first comprehensive original study done with diet biscuits. For this reason, the study will provide positive contributions to the literature in terms of originality. When we look at the literature, we see that food analysis is carried out with laborious, time-consuming traditional test methods. This study was carried out using modern instrumental techniques. The techniques used have enabled us to make interpretations both faster and with more precise results. The study has also brought a different perspective to food analysis.

Conflict of interest

The authors declare that they have no conflict of interests.

References

- [1] Caleja C., Barros L., Antonio A.L., Oliveira M.B.P.P., Ferreira I.C.F.R., A comparative study between natural and synthetic antioxidant: Evaluation of their performance after incorporation into biscuits, *Food Chem.*, 216 (2017) 342-346.
- [2] Chauhan A., Saxena D.C., Singh, S., Total dietary fibre and antioxidant activity of gluten free cookies made from raw and germinated amaranth (*Amaranthus spp.*) flour, *LWT-Food Sci Technol.*, 63(2) (2015) 939-945.
- [3] Psodorov Đ., Ačanski M., Psodorov D., Vujić, Đ., Pastor K., Determination of the content of buckwheat and wheat flours in bread using GC-MS and multivariate analysis, *J. Food Nutr. Res.*, 54(2) (2015) 179-183.
- [4] Vujic' L., Cepo D.V., Sebecic B., Dragojevic' I.V., Effects of pseudocereals, legumes and inulin addition on selected nutritional properties and glycemic index of whole grain wheat-based biscuits, *J. Food Nutr. Res.*, 53(2) (2014) 152-161.
- [5] Boobier WJ., Baker JS., Davies B., Development of a healthy biscuit: an alternative approach to biscuit manufacture, *Nutr.*, 5(7) (2006) 1-7.
- [6] Klunkin W., Savage G., Biscuits: A substitution of wheat flour with purple rice flour, *AFSE.*, 2(3) (2018) 81-97.
- [7] Nakov G., Stamatovska V., Ivanova N., Damyanova S., Godjevargova T., Komlenic D.K., Physicochemical characteristics of functional biscuits and in vivo determination of glucose in blood after consumption of functional biscuits, *J. Hyg. Eng. Des.*, 22 (2018) 25-32.
- [8] Kolberg DI., Prestes OD., Adaimo M.B., Zanella R. A New Gas Chromatography/Mass Spectrometry (GC-MS) Method for the Multiresidue Analysis of Pesticides in Bread., *J. Braz. Chem. Soc.*, 21(6) (2010) 1065-1070.
- [9] Cerci A., Cakmak Aksan A., Gümüs D., Pazarbası İ., Determination of the diet product consumption status of adults between, *Hacettepe University Faculty of Health Sciences Journal.*, 7891 (2015) 103857.
- [10] Yıldırım Mavis Ç., Ozay Arancioğlu İ., Aldemir N., Assessment of clients'awareness and consumption frequency of diet food products who consulted to nutrition and diet counseling, *Haliç University Journal of Health Sciences.*, 1 (2018) 15-29.
- [11] Guinë RPF., Barroca M.J., Pereira D., Correia P.M.R., Adsorption isotherms of Maria biscuits from different brands, *J. Food Process Eng.*, 37(3) (2014) 329-337.
- [12] Diukareva G., Pak A., Gasanova A., Determination of storage conditions for new biscuits using their sorption isotherms, *Ukrainian Food Journal.*, 3(2) (2014) 249-256.
- [13] Passos M.E.A. dos, Moreira C.F.F., Pacheco M.T.B., Takas I., Lopes, M.L.M, Valente-Mesquita V.L., Proximate and mineral composition of industrialized biscuits, *Food Sci. Technol.*, 33(2) (2013) 323-331.
- [14] Cayuela-Sánchez Y.A., Palarea-Albaladejo J., Zira T.P., Moriana-Correro E., Compositional method for measuring the nutritional label

- components of industrial pastries and biscuits based on Vis/NIR spectroscopy, *J. Food Compos. Anal.*, 92 (2020) 103572.
- [15] Kalendar M., Akosman C., Drying behavior of sunflower seeds in infrared dryer and adaptation analysis to during models, *Firat University Journal of Engineering*, 27(1) (2015) 51-56.
- [16] Adeola A.A., Ohizua E.R., Physical, chemical and sensory properties of biscuits prepared from flour blends of unripe cooking banana, pigeon pea, and sweet potato, *Food Sci. Nutr.*, 6(3) (2018) 532-540.
- [17] Ullah F., Ahmad S., Wahap S., Zeb A., Khattak M.K., Khan S., Kang M., Quality evaluation of biscuits supplemented with alfaalfa seed flour, *Foods.*, 5(4) (2016) 68.
- [18] Kumar A., Krishnamoorthy E., Devi H.M., Uchoi D., Tejpal C.S., Ninan G., Zynudheen A.A., Influence of sea grapes (*caulerpa racemosa*) supplementation on physical, functional and antioxidant properties of semi-sweet biscuits, *J. Appl. Phycol.*, 30 (2018) 1393-1403.
- [19] Ag H.O., Okoli, N.A., Physico-chemical, sensory, and microbiological assessments of wheat-based biscuit improved with beniseed and unripe plantain, *Food Sci. Nutr.*, 2(5) (2014) 464-469.
- [20] Erinc H., Mert B., Tekin A., Different sized wheat bran fibers as fat mimetic in biscuits: its effects on dough rheology and biscuit quality, *J. Food Sci. Technol.*, 55(10) (2018) 3960-3970.
- [21] Amin. T., Naik H.R., Hussain S.Z., Mir M.A., Jabeen A., In vitro digestion, physicochemical and morphological properties of low glycemic index rice flour prepared through enzymatic hydrolysis, *Int. J. Food Prop.*, 21(1) (2018) 2632-2645.
- [22] Costa L.A. Des., Fonsèc A.F., Pereira, F.V., Druzia J.I., Extraction and characterization of cellulose nanocrystals from corn stover, *Cell Chem Technol.*, 49(2) (2015) 127-133.
- [23] Majzoobi M., Hansouri H., Mesbahi G.H., Farahnaky A., Golmakani M.T., Effects of sucrose substitution with date syrup and date liquid sugar on the physiochemical properties of dough and biscuits, *J. Agric. Sci. Technol.*, 18 (2018) 643-656.
- [24] Díaz A., Bomben R., Dini C., Viña S.Z., García M.A., Ponzi M., Comelli N., Jerusalem artichoke tuber flour as a wheat flour substitute for biscuit elaboration, *LWT-Food Sci. Technol.*, 108 (2019) 361-369.
- [25] Ahmad N., Sahrin N., Talib N., Ghani F.S.A., Characterization of energy content in food waste by using thermogravimetric analyser (TGA) and elemental analyser (CHNS-O), *J. Phys. Conf. Ser.*, 1349 (2019) 1-8.
- [26] Esselink E.F.J., Aalst H.van., Maliepaar M., Duynhoven, J.P.M. van., Long-term storage effect in frozen dough by spectroscopy and microscopy, *Cereal Chem.*, 80(4) (2003) 396-403.
- [27] Van Velzen E.J.J., Van Duynhove J.P.M., Pudney P., Weegels P.L., van der Maas J.H., Factor associated with dough stickiness as sensed by attenuated total reflectance infrared spectroscopy, *Cereal Chem.*, 80(4) (2003) 378-382.
- [28] Doner G., Ege A., Evaluation of digestion procedures for the determination of iron and zinc in biscuits by flame atomic absorption spectrometry, *Anal. Chim. Acta.*, 520 (2004) 217-222.
- [29] Pereira D., Correi P.M.R., Guinè, R.P.F., Analysis of the physical-chemical and sensorial properties of Maria type cookies, *Acta Chim. Slov.*, 6(2) (2013) 269-280.
- [30] Tavares B.O., Silva E-P da., Silva V-S-N.da., Soares Júnio M.S., Ida E.I., Damiani C., Stability of gluten free sweet biscuit elaborated with rice bran, broken rice and okara, *Food Sci. Technol.*, 36(2) (2016) 296-303.
- [31] Barbarisi C., De Vito V., Pellicano MP., Boscaino F., Balsamo S., Laurino C., Sorrentino G., Volpe MG., Bread chemical and nutritional characteristics as influenced by food grade sea water, *Int. J. Food Prop.*, 22(1) (2019) 280-289.
- [32] Gül H., Determination of the effects of corn and wheat brans addition on dough and bread characteristics, Ph.D. Thesis., Department of Food Engineering Institute of Natural and Applied Sciences University of Çukurova, (2007).
- [33] Ravindran V., Ravindran G., Sivalogan S., Total and phytate phosphorus contents of various foods and foodstuffs of plant origin, *Food Chem.*, 50 (1994) 133-136.
- [34] Zaky AS., Pensupa N., Andrade-Eiroa Á., Tucker G.A., Du C., A new HPLC method for simultaneously measuring chloride, sugars, organic acids and alcohols in food samples, *J. Food Compos. Anal.*, 56 (2017) 25-33.



Environmental risk assessment of commonly used anti-cancer drugs

Hamdi MIHÇIÖKUR ^{1,*}

¹Erciyes University, Faculty of Engineering, Department of Environmental Engineering, Kayseri/TURKEY

Abstract

This study has been focused on the commonly used anti-cancer drugs (ACDs) in Turkey in terms of environmental toxicity, behaviors in sewage treatment plants (STPs), biodegradability and physicochemical properties. For this purpose, EPI Suite, estimation programme, has been used by employing BCFWIN, KOWWIN, KOCWIN, HENRYWIN, AEROWIN, ECOSAR, BIOWIN, STPWIN suites. Among 13 selected ACDs, Tamoxifen has been found as the most risky pharmaceutical due to its high Predicted Environmental Concentration (PEC) / Predicted No Effect Concentration (PNEC) value (2.96350). Even if the total removal efficiency of Tamoxifen is rather high (97.24%), the considerable portion (71.50%) has been retained on the treatment sludge leading to compose hazardous waste. Additionally, physicochemical parameters, log Kow (6.30), Kd (62230 L/g), log Koc (4.400) and BCF (6689 L/kg), calculated for Tamoxifen indicate that Tamoxifen has the highest sorption potential and tends to bioaccumulate in organisms, respectively.

Article info

History:

Received: 23.01.2021

Accepted: 07.06.2021

Keywords:

Anti-cancer drugs,
Environmental risks
Pharmaceuticals;
Predicted
environmental
concentration,
Predicted no effect
concentration.

1. Introduction

Anti-cancer drugs (ACDs) are classified to two main groups as antineoplastic and immunomodulating agents (class L) by the Anatomical Therapeutic Classification (ATC) system based on their therapeutic purposes [1]. Antineoplastic agents are categorized into 5 sub-groups upon to their chemical structures and therapeutic properties such that; L01A: Alkylating agents; L01B: Antimetabolites; L01C: Plant alkaloids; and other natural products; L01D: Cytotoxic antibiotics and related substances; L01X: Other antineoplastic agents [1]. These antineoplastic drugs are discriminated from each other due to their different mode of actions [1]. Most chemotherapy drugs which are used to kill cancer cells and to inhibit the growth of these cells act as cytotoxic agents (L01D), so cytotoxic agents are considered to be in the most risky group from environmental point of view compared to the other antineoplastic agents [1]. On the other hand, cytostatic agents (L01X) used for treatment of cancer and other illnesses are differentiate from cytotoxic agents because of their specific action mechanism [1]. Cytostatic agents prevent cancer cells growing and spreading, without killing them in contrast to cytotoxic agents [2]. As well as antineoplastic agents, immunomodulating agents are also classified into sub-groups and these drugs are defined by their ATC codes like that; L02A: Hormone and related agents; L02B:

Hormone antagonists and related agents; L03A: Immunostimulants, L04A: Immunosuppressants [3].

The amount of use for anti-cancer drugs is considerably high in many countries in the world [4]. Today, more than fifty different anti-cancer drugs have been used routinely in cancer care in United Kingdom [1]. According to the Pharmaceuticals and Medical Devices Institution report of Republic of Turkey Ministry of Health, the consumption of antineoplastic and immunomodulating drugs known as anti-cancer drugs were increased in 2007-2014 years associated with increasing cancer cases explained above. While 4.7 million boxes of anti-cancer drugs were consumed in 2007, this number was raised up to 9.3 million boxes in 2014. Also, box sales of anti-cancer drugs increased from 6.9 to 9.8 million boxes in the range of 2011-2016 years depending on the increment in cancer cases in respect to the Turkish Medicines and Medical Devices Agency report. Nowadays, the amount of use of anti-cancer drugs in hospitals and outpatients has been gradually increased due to the tendency in the increment of cancer cases and therapeutic and inhibitory effects of these drugs [5]. The main sources of anti-cancer drugs in aquatic environment are domestic and hospital wastewaters [6,7]. The penetration of these drugs to domestic wastewaters is performed through the excreted urine of chemotherapy patients as the other pharmaceuticals [5]. The anti-

*Corresponding author. e-mail address: hamdi@erciyes.edu.tr

cancer agents by which excreted through urine may damage [1,3,8] the genetic and cell structure of living organisms in the aquatic environment [9,10] since they have potential to show carcinogenic, teratogenic, mutagenic and adverse effects on normal and immune system cells. Therefore, the physical and biological removal of anti-cancer drugs from wastewaters should be performed, but this process is rather difficult [9] because these drugs are poorly biodegradable and are not fully metabolized in the human body [1].

Al-Ahmed and Kümmerer reported that among pharmaceuticals, drugs used for cancer treatment, referred to as anticancer or antineoplastic drugs, are suspected to represent a specific risk for aquatic non-target species [11]. Data on the toxicity of anti-cancer agents suggest that some of these drugs are toxic at three-fold or higher concentrations than that of their known environmental concentrations [5, 12]. Environmental risk assessment of anti-cancer drugs should be done to determine biodegradability (biodegradation period) and behaviors (total removal (%), total biodegradation (%), total sludge adsorption (%)) of these drugs in sewage treatment plants (STPs) due to the toxic effects of these agents to the aquatic environment. Additionally, physicochemical properties of anti-cancer drugs should be investigated for understanding the potential risks of these drugs to the environment. During the chemotherapy medication, physicochemical parameters of anti-cancer drugs (polarity, non-volatile, solubility, etc..) can increase with the entering of these drugs to waste waters through hospital effluents and domestic dwellings [1]. This case can cause environmental risk for aquatic media. So, researching some critical physicochemical properties of anti-cancer drugs is crucial to get information whether it would be difficult to remove them from aquatic environment or not when they have penetrated it [5].

Generally, only limited studies have been performed on the ecotoxicity of both cytotoxic and cytostatic drugs. Until now, a detailed study has not been reported on the environmental significance of most frequently used anti-cancer drugs in Turkey in respect to predicting and assessing environmental risks due to the restricted and lower consumption compared to other pharmaceuticals. Furthermore, based on the tendency in the increasing usage of anti-cancer drugs in different fields (cancer treatment of pets, other treatments excluding cancer, etc.) [5]. In several countries, extra consumption data of these agents should be accounted. In this case, the existence of these drugs into the environment will be expected to increase further and there will be more need to the

environmental risk assessment of anti-cancer drugs in the future.

In the present study, the calculations have been performed in order to assess the environmental risks of anti-cancer drugs as theoretically. The programme of EPA is used in the calculations. In these calculations, the structural analysis and the physical properties of anti-cancer drugs have been estimated. Due to the reason of increasing consumption of these anti cancer drugs, determining the environmental risks of these drugs is critical in future time. So, this study is original for this point of view.

2. Materials and Methods

In the present study, the consumption data (number of boxes/units) of imported oncology drugs by pharmacological firms were taken from IMS-Health (Intercontinental Marketing Services Health) Turkey for the year of 2017. Totally 13 anti-cancer drugs, widely used in Turkey, were selected for getting knowledge about fate and behaviors of these drugs, since examination of a group of anti-cancer drugs having high consumption as detailed is worthy. In this study, all calculations have been carried out using EPI Suite™ (Estimation Programs Interface) program which includes physical/chemical and environmental fate estimation suites (BCFWIN, KOWWIN, KOCWIN, HENRYWIN, AEROWIN, ECOSAR, BIOWIN, STPWIN) developed by EPA's and Syracuse Research Corp. (SRC) [13]. EPI Suite program is based on Quantitative Structure Activity Relationships (QSARs) methodologies which are used in estimation of toxicity measures of chemicals from the physical properties based on their molecular structures and in prediction of the effects of chemicals on biota [13].

The Predicted Environmental Concentration (PEC) and the Predicted No Effect Concentration (PNEC) values of selected drugs have been calculated to obtain the PEC/PNEC ratios which indicate the risks of drugs. Risk assessment, assigned as insignificant, low, moderate and high depending on PEC/PNEC ratios, has been performed according to Stockholm Council Report and given in Table 1. PNEC values have been calculated by using Effective Concentration (EC50) and Lethal Concentration (LC50) values which are computed by Ecological Structure-Activity Relationships (ECOSAR) Interface of EPA's [13]. As physicochemical parameters of anti-cancer drugs, Bioconcentration factor (BCF), Octanol-water partition coefficient (log Kow), Organic carbon-normalized sorption coefficient (log Koc), vapour pressures and Henry Law constants have been

calculated by employing BCFWINTM, KOWWINTM, KOCWINTM, AEROWINTM and HENRYWINTM suites of EPA, respectively [13]. In addition, the biodegradability of drugs under aerobic and anaerobic conditions has been estimated by using the BIOWIN 3, BIOWIN 5 and BIOWIN 7 modules of the Biodegradation Probability Program (BIOWIN) which estimates the probable biodegradation of chemicals as rapidly or slowly. EPI Suite User Guide [13] has been used in the evaluation of the results obtained from BIOWIN output data. Also, STPWIN interface of EPA/EPI Suite [13] has been applied to evaluate the biological behaviors (total removal, total biodegradation and total sludge adsorption) of ACDs in STPs.

Among the BIOWIN modules, the results of BIOWIN 3, BIOWIN 5 and BIOWIN 7 have been evaluated heavily in this study. The ultimate biodegradation time has been calculated by BIOWIN 3, if the aerobic biodegradation occurs or not has been discussed by the way of the results of BIOWIN 5 and the anaerobic biodegradation conditions have been informed by BIOWIN 7. Due to the similar results of BIOWIN 1 and BIOWIN 2 modules with BIOWIN 3, also the insufficient information about biodegradation time, the non-linearity of BIOWIN 6 compared to BIOWIN 5, the primary biodegradation time obtained by BIOWIN 4 instead of ultimately, it is not required to evaluate the BIOWIN 1, BIOWIN 2, BIOWIN 4 and BIOWIN 6.

Also, total removal, total biodegradation and total sludge adsorption parameters that determine biological treatability of drugs in STPs have been calculated using STPWIN interface of EPA/EPI Suite [13]. Generally, PEC values of pharmaceuticals have been calculated according to Equation 1 (Eq.1) that following formula is given below with the explanations of parameters [14, 15].

$$PEC (\mu\text{g/L}) = \frac{Ax10^9x(100-R)}{365\frac{\text{day}}{\text{year}}xPxVxDx100} \quad (1)$$

A: The amount of annual use of pharmaceuticals (kg)

R: Removal rate of pharmaceuticals before mixing with the water bodies by using different processes (adjusted as 0) [14].

P: Population of Turkey (80810525 persons) [16].

V: The amount of wastewater produced by per person per day (180 L/person/day [17])

D: Environmental dilution factor (usually 10) [14,15].

In calculation of PNEC values of pharmaceuticals, toxicological dose descriptors (EC50/LC50/NOECs)

obtained by toxicity studies are usually divided by different assessment factors. In that study, the PNEC values of the selected ACDs have been determined by dividing computed EC50 and LC50 values to the assessment factor taken as 1000. The following equation (Eq.2) has been used in the calculation of PNEC values [18].

$$PNEC = \text{Lowest Acute (EC50 or LC 50)}/\text{Assessment Factor} \quad (2)$$

Bioconcentration factors (BCF) for the selected drugs, predicted with EPI Suite BCFWIN interface, have been calculated in order to get information about bioaccumulation potentials of ACDs on living organisms. BCF parameter, given in the following equation (Eq.3), can be expressed as the ratio between the concentrations of chemical in organism and aquatic media [19].

$$BCF = \text{Concentration Biota}/\text{Concentration Water} \quad (3)$$

Concentration Biota = Concentration of a chemical in an organism

Concentration Water = Concentration of a chemical in an aquatic media.

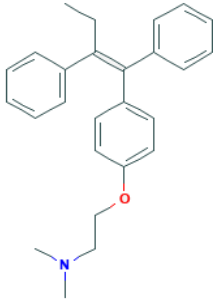
Kd values have been used to verify the adsorption capacities of pharmaceuticals on surfaces. The following equation (Eq.4) has been used in the calculation of Kd value of each drug [20].

$$Kd = 10(0.58 \log Kow + 1.14) \quad (4)$$

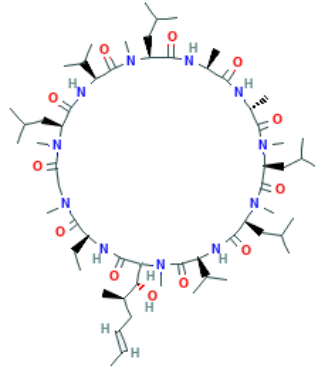
Herein, Kow and Kd parameters express octanol-water partition coefficient and particle-water distribution ratio of pharmaceuticals, respectively [20].

Totally 13 anti-cancer drugs, widely used in Turkey, were selected for getting knowledge about fate and behaviors of these drugs. The two-dimensional representation and chemical structure of the ACDs used in this study are shown in Figure 1.

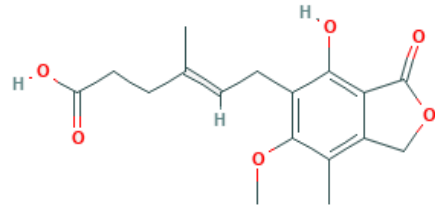
Tamoxifen



Ciclosporin



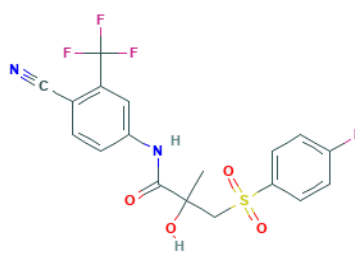
Mycophenolic acid



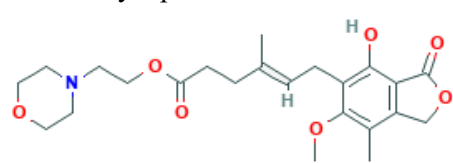
Azathioprine



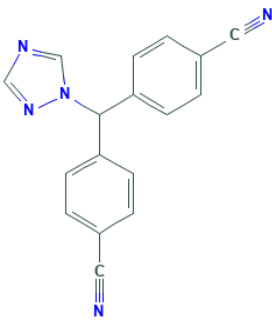
Bicalutamide



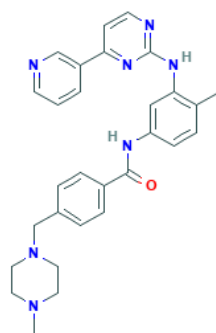
Mycophenolate mofetil



Letrozole



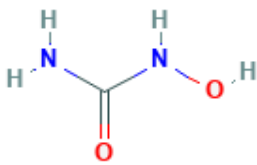
Imatinib



Capecitabine



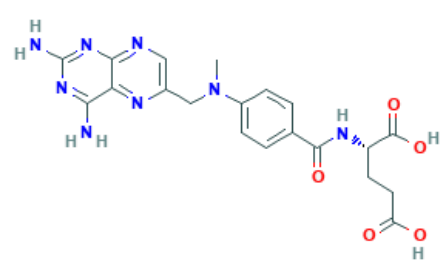
Hydroxycarbamide



Temozolomide



Methotrexate



5-Fluorouracil

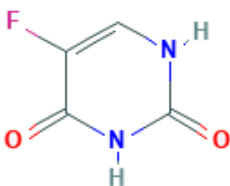


Figure 1. Chemical structure of the ACDS

3. Results and Discussion

3.1. Environmental risk assessment of ACDs

Predicted Environmental Concentration (PEC), Predicted No Effect Concentration (PNEC) and PEC/PNEC values have been calculated to assess the environmental risks of pharmaceuticals. [14, 21-24]. The following criteria that define the PEC and PEC / PNEC values is considered in the assessment of the environmental risks of pharmaceuticals.

- PEC<0.01 µg/L: There is no need to have done some tests and researches.
- 0.01µg/L <PEC<0.1µg/L: PEC/PNEC ratio should be considered and investigated.
- PEC/PNEC >1: Pharmaceutical can lead serious risks in environment, so precautions should be taken to

avoid environmental risks [23].

To classify the risk groups of ACDs and to specify the environmental risks of them, the data taken from Stockholm County Council report was used in that study. In this report, the potential risk groups determined to PEC/PNEC values are as follows; PEC/PNEC<0.1: Insignificant, 0.1<PEC/PNEC<1: Low, 1<PEC/PNEC<10: Moderate PEC/PNEC>10: High [22].

In the present study, the environmental risk assessment of 13 ACDs has been done by the aid of calculated PEC, PNEC and PEC/PNEC values which are given in Table 1.

Table 1. Environmental risk assessment of the selected ACDs

Drug Name	PEC (µg/L)	PNEC (µg/L)	Lowest Effect Level Toxicity Test /Test Organism/ECOSAR Class	PEC/PNEC	Risk Assessment	
					This Study*	Others [1,4,5]
Mycophenolic acid	0.0078	1.8750	LC ₅₀ /Daphnid/Neutral Organic	0.00414	Insignificant	-
Ciclosporin	0.0315	47.5790	EC ₅₀ /Green Algae/Amides	0.00066	Insignificant	-
Mycophenolate mofetil	0.2707	0.4290	EC ₅₀ / Green Algae/ Aliphatic Amines	0.63091	Low risk	-
Azathioprine	0.0267	1.2710	EC ₅₀ / Green Algae/Imidazoles	0.02103	Insignificant	-
Bicalutamide	0.0161	2.6430	EC ₅₀ / Green Algae/Amides	0.00611	Insignificant	Need to confirm its presence in environment.
Tamoxifen	0.0178	0.0060	EC ₅₀ / Green Algae/Aliphatic Amines	2.96350	Moderate	Potential risk
Letrozole	0.0006	7.7720	EC ₅₀ / Green Algae/Triazoles	0.00008	Insignificant	-
Capecitabine	0.1262	0.9880	EC ₅₀ / Green Algae/Carbamate Esters	0.12774	Low risk	Potential risk
Methotrexate	0.0014	34.9260	LC ₅₀ /Daphnid/Anilines	0.00004	Insignificant	No need to assess
Temozolomide	0.0036	1.8180	EC ₅₀ / Green Algae/Imidazoles	0.00199	Insignificant	No need to assess
Hydroxycarbamide	0.1014	318.00	LC ₅₀ /Earthworm/Neutral Organic	0.00032	Insignificant	Potential risk
Imatinib	0.0122	1.0880	EC ₅₀ / Green Algae/Amides	0.01120	Insignificant	Need to confirm its presence in environment
5-Fluorouracil	0.0031	0.0100	EC ₅₀ / Green Algae/Carbonyl Ureas	0.31418	Low risk	Need to confirm its presence in environment

* Risk assessment for the selected ACDs was performed based on the criteria of Stockholm County Council report. According to this report, environmental risks are determined by taken into account PEC/PNEC values (If PEC/PNEC<0.1: Insignificant; if PEC/PNEC 0.1-1.0: Low; if PEC/PNEC 1-10: Moderate; if PEC/PNEC >10: High).

Among 13 ACDs given in Table 1. Tamoxifen, included in Endocrine Therapy class, was considered to be the most toxic drug for environment due to the calculated highest PEC/PNEC (2.96350) and the lowest PNEC (0.0060($\mu\text{g/L}$)) values. According to the risk assessment report of Stockholm Country Council [21], Tamoxifen was assessed as moderate risky. On the other hand, Mycophenolate Mofetil, 5-Fluorouracil and Capecitabine were classified as “low risk” depending on PEC/PNEC values (0.63091, 0.31418, 0.12774) in descending order, respectively. Although, these three drugs are in low risk group, the potential risk levels may increase as to the increment in the amounts of use. The other ACDs excluding from Tamoxifen, Mycophenolate Mofetil, 5-Fluorouracil

and Capecitabine have been considered as “insignificant” in terms of their risk assessment due to their calculated PEC/PNEC values lower than 0.1 ($\text{PEC/PNEC} < 0.1$).

3.2. Biodegradation times of ACDs with their behaviors in STPs

The estimated biodegradation times of totally 13 ACDs, given in Table 2, were calculated by using BIOWIN suite involving BIOWIN 3, BIOWIN 5 and BIOWIN 7 models [13].

Table 2. Estimation of biodegradation times of the selected ACDs with their behaviors in sewage treatment plants.

Drug Name	*Estimated Biodegradation Times Of ACDs				*Estimated Behaviors Of ACDs In Sewage Treatment Plants (STPs) (%)				
	BIOWIN 3		BIOWIN 5		BIOWIN 7		Total Rem.*	Total B.D.*	Total S.A.*
	Cal.* ratings	Complete B.D.* time units	Cal.* values	Readily B.D.*	Cal.* values	Rapid B.D.*			
Mycophenolic acid	2.8446	Weeks	0.9028	Yes	0.7719	Yes	99.39	85.88	13.51
Ciclosporin	0.4035	Recalcitrant	-0.2050	No	-8.5487	No	5.07	0.12	4.95
Mycophenolate mofetil	2.1067	Months	0.5660	No	-1.0032	No	48.06	46.25	1.81
Azathioprine	2.4169	Weeks to Months	-0.0318	No	0.2562	No	21.99	20.54	1.45
Bicalutamide	0.9795	Recalcitrant	0.1007	No	-0.7876	No	2.64	0.10	2.54
Tamoxifen	2.1092	Months	0.0803	No	-1.1212	No	97.24	25.74	71.5
Letrozole	2.4039	Weeks to Months	0.0357	No	-0.0851	No	23.49	21.46	2.03
Capecitabine	2.9679	Weeks	0.3146	No	0.5557	Yes	75.09	74.46	0.63
Methotrexate	2.3452	Weeks to Months	0.1288	No	-1.6667	No	21.97	20.53	1.44
Temozolomide	2.7159	Weeks to Months	0.3183	No	0.0932	No	21.97	20.53	1.44
Hydroxycarbamide	3.0311	Weeks	0.4344	No	0.8361	Yes	75.06	74.44	0.62
Imatinib	1.1206	Recalcitrant	-0.5364	No	-3.6976	No	5.77	0.12	5.65
5-Fluorouracil	2.9117	Weeks	0.3981	No	0.7626	Yes	75.06	74.44	0.62

* Biowin/EPA draft method is used in order to assign biodegradation time of compounds [13], Cal: Calculated, B.D: Biodegradation, Rem: Removal, S.A: Sludge Adsorption

Each model predicts different biodegradation periods of drugs (i.e. complete biodegradation, ready for biodegradation, fast or slow biodegradation). BIOWIN 3 model estimates the time required for complete biodegradation of compound in a typical aquatic environment under aerobic conditions. Boethling and Sabljic have been rated the ultimate biodegradation of compounds as a scale of 1-5 according to the calculated

numerical values by employing BIOWIN 3 model [25]. In this study, the calculated ratings have been attributed to the biodegradation time units of compounds (5: Hours, 4: Days, 3: Weeks, 2: Months, 1: Longer). If the calculated rating is a decimal value changing in the range of 1-5, it is considered that the ultimate biodegradation time of the compound cannot be determined exactly, that means the compound can

biodegrade completely in an uncertain time (i.e. days to weeks, weeks to months, etc.). As to BIOWIN 3 results, the calculated ratings of 0.4035, 0.9795, 1.1206, respectively for Ciclosporin, Bicalutamide and Imatinib, indicated these drugs being highly persistent in environment and resistant against biodegradation. Therefore, these drugs were called as "Recalcitrant". BIOWIN 5, which is one of several models of BIOWIN suite, is utilized to estimate whether the compounds are ready for biodegradability or not under aerobic conditions [13]. In predicting "ready biodegradability" of compounds, the results obtained from both BIOWIN 3 and BIOWIN 5 models are evaluated as common. With respect to the approach described by [26], if BIOWIN 3 result is defined as "Weeks" or faster than weeks (i.e. "Days", "Days to Weeks", or "Weeks") and BIOWIN 5 value is higher than 0.5, then the compound is considered as "ready for biodegradation"; if not so the compound is considered as "not ready for biodegradation". Considering BIOWIN 3 results, Mycophenolic acid, Capecitabine, Hydroxycarbamide and 5-Fluorouracil have been evaluated as easily biodegradable drugs due to the shorter biodegradation time which are described as "Weeks". Among these 4 drugs, Mycophenolic acid is considered as "ready for biodegradation" drug because of the calculated BIOWIN 5 value (0.9028) that is higher than that of 0.5. BIOWIN 7, an anaerobic biodegradation model, estimates the probability of rapid biodegradation under anaerobic conditions [13]. The calculated values by BIOWIN 7 higher than that of 0.5 (>0.5) indicate that compounds can biodegrade rapidly [13]. In this context, Hydroxycarbamide, Mycophenolic acid, 5-Fluorouracil and Capecitabine ACDs can biodegrade rapidly under anaerobic conditions in respect to the calculated values of 0.8361, 0.7719, 0.7626 and 0.5557, respectively.

It is essential to know the behaviors of pharmaceuticals in sewage treatment plants due to the probable toxic effects of these drugs. The estimated behaviors of 13 ACDs in sewage treatment plants (STPs), total removal (%), total biodegradation (%) and total sludge adsorption (%) were given in Table 2. It was noted that the total removal efficiencies of Bicalutamide, Ciclosporin and Imatinib in STPs were found to be lower than the other ACDs in Table 2 due to the lower calculated values as 2.64, 5.07 and 5.77, respectively. This result indicates that the giant proportion of Bicalutamide, Ciclosporin and Imatinib can enter to aquatic media without treatment. Although these ACDs were considered to be non-risky according to the low PEC/PNEC ratios calculated as 0.00611 (Bicalutamide), 0.00066 (Ciclosporin) and 0.01120 (Imatinib); their potential to enter in receiving

water was rather high due to their lower removal efficiencies. The calculated values of total sludge adsorption as 2.54, 4.95 and 5.65 for Bicalutamide, Ciclosporin and Imatinib, respectively indicate that the large amount of these ACDs were removed from wastewater by being adsorbed to sludge based on their lower calculated removal efficiencies (2.64, 5.07 and 5.77) and this case can cause hazardous waste for environment. The calculated total biodegradation values for Bicalutamide, Ciclosporin and Imatinib as 0.10, 0.12 and 0.12, respectively showed that these ACDs were poorly biodegrade in aquatic media. This estimation is also in harmony with the predicted BIOWIN results since the results from BIOWIN explain that these ACDs are "Recalcitrant" against biodegradation and possess longer biodegradation time. On the other hand, even if Tamoxifen is the most risky agent depending on the highest PEC/PNEC ratio (2.96350); the amount of 97.24% for Tamoxifen can be removed from aquatic media. Although the total removal efficiency of Tamoxifen is rather high, the considerable portion of this amount (71.50%) is adsorbed on the treatment sludge causing to compose hazardous waste. Hence, the sludge adsorption of Tamoxifen is an undesired case due to its toxicity, leading environmental risk.

3.3. Physicochemical properties of ACDs

In combination with environmental risk assessment of pharmaceuticals, it should be required to investigate also the physicochemical properties of them which inform us for how difficult it would be remove these drugs from the aquatic environment when they have entered it. In the present study, the physicochemical parameters calculated by applying different suites of EPA, have been presented as collectively in **Table 3** for 13 ACDs. The chemical structures of the related ACDs, given as Supplementary Data, contribute in the assessment of some critical physicochemical parameters such as solubility, Kow, Kd.

Considering that most of the pharmaceuticals possess lipophilic character, namely dissolved in membrane lipids, it should be required to be investigated the bioaccumulation of drugs on organisms, in terms of their toxicity. In this context, bioconcentration factor (BCF), described as the ratio between the concentrations of chemical in living organism and in aquatic media, provides us to understand whether these drugs are causing accumulation or not in the organisms.

Table 3. Physicochemical properties of the selected ACDs

Drug Names	BCF (L/kg)	Log K _{ow}	Log K _{oc}	K _d (L/g)	Vapour Pressure (Pa)	Henry's Law Constant (Pa·m ³ /mole)	Water Solubility (mg/L) 25°C
Mycophenolic acid	3.162	4.22	2.647	3869	3.15E-007	3.87E-007	22.07
Ciclosporin	39.23	2.92	1.729	682	*NC	*NC	4.239E-005
Mycophenolate mofetil	17.27	2.38	2.177	331	6.05E-009	5.59E-01	680.1
Azathioprine	3.162	0.10	2.395	16	7.48E-008	2.68E-010	272.3
Bicalutamide	15.23	2.30	2.177	298	2.33E-010	2.85E-010	11.75
Tamoxifen	6689	6.30	4.400	62230	2.31E-005	4.55E-005	0.1916
Letrozole	13.58	2.22	3.010	268	5.05E-005	2.01E-006	102.8
Capecitabine	3.162	0.56	0.173	29	1.35E-008	2.96E-014	1821
Methotrexate	3.162	-1.85	-0.387	1	1.23E-013	1.56E-026	2600
Temozolomide	3.162	-1.32	0.554	2	1.51E-005	8.10E-009	1.148E+004(11480)
Hydroxycarbamide	3.162	-1.80	-0.081	1	0.585	5.49E-006	2.242E+005(224200)
Imatinib	45.18	3.01	2.762	769	8.41E-012	8.17E-019	2.103
5-Fluorouracil	3.162	-0.89	0.442	4	0.0068	1.68E-005	2.59E+004 (25900)

*NC: non calculated

Eq.3 explains that there is a proportion between the calculated BCF value and the concentration of pharmaceutical on biota that means in the case of BCF value increases, tendency for bioaccumulation of pharmaceutical within the tissue will increase. Tamoxifen, with the calculated BCF value of 6689 L/kg, has the highest BCF value, compared to others, that means Tamoxifen extremely tends to accumulate in organisms due to its high concentration. Lipophilicity, a key physicochemical parameter associated with solubility, membrane permeability, and hence drug absorption and distribution with route and rate of clearance, is a measure of interaction with lipids [27]. From the structural point of view, apolar (non-polar) or lipophilic groups found in molecular structure of compound, makes molecule more lipophilic due to low water solubility of these fragments. Herein, Tamoxifen is considered as highly lipophilic since the structure of Tamoxifen is composed mostly of apolar groups, such as aromatic (C₆H₅-) and aliphatic groups (-CH₃, -CH₂-, H₂C=CH₂), which enhance the lipophilicity of Tamoxifen. So, Tamoxifen may cause toxic effect on the organisms by accumulating in the lipid part of the cell membranes. On the other hand, Mycophenolic acid, Azathioprine, Capecitabine, Methotrexate, Temozolomide and Hydroxycarbamide are unlikely to be expected for accumulation due to their low BCF values calculated as 3.162 L/kg for all.

Looking at the solubility of ACDs, Hydroxycarbamide has the highest aqueous solubility (2.242x10⁵ mg/L). Presence of many deprotonated forms, (-HN-CO-NHOH), (H₂N-CO-N(OH)-), (H₂N-CO-N(H)O⁻) and consisting of ionizable functional groups (primer, secondary amine and hydroxyl) make Hydroxycarbamide, more soluble in water, hence render it more hydrophilic. As different from other ACDs, Ciclosporin, a polypeptide consisting of 11 amino acid moieties with their hydrophobic aliphatic groups, has a complex structure. Amino acids, possessing hydrophobic -R groups, are found in the interior part of the polypeptide where does not come into contact with water [28]. Ciclosporin has low water solubility (4.239x10⁻⁵) due to the presence of hydrophobic CH₃ and CH₂ groups binding to amino acid units of polypeptide. Kow is defined as a concentration ratio of compound, distributed between n-octanol and aqueous phase. In order to estimate the sorption efficiencies of ACDs, the following general statements [5, 29, 30], defining the sorption potentials of these drugs according to the calculated Kow values, were taken in consideration. A.P. Toolaram et al. have suggested that the pharmaceuticals having log Kow values below 1 (log Kow<1) are highly mobile in the aquatic media, therefore they remain in liquid phase in contrast to sorption of them onto particles, sediments or sludge [5]. Based on that survey, the drugs of Azathioprine (0.10), Capecitabine (0.56), Methotrexate (-1.85), Temozolomide (-1.32), Hydroxycarbamide (-1.80) and 5-Fluorouracil (-0.89)

are considered to remain in the aqueous phase and to show weak tendency for sorption due to their low log Kow values. The values given in parenthesis above represent the calculated log Kow values for the related drug. In another study, have determined the effectiveness of adsorption for pharmaceuticals using the following criteria [29, 31]

- $\log Kow < 2.5$: low adsorption potential;
- $4.0 < \log Kow < 2.5$: moderate adsorption potential;
- $\log Kow > 4.0$: high adsorption potential;

According to the explanation above, Tamoxifen (6.30) and Mycophenolic acid (4.22) are considered to have higher adsorption potentials than the other ACDs due to the calculated log Kow values above 4.0. In Tamoxifen, the hydrophobic interactions between, aromatic (benzene rings), alkyl (-CH₃, -CH₂-) groups and lipid fractions of sludge, may be efficient in sorption due to the highly lipophilic character of these groups. Imatinib and Ciclosporin have moderate adsorption potentials with the calculated log Kow values of 3.01 and 2.92, respectively. Excluding Tamoxifen, Mycophenolic acid, Imatinib, and Ciclosporin, the sorption of other ACDs on the activated sludge is rather poor. The pharmaceuticals possessing log Kow values higher than 4.5, are considered as bioaccumulative according to the European Medicines Agency's (EMA) guideline associated with the environmental risk assessment of medicinal products [5, 32]. In this context, Tamoxifen is supposed to have tendency in terms of persistency and bioaccumulation due to its high calculated log Kow value.

Since ACDs are complex molecules which possess different functional groups, involving acidic and/or basic groups within the same molecule, it is difficult to determine if molecules may be sorbed onto surface or not. Log Kow data is not sufficient in the assessment of sorption behaviors due to the several factors affecting sorption process, such as pH, redox potential, chemical nature of sorbent and sorbed molecules, etc [31]. Hence, in order to clarify sorption of pharmaceuticals exactly, experimental studies have to be done accompanied with theoretical studies. The theoretical data from this study will guide the experimental studies to be carried out on this subject.

K_d , defined as solid-water distribution coefficient, is used to understand the sorption capacities of pharmaceuticals on surfaces. All K_d values are obtained by using calculated Kow values, previously.

The relation between K_d and K_{ow} is given as a mathematical expression in Eq.4. From the results of K_d , it can be concluded that Tamoxifen has the highest capacity for sorption due to its considerable high K_d value calculated as 2230. Mycophenolic acid with the calculated K_d value of 3869 is in the second order after Tamoxifen in terms of its sorption capacity. Methotrexate, Temozolomide, Hydroxycarbamide and 5-Fluorouracil are considered to exhibit extremely weak sorption potential with their rather low K_d values calculated as 1, 2, 1 and 4 L/g, respectively.

Henry's Law constant, defined as a fixed ratio between the concentration of a compound in water and its partial pressure in air, is proportional with vapour pressure. [33]. That means, the lower Henry's Law constant indicates the lower vapour pressure, hence slightly volatilization of compounds. Generally, vapour pressures and Henry's Law constants of pharmaceuticals are changing in the range of 10^{-7} - 10^{-2} Pa and 10^{-10} to 10^{-5} Pa·m³/mol, respectively [1]. In this study, Methotrexate's vapour pressure and hence Henry's Law constant were calculated as $1.23 \cdot 10^{-13}$ Pa and $1.56 \cdot 10^{-26}$ Pa·m³/mole respectively, as the lowest values of all, that indicates unlikely to volatilize of Methotrexate from aqueous media at ambient temperatures. Furthermore, the existence of ionisable functional groups in Methotrexate's structure, such as carboxylic acid (COOH) and amino (R-NH₂) groups, increase hydrophilicity of it, so Methotrexate may be considered to present mostly in dissolved phase instead of gaseous.

4. Conclusion

In the present study, the environmental risk assessment has been done for widely used ACDs in Turkey. Although there are many studies related to the estimation of environmental risks of ACDs in many countries, that study is the first for Turkey. Of the 13 ACDs mostly used in Turkey, Tamoxifen was recognized as the most risky for environment due to its high PEC / PNEC ratio (2.96350) compared to others. Although the 97.24% of Tamoxifen seems to be removed in STPs, the giant portion of this amount (71.5%) is sorbed into the treatment sludge, that means the micro-pollutant is not removed from environment completely, but just changes its physical phase. In other words 71.5% of Tamoxifen is passing from the aquatic phase to the sludge phase. According to the BIOWIN results, Ciclosporin, Bicalutamide and Imatinib are considered to biodegrade as poorly due to their high persistency in environment. Also, the removal of these drugs in STPs is rather difficult when compared to other ACDs. Although these ACDs have been found to be non-risky according to the calculated

PEC/PNEC ratios; their potential to enter in receiving water is considered to be rather high due to their low removal efficiencies in STPs. In other words, the giant amount of these drugs may enter to aquatic media without treatment, causing toxic effect for environment.

Bioaccumulation of drugs on organisms is an important task in investigation of drugs with respect to their toxicity. In that study, Tamoxifen was found to have the biggest tendency to accumulate in the lipid fragments of cell membranes in the organisms due to its high BCF value (6689 L/kg) and high lipophilic character. Compared to other ACDs, the sorption potentials of Tamoxifen and Mycophenolic acid on sludge were considered as high due to their high K_{ow} and K_d values. Although the huge portion (85.88%) of Mycophenolic acid can be removed from environment by biodegradation, Tamoxifen could not biodegrade due to its partially metabolized and the large amount of it (71.5%) was sorbed to sludge composing hazardous waste for environment. Based on the results in that study, it can be concluded that more precautions should be taken for reducing the release of Tamoxifen into the environment.

Conflicts of interest

The author state that did not have conflict of interests

References

- [1] Booker V., Halsall C., Llewellyn N., Johnson A., Williams R., Prioritising Anticancer Drugs for Environmental Monitoring and Risk Assessment Purposes, *Science of the Total Environment*, 473–474 (2014) 159–170.
- [2] Caley A., Jones R., The Principles of Cancer Treatment by Chemotherapy, *Surgery (Oxford)*, 30(4) (2012) 186–190.
- [3] WHO CCDSM (World Health Organization Collaborating Centre for Drug Statistics Methodology), ATC/DDD index 2021, Available at: https://www.whocc.no/atc_ddd_index/, Retrieved December 17, (2020).
- [4] Besse J.P., Latour J.F., Garric J., Anticancer Drugs in Surface Waters: What can We Say About The Occurrence and Environmental Significance of Cytotoxic, Cytostatic and Endocrine Therapy Drugs?, *Environmental International*, 39(1) (2012) 73–86.
- [5] Toolaram A.P., Kümmerer K., Schneider M., Environmental Risk Assessment of Anti-Cancer Drugs and Their Transformation Products: A Focus on Their Genotoxicity Characterization-State of Knowledge and Shortcomings, *Mutation Research*, 760 (2014) 18–35.
- [6] Stanford B.D., Weinberg H.S., Evaluation of on-site Wastewater Treatment Technology to Remove Estrogens, Nonylphenols, and Estrogenic Activity from Wastewater, *Environmental Science & Technology*, 44(8) (2010) 2994–3001.
- [7] Du B., Price A.E., Scott W.C., Kristofco L.A., Ramirez A.J., Chambliss C.K., Yelderman J.C., Brooks B.W., Comparison of Contaminants of Emerging Concern Removal, Discharge, and Water Quality Hazards among Centralized and on-site Wastewater Treatment System Effluents Receiving Common Wastewater Influent, *Science of The Total Environment*, 466-467 (2014) 976-984.
- [8] Allwood M., Stanley A., Wright P., The cytotoxics handbook. 4th ed. Oxford: Radcliffe Medical Press, (2002) 400-425.
- [9] Johnson A.C., Jürgens M.D., Williams J., Kümmerer K., Kortenkamp A., Sumpter J.P., Do Cytotoxic Chemotherapy Drugs Discharged into Rivers Pose a Risk to the Environment and Human Health? an Overview and UK Case Study, *Journal of Hydrology*, 348 (1–2) (2008) 167–175.
- [10] Rowney N.C., Johnson A.C., Williams R.J., Cytotoxic Drugs in Drinking Water: A Prediction and Risk Assessment Exercise for the Thames Catchment in the United Kingdom, *Environmental Toxicology and Chemistry*, 28(12) (2009) 2733–2743.
- [11] Al-Ahmad A., Kümmerer K., Biodegradation of the Antineoplastics Vindesine, Vincristine, and Vinblastine and Their Toxicity Against Bacteria in the Aquatic Environment, *Cancer Detection and Prevention*, 25(1) (2001) 102-107.
- [12] Zhang J., Chang Victor W.C., Apostolos G., Wang J.Y., Removal of Cytostatic Drugs From Aquatic Environment: A Review, *Science of The Total Environment*, 445-446 (2013) 281-298.
- [13] US Environmental Protection Agency, 2012. Estimation Program Interface Suite™ for Microsoft® Windows, version 4.11. United States Environmental Protection Agency, Washington, DC, USA.
- [14] Jones O.A.H., Voulvoulis N., Lester J.N., Aquatic Environmental Assessment of The Top 25 English Prescription Pharmaceuticals, *Water Research*, 36 (2002) 5013–5022.

- [15] Stuer-Lauridsen F, Birkved M, Hansen LP, Holten Lützhof HC, Halling Sorensen B., Environmental Risk Assessment of Human Pharmaceuticals in Denmark After Normal Therapeutic Use, *Chemosphere*, 40 (2000) 783–793.
- [16] TSIa (Turkish Statistical Institute a). Available at: <http://www.tuik.gov.tr/UstMenu.do?metod=temeliste>. Retrieved April 19, 2018.
- [17] TSIb (Turkish Statistical Institute b). Available at: <http://tuikapp.tuik.gov.tr/cevredagitimapp/belediyeatiksu.zul>. Retrieved April 19, 2018.
- [18] Chem Safety Proa, How to calculate Predicted No-Effect Concentration (PNEC). Available at: [https://www.chemsafetypro.com/Topics/CRA/How_to_Calculate_Predicted_NoEffect_Concentration_\(PNEC\).html](https://www.chemsafetypro.com/Topics/CRA/How_to_Calculate_Predicted_NoEffect_Concentration_(PNEC).html). Retrieved May 28, 2019.
- [19] Morrison H.A., Bioconcentration and biomagnification in the aquatic environment In Boethling RS, Mackay D, eds. Handbook of Property Estimation methods for Chemicals: Environmental and Health Sciences, Boca Raton, FL, USA: Lewis, (2000) 89-221.
- [20] Dobbs R.A., Wang L., Govind L., Sorption of Toxic Organic Compounds on Wastewater Solids: Correlation with Fundamental Properties, *Environmental Science and Technology*, 23 (1989) 1092-1097.
- [21] Halling-Sorensen B., Nors Nielsen S., Lansky P.F., Ingerslev F., Holten Lützhof H.C., Jorgensen S.E., Occurrence, Fate, and Effects of Pharmaceutical Substances in The Environment, *Chemosphere*, 36 (2) (1998) 357-393.
- [22] Stockholm County Council, Environmentally Classified Pharmaceuticals Report, 2012.
- [23] Sebastine I.M., Wakeman R.J., Consumption and Environmental Hazards of Pharmaceutical Substances in the UK., *Process Safety and Environmental Protection*, 81 (4) (2003) 229-235.
- [24] Kummerer K., Pharmaceuticals in the environment: sources, fate, effects and risks. 1st ed. Berlin: Springer-Verlag, (2008) 450-485.
- [25] Boethling R.S., Sabljic A., Screening-level Model For Aerobic Biodegradability Based on a Survey of Expert Knowledge, *Environmental Science and Technology*, 23 (1989) 672-679.
- [26] Boethling R.S., Lynch D.G., Jaworska J.S., Tunkel J.L., Thom G.C., Webb S., Using BIOWIN, Bayes, and Batteries to Predict Ready Biodegradability, *Environmental Toxicology and Chemistry*, 23 (2004) 911-920.
- [27] Comprehensive Medicinal Chemistry II, 2007. Lipophilicity. Available at: <https://www.sciencedirect.com/topics/chemistry/lipophilicity>. Retrieved May 11, 2019.
- [28] Bagno A., Comuzzi C., Deprotonation of Amides and Polyfunctional Imides Probed by Heteronuclear NMR and Quantum Chemical Calculations, *European Journal of Organic Chemistry*, 1 (1999) 287-295.
- [29] Jones O.A.H., Voulvoulis N., Lester J.N., The Occurrence and Removal of Selected Pharmaceutical Compounds in a Sewage Treatment Works Utilizing Activated Sludge Treatment, *Environmental Pollution*, 145 (2007) 738-744.
- [30] Oğuz M., Mihçioğur H. Environmental Risk Assessment of Selected Pharmaceuticals in Turkey, *Environmental Toxicology and Pharmacology*, 38(1) (2014) 79-83.
- [31] Mihçioğur H., Oğuz M., Removal of oxytetracycline and Determining its Biosorption Properties on Aerobic Granular Sludge, *Environmental Toxicology and Pharmacology*, 46 (2016) 174-182.
- [32] European Medicines Agency (EMA), Guideline on the environmental risk assessment of medicinal products for human use 2006, Available at: http://www.ema.europa.eu/ema/pages/includes/document/open_document.jsp?webContentId=WC500003978. Retrieved May 10, 2019).
- [33] Chem Safety Proa, 2016. Henry's Law Constant. Available at: https://www.chemsafetypro.com/Topics/CRA/Henry_Law_Constant.html, Retrieved May 27, (2019).



Remarks on the group of units of a corner ring

Tülay YILDIRIM^{1,*}

¹Karabük University, Eskipazar Vocational College, Karabük/TURKEY

Abstract

The aim of this study is to characterize rings having the following properties for a non-trivial idempotent element e of R , $U(eRe) = e + eJ(R)e = e + J(eRe)$ (and $U(eRe) = e + N(eRe)$), where $U(-)$, $N(-)$ and $J(-)$ denote the group of units, the set of all nilpotent elements and the Jacobson radical of R , respectively. In the present paper, some characterizations are also obtained in terms of every element is of the form $e + u$, where $e^2 = e \in R$ and $u \in U(eRe)$.

Article info

History:
Received: 03.06.2020
Accepted: 12.02.2021

Keywords:
Uj-rings,
Corner Rings,
Clean Elements,
Lifting Idempotents

1. Introduction

Throughout the paper all rings considered are associative and unital. For a ring R , the Jacobson radical, the group of units and the set of all nilpotent elements are denoted by $J(R)$, $U(R)$ and $N(R)$, respectively.

One always has $1 + J(R) \subseteq U(R)$. In [1], authors defined a ring to be UJ if it satisfies the above property as two sided, that is a ring R is a UJ -ring if $1 + J(R) = U(R)$ and also they showed that the problem of lifting the UJ property from a ring R to the polynomial ring $R[x]$ is equivalent to the Köthe's problem for F_2 -algebras. They also proved that if e is an idempotent element and R is UJ -ring then the corner rings eRe and $(1 - e)R(1 - e)$ are also UJ . But the converse is true with an additional property that $eR(1-e), (1-e)Re \subseteq J(R)$.

One can see easily that $e(1 + J(R))e \subseteq eU(R)e$ for $e^2 = e \in R$ since $1 + J(R)$ is always contained in $U(R)$. So it makes sense to think about the equality as following:

$$U(eRe) = e + eJ(R)e = e + J(eRe). \quad (1)$$

Every UJ -ring satisfies this property. Also, we give examples and some characterizations and basic properties of rings having this property. For example, a ring R satisfies this property iff $U(eRe / J(eRe)) = \{e\}$, and the ring $\prod_{i \in I} R_i$ satisfies this property if and

only if each ring R_i satisfies this property, for all $i \in I$. Recall that a ring is called semilocal if $R / J(R)$ is a semisimple ring. It is also shown that a semilocal ring R satisfies the (1)-property if and only if $eRe / J(eRe) \cong F_2 \times \dots \times F_2$.

The behavior of this property under some classical ring constructions is studied. In particular, it is proved that if the polynomial ring $R[x]$ satisfies this property, then R satisfies this property and $J(eRe)$ is a nil ideal of eRe . It is also shown that Morita context satisfies this property.

An element is called clean if it can be written as a sum of an idempotent and a unit. A ring is called clean if each of its element is clean. Clean rings were firstly introduced by Nicholson [2]. Several people work on this subject and investigate properties of clean rings, for example see [3]. Rings for which every element is a sum of an element from the Jacobson radical and an idempotent is called J-clean. We obtain that: (1) R satisfies the (1)-property iff all clean elements of eRe are J-clean, (2) eRe is a clean ring and R satisfies the (1)-property if and only if $eRe / J(eRe)$ is a Boolean ring and idempotents lift modulo $J(eRe)$ iff eRe is a J-clean ring.

As a clean element representation of a ring, we can consider the following: Let R be a ring and a be a non-unit element of R . We say that a is of the form (*) if $a = e + u$, where $e^2 = e \in R$ and $u \in U(eRe)$. It is easy to see that an element a of a ring R is of the form (*) if

*Corresponding author. e-mail address: tulayturan@karabuk.edu.tr
<http://dergipark.gov.tr/csj> ©2021 Faculty of Science, Sivas Cumhuriyet University

and only if it is quasi-regular, and an element of a ring is of the form (*) is clean. Hence we also obtain that every element ($\neq 1$) of a ring R has the form $e + u$, where $e^2 = e \in R$ and $u \in U(eRe)$ if and only if R is a division ring.

2. The Results

We begin with the following well known facts / notions will be referred to several times.

Remark 1.1. For any idempotent element e of a ring R ,

1. $J(eRe) = \{exe \in eRe : e - exeye \in U(eRe), \forall eye \in eRe\}$.
2. $N(eRe) = \{exe \in eRe : (exe)^n = 0, \text{ for some } n \in \mathbb{Z}^+\}$.
3. $U(eRe) \subseteq eU(R)e$ for $e^2 = e \in R$.
4. $U(\prod_{i \in I} eR_i e) = \prod_{i \in I} U(eR_i e)$, where

$$U(\prod_{i \in I} eR_i e) = \{ \prod_{i \in I} ex_i e \text{ is unit where } ex_i e \in eR_i e \}, \text{ and}$$

$$\prod_{i \in I} (U(eR_i e)) = \{ \prod_{i \in I} ex_i e : ex_i e \in eR_i e \text{ is unit for every } i \in I \}$$

5. $J(\prod_{i \in I} eR_i e) = \prod_{i \in I} J(eR_i e)$.

We consider the following property (1):

A ring R satisfies (1) if for any idempotent element e of R , $U(eRe) = e + eJ(R)e = e + J(eRe)$.

Example 1.2. Every UJ -ring satisfies the (1)-property by [1, Proposition 2.7]. Furthermore, if R is a UJ -ring, then $eU(R)e = U(eRe)$.

Given a ring R , we define an operation \circ on R , called quasi-multiplication, by $a \circ b = a + b - ab$. It is easy to see that (R, \circ) is a monoid with identity element 0. An element $a \in R$ is called quasi-regular if it is invertible in (R, \circ) , i.e., if there exists $a' \in R$ such that $a \circ a' = 0 = a' \circ a$. In this case we say that a' is the quasi-inverse of a . If R is unital then this is equivalent to $1 - a \in U(R)$. The set of all quasi-regular elements of R will be denoted by $Q(R)$. Clearly, $(Q(R), \circ)$ is a group since this is just the group of invertible elements of the monoid (R, \circ) .

Theorem 1.3. Every element ($\neq 1$) of a ring R is quasi-regular if and only if R is a division ring.

Proof: Suppose that $0, 1 \neq a$ is an arbitrary element of R . Since $(1 - a)$ is a unit then there exists $1 \neq u \in U(R)$ such that $(1 - a)u = 1$. Therefore, we have $(-au) = (1 - u)$. By assumption, $1 - u$ is a unit element and hence $a = -(1 - u)(1 - a)$ is a unit element. Hence, R is a division ring. The converse is clear.

Remark 1.4: If ere is a quasi-regular element of eRe then r is quasi-regular element of R by Remark 1.1.

Proposition 1.5. For a ring R and any non-trivial idempotent $e \in R$, the following conditions are equivalent:

1. $U(eRe) = e + J(eRe)$, i.e., R satisfies the (1)-property.
2. $U(eRe / J(eRe)) = \{e\}$.
3. $Q(eRe)$ is an ideal of eRe (then $Q(eRe) = J(eRe)$).
4. $erebe - ecere \in J(eRe)$ for any $ere \in eRe$ and $ebe, ece \in Q(eRe)$.
5. $ereue - evere \in J(eRe)$ for any $eue, eve \in U(eRe)$ and $ere \in eRe$.
6. $U(eRe) + U(eRe) \subseteq J(eRe)$ (then $U(eRe) + U(eRe) = J(eRe)$).

Proof: (1) \Rightarrow (2) If we take $eRe / J(eRe)$ instead of eRe in (1), then we get $U(eRe / J(eRe)) = e + J(eRe / J(eRe)) = e$, as desired.

(1) \Rightarrow (3) Let $exe \in Q(eRe)$. Then $e - exe \in U(eRe)$, and so there exists an element $eue \in U(eRe)$ such that $e - exe = eue$ which gives $exe = e - eue$, where $eue \in U(eRe) = (e + J(eRe))$. Hence there exists $eje \in J(eRe)$ such that $eue = e + eje$. Since $exe = e - eue = e - (e + eje) = -eje \in J(eRe)$, we get $Q(eRe) \subseteq J(eRe)$. But by the definition we have $J(eRe) \subseteq Q(eRe)$ so we are done.

(2) \Rightarrow (1) Clearly $e + J(eRe) \subseteq U(eRe)$. For the converse, first we prove the following claim:

Claim: $[U(eRe) + J(eRe)] / J(eRe) = U(eRe / J(eRe))$: Let $exe + J(eRe) \in U(eRe / J(eRe))$. By the hypothesis, we have $U(eRe / J(eRe)) = \{e\}$ and so $exe + J(eRe) = e$ which gives $e - exe \in J(eRe)$. By Remark 1.1, one obtains $exe \in U(eRe)$ and so $exe + J(eRe) \in [U(eRe) + J(eRe)] / J(eRe)$. For the converse, let $exe + J(eRe) \in [U(eRe) + J(eRe)] / J(eRe)$.

Since exe is invertible, there exists $eye \in eRe$ such that $exeye = eyexe = e$. The equation $(exe + J(eRe))(eye + J(eRe)) = exeye + J(eRe) = e + J(eRe)$ implies $exe + J(eRe) \in U(eRe / J(eRe))$. Now for the converse, let $exe \in U(eRe)$. By the Claim, $exe + J(eRe) \in U(eRe) / J(eRe) = \{e\}$. Therefore $exe + eje = e$ for all $eje \in J(eRe)$ which implies $exe = e - eje \in e + J(eRe)$.

(3) \Rightarrow (4) Since $Q(eRe)$ is an ideal of eRe , we get $erebe - ece \in Q(eRe)$ for $ebe, ece \in Q(eRe)$ and $exe \in eRe$. Hence $Q(eRe) = J(eRe)$ implies $erebe - ece \in J(eRe)$.

(4) \Rightarrow (5) Setting $ece = e - eue$ and $ebe = e - eve$ for $eue, eve \in U(eRe)$, we get $ebe, ece \in Q(eRe)$. The rest follows from (4).

(5) \Rightarrow (6) If we take $ere = e$ in (5), then $eue - eve \in J(eRe)$, for any $eue, eve \in U(eRe)$ which gives $U(eRe) + U(eRe) \subseteq J(eRe)$. Hence, every $ere \in J(eRe)$ can be written as a sum of two invertible element as $ere = e + (ere - e) \in U(eRe) + U(eRe)$.

(6) \Rightarrow (1) Clearly $e + J(eRe) \subseteq U(eRe)$. Using (6), we get $U(eRe) - e \subseteq J(eRe)$, i.e. $U(eRe) \subseteq e + J(eRe)$ which completes the proof.

Remark 1.6. For $e = 1$, one has [1, Lemma 1.1].

In the following observation, we collect some basic properties of rings having the (1)- property.

Proposition 1.7. Assume that a ring R satisfies the (1)-property for any non-trivial idempotent element e of R . Then:

1. $2e \in J(eRe)$;
2. If eRe is a division ring, then $eRe = K_2 \cong F_2$ where $K_2 = \{0, e\}$;
3. $eRe / J(eRe)$ is reduced (i.e., it has no nonzero nilpotent elements) and hence abelian (i.e., every idempotent is central);
4. If $exe, eye \in eRe$ are such that $exeye \in J(eRe)$, then $eyexe \in J(eRe)$ and $exeReye, eyeRexe \in J(eRe)$;
5. Let $I \subseteq J(eRe)$ be an ideal of eRe . Then R satisfies (1)-property if and only if R/I satisfies (1)-property;
6. eRe is Dedekind finite;

7. The ring $\prod_{i \in I} R_i$ satisfies the (1)-property if and only rings R_i satisfy the (1)- property for all $i \in I$.

Proof: (1) By Proposition 1.5 (6), we have $U(eRe) + U(eRe) = J(eRe)$. So $e + e = 2e \in J(eRe)$.

(2) If eRe is a division ring, then every nonzero element of eRe has an inverse and also $U(eRe) = e + J(eRe)$, by Proposition 1.5(1). Therefore $e + J(eRe) \in eRe / J(eRe)$ is an only element which has an inverse. By Proposition 1.5(2), $U(eRe / J(eRe)) = \{e\}$.

(3) For a nilpotent element $ere + J(eRe)$ in $eRe / J(eRe)$, we shall show that $ere \in J(eRe)$. There exists $n \in \mathbb{N}$ such that $(ere)^n + J(eRe) = J(eRe)$. Then

$$\begin{aligned} e + J(eRe) &= [(ere)^n + J(eRe)] + (e + J(eRe)) \\ &= ((ere)^n + e) + J(eRe) \\ &= ((ere) + e)((-1)^{n-1} (ere)^{n-1} + \dots + (-1)^2 (ere)^2 - ere + 1) + J(eRe) \\ &= [((ere) + e) + J(eRe)][((-1)^{n-1} (ere)^{n-1} + \dots + (-1)^2 (ere)^2 - ere + 1) + J(eRe)]. \end{aligned}$$

By Proposition 1.5(2), $(ere + e) + J(eRe) \in U(eRe / J(eRe))$. So there exists $eje \in J(eRe)$ such that $(ere + e) + eje = e$, that is $ere = -eje \in J(eRe)$. Hence it has no nonzero nilpotent elements.

(4) Let $exeye \in J(eRe)$. Then $exeye + J(eRe) = J(eRe)$. After multiplying the equation by $eye + J(eRe)$ (on the left and by $exe + J(eRe)$ on the right, we get $eyexeyexe + J(eRe) = (eyexe)^2 + J(eRe) = J(eRe)$. By (3), $eRe / J(eRe)$ is reduced and so $eyexe + J(eRe) = J(eRe)$. Hence $eyexe \in J(eRe)$. The rest follows from (3).

(5) Let $I \subseteq J(eRe)$. Then $J(eRe) / I = J(eRe / I)$. Indeed, clearly, $J(eRe) / I \subseteq J(eRe / I)$. For the converse, let $exe + I \in J(eRe / I)$. Then $(e - exeye) + I$ is a unit of eRe / I for every $eye \in eRe$. Hence $e - exeye$ is a unit for every $eye \in eRe$ which implies that $exe \in J(eRe)$.

Now $exe + I \in J(eRe) + I$ and $\frac{eRe/I}{J(eRe/I)} = \frac{eRe/I}{J(eRe)/I} = eRe / J(eRe)$. The rest follows from Proposition 1.5(2).

(6) $eRe / J(eRe)$ is Dedekind finite since it is reduced. Let $exeye = e$ for $exe, eye \in eRe$. Then $exeye + J(eRe) = e + J(eRe)$ but $eRe / J(eRe)$ is Dedekind finite so $eyexe + J(eRe) = e + J(eRe)$ that is $eyexe$ is invertible. Clearly $eyexe$ is an idempotent so $eyexe = e$.

(7) This follows from Remark 1.1.

Remark 1.8. For $e = 1$, one has [1, Proposition 1.3]

Proposition 1.9. A semilocal ring R satisfies the (1)-property if and only if $eRe / J(eRe) \cong F_2 \times \dots \times F_2$.

Proof. Since $eRe / J(eRe)$ is semisimple by the definition and reduced by Proposition 1.7(3), so $eRe / J(eRe)$ is a finite direct product of division ring. But it is isomorphic to F_2 by Proposition 1.7(2).

We focus on some algebraic constructions of rings having the (1)-property.

Proposition 1.10. If a ring R satisfies the (1)-property and S is a subring of R such that $U(eSe) = U(eRe) \cap eSe$, then S also satisfies the (1)-property.

Proof. Since $U(eSe) = U(eRe) \cap eSe$, we also have $J(eRe) \cap eSe \subseteq J(eSe)$. Thus, using $U(eRe) = e + J(eRe)$ we get

$$e + J(eSe) \subseteq U(eSe) = U(eRe) \cap eSe = (e + J(eRe)) \cap eSe = e + (J(eRe) \cap eSe) \subseteq e + J(eSe).$$

Therefore $U(eSe) = e + J(eSe)$. We consider the following property (2):

A ring R satisfies (2) if for any non-trivial idempotent element e of R , $U(eRe) = e + N(eRe)$.

Lemma 1.11. Let e be a non-trivial idempotent and eRe be a ring such that its unit element is only e . Then $U(eRe[X]) = \{e\}$, where $eRe[X]$ denotes the polynomial ring in the set X of commuting indeterminates.

Proof. Since being a unit in $eRe[X]$ is a local property, i.e., depends only on finitely many indeterminates, we may assume that X is a finite set. By assumption $U(eRe) = \{e\}$, so eRe does not contain non-trivial nilpotent elements, i.e., it is a reduced ring. [1, Corollary 1.7] characterizes reduced rings as rings such that $U(eRe[x]) = U(eRe)$ and the thesis follows easily.

Let us recall that a ring R is 2-primal if its prime radical $B(R)$ coincides with the set of all its nilpotent elements.

Proposition 1.12. Let R be a 2-primal having the (2)-property. Then, for any set X of commuting indeterminates, the polynomial ring $R[X]$ satisfies the (1)-property.

Proof. It is known that $B(eRe[X]) = B(eRe)[X]$ (cf.[4, Theorem 10.19]). Thus the assumptions imposed on R and Lemma 1.11 imply that the ring $eRe[X] / B(eRe[X]) \cong (eRe / B(eRe))[X]$ has trivial units. Now, by Proposition 1.7(5), $R[X]$ satisfies the (1)-property.

Proposition 1.13. If the polynomial ring $R[x]$ satisfies the (1)-property, then R satisfies the (1)-property and $J(eRe)$ is a nil ideal of eRe .

Proof. It is known that $J(eRe[x]) = I[x]$ for some nil ideal I of eRe . Thus, as $R[x]$ satisfies the (1)-property, we have $e + J(eRe) \subseteq U(eRe[x]) = e + J(eRe[x]) = e + I[x]$. This implies that $J(eRe) = I$ is nil. As $R[x]$ satisfies the (1)-property, then $\{e\} = U(eRe[x] / J(eRe[x])) = U((eRe / J(eRe))[X])$. Hence also $U(eRe / J(eRe)) = \{e\}$, i.e. R satisfies the (1)-property.

A Morita context is a 4-tuple $\begin{pmatrix} R & M \\ N & S \end{pmatrix}$, where R, S are rings, ${}_R M_S$ and ${}_S N_R$ are bimodules, and there exist context products $M \times N \rightarrow R$ and $N \times M \rightarrow S$ written multiplicatively as $(x, y) \rightarrow xy$ and $(y, x) \rightarrow yx$, such that $\begin{pmatrix} R & M \\ N & S \end{pmatrix}$ is an associative ring with the obvious matrix operations. A Morita context $\begin{pmatrix} R & M \\ N & S \end{pmatrix}$ is called trivial if the context products are trivial, i.e., $MN = 0$ and $NM = 0$. A trivial Morita context is also called the ring of a Morita context with zero pairings in [5]. A trivial Morita context $\begin{pmatrix} R & M \\ N & S \end{pmatrix}$ with $N = 0$ is commonly called a formal triangular matrix ring. Given a ring R and a bimodule V over R , we can easily see that $\left\{ \begin{pmatrix} a & v \\ 0 & a \end{pmatrix} : a \in R, v \in V \right\}$ is a subring of the formal triangular matrix ring $\begin{pmatrix} R & V \\ 0 & R \end{pmatrix}$, and this subring is the just trivial extension of R by V . By [6, Lemma 2], trivial Morita contexts (in particular, formal triangular matrix rings) are special cases of trivial extensions.

Theorem 1.14. Let (eRe, eVf, fWe, fSf) be a Morita context and $T := \begin{pmatrix} eRe & eVf \\ fWe & fSf \end{pmatrix}$ where e and f are non-trivial idempotents. The following conditions are equivalent:

1. T satisfies the (1)- property for an idempotent $E = \begin{pmatrix} e_R & 0 \\ 0 & f_S \end{pmatrix}$, where e and f are non-trivial idempotents.
2. R satisfies the (1)- property for an idempotent e , S satisfies the (1)- property for an idempotent f and $eVfWe \subseteq J(eRe)$, $WV \subseteq J(fSf)$.
3. R satisfies the (1)- property for an idempotent e , S satisfies the (1)- property for an idempotent f and $T / J(ETE) \cong eRe / J(eRe) \oplus fSf / J(fSf)$.

Proof: (1) \Rightarrow (2) Suppose T satisfies the (1)- property for an idempotent $E = \begin{pmatrix} e_R & 0 \\ 0 & f_S \end{pmatrix}$ where e and f are non-trivial idempotents. Hence $ETE / J(ETE)$ has no nonzero nilpotent elements. Let $\begin{pmatrix} 0 & eVf \\ 0 & 0 \end{pmatrix}$,

$$\begin{pmatrix} 0 & 0 \\ fWe & 0 \end{pmatrix} \subseteq J(ETE) = \begin{pmatrix} J(eRe) & B \\ C & J(fSf) \end{pmatrix}, \text{ where } B \\ = \{evf : fWevf \subseteq J(fSf)\} = \{evf : evfWe \\ \subseteq J(eRe)\}, \text{ and } C = \{fwe : fweVf \subseteq J(fSf)\} = \{fwe \\ : eVfwe \subseteq J(eRe)\}.$$

Clearly, $B = eVf$ and $C = fWe$. We have also obtain that $B = eVf$, $C = fWe$, $eVfWe \subseteq J(eRe)$, $fWeVf \subseteq J(fSf)$ and $ETE / J(ETE) \cong eRe / J(eRe) \oplus fSf / J(fSf)$. Since T satisfies the (1)-property for an idempotent E , we get $U(ETE / J(ETE)) = \{E\}$.

We also know that $U(ETE / J(ETE)) \cong U(eRe / J(eRe)) \oplus U(fSf / J(fSf))$ which implies R satisfies the (1)-property for an idempotent e , and S satisfies the (1)-property for an idempotent f .

(2) \Rightarrow (3) It is clear by the fact that $B = eVf$ and $C = fWe$.

(3) \Rightarrow (1) It is a consequence of Proposition 1.5.

Recall that an element $r \in R$ is clean (J -clean) provided there exist an idempotent $e \in R$ and an element $t \in U(R)$ ($t \in J(R)$) such that $r = e + t$. A ring R is clean (J -clean) if every element of R has such clean (J -clean) decomposition. It is known that every J -clean ring is clean (in fact if $-r = e + j$ is a J -clean decomposition of $-r \in R$, then $r = (1 - e) + (-1 - j)$ is a clean decomposition of r).

Proposition 1.15. For a ring R , the following conditions are equivalent:

1. R satisfies the (1)-property.
2. All clean elements of eRe are J -clean.

Proof: (1) \Rightarrow (2) Assume that $r \in R$ is a clean element of eRe and $r = f + u$ is its clean decomposition for $f \in Id(eRe)$ and $u \in U(eRe)$. Then $r = f + u + e - e + f - f = (2f + u - e) + (e - f)$.

Claim 1. $(e - f)$ is an idempotent element of eRe : Indeed, $(e - f)^2 = e - f$ since $ef = f$ and $fe = f$.

Claim 2. $2f \in J(eRe)$: By Proposition 1.7, $2f \in J(fRf) = fJ(R)f = exeJ(R)exe \subseteq eJ(R)e = J(eRe)$. Also by Proposition 1.5, $u - e \in J(eRe)$ and so one obtains $2f + u - e \in J(eRe)$.

(2) \Rightarrow (1) Let $e^2 = e \in R$ and $u \in U(eRe)$. Then u is a clean element of eRe and, by the hypothesis, u is J -clean. Let $u = f + j$ be a J -clean decomposition of u . Since $e = fu^{-1} + ju^{-1}$, we obtain that $fu^{-1} = e - ju^{-1}$ is a unit

of eRe . Hence, $e = f$. This means that $u = f + j = e + j$ and $U(eRe) = e + J(eRe)$ as desired.

Theorem 1.16. For a ring R and for any idempotent $e \in R$, the following conditions are equivalent:

1. eRe is a clean ring and R satisfies the (1)-property.
2. $eRe / J(eRe)$ is a Boolean ring and idempotents lift modulo $J(eRe)$.
3. eRe is a J -clean ring and R satisfies the (1)-property.
4. eRe is a J -clean ring.

Proof: (1) \Rightarrow (2) By the assumptions, $eRe / J(eRe)$ is a clean ring such that $U(eRe) = \{e\}$. In particular, $2e = 0$ in $(eRe / J(eRe))$ and every element $r \in eRe / J(eRe)$ is of the form $r = f + e$, for a suitable idempotent f . Hence $r^2 = r$, i.e., $eRe / J(eRe)$ is Boolean. By (cf.[7, Lemma 17]), idempotents lift modulo every ideal I of a clean ring R , which gives (2).

(2) \Rightarrow (3) Suppose (2) holds and let $a \in eRe$. Then $a + J(eRe) \in eRe / J(eRe)$ is idempotent. Hence, there exists an idempotent $f \in eRe$ such that $a - f \in J(eRe)$, i.e. a is a J -clean element. This shows that eRe is J -clean. If $u \in U(eRe)$, then $u + J(eRe)$ is a unit in a Boolean ring $eRe / J(eRe)$. Thus $u - e \in J(eRe)$, so satisfies the (1)-property.

(3) \Rightarrow (4) Trivial.

(4) \Rightarrow (1) This follows from Proposition 1.15.

Let us continue on a clean decomposition for a non-unit element of a ring.

Lemma 1.17. For a non-unit element a of ring R , the following conditions are equivalent:

1. $a = e + u$ (and $eu = ue$), where $e^2 = e \in R$ and $u \in U(eRe)$;
2. $a \in 1 + U(R)$ (and $u \in Z(U(R))$).

Proof: Assume that a non-unit element a of ring R is of the form $e + u$, where $e^2 = e \in R$ and $u \in U(eRe)$. It is easy to check (or well known) that $U(eRe) = eRe \cap ((1 - e) + U(R))$, where $e^2 = e \in R$. Hence $u = (1 - e) + v$ for some $v \in U(R)$. Now, $a = e + (1 - e) + v = 1 + v \in 1 + U(R)$, as desired.

Now assume that a non-unit element a of ring R is of the form $e + u$ and $eu = ue$, where $e^2 = e \in R$ and $u \in U(eRe)$. Then $au = eu + u^2$ and $ua = ue + u^2$ which imply $au = ua$. Since $a \in 1 + U(R)$, we write $a = 1 +$

v for some $v \in U(R)$. Hence $au = u(1+v)$ and $ua = (1+v)u$ that implies $uv = vu$.

Corollary 1.18. An element a of ring R is of the form (*) if and only if it is quasi-regular.

Example 1.19. 1. An element a of ring R is of the form (*) is clean.

2. It is well known that the units, idempotents, and quasi-regular elements of any ring are clean, but units and idempotents are not of the form (*).

3. Any element Z_2 is of the form (*). Consider its matrix ring $M(Z_2)$. The set of units of $M(Z_2)$ is $U(M(Z_2)) = \left\{ \begin{pmatrix} 1 & 0 \\ 0 & 1 \end{pmatrix}, \begin{pmatrix} 0 & 1 \\ 1 & 0 \end{pmatrix}, \begin{pmatrix} 0 & 1 \\ 1 & 1 \end{pmatrix}, \begin{pmatrix} 1 & 0 \\ 1 & 1 \end{pmatrix}, \begin{pmatrix} 1 & 1 \\ 1 & 0 \end{pmatrix}, \begin{pmatrix} 1 & 1 \\ 0 & 1 \end{pmatrix} \right\}$.

Consider the non-unit element $a = \begin{pmatrix} 1 & 1 \\ 0 & 0 \end{pmatrix} \in M(Z_2)$.

Then, there is no unit in $U(M(Z_2))$ such that $a \in 1 + U(M(Z_2))$.

Remark 1.20. We should remind the reader that $1 \in R$ never has the form $e + u$, where $e^2 = e \in R$ and $u \in U(eRe)$. To see this,

1. If $e = 1$ then we conclude that $u = 0$. By assumption, $0 = u \in U(1R1) = U(R)$ is a unit element that is impossible.

2. If $e = 0$ then we conclude that $u = 1$. By assumption, $1 - u \in U(0R0) = 0$ that is impossible.

3. If $e \neq 0, 1$ then $1 - e = u$ and we conclude that $1 - e$ is a unit element of eRe while $1 - e$ is a zero-divisor of eRe and that is a contradiction.

Corollary 1.21. Let R be a ring in which every element ($\neq 1$) of R has the form $e + u$, where $e^2 = e \in R$ and $u \in U(eRe)$. Then $Id(R) = \{0, 1\}$.

Proof: We claim that R has the only trivial idempotents. To see this, let $e \neq 0, 1$ be an idempotent of R . By Lemma 1.17, since e is a non-unit element, there exists $u \in U(R)$ in which $e = 1 + u$. Hence, we have $-u = 1$

- e . It is clear that $1 - e$ is a zero divisor thus u is a zero-divisor that is a contradiction. Therefore, R has the only trivial idempotents.

Corollary 1.22. Every element ($\neq 1$) of a ring R has the form $e + u$, where $e^2 = e \in R$ and $u \in U(eRe)$ if and only if R is a division ring.

Proof. By Corollary 1.21, R has only trivial idempotents. Hence every element of R has either the form $0 + u$ where $u \in U(0R0)$ (that is impossible) or the form $1 + u$ where $u \in U(1R1) = U(R)$. Therefore, every element ($\neq 1$) of R has the form $1 + u$ where $u \in U(R)$. Hence every element ($\neq 1$) of R is quasi-regular and we conclude that R is a division ring by Lemma 1.3.

The converse is clear.

Conflicts of interest

The authors state that did not have a conflict of interests.

References

- [1] Kosan M. T., Lero A., Matczuk J. UJ rings, *Commun. Algebra*, 46 (5) (2018) 2297-2303.
- [2] Nicholson W.K., Lifting idempotent and exchange rings, *Trans. Amer. Math. Soc.*, 229 (1977) 269-278.
- [3] Nicholson W.K., Zhou Y., Clean general rings, *J. Algebra*, 291 (2005) 297-311.
- [4] Lam T.Y., A First Course in Noncommutative Rings, GTM 131, 2nd ed. Verlag: Springer, (1991) 53-82.
- [5] Haghany A., Hopficity and co-hopficity for Morita contexts, *Commun. Algebra*, 27 (1999) 477-492.
- [6] Kosan M. T., The p.p. property of trivial extensions, *J. Algebra Appl.*, 14 (8) (2015) 1550124.
- [7] Nicholson W.K., Zhou Y., Rings in which elements are uniquely the sum of an idempotent and a unit, *Glasgow Math. J.*, 46 (2004) 227-236.

Existence of nonoscillatory solutions of second-order neutral differential equations

M. Tamer ŞENEL¹ , Bengü ÇINA^{2,*} 

¹Erciyes University, Faculty of Sciences, Typo of Mathematics, Kayseri/ TURKEY

²Sivas Cumhuriyet University, University, Zara Veysel Dursun UBYO, Sivas/ TURKEY

Abstract

In this study we shall obtain some sufficient conditions for the existence of positive solutions of variable coefficient nonlinear second-order neutral differential equation with distributed deviating arguments. For some different cases of the range of $p(t)$ by using Banach contraction principle we will give some sufficient conditions for the nonoscillatory solutions of second-order neutral differential equation. With this purpose we will use fixpoint theorem. At the end of the research, there is an example that meets the conditions we have given. Our results improve and extend some existing results.

Article info

History:
Received: 14.11.2020
Accepted: 26.04.2021

Keywords:
Nonoscillatory solutions, Fixpoint, Second-order.

1. Introduction

In this work we consider the second-order neutral nonlinear differential equation with distributed deviating arguments of the form

$$\left(x(t) - \int_a^b P(t, \xi)x(t - \xi)d\xi\right)'' + \int_{a_1}^{b_1} f_1(t, x(\sigma_1(t, \xi)))d\xi - \int_{a_2}^{b_2} f_2(t, x(\sigma_2(t, \xi)))d\xi = g(t), \quad (1)$$

where $g \in C([t_0, \infty), \mathbb{R})$, $P(t, \xi) \in C([t_0, \infty) \times [a, b], \mathbb{R})$ for $0 < a < b$ and $\sigma_i(t, \xi) \in C([t_0, \infty) \times [a_i, b_i], \mathbb{R})$ with $\lim_{t \rightarrow \infty} \sigma_i(t, \xi) = \infty$ and $0 \leq a_i < b_i$, $i = 1, 2$.

In this paper, we assume that $f_i(t, x) \in C([t_0, \infty) \times \mathbb{R}, \mathbb{R})$ is a nondecreasing in x for $i = 1, 2$, $xf_i(t, x) > 0$ for $x \neq 0$, $i = 1, 2$ and satisfies

$$|f_i(t, x) - f_i(t, y)| \leq q_i(t)|x - y| \text{ for } t \in [t_0, \infty) \text{ and } x, y \in [e, f], \quad (2)$$

where $q_i \in C([t_0, \infty), \mathbb{R}^+)$, $i = 1, 2$ and $[e, f]$ ($0 < e < f$ or $e < f < 0$) is any closed interval.

Furthermore, suppose that

$$\int_{t_0}^{\infty} sq_i(s)ds < \infty, \quad i = 1, 2, \quad (3)$$

$$\int_{t_0}^{\infty} s|f_i(s, d)|ds < \infty, \text{ for some } d \neq 0, \quad i = 1, 2, \quad (4)$$

$$\int_{t_0}^{\infty} s|g(s)|ds < \infty. \quad (5)$$

The nonoscillatory behavior of solutions of neutral differential equations has been considered by different authors in the past. This work was motivated by the paper of Yang, Zhang and Ge in [1] which is concerned with the existence of nonoscillatory solutions of second-order differential equation of the form

$$(x(t) - p(t)x(t - \tau))'' + f_1(t, x(\sigma_1(t))) - f_2(t, x(\sigma_2(t))) = 0 \quad (6)$$

and T. Candan and R.S. Dahiya in [2] which is concerned with the existence of first and second-order neutral differential equations of the form

$$\frac{d^k}{dt^k} [x(t) + P(t)x(t - \tau)] + \int_a^b q_1(t, \xi)x(t - \xi)d\xi - \int_c^d q_2(t, \mu)x(t - \mu)d\mu = 0. \tag{7}$$

In 2016, Candan [3] investigated nonoscillatory solutions of higher-order neutral differential equations of the form

$$\left[r(t) \left[\left[x(t) - \int_a^b p_2(t, \xi)x(t - \xi)d\xi \right]^{(n-1)} \right]^{\gamma'} + (-1)^n \int_c^d Q_2(x, \xi)G(x, \xi)d\xi = 0.$$

Neutral differential equations have numerous applications in natural sciences and engineering. Especially, neutral differential equations arise in a variety of real world problems such as in the study of non-Newtonian fluid theory and porous medium problems. In recent years, there have been many studies concerning the oscillatory and nonoscillatory behavior of neutral differential equations. For example, Li, Pintus, and Viglialoro [4] studied “Properties of solutions to porous medium problems with different sources and boundary conditions” in 2019. Also, Li and Rogovchenko [5] studied “On the asymptotic behavior of solutions to a class of third-order nonlinear neutral differential equations” in 2020. Many authors have investigated existence of oscillation and nonoscillation solutions of neutral differential equations. Please, see [1-16] and references cited therein.

The purpose of this article is to give some sufficient conditions for the existence of nonoscillatory solutions of (1) according to different cases of the range of $p(t)$ by using Banach contraction principle.

Let $T_0 = \min \{t_1 - b, \inf_{t \geq t_1} \min_{\xi \in [a_1, b_1]} \sigma_1(t, \xi), \inf_{t \geq t_1} \min_{\xi \in [a_2, b_2]} \sigma_2(t, \xi)\}$ for $t_1 \geq t_0$. By a solution of equation (1), we mean a function $x \in C([T_1, \infty), \mathbb{R})$ in the sense that $x(t) - \int_{a_3}^{b_3} p(t, \xi)x(t - \xi)d\xi$

is two times continuously differentiable on $[t_1, \infty)$ and such that equation (1) is satisfied for $t \geq t_1$.

As is customary, a solution of (1) is said to be oscillatory if it has arbitrarily large zeros. Otherwise the solution is called nonoscillatory.

2. Main Results

Theorem 2.1. Assume that (3) - (5) hold, $P(t, \xi) \geq 0$ and $\int_a^b P(t, \xi)d\xi \leq p < 1$. Then (1) has a bounded nonoscillatory solution.

Proof. Suppose (4) holds with $d > 0$. A similar argument holds for $d < 0$. Let $N_2 = d$.

Set

$$A = \{x \in X : N_1 \leq x(t) \leq N_2, \quad t \geq t_0\},$$

where N_1 and N_2 are positive constants such that

$$N_1 + pN_2 < N_2.$$

It is obvious that A is a closed, bounded and convex subset of X . Because of (3) - (5), we can take a $t_1 > t_0$ sufficiently large such that $t - b \geq t_0$, $\sigma_i(t, \xi) \geq t_0$, $\xi \in [a_i, b_i]$, $i = 1, 2$ for $t \geq t_1$ and

$$p + \int_{t_1}^{\infty} s[(b_1 - a_1)q_1(s) + (b_2 - a_2)q_2(s)] ds \leq \theta_1 < 1, \tag{8}$$

$$\int_{t_1}^{\infty} s[(b_1 - a_1)f_1(s, d) + |g(s)|] ds \leq \alpha - N_1 - pN_2, \tag{9}$$

and

$$\int_{t_1}^{\infty} s[(b_2 - a_2)f_2(s, d) + |g(s)|] ds \leq N_2 - \alpha, \tag{10}$$

where $\alpha \in (N_1 + pN_2, N_2)$. Define a mapping $S : A \rightarrow X$ as follows:

$$(Sx)(t) = \begin{cases} \alpha - \int_a^b P(t, \xi)x(t - \xi)d\xi - \int_t^\infty (s - t) \left[\int_{a_1}^{b_1} f_1(s, x(\sigma_1(s, \xi)))d\xi \right. \\ \left. - \int_{a_2}^{b_2} f_2(s, x(\sigma_2(s, \xi)))d\xi - g(s) \right] ds, & t \geq t_1 \\ (Sx)(t_1), & t_0 \leq t \leq t_1 \end{cases}$$

It is easy to see that Sx is continuous. For every $x \in A$ and $t \geq t_1$ dealing with (10) we can get

$$\begin{aligned} (Sx)(t) &= \alpha - \int_a^b P(t, \xi)x(t - \xi)d\xi - \int_t^\infty (s - t) \left[\int_{a_1}^{b_1} f_1(s, x(\sigma_1(s, \xi)))d\xi \right. \\ &\quad \left. - \int_{a_2}^{b_2} f_2(s, x(\sigma_2(s, \xi)))d\xi - g(s) \right] ds \\ &\leq \alpha + \int_{t_1}^\infty s[(b_2 - a_2)f_2(s, d) + |g(s)|] ds \\ &\leq N_2 \end{aligned}$$

and taking (9) into account, we can get

$$\begin{aligned} (Sx)(t) &= \alpha - \int_a^b P(t, \xi)x(t - \xi)d\xi - \int_t^\infty (s - t) \left[\int_{a_1}^{b_1} f_1(s, x(\sigma_1(s, \xi)))d\xi \right. \\ &\quad \left. - \int_{a_2}^{b_2} f_2(s, x(\sigma_2(s, \xi)))d\xi - g(s) \right] ds \\ &\geq \alpha - pN_2 - \int_{t_1}^\infty s[(b_1 - a_1)f_1(s, d) + |g(s)|] ds \\ &\geq N_1. \end{aligned}$$

Thus we proved that $SA \subset A$. Now we shall show that S is a contraction mapping on A .

In fact, for $x, y \in A$ and $t \geq t_1$, in view of (2) and (8) we have

$$\begin{aligned} |(Sx)(t) - (Sy)(t)| &\leq \int_a^b P(t, \xi)|x(t - \xi) - y(t - \xi)|d\xi \\ &+ \int_t^\infty (s - t) \int_{a_2}^{b_2} |f_2(s, x(\sigma_2(s, \xi))) - f_2(s, y(\sigma_2(s, \xi)))|d\xi ds \\ &+ \int_t^\infty (s - t) \int_{a_1}^{b_1} |f_1(s, x(\sigma_1(s, \xi))) - f_1(s, y(\sigma_1(s, \xi)))|d\xi ds \\ &\leq \int_a^b P(t, \xi)|x(t - \xi) - y(t - \xi)|d\xi \\ &+ \int_{t_1}^\infty s \int_{a_1}^{b_1} q_1(s)|x(\sigma_1(s, \xi)) - y(\sigma_1(s, \xi))|d\xi ds \\ &+ \int_{t_1}^\infty s \int_{a_1}^{b_1} q_2(s)|x(\sigma_2(s, \xi)) - y(\sigma_2(s, \xi))|d\xi ds \\ &\leq \|x - y\| \left(p + \int_{t_1}^\infty s[(b_1 - a_1)q_1(s) + (b_2 - a_2)q_2(s)] ds \right) \leq \theta_1 \|x - y\|, \end{aligned}$$

which implies with the sup norm that

$$\|Sx - Sy\| \leq \theta_1 \|x - y\|.$$

Since $\theta_1 < 1$, S is a contraction mapping on A . By Banach Contraction Mapping Principle, there exists a unique fixed point $x \in A$ such that $Sx = x$, which is obviously a positive solution of (1). This completes the proof.

Theorem 2.2. Assume that (3) - (5) hold, $P(t, \xi) \leq 0$ and $-1 < p \leq \int_a^b P(t, \xi)d\xi$. Then (1) has a bounded nonoscillatory solution.

Proof. Suppose (4) holds with $d > 0$. A similar argument holds for $d < 0$. Let $N_4 = d$.

Set

$$A = \{x \in X : N_3 \leq x(t) \leq N_4, \quad t \geq t_0\},$$

where N_3 and N_4 are positive constants such that

$$N_3 < (1 - p)N_4.$$

It is obvious that A is a closed, bounded and convex subset of X . Because of (3) - (5), we can take a $t_1 > t_0$ sufficiently large such that $t - b \geq t_0$, $\sigma_i(t, \xi) \geq t_0$, $\xi \in [a_i, b_i]$, $i = 1, 2$ for $t \geq t_1$ and

$$p + \int_{t_1}^{\infty} s[(b_1 - a_1)q_1(s) + (b_2 - a_2)q_2(s)] ds \leq \theta_2 < 1, \tag{11}$$

$$\int_{t_1}^{\infty} s[(b_1 - a_1)f_1(s, d) + |g(s)|] ds \leq \alpha - N_3, \tag{12}$$

and

$$\int_{t_1}^{\infty} s[(b_2 - a_2)f_2(s, d) + |g(s)|] ds \leq (1 - p)N_4 - \alpha, \tag{13}$$

where $\alpha \in (N_3, (1 - p) - N_4)$. Define a mapping $S : A \rightarrow X$ as follows:

$$(Sx)(t) = \begin{cases} \alpha - \int_a^b P(t, \xi)x(t - \xi)d\xi - \int_t^{\infty} (s - t) \left[\int_{a_1}^{b_1} f_1(s, x(\sigma_1(s, \xi)))d\xi \right. \\ \left. - \int_{a_2}^{b_2} f_2(s, x(\sigma_2(s, \xi)))d\xi - g(s) \right] ds, & t \geq t_1 \\ (Sx)(t_1), & t_0 \leq t \leq t_1 \end{cases}$$

It is easy to see that Sx is continuous. For every $x \in A$ and $t \geq t_1$ dealing with (13) we can get

$$\begin{aligned} (Sx)(t) &= \alpha - \int_a^b P(t, \xi)x(t - \xi)d\xi - \int_t^{\infty} (s - t) \left[\int_{a_1}^{b_1} f_1(s, x(\sigma_1(s, \xi)))d\xi \right. \\ &\quad \left. - \int_{a_2}^{b_2} f_2(s, x(\sigma_2(s, \xi)))d\xi - g(s) \right] ds \\ &\leq \alpha + pN_4 + \int_{t_1}^{\infty} s[(b_2 - a_2)f_2(s, d) + |g(s)|] ds \leq N_4 \end{aligned}$$

and taking (12) in to account, we can get

$$\begin{aligned} (Sx)(t) &= \alpha - \int_a^b P(t, \xi)x(t - \xi)d\xi - \int_t^{\infty} (s - t) \left[\int_{a_1}^{b_1} f_1(s, x(\sigma_1(s, \xi)))d\xi \right. \\ &\quad \left. - \int_{a_2}^{b_2} f_2(s, x(\sigma_2(s, \xi)))d\xi - g(s) \right] ds \\ &\geq \alpha - \int_{t_1}^{\infty} s[(b_1 - a_1)f_1(s, d) + |g(s)|] ds \geq N_3. \end{aligned}$$

Thus we proved that $SA \subset A$. Now we shall show that S is a contraction mapping on A .

In fact, for $x, y \in A$ and $t \geq t_1$, in view of (2) and (11) we have

$$\begin{aligned} |(Sx)(t) - (Sy)(t)| &\leq \int_a^b (-P(t, \xi))|y(t - \xi) - x(t - \xi)|d\xi \\ &+ \int_t^{\infty} (s - t) \int_{a_2}^{b_2} |f_2(s, x(\sigma_2(s, \xi))) - f_2(s, y(\sigma_2(s, \xi)))|d\xi ds \\ &+ \int_t^{\infty} (s - t) \int_{a_1}^{b_1} |f_1(s, x(\sigma_1(s, \xi))) - f_1(s, y(\sigma_1(s, \xi)))|d\xi ds \\ &\leq \int_a^b (-P(t, \xi))|x(t - \xi) - y(t - \xi)|d\xi \\ &+ \int_{t_1}^{\infty} s \int_{a_1}^{b_1} q_1(s)|x(\sigma_1(s, \xi)) - y(\sigma_1(s, \xi))|d\xi ds \\ &+ \int_{t_1}^{\infty} s \int_{a_1}^{b_1} q_2(s)|x(\sigma_2(s, \xi)) - y(\sigma_2(s, \xi))|d\xi ds \end{aligned}$$

$$\begin{aligned} &\leq \|x - y\| \left(p + \int_{t_1}^{\infty} s[(b_1 - a_1)q_1(s) + (b_2 - a_2)q_2(s)] ds \right) \\ &\leq \theta_2 \|x - y\|, \end{aligned}$$

which implies with the sup norm that

$$\|Sx - Sy\| \leq \theta_2 \|x - y\|.$$

Since $\theta_2 < 1$, S is a contraction mapping on A . By Banach Contraction Mapping Principle, there exists a unique fixed point $x \in A$ such that $Sx = x$, which is obviously a positive solution of (1). This completes the proof.

Example 2.3. For $t > 0$ consider the equation

$$\begin{aligned} &\left(x(t) - \int_0^1 \exp(-t - 3\xi)x(t - \xi)d\xi \right)'' + \int_1^3 2 \exp(-t)x(t - 2\xi)d\xi - \int_2^6 \exp(-t)x(t - \xi)d\xi \\ &= \frac{1}{3} \exp(-t) - \exp(-t - 3) + 9 \exp(-3t) + 16 \exp(-4t). \end{aligned} \tag{14}$$

Note that $P(t, \xi) = \exp(-t - 3\xi)$, $\sigma_1(t, \xi) = t - 2\xi$, $\sigma_2(t, \xi) = t - \xi$, $f_1(t, u) = 2\exp(-t)u$, $f_2(t, u) = \exp(-t)u$ and $g(t) = \frac{1}{3} \exp(-t) - \exp(-t - 3) + 9 \exp(-3t) + 16 \exp(-4t)$. We can check that the conditions of Theorem 2.1 are all satisfied. We note that $x(t) = \exp(-3t) + 1$ is a nonoscillatory solution of (14).

Conflicts of interest

The authors state that did not have a conflict of interests.

References

- [1] Yang A., Zhang Z., Ge W., Existence of nonoscillatory solutions of second-order nonlinear neutral differential equations, *Indian J. Pure Appl. Math.*, 39 (3) (2008).
- [2] Candan T., and Dahiya R. S., Existence of nonoscillatory solutions of first and second order neutral differential equations with distributed deviating arguments, *J. Franklin Inst.*, 3 (47) (2010) 1309-1316.
- [3] Candan T., Existence of Nonoscillatory Solutions of Higher Order Neutral Differential Equations, *Filomat*, 30 (8) (2016) 2147-2153.
- [4] Li T., Pintus N., Vignali G., Properties of solutions to porous medium problems with different sources and boundary conditions, *Z. Angew. Math. Phys.*, 70 (3) (2019) 1-18.
- [5] Li T., Rogovchenko Yu. V., On the asymptotic behavior of solutions to a class of third-order nonlinear neutral differential equations, *Appl. Math. Lett.*, 105 (2020) 1-7.
- [6] Candan T., Dahiya R. S., Existence of nonoscillatory solutions of higher order neutral differential equations with distributed deviating arguments, *Math. Slovaca*, 63(1) (2013) 183-190.
- [7] Candan T., Nonoscillatory solutions of higher order differential and delay differential equations with forcing term, *Appl. Math. Lett.*, 39 (2015), 67-72.
- [8] Tian Y., Cai Y., Li T., Existence of nonoscillatory solutions to second-order nonlinear neutral difference equations, *J. Nonlinear Sci. Appl.*, 8 (2015) 884-892.
- [9] Györi I., Ladas G., Oscillation Theory of Delay Differential Equations With Applications, Oxford: Clarendon Press, (1991).
- [10] Erbe L. H., Kong Q., Zang B. G., Oscillation Theory for Functional Differential Equations, New York: Marcel Dekker, Inc., (1995).
- [11] Agarwal R. P., Grace S. R., O'Regan D., Oscillation Theory for Difference and Functional Differential Equations Oscillation Theory for Difference and Functional Differential Equations, Kluwer Academic Publishers, (2000).
- [12] Yu Y., Wang H., Nonoscillatory Solutions of Second Order Nonlinear Neutral Delay Equations, *J. Math. Anal. Appl.*, 311(2005) 445-456.
- [13] Li T., Han Z., Sun S., Yang D., Existence of nonoscillatory solutions to second-order neutral delay dynamic equations on time scales, *Adv. Difference Equ.*, 2009 (2009) 562329.
- [14] Agarwal R. P., Bohner M., Li T., Zang C., A new approach in the study of oscillatory behavior of even-order neutral delay differential equations, *Appl. Math. Comput.*, 225 (2013) 787-794.

- [15] Džurina J., Grace S. R., Jadlovská I., Li T., Oscillation criteria for second-order Emden-Fowler delay differential equations with a sublinear neutral term, *Math. Nachr.*, 293(5) (2020) 910-922.
- [16] Li T., Rogovchenko Yu. V., Oscillation of second-order neutral differential equations, *Math. Nachr.*, 88(10) (2015) 1150-1162.

Quasi ideals of nearness semirings

Özlem TEKİN^{1,*} 

¹Adiyaman University, Faculty of Science, Department of Mathematics, Adiyaman / TURKEY

Abstract

This article introduces quasi-ideals in semirings on weak nearness approximation spaces. Concepts and definitions are given to clarify the subject of quasi ideals in semirings on weak nearness approximation spaces. Some basic properties of quasi ideals are also given. Furthermore, it is given that the definition of upper-near quasi ideals. And, it is examined that the relationship between quasi ideals and upper near quasi ideals. Therefore, the features described in this study will contribute greatly to the theoretical development of the nearness semirings theory.

Article info

History:
Received: 22.01.2021
Accepted: 04.05.2021

Keywords:
Nearness approximation space, Semirings, Nearness semiring, Quasi ideals.

1. Introduction

Peters defined near sets theory that is a generalization of rough sets [1]. Peters introduced new form of indiscernibility relation by using the characteristics of the objects to find the nearness of the objects [2]. Afterward, he generalized approaching theory in the study of the nearness of non-empty sets which are similar to each other [3], [4]. İnan and Öztürk introduced the notion of nearness groups and nearness semigroups [5], [6], [7]. Also, other approaches have been studied in [8], [9], [10], [11], [12], [13].

Vandier introduced the concept of semiring theory in 1934 [14] and many mathematicians proved important properties for semiring theory. Especially, semirings are very important for determinants and matrices. One of the most important notions for semirings is ideals. Shabir et al. [15] defined ideals for semirings. The subject of quasi ideals for semigroups and rings was formally defined by Steinfield in 1956 [16]. Iseki defined the concept of quasi-ideal for a semiring [17]. Rao introduced other types of ideals and their properties for semirings [18], [19].

In this article, quasi ideals in semirings are defined and some of the concepts and definitions on weak nearness approximation spaces are explained. Then, we study some basic properties of quasi ideals.

2. Preliminaries

An object characterization is specified by means a tuple of function values $\Phi(x)$ deal with an $x \in X$. $B \subseteq \mathcal{F}$ is a set of probe functions and these functions stand

for characteristics of sampling objects $X \subseteq \mathcal{O}$. Let $\varphi_i \in B$, that is $\varphi_i : \mathcal{O} \rightarrow \mathbb{R}$. The functions showing object characteristics supply a basis for $\Phi: \mathcal{O} \rightarrow \mathbb{R}^L$, $\Phi(x) = (\varphi_1(x), \varphi_2(x), \dots, \varphi_L(x))$ a vector consisting of measurements deal with every functional value $\varphi_i(x)$ with the description length $|\Phi| = L$ ([2]).

The selection of functions $\varphi_i \in B$ is very fundamental by using to determine sampling objects. $X \subseteq \mathcal{O}$ are near each other if and only if the sample items have alike characterizations. Every φ shows a descriptive pattern of an object. Hence, Δ_{φ_i} means $\Delta_{\varphi_i} = |\varphi_i(x) - \varphi_i(x')|$ such that $x, x' \in \mathcal{O}$. Δ_{φ_i} means to a description of the indiscernibility relation " \sim_B " defined by Peters in [2]. B_r is probe functions in B for $r \leq |B|$.

Definition 2.1 [2]

$$\sim_B = \{(x, x') \in \mathcal{O} \times \mathcal{O} \mid \Delta_{\varphi_i} = 0, \forall \varphi_i \in B, B \subseteq \mathcal{F}\}$$

means an indiscernibility relation on \mathcal{O} with $i \leq |\Phi|$. \sim_{B_r} is also indiscernibility relation determined by utilizing B_r .

Near equivalence class is stated as $[x]_{B_r} = \{x' \in \mathcal{O} \mid x \sim_{B_r} x'\}$. After getting near equivalence classes, quotient set $\mathcal{O} / \sim_{B_r} = \{[x]_{B_r} \mid x \in \mathcal{O}\} = \xi_{\mathcal{O}, B_r}$ and set of partitions $N_r(B) = \{\xi_{\mathcal{O}, B_r} \mid B_r \subseteq B\}$ can be found. By using near equivalence classes, $N_r(B)^* X = \bigcup_{[x]_{B_r} \cap X \neq \emptyset} [x]_{B_r}$ upper approximation set can be attained.

Definition 2.1 [9] Let \mathcal{O} be a set of sample objects, F a set of the probe functions, \sim_{B_r} an indiscernibility relation, and $N_r(B)$ a collection of partitions. Then,

$(\mathcal{O}, \mathcal{F}, \sim_{B_r}, N_r(B))$ is called a weak nearness approximation space.

Theorem 2.1 [9] Let $(\mathcal{O}, \mathcal{F}, \sim_{B_r}, N_r(B))$ be a weak nearness approximation space and $X, Y \subset \mathcal{O}$. The followings are held:

- 1) $X \subseteq N_r(B)^*X$,
- 2) $N_r(B)^*(X \cup Y) = (N_r(B)^*X) \cup (N_r(B)^*Y)$,
- 3) $X \subseteq Y$ implies $N_r(B)^*X \subseteq N_r(B)^*Y$,
- 4) $N_r(B)^*(X \cap Y) \subseteq (N_r(B)^*X) \cap (N_r(B)^*Y)$.

After this, \mathcal{O} means a $(\mathcal{O}, \mathcal{F}, \sim_{B_r}, N_r(B))$ is weak near approximation spaces unless otherwise stated.

Definition 2.3 [13] If S is a nearness semigroup and there exists an $e \in N_r(B)^*S$ satisfying $x \cdot e = x = e \cdot x$ for all $x \in S$, then (S, \cdot) is called a nearness monoid. If $x \cdot y = y \cdot x$ ($x + y = y + x$) for all $x, y \in S$, then (S, \cdot) ($(S, +)$) is called a commutative (abelian).

Definition 2.4 [13] Let $S \in \mathcal{O}$. Then, S is called a semiring on weak near approximation spaces \mathcal{O} if the following properties hold:

- SR_1) $(S, +)$ is an abelian monoid on \mathcal{O} with identity element 0 ,
- NSR_2) (S, \cdot) is a monoid on \mathcal{O} with identity element 1 ,
- NSR_3) for all $x, y, z \in S$,
 $x \cdot (y + z) = (x \cdot y) + (x \cdot z)$ and $(x + y) \cdot z = (x \cdot z) + (y \cdot z)$
- properties hold in $N_r(B)^*S$,
- NSR_4) for all $x \in S$, $0 \cdot x = 0 = x \cdot 0$
- properties hold in $N_r(B)^*$,
- NSR_5) $1 \neq 0$.

Theorem 2.2 [13] Let S be a nearness semiring, \sim_{B_r} a complete congruence indiscernibility relation on S , and X, Y two non-empty subsets of S . The following properties hold:

- 1) $(N_r(B)^*X) + (N_r(B)^*Y) = N_r(B)^*(X + Y)$,
- 2) $(N_r(B)^*X) \cdot (N_r(B)^*Y) = N_r(B)^*(X \cdot Y)$.

Definition 2.5 [13] Let S be a nearness semiring, and A is a non-empty subset of S .

- 1) A is called a subnearness semiring of S , if $A + A \subseteq N_r(B)^*A$ and $A \cdot A \subseteq N_r(B)^*A$.
- 2) A is called a upper-near subnearness semiring of S , if $(N_r(B)^*A) + (N_r(B)^*A) \subseteq N_r(B)^*A$ and $(N_r(B)^*A) \cdot (N_r(B)^*A) \subseteq N_r(B)^*A$.

Definition 2.6 [13] Let S be a nearness semiring, and A be a subnearness semigroup of S , where $A \neq S$.

- 1) A is called a right (left) ideal of S , if $A \cdot S \subseteq N_r(B)^*A$ ($S \cdot A \subseteq N_r(B)^*A$).
- 2) A is called a upper-near right (left) ideal of S , if $(N_r(B)^*A) \cdot S \subseteq N_r(B)^*A$ ($S \cdot (N_r(B)^*A) \subseteq$

$N_r(B)^*A$).

Definition 2.7 [20] Let S be a semiring and A be a non-empty subset of semiring S , where $A \neq S$.

- 1) If A is a subsemigroup of S , $AS \subseteq A$ and $SA \subseteq A$, then A is called an ideal of S .
- 2) If A is a subsemigroup of S and $AS \cap SA \subseteq A$, then A is called a quasi-ideal of S .

3. Quasi Ideals of Nearness Semirings

Definition 3.1 Let S be a nearness semiring and Q be a non-empty subset of S , where $Q \neq S$.

- 1) Q is called quasi-ideal of S if Q is a subnearness semigroup of S and $QS \cap SQ \subseteq N_r(B)^*Q$.
- 2) Q is called a upper-near quasi ideal of S if Q is a subnearness semigroup of S and $(N_r(B)^*Q)S \cap S(N_r(B)^*Q) \subseteq N_r(B)^*Q$.

Example 3.1

Let $\mathcal{O} = \{a, b, c, d, e, f, g, h, j, k, l, m, n\}$ be a set of perceptual objects where

$$a = \begin{bmatrix} 0 & 0 \\ 0 & 0 \end{bmatrix}, b = \begin{bmatrix} 1 & 0 \\ 0 & 1 \end{bmatrix}, c = \begin{bmatrix} 2 & 0 \\ 0 & 2 \end{bmatrix}, d = \begin{bmatrix} 1 & 0 \\ 0 & 2 \end{bmatrix},$$

$$e = \begin{bmatrix} 2 & 0 \\ 0 & 1 \end{bmatrix}, f = \begin{bmatrix} 1 & 0 \\ 0 & 0 \end{bmatrix}, g = \begin{bmatrix} 2 & 0 \\ 0 & 0 \end{bmatrix}, h = \begin{bmatrix} 0 & 0 \\ 0 & 2 \end{bmatrix},$$

$$j = \begin{bmatrix} 0 & 0 \\ 0 & 1 \end{bmatrix}, k = \begin{bmatrix} 1 & 1 \\ 0 & 0 \end{bmatrix}, l = \begin{bmatrix} 1 & 0 \\ 1 & 0 \end{bmatrix}, m = \begin{bmatrix} 1 & 1 \\ 0 & 1 \end{bmatrix},$$

$$n = \begin{bmatrix} 2 & 1 \\ 0 & 0 \end{bmatrix}$$

for $\mathcal{O} = \{[a_{ij}]_{2 \times 2} | a_{ij} \in \mathbb{Z}_3\}$, $r = 1$, $B, \{\varphi_1, \varphi_2, \varphi_3\} \subseteq \mathcal{F}$ is a set of probe functions. Let $S = \{c, d, e, f\} \subset \mathcal{O}$. Probe functions' values

$$\varphi_1: \mathcal{O} \rightarrow V_1 = \{\alpha_1, \alpha_2, \alpha_3, \alpha_4, \alpha_5\},$$

$$\varphi_2: \mathcal{O} \rightarrow V_2 = \{\alpha_2, \alpha_3, \alpha_5, \alpha_6, \alpha_7\},$$

$$\varphi_3: \mathcal{O} \rightarrow V_3 = \{\alpha_2, \alpha_3, \alpha_4, \alpha_5, \alpha_6\}$$

are presented in Table 1.

Table 1: Features' Table

	a	b	c	d	e	f	g	h	j	k	l	m	n
φ_1	α_1	α_2	α_4	α_5	α_4	α_5	α_3	α_4	α_5	α_1	α_2	α_1	α_3
φ_2	α_3	α_5	α_6	α_3	α_3	α_2	α_6	α_6	α_6	α_5	α_5	α_7	α_7
φ_3	α_2	α_3	α_2	α_4	α_3	α_2	α_4	α_5	α_6	α_5	α_5	α_6	α_6

Now, we find the nearness equivalence classes as follows;

$$\begin{aligned}
 [a]_{\varphi_1} &= \{x' \in \mathcal{O} \mid \varphi_1(x') = \varphi_1(a) = \alpha_1\} = \{a, k, m\} \\
 &= [k]_{\varphi_1} = [m]_{\varphi_1}, \\
 [b]_{\varphi_1} &= \{x' \in \mathcal{O} \mid \varphi_1(x') = \varphi_1(b) = \alpha_2\} = \{b, l\} \\
 &= [l]_{\varphi_1}, \\
 [c]_{\varphi_1} &= \{x' \in \mathcal{O} \mid \varphi_1(x') = \varphi_1(c) = \alpha_4\} = \{c, e, h\} \\
 &= [e]_{\varphi_1} = [h]_{\varphi_1}, \\
 [d]_{\varphi_1} &= \{x' \in \mathcal{O} \mid \varphi_1(x') = \varphi_1(d) = \alpha_5\} = \{d, f, j\}, \\
 &= [f]_{\varphi_1} = [j]_{\varphi_1}, \\
 [g]_{\varphi_1} &= \{x' \in \mathcal{O} \mid \varphi_1(x') = \varphi_1(g) = \alpha_3\} = \{g, n\}, \\
 &= [n]_{\varphi_1}.
 \end{aligned}$$

Then, we have that

$$\begin{aligned}
 \xi_{\varphi_1} &= \{[a]_{\varphi_1}, [b]_{\varphi_1}, [c]_{\varphi_1}, [d]_{\varphi_1}, [g]_{\varphi_1}\}. \\
 [a]_{\varphi_2} &= \{x' \in \mathcal{O} \mid \varphi_2(x') = \varphi_2(a) = \alpha_3\} = \{a, d, e\} \\
 &= [d]_{\varphi_2} = [e]_{\varphi_2}, \\
 [b]_{\varphi_2} &= \{x' \in \mathcal{O} \mid \varphi_2(x') = \varphi_2(b) = \alpha_5\} = \{b, k, l\} \\
 &= [k]_{\varphi_2} = [l]_{\varphi_2}, \\
 [c]_{\varphi_2} &= \{x' \in \mathcal{O} \mid \varphi_2(x') = \varphi_2(c) = \alpha_6\} = \{c, g, h, j\} \\
 &= [g]_{\varphi_2} = [h]_{\varphi_2} = [j]_{\varphi_2}, \\
 [f]_{\varphi_2} &= \{x' \in \mathcal{O} \mid \varphi_2(x') = \varphi_2(f) = \alpha_2\} = \{f\}, \\
 [m]_{\varphi_2} &= \{x' \in \mathcal{O} \mid \varphi_2(x') = \varphi_2(m) = \alpha_7\} = \{m, n\} \\
 &= [n]_{\varphi_2}.
 \end{aligned}$$

We attain that

$$\begin{aligned}
 \xi_{\varphi_2} &= \{[a]_{\varphi_2}, [b]_{\varphi_2}, [c]_{\varphi_2}, [f]_{\varphi_2}, [m]_{\varphi_2}\}. \\
 [a]_{\varphi_3} &= \{x' \in \mathcal{O} \mid \varphi_3(x') = \varphi_3(a) = \alpha_2\} = \{a, c, f\} \\
 &= [c]_{\varphi_3} = [f]_{\varphi_3}, \\
 [b]_{\varphi_3} &= \{x' \in \mathcal{O} \mid \varphi_3(x') = \varphi_3(b) = \alpha_3\} = \{b, e\} \\
 &= [e]_{\varphi_3}, \\
 [d]_{\varphi_3} &= \{x' \in \mathcal{O} \mid \varphi_3(x') = \varphi_3(d) = \alpha_4\} = \{d, g\} \\
 &= [g]_{\varphi_3}, \\
 [h]_{\varphi_3} &= \{x' \in \mathcal{O} \mid \varphi_3(x') = \varphi_3(h) = \alpha_5\} = \{h, k, l\} \\
 &= [k]_{\varphi_3} = [l]_{\varphi_3}, \\
 [j]_{\varphi_3} &= \{x' \in \mathcal{O} \mid \varphi_3(x') = \varphi_3(j) = \alpha_6\} = \{j, m, n\} \\
 &= [m]_{\varphi_3} = [n]_{\varphi_3}.
 \end{aligned}$$

From here, we get that $\xi_{\varphi_3} = \{[a]_{\varphi_3}, [b]_{\varphi_3}, [d]_{\varphi_3}, [h]_{\varphi_3}, [j]_{\varphi_3}\}$. Consequently, a set of partitions of \mathcal{O} is $N_r(B) = \{\xi_{\varphi_1}, \xi_{\varphi_2}, \xi_{\varphi_3}\}$ for $r = 1$.

Hence,

$$\begin{aligned}
 N_1(B)^*S &= \cup_{[x]_{\varphi_i} \cap S \neq \emptyset} [x]_{\varphi_i} \\
 &= [c]_{\varphi_1} \cup [d]_{\varphi_1} \cup [a]_{\varphi_2} \cup [c]_{\varphi_2} \cup [f]_{\varphi_2} \cup [a]_{\varphi_3} \cup \\
 &[b]_{\varphi_3} \cup [d]_{\varphi_3} \\
 &= \{a, b, c, d, e, f, g, h, j\}.
 \end{aligned}$$

Taking operation tables for S in Table 2 and Table 3.

Table 2: “+” operation table for S .

+	c	d	e	f
c	b	j	f	h
d	j	e	a	c
e	f	a	d	j
f	h	c	j	g

Table 3: “.” operation table for S .

.	c	d	e	f
c	b	e	d	g
d	e	b	c	f
e	d	c	b	g
f	g	f	g	f

In this case, $(S, +, \cdot)$ is a nearness semiring. Let take $Q = \{d, e, f\}$ is subset of S . Considering operation tables for Q in Table 4 and Table 5.

Table 4: “+” operation table for \cdot .

+	d	e	f
d	e	a	c
e	a	d	j
f	c	j	g

Table 5: “+” operation table for Q .

\cdot	d	e	f
d	b	c	f
e	c	b	g
f	f	g	f

$$N_1(B)^*Q = \cup_{[x]_{\varphi_i} \cap Q \neq \emptyset} [x]_{\varphi_i}$$

$$= [c]_{\varphi_1} \cup [d]_{\varphi_1} \cup [a]_{\varphi_2} \cup [f]_{\varphi_2} \cup [a]_{\varphi_3}$$

$$\cup [b]_{\varphi_3} \cup [d]_{\varphi_3}$$

$$= \{a, b, c, d, e, f, g, h, j\}.$$

Since Q is a subnearness semiring of S and $QS \cap SQ \subseteq N_r(B)^*Q$, Q is quasi-ideal of S .

Lemma 3.1 Let S be a nearness semiring. If S is commutative, then each quasi-ideal of S is two-sided ideal of S .

Proof Let S be a commutative nearness semiring and Q be a quasi-ideal of S . Then $QS \cap SQ \subseteq N_r(B)^*Q$. Moreover, S is commutative and $Q \subseteq S$, then $SQ = QS$, and so $SQ \subseteq N_r(B)^*Q$. Therefore, Q is a left ideal of semiring S . Similarly, Q is right ideal of S . Hence, each quasi-ideal of S is a two-sided ideal of S .

Example 3.2 Let $\mathcal{O} = \{a, b, c, d, e, f, g, h, m\}$ be a set of perceptual objects where for $r = 1$, $B = \{\varphi_1, \varphi_2\} \subseteq \mathcal{F}$ be a set of probe functions. Let $S = \{a, b, c, d\} \subset \mathcal{O}$. Here are some sample probe functions values

$$\varphi_1: \mathcal{O} \rightarrow V_1 = \{\alpha_1, \alpha_2, \alpha_3, \alpha_4\},$$

$$\varphi_2: \mathcal{O} \rightarrow V_2 = \{\alpha_1, \alpha_3, \alpha_4, \alpha_5, \alpha_7\}$$

are presented in Table 6.

Table 6: Features' Table

	a	b	c	d	e	f	g	h	m
φ_1	α_1	α_2	α_2	α_1	α_3	α_4	α_3	α_3	α_4
φ_2	α_3	α_7	α_7	α_1	α_3	α_1	α_4	α_5	α_5

Now, we find the nearness equivalence classes according to the indiscernibility relation \sim_{B_r} of elements in \mathcal{O} :

$$[a]_{\varphi_1} = \{x' \in \mathcal{O} | \varphi_1(x') = \varphi_1(a) = \alpha_1\} = \{a, d\}$$

$$= [d]_{\varphi_1},$$

$$[b]_{\varphi_1} = \{x' \in \mathcal{O} | \varphi_1(x') = \varphi_1(b) = \alpha_2\} = \{b, c\}$$

$$= [c]_{\varphi_1},$$

$$[e]_{\varphi_1} = \{x' \in \mathcal{O} | \varphi_1(x') = \varphi_1(e) = \alpha_3\} = \{e, g, h\}$$

$$= [g]_{\varphi_1} = [h]_{\varphi_1},$$

$$[f]_{\varphi_1} = \{x' \in \mathcal{O} | \varphi_1(x') = \varphi_1(f) = \alpha_5\} = \{f, m\},$$

$$= [m]_{\varphi_1}.$$

Then, we have that $\xi_{\varphi_1} = \{[a]_{\varphi_1}, [b]_{\varphi_1}, [e]_{\varphi_1}, [f]_{\varphi_1}\}$.

$$[a]_{\varphi_2} = \{x' \in \mathcal{O} | \varphi_2(x') = \varphi_2(a) = \alpha_3\} = \{a, e\}$$

$$= [e]_{\varphi_2},$$

$$[b]_{\varphi_2} = \{x' \in \mathcal{O} | \varphi_2(x') = \varphi_2(b) = \alpha_7\} = \{b, c\}$$

$$= [c]_{\varphi_2},$$

$$[d]_{\varphi_2} = \{x' \in \mathcal{O} | \varphi_2(x') = \varphi_2(d) = \alpha_1\} = \{d, f\}$$

$$= [f]_{\varphi_2},$$

$$[g]_{\varphi_2} = \{x' \in \mathcal{O} | \varphi_2(x') = \varphi_2(g) = \alpha_4\} = \{g\},$$

$$[h]_{\varphi_2} = \{x' \in \mathcal{O} | \varphi_2(x') = \varphi_2(h) = \alpha_5\} = \{h, m\}$$

$$= [m]_{\varphi_2}.$$

We attain that

$$\xi_{\varphi_2} = \{[a]_{\varphi_2}, [b]_{\varphi_2}, [d]_{\varphi_2}, [g]_{\varphi_2}, [h]_{\varphi_2}\}.$$

Consequently, we obtain that a set of partitions of \mathcal{O} is

$$N_r(B) = \{\xi_{\varphi_1}, \xi_{\varphi_2}\} \text{ for } r = 1. \text{ Hence,}$$

$$N_1(B)^*S = \cup_{[x]_{\varphi_i} \cap S \neq \emptyset} [x]_{\varphi_i}$$

$$= [a]_{\varphi_1} \cup [b]_{\varphi_1} \cup [a]_{\varphi_2} \cup [b]_{\varphi_2} \cup [d]_{\varphi_2}$$

$$= \{a, b, c, d, e, f\}.$$

Taking operation tables for S in Table 7 and Table 8.

Table 7: “+” operation table for S .

$+$	a	b	c	d
a	a	b	c	d
b	b	c	d	e
c	c	d	e	f
d	d	e	f	a

Table 8: “.” operation table for S .

.	a	b	c	d
a	b	d	f	a
b	d	a	e	b
c	f	e	d	c
d	a	b	c	d

In this case, $(S, +, \cdot)$ is a nearness semiring. Let take $Q = \{b, c, d\}$ is subset of S . Let’s find $N_1(B)^*Q$:

$$\begin{aligned} N_1(B)^*Q &= \cup_{[x]_{\varphi_i} \cap Q \neq \emptyset} [x]_{\varphi_i} \\ &= [a]_{\varphi_1} \cup [b]_{\varphi_1} \cup [b]_{\varphi_2} \cup [d]_{\varphi_2} \\ &= \{a, b, c, d, f\}. \end{aligned}$$

Hence, it can be easily seen that Q is not quasi-ideal of nearness semiring S . Since $e \in QS \cap SQ$, but $e \notin N_r(B)^*Q$.

Proposition 3.1 Let S be a nearness semiring. Each one or two-sided ideal of S is a quasi-ideal of S .

Proof. Assume that Q is left ideal of S . From Definition 3.1. (1), $SQ \subseteq N_r(B)^*Q$. Then, $QS \cap SQ \subseteq SQ \subseteq N_r(B)^*Q$. We get $QS \cap SQ \subseteq N_r(B)^*Q$, and so Q is a quasi-ideal of S . Similarly, we can show that if Q is a right ideal of S , then Q is a quasi-ideal of S . $QS \subseteq N_r(B)^*Q$. Thus, $QS \cap SQ \subseteq QS \subseteq N_r(B)^*Q$. Hence, Q is a quasi-ideal of S .

Theorem 3.1 Let S be a nearness semiring and $\{Q_i | i \in I\}$ be set of quasi-ideals of the nearness semiring S where I is index set. If $N_r(B)^* \left(\bigcap_{i \in I} Q_i \right) = \bigcap_{i \in I} N_r(B)^*Q_i$, then $\bigcap_{i \in I} Q_i = \emptyset$ or $\bigcap_{i \in I} Q_i$ is a quasi-ideal of S .

Proof. Let $\bigcap_{i \in I} Q_i = Q$. Let show that Q is either empty or a quasi-ideal of S . Assume that Q is non-empty. Since Q_i is quasi-ideals of S for $i \in I$. We get that $Q_i S \cap S Q_i \subseteq N_r(B)^*Q_i$ for all $i \in I$.

$$SQ = S \left(\bigcap_{i \in I} Q_i \right) = \bigcap_{i \in I} (S Q_i) \subseteq S Q_i$$

and

$$QS = \left(\bigcap_{i \in I} Q_i \right) S = \bigcap_{i \in I} (Q_i S) \subseteq Q_i S$$

Then, we obtain

$$QS \cap SQ \subseteq Q_i S \cap S Q_i \subseteq N_r(B)^*Q_i, \quad \forall i \in I.$$

Therefore, we have that $QS \cap SQ \subseteq N_r(B)^*Q$. Hence, Q is a quasi-ideal of S .

Lemma 3.2 Let S be a nearness semiring, L be a left

ideal and R be a right ideal of S . If $(N_r(B)^*R) \cap (N_r(B)^*L) \subseteq N_r(B)^*(R \cap L)$, then

- 1) $RL \subseteq N_r(B)^*(L \cap R)$.
- 2) $Q = L \cap R$ is a quasi-ideal of S .

Proof. 1) Let L be left ideal and R be right ideal of S . Since $R \subseteq S$ and L is left ideal of S , $RL \subseteq SL \subseteq N_r(B)^*L$.

Similarly, since $L \subseteq S$ and R is right ideal of S , $RL \subseteq RS \subseteq N_r(B)^*R$. Then, considering these $RL \subseteq (N_r(B)^*R) \cap (N_r(B)^*L)$. Hence, we get $RL \subseteq N_r(B)^*(L \cap R)$ by the hypothesis.

2) Let show that $QS \cap SQ \subseteq N_r(B)^*Q$. Since L is a left ideal and R is a right ideal of S ,

$$SQ = S(L \cap R) = SL \cap SR \subseteq SL \subseteq N_r(B)^*L$$

and

$$QS = (L \cap R)S = LS \cap RS \subseteq RS \subseteq N_r(B)^*R.$$

Thus,

$$QS \cap SQ \subseteq (N_r(B)^*L) \cap (N_r(B)^*R) \subseteq N_r(B)^*(L \cap R) = N_r(B)^*Q$$

by the hypothesis.

Theorem 3.2 Let Q be quasi ideal of nearness semiring S such that $N_r(B)^*(N_r(B)^*Q) = N_r(B)^*Q$. If S is commutative, then Q is an upper-near quasi ideal of S .

Proof. $(N_r(B)^*Q)S \cap S(N_r(B)^*Q) \subseteq (N_r(B)^*Q)(N_r(B)^*S) \cap (N_r(B)^*S)(N_r(B)^*Q)$ by Theorem 2.1.(1). From Theorem 2.2. (2) we get that $(N_r(B)^*Q)S \cap S(N_r(B)^*Q) \subseteq N_r(B)^*(QS) \cap N_r(B)^*(SQ)$. Since $QS \subseteq N_r(B)^*Q$ and $SQ \subseteq N_r(B)^*Q$ by Lemma 3.1, we have $(N_r(B)^*Q)S \cap S(N_r(B)^*Q) \subseteq (N_r(B)^*(N_r(B)^*Q)) \cap (N_r(B)^*(N_r(B)^*Q))$.

Thus, we obtain $(N_r(B)^*Q)S \cap S(N_r(B)^*Q) \subseteq N_r(B)^*Q$ by the hypothesis.

Conflicts of interest

The authors state that did not have a conflict of interests

References

- [1] Pawlak Z., Rough sets, *Int. J. Comput. Inform. Sci.*, 11 (5) (1982) 341–356.
- [2] Peters J. F., Near sets, General theory about nearness of objects, *Appl. Math. Sci.*, 1 (53-56) (2007) 2609–2629.
- [3] Peters J. F., Near sets, Special theory about nearness of objects, *Fund. Inform.*, 75 (1-4) (2007) 407–433.
- [4] Peters J. F., Near sets: An introduction, *Math. Comput. Sci.*, 7 (1) (2013) 3–9.

- [5] İnan E., Öztürk M. A., Near groups on nearness approximation spaces, *Hacet. J. Math. Stat.*, 41 (4) (2012) 545-558.
- [6] İnan E., Öztürk M. A., Erratum and notes for near groups on nearness approximation spaces, *Hacet. J. Math. Stat.*, 43 (2) (2014) 279-281.
- [7] İnan E., Öztürk M. A., Nearness rings, *Ann. Fuzzy Math. Inform.*, 17(2) (2019) 115-132.
- [8] Öztürk M. A., Bekmezci İ. H., Gamma nearness semirings, *Southeast Asian Bull. Math.*, 44(4) (2020) 567-586.
- [9] Öztürk M. A., Jun Y. B., İz A., Gamma semigroups on weak nearness approximation spaces, *J. Int. Math. Virtual Inst.*, 9(1) (2019) 53-72.
- [10] Öztürk M. A., Prime ideals of gamma semigroups on weak nearness approximation spaces, *Asian-Eur. J. Math.*, 12 (2019).
- [11] Öztürk M. A., Bekmezci İ. H., Gamma nearness semirings, *Southeast Asian Bull. Math.*, 44(4) (2020) 567-586.
- [12] Öztürk, M. A., and Temur, İ., Prime ideals of nearness semirings, *Commun. Fac. Sci. Univ. Ank. Ser. A1 Math. Stat.*, 68(2) (2019) 1867-1878.
- [13] Öztürk M. A., Semiring on weak nearness approximation spaces, *Ann. Fuzzy Math. Inform.*, 15(3) (2018) 227-241.
- [14] Vandier H. S., Note on a simple type of algebra in which cancellation law of addition does not hold, *Bull. Am. Math. Soc.*, 40(12) (1934) 914-920.
- [15] Shabir A. M, Ali A., Batol S., A note on quasi ideal in semirings, *Southeast Asian Bull. Math.*, 27 (5) (2004) 923-928.
- [16] Steinfeld, O, Quasi-Ideals in Rings and Semigroups, Akad'emiai Kiad'o, Budapest (1978).
- [17] Iseki K., Quasi-ideals in semirings without zero, *Proc. Japan Acad.*, 34 (1958) 79-81.
- [18] Rao M. M. K., A study of quasi-interior ideals of semirings, *Bull. Int. Math. Virtual Inst.*, 9(1) (2019) 287-300.
- [19] Rao M. M. K., Bi-quasi ideals and fuzzy bi-quasi ideals of Γ -semirings, *Bull. Int. Math. Virtual Inst.*, 8(1) (2018) 45-53.
- [20] El-Madhoun N. R., Quasi ideals and bi-ideals on semigroups and semirings, MSc Thesis, The Islamic University of Gaza, Faculty of Science, 2007.
- [21] Golan J. S., Semirings and Their Applications, Kluwer Academic Publishers, 1999.



Algebra of frontier points via semi-kernels

Jiarul HOQUE ¹, Shyamapada MODAK ^{1,*}

¹University of Gour Banga, Department of Mathematics, Malda/INDIA

Abstract

In topological spaces, the study of interior and closure of a set are renowned concepts where the interior is defined as the union of open sets and the closure is defined as the intersection of closed sets. In literature, it is also a significant study while a set is defined as the intersection of open sets, and the union of closed sets. These respective ideas are known as the kernel of a set and its complementary function. Utilizing these ideas, some authors have introduced various kinds of results in topological spaces. Some mathematicians have extended these concepts via Levine's semi-open sets to semi-kernel and its complementary function. The study of these notions is also a remarkable part of the field of topological spaces as the collection of semi-open sets does not form a topology again. In this paper, we have taken the semi-kernel and its complementary function into account to introduce new types of frontier points. After that we have studied and presented several characterizations of these new types of frontiers and established relationships among them. Finally, we have shown that semi-homeomorphic images of these new types of frontiers are invariant.

Article info

History:

Received: 22.08.2020

Accepted: 31.05.2021

Keywords:

Frontier point,
Semi-homeomorphism,

\wedge_s -set,

\vee_s -set.

1. Introduction

The semi-open set in a topological space was first introduced by Levine [1] and its notion has opened a new branch in the research field by the name of generalized open set. A good number of mathematicians have studied this set extensively [2-11]. The study of \wedge -sets and \vee -sets in topological spaces was introduced by Maki [12]. These two types of sets are not defined in the traditional way using interior (denoted as 'Int') and closure (denoted as 'Cl') operators in topological spaces. Though the set \wedge is not an open set and the set \vee is not a closed set, they are dual to each other. These two sets have been utilized in the study of separation axioms (see [7,10]). Dontchev and Maki [13], and Maheshwari and Prasad [14] imposed these notions in the field of semi-open sets by the name of \wedge_s -set and \vee_s -set. These sets help us to study generalized separation axioms in detail (see [3,4,8,9,11,13,15]).

In this paper, our main work is to study some new types of boundaries or frontiers with the help of \wedge_s -sets and \vee_s -sets that are not conventional type frontiers (see [16-22]) because they are not defined in terms of 'Int' and 'Cl' operators. Throughout this paper, the

notations \mathcal{T} and \mathcal{S} are used to denote the topological spaces (X, τ) and (Y, σ) respectively. In a topological space \mathcal{T} , the family of all closed (resp. semi-open) sets is identified by the notations $C(\mathcal{T})$ (resp. $SO(\mathcal{T})$).

In a topological space \mathcal{T} , a subset P of X is a \wedge_s (resp. \vee_s)-set [23] if $P = P^{\wedge_s}$ (resp. P^{\vee_s}), where $P^{\wedge_s} = \bigcap \{N : N \supseteq P, N \in SO(\mathcal{T})\}$ and $P^{\vee_s} = \bigcup \{M : M \subseteq P, X \setminus M \in SO(\mathcal{T})\}$. In [13,14], P^{\wedge_s} is called the semi-kernel of P .

The aim of this paper is to solve the question: What happens if the frontier points are defined by semi-open sets related to the operators $()^{\wedge_s}$ and $()^{\vee_s}$?

2. Frontier Points Via Semi-kernels

We begin this section with the following example:

*Corresponding author. e-mail address: spmadak2000@yahoo.co.in
<http://dergipark.gov.tr/csj> ©2021 Faculty of Science, Sivas Cumhuriyet University

Example 2.1. Let $X = \{p, q, r\}$ and $\tau = \{\emptyset, \{p\}, \{q, r\}, X\}$. Then $C(\mathcal{T}) = \{\emptyset, \{p\}, \{q, r\}, X\}$. For $\{p\}$, $\{p\} \subseteq Cl(Int(\{p\}))$; for $\{q\}$, $\{q\} \not\subseteq Cl(Int(\{q\}))$; for $\{r\}$, $\{r\} \not\subseteq Cl(Int(\{r\}))$; for $\{p, q\}$, $\{p, q\} \not\subseteq Cl(Int(\{p, q\}))$; for $\{p, r\}$, $\{p, r\} \not\subseteq Cl(Int(\{p, r\}))$; for $\{q, r\}$, $\{q, r\} \subseteq Cl(Int(\{q, r\}))$ and for X , $X \subseteq Cl(Int(X))$. Thus $SO(\mathcal{T}) = \{\emptyset, \{p\}, \{q, r\}, X\}$. Consider $P = \{q\}$. Then $P^{\wedge_s} = \{q, r\}$ and $(X \setminus P)^{\wedge_s} = X$. Therefore $P^{\wedge_s} \cap (X \setminus P)^{\wedge_s} \neq \emptyset$.

In this regards, we define:

Definition 2.2. Let \mathcal{T} be a topological space. Define the frontier operator $Bd^{\wedge_s} : \wp(X) \rightarrow \wp(X)$ by $Bd^{\wedge_s}(P) = P^{\wedge_s} \cap (X \setminus P)^{\wedge_s}$, $P \in \wp(X)$, where $\wp(X)$ is the power set of X .

Theorem 2.3. Let P and Q be two subsets of a topological space \mathcal{T} . Then

1. $Bd^{\wedge_s}(\emptyset) = \emptyset = Bd^{\wedge_s}(X)$;
2. $Bd^{\wedge_s}(P) = Bd^{\wedge_s}(X \setminus P)$;
3. $Bd^{\wedge_s}(P) = P^{\wedge_s} \setminus P^{\vee_s}$;
4. for $P \in SO(\mathcal{T})$, $Bd^{\wedge_s}(P) = P \setminus P^{\vee_s}$;
5. for semi-closed and semi-open set P , $Bd^{\wedge_s}(P) = \emptyset$;
6. for $P \in \tau$, $Bd^{\wedge_s}(P) = P \setminus P^{\vee_s}$;
7. for \wedge_s -set P , $Bd^{\wedge_s}(P) = P \setminus P^{\vee_s}$;
8. for \vee_s -set P , $Bd^{\wedge_s}(P) = P^{\wedge_s} \setminus P$;
9. $Bd^{\wedge_s}(Bd^{\wedge_s}(P)) \neq Bd^{\wedge_s}(P)$;
10. $Bd^{\wedge_s}(P \cup Q) \subseteq Bd^{\wedge_s}(P) \cup Bd^{\wedge_s}(Q)$.

Proof. 1. Follows from the fact that $\emptyset^{\wedge_s} = \emptyset$.

3. $Bd^{\wedge_s}(P) = P^{\wedge_s} \cap (X \setminus P)^{\wedge_s} = P^{\wedge_s} \cap (X \setminus P^{\vee_s})$ ([23]) $= P^{\wedge_s} \setminus P^{\vee_s}$.

4. $Bd^{\wedge_s}(P) = P^{\wedge_s} \cap (X \setminus P)^{\wedge_s} = P \cap (X \setminus P^{\vee_s}) = P \setminus P^{\vee_s}$.

5. Follows from the fact that for semi-open and semi-closed set P , $P^{\vee_s} = P^{\wedge_s} = P$.

6. Follows from $\tau \subseteq SO(\mathcal{T})$.

7, 8. Follows from Definitions of \wedge_s -set and \vee_s -set.

9. It will be followed by the Example 2.4.

10. $Bd^{\wedge_s}(P \cup Q) = (P \cup Q)^{\wedge_s} \cap [X \setminus (P \cup Q)]^{\wedge_s} = (P \cup Q)^{\wedge_s} \cap [(X \setminus P) \cap (X \setminus Q)]^{\wedge_s} \subseteq (P \cup Q)^{\wedge_s} \cap [(X \setminus P)^{\wedge_s} \cap (X \setminus Q)^{\wedge_s}] = (P^{\wedge_s} \cup Q^{\wedge_s}) \cap [(X \setminus P)^{\wedge_s} \cap (X \setminus Q)^{\wedge_s}] = [((X \setminus P)^{\wedge_s} \cap (X \setminus Q)^{\wedge_s}) \cap P^{\wedge_s}] \cup [((X \setminus P)^{\wedge_s} \cap (X \setminus Q)^{\wedge_s}) \cap Q^{\wedge_s}] \subseteq [(X \setminus P)^{\wedge_s} \cap P^{\wedge_s}] \cup [(X \setminus Q)^{\wedge_s} \cap Q^{\wedge_s}] = Bd^{\wedge_s}(P) \cup Bd^{\wedge_s}(Q)$.

Example 2.4. Let $X = \{p, q, r\}$ and $\tau = \{\emptyset, \{p\}, \{q, r\}, X\}$. Then $SO(\mathcal{T}) = \{\emptyset, \{p\}, \{q, r\}, X\}$. Consider $P = \{q\}$. Then $Bd^{\wedge_s}(P) = \{q, r\}$ and $Bd^{\wedge_s}(Bd^{\wedge_s}(P)) = \emptyset$. Thus $Bd^{\wedge_s}(Bd^{\wedge_s}(P)) \neq Bd^{\wedge_s}(P)$.

Note that $Bd^{\wedge_s}(P)$ is not a semi-open set, in general.

For the converse of the relation (5) of Theorem 2.3, we have the following result:

Theorem 2.5. Let P be a subset of a topological space \mathcal{T} . Then for $Bd^{\wedge_s}(P) = \emptyset$, $P^{\wedge_s} = P = P^{\vee_s}$.

Proof. Given that $P^{\wedge s} \cap (X \setminus P)^{\wedge s} = \emptyset$. Then $P^{\wedge s} \subseteq X \setminus (X \setminus P)^{\wedge s}$. This implies that $P^{\wedge s} \subseteq P^{\vee s}$ and hence $P \subseteq P^{\wedge s} \subseteq P^{\vee s} \subseteq P$ [23].

Lemma 2.6. Let P and Q be two subsets of a topological space \mathcal{T} . Then

$$Bd^{\wedge s}(P) \cup Bd^{\wedge s}(Q) = Bd^{\wedge s}(P \setminus Q) \cup Bd^{\wedge s}(Q \setminus P) \cup Bd^{\wedge s}(P \cap Q).$$

Proof. For the proof of this theorem, we consider following relations:

- $Bd^{\wedge s}(P \cap Q) = Bd^{\wedge s}[X \setminus (P \cap Q)] = Bd^{\wedge s}[(X \setminus P) \cup (X \setminus Q)] \subseteq Bd^{\wedge s}(X \setminus P) \cup Bd^{\wedge s}(X \setminus Q) = Bd^{\wedge s}(P) \cup Bd^{\wedge s}(Q)$.
- $Bd^{\wedge s}(P \setminus Q) = Bd^{\wedge s}[P \cap (X \setminus Q)] \subseteq Bd^{\wedge s}(P) \cup Bd^{\wedge s}(X \setminus Q) = Bd^{\wedge s}(P) \cup Bd^{\wedge s}(Q)$.
- $Bd^{\wedge s}(Q \setminus P) = Bd^{\wedge s}[Q \cap (X \setminus P)] \subseteq Bd^{\wedge s}(Q) \cup Bd^{\wedge s}(X \setminus P) = Bd^{\wedge s}(Q) \cup Bd^{\wedge s}(P)$.

Therefore from the above three relations, we have

$$Bd^{\wedge s}(P \cap Q) \cup Bd^{\wedge s}(P \setminus Q) \cup Bd^{\wedge s}(Q \setminus P) \subseteq Bd^{\wedge s}(P) \cup Bd^{\wedge s}(Q).$$

On the other hand, $Bd^{\wedge s}(P) \cup Bd^{\wedge s}(Q) = Bd^{\wedge s}[(P \setminus Q) \cup (P \cap Q)] \cup Bd^{\wedge s}[(Q \setminus P) \cup (P \cap Q)] \subseteq Bd^{\wedge s}(P \setminus Q) \cup Bd^{\wedge s}(P \cap Q) \cup Bd^{\wedge s}(Q \setminus P)$.

Hence $Bd^{\wedge s}(P) \cup Bd^{\wedge s}(Q) = Bd^{\wedge s}(P \setminus Q) \cup Bd^{\wedge s}(Q \setminus P) \cup Bd^{\wedge s}(P \cap Q)$.

Theorem 2.7. Let P and Q be two subsets of a topological space \mathcal{T} . Then following properties hold:

1. $Bd^{\wedge s}(P) \cup Bd^{\wedge s}(Q) = Bd^{\wedge s}(P \cap Q) \cup Bd^{\wedge s}(P \setminus Q) \cup Bd^{\wedge s}(P \cup Q)$;
2. $Bd^{\wedge s}(P) \cup Bd^{\wedge s}(Q) = Bd^{\wedge s}(P \cup Q) \cup Bd^{\wedge s}(Q \setminus P) \cup Bd^{\wedge s}(P \cap Q)$;
3. $Bd^{\wedge s}(P) \cup Bd^{\wedge s}(Q) = Bd^{\wedge s}(P \setminus Q) \cup Bd^{\wedge s}(Q \setminus P) \cup Bd^{\wedge s}(P \cup Q)$;
4. $Bd^{\wedge s}(P) \cup Bd^{\wedge s}(P \Delta Q) = Bd^{\wedge s}(P \setminus Q) \cup Bd^{\wedge s}(P \cap Q) \cup Bd^{\wedge s}(Q \setminus P)$;
5. $Bd^{\wedge s}(Q) \cup Bd^{\wedge s}(P \Delta Q) = Bd^{\wedge s}(P \setminus Q) \cup Bd^{\wedge s}(P \cap Q) \cup Bd^{\wedge s}(Q \setminus P)$,

where Δ stands for symmetric difference.

Proof. 1. Putting $X \setminus Q$ in place of Q in Lemma 2.6, we have $Bd^{\wedge s}(P) \cup Bd^{\wedge s}(X \setminus Q) = Bd^{\wedge s}[P \setminus (X \setminus Q)] \cup Bd^{\wedge s}[(X \setminus Q) \setminus P] \cup Bd^{\wedge s}[P \cap (X \setminus Q)]$. This implies that $Bd^{\wedge s}(P) \cup Bd^{\wedge s}(Q) = Bd^{\wedge s}(P \cap Q) \cup Bd^{\wedge s}[X \setminus (P \cup Q)] \cup Bd^{\wedge s}(P \setminus Q) = Bd^{\wedge s}(P \cap Q) \cup Bd^{\wedge s}(P \cup Q) \cup Bd^{\wedge s}(P \setminus Q)$.

2. Putting $X \setminus P$ in place of P in Lemma 2.6, we have $Bd^{\wedge s}(X \setminus P) \cup Bd^{\wedge s}(Q) = Bd^{\wedge s}[(X \setminus P) \setminus Q] \cup Bd^{\wedge s}[Q \setminus (X \setminus P)] \cup Bd^{\wedge s}[(X \setminus P) \cap Q]$. This implies that $Bd^{\wedge s}(P) \cup Bd^{\wedge s}(Q) = Bd^{\wedge s}[X \setminus (P \cup Q)] \cup Bd^{\wedge s}(P \cap Q) \cup Bd^{\wedge s}(Q \setminus P) = Bd^{\wedge s}(P \cup Q) \cup Bd^{\wedge s}(P \cap Q) \cup Bd^{\wedge s}(Q \setminus P)$.

3. Putting $X \setminus P$ in place of P and $X \setminus Q$ in place of Q in Lemma 2.6, we have $Bd^{\wedge s}(X \setminus P) \cup Bd^{\wedge s}(X \setminus Q) = Bd^{\wedge s}[(X \setminus P) \setminus (X \setminus Q)] \cup Bd^{\wedge s}[(X \setminus Q) \setminus (X \setminus P)] \cup Bd^{\wedge s}[(X \setminus P) \cap (X \setminus Q)]$. This implies that $Bd^{\wedge s}(P) \cup Bd^{\wedge s}(Q) = Bd^{\wedge s}(Q \setminus P) \cup Bd^{\wedge s}(P \setminus Q) \cup Bd^{\wedge s}[X \setminus (P \cup Q)] = Bd^{\wedge s}(Q \setminus P) \cup Bd^{\wedge s}(P \setminus Q) \cup Bd^{\wedge s}(P \cup Q)$.

4. From Lemma 2.6, we have $Bd^{\wedge s}(P) \cup Bd^{\wedge s}(P \Delta Q) = Bd^{\wedge s}[P \setminus (P \Delta Q)] \cup Bd^{\wedge s}[P \cap (P \Delta Q)] \cup Bd^{\wedge s}[(P \Delta Q) \setminus P] = Bd^{\wedge s}(P \cap Q) \cup Bd^{\wedge s}(P \setminus Q) \cup Bd^{\wedge s}(Q \setminus P)$.

5. Similar to (4).

It is noticeable that for a subset P of a topological space \mathcal{T} , $P^{\vee_s} \cap (X \setminus P)^{\vee_s} = \emptyset$. But their union is neither empty nor the whole space, in general.

Example 2.8. Let $X = \{p, q, r\}$ and $\tau = \{\emptyset, \{p\}, \{p, q\}, X\}$. Then closed sets are $\emptyset, \{r\}, \{q, r\}$ and X . Now for $\{p\}$, $\{p\} \subseteq Cl(Int(\{p\}))$; for $\{q\}$, $\{q\} \not\subseteq Cl(Int(\{q\}))$; for $\{r\}$, $\{r\} \not\subseteq Cl(Int(\{r\}))$; for $\{p, q\}$, $\{p, q\} \subseteq Cl(Int(\{p, q\}))$; for $\{p, r\}$, $\{p, r\} \subseteq Cl(Int(\{p, r\}))$; for $\{q, r\}$, $\{q, r\} \not\subseteq Cl(Int(\{q, r\}))$. Therefore $SO(\mathcal{T}) = \{\emptyset, \{p\}, \{p, q\}, \{p, r\}, X\}$ and the semi-closed sets are $\emptyset, \{q\}, \{r\}, \{q, r\}$ and X . Let $P = \{p, q\}$. Then $P^{\vee_s} = \{q\}$ and $(X \setminus P)^{\vee_s} = \{r\}$. Therefore $P^{\vee_s} \cup (X \setminus P)^{\vee_s} \neq X, \emptyset$.

In view of the Example 2.8, we define a new frontier operator as:

Definition 2.9. Let \mathcal{T} be a topological space. Define the frontier operator $Bd^{\vee_s} : \wp(X) \rightarrow \wp(X)$ by $Bd^{\vee_s}(P) = P^{\vee_s} \cup (X \setminus P)^{\vee_s}$, $P \in \wp(X)$.

Theorem 2.10. Let P be a subset of a topological space \mathcal{T} . Then following results hold:

1. $Bd^{\vee_s}(\emptyset) = Bd^{\vee_s}(X) = X$;
2. $Bd^{\vee_s}(P) = Bd^{\vee_s}(X \setminus P)$;
3. $Bd^{\vee_s}(P) = P^{\vee_s} \cup (X \setminus P^{\wedge_s})$;
4. for $P \in SO(\mathcal{T})$, $Bd^{\vee_s}(P) = P^{\vee_s} \cap (X \setminus P)$;
5. for semi-closed set P , $Bd^{\vee_s}(P) = P \cup (X \setminus P^{\wedge_s})$;
6. for \wedge_s -set P , $Bd^{\vee_s}(P) = P^{\vee_s} \cup (X \setminus P)$;
7. for \vee_s -set P , $Bd^{\vee_s}(P) = P \cup (X \setminus P^{\wedge_s})$;
8. for semi-closed and semi-open set P , $Bd^{\vee_s}(P) = X$;
9. $X \setminus Bd^{\vee_s}(P) = Bd^{\wedge_s}(P)$.

Proof. 1, 2. Obvious from Definition.

3. Obvious from the fact $(X \setminus P)^{\wedge_s} = X \setminus P^{\vee_s}$.

4. $Bd^{\vee_s}(P) = P^{\vee_s} \cup (X \setminus P)^{\vee_s} = P^{\vee_s} \cup (X \setminus P)$, since $X \setminus P$ is semi-closed.

5. $Bd^{\vee_s}(P) = P^{\vee_s} \cup (X \setminus P)^{\vee_s} = P \cup (X \setminus P^{\wedge_s})$, since $P = P^{\vee_s}$ [23].

7. $Bd^{\wedge_s}(P) = P^{\vee_s} \cup (X \setminus P)^{\vee_s} = P \cup (X \setminus P^{\wedge_s})$.

9. $X \setminus Bd^{\vee_s}(P) = X \setminus [P^{\vee_s} \cup (X \setminus P)^{\vee_s}] = (X \setminus P^{\vee_s}) \cap [X \setminus (X \setminus P)^{\vee_s}] = P^{\wedge_s} \setminus P^{\vee_s} = Bd^{\wedge_s}(P)$.

Example 2.11. Let $X = \{p, q, r\}$ and $\tau = \{\emptyset, \{p\}, \{q, r\}, X\}$. Then the semi-closed sets are $\emptyset, \{p\}, \{q, r\}$ and X . Consider $P = \{p, q\}$. Then $Bd^{\vee_s}(P) = \{p\}$ and $Bd^{\vee_s}(Bd^{\vee_s}(P)) = X$. Thus $Bd^{\vee_s}(Bd^{\vee_s}(P)) \neq Bd^{\vee_s}(P)$.

Note that $Bd^{\vee_s}(P)$ is not a semi-closed set, in general.

Definition 2.12. Let \mathcal{T} be a topological space. We define the frontier operator $Bd_{\vee_s} : \wp(X) \rightarrow \wp(X)$ by $Bd_{\vee_s}(P) = P \setminus P^{\vee_s}$, $P \in \wp(X)$.

Theorem 2.13. Let P be a subset of a topological space \mathcal{T} . Then

1. $P = P^{\vee_s} \cup Bd_{\vee_s}(P)$;
2. $P^{\vee_s} \cap Bd_{\vee_s}(P) = \emptyset$;
3. for $Bd_{\vee_s}(P) = \emptyset$, $P = P^{\vee_s}$;

4. for a semi-closed set P , $Bd_{\vee_s}(P) = \emptyset$.

Proof. 1, 2. Obvious from Definition.

3. Follows from 1.

4. For semi-closed set P , $P = P^{\vee_s}$ and hence $Bd_{\vee_s}(P) = P \setminus P^{\vee_s} = \emptyset$.

Theorem 2.14. Let P be a subset of a topological space \mathcal{T} . Then $Bd_{\vee_s}(P) = \emptyset$ if and only if P is a \vee_s -set.

Proof. Suppose $Bd_{\vee_s}(P) = \emptyset$. Then $P \setminus P^{\vee_s} = \emptyset$ implies $P \subseteq P^{\vee_s}$. Furthermore, $P^{\vee_s} \subseteq P$.

Conversely, suppose that P is a \vee_s -set. Then $P = P^{\vee_s}$ and hence $Bd_{\vee_s}(P) = \emptyset$.

Definition 2.15. Let \mathcal{T} be a topological space. We define the frontier operator $Bd_{\wedge_s} : \wp(X) \rightarrow \wp(X)$ by $Bd_{\wedge_s}(P) = P^{\wedge_s} \setminus P$, $P \in \wp(X)$.

Theorem 2.16. Let P be a subset of a topological space \mathcal{T} . Then

1. $P \cup Bd_{\wedge_s}(P) = P^{\wedge_s}$;
2. $P \cap Bd_{\wedge_s}(P) = \emptyset$;
3. $Bd_{\wedge_s}(P) = \emptyset$ if and only if $P = P^{\wedge_s}$;
4. for semi-open set P , $Bd_{\wedge_s}(P) = \emptyset$.

Proof. 1, 2. Obvious from Definition.

3. Assume $Bd_{\wedge_s}(P) = \emptyset$. Then $P^{\wedge_s} \subseteq P$, and from Definition of $(\)^{\wedge_s}$, $P \subseteq P^{\wedge_s}$. Thus $P^{\wedge_s} = P$.

Converse is trivial.

4. Since P is semi-open, so $P^{\wedge_s} = P$. Hence the result.

Theorem 2.17. Let P be a subset of a topological space \mathcal{T} . Then $Bd_{\wedge_s}(P) = \emptyset$ if and only if P is a \wedge_s -set.

Theorem 2.18. Let P be a subset of a topological space \mathcal{T} . Then

1. $Bd_{\vee_s}(P) \cap Bd_{\wedge_s}(P) = \emptyset$;
2. $Bd_{\wedge_s}(P) \cup Bd_{\vee_s}(P) = Bd^{\wedge_s}(P)$;
3. $Bd_{\wedge_s}(P) = Bd^{\wedge_s}(P) \setminus Bd_{\vee_s}(P)$;
4. $Bd_{\vee_s}(P) = Bd^{\wedge_s}(P) \setminus Bd_{\wedge_s}(P)$.

Proof. 1. $Bd_{\vee_s}(P) \cap Bd_{\wedge_s}(P) = (P \setminus P^{\vee_s}) \cap (P^{\wedge_s} \setminus P) = \emptyset$.

2. $Bd_{\wedge_s}(P) \cup Bd_{\vee_s}(P) = (P^{\wedge_s} \setminus P) \cup (P \setminus P^{\vee_s}) = P^{\wedge_s} \setminus P^{\vee_s} = Bd^{\wedge_s}(P)$.

3, 4. Follows from (1) and (2) because $\{Bd_{\vee_s}(P), Bd_{\wedge_s}(P)\}$ is a partition of $Bd^{\wedge_s}(P)$.

We conclude this paper with the following definition and result.

Definition 2.19. [24] Let \mathcal{T} and \mathcal{S} be two topological spaces. A mapping $f : \mathcal{T} \rightarrow \mathcal{S}$ is called semi-homeomorphism if f is a bijection and images and pre-images of semi-open sets are semi-open.

Theorem 2.20. Let \mathcal{T} and \mathcal{S} be two topological spaces and $f : \mathcal{T} \rightarrow \mathcal{S}$ be a semi-homeomorphism. Then for a subset P of X ,

1. $f(P^{\wedge_s}) = [f(P)]^{\wedge_s}$;
2. $f(P^{\vee_s}) = [f(P)]^{\vee_s}$.

Proof. We give the proof of (1) only. We shall first show that $f(P^{\wedge_s}) \subseteq [f(P)]^{\wedge_s}$.

If not, there exists $y \in f(P^{\wedge_s})$ but $y \notin [f(P)]^{\wedge_s}$. This implies that $y \notin \cap\{V \in SO(\mathcal{S}) : f(P) \subseteq V\}$. Then there exists $U \in SO(\mathcal{S})$ such that $f(P) \subseteq U$ but $y \notin U$. Therefore $f^{-1}(U) \in SO(\mathcal{T})$, $P = f^{-1}(f(P)) \subseteq f^{-1}(U)$ and $f^{-1}(y) \notin f^{-1}(U)$ (because if $f^{-1}(y) \in f^{-1}(U)$, then $f(f^{-1}(U)) = U$ implies $y \in U$, a contradiction). Thus $f^{-1}(y) \notin P^{\wedge_s}$ and hence $y \notin f(P^{\wedge_s})$, a contradiction. Therefore $f(P^{\wedge_s}) \subseteq [f(P)]^{\wedge_s}$.

We shall now show that $[f(P)]^{\wedge_s} \subseteq f(P^{\wedge_s})$.

If not, there exists $y \in [f(P)]^{\wedge_s}$ but $y \notin f(P^{\wedge_s})$. Then $f^{-1}(y) \notin P^{\wedge_s} = \cap\{V \in SO(\mathcal{T}) : P \subseteq V\}$. This implies that there exists $U \in SO(\mathcal{T})$ such that $P \subseteq U$ but $f^{-1}(y) \notin U$. Thus $f(P) \subseteq f(U)$ but $y \notin f(U)$. Moreover, $f(U) \in SO(\mathcal{S})$. So $y \notin [f(P)]^{\wedge_s}$, a contradiction. Thus $[f(P)]^{\wedge_s} \subseteq f(P^{\wedge_s})$. Hence the result follows.

Conclusions

The mathematical findings are:

- The frontier operator $Bd^{\wedge_s} : \wp(X) \rightarrow \wp(X)$ is \emptyset -preserving and sub-additive but not X -preserving and not idempotent.
- The frontier operator $Bd^{\vee_s} : \wp(X) \rightarrow \wp(X)$ is X -preserving but not \emptyset -preserving and not idempotent.
- For any set $P \subseteq X$, its images under the frontier operators Bd_{\wedge_s} , $Bd_{\vee_s} : \wp(X) \rightarrow \wp(X)$ are disjoint. Moreover, $\{Bd_{\wedge_s}(P), Bd_{\vee_s}(P)\}$ forms a partition of $Bd^{\wedge_s}(P)$.
- Semi-homeomorphic image of \wedge_s (resp. \vee_s)-set is again \wedge_s (resp. \vee_s)-set.
- For a semi-homeomorphism $f : \mathcal{T} \rightarrow \mathcal{S}$, $f[Bd^{\wedge_s}(P)] = Bd^{\wedge_s}[f(P)]$; $f[Bd^{\vee_s}(P)] = Bd^{\vee_s}[f(P)]$; $f[Bd_{\wedge_s}(P)] = Bd_{\wedge_s}[f(P)]$ and $f[Bd_{\vee_s}(P)] = Bd_{\vee_s}[f(P)]$.

Acknowledgment

The first author is thankful to University Grants Commission (UGC), New Delhi-110002, India for granting UGC-NET Junior Research Fellowship (1173/(CSIR-UGC NET DEC. 2017)) during the tenure of which this work was done.

The authors are thankful to the referees for their valuable comments and suggestions for improving the paper.

Conflicts of interest

The authors state that they did not have a conflict of interests.

References

- [1] Levine N., Semi-open sets and semi-continuity in topological spaces, *Amer. Math. Monthly*, 70 (1963) 36-41.
- [2] Ahmad B., Khan M., Noiri T., A note on semi-frontier, *Indian J. Pure Appl. Math.*, 22 (1) (1991) 61-62.
- [3] Caldas M., Semi- $T_{\frac{1}{2}}$ -spaces, *Pro. Math.*, 8 (1994) 115-121.
- [4] Caldas M., A separation axiom between semi- T_0 and semi- T_1 , *Mem. Fac. Sci. Kochi Univ. (Math.)*, 18 (1997) 37-42.
- [5] Crossley S.G., Hildebrand S.K., Semi-closure, *Texas J. Sci.*, 22 (1971) 99-112.
- [6] Das P., Note on some applications of semi-open sets, *Progr. Math.*, 7 (1973) 33-44.
- [7] Davis A.S., Indexed systems of neighbourhoods for general topological spaces, *Amer. Math. Monthly*, 68 (1961) 886-894.
- [8] Maio G.D., On semi topological operators and semi separation axioms, *Rend. Circ. Mat. Palermo (2) Suppl. Second Topology Conference (4 Taormina 1984)*, 12 (1986) 219-230.
- [9] Jankovic D.D., Reilly I.L., On semi separation properties, *Indian J. Pure Appl. Math.*, 16 (9) (1985) 957-964.

- [10] Maheshwari S.N., Prasad R., Some new separation axioms, *Ann. Soc. Sci. Bruxelles*, 89 (1975) 395-402.
- [11] Sundaram P., Maki H., Balachandran K., Semi-generalized continuous maps and semi- $T_{\frac{1}{2}}$ spaces, *Bull. Fukuoka Univ. Ed. Part III*, 40 (1991) 33-40.
- [12] Maki H., Generalized \wedge -sets and the associated closure operator, *The Special Issue in Commemoration of Prof. Kazusada Ikeda's Retirement*, (1986) 139-146.
- [13] Dontchev J., Maki H., On sg-closed sets and semi- λ -closed sets, *Questions Answers Gen. Topology*, 15 (2) (1997) 259-266.
- [14] Maheshwari S.N., Prasad R., On R_{0_s} -spaces, *Port. Math.*, 34 (1975) 213-217.
- [15] Bhattacharya P., Lahiri B.K., Semi-generalized closed set in topology, *Indian J. Math.*, 29 (1987) 375-382.
- [16] Gabai H., The exterior operator and boundary operator, *Amer. Math. Monthly*, 71 (9) (1964) 1029-1031.
- [17] Khodabocus M.I., Sookia N.U.H., Theory of generalized exterior and generalized frontier operators in generalized topological spaces: Definitions, Essential Properties and, Consistent, Independent Axioms, *Research Series in Pure Mathematics Topology. Exterior and Frontier Operators, Series.*, 7 (2018-2019) 1-59.
- [18] Kleiner I.Z., Closure and boundary operators in topological spaces, *Ukr. Math. J.*, 29 (1977) 295-296.
- [19] Modak S., Some points on generalized open sets, *Casp. J. Math. Sci.*, 6 (2) (2017) 99-106.
- [20] Modak S., Hoque J., Sk Selim., Homeomorphic image of some kernels, *Cankaya Uni. J. Sci. Eng.*, 17 (1) (2020) 052-062.
- [21] Nour T.M., A note on some applications of semi-open sets, *Int. J. Math. & Math. Sci.*, 21 (1998) 205-207.
- [22] Sk Selim., Modak S., Islam Md.M., Characterizations of Hayashi-Samuel spaces via boundary points, *Commun. Adv. Math. Sci.*, II (3) (2019) 219-226.
- [23] Cueva M.C., Dontchev J., $G.\wedge_s$ -sets and $G.\vee_s$ -sets, *arXiv:math/9810080v1*, (1998).
- [24] Sabah A., Khan M., Kočinac L. D. R., Covering properties defined by semi-open sets, *J. Nonlinear Sci. Appl.*, 9 (2016) 4388-4398.



The relations between bi-periodic jacobsthal and bi-periodic jacobsthal lucas sequence

Şükran UYGUN^{1,*}

¹Gaziantep University, Faculty of Science And Arts, Department of Mathematics, Gaziantep / TURKEY

Abstract

In this paper, one of the special integer sequences, Jacobsthal and Jacobsthal Lucas sequences which are encountered in computer science is generalized according to parity of the index of the entries of the sequences, called bi-periodic Jacobsthal and Jacobsthal Lucas sequences. The definitions of the bi-periodic Jacobsthal and Jacobsthal Lucas sequences are given by using classic Jacobsthal and Jacobsthal Lucas sequences. In literature, there were some relations for the bi-periodic Jacobsthal and Jacobsthal Lucas sequences. We find new identities for these sequences. If we substitute $a = b = 1$ in the results, we get identities for classic Jacobsthal and Jacobsthal Lucas sequences.

Article info

History:
Received: 16.07.2020
Accepted: 02.06.2021

Keywords:
Bi-periodic Jacobsthal sequence,
Generalized Jacobsthal Lucas sequence,
Binet formula.

1. Introduction

The classical Jacobsthal sequence is defined as $j_n = j_{n-1} + 2j_{n-2}$ with initial conditions $j_0 = 0, j_1 = 1$ and the Jacobsthal Lucas sequence is defined as with the initial conditions $c_0 = 2, c_1 = 1$ [1]. There are many generalizations on special integer sequences. With this in mind, we proceed with the introduction as follows. In the year 2009, a paper entitled, the generalized Fibonacci sequence has been published by Edson and Yayenie [2,3]. Jun, Choi gave some properties of the bi-periodic Fibonacci sequence by using a special matrix in [4]. Bilgici [5] introduced the bi-periodic Lucas sequence into literature in 2014. Uygun and Owusu demonstrated a new generalization for the Jacobsthal sequence called bi-periodic Jacobsthal sequence in [6]. The authors evaluated some relations for bi-periodic Jacobsthal sequence in [7]. In [8], Uygun and Owusu demonstrated the bi-periodic Jacobsthal Lucas sequence. Uygun, Karatas defined a new generalization of Pell-Lucas numbers which is called bi-periodic Pell-Lucas sequence in [9]. Choo studied some identities of generalized bi-periodic Fibonacci sequence in [10]. Gul studied bi-periodic Jacobsthal and Jacobsthal-Lucas quaternions in [11]. Komatsu, Ramírez studied on convolutions of the bi-periodic Fibonacci numbers in [12].

For every integer n , any nonzero real numbers a, b the generalized Jacobsthal sequence $\{J_m\}_{m=0}^{\infty}$ and the generalized Jacobsthal Lucas sequence $\{C_m\}_{m=0}^{\infty}$ satisfy the following equations.

$$J_n = \begin{cases} aJ_{n-1} + 2J_{n-2} & \text{if } n \text{ is even} \\ bJ_{n-1} + 2J_{n-2} & \text{if } n \text{ is odd} \end{cases} \quad (n \geq 2)$$

with initial values $J_0 = 0$ and $J_1 = 1$.

$$C_n = \begin{cases} bC_{n-1} + 2C_{n-2} & \text{if } n \text{ is even} \\ aC_{n-1} + 2C_{n-2} & \text{if } n \text{ is odd} \end{cases} \quad (n \geq 2)$$

with initial values, $C_0 = 2$ and $C_1 = a$ in [6,8]. If we take $a = b = 1$ then we have the classic Jacobsthal and classic Jacobsthal Lucas sequences respectively.

The sequence $\{J_n\}_{n=0}^{\infty}$ satisfies the following properties

$$\begin{aligned} J_{2n} &= (ab + 4)J_{2n-2} - 4J_{2n-4} \\ J_{2n+1} &= (ab + 4)J_{2n-1} - 4J_{2n-3} \end{aligned}$$

The sequence $\{C_n\}_{n=0}^{\infty}$ also satisfies the following properties

$$\begin{aligned} C_{2n} &= (ab + 4)C_{2n-2} - 4C_{2n-4} \\ C_{2n+1} &= (ab + 4)C_{2n-1} - 4C_{2n-3} \end{aligned}$$

For every n belonging to the set of natural numbers, the Binet formula for the bi-periodic Jacobsthal sequence is given by

*Corresponding author. e-mail address: suygun@gantep.edu.tr
<http://dergipark.gov.tr/csj> ©2021 Faculty of Science, Sivas Cumhuriyet University

$$J_n = \frac{a^{1-\xi(n)}}{(ab)^{\lfloor \frac{n}{2} \rfloor}} \left(\frac{\alpha^{n-\beta^n}}{\alpha-\beta} \right) \quad (1)$$

where

$$\alpha = \frac{ab + \sqrt{a^2b^2 + 8ab}}{2} \quad \text{and} \quad \beta = \frac{ab - \sqrt{a^2b^2 + 8ab}}{2}$$

are the roots of the characteristic polynomial given by $x^2 - abx - 2ab = 0$. Similarly, Binet formula for the bi-periodic Jacobsthal Lucas sequence is given by

$$C_n = \frac{a^{\xi(n)}}{(ab)^{\lfloor \frac{n+1}{2} \rfloor}} (\alpha^n + \beta^n). \quad (2)$$

The authors evaluated some relations of bi-periodic Jacobsthal sequence in [7] as:

- a) $\alpha^n = a^{\lfloor \frac{n}{2} \rfloor - \xi(n-1)} b^{\lfloor \frac{n}{2} \rfloor} J_n \alpha + 2a^{\lfloor \frac{n}{2} \rfloor} b^{\lfloor \frac{n}{2} \rfloor + \xi(n)} J_{n-1}$
- b) $\beta^n = a^{\lfloor \frac{n}{2} \rfloor - \xi(n-1)} b^{\lfloor \frac{n}{2} \rfloor} J_n \beta + 2a^{\lfloor \frac{n}{2} \rfloor} b^{\lfloor \frac{n}{2} \rfloor + \xi(n)} J_{n-1}$
- c) $J_{n+6} = (ab + 6)a^{1-\xi(n)} b^{\xi(n)} J_{n+3} - 8J_n$
- d) $aJ_{2n-1} = J_{n+1}J_n + J_{n-1}J_{n-2}$
- e) $J_{m+n-1} = \left(\frac{b}{a}\right)^{1-\xi(mn+n-m)} J_m J_n + 2\left(\frac{b}{a}\right)^{\xi(mn)} J_{m-1} J_{n-1}$
- f) $J_{2m-1} = \left(\frac{b}{a}\right)^{\xi(m+1)} (J_m)^2 + 2\left(\frac{b}{a}\right)^{\xi(m)} (J_{m-1})^2$
- g) $J_n J_{n+2} = \left(\frac{a}{b}\right)^{\xi(n+1)} \left[\left(\frac{b}{a}\right)^{\xi(n)} J_{n+1}^2 - (-2)^{n+1} \right]$
- h) $J_m = a^{\xi(m-1)} \sum_{k=0}^{\lfloor \frac{m-1}{2} \rfloor} \binom{m-k-1}{k} (ab)^{\lfloor \frac{m-1}{2} \rfloor - k} 2^k$
- i) $J_m = \frac{a^{\xi(m+1)}}{2^{m-1}} \sum_{k=0}^{\lfloor \frac{m-1}{2} \rfloor} \binom{m}{2k+1} (ab)^{\lfloor \frac{m-1}{2} \rfloor - k} (ab + 8)^k$

The authors evaluated some relations between the bi-periodic Jacobsthal sequence and the bi-periodic Jacobsthal Lucas sequences for all integers m and n in as:

- a) $(ab + 8)J_m = 2C_{m-1} + C_{m+1}$
- b) $J_{m+n} = \frac{1}{2} \left[\left(\frac{b}{a}\right)^{\xi(m+1)\xi(n)} J_m C_n + \left(\frac{b}{a}\right)^{\xi(m)\xi(n+1)} J_n C_m \right]$
- c) $J_{m-n} = \frac{(-1)^n}{2^{n+1}} \left[\left(\frac{b}{a}\right)^{\xi(m+1)\xi(n)} J_m C_n - \left(\frac{b}{a}\right)^{\xi(m)\xi(n+1)} J_n C_m \right]$
- d) $C_{m+n} = \frac{1}{2} \left[(a^2b^2 + 8ab) \left(\frac{1}{a^2}\right)^{\xi(m+1)\xi(n+1)} \left(\frac{1}{ab}\right)^{1-\xi(m+1)\xi(n+1)} J_m J_n + \left(\frac{b}{a}\right)^{\xi(m)\xi(n)} C_m C_n \right]$

- e) $C_{m-n} = \frac{(-1)^n}{2^{n+1}} \left[\begin{matrix} \left(\frac{b}{a}\right)^{\xi(m)\xi(n)} C_m C_n \\ -(a^2 b^2 + 8ab) \left(\frac{1}{a^2}\right)^{\xi(m+1)\xi(n+1)} \left(\frac{1}{ab}\right)^{1-\xi(m+1)\xi(n+1)} J_m J_n \end{matrix} \right]$
- f) $J_{n+1} = \frac{1}{2}(C_n + a^{\xi(n)} b^{\xi(n+1)} J_n)$
- g) $C_{n+1} = \frac{1}{2}[(ab + 8)J_n + a^{\xi(n+1)} b^{\xi(n)} C_n]$
- h) $\left(\frac{b}{a}\right)^{\xi(n)} C_n^2 - (a^2 b^2 + 8ab) \left(\frac{1}{a^2}\right)^{\xi(n+1)} \left(\frac{1}{ab}\right)^{\xi(n)} J_n^2 = 4(-2)^n$
- i) $C_{2n} = \frac{1}{2} \left[(a^2 b^2 + 8ab) \left(\frac{1}{a^2}\right)^{\xi(n+1)} \left(\frac{1}{ab}\right)^{\xi(n)} J_n^2 + \left(\frac{b}{a}\right)^{\xi(n)} C_n^2 \right]$
- j) $C_{2m} C_{2n} = C_{2m+2n} + 4^m C_{2n-2m}$
- k) $C_{2m} C_{2n} = \left(\frac{b}{a}\right)^{\xi(m+n)} [C_{2m+n}^2 + (2)^{2n} C_{2m-n}^2] - 4(-2)^{m+n}$
- l) $C_{2m} C_{2n} = a^{-2\xi(m+n+1)} (ab)^{-\xi(m+n)} (a^2 b^2 + 8ab) J_{m+n}^2 + 2^{2n} \left(\frac{b}{a}\right)^{\xi(m+n)} C_{m-n}^2$
- m) $C_{2m} C_{2n} = a^{-2\xi(m+n+1)} (ab)^{-\xi(m+n)} (a^2 b^2 + 8ab) J_{m+n}^2 + 2^{2n} \left(\frac{b}{a}\right)^{\xi(m+n)} C_{m-n}^2$
- n) $C_{2m} C_{2n} = 2^{2n} a^{-2\xi(m+n+1)} (ab)^{-\xi(m+n)} (a^2 b^2 + 8ab) J_{m-n}^2 \left(\frac{b}{a}\right)^{\xi(m+n)} C_{m+n}^2$
- o) $C_n C_{n+1} = C_{2n+1} + (-2)^n a$
- p) $2 \left(\frac{b}{a}\right)^{\xi(n)} C_n^2 + \left(\frac{b}{a}\right)^{\xi(n+1)} C_{n+1}^2 = (ab + 8) J_{2n+1}$

2. Main Results

2.1. New properties between the bi-periodic jacobsthal sequence and the bi-periodic jacobsthal lucas sequences

Jacobsthal numbers have applications in such areas as tiling, graph matching, alternating sign matrices, etc. [13-16]. So, in this part we want to develop this number sequence and find new properties of the sequence.

Theorem 2.1 For any integers m and n , we have

- a) $J_{3n} = J_n [C_{2n} + (-2)^n],$
- b) $J_{3n} = \left(\frac{b}{a}\right)^{\xi(n)} [J_{2n} C_n - (-2)^n J_n].$

Proof: For the proof of a) we use Binet formula for bi-periodic Jacobsthal sequence and bi-periodic Jacobsthal Lucas sequences

$$\begin{aligned}
 J_n C_{2n} &= \left(\frac{a^{1-\xi(n)}}{(ab)^{\lfloor \frac{n}{2} \rfloor}}\right) \left(\frac{a^{\xi(2n)}}{(ab)^{\lfloor \frac{2n+1}{2} \rfloor}}\right) (\alpha^{2n} + \beta^{2n}) \left(\frac{\alpha^n - \beta^n}{\alpha - \beta}\right) \\
 &= \frac{a^{\xi(n+1)}}{(ab)^{\lfloor \frac{n}{2} \rfloor + \lfloor \frac{2n+1}{2} \rfloor}} \frac{1}{\alpha - \beta} (\alpha^{3n} - \beta^{3n} + \alpha^n \beta^{2n} - \alpha^{2n} \beta^n) \\
 &= \frac{a^{\xi(n+1)}}{(ab)^{\lfloor \frac{3n}{2} \rfloor}} \frac{1}{\alpha - \beta} (\alpha^{3n} - \beta^{3n} - \alpha^n \beta^n (\alpha^n - \beta^n)) \\
 &= \frac{a^{\xi(n+1)}}{(ab)^{\lfloor \frac{3n}{2} \rfloor}} \frac{\alpha^{3n} - \beta^{3n}}{\alpha - \beta} - \frac{a^{\xi(n+1)}}{(ab)^{\lfloor \frac{3n}{2} \rfloor}} (-2ab)^n \frac{\alpha^n - \beta^n}{\alpha - \beta} \\
 &= \frac{a^{\xi(n+1)}}{(ab)^{\lfloor \frac{3n}{2} \rfloor}} \frac{\alpha^{3n} - \beta^{3n}}{\alpha - \beta} - (-2)^n \frac{a^{1-\xi(n)}}{(ab)^{\lfloor \frac{n}{2} \rfloor}} \frac{\alpha^n - \beta^n}{\alpha - \beta} \\
 &= J_{3n} - (-2)^n J_n
 \end{aligned}$$

For the proof of b)

$$J_{2n}C_n = \left(\frac{a^{1-\xi(2n)}}{(ab)^n}\right) \left(\frac{a^{\xi(n)}}{(ab)^{\lfloor \frac{n+1}{2} \rfloor}}\right) (\alpha^n + \beta^n) \left(\frac{\alpha^{2n}-\beta^{2n}}{\alpha-\beta}\right)$$

$$= \frac{a^{1+\xi(n)}}{(ab)^{n+\lfloor \frac{n+1}{2} \rfloor}} \frac{1}{\alpha-\beta} (\alpha^{3n} - \beta^{3n} + \alpha^{2n}\beta^n - \alpha^n\beta^{2n})$$

If n is odd, we have

$$J_{2n}C_n = \frac{a^2}{(ab)^{\lfloor \frac{3n}{2} \rfloor + 1}} \frac{1}{\alpha-\beta} (\alpha^{3n} - \beta^{3n} + \alpha^n\beta^n(\alpha^n - \beta^n))$$

$$= \frac{a}{b} \frac{ab}{(ab)^{\lfloor \frac{3n}{2} \rfloor + 1}} \frac{1}{\alpha-\beta} (\alpha^{3n} - \beta^{3n} + (-2ab)^n(\alpha^n - \beta^n))$$

$$= \frac{a}{b} \frac{1}{(ab)^{\lfloor \frac{3n}{2} \rfloor}} \frac{\alpha^{3n}-\beta^{3n}}{\alpha-\beta} + \frac{a}{b} \frac{1}{(ab)^{\lfloor \frac{3n}{2} \rfloor - n}} (-2)^n \left(\frac{\alpha^n-\beta^n}{\alpha-\beta}\right)$$

$$= \frac{a}{b} \frac{1}{(ab)^{\lfloor \frac{3n}{2} \rfloor}} \frac{\alpha^{3n}-\beta^{3n}}{\alpha-\beta} + \frac{a}{b} (-2)^n \frac{1}{(ab)^{\lfloor \frac{n}{2} \rfloor}} \left(\frac{\alpha^n-\beta^n}{\alpha-\beta}\right)$$

$$= \frac{a}{b} J_{3n} + \frac{a}{b} (-2)^n J_n$$

Proof:

$$J_m C_{m+n} = \left(\frac{a^{1-\xi(m)}}{(ab)^{\lfloor \frac{m}{2} \rfloor}}\right) \left(\frac{a^{\xi(m+n)}}{(ab)^{\lfloor \frac{m+n+1}{2} \rfloor}}\right) (\alpha^{m+n} + \beta^{m+n}) \left(\frac{\alpha^m-\beta^m}{\alpha-\beta}\right)$$

$$= \frac{a^{1-\xi(m)+\xi(m+n)}}{(ab)^{\lfloor \frac{m}{2} \rfloor + \lfloor \frac{m+n+1}{2} \rfloor}} \frac{\alpha^{2m+n}-\beta^{2m+n} + \alpha^m\beta^{m+n} - \alpha^{m+n}\beta^m}{\alpha-\beta}$$

If both m and n are even, $m + n$ is even as well and hence we have

$$J_m C_{m+n} = \frac{a}{(ab)^{\lfloor \frac{2m+n}{2} \rfloor}} \frac{\alpha^{2m+n}-\beta^{2m+n}-\alpha^m\beta^m(\alpha^n-\beta^n)}{\alpha-\beta}$$

$$= \frac{a}{(ab)^{\lfloor \frac{2m+n}{2} \rfloor}} \frac{\alpha^{2m+n}-\beta^{2m+n}}{\alpha-\beta} - (-2)^m \frac{a}{(ab)^{\lfloor \frac{2m+n}{2} \rfloor - m}} \frac{\alpha^n-\beta^n}{\alpha-\beta}$$

$$= J_{2m+n} - (-2)^m J_n$$

If m and n are both odd, $m + n$ even and hence we have

$$J_m C_{m+n} = \frac{1}{(ab)^{\lfloor \frac{2m+n}{2} \rfloor}} \frac{\alpha^{2m+n}-\beta^{2m+n} + \alpha^m\beta^{m+n} - \alpha^{m+n}\beta^m}{\alpha-\beta}$$

Now if n is even, we have

$$J_{2n}C_n = \frac{a}{(ab)^{\lfloor \frac{3n}{2} \rfloor}} \frac{1}{\alpha-\beta} (\alpha^{3n} - \beta^{3n} - \alpha^n\beta^n(\alpha^n - \beta^n))$$

$$= \frac{a}{(ab)^{\lfloor \frac{3n}{2} \rfloor}} \frac{1}{\alpha-\beta} (\alpha^{3n} - \beta^{3n} - (-2ab)^n(\alpha^n - \beta^n))$$

$$= \frac{a}{(ab)^{\lfloor \frac{3n}{2} \rfloor}} \frac{\alpha^{3n}-\beta^{3n}}{\alpha-\beta} - \frac{a}{(ab)^{\lfloor \frac{3n}{2} \rfloor - n}} (-2)^n \left(\frac{\alpha^n-\beta^n}{\alpha-\beta}\right)$$

$$= \frac{a}{(ab)^{\lfloor \frac{3n}{2} \rfloor}} \frac{\alpha^{3n}-\beta^{3n}}{\alpha-\beta} - (-2)^n \frac{a}{(ab)^{\lfloor \frac{n}{2} \rfloor}} \left(\frac{\alpha^n-\beta^n}{\alpha-\beta}\right)$$

$$= J_{3n} - (-2)^n J_n$$

By condensing the result gives us the desired result. ■

Now taking $a = b = 1$ into Theorem 2.1 gives

$$j_{3n} = j_n [c_{2n} + (-2)^n] = j_{2n}c_n + (-2)^n j_n.$$

Theorem 2.2 For any integers m and n , we have the following property for bi-periodic Jacobsthal sequence and bi-periodic Jacobsthal Lucas sequences

$$J_{2m+n} = \left(\frac{b}{a}\right)^{\xi(m+1)\xi(n)} J_m C_{m+n} + (-2)^m J_n.$$

$$\begin{aligned}
 &= \frac{1}{(ab)^{\lfloor \frac{2m+n}{2} \rfloor}} \frac{\alpha^{2m+n} - \beta^{2m+n}}{\alpha - \beta} - (-2)^m \frac{1}{(ab)^{\lfloor \frac{2m+n}{2} \rfloor - m}} \left(\frac{\alpha^n - \beta^n}{\alpha - \beta} \right) \\
 &= J_{2m+n} - (-2)^m J_n
 \end{aligned}$$

If m is odd and n is even, then $m + n$ is odd and hence we have

$$\begin{aligned}
 J_m C_{m+n} &= \frac{a}{(ab)^{\lfloor \frac{2m+n}{2} \rfloor}} \frac{1}{\alpha - \beta} (\alpha^{2m+n} - \beta^{2m+n} + \alpha^m \beta^{m+n} - \alpha^{m+n} \beta^m) \\
 &= \frac{a}{(ab)^{\lfloor \frac{2m+n}{2} \rfloor}} \frac{1}{\alpha - \beta} (\alpha^{2m+n} - \beta^{2m+n} - \alpha^m \beta^m (\alpha^n - \beta^n)) \\
 &= \frac{a}{(ab)^{\lfloor \frac{2m+n}{2} \rfloor}} \frac{\alpha^{2m+n} - \beta^{2m+n}}{\alpha - \beta} - \frac{(-2)^m a}{(ab)^{\lfloor \frac{2m+n}{2} \rfloor - m}} \left(\frac{\alpha^n - \beta^n}{\alpha - \beta} \right) \\
 &= J_{2m+n} - (-2)^m J_n
 \end{aligned}$$

Finally if m is even and n is odd, $m + n$ is odd

$$\begin{aligned}
 J_m C_{m+n} &= \frac{a^2}{(ab)^{\lfloor \frac{2m+n}{2} \rfloor + 1}} \frac{\alpha^{2m+n} - \beta^{2m+n} + \alpha^m \beta^{m+n} - \alpha^{m+n} \beta^m}{\alpha - \beta} \\
 &= \frac{a}{b} \frac{ab}{(ab)^{\lfloor \frac{2m+n}{2} \rfloor + 1}} \frac{\alpha^{2m+n} - \beta^{2m+n} - \alpha^m \beta^m (\alpha^n - \beta^n)}{\alpha - \beta} \\
 &= \frac{a}{b} \frac{1}{(ab)^{\lfloor \frac{2m+n}{2} \rfloor}} \frac{\alpha^{2m+n} - \beta^{2m+n}}{\alpha - \beta} - \frac{a}{b} (-2)^m \frac{1}{(ab)^{\lfloor \frac{2m+n}{2} \rfloor - m}} \left(\frac{\alpha^n - \beta^n}{\alpha - \beta} \right) \\
 &= \frac{a}{b} J_{2m+n} - \frac{a}{b} (-2)^m J_n.
 \end{aligned}$$

Therefore, condensing the above with the help of the parity function gives

$$J_{2m+n} = \left(\frac{b}{a} \right)^{\xi(m+1)\xi(n)} J_m C_{m+n} + (-2)^m J_n$$

which completes the proof.

Now taking $a = b = 1$ into Theorem 2.2 gives

$$j_{2m+n} = j_m C_{m+n} + (-2)^m j_n.$$

Theorem 2.3 The following identity is satisfied by bi-periodic Jacobsthal sequence and bi-periodic Jacobsthal Lucas sequence for any integer n

$$(\alpha - \beta)^2 J_{2n+3} J_{2n-3} = C_{4n} - (-2)^{2n-3} C_6.$$

Proof: By (1) and (2), we establish

$$\begin{aligned}
 J_{2n+3} J_{2n-3} &= \left(\frac{a^{1-\xi(2n+3)}}{(ab)^{\lfloor \frac{2n+3}{2} \rfloor}} \frac{\alpha^{2n+3} - \beta^{2n+3}}{\alpha - \beta} \right) \left(\frac{a^{1-\xi(2n-3)}}{(ab)^{\lfloor \frac{2n-3}{2} \rfloor}} \frac{\alpha^{2n-3} - \beta^{2n-3}}{\alpha - \beta} \right) \\
 &= \frac{1}{(ab)^{\lfloor \frac{2n+3}{2} \rfloor + \lfloor \frac{2n-3}{2} \rfloor}} \frac{\alpha^{4n} + \beta^{4n} - \alpha^{2n-3} \beta^{2n-3} (\alpha^6 + \beta^6)}{(\alpha - \beta)^2}.
 \end{aligned}$$

Multiplying through by $(\alpha - \beta)^2$ gives the following

$$\begin{aligned} (\alpha - \beta)^2 J_{2n+3} J_{2n-3} &= \frac{\alpha^{4n} + \beta^{4n} - (-2ab)^{2n-3} (\alpha^6 + \beta^6)}{(ab)^{2n}} \\ &= \frac{a^{\xi(4n)}}{(ab)^{\lfloor \frac{4n+1}{2} \rfloor}} (\alpha^{4n} + \beta^{4n}) - (-2)^{2n-3} \frac{a^{\xi(6)}}{(ab)^{\lfloor \frac{6+1}{2} \rfloor}} (\alpha^6 + \beta^6) \\ &= C_{4n} - (-2)^{2n-3} C_6 \end{aligned}$$

which completes the proof.

Now taking $a = b = 1$ into Theorem 2.3 gives

$$9j_{2n+3}j_{2n-3} = c_{4n} - (-2)^{2n-3}c_6.$$

Theorem 2.4 For any integer n , we have for bi-periodic Jacobsthal sequence and bi-periodic Jacobsthal Lucas sequences

$$2J_{2n+1} = \left(\frac{b}{a}\right)^{\xi(n)} J_{n+1}C_{n+2} - bJ_{n+2}C_n + (-2)^n(ab - 2).$$

Proof:

$$\begin{aligned} \left(\frac{b}{a}\right)^{\xi(n)} J_{n+1}C_{n+2} &= \left(\frac{b}{a}\right)^{\xi(n)} \left(\frac{a^{\xi(n)} \alpha^{n+1} - \beta^{n+1}}{(ab)^{\lfloor \frac{n+1}{2} \rfloor} \alpha - \beta} \right) \left(\frac{a^{\xi(n+2)} (\alpha^{n+2} + \beta^{n+2})}{(ab)^{\lfloor \frac{n+3}{2} \rfloor}} \right) \\ &= \left(\frac{b}{a}\right)^{\xi(n)} \left(\frac{a^{2\xi(n)} \alpha^{2n+3} - \beta^{2n+3} - (\alpha\beta)^{n+1} (\alpha - \beta)}{(ab)^{2\lfloor \frac{n+1}{2} \rfloor + 1} \alpha - \beta} \right) \\ &= \left(\frac{(ab)^{\xi(n)} \alpha^{2n+3} - \beta^{2n+3}}{(ab)^{n+1+\xi(n)} \alpha - \beta} \right) - \frac{(2ab)^{n+1} (\alpha - \beta)}{(ab)^{n+1}} \\ &= J_{2n+3} - (-2)^{n+1} \end{aligned}$$

$$\begin{aligned} bJ_{n+2}C_n &= b \left(\frac{a^{1-\xi(n+2)} \alpha^{n+2} - \beta^{n+2}}{(ab)^{\lfloor \frac{n+2}{2} \rfloor} \alpha - \beta} \right) \left(a^{\xi(n)} \frac{\alpha^n + \beta^n}{(ab)^{\lfloor \frac{n+1}{2} \rfloor}} \right) \\ &= \left(\frac{ab \alpha^{2n+2} - \beta^{2n+2} + (\alpha\beta)^n (\alpha^2 - \beta^2)}{(ab)^{n+1} \alpha - \beta} \right) \\ &= b \left(\frac{a^{1-\xi(2n+2)} \alpha^{2n+2} - \beta^{2n+2}}{(ab)^{n+1} \alpha - \beta} \right) + \frac{(-2ab)^n ab (\alpha + \beta)}{(ab)^{n+1}} \\ &= bJ_{2n+2} + (-2)^n ab \end{aligned}$$

Therefore we have

$$\begin{aligned} \left(\frac{b}{a}\right)^{\xi(n)} J_{n+1}C_{n+2} - bJ_{n+2}C_n + (-2)^n(ab - 2) \\ = J_{2n+3} - (-2)^{n+1} - bJ_{2n+2} - (-2)^n ab + (-2)^n(ab - 2) \\ = J_{2n+3} - bJ_{2n+2} = 2J_{2n+1}. \end{aligned}$$

Now taking $a = b = 1$ into Theorem 2.4 gives

$$2j_{2n+1} = j_{n+1}c_{n+2} - j_{n+2}c_n - (-2)^n.$$

Theorem 2.5 For any n , n th element of bi-periodic Jacobsthal Lucas sequence is demonstrated by the following equality:

$$C_n = \left(\frac{b}{a}\right)^{\xi(n+1)\xi(m)} C_m J_{n-m+1} + 2 \left(\frac{b}{a}\right)^{\xi(n+1)\xi(m+1)} C_{m-1} J_{n-m}.$$

Proof: For proof we use the following properties

$$\frac{1}{2}(\xi(n) + \xi(m) - \xi(m+n)) = \xi(n)\xi(m)$$

$$n - \xi(n) = 2 \left\lfloor \frac{n}{2} \right\rfloor.$$

By Binet formulas (1, 2), we have

$$\begin{aligned} & \left(\frac{b}{a}\right)^{\xi(n+1)\xi(m)} C_m J_{n-m+1} + 2 \left(\frac{b}{a}\right)^{\xi(n+1)\xi(m+1)} C_{m-1} J_{n-m} \\ &= \left(\frac{b}{a}\right)^{\frac{1}{2}(\xi(n+1)+\xi(m)-\xi(m+n+1))} \left(\frac{a^{\xi(m)}}{(ab)^{\lfloor \frac{m+1}{2} \rfloor}} (\alpha^m + \beta^m)\right) \left(\frac{a^{1-\xi(n-m+1)} \alpha^{n-m+1} - \beta^{n-m+1}}{(ab)^{\lfloor \frac{n-m+1}{2} \rfloor} (\alpha - \beta)}\right) + \\ & 2 \left(\frac{b}{a}\right)^{\frac{1}{2}(\xi(n+1)+\xi(m+1)-\xi(m+n+2))} \left(\frac{a^{\xi(m-1)}}{(ab)^{\lfloor \frac{m}{2} \rfloor}} (\alpha^{m-1} + \beta^{m-1})\right) \left(\frac{a^{1-\xi(n-m)} \alpha^{n-m} - \beta^{n-m}}{(ab)^{\lfloor \frac{n-m}{2} \rfloor} (\alpha - \beta)}\right) \\ &= \frac{1}{a^{\lfloor \frac{n}{2} \rfloor} b^{\lfloor \frac{n+1}{2} \rfloor}} \frac{1}{\alpha - \beta} \left(\alpha^{n+1} - \beta^{n+1} - \alpha^m \beta^{n-m+1} + \alpha^{n-m+1} \beta^m \right. \\ & \quad \left. + 2ab(\alpha^{n-1} - \beta^{n-1} - \alpha^{m-1} \beta^{n-m} + \alpha^{n-m} \beta^{m-1}) \right) \\ &= \frac{1}{a^{\lfloor \frac{n}{2} \rfloor} b^{\lfloor \frac{n+1}{2} \rfloor}} \frac{1}{\alpha - \beta} \left(\alpha^{n+1} - \beta^{n+1} - \alpha^m \beta^{n-m+1} + \alpha^{n-m+1} \beta^m \right. \\ & \quad \left. - \alpha^n \beta + \alpha \beta^n + \alpha^m \beta^{n-m+1} - \alpha^{n-m+1} \beta^m \right) \end{aligned}$$

After simplifications we have

$$= \frac{1}{a^{\lfloor \frac{n}{2} \rfloor} b^{\lfloor \frac{n+1}{2} \rfloor}} \frac{1}{\alpha - \beta} (\alpha^{n+1} - \beta^{n+1} - \alpha^n \beta + \alpha \beta^n) = \frac{1}{a^{\lfloor \frac{n}{2} \rfloor} b^{\lfloor \frac{n+1}{2} \rfloor}} \frac{1}{\alpha - \beta} (\alpha^n + \beta^n)(\alpha - \beta) = C_n.$$

Now taking $a = b = 1$ into Theorem 2.5 gives

$$c_n = c_m j_{n-m+1} + 2c_{m-1} j_{n-m}.$$

Theorem 2.6 For any m, n the m th element of bi-periodic Jacobsthal sequence is given by

$$J_{mn} = \left(\frac{b}{a}\right)^{\xi(n)\xi(m)} C_m J_{m(n-1)} - (-2)^m J_{m(n-2)}.$$

Proof: By using the following property,

$$\xi(n)\xi(m) = \left\lfloor \frac{m+n}{2} \right\rfloor - \left\lfloor \frac{m}{2} \right\rfloor - \left\lfloor \frac{n}{2} \right\rfloor$$

we have

$$\left(\frac{b}{a}\right)^{\xi(n)\xi(m)} C_m J_{m(n-1)} + J_{m(n-2)}$$

$$\begin{aligned}
 &= \left(\frac{a^{-\lfloor \frac{m+n}{2} \rfloor + \lfloor \frac{n}{2} \rfloor - \lfloor \frac{m(n-1)-1}{2} \rfloor} b^{\lfloor \frac{m+n}{2} \rfloor - \lfloor \frac{n}{2} \rfloor - \lfloor \frac{m+1}{2} \rfloor - \lfloor \frac{m(n-1)}{2} \rfloor}}{\alpha - \beta} (\alpha^m + \beta^m) (\alpha^{m(n-1)} - \beta^{m(n-1)}) \right) + \\
 &(-2)^{m+1} \left(\frac{a^{-\lfloor \frac{m(n-2)-1}{2} \rfloor} b^{-\lfloor \frac{m(n-2)}{2} \rfloor}}{\alpha - \beta} (\alpha^{m(n-2)} - \beta^{m(n-2)}) \right) \\
 &= \frac{1}{a^{\lfloor \frac{mn-1}{2} \rfloor} b^{\lfloor \frac{mn}{2} \rfloor}} \frac{\alpha^{mn} - \beta^{mn}}{\alpha - \beta} + \frac{1}{a^{\lfloor \frac{mn-1}{2} \rfloor} b^{\lfloor \frac{mn}{2} \rfloor}} \frac{(-\alpha^m \beta^{m(n-1)} + \alpha^{m(n-1)} \beta^m - (-2)^m (ab)^m (\alpha^{m(n-2)} - \beta^{m(n-2)}))}{\alpha - \beta} \\
 &= \frac{1}{a^{\lfloor \frac{mn-1}{2} \rfloor} b^{\lfloor \frac{mn}{2} \rfloor}} \frac{\alpha^{mn} - \beta^{mn}}{\alpha - \beta} = J_{mn}.
 \end{aligned}$$

Now taking $a = b = 1$ into Theorem 2.6 gives

$$j_{mn} = j_{m(n-1)} - (-2)^m j_{m(n-2)}.$$

Theorem 2.7 For any n , we have the following identities for bi-periodic Jacobsthal sequence and bi-periodic Jacobsthal Lucas sequence:

$$J_{4n+1} - 2^{2n} = \left(\frac{b}{a}\right) C_{2n+1} J_{2n},$$

and

$$J_{4n+3} - 2^{2n+1} = \left(\frac{b}{a}\right) C_{2n+1} J_{2n+2}.$$

Proof: (1)

$$\begin{aligned}
 C_{2n+1} J_{2n} &= \left(\frac{a^{\xi(2n+1)}}{(ab)^{\lfloor \frac{2n+2}{2} \rfloor}} (\alpha^{2n+1} + \beta^{2n+1}) \right) \left(\frac{a^{1-\xi(2n)} \alpha^{2n} - \beta^{2n}}{(ab)^{\lfloor \frac{2n}{2} \rfloor} \alpha - \beta} \right) \\
 &= \frac{a^2}{(ab)^{2n+1}} \left(\frac{\alpha^{4n+1} - \beta^{4n+1} - \alpha^{2n+1} \beta^{2n} + \beta^{2n+1} \alpha^{2n}}{\alpha - \beta} \right) \\
 &= \frac{a^2}{(ab)^{2n+1}} \left(\frac{\alpha^{4n+1} - \beta^{4n+1} - \alpha^{2n} \beta^{2n} (\alpha - \beta)}{\alpha - \beta} \right) \\
 &= \frac{a}{b} \left[\frac{1}{(ab)^{2n}} \frac{\alpha^{4n+1} - \beta^{4n+1}}{\alpha - \beta} \right] - \frac{a}{b} \frac{1}{(ab)^{2n}} (ab)^{2n} (-2)^{2n} \\
 &= \frac{a}{b} \left[\frac{1}{(ab)^{2n}} \frac{\alpha^{4n+1} - \beta^{4n+1}}{\alpha - \beta} \right] - \frac{a}{b} \frac{1}{(ab)^{2n}} (ab)^{2n} (-2)^{2n} \\
 &= \frac{a}{b} \left[\frac{a^{1-\xi(4n+1)} \alpha^{4n+1} - \beta^{4n+1}}{(ab)^{\lfloor \frac{4n+1}{2} \rfloor} \alpha - \beta} \right] - \frac{a}{b} 2^{2n} \\
 &= \frac{a}{b} J_{4n+1} - \frac{a}{b} 2^{2n}
 \end{aligned}$$

(2)

$$\begin{aligned}
 C_{2n+1} J_{2n+2} &= \left(\frac{a^{\xi(2n+1)}}{(ab)^{\lfloor \frac{2n+2}{2} \rfloor}} (\alpha^{2n+1} + \beta^{2n+1}) \right) \left(\frac{a^{1-\xi(2n+2)} \alpha^{2n+2} - \beta^{2n+2}}{(ab)^{\lfloor \frac{2n+2}{2} \rfloor} \alpha - \beta} \right) \\
 &= \frac{a^2}{(ab)^{2n+2}} \left(\frac{\alpha^{4n+3} - \beta^{4n+3} + \alpha^{2n+1} \beta^{2n+1} (\alpha - \beta)}{\alpha - \beta} \right)
 \end{aligned}$$

$$\begin{aligned}
 &= \frac{a}{b} \frac{ab}{(ab)^{2n+2}} \frac{\alpha^{4n+3} - \beta^{4n+3}}{\alpha - \beta} + \frac{a}{b} \frac{ab}{(ab)^{2n+2}} \frac{(\alpha\beta)^{2n+1}(\alpha - \beta)}{\alpha - \beta} \\
 &= \frac{a}{b} \frac{1}{(ab)^{2n+1}} \frac{\alpha^{4n+3} - \beta^{4n+3}}{\alpha - \beta} + \frac{a}{b} \frac{1}{(ab)^{2n+1}} (-2ab)^{2n+1} \\
 &= \frac{a}{b} \frac{a^{1-\xi(4n+3)}}{(ab)^{\lfloor \frac{4n+3}{2} \rfloor}} \frac{\alpha^{4n+3} - \beta^{4n+3}}{\alpha - \beta} + \frac{a}{b} (-2)^{2n+1} \\
 &= \frac{a}{b} J_{4n+3} - \frac{a}{b} 2^{2n+1}.
 \end{aligned}$$

Now if we take $a = b = 1$, we obtain the following

$$c_{4n+1} - (-2)^{2n} = c_{2n+1}j_{2n},$$

and

$$c_{4n+3} - (-2)^{2n+1} = c_{2n+1}j_{2n+2}.$$

Theorem 2.8 For any integer n , the identity for bi-periodic Jacobsthal sequence and bi-periodic Jacobsthal Lucas sequence is denoted by

$$C_n C_{n+2} - (ab + 8) J_{n-1} J_{n+3} = (-2)^{n-1} a^{1+\xi(n)} b^{\xi(n+1)} (ab + 6).$$

Proof:

$$\begin{aligned}
 C_n C_{n+2} - (ab + 8) J_{n-1} J_{n+3} &= \frac{(\alpha^n + \beta^n)}{a^{\lfloor \frac{n}{2} \rfloor} b^{\lfloor \frac{n+1}{2} \rfloor}} \frac{(\alpha^{n+2} + \beta^{n+2})}{a^{\lfloor \frac{n+2}{2} \rfloor} b^{\lfloor \frac{n+3}{2} \rfloor}} - \frac{(ab+8)}{(\alpha - \beta)^2} \frac{(\alpha^{n-1} - \beta^{n-1})}{a^{\lfloor \frac{n-2}{2} \rfloor} b^{\lfloor \frac{n-1}{2} \rfloor}} \frac{(\alpha^{n+3} - \beta^{n+3})}{a^{\lfloor \frac{n+2}{2} \rfloor} b^{\lfloor \frac{n+3}{2} \rfloor}} \\
 &= \frac{(\alpha^{2n+2} + \beta^{2n+2} + \alpha^n \beta^{n+2} + \alpha^{n+2} \beta^n)}{a^{2\lfloor \frac{n}{2} \rfloor} b^{2\lfloor \frac{n+1}{2} \rfloor} (ab)} - \frac{(\alpha^{2n+2} + \beta^{2n+2} - \alpha^{n-1} \beta^{n+3} - \alpha^{n+3} \beta^{n-1})}{a^{2\lfloor \frac{n}{2} \rfloor} b^{2\lfloor \frac{n+1}{2} \rfloor} (ab)} \\
 &= \frac{\alpha^{2n+2} + \beta^{2n+2} + \alpha^n \beta^n (\beta^2 + \alpha^2) - [\alpha^{2n+2} + \beta^{2n+2} - \alpha^n \beta^n (\frac{\beta^3}{\alpha} + \frac{\alpha^3}{\beta})]}{a^{2\lfloor \frac{n}{2} \rfloor} b^{2\lfloor \frac{n+1}{2} \rfloor} (ab)} \\
 &= \frac{\alpha^n \beta^n (\beta^2 + \alpha^2) + \alpha^n \beta^n (\frac{\beta^3}{\alpha} + \frac{\alpha^3}{\beta})}{a^{2\lfloor \frac{n}{2} \rfloor} b^{2\lfloor \frac{n+1}{2} \rfloor} (ab)} \\
 &= \frac{\alpha^n \beta^n (\beta^2 + \alpha^2 + \frac{\beta^3}{\alpha} + \frac{\alpha^3}{\beta})}{a^{2\lfloor \frac{n}{2} \rfloor} b^{2\lfloor \frac{n+1}{2} \rfloor} (ab)} \\
 &= \frac{\alpha^n \beta^n [\beta^2 (1 + \frac{\beta}{\alpha}) + \alpha^2 (1 + \frac{\alpha}{\beta})]}{a^{2\lfloor \frac{n}{2} \rfloor} b^{2\lfloor \frac{n+1}{2} \rfloor} (ab)} \\
 &= \frac{\alpha^n \beta^n [(\alpha + \beta) (\frac{\beta^2}{\alpha} + \frac{\alpha^2}{\beta})]}{a^{2\lfloor \frac{n}{2} \rfloor} b^{2\lfloor \frac{n+1}{2} \rfloor} (ab)} \\
 &= \frac{\alpha^n \beta^n [(\alpha + \beta) (\frac{\beta^3 + \alpha^3}{\alpha\beta})]}{a^{2\lfloor \frac{n}{2} \rfloor} b^{2\lfloor \frac{n+1}{2} \rfloor} (ab)}
 \end{aligned}$$

$$\begin{aligned}
 &= \frac{(\alpha\beta)^n \left[\frac{ab}{-2} [(ab)^2 + 6ab] \right]}{a^{2\lfloor \frac{n}{2} \rfloor} b^{2\lfloor \frac{n+1}{2} \rfloor} (ab)} \\
 &= \frac{a^2 b^2 (-2ab)^n (ab+6)}{-2 a^{2\lfloor \frac{n}{2} \rfloor} b^{2\lfloor \frac{n+1}{2} \rfloor} (ab)} \\
 &= \frac{(-2)^n (ab)^{n+1} (ab+6)}{-2 a^{2\lfloor \frac{n}{2} \rfloor} b^{2\lfloor \frac{n+1}{2} \rfloor}} \\
 &= (-2)^{n-1} a^{1+n-2\lfloor \frac{n}{2} \rfloor} b^{n+1-2\lfloor \frac{n+1}{2} \rfloor} (ab+6) \\
 &= (-2)^{n-1} a^{1+\xi(n)} b^{\xi(n+1)} (ab+6).
 \end{aligned}$$

Now if we take $a = b = 1$, we obtain the following

$$c_n c_{n+2} - 9 j_{n-1} j_{n+3} = 7(-2)^{n-1}.$$

Theorem 2.9 For any integer $m, n \geq 2$, the relation between bi-periodic Jacobsthal sequence and bi-periodic Jacobsthal Lucas sequence is given as

$$J_m J_n - 4J_{m-2} J_{n-2} = a^{1-\xi(mn)} b^{\xi(mn)} J_{m+n-2}.$$

Proof: By (1, 2), we get

$$\begin{aligned}
 J_m J_n &= \frac{a^{2-\xi(m)-\xi(n)} [\alpha^{m+n} + \beta^{m+n} - (\alpha^n \beta^m + \alpha^m \beta^n)]}{(ab)^{\lfloor \frac{m}{2} \rfloor + \lfloor \frac{n}{2} \rfloor} (\alpha - \beta)^2} \\
 J_{m-2} J_{n-2} &= \frac{a^{2-\xi(m)-\xi(n)} (ab)^2 [\alpha^{m+n-4} + \beta^{m+n-4} - (\alpha\beta)^{-2} (\alpha^n \beta^m + \alpha^m \beta^n)]}{(ab)^{\lfloor \frac{m}{2} \rfloor + \lfloor \frac{n}{2} \rfloor} (\alpha - \beta)^2}
 \end{aligned}$$

Then we subtract the equalities

$$J_m J_n - 4J_{m-2} J_{n-2} = \frac{a^{2-\xi(m)-\xi(n)}}{(ab)^{\lfloor \frac{m}{2} \rfloor + \lfloor \frac{n}{2} \rfloor} (\alpha - \beta)^2} \left[\begin{aligned} &\alpha^{m+n} \left(1 - \frac{4(ab)^2}{\alpha^4} \right) + \beta^{m+n} \left(1 - \frac{4(ab)^2}{\beta^4} \right) - \\ &(\alpha^n \beta^m + \alpha^m \beta^n) \left(1 - \frac{4(ab)^2}{(\alpha\beta)^2} \right) \end{aligned} \right]$$

By $\alpha\beta = -2ab$ and $\xi(m) + \xi(n) - \xi(mn) = \xi(m+n)$, we get

$$\begin{aligned}
 J_m J_n - 4J_{m-2} J_{n-2} &= \frac{a^{2-\xi(m)-\xi(n)} (\alpha + \beta)}{(ab)^{\lfloor \frac{m}{2} \rfloor + \lfloor \frac{n}{2} \rfloor} (\alpha - \beta)} (\alpha^{m+n-2} - \beta^{m+n-2}) \\
 &= \frac{a^{2-\xi(mn)-\xi(m+n)}}{(ab)^{\lfloor \frac{m}{2} \rfloor + \lfloor \frac{n}{2} \rfloor - 1} (\alpha - \beta)} (\alpha^{m+n-2} - \beta^{m+n-2}) \\
 &= a^{1-\xi(mn)} \frac{a^{1-\xi(m+n-2)}}{(ab)^{\lfloor \frac{m}{2} \rfloor + \lfloor \frac{n-2}{2} \rfloor} (\alpha - \beta)} (\alpha^{m+n-2} - \beta^{m+n-2}) \\
 &= a^{1-\xi(mn)} b^{\xi(mn)} \frac{a^{1-\xi(m+n-2)}}{(ab)^{\lfloor \frac{m+n-2}{2} \rfloor} (\alpha - \beta)} (\alpha^{m+n-2} - \beta^{m+n-2}) \\
 &= a^{1-\xi(mn)} b^{\xi(mn)} J_{m+n-2}
 \end{aligned}$$

Therefore, the proof is completed.

Now if we take $a = b = 1$, we obtain the following

$$j_m j_n - 4j_{m-2} j_{n-2} = j_{m+n-2}.$$

Theorem 2.10 A summation formula of bi-periodic Jacobsthal sequence with even index term is given by

$$J_{2m} = -(ab + 4)^{m-1} \left[-a + 4 \sum_{k=0}^{m-2} (ab + 4)^{-k-1} J_{2k} \right].$$

Proof:

$$\begin{aligned} \sum_{k=0}^{m-2} (ab + 4)^{-k-1} J_{2k} &= \sum_{k=0}^{m-2} (ab + 4)^{-k-1} \frac{a^{1-\xi(2k)}}{(ab)^{\lfloor \frac{2k}{2} \rfloor}} \left(\frac{\alpha^{2k} - \beta^{2k}}{\alpha - \beta} \right) \\ &= \frac{a}{(ab+4)(\alpha - \beta)} \sum_{k=0}^{m-2} \frac{\alpha^{2k} - \beta^{2k}}{(ab+4)^k (ab)^k} \\ &= \frac{a}{(ab+4)(\alpha - \beta)} \sum_{k=0}^{m-2} \left[\left(\frac{\alpha^2}{ab(ab+4)} \right)^k - \left(\frac{\beta^2}{ab(ab+4)} \right)^k \right] \\ &= \frac{a}{(ab+4)(\alpha - \beta)} \left(\frac{\left(\frac{\alpha^2}{ab(ab+4)} \right)^{m-1} - 1}{\frac{\alpha^2}{ab(ab+4)} - 1} - \frac{\left(\frac{\beta^2}{ab(ab+4)} \right)^{m-1} - 1}{\frac{\beta^2}{ab(ab+4)} - 1} \right) \\ &= \frac{a}{(ab+4)(\alpha - \beta)} \left(\frac{\alpha^{2m-2} - (ab)^{m-1} (ab+4)^{m-1}}{(\alpha^2 - ab(ab+4))(ab)^{m-2} (ab+4)^{m-2}} - \frac{\beta^{2m-2} - (ab)^{m-1} (ab+4)^{m-1}}{(\beta^2 - ab(ab+4))(ab)^{m-2} (ab+4)^{m-2}} \right) \\ &= \frac{a}{(ab+4)^{m-1} (ab)^{m-2} (\alpha - \beta)} \left(\frac{\alpha^{2m-2} - (ab)^{m-1} (ab+4)^{m-1}}{\alpha^2 - ab(ab+4)} - \frac{\beta^{2m-2} - (ab)^{m-1} (ab+4)^{m-1}}{\beta^2 - ab(ab+4)} \right) \end{aligned}$$

It is noticed that,

$$\begin{aligned} \sum_{k=0}^{m-2} (ab + 4)^{-k-1} J_{2k} &= \frac{a}{(ab+4)^{m-1} (ab)^{m-2} (\alpha - \beta)} \left(\frac{4(ab)^2 (\alpha^{2m-4} - \beta^{2m-4}) - ab(ab+4)(\alpha^{2m-2} - \beta^{2m-2})}{4(ab)^2} + (ab)^{m-1} (ab+4)^{m-1} (\alpha^2 - \beta^2) \right) \\ &= \frac{a(\alpha^{2m-4} - \beta^{2m-4})}{(ab+4)^{m-1} (ab)^{m-2} (\alpha - \beta)} - \frac{a(\alpha^{2m-2} - \beta^{2m-2})}{4(ab+4)^{m-2} (ab)^{m-1} (\alpha - \beta)} + \frac{a}{4} \\ &= \frac{J_{2m-4}}{(ab+4)^{m-1}} - \frac{J_{2m-2}}{4(ab+4)^{m-2}} + \frac{a}{4} \\ &= \frac{4J_{2m-4} - (ab+4)J_{2m-2}}{4(ab+4)^{m-1}} + \frac{a}{4} \end{aligned}$$

Consequently,

$$\sum_{k=0}^{m-2} (ab + 4)^{-k-1} J_{2k} = -\frac{1}{4(ab + 4)^{m-1}} J_{2m} + \frac{a}{4}$$

The proof is completed.

Now if we take $a = b = 1$, we obtain the following

$$j_{2m} = -5^{m-1} \left[-a + 4 \sum_{k=0}^{m-2} (5)^{-k-1} j_{2k} \right].$$

Acknowledgment

I would like to acknowledge Prof. Dr. Baki KESKİN for technical and editorial assistance and referees for their valuable comments.

Conflicts of interest

The authors state that did not have a conflict of interests.

References

- [1] Horadam A. F., Jacobsthal Representation Numbers, *The Fibonacci Quarterly*, 37 (2) (1996) 40-54.
- [2] Edson M, Yayenie O., A New Generalization of Fibonacci Sequences and Extended Binet's Formula, *Integers*, 9 (2009) 639-654.
- [3] Yayenie O., A Note on Generalized Fibonacci Sequence, *Applied Mathematics and Computation*, 217 (2011) 5603-5611.
- [4] Jun S.P, Choi K.H., Some Properties of the Generalized Fibonacci Sequence $\{q_n\}$ by Matrix Methods, *The Korean Journal of Mathematics*, 24 (4) (2016) 681-691.
- [5] Bilgici G, Two Generalizations of Lucas Sequence, *Applied Mathematics and Computation*, 245 (2014) 526-538.
- [6] Uygun S., Owusu E., A New Generalization of Jacobsthal Numbers (Bi-Periodic Jacobsthal Sequences), *Journal of Mathematical Analysis*, 5 (2016) 728-39.
- [7] Uygun S., Karatas H., Akıncı E., Relations on Bi-periodic Jacobsthal Sequence, *Transylvanian Journal of Mathematics and Mechanics*, 10 (2) (2018) 141-151.
- [8] Uygun S., Owusu E., A Note on bi-periodic Jacobsthal Lucas Numbers, *Journal of Advances in Mathematics and Computer Science*, 34 (5) (2019) 1-13.
- [9] Uygun S., Karatas H., A New Generalization of Pell-Lucas Numbers (Bi-Periodic Pell-Lucas Sequence), *Communications in Mathematics and Applications*, 10 (3) (2019) 1-12.
- [10] Choo Y., Some Identities on Generalized Bi-periodic Fibonacci Sequences, *International Journal of Mathematical Analysis*, 13 (6) (2019) 259-267.
- [11] Gul K., On Bi-periodic Jacobsthal and Jacobsthal-Lucas Quaternions, *Journal of Mathematics Research*, 11 (2) (2019) 44-52.
- [12] Komatsu T., Ramírez J.L., Convolutions of the Bi-periodic Fibonacci Numbers, *Hacettepe Journal of Mathematics & Statistics*, (2019) Early Access: 1-13.
- [13] Brigham R., Chinn P., Grimaldi R., Tiling and Patterns of Enumeration, *Congressus Numerantium*, 137 (1999) 207-219.
- [14] Frey D., Sellers J., Jacobsthal Numbers and Alternating Sign Matrices, *Journal. of Integer Sequences*, 3 (2000).
- [15] Grimaldi R., Binary Strings and the Jacobsthal Numbers, *Congressus Numerantium*, 174 (2005) 3-22.
- [16] Grimaldi R., The Distribution of 1's in Jacobsthal Binary Sequences, *Congressus Numerantium*, 190 (2008) 47-64.



Simulation study for 3D dynamic characteristics of voltage losses in PEM fuel cell

Abdurrahman BAYTAR^{1,*} , Deniz SUNAR ÇERÇİP² , Salim ÇERÇİP² 

¹Adiyaman University, Graduate School of Natural and Applied Sciences, 02040, Adiyaman/TURKEY

²Adiyaman University, Faculty of Arts and Sciences, Department of Physics, 02040, Adiyaman/TURKEY

Abstract

Fuel cells, providing an advanced alternative energy source, are devices that can convert chemical energy into electrical energy. Modeling of a fuel cell provides improvements to the design of the fuel cells as well as providing cheaper, better and more efficient fuel cells. Three basic voltage losses occur in the fuel cell: activation polarization, ohmic polarization and concentration polarization. In this study, simulation of voltage losses in PEM (proton exchange membrane) fuel cells was performed by using Matlab@Simulink program. Polarization and power curves were obtained for different operating temperatures by considering these losses.

Article info

History:
Received: 21.02.2020
Accepted: 30.01.2021

Keywords:
Proton exchange membrane (PEM),
Fuel cell,
Voltage losses,
Simulation.

1. Introduction

Energy consumption is one of the most important requirements of countries with high levels of development and has been continuously increasing. In fact, most of the energy we consume is supplied from fossil fuel sources such as coal, oil and natural gas [1, 2]. However, there are basically three problems in the use of such fuels worldwide [3]. The first problem is that fossil fuels will be depleted in the near future, and the second problem is the increase in environmental pollution, and finally the increase in human health. It is possible to define renewable energy as an energy source that can be obtained from natural resources and renews itself continuously [4]. The most important feature that distinguishes renewable energy from other types of energy is that it can renew itself naturally and does not disappear. In addition, renewable energy types are very important in terms of reducing the carbon emissions that can harm the environment [5, 6].

Fuel cells are one of the renewable energy sources that will become the power source of the near future. Fuel cells have energy efficiency, low environmental pollution and unlimited fuel supply, as well as the potential to meet environmental expectations while moving confidently towards commercialization [7, 8]. Fuel cells can power everything from cell phones to tools at home and even cars.

Polymer electrolyte membrane (PEM) fuel cells, one of the most popular, are available in a variety of fuels,

from hydrogen to ethanol to biomass-derived materials [9]. A PEM type fuel cell [10] consists of two electrodes one is positively charged (cathode), another is negatively charged (anode), and an electrolyte membrane. Oxygen is reduced to the cathode while hydrogen is oxidized to the anode. Transportation of protons from the anode to the cathode occurs through the electrolyte membrane, whereas electrons are transported to the cathode above the outer circuit. Hydrogen protons in fuel cells remain ionic by passing from molecule to molecule using special materials. Protons circulate through a polymer membrane consisting of persulfonic acid groups with a Teflon backbone. Electrons are attracted by conductive materials and go to the charge if necessary. In the cathode, oxygen reacts with protons and electrons to form water and generate heat. The stabilization of the electrode structure and minimization of the catalyst particle play important role for future material developments. The studies on the highly efficient electrocatalysts for the oxygen evolution reaction (OER) were presented in [11-14]. A basic PEM fuel cell stack consists of a proton exchange membrane, catalyst and gas diffusion layers, flow field plates, gaskets, and end plates. A stack with multiple cells has “membrane electrode assembly (MEA)” sandwiched between bipolar flow field plates and only one set of end plates.

Fuel cells are still showing intense development. The combination of new and optimized materials, advanced

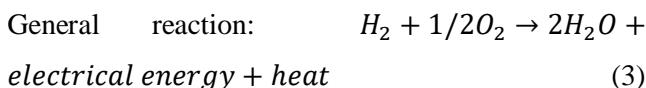
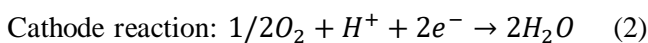
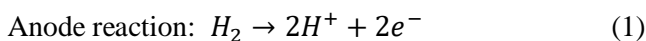
*Corresponding author. e-mail address: abdurrahmanbaytar2020@gmail.com
<http://dergipark.gov.tr/csj> ©2021 Faculty of Science, Sivas Cumhuriyet University

product development, new architectures, more efficient handling processes, design optimization and integration are expected to result in significant gains in performance, efficiency, reliability, productivity and cost effectiveness. Computational Fuel Cell Engineering (CFCE) tools that allow systematic simulation, design and optimization of fuel cell systems may facilitate the integration of such advances, allow less reliability of hardware prototyping, and reduce development cycles. A new model for combined protonics and water transport in polymer membranes is presented in [15]. A method for reducing the model of a nonlinear dynamic fuel cell stack suitable for control and diagnostic studies is performed in Ref. [16]. In order to meet the increasingly stringent application requirements in the PEM type fuel cell, performance gains and productivity gains are crucial. Computational fluid dynamics (CFD) is an ideal tool for achieving these improvements. A comprehensive CFD-based vehicle that can accurately simulate the main transport event occurring in a PEM fuel cell was presented in Ref. [17]. The results of the study were compared with the numerical model results and the results of Ref. [18]. It is seen that the study performed at low current values shows better agreement. A study on the modeling, simulation and analysis of the dynamic behavior of the 5kW PEM fuel cell system [19]. The model used in the study includes hydrogen fuel regulator and PEM fuel cell stack. The model was used to investigate the effect of temperature on fuel cell voltage and power flow at various temperatures. A series of fuel cell studies have been performed to investigate heat and mass transfer in reactive gas channels and water supply to protect the moisture of the membrane [20-26].

Although operating conditions are important for a fuel cell performance, the main factors in this performance are the structure, material and performance of the elements used in each unit of the fuel cell. For this reason, studies on materials and equipment used in fuel cells are of great importance. In this study, performances of fuel cell elements were simulated using Matlab@Simulink simulation program.

2. Materials and Methods

A typical PEM fuel cell has the following reactions:



The reactants are carried by diffusion and/or convection to the catalyzed electrode surfaces where electrochemical reactions take place. Water and waste heat generated by the fuel cell must be removed continuously. Otherwise, PEM may cause critical problems for fuel cells. The maximum electrical energy output and the voltage difference between the cathode and the anode are obtained when the fuel cell is operated under thermodynamically reversible conditions. This maximum possible cell potential is called “reversible cell potential”. The net output voltage of a fuel cell at a given current density is the reversible potential minus the irreversible potential and can be written as:

$$V(i) = V_r - V_{irr} \tag{4}$$

Here V_r is the maximum voltage of the fuel cell (i.e., = E_r) and V_{irr} is non-reversible voltage loss (i.e, over-voltage) occurring in the fuel cell. The actual work in the fuel cell is less than the maximum useful work due to other irreversible processes in the process. The irreversible voltage loss is indeed the summation of activation potential (v_{act}), ohmic over-voltage (v_{ohmic}) and concentration over-voltage (v_{consan}) and it is represented by the following equations:

$$V_{overvoltage} = V_{irr} = v_{act} + v_{ohmic} + v_{consan} \tag{5}$$

$$V(i) = V_r - v_{act_a} - v_{act_c} - v_{consan_a} - v_{consan_c} - v_{ohmic} \tag{6}$$

As can be seen from Eqn. 6, activation polarization (v_{act_a} and v_{act_c}) and concentration polarization (v_{consan_a} and v_{consan_c}) occur at both in the anode and cathode, while the resistive polarization (v_{ohmic}) represents ohmic losses across the fuel cell. The equation for the fuel cell polarization curve is the relationship between fuel cell potential and current density. It can be written as follows:

$$E = E_r - \frac{RT}{\alpha_c F} \ln\left(\frac{i}{i_{0,c}}\right) - \frac{RT}{\alpha_a F} \ln\left(\frac{i}{i_{0,a}}\right) - \frac{RT}{nF} \ln\left(\frac{i_{L,c}}{i_{L,c}-i}\right) - \frac{RT}{nF} \ln\left(\frac{i_{L,a}}{i_{L,a}-i}\right) - iR_i \tag{7}$$

where E_r is the standard reversible voltage, R is the ideal gas constant, T is the absolute temperature, F is the Faraday constant, n is the number of moles of electrons transferred per fuel consumed, α is the charge transport constant, $i_{L,a}$ and $i_{L,c}$ are the limiting current density at the anode and cathode, and i is the operating current density of fuel cell, respectively.

3. Results and Discussion

3.1. Voltage losses from activation

Although many progresses have been achieved in the area of electrode kinetics, however, it is clear that methods still need to be developed to fully understand the anode and cathode kinetics. The electrochemical reactions that occur in the anode and cathode when modeling fuel cells need to be understood as they control the power generation rate and cause activation voltage losses. The over-voltage required to cross the energy barrier for the electrochemical reaction to take place is called polar activation polarization. Such polarization dominates losses at low current density and measures catalyst activity at a given temperature. The catalyst lowers the height of the activation barrier but causes voltage loss due to the slow oxygen reaction. The total activation polarization over-potential generally ranges from 0.1 to 0.2 V, which reduces the maximum potential to less than 1.0 V even in open circuit conditions. Activation over-potential expressions can be derived from the Butler-Volmer equation. In PEM fuel cells, the anode for hydrogen oxidation is very high compared to the cathode for oxygen reduction. Therefore, the contribution of the cathode to activation polarization is often neglected.

The parameters in the equations to be used in polarization and power curves modeling for the fuel cell are: cell area, hydrogen pressure, air pressure, temperature, Faraday constant, ideal gas constant, internal resistance and Gibbs energy in liquid state (J/mol). The parameters and their values used in the present study for the simulation of polarization and power curves are given in Table 1.

Table 1. The parameters and their values used in the present study for the simulation of polarization and power curves

Parameters	Values
Ideal gas constant (R)	8.314 J/molK
Faraday's constant (F)	96487 Columbs
Hydrogen pressure	2 atm
Air pressure	2 atm
Cell area	55 cm ²
Number of cells	1
Inner resistance	0.245 Ohm-cm ²
Charge transport constant	0.4
Amplification constant	0.1
Exchange current density	10 ^{-9.486} (A/cm ²)
Limiting current density	1.5 (A/cm ²)
Gibbs energy	-228170 (J/mol)
Mass transport constant	1.1
Ideal gas constant (R)	8.314 J/molK

In this study, activation losses in anode and cathode as function of temperature and current density were simulated with Matlab® Simulink program. The variation of activation loss was investigated for 4 °C increased temperature values in the range 40 to 80 °C and increased current density values in the range 0 to 1.1 A / cm². As shown in Figure 1, the loss resulting

from activation increases linearly with temperature, while a functional change as in the graph is observed with the current density. The increased temperature appears to cause a voltage drop in the activation polarization zone.

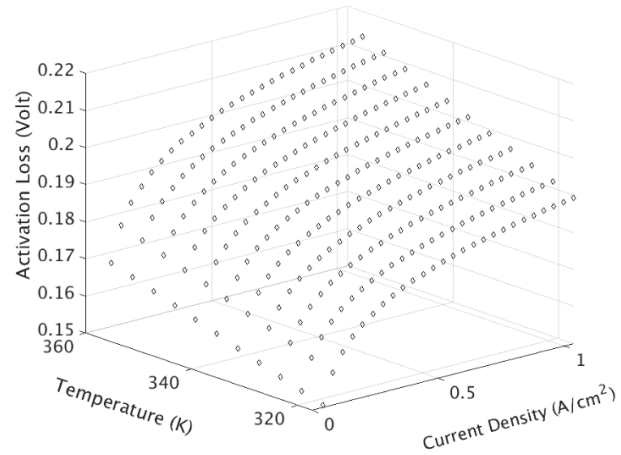


Figure 1. Change of activation loss with respect to current density (A/cm²) and temperature (K).

3.2. Ohmic losses

The voltage loss due to the charge carrying resistance of electrons and ions, which are charged particles, is defined as “ohmic losses”. General methods of reducing ohmic losses are to make the electrolytes as thin as possible and to use high conductivity materials that are well connected to each other. In this study, the ohmic loss was simulated by using the effective surface area of the fuel cell, the thickness of the electrolyte layer and electrical conductivity parameters. The obtained result is shown in Figure 2. The change in ohmic loss was investigated by increasing the cell area with 10 in the range of 50 to 100 cm² and the current density with 0.1 in the range of 0.1 to 1.1 A. As shown in the graph, ohmic loss is very sensitive to current density and surface area of the cell. At the same time 5 different thickness electrodes were used to see how this sensitivity of ohmic loss changes with the thickness of the electrode. In order to see the effect of electrolyte thickness in detail, the change in ohmic loss according to the current density for a 100 cm² cell is shown in Figure 3. It is clear that ohmic loss increases with respect to electrolyte thickness.

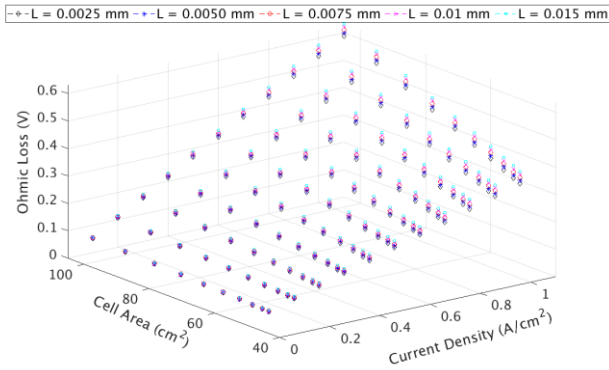


Figure 2. Change of ohmic loss as a function cell area (cm²) and current density (A/cm²)

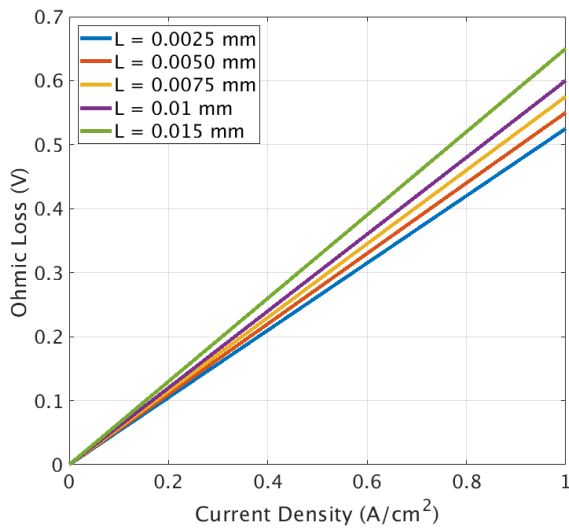


Figure 3. Change of ohmic loss (V) with respect to current density (A/cm²) for an electrolyte having different thicknesses.

3.3. Voltage losses from concentration

When a fuel cell is filled by fuel and oxygen generates electricity, the product water must be continuously removed to maintain efficiency and provide appropriate fuel and oxidant in the catalyst layers. Another source of voltage losses is mass transport constraints, which can significantly affect fuel cell performance. Losses caused by mass transport are also called “concentration losses”. In the simulations performed in this study, the limiting current density values in the cathode and anode were taken as 1.5A/cm².

The polarization curve and the power curve with respect to the different operating temperatures obtained using the Matlab® Simulink program are shown in Figure 4.

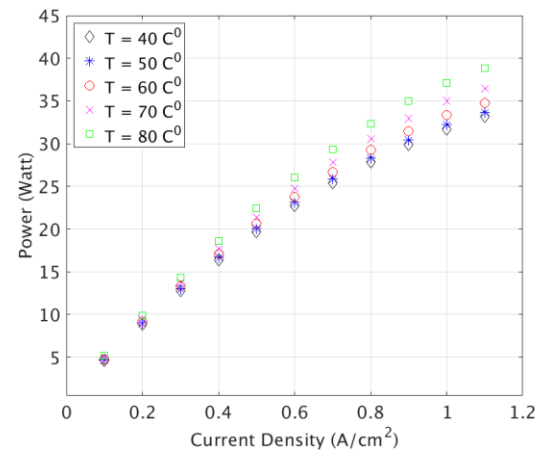
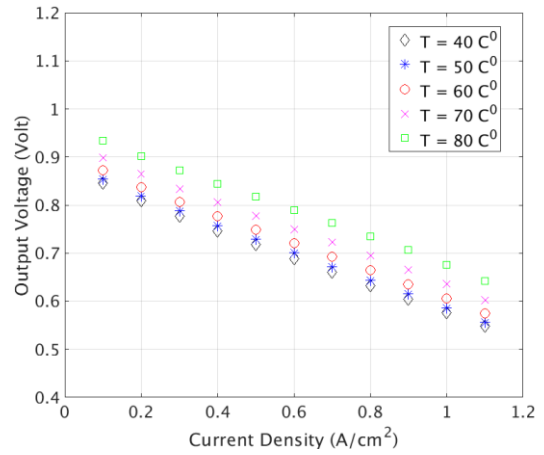


Figure 4. a) Polarization curves and b) power curves obtained for a PEM type fuel cell at different temperatures

These curves may not exactly match the actual curves obtained for a fuel cell stack. However, it is a good start to perform simulation of a PEM fuel cell. Individual modeling of the structure of the proton exchange, the gas diffusion layer, the catalyst layers and the fuel flow plates for a complete PEM fuel cell simulation will allow for more realistic polarization and power curves.

4. Conclusion

With a wide range of applications, from dynamic mobile systems to stationary systems, PEM fuel cells are one of the potential tools for generating clean energy. Although it has important features such as wide usage range and high efficiency, it has a disadvantage in terms of durability and cost. In order to compete with other power systems today, many studies focus on reducing PEM fuel cell costs and better durability. It is important to model and simulate these technological developments before the application.

In this study, our aim is to simulate voltage losses that can occur in PEM fuel cells by considering the various operating temperatures and thickness of electrodes.

According to the simulation, the increased temperature leads to a voltage drop in the activation polarization. As a result, to derive a final decision on the PEM fuel cell properties, all the parameters need to be taken into account during the simulation.

Acknowledgment

This study was supported by the project performed in Adiyaman University Scientific Research Fund (ADYUBAP) with the grant number: FEFGAP/2018-0001.

Conflicts of interest

The authors state that did not have conflict of interests.

References

- [1] Miller B. G., Clean coal engineering technology, Coal as fuel: past, present, and future, 1st ed. Boston: Butterworth-Heinemann, (2011) 1-51.
- [2] Zou C., Zhao Q., Zhang G., Xiong B., Energy revolution: From a fossil energy era to a new energy era, *Natural Gas Industry B*, 3(1) (2016) 1-11
- [3] Staffell I., Scamman D., Abad A.V., Balcombe P., Dodds P.E., Ekins P., Shah N., Ward K.R., The role of hydrogen and fuel cells in the global energy system, *Royal Society of Chemistry-Energy Environ. Sci.*, 12(1) (2019) 463-491.
- [4] Harting C., Jörissen L., Kerres J., Lehnert W., Scholta J., Polymer electrolyte membrane fuel cells, *Materials for Fuel Cells*, Woodhead Publishing Series in Electronic and Optical Materials, 8(3) (2008), 101-184.
- [5] Panwar N.L, Kaushik S.C., Kothari S., Role of renewable energy sources in environmental protection: A review, *Renewable and Sustainable Energy Reviews*, 15 (2011) 1513–1524.
- [6] Fahmy F.H., Abdel-Rehim Z.S., Hydrogen gas production an dutilization as electricity using a renewable energy source. *Energy Sources, Part A: Recovery, Utilization, and Environmental Effects*, 21(7) (1999) 629–641.
- [7] Bauen A., Foradini F., Hart D., Fuel Cell-Based Renewable Energy Supply: Sustainable Energy for Isolated and Island Communities. In: Afgan N.H., Carvalho M.G., (Eds). *New and Renewable Technologies for Sustainable Development*. 1st ed. Boston: Springer, (2002) 421-428 .
- [8] Bauen A., Hart D., Assessment of the environmental benefits of transport and stationary fuel cells, *Journal of Power Sources*, 86 (1-2) (2000) 482-494.
- [9] Wang Y., Chen K.S., Mishler M., Cho S.C., Adrohera X.A., A review of polymer electrolyte membrane fuel cells: Technology, applications, and needs on fundamental research, *Applied Energy*, 88(4) (2011) 981-1007.
- [10] Peighambardoust S.J., Rowshanzamir S., Amjadia M., Review of the proton exchange membranes for fuel cell applications, *International Journal of Hydrogen Energy*, 35 (17) (2010) 9349-9384
- [11] Elmacı G., Ertürk A.S, Sevim M., Metin Ö., MnO₂ nanowires anchored on mesoporous graphitic carbon nitride (MnO₂@mpg-C₃N₄) as a highly efficient electrocatalyst for the oxygen evolution reaction, *Journal of Hydrogen Energy* 44 (33) (2019) 17995-18006.
- [12] Elmacı G., Frey C.E., Kurz P., Zümreoğlu-Karan B., Water oxidation catalysis by using nano-manganese ferrite supported 1D-(tunnelled), 2D-(layered) and 3D-(spinel) manganese oxides, *Journal of Materials Chemistry A* 4 (22) (2016) 8812-8821.
- [13] Elmacı G., Frey C.E., Kurz P., Zümreoğlu-Karan B., Water Oxidation Catalysis by Birnessite@Iron Oxide Core-Shell Nanocomposites, *Inorganic Chemistry*, 54 (6) (2015) 2734-2741.
- [14] Elmacı G., Microwave Assisted Green Synthesis of Ag/AgO Nanocatalyst as An Efficient OER Catalyst in Neutral Media, *Hittite Journal of Science & Engineering*, 7 (1) (2020) 61-65.
- [15] Djilali N., Computational modelling of polymer electrolyte membrane (PEM) fuel cells: Challenges and opportunities, *Energy* 32 (2007) 269–280.
- [16] Najafi N., Dipenta D., Bencherif K., Sorine M., Modeling and simulation of a reformatte supplied PEM fuel cell stack, application to fault detection, *HAL Applications and Tools of Automatic Control*, 21 (1) (2007) 1-18.
- [17] Kone J.P, Zhang X., Yan Y., Hu G., Ahmadi G., CFD modeling and simulation of PEM fuel cell using OpenFOAM, *Energy Procedia*, 145 (1) (2018) 64-69.
- [18] Yuan W., Tang Y., Pan M.Q., Li Z.T., Tang B., Model prediction of effects of operating parameters on proton exchange membrane fuel cell performance, *Renewable Energy*, 35 (2010) 656-666.
- [19] Salam A.A., Mohamed A., Hannan M.A., Modeling and Simulation of a PEM Fuel Cell System Under Various Temperature Conditions, 2nd WSEAS/IASME International Conference on Renewable Energy Sources (Res'08) Corfu, Greece, October 2008, 26-28.

- [20] Djilali N., Lu D., Influence of Heat Transfer on Gas and Water Transport in Fuel Cells, *Int. J. Therm. Sci.*, 41 (1) (2002) 29-40.
- [21] Musser J., Wang C.Y., Heat Transfer in a Fuel Cell Engine, Proceedings of NHTC'00, 34th National Heat Transfer Conference, Pittsburgh, 2000, 1-7.
- [22] Verbrugge M.W., Hill R.F., Transport Phenomena in Perfluorosulfonic Acid Membranes During the Passage of Current, *J. Electrochem. Soc.*, 137 (4) (1990) 1131-1138.
- [23] Springer T.E., Zawodzinski T.A., Gottesfeld S., Polymer Electrolyte Fuel Cell Model, *J. Electrochem. Soc.*, 138 (8) (1991) 2334-2342.
- [24] Fuller T.F., Newman J., Water and Thermal Management in Solid-Polymer-Electrolyte Fuel Cells, *J. Electrochem. Soc.*, 140 (5) (1993) 1218-1225.
- [25] Nguyen T.V., White R.E., A Water and Heat Management Model for Proton-Exchange-Membrane Fuel Cells, *J. Electrochem. Soc.*, 140 (8) (1993) 2178-2186.
- [26] Woehr M., Bowlin K., Schnurnberger W., Fischer M., Neubrand W., Eigenberger G., Dynamic Modeling and Simulation of a Polymer Membrane Fuel Cell Including Mass Transport Limitation, *Int. J. Hydrogen Energy*, 23 (2), (1998) 213-218.



Analysis and calculations of decentration amount and prism in eyeglass lenses

Hülya KURU MUTLU^{1,*} , Naci EKEM² 

¹Eskisehir Osmangazi University, Health Service Vocational School of Higher Education, Opticianry Program/Eskisehir, TURKEY

²Eskisehir Osmangazi University, Faculty of Arts and Sciences, Department of Physics, Eskisehir/TURKEY

Abstract

The error of refraction is a very common eye disorder. Untreated vision problems put a lot of burden on the global economy annually. One of the most important parameters in the correct treatment of visual defects is the correct assembly of the focal point of the glass. The study was carried out to reveal the decentration differences and the analysis of prism formation after glass assembly according to the prescriptions of 150 customers who came to an optical shop in Eskisehir on Saturdays, 2015-2016. A digital lensmeter was used for the measurement of glasses, and a digital and photographic pupillometer was used to measure pupillary distances. Chi-square test was used in the frequency study, and differences in glass numbers were used the Marginal Homogeneity Test was used in the analysis of the accuracy of the data. Glass assemblies without decentration were achieved at a rate of 94.66% in distance glasses and 93.33 % in near glasses. When the errors made in applied physics are analyzed, the amount of decentration in the assembly of the glasses that are frequently used in daily life draws attention. In this case, it caused unwanted prism formation.

Article info

History:
Received: 16.01.2021
Accepted: 12.03.2021

Keywords:
Decentration amount, prismatic effect, Chi-square test, Marginal homogeneity test, spectacle glass errors.

1. Introduction

Globally, approximately 1.3 billion people are estimated to experience some form of visual impairment. 441.5 million People have visual impairment with regard to distance vision. Also, 826 million people suffer from near vision. 80% of visual impairment can be prevented [1, 2]. Top reasons of visual impairment are uncorrected refraction errors.

The error of refraction is a very common eye disorder. It occurs when the eye cannot clearly focus the images in the outside world. The result of refraction errors is blurred vision, sometimes severe enough to cause visual impairment [3]. According to W.H.O., untreated vision problems cost the global economy \$ 200 billion annually [4].

Uncorrected refractive errors are one of the most important causes of preventable blindness in undeveloped or underdeveloped societies [5]. Therefore, when these refractive errors are not corrected or are wrongly corrected, they become an important health problem globally that causes serious health disorders [3, 6-8]. Uncorrected refractive defects lead to asthenopic symptoms such as pain,

eyestrain and frontal headaches [9-11]. The number of people suffering from these complaints is very high.

If the corrective glasses are not installed correctly, a person experiencing difficulties with vision has trouble performing routine daily activities such as reading, writing, socializing, traveling and work life [12]. As a result, because the person's quality of life decreases, the person can become unhappy, stressed, and so on. which sometimes, it can cause various accidents at home, at work, at school[13].

When people go optic store to buy corrective glasses, they generally think various factors such as frame color, model and design [14-16]. But the main point to be considered here is personal measurement. As your personal measurement, the distance between the pupils (IPD) is defined as the distance between the centers of the pupils [14, 17].

Transferring the patient's personal measurement data to the frame and overlapping and assembling the glasses provided on the prescription with this data will prevent possible unwanted prismatic effects. However, in the case of troubles such as dioptric changes, axial

differences and mismatch of the pupil and optical axis, machine errors, the image of an object will be perceived at a different location from the actual location (prismatic effect) [18-20]

The other important point that can cause prismatic effect is that the measurement of the exact center of the pupil is very difficult because the proper parallelity cannot be provided between the floor and the ruler [14].

In this study, in order to correct the refractive errors properly, we have measured and statistically analyzed the reasons of the unwanted prismatic effects that occur when the optician is installing the glass to the frame. Taking data from a digital and photographic pupilometers, and the prismatic effects were calculated from the resulting differences. Unwanted prismatic effects are calculated with Prentice's rule [21, 22].

Our aim is to calculate the mistakes made by raising awareness about faulty eyeglass mounting that causes financial losses and health problems worldwide. A database has been created by performing prismatic effects, optical characterization and surface analysis of the glasses of glasses wearers who have been assembled glasses. Optical prism calculations made regarding the optic store in terms of being the first study in Turkey are expected to lead to other studies.

2. Materials and Methods

The study was carried out for decentration calculations and analysis as a result of the analysis of the glass values assembled according to the prescriptions of 150 customers who visited an optical store in Eskisehir on Saturday 2015-2016. The aim of the study is to check the conformity of the glasses mounted by the optician to the prescription and to calculate the prism values formed. 150 people participated in the study and there is no one among them whose data were not obtained. Out of a total of 361 glasses in the study, 214 were distant glasses and 147 were close to lenses.

In order for the results of the study to be interpreted by physics, opticianry, statistics departments, a form was created. In this form, it consists of the measurement values taken by the optician for the glass assembly and the glass values taken after the assembly.

The measurement of the glasses was taken with lensmeter (LM-1000P model, Nidek brand) [23]. The values in the prescription and the lensmeter measurement values of the glasses made by the optician were noted on the form and all data were entered into the SPSS program. Marginal Homogeneity test [24] was used to statistically

evaluate the accuracy of sph, cyl, ax values of the glasses written in the recipe and assembled. The difference between glass numbers causes prism and makes an important contribution to the decentration calculation [21].

Another major assembly error is that the distance between pupillary points is not measured accurately. The distance of difference between the focal point of the glass and the pupillary point is another parameter that contributes to decentralization. The distance between the pupils was measured with the Digital Pupilometer [25], Nidek brand PM-600 model and Photometric Focusing Measuring Device, Elegance Mirror Marked. Data entered into the SPSS.

Chi-square test was used in the frequency study [26], and the Marginal Homogeneity Test was used in the analysis of the accuracy of the data. $P < 0.001$ was used considered significant.

The surface images of the glasses presented to the glasses wearers in the optician store were taken with the Zeiss Ultra Plus model FESEM. To obtain FESEM images, the glasses were coated with 30 nm gold (Au) at 50 mA for 2 minutes.

For the optical characterization of the glasses, absorption-transmittance measurements were taken using 4802 UV / VIS Dual Beam Spectrophotometer, the data were marked as Pro 8 origin and graphics were created.

3. Results

61 (40.7 %) are male and 89 (59.3 %) are female of the participants. When the ages of the participants are examined, the smallest participant is 5 years old and the largest is 88 years old. According to Table 1, the average age of the participants is 45.47.

Table 1. Descriptive Statistics for Age

N	Average age	Standard Error
150	45.470	1.654

The distribution of age groups is as shown in Table 4. There are 10 persons in the age range of 5-14 years, 23 persons in the age range of 15-24 years, 14 persons in the age range of 25-34 years, 18 persons in the age range of 35-44 years, 37 persons in the range of 45-54 years, 16 persons in the range of 55-64 years, 21 persons in the age group of 65-74, and 11 persons in the age group of 75 and over.

Table 2. Distribution between distant glass and close glass groups

Glass group	Distant Glass		Close Glass	
	Number	%	Number	%
0-2	57	19.0	32	10.6
2-4	16	5.3	48	16.0
4-6	2	0.7	6	2.0
14-16	2	0.7	-	-
2/2	78	26.0	10	3.3
2/4	3	1.0	4	1.3
4/2	34	11.3	34	11.3
4/4	8	2.6	2	0.7
6/2	9	3.0	10	3.3
6/4	3	1.0	-	-
8/2	1	0.3	-	-
8/4	1	0.3	-	-
No Prescription	86	28.6	153	51.0
Total	300	100	300	100

When Table 2 is examined, it is found that the number of 2/2 spherocylindrical glass group used by the optician is 78 and it is the most used glass, constituting 26.0% in the distant glasses. 0-2 spherical glass group constitutes 19.0% (57 pieces) of the distant glasses and it is the most used second glass group. Statistically, there was no significant difference between the groups of distant right and left glasses ($p = 0.921$). No Prescription statement in the last line means that the doctor did not write the distant prescription value in the prescription and wrote the close prescription value.

In the distribution of the close right-left glass group written in the prescriptions of the participants of the

Table 3. Distribution between Distance Glass Group and Axis Value

Axis value	Distant Right Glass	Distant Left Glass	Total
	Number	Number	Number
0°-45°	13	16	29
46°-90°	19	22	41
91°-145°	14	7	21
146°-180°	24	22	46
Total	70	67	137

Table 3 gives the distribution of the distant glass axis. 46 of the astigmatic refraction defect have axis values between 146°-180°, 41 between 46°-90°, 29 between 0°-45°, and 21 between 91°-145°. Statistically, there is no difference between the distant right and left glass axes (Chi-square test, $p = 0.410$).

The glasses assembled by the optician did not show any change in the right and left glasses in reverse. This is a positive development because otherwise it would cause unwanted prism.

study (Table 2), while 48 (16.0%) constitutes spherical glass groups, the second 34 (11.33 %) constitutes spherocylindrical glass group. Statistically, p value between the right and left glass groups in the prescription was 0,785 and no difference was found.

When the glass group frequency distributions are examined (Table 2), when the close spectacle glass values have higher value, it will have more prismatic effect when faulty glass assembly is done. Therefore, it is necessary to assemble close glass more carefully than distant glass.

At firstly, glasses were measured with lensmeter after assembly. All data were entered into the SPSS. Prescription values and post-assembly values of the glasses were compared with Marginal Homogeneity Test. Statistical coherence analysis of the sph, cyl and axial values are shown in Table 4. Although the glass and axis values were not in full agreement, the statistical coherence analysis results showed that $p > 0.05$ ie values are in harmony and small number changes. It has been observed that small variations in glass numbers will produce a small amount of unwanted prism.

Table 4. Lens number differences resulting from measuring the glasses

Lens	p-Sph	p-Cyl	p-Axial
D-R	1.00	1.00	0.414
D-L	0.317	1.00	0.329
C-R	0.317	1.00	1.00
C-L	0.317	1.00	0.317

*D:distant C:Close R:Right L:Left *Marginal Homogeneity testi

Axis differences resulting from measuring the glasses with a lens meter after assembly were determined (Table 5). 0° axis change is in 67 people with distant right glass assembly, in 64 people with distant left glass assembly, in 31 people with close right glass assembly

and in 29 people with close left glass assembly, in total 191 people. According to the Prentice rule, the angle change distribution contributes to the formation of undesirable prisms [21, 22].

Table 5. Axis differences resulting from measuring the glasses

Axis change	D-Right Glass	D- Left Glass	C- Right Glass	C- Left Glass	Total
	Number	Number	Number	Number	Number
0°	67	64	31	29	191
1°	2	0	0	0	2
2°	1	2	0	0	3
5°	0	1	0	1	2
Total	70	67	31	30	198

D-R: Distant Right D-L: Distant Left C-R: Close Right C-L: Close Left

Other axis changes cause a prismatic error and are calculated with the formula given below. α stands for required angle difference between the meridian and the axle value D_{cyl} for the cylindrical glass value of the glasses, D_{sph} for the spherical glass value of the glasses. D_T , stands for the power of the glasses, prismatic effect Δ , the resultant of the distance of the pupil point to the desired point in cm, can be calculated after measuring (Equations 1,2).

$$D_T = D_{sph} + D_{cyl} \sin^2 \alpha \tag{1}$$

$$\Delta = D_T C \tag{2}$$

After the glasses were mounted, the pupil measurement of the user was taken and compared with the measurement of the optician. The pupil

measurements were measured with the pupilometer. The differences between the pupil values cause prismatic faults according to Equation 1.2 above. For this reason, the decentralization differences between the pupil values are given in Tables 6, 7.

When Table 6 is examined, the amounts and directions of decentralization are seen for the distant glasses. The glasses were assembled without any problems for 142 people with distant right glasses, 143 people with distant left glasses. There is no decentralization for the right and left eyes in the upward and outward directions. Decentralization in the downward direction was observed in 0.66% of the total glasses, that is for only 1 person. Decentralization in the inward direction was observed for 7 people in the right eyes and 6 people in the left eyes.

Table 6. Decentralization amount and directions of distant glasses

Directions	Decentralization amount (cm)	0		0.1 – 0.5		0.6 – 1.0	
		Number	%	Number	%	Number	%
Centralize	D-R	142	94.66	0	0.0	0	0.0
	D-L	143	95.33	0	0.0	0	0.0
Upward	D-R	150	100.0	0	0.0	0	0.0
	D-L	150	100.0	0	0.0	0	0.0
Downward	D-R	149	99.33	1	0.66	0	0.0
	D-L	149	99.33	1	0.66	0	0.0
Inward	D-R	143	95.33	5	3.33	2	1.33
	D-L	144	0.96	6	4.0	0	0.0
Outward	D-R	150	100.0	0	0.0	0	0.0
	D-L	150	100.0	0	0.0	0	0.0

D-R: Distant Right D-L: Distant Left

Table 7 shows the amounts and directions of decentralization of close glasses. Of all close glasses, 149 are faultless. There is decentralization in the upward direction in the 2 glasses which constituted 1.32% of the close glasses. No decentralization is seen in downward, inward, and outward directions.

Table 7. Decentralization amount and directions of close right and left glasses

Decentralization amount (cm)		0		0.1 – 0.5		0.6 – 1.0	
Directions		Number	%	Number	%	Number	%
Centralize	C-R	149	99.33	0	0.0	0	0.0
	C-L	149	99.33	0	0.0	0	0.0
Upward	C-R	149	99.33	1	0.66	0	0.0
	C-L	149	99.33	1	0.66	0	0.0
Downward	C-R	150	100.0	0	0.0	0	0.0
	C-L	150	100.0	0	0.0	0	0.0
Inward	C-R	150	100.0	0	0.0	0	0.0
	C-L	150	100.0	0	0.0	0	0.0
Outward	C-R	150	100.0	0	0.0	0	0.0
	C-L	150	100.0	0	0.0	0	0.0

C-R: Close Right C-L: Close Left

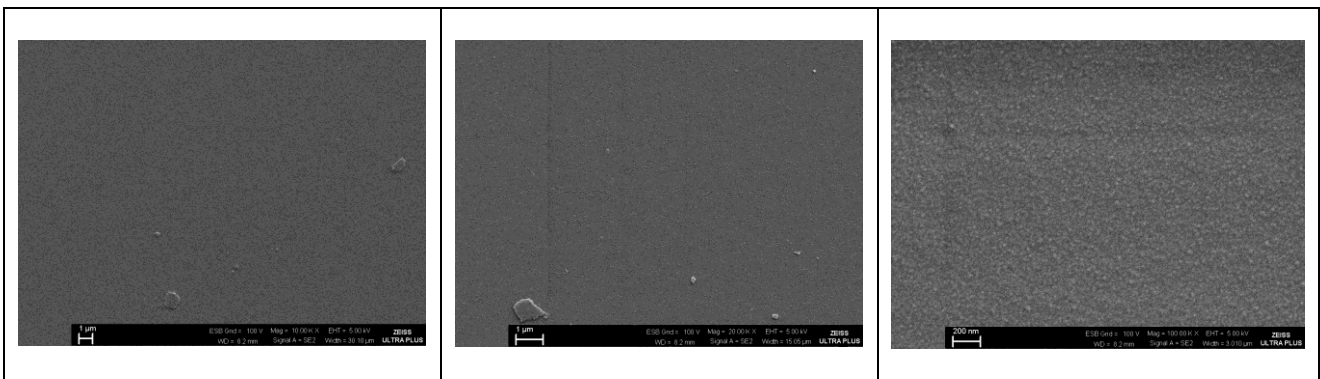


Figure 1. FESEM image of the lens at 10000, 20000, 100000 magnifications

Examining the spectacle lens analysis of eyeglass wearers (Figure 1), it is seen that the glass surfaces are quite smooth and homogeneous at 10000 and 20000 magnifications. When FESEM analyzes are examined at 100000 magnifications, ridges of about 20-25 nm in size appear. The eyeglass lenses are quite smooth and homogeneous compared to other glass works [29-31].

When the uncoated and coated glasses of eyeglass lenses were examined (Figure 2), it was observed that

the light transmittance of coated glasses increased in the entire spectrum. While uncoated glasses have 85% light transmittance at 550 nm, light transmittance has increased to 97 % in anti-reflective glasses. When looking at similar studies [29,30], the spectra of the glass contributed positively to the quality of vision and did not cause a prismatic effect. The fluctuations in the spectrum in similar studies are not seen in our study, and the smoothness of the spectrum increased the vision quality of the eyeglass wearer.

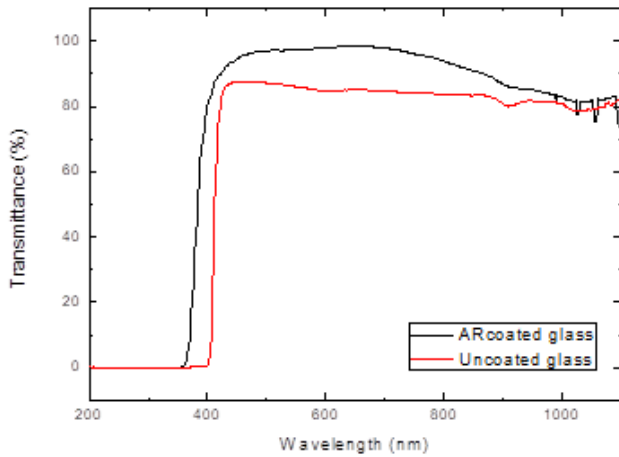


Figure 2. Transmittance graphs of lenses

When Figure 3 is examined, it is seen that two types of glass absorb in the UV region. It can be said that anti-reflective glasses absorb more in the UV region than normal glasses.

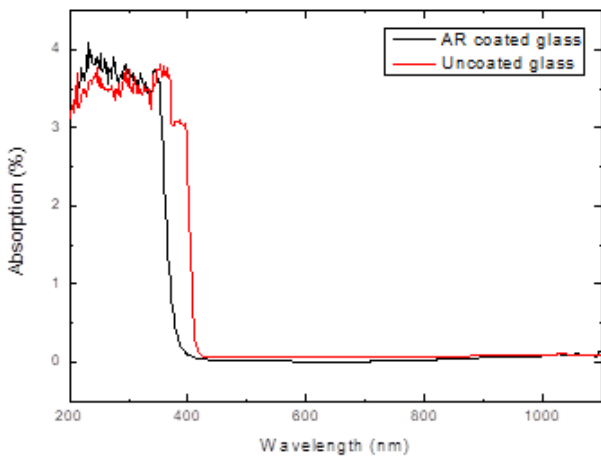


Figure 3. Absorption graphs of lenses

4. Conclusion and Recommendations

In this study, decentralization calculations and analyzes were performed as a result of glass analysis after assembly according to the prescriptions of 150 customers who visited an optical store between 2015 and 2016. The optician made mistakes while assembling the glass and measuring the pupillary distance. These errors arise from various difficulties [14, 17] and cause the unwanted prismatic effect [21, 22] to occur.

A study [27] similar to our study tested the accuracy of glasses on 100 people on a campus. There is a prismatic effect caused by faulty assembly in 100% of the glasses used by people. The difference of this study from our study is that it includes user errors as well as errors caused by the optician.

In another study [28] similar to our study, it is the calculation of the prismatic effects of glasses wearers who come to the hospital. In this study, a statistically significant difference was found due to the fact that pd values were not written on the prescription, the users went to different opticians and the opticians did not measure the pd distance ($p < 0.001$).

When the data are examined, it is seen that the amount of decentration is very low. When glass numbers were also included, low prismatic effects occurred. According to other studied [18, 25, 27, 28] in the literature, one of the important points of observing low prismatic effects in our study is due to the careful use of the pupilometer during assembly and the more careful assembly because we are with the optician. Faults that occur despite careful assembly are caused by the suction pads getting wet and slipping during the cutting phase in the automatic glass cutting machine.

The use of non-parallel pupilometer to measure the distance between pupils causes pupil measurement errors. To avoid this, photographic and digital Pupilometer with the same length working with sensors had been used in the pd measurements. With this system, which is not used in most optical stores, we have prevented many of the errors.

Since the education status of each optician and the facilities available in his shop are not the same, different decentrations will occur during the welding of the eyeglass lenses, which will create an undesirable prismatic effect. Therefore, the results will differ when the study is done in different optical facilities.

When the surface analysis, transmittance and absorption spectra of the glasses worn by the eyeglass wearers were examined, it was seen that the wearer's vision quality increased and did not cause prismatic effects.

In the literature, there is no study in the optic shop related to the decentration calculation after prescription and eyeglass assembling and the statistical analysis of distant-close lens groups. Prismatic effects, optical characterization and surface analysis of the users were made. In this case, it will shed light on the studies of optics in optician programs, which have been developing rapidly recently, where physicists work.

Acknowledgment

This study was produced from the PhD thesis, and I would like to thank Prof. Dr. Suat PAT and Prof. Dr. Müjdat ÇAĞLAR for opportunity to take measurements of my samples. Thanks to Prof. Dr.

Setenay Kevser Dincer Oner for contributions regarding the statistics used.

Conflicts of interest

The authors state that did not have a conflict of interests.

References

- [1] Bourne R.R.A., Flaxman S.R., Braithwaite T., Cicinelli M.V., Das A., Jonas J.B., Keeffe J., Kempen J.H., Leasher J., Limburg H., Naidoo K., Pesudovs K., Resnikoff S., Silvester A., Stevens G.A., Tahhan N., Wong T.Y., Taylor H.R., Grp V.L.E., Magnitude, temporal trends, and projections of the global prevalence of blindness and distance and near vision impairment: a systematic review and meta-analysis, *Lancet Global Health*, 5(9) (2017) 888-897.
- [2] Fricke T.R., Tahhan N., Resnikoff S., Papas E., Burnett A., Ho S.M., Naduvilath T., Naidoo K.S., Global Prevalence of Presbyopia and Vision Impairment from Uncorrected Presbyopia Systematic Review, Meta-analysis, and Modelling, *Ophthalmology*, 125(10) (2018) 1492-1499.
- [3] Organization W.H. *Blindness and vision impairment: Refractive errors*. 2013 08.01.2021]; Available from: <https://www.who.int/news-room/q-a-detail/blindness-and-vision-impairment-refractive-errors>.
- [4] Anonymous, *A Simple Way to Improve a Billion Lives: Eyeglasses*, in *The New York Times* 2018.
- [5] Pi L.H., Chen L., Liu Q., Ke N., Fang J., Zhang S., Xiao J., Ye W.J., Xiong Y., Shi H., Zhou X.Y., Yin Z.Q., Prevalence of Eye Diseases and Causes of Visual Impairment in School-Aged Children in Western China, *Journal of Epidemiology*, 22(1) (2012) 37-44.
- [6] Dandona R., Dandona L., Naduvilath T.J., Srinivas M., McCarty C.A., Rao G.N., Refractive errors in an urban population in southern India: The Andhra Pradesh Eye Disease Study, *Investigative Ophthalmology & Visual Science*, 40(12) (1999) 2810-2818.
- [7] Thorn F., Cruz A.A.V., Machado A.J., Carvalho R.A.C., Refractive status of indigenous people in the northwestern Amazon region of Brazil, *Optometry and Vision Science*, 82(4) (2005) 267-272.
- [8] Attebo K., Ivers R.Q., Mitchell P., Refractive errors in an older population - The blue mountains eye study, *Ophthalmology*, 106(6) (1999) 1066-1072.
- [9] Abdi S., Lennerstrand G., Pansell T., Rydberg A., Orthoptic findings and asthenopia in a population of Swedish schoolchildren aged 6 to 16 years, *Strabismus*, 16(2) (2008) 47-55.
- [10] Ayanniyi A.A., Folorunso F.N., Adepoju F.G., Refractive ocular conditions and reasons for spectacles renewal in a resource-limited economy, *BMC Ophthalmol*, 10 (2010) 12.
- [11] Borsting E., Chase C., Tosha C., Ridder W.H., 3rd, Longitudinal study of visual discomfort symptoms in college students, *Optom Vis Sci*, 85(10) (2008) 992-8.
- [12] Kosnik W., Winslow L., Kline D., Rasinski K., Sekuler R., Visual changes in daily life throughout adulthood, *J Gerontol*, 43(3) (1988) P63-70.
- [13] McGregor L.N., Chaparro A., Visual difficulties reported by low-vision and nonimpaired older adult drivers, *Hum Factors*, 47(3) (2005) 469-78.
- [14] Brooks C.W., Borish I.M., Measuring the Interpupillary Distance in System for Ophthalmic Dispensing, H. C.M., Editor, New York: Professional Press, (2007) 25-30.
- [15] Obstfeld H., *Spectacle Frames and their Dispensing in Clinical and Experimental Optometry*. 1997.
- [16] Sasieni L.S., *The Principles and Practice of Optical Dispensing and Fitting*, London: Butterworths, (1962).
- [17] Osuobeni E.P., Al-Fahdi M., Differences between anatomical and physiological interpupillary distance, *J Am Optom Assoc*, 65(4) (1994) 265-71.
- [18] Valiyaveetil B., Asmin P.T., Vallon R.K., Predictors of Unwanted Prismatic Effect Among Bespectacled Symptomatic Ammetropes (Refractive Error Less Than 4D) With Displaced Optical Centre. , *Delhi Journal of Ophthalmology*, 28 (2018) 29-31.
- [19] Jalie M., *Ophthalmic lenses and dispensing*, London: Butterworth - Heinemann, (2003) 39-52.

- [20] Khurana A., *Theory and practice of optics and refraction*. India: Elsevier 2008; pp190-191.
- [21] Shukla A.V., *Clinical Optics Primer for Ophthalmic Medical Personnel (A Guide to Laws, Formulae, Calculations, and Clinical Applications)*. USA: SLACK Inc. 1950.
- [22] Topliss W.S., *Optical dispensing & workshop practice*. London: Butterworths 1975.
- [23] Tomas J.E., Candela D.M., Amigot B.D., Rodriguez J.P., Ferri C.V., Information and Communication Technologies Applied to Learning the Use of the Lensmeter, *10th International Conference of Education, Research and Innovation (Iceri2017)*, (2017) 2281-2287.
- [24] Iki K., Yamasaki S., Test and Measure on Difference of Marginal Homogeneity between Several Square Contingency Tables, *International Journal of Applied Mathematics & Statistics*, 53(6) (2015) 1-9.
- [25] Tsalpatouros A., Panoudiamandi O., Papageorgiou C., Rambavillas A., Stefanis C., Uzunoglu N., Koutsouris D., Eye Pupil Diameter Measurement and Assessment Via a Novel Pupilometer System, *Technology and Health Care*, 2(3) (1994) 209-213.
- [26] Cidota M.A., Blind Separation for Speech Signals by Minimizing the Contingency Coefficient in the Chi-Square Independence Test, *Romanian Journal of Information Science and Technology*, 12(1) (2009) 3-12.
- [27] Moodley V.R., Kadwa F., Nxumalo B., Penceliah S., Ramkalam B., Zama A., Induced prismatic effects due to poorly fitting spectacle frames, *The South African Optometrist*, 70(4) (2011) 168-174.
- [28] Ilhan N., Dogan H., Ilhan O., Coskun M., Bulut B.T., Ersekerci T.K., Compatibility of spectacles with their prescriptions in central Anatolia, *Semin Ophthalmol*, 30(1) (2015) 29-35.
- [29] Mahadik D. B., Lakshmi R. V., Barshilia H. C., High performance single layer nano-porous antireflection coatings on glass by sol-gel process for solar energy applications. *Solar Energy Materials and Solar Cells*, 140 (2015) 61-68.
- [30] Yao L., He J. H., Broadband Antireflective Superhydrophilic Thin Films with Outstanding Mechanical Stability on Glass Substrates. *Chinese Journal of Chemistry*, 32(6) (2014) 507-512.
- [31] Yuan J. J., Yan S. Y., Zhang X., Superhydrophilic antifogging broadband antireflective coatings with worm-like nanostructures fabricated by one dip-coating method and calcination. *Applied Surface Science*, 506 (2020).

Numerical solutions of the randall-wilkins and one trap one recombination models for first order kinetic

Erdem UZUN ^{1,*} 

¹ Karamanoğlu Mehmetbey University, Department of Physics, 70200, Karaman / TURKEY

Abstract

Randall-Wilkins and One Trap One Recombination (otor) models have been proposed to explain thermoluminescence emission and it should be emphasized that each model has its own allowed charge carrier transitions, trapping parameters and differential equations set. The equations are generally first or higher order linear differential equations with constant coefficients and their numerical solutions are an initial value problem. From this point on, numerical solutions of the thermoluminescence equations have been effectively used. In this paper the models were solved, numerically by using Euler and Runge-Kutta methods on Mathematica 8.0. In this work, although the fastest result calculated by Explicit Euler method, the most accurate results were calculated Linearly Implicit Euler method.

Article info

History:
Received: 17.10.2020
Accepted: 18.03.2021

Keywords:
Thermoluminescence,
Simulation
Euler, Runge-Kutta,
Otor.

1. Introduction

Although differential equations proposed by thermoluminescence (TL) models are relatively basic, their analytic solutions are not possible. One of the ways to overcome the difficulty is to simplify the equations under various assumptions and the another is to perform numerical solutions. Numerical solutions of the TL equations are widely used in TL applications [1,2]. Pros and cons arguments of the numerical solutions of the TL equations were argued by McKeever[3] and many others[1,4]. The first numerical approximation of the TL equations was performed by Kemmeyer et al[5] but exact numerical solutions were given by Kelly et al[6] for the first time. Moreover, Shenker and Chen[7], Chen et al[8] and many others have published numerical solutions of the TL equations up to now.

In this paper we discuss numerical solutions of the Randall-Wilkins and otor models by using different numerical methods such as Euler's and Runge-Kutta methods. All solutions are performed in Mathematica 8.0.

2. Randall and Wilkins Model

The simplest model of TL emission is proposed by Randall and Wilkins and it consists of an electron trap level (N), and a recombination center^[9,10]. Randall and Wilkins assumed that recombination rate of the free charge carrier is significantly faster than re-trapping and thus, TL emission can be given as Eq.1. Energy

band diagram and allowed transitions are given in Fig. Figure 1.

$$I_{TL} = n.s.\exp\left\{-\frac{E_e}{k.T}\right\} \quad (1)$$

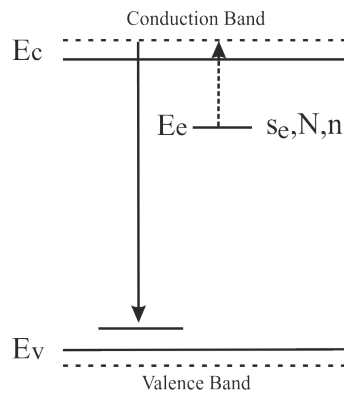


Figure 1. Schematic energy level diagram of Randall-Wilkins model

Here, N is trapping states (in cm^{-3}) and with instantaneous occupancy n. The activation energy for the electron trap is E_e (in eV) and the frequency factor is s_e (s^{-1}). k is the Boltzmann constant ($k = 8.617 \times 10^{-5}$ eV K^{-1})

3. OTOR Model

OTOR model consists of an electron trap level, and a recombination center (Fig. Figure 2), but there are three allowed transitions are available; trapped electrons can

*Corresponding author. e-mail address: erdemuzun@kmu.edu.tr
<http://dergipark.gov.tr/csj> ©2021 Faculty of Science, Sivas Cumhuriyet University

be released by thermally; free electrons are trapped by N or recombined in center^[11,12]. Differential equations representing the charge carrier traffic as a function of temperature and time are given:

$$\frac{dn_c}{dt} = n \cdot s_e \cdot \exp\left\{-\frac{E_e}{k.T}\right\} - n_c \cdot (N - n) A_{te} - n_c \cdot (n + n_c) \cdot A_{re} \quad (2)$$

$$\frac{dn}{dt} = n_c \cdot (N - n) A_{te} - n \cdot s_e \cdot \exp\left\{-\frac{E_e}{k.T}\right\} \quad (3)$$

$$I_{TL} = -\eta \cdot n_c \cdot (n + n_c) \cdot A_{re} \quad (4)$$

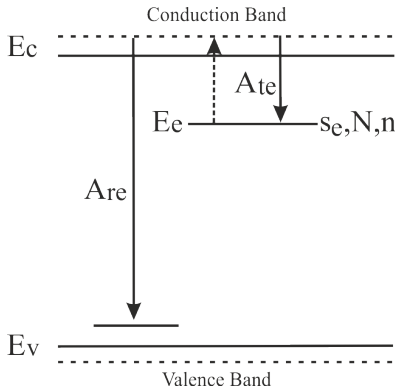


Figure 2 Schematic energy level diagram of OTOR model

Here, A_{te} and A_{re} are re-trapping and recombination probability coefficients. Moreover, if $A_{re}=1$ and $A_{te}=0$ are taken, OTOR model transforms into Randall and Wilkins model.

3.1. Experimental methods

Samples used in this study is α - Al_2O_3 powder. α - Al_2O_3 has four glow peaks[13,14] (Figure Figure 1) and the first peak is located at $117 \pm 2^\circ C$. The first peak has first ordered kinetic and it is used for the comparisons of the simulations. In order to isolate of the first peak, some experimental procedures are performed. Firstly, α - Al_2O_3 sample is annealed at $600^\circ C$ for 15 min to erase any residual radiation effects. Then, it is spread on thin aluminum disk about 10mg and it is irradiated at room temperature using the beta rays from a calibrated ^{90}Sr - ^{90}Y source. Glow curve of the sample is recorded between 40 - $400^\circ C$ temperature ranges using linear heating rate as reference. Thereafter, the annealing and irradiation procedure repeated and the sample is heated up to T_s and cooled to room temperature. Lastly, glow curve of the sample is recorded between 40 - $400^\circ C$ temperature ranges. Last glow curve is subtracted from the first one and the peak is obtained in isolated manner. The procedures are repeated several times for different T_s and T_s 's are chosen between $100^\circ C$ - $140^\circ C$. After then trap parameters are calculated by using peak

shape[4,15,16], various heating rate[4,17] and initial rise[4,18] methods. Moreover, initial trap occupancy was also measured by using area under the glow curve. Results are given in Table Table 1 and Figure Figure 4.

Table 1. Experimental trap parameters

	E_e (eV)	S_e (s^{-1})	b	n_0 ($cm^3 s^{-1}$)
FOK peak	0.89 ± 0.02	$2.17 \pm 0.07 \times 10^{10}$	1.00	1.18×10^5

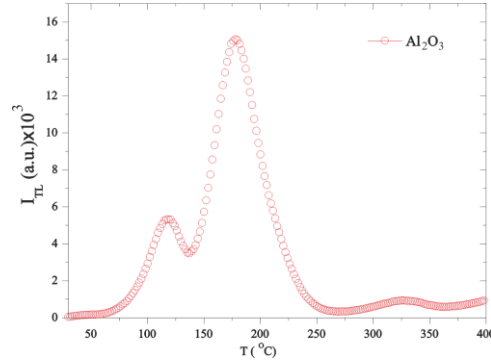


Figure 3. Thermoluminescence glow curve of the α - Al_2O_3

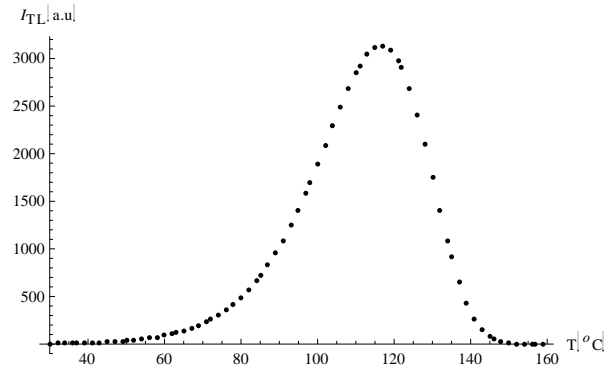


Figure 4. First peak of the α - Al_2O_3 used in this study

4. Numerical Analysis

In this study, all numerical solutions are calculated iteratively. Each solution is started from a given initial particular value of I_{TL} (n_0, n_{co}) at T_{min} , and then takes a sequence of steps, trying eventually to cover the whole range T_{min} to T_{max} . Experimental trap parameters (Table 1) are taken as initial conditions and other parameters such as A_{re} , A_{te} et al are chosen realistically but in a broad range. Numerical solutions of the equations are performed using Explicit Euler[19,20], Generalized Euler[19], Classical Runge-Kutta[21], and Implicit Runge-Kutta methods [21–23]. The techniques are summarized in Figure Figure 5. Simulations of the models are performed on Mathematica 8.0[24,25].

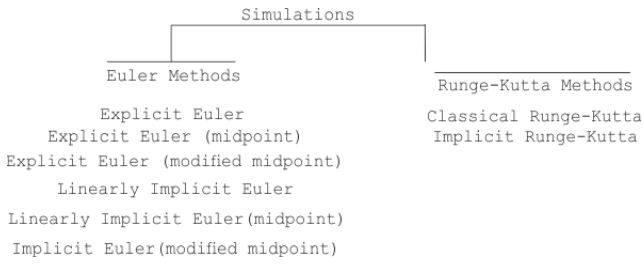


Figure 5. Numerical methods and sub methods used in this study

5. Results and Discussions

Numerical solutions of the models are performed for different step sizes and differential orders. In order to make comparison easier, figure of merit[26] (FOM) and step sizes are drawn together. All the simulations were performed by using experimentally measured trap parameters from Table Table 1. It is important to

Table 2. Although the Euler methods can simulate the Randall-Wilkins model by wide range of steps (10^{-1} -

point out that that although the numerical solutions of the TL models are successful in explaining some TL behaviors of the materials theoretically, they do not match the results of the experiments. However, Uzun[27–30] and many others[3,8,11] shown that the simulations are in good agreement with experiment only when the simulation is started with the assumption of $n_0=N$. Thus, $N=1.20 \times 10^5 \text{cm}^3 \text{s}^{-1}$ was taken in all the simulations.

Randall-Wilkins and OTOR models were solved numerically by using Explicit Euler, Explicit Euler (midpoint), Explicit Euler (modified midpoint), Linearly Implicit Euler, Linearly Implicit Euler (midpoint), Implicit Euler (modified midpoint), Classical Runge-Kutta and Implicit Runge-Kutta.

Randall-Wilkins model was solved numerically by using Explicit Euler methods and results are given in

10^{-4}), the methods can be solved the OTOR model for a restricted step range (step size $\leq 2.0 \times 10^{-5}$).

Table 2. Simulation results of the Explicit Euler

It. Nu.	St. Sz.	FOM	It. Nu.	St. Sz.	FOM
fok			otor		
1.59×10^3	10^{-1}	0.45(5266)	3.18×10^7	0.5×10^{-5}	0.29(0760)
1.59×10^4	10^{-2}	0.30(5387)	1.59×10^7	1.0×10^{-5}	0.29(0767)
1.59×10^5	10^{-3}	0.29(2113)	1.06×10^7	1.5×10^{-5}	0.29(0776)
1.59×10^6	10^{-4}	0.29(0889)	7.95×10^7	2.0×10^{-5}	0.29(0781)

Table 3. Simulation results of the Explicit Euler (midpoint)

It. Nu.	St. Sz.	FOM	It. Nu.	St. Sz.	FOM
fok			otor		
2.03×10^5	10^{-1}	0.29(0753912)	1.30×10^7	0.5×10^{-5}	0.29(0760)
2.03×10^5	10^{-2}	0.29(0753989)	1.30×10^7	1.0×10^{-5}	0.29(0767)
2.03×10^5	10^{-3}	0.29(0753945)	1.30×10^7	1.5×10^{-5}	0.29(0776)
2.03×10^5	10^{-4}	0.29(0754040)	1.30×10^7	2.0×10^{-5}	0.29(0781)

Table 4. Simulation results of the Explicit Euler (modified midpoint)

It. Nu.	St. Sz.	FOM	It. Nu.	St. Sz.	FOM
fok			otor		
3.05×10^5	10^{-1}	0.29(0753)	1.19×10^7	0.5×10^{-5}	0.29(0754)
3.05×10^5	10^{-2}	0.29(0753)	1.21×10^7	1.0×10^{-5}	0.29(0754)
3.05×10^5	10^{-3}	0.29(0753)	1.16×10^7	1.5×10^{-5}	0.29(0754)
3.05×10^5	10^{-4}	0.29(0753)	1.17×10^7	2.0×10^{-5}	0.29(0754)

Table 5. Simulation results of the Linearly Implicit Euler

It. Nu.	St. Sz.	FOM	It. Nu.	St. Sz.	FOM
fok			otor		
3.18×10^4	10^{-1}	0.24(6577)	6.36×10^7	0.5×10^{-5}	0.29(0747)
3.18×10^5	10^{-2}	0.27(8494)	3.18×10^7	1.0×10^{-5}	0.29(0740)
3.18×10^6	10^{-3}	0.28(9486)	2.12×10^7	1.5×10^{-5}	0.29(0731)
3.18×10^7	10^{-4}	0.29(0618)	1.59×10^7	2.0×10^{-5}	0.29(0726)

Table 6. Simulation results of the Linearly Implicit Euler (midpoint)

It. Nu.	St. Sz.	FOM	It. Nu.	St. Sz.	FOM
fok			otor		
1.44×10^5	10^{-1}	0.29(0801)	5.75×10^6	0.5×10^{-5}	0.29(0767)
1.44×10^5	10^{-2}	0.29(0802)	5.75×10^6	1.0×10^{-5}	0.29(0759)
1.44×10^5	10^{-3}	0.29(0829)	5.75×10^6	1.5×10^{-5}	0.29(0764)
1.44×10^5	10^{-4}	0.29(0816)	5.75×10^6	2.0×10^{-5}	0.29(0760)

Table 7. Simulation results of the Linearly Implicit Euler (modified midpoint)

It. Nu.	St. Sz.	FOM	It. Nu.	St. Sz.	FOM
fok			otor		
1.92×10^5	10^{-1}	0.29(0769)	9.05×10^6	0.5×10^{-5}	0.29(1068)
1.92×10^5	10^{-2}	0.29(0586)	9.05×10^6	1.0×10^{-5}	0.29(1187)
1.92×10^5	10^{-3}	0.29(0846)	9.05×10^6	1.5×10^{-5}	0.29(1158)
1.92×10^5	10^{-4}	0.29(0633)	9.05×10^6	2.0×10^{-5}	0.29(1068)

Table 8. Simulation results of the Classical Runge-Kutta

Diff. Ord.	It. Nu.	St. Sz.	FOM	It. Nu.	St. Sz.	FOM
	fok			otor		
3	6.36×10^3	10^{-1}	0.29(0754)	1.27×10^8	0.5×10^{-5}	0.29(0754)
	6.36×10^4	10^{-2}	0.29(0754)	6.36×10^7	1.0×10^{-5}	0.29(0754)
	6.36×10^5	10^{-3}	0.29(0754)	4.24×10^7	1.5×10^{-5}	0.29(0754)
	6.36×10^6	10^{-4}	0.29(0754)	3.18×10^7	2.0×10^{-5}	0.29(0754)
4	7.65×10^3	10^{-1}	0.29(0754)	-		
	7.65×10^4	10^{-2}	0.29(0754)			
	7.65×10^5	10^{-3}	0.29(0754)			
	7.65×10^6	10^{-4}	0.29(0754)			
5	6.36×10^3	10^{-1}	0.29(0754)	-		
	6.36×10^4	10^{-2}	0.29(0754)			
	6.36×10^5	10^{-3}	0.29(0754)			
	6.36×10^6	10^{-4}	0.29(0754)			
6	6.36×10^3	10^{-1}	0.29(0754)	-		
	6.36×10^4	10^{-2}	0.29(0754)			
	6.36×10^5	10^{-3}	0.29(0754)			
	6.36×10^6	10^{-4}	0.29(0754)			
7	6.36×10^3	10^{-1}	0.29(0754)	-		
	6.36×10^4	10^{-2}	0.29(0754)			
	6.36×10^5	10^{-3}	0.29(0754)			
	6.36×10^6	10^{-4}	0.29(0754)			
8	6.36×10^3	10^{-1}	0.29(0754)	-		
	6.36×10^4	10^{-2}	0.29(0754)			
	6.36×10^5	10^{-3}	0.29(0754)			
	6.36×10^6	10^{-4}	0.29(0754)			
9	6.36×10^3	10^{-1}	0.29(0754)	-		
	6.36×10^4	10^{-2}	0.29(0754)			
	6.36×10^5	10^{-3}	0.29(0754)			
	6.36×10^6	10^{-4}	0.29(0754)			

Table 9. Simulation results of the Implicit Runge-Kutta

Diff. Ord.	It. Nu.	St. Sz.	FOM	It. Nu.	St. Sz.	FOM
	fok			otor		
3	8.06×10^3	10^{-1}	0.29(0754)	9.14×10^3	10^{-1}	0.29(0754)
	7.94×10^4	10^{-2}	0.29(0754)	7.95×10^4	10^{-2}	0.29(0754)
	6.63×10^5	10^{-3}	0.29(0754)	7.26×10^5	10^{-3}	0.29(0754)
	4.77×10^6	10^{-4}	0.29(0754)	5.58×10^6	10^{-4}	0.29(0754)
4	9.36×10^3	10^{-1}	0.29(0754)	1.04×10^4	10^{-1}	0.29(0754)
	9.23×10^4	10^{-2}	0.29(0754)	9.24×10^4	10^{-2}	0.29(0754)
	7.92×10^5	10^{-3}	0.29(0754)	8.55×10^5	10^{-3}	0.29(0754)
	6.06×10^6	10^{-4}	0.29(0754)	6.87×10^6	10^{-4}	0.29(0754)
5	1.50×10^4	10^{-1}	0.29(0754)	1.70×10^4	10^{-1}	0.29(0754)
	1.09×10^5	10^{-2}	0.29(0754)	1.46×10^5	10^{-2}	0.29(0754)
	1.02×10^6	10^{-3}	0.29(0754)	1.27×10^6	10^{-3}	0.29(0754)
	1.02×10^7	10^{-4}	0.29(0754)	1.16×10^7	10^{-4}	0.29(0754)
6	1.89×10^4	10^{-1}	0.29(0754)	2.09×10^4	10^{-1}	0.29(0754)
	1.48×10^5	10^{-2}	0.29(0754)	1.85×10^5	10^{-2}	0.29(0754)
	1.41×10^6	10^{-3}	0.29(0754)	1.66×10^6	10^{-3}	0.29(0754)
	1.41×10^7	10^{-4}	0.29(0754)	1.54×10^7	10^{-4}	0.29(0754)
7	2.29×10^4	10^{-1}	0.29(0754)	3.02×10^4	10^{-1}	0.29(0754)
	2.08×10^5	10^{-2}	0.29(0754)	2.64×10^5	10^{-2}	0.29(0754)
	2.08×10^6	10^{-3}	0.29(0754)	2.43×10^6	10^{-3}	0.29(0754)
	2.08×10^7	10^{-4}	0.29(0754)	2.28×10^7	10^{-4}	0.29(0754)
8	2.94×10^4	10^{-1}	0.29(0754)	3.66×10^4	10^{-1}	0.29(0754)
	2.73×10^5	10^{-2}	0.29(0754)	3.29×10^5	10^{-2}	0.29(0754)
	2.73×10^5	10^{-3}	0.29(0754)	3.07×10^6	10^{-3}	0.29(0754)
	2.73×10^7	10^{-4}	0.29(0754)	2.92×10^7	10^{-4}	0.29(0754)
9	3.66×10^4	10^{-1}	0.29(0754)	4.85×10^4	10^{-1}	0.29(0754)
	3.66×10^5	10^{-2}	0.29(0754)	4.37×10^5	10^{-2}	0.29(0754)
	3.66×10^6	10^{-3}	0.29(0754)	4.10×10^6	10^{-3}	0.29(0754)
	3.66×10^7	10^{-4}	0.29(0754)	3.91×10^7	10^{-4}	0.29(0754)

Conclusions

In this paper Randall-Wilkins and One Trap One Recombination models were solved, numerically by using Mathematica for Euler and Runge-Kutta methods. In order to comparison of the simulations,

some experiments were also performed. Fundamental trap parameters were measured, experimentally and used as initial conditions. each simulation was compared by the experiments and FOM was calculated. The fastest results were calculated by Linear Euler method but, the most accurate results

were calculated by Linearly Implicit Euler method. In the application, not only precision but also machine time is important and here Linearly Implicit Euler method is suggested by the authors.

Acknowledge

This work has been funded by Karamanoğlu Mehmetbey University Commission of Scientific Research Projects (Project Number: 20-M-16).

Conflicts of interest

The authors state that did not have conflict of interests.

References

- [1] Chen R., Pagonis V., Thermally and Optically Stimulated Luminescence: A Simulation Approach. 1st ed. Wilthshire, (2011) 245-272.
- [2] Pagonis V., Kitis G., Furetta C., Numerical and Practical Exercises in Thermoluminescence. 1st ed. New York, (2006) 1-21.
- [3] McKeever S. W. S., Thermoluminescence of Solids. 1st ed. Cambridge, (1985) 20-198.
- [4] Chen R., McKeever S. W. S., Theory of Thermoluminescence and Related Phenomena. 1st ed. Singapore, (1997) 17-205.
- [5] Kemmey P. J., Townsend P. D. Levy, P. W., Numerical Analysis of Charge-Redistribution Processes Involving Trapping Centers, *Phys. Rev.*, 155 (1967) 917-920.
- [6] Kelly P., Laubitz M. J., Bräunlich P., Exact Solutions of the Kinetic Equations Governing Thermally Stimulated Luminescence and Conductivity, *Phys. Rev. B.*, 4 (1971) 1960-1968.
- [7] Shenker D., Chen R., Numerical Solution of the Glow Curve Differential Equations, *J. Comput. Phys.*, 10 (1972) 272-283.
- [8] Chen R., Hornyak W. F., Mathur V. K., Competition Between Excitation and Bleaching of Thermoluminescence, *J. Phys. D. Appl. Phys.*, 23 (1990) 724-728.
- [9] Randall J. T., Wilkins M. H. F., Phosphorescence and Electron Traps - I. The Study of Trap Distributions, *Proc. R. Soc. London. Ser. A. Math. Phys. Sci.*, 184 (1945) 365-389.
- [10] Randall J. T., Wilkins M. H. F., Phosphorescence and Electron Traps II. The Interpretation of Long-Period Phosphorescence, *Proc. R. Soc. London. Ser. A. Math. Phys. Sci.*, 184 (1945) 390-407.
- [11] McKeever S. W. S., Chen R., Luminescence Models, *Radiat. Meas.*, 27 (1997) 625-661.
- [12] Bos A. J. J., Theory of Thermoluminescence, *Radiat. Meas.*, 41 (2006) 45-56.
- [13] Uzun E., Characterization of Thermoluminescent Properties of Seydisehir Alumina and Investigation of Properties of Dose Response, PD, Yıldız Technical University, Science and Engineering, 2008.
- [14] Uzun E., Yazar Y., Yazıcı A. N., Electron Immigration From Shallow Traps to Deep Traps by Tunnel Mechanism on Seydiehir Aluminas, *J. Lumin.*, 131 (2011) 2625-2629.
- [15] Kitis G., Pagonis V., Peak Shape Methods for General Order Thermoluminescence Glow-Peaks: A Reappraisal, *Nucl. Instruments Methods Phys. Res. Sect. B Beam Interact. with Mater. Atoms.*, 262 (2007) 313-322.
- [16] Sunta C. M., Feria A. W. E., Piters T. M., Watanabe S., Limitation of Peak Fitting and Peak Shape Methods for Determination of Activation Energy of Thermoluminescence Glow Peaks, *Radiat. Meas.*, 30 (1999) 197-201.
- [17] Chen R., Winer S. A. A., Effects of Various Heating Rates on Glow Curves, *J. Appl. Phys.*, 41 (1970) 5227-5232.
- [18] Chen R., Methods for Kinetic Analysis of Thermally Stimulated Processes, *J. Mater. Sci.*, 11 (1976) 1521-1541.
- [19] Stoer J., Bulirsch R., Introduction to Numerical Analysis, 3rd ed. New York, (2002) 471-480.
- [20] Hoffman J. D., Numerical Methods for Engineers and Scientists, 2nd ed. West Lafayette, (2015) 352-414.
- [21] Conte S. D. D., de Boor C., The Solution of Differential Equations. In: Conte S. D. D., de Boor C., (Eds). Elementary Numerical Analysis: An Algorithmic Approach, 1st ed. Philadelphia: Siam, (2017) 346-405.
- [22] Shampine L. F., Some practical Runge-Kutta formulas, *Math. Comput.*, 46 (1986) 135-135.
- [23] Dormand J. R., Prince P. J., Runge-Kutta triples, *Comput. Math. with Appl.*, 12 (1986) 1007-1017.
- [24] Nearing J., Mathematical Tools for Physics, 1st ed. Miami, (2010) 320-350.
- [25] Sofroniou M., Knapp R., Advanced Numerical Differential Equation Solving in Mathematica, 1st ed. Online, (2008) 17-162.

- [26] Balian H. G., Eddy N. W., Figure-of-merit (FOM), an improved criterion over the normalized chi-squared test for assessing goodness-of-fit of gamma-ray spectral peaks, *Nucl. Instruments Methods*, 145 (1977) 389–395.
- [27] Uzun E., Theoretical Modeling and Numerical Solutions of the Some Standard Thermoluminescence Detector Crystals, *Turkish J. Phys.*, 37 (2013) 304–311.
- [28] Uzun E., On the Numerical Solution of the One Trap One Recombination Model for First Order Kinetic, *AASCIT J. Phys.*, 3(5) 2017 36-43.
- [29] Uzun E., Korkmaz M. E., Numerical Solutions of Schön-Klasens Model for Luminescence Efficiency, *EPJ Web Conf.*, 100 (2015) 04005p1-p3.
- [30] Uzun E., Discussions on the Numerical Solutions of Schön-Klasens Model: Charge Carrier Traps Depth, *Sigma J. Eng. Nat. Sci.*, 33 (2015) 421–426.



Velocity-dependent potential effects on two interacting electrons in Cornell quantum dot planted in plasma medium

Mustafa Kemal BAHAR^{1,*}

¹Sivas Cumhuriyet University, Department of Physics, Sivas/ TURKEY

Abstract

In this study, the energy levels of two-electron Cornell quantum dot (TECQD) immersed in Debye and quantum plasma mediums are probed. To model plasma mediums, the more general exponential cosine screened Coulomb (MGECS) is suggested. The presence of TECQD in plasma environment and velocity-dependent potential (VDP) effect in the system render very difficult to solve the relevant wave equation. Since the analytical solution of the relevant wave equation is very difficult, the numerical asymptotic iteration method (AIM) is used. As well as the effects of the encompassing parameters on the energy levels and possible radiations of TECQD, the effects of VDP and quantum (and Debye) plasma medium are also presented in detail. In addition, the alternativeness of VDP, quantum (and Debye) plasma and encompassing parameters to each other on these effects are also discussed.

Article info

History:

Received: 25.11.2020

Accepted: 22.03.2021

Keywords:

Quantum dot,
Debye plasma,
Quantum plasma,
Velocity-dependent
potential,
Cornell confinement.

1. Introduction

Quantum dots are systems that are very popular and studied intensively due to their wide range of uses in technology. Studies on quantum dots consist of two basic points: experimental production and the control of the frequency of the light emitted afterwards. Plasma medium provides great advantages in experimental production, and it is also an effective experimental argument for modification of the quantum dot. External fields such as electric, magnetic and laser fields provide a highly functional control mechanism for the radiations produced by the quantum dot. Considering the complicated structure of the plasma medium and the complex correlations of the plasma particles, it is clear that the velocity-dependent potential (VDP) effects will also have important effects. The restricting effects of electrons in the quantum dot are very important for the electronic, optical and statistical properties displayed by the quantum dot. The encompassing effects affect directly the possible radiation frequencies of the quantum dot. These frequencies can be finely tuned by changing the size, shape, encompassing effects, and material of the quantum dot. Quantum dots can be generated using many methods. With the development of nanofabrication technology, it has been possible to manufacture quantum dots containing one, two or more electrons, and such structures have been extensively studied theoretically and experimentally

[1]. However, the use of plasma for production processes of quantum dots is also an important experimental argument. The size, shape and surface composition of quantum dots can be controlled in a non-thermal plasma medium [2,3]. Quantum dots that contain two electrons are the simplest structures to study the electron-electron interactions involving exchange and correlation [4]. Due to the fact that plasma screening effects have very important effects on atomic systems immersed in the plasma medium, remarkable studies have been carried out in recent years on the examination of atomic systems in plasma mediums [5-10]. Atomic excitation and ionization processes play an important role in the interpretation of various phenomena associated with hot plasma physics, astrophysics, and experiments with positively charged ions. Excitation processes have attracted great attention in the history of plasma, as the emission line formed by excitation provides detailed information about the physical processes of the plasma. In this manner, the results obtained in these studies contain accurate atomic data ready to use in the literature for atomic systems in various plasma medium, and these data are of great importance for the technological applications that have been and will be made in the future.

VDPs were first considered to study the scattering of mesons off the complex nucleus [11]. These potentials

*Corresponding author. e-mail address: mussiv58@gmail.com

can be used in the field of nuclear and atomic physics, such as nucleon-nucleon interactions and scattering of electrons off atoms [12-14]. Soylu et al. [15], using AIM, the effect of VDPs on the energy eigenvalues of Morse potential; Bayrak et al. [16], using AIM, the VDP effect on energy eigenvalues of Coulomb and harmonic oscillator potentials; Jaghoub [17], Schrödinger equation with the VDP in consideration of scattering cases in the framework of perturbative theory; Eed [18], using a variation iteration method, Schrödinger equation with the VDP for scattering states has investigated. Bahar [19] has examined the VDP effect on the energies of the hydrogen atom in Debye and quantum plasma, modeled by the MGECS potential, using AIM. The Schrödinger equation involving the velocity-dependent interaction can be rearranged into a form that describes a particle with position dependent effective mass. The Schrödinger equation with position-dependent mass has been an important model in defining the dynamics of electrons in semiconductor heterostructures such as quantum dots [20], liquid crystals [21] and graded crystals [22]. It is noteworthy that some external effects (for example, perturbative effects) that are not included in the model potential on two electrons interacting in the plasma medium can be included in the study by modeling with a VDP, in short, to examine the VDP effect.

Most of the plasmas found in nature such as solar chromosphere, ionosphere and laboratory produced plasmas such as fusion reactor, methane gas pulse discharge (10^6 - 10^{14} cm⁻³ electron density and 10^{-1} - 10^4 eV temperature) are weakly coupled (classical or Debye) plasmas. The Debye model and the related screened Coulomb (SC) potential is a suitable model for studying the interactions of atomic systems embedded in such classical plasmas. As the plasma density increases, it is more convenient to use exponential cosine screened Coulomb (ECSC) and MGECS potentials to model interactions [23,24]. In the literature, except for the studies by Bahar and/or Soylu, the potentials used to model interactions in plasmas are SC and ECSC potentials. The potential model used in this study is the MGECS potential which is given by

$$V_{MGECS}(r) = \frac{e^2}{r}(1 + br)\exp(-r/\lambda)\cos(ar/\lambda), \quad (1)$$

where, e is the electron charge; a , b and λ are the plasma screening parameters. Thanks to these parameters in the structure of MGECS potential, it can be reduced to SC, ECSC and pure Coulomb (PC) (only Coulomb) potentials, so it has a more compact structure. Also, the MGECS potential is more

physical and advantageous for modeling Debye and quantum plasma environments [25].

Due to the fact that plasma mediums modeled by MGECS potential has both the experimental advantage and the ability to create a new encompassing mechanism, the two-electron interaction is an important basic model, and the VDP effects model some factors that are in the plasma medium but not modeled by the MGECS potential, and affect two-electron interaction, and the confinement characteristic of the Cornell quantum dot is the main motivation for the present study. In this context, the effect of plasma, VDP and encompassing on energy levels of TECQD will be examined in detail.

The study is organized as follows: In the Section 2, the theoretical model and method are presented. In Section 3, the results obtained are discussed. The last paragraph is devoted to the conclusions.

2. Theoretical Model and Computation Method

The velocity-dependent total potential as a superposition of the local potential ($V_{eff}(r)$) and the isotropic velocity-dependent local potential ($V(r, p)$) is given by [26-30]:

$$V_{total}(r, p) = V_{eff}(r) + \frac{\hbar^2}{2\mu}(F(r) \cdot \nabla^2 + \nabla F(r) \cdot \nabla), \quad (2)$$

where $F(r)$ is the isotropic form factor function of the radial variable r . On the other hand, Hamiltonian for two-electron interacting in plasma medium is expressed as $H = H_{cm} + H_{rm}$, where H_{cm} associates with the motion of the center-of-mass and H_{rm} is for the relative motion, and they are written by:

$$H_{cm} = \frac{1}{2M} \mathbf{P}^2 + V_{dot}(\mathbf{R}), \quad (3)$$

$$H_{rm} = \frac{1}{2\mu} \mathbf{p}^2 + V_{dot}(r) + V_{MGECS}(|\mathbf{r}|), \quad (4)$$

where, while (R, P) is center-of-mass coordinates; (r, p) is the relative coordinates. H_{cm} does not contain plasma effects and therefore it is easy to find eigenvalues within the VDP effect. However, since our purpose is to investigate the VDP effects in the plasma environment, we focus on finding the eigenvalues of H_{rm} with VDP. Being the total wave function of two-electron system is $\Psi(r, R) = \varphi(r)\theta(R)$, its energy is $E = E_{cm} + E_{rm}$, the Schrödinger equation is $H\Psi(r, R) = E\Psi(r, R)$. The wave equation to be solved is $H_{rm}\varphi(r) = E_{rm}\varphi(r)$. In this case, within the VDP, the wave equation becomes:

$$\left[-\frac{\hbar^2}{2\mu} \nabla^2 + V_{total}(r, p) - E_{rm} \right] \varphi(\mathbf{r}) = 0, \quad (5)$$

where, by employing $\varphi(\mathbf{r}) = r^{-1}u(r)$, and then considering $F(r) = \gamma\rho(r)$ (γ is a constant), the following equation is obtained in units of $2\mu = \hbar = 1$:

$$u''(r) - \left[u'(r) - \frac{u(r)}{r} \right] \frac{\gamma\rho'(r)}{1-\gamma\rho(r)} + \frac{E_{rm} - V_{eff}(r)}{1-\gamma\rho(r)} u(r) = 0, \tag{6}$$

where, $V_{eff}(r)$ is the effective potential, and it is given by

$$V_{eff}(r) = \frac{l(l+1)}{r^2} + V_{dot}(r) + V_{MGECSC}(r) \tag{7}$$

The quantum dot confinement is chosen as parabolic-linear-Coulomb (that is, Cornell) as follows:

$$V_{dot}(r) = a_1 r^2 + b_1 r - \frac{c_1}{r}, \tag{8}$$

where, a_1, b_1 and c_1 are the quantum dot parameters. $\gamma = 1$ is taken throughout the VDP investigations. The isotropic form factor, in other words, the VDP term is chosen in the harmonic oscillator type, as $\rho(r) = \rho_0 r^2$. ρ_0 is a constant, and determines the strength of the isotropic dependence of the VDP. The following physical transformation is proposed by examining the asymptotic behaviors of Eq.(6):

$$u(r) = r^{t+1} e^{-\beta_1 r - \beta_2 r^2} f(r), \tag{9}$$

where, $\beta_{1,2}$ are important constants that affect the stabilization and speed of solution iterations as mentioned before. Details on the use of asymptotic iteration method (AIM) are detailed below.

Analytically solving the Schrödinger equation for Hamiltonians given in Section 3 is currently not possible. Therefore, numerical computation will be carried out by considering AIM [31-33]. This method was developed the second-order differential equations in the following form:

$$p_n''(r) = \lambda_0(r)p_n'(r) + s_0(r)p_n(r). \tag{10}$$

$s_0(r)$ and $\lambda_0(r)$ are differentiable functions, as well as $\lambda_0(r) \neq 0$. $s_0(r)$ and $\lambda_0(r)$ are defined in $C_\infty[a, b]$. At sufficiently large values of k , it is

$$(s_k/\lambda_k) = (s_{k-1}/\lambda_{k-1}) = \alpha(r) \tag{11}$$

and, for λ_k and s_k , it is obtained

$$\lambda_k = \lambda'_{k-1} + s_{k-1} + \lambda_0 \lambda_{k-1}, \quad s_k = s'_{k-1} + s_{k-1} + s_0 \lambda_{k-1}, \quad k = 1, 2, 3, \dots, n \tag{12}$$

The relevant wave equation for the system to be examined is converted to Eq.(10) form. Then $s_0(r)$ and $\lambda_0(r)$ are determined, $s_k(r)$ and $\lambda_k(r)$ expressions are obtained using Eq.(12). Eigenvalues are calculated using the quantization condition in Eq.(11). In this case, the quantization condition of the model is determined as follows:

$$\delta_k = \lambda_k s_{k-1} - \lambda_{k-1} s_k = 0, \tag{13}$$

where, k is iteration number, and in form of $k=1, 2, 3, \dots$. An appropriate r_0 point should be chosen for the fundamental quantum number considered in eigenvalue equation calculations that require numerical solutions. This point can be obtained from the maximum value of the proposed wave function to obtain the form Eq.(10), which is essential for the speed and convergence of these iterations. In other words, the solution should be sought where the probability of the wave function of the relevant particle is greatest. The success of AIM in examining such quantum dot-external (or internal) field-plasma combined systems is undeniable [34-36].

3. Results and Discussion

In this study, the effects of the VDP on the energies of the two-electron Cornell quantum dot are investigated. There are seven parameters on the energies of the TECQD as plasma shielding parameters (a, b, λ); quantum dot confinement parameters (a_1, b_1, c_1), and the intensity of the isotropic dependence of the VDP (in other words, the form factor) (ρ_0). Throughout the study, different values of λ parameter from 10 to 1000, b parameter from 0.1 to 7, and a parameter from 0.1 to 7 are taken into consideration. As can be seen from Table 1, λ parameter causes the energies to increase monotonously, while the a parameter causes them to decrease monotonously. On the other hand, b parameter causes a significant increase in energies.

Table 1: Under the influence of the VDP ($\rho_0=0.2-2$), the energies of some quantum states of TECQD ($a_1=0.1-2$, $b_1=0.1-2$, $c_1=0.1-2$) immersed in the quantum plasma modeled by the MGECSC potential ($a = 0.1-7$, $b = 0.1-7$, $l = 10-1000$), in atomic units.

$a_1=b_1=c_1=1, a=1, b=1, \rho_0=0.5$						
(n,l)	$\lambda=10$	$\lambda=50$	$\lambda=150$	$\lambda=250$	$\lambda=500$	$\lambda=1000$
(0,0)	2.931564	3.088418	3.114647	3.119893	3.123828	3.125795
(1,0)	7.816014	7.927719	7.998968	8.004219	8.008157	8.010127
(2,0)	16.749875	16.903294	16.928980	16.934118	6.937972	16.939899
(0,1)	5.334427	5.504695	5.533211	5.538916	5.543194	5.545333
(1,1)	11.936109	12.096445	12.123292	12.128663	12.132691	12.134705
(2,1)	22.827264	22.983708	23.009899	23.015138	23.019067	23.021032
(0,2)	8.541594	8.718016	8.747583	8.753498	8.757934	8.760153
(1,2)	17.075597	17.240152	17.267709	17.273222	17.277356	17.279423
(2,2)	29.921006	30.080717	30.107456	30.112805	30.116817	30.118823
$\lambda=300, a_1=b_1=c_1=1, a=1, \rho_0=0.5$						
(n,l)	b=0.1	b=0.5	b=1	b=3	b=5	b=7
(0,0)	2.224106	2.622817	3.121205	5.114756	7.108305	9.101853
(1,0)	7.108439	7.507147	8.005532	9.999070	11.992609	13.986149
(2,0)	16.038184	16.436948	16.935403	18.929224	20.923044	22.916865
(0,1)	4.643759	5.042240	5.540342	7.532747	9.525152	11.517556
(1,1)	11.233048	11.631696	12.130005	14.123245	16.116485	18.109725
(2,1)	22.119342	22.518056	23.016448	25.010016	27.003584	28.997153
(0,2)	7.858631	8.257007	8.754977	10.746856	12.738734	14.730612
(1,2)	16.377801	16.776378	17.274600	19.267485	21.260370	23.253255
(2,2)	29.217603	29.615819	30.114142	32.107436	34.100730	36.094024
$\lambda=300, a_1=b_1=c_1=1, b=1, \rho_0=0.5$						
(n,l)	a=0.1	a=0.5	a=1	a=3	a=5	a=7
(0,0)	3.121216	3.121213	3.121205	3.121117	3.120940	3.120676
(1,0)	8.005543	8.005540	8.005532	8.005440	8.005256	8.004980
(2,0)	16.935414	16.935411	16.935403	16.935316	16.935142	16.934881
(0,1)	5.540355	5.540352	5.540342	5.540232	5.540012	5.539682
(1,1)	12.130017	12.130014	12.130005	12.129910	12.129720	12.129434
(2,1)	23.016459	23.016456	23.016448	23.016358	23.016178	23.015908
(0,2)	8.754992	8.754988	8.754977	8.754856	8.754614	8.754252
(1,2)	17.274612	17.274609	17.274600	17.274499	17.274294	17.273994
(2,2)	30.114154	30.114151	30.114142	30.114048	30.113860	30.113578
$\lambda=300, a_1=b_1=c_1=1, a=1, b=1$						
(n,l)	$\rho_0=0.2$	$\rho_0=0.3$	$\rho_0=0.5$	$\rho_0=1$	$\rho_0=1.5$	$\rho_0=2$
(0,0)	4.283639	3.836447	3.121205	2.323289	1.999651	1.821674
(1,0)	7.547317	7.141334	8.005532	17.170975	16.874575	21.716203
(2,0)	10.832108	12.337350	16.935403	30.146865	43.858615	57.703652
(0,1)	6.365500	5.833800	5.540342	6.532451	8.147853	9.939589
(1,1)	9.248909	9.625825	12.130005	20.266625	28.949201	37.778209
(2,1)	13.280956	16.028588	23.016448	42.201187	61.900465	81.738399
(0,2)	8.357383	8.047013	8.754977	12.641884	17.225630	22.001442
(1,2)	11.384459	12.799661	17.274600	30.356719	44.016430	57.832941
(2,2)	16.220	20.359728	30.114142	56.261547	82.945828	109.775512
$\lambda=300, b_1=c_1=1, a=1, b=1, \rho_0=0.5$						
(n,l)	$a_1=0.1$	$a_1=0.5$	$a_1=0.75$	$a_1=1$	$a_1=1.5$	$a_1=2$
(0,0)	2.152254	2.594734	2.861671	3.121205	3.618290	4.086863
(1,0)	7.032230	7.458709	7.730214	8.005532	8.567339	9.143173
(2,0)	16.009750	16.419311	16.676779	16.935403	17.456152	17.981634
(0,1)	4.305607	4.860285	5.202204	5.540342	6.204880	6.853170
(1,1)	11.113172	11.563297	11.846048	12.130005	12.701893	13.279607
(2,1)	22.059060	22.483605	22.749722	23.016448	23.551753	24.089858
(0,2)	7.381410	7.995012	8.375996	8.754977	9.506713	10.249775
(1,2)	16.183036	16.667980	16.971210	17.274600	17.882042	18.490673
(2,2)	29.109256	29.555450	29.934661	30.114142	30.673943	31.234908

$\lambda=300, a_1=c_1=1, a=1, b=1, \rho_0=0.5$						
(n,l)	$b_1=0.1$	$b_1=0.5$	$b_1=0.75$	$b_1=1$	$b_1=1.5$	$b_1=2$
(0,0)	2.236842	2.633289	2.878317	3.121205	3.600489	4.071045
(1,0)	7.139139	7.522755	7.763682	8.005532	8.492060	8.982429
(2,0)	16.103396	16.472623	16.703839	16.935403	17.399577	17.865156
(0,1)	4.509396	4.969034	5.255120	5.540342	6.108131	6.672276
(1,1)	11.218208	11.623253	11.876562	12.130005	12.637348	13.145386
(2,1)	22.148896	22.534293	22.775313	23.016448	23.499069	23.982174
(0,2)	7.656047	8.145092	8.450234	8.754977	9.363239	9.969827
(1,2)	16.313696	16.740861	17.007759	17.274600	17.808126	18.341476
(2,2)	29.209936	29.611222	29.862673	30.114142	30.617141	31.120229

$\lambda=300, a_1=b_1=1, a=1, b=1, \rho_0=0.5$						
(n,l)	$c_1=0.1$	$c_1=0.5$	$c_1=0.75$	$c_1=1$	$c_1=1.5$	$c_1=2$
(0,0)	4.168043	3.712976	3.420554	3.121205	2.498743	1.838832
(1,0)	9.264837	8.709131	8.358519	8.005532	7.293198	6.574156
(2,0)	18.390545	17.747343	17.342443	16.935403	16.115296	15.287957
(0,1)	6.365889	6.000598	5.770994	5.540342	5.075711	4.606314
(1,1)	13.145904	12.695701	12.413263	12.130005	11.561024	10.988759
(2,1)	24.169570	23.658221	23.337693	23.016448	22.371808	21.724319
(0,2)	9.510186	9.175027	8.965158	8.754977	8.333652	7.910993
(1,2)	18.184099	17.780463	17.527715	17.274600	16.767253	16.258403
(2,2)	31.135729	30.682242	30.398365	30.114142	29.544654	28.973769

As can be seen from Table 1, the increase of a_1 parameter increases the repulsion of the total interaction potential and causes an enhancement in the localizations of energy levels. The b_1 parameter also increases the repulsion of the total interaction potential and causes the localizations to enhance. The c_1 parameter exhibits the opposite behavior, increasing the attractiveness of the total interaction potential, causing a descend in localizations. However, according to the data of Table 1, the encompassing parameters do not have a significant effect on energy gaps. For quantum plasma environment in Table 1, the intensity of the isotropic dependence of the VDP, in other words, the intensity of the harmonic form factor

(ρ_0) descends the localization of the (0,0) state and enhances the localizations of other statements. Therefore, it can be said that the inclusion of harmonic isotropic dependence in the system interaction causes an asymmetric situation in the total interaction potential. However, the increase of ρ_0 has a significant effect on energy gaps. According to the data of Table 1; $\Delta E = E_{10} - E_{00} = 3.304887$ a.u. for $\rho_0 = 0.3$, $\Delta E = 9.847686$ a.u. for $\rho_0 = 1$, $\Delta E = 19.894529$ a.u. for $\rho_0 = 2$. As can be seen, the increment in the VDP effect causes to increase in the energy gaps of TECQD. Also, the most dominant influence on energy levels and energy gaps belongs to ρ_0 parameter (See Table 1).

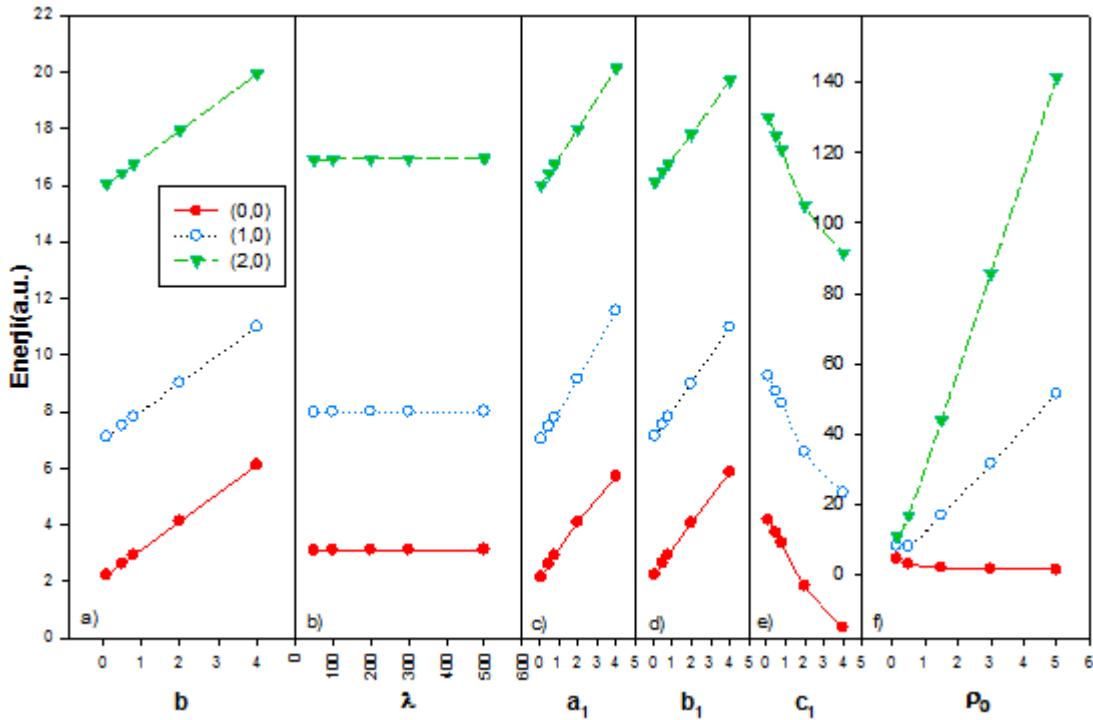


Figure 1: a) Under the influence of VDP ($\rho_0=0.5$), the energies of some quantum states of TECQD ($a_1=b_1=c_1=1$) in the quantum plasma modeled by the MGECS potential ($a=1, b=0.1-4, \lambda=500$), in atomic units, b) Under the influence of VDP ($\rho_0=0.5$), the energies of some quantum states of TECQD ($a_1=b_1=c_1=1$) in the quantum plasma modeled by the MGECS potential ($a=1, b=1, \lambda=50-500$), in atomic units, c) Under the influence of VDP ($\rho_0=0.5$), the energies of some quantum states of TECQD ($a_1=0.1-4, b_1=c_1=1$) in the quantum plasma modeled by the MGECS potential ($a=1, b=1, \lambda=500$), in atomic units, d) Under the influence of VDP ($\rho_0=0.5$), the energies of some quantum states of TECQD ($a_1=1, b_1=0.1-4, c_1=1$) in the quantum plasma modeled by the MGECS potential ($a=1, b=1, \lambda=500$), in atomic units, e) Under the influence of VDP ($\rho_0=0.5$), the energies of some quantum states of TECQD ($a_1=1, b_1=1, c_1=0.1-4$) in the quantum plasma modeled by the MGECS potential ($a=1, b=1, \lambda=500$), in atomic units, f) Under the influence of VDP ($\rho_0=0.15-5$), the energies of some quantum states of TECQD ($a_1=1, b_1=1, c_1=0.1$) in the quantum plasma modeled by the MGECS potential ($a=1, b=1, \lambda=500$), in atomic units.

Figure 1 shows the similarities of the parameters on the energies of TECQD in the quantum plasma environment described by MGECS potential. As can be seen, b, a_1 and b_1 parameters can be alternatives to each other in this context since they behave similarly on energies. The parameter λ can be an alternative to the parameters b, a_1, b_1 , with a monotonous effect. However, the main point here is that this

alternativeness can be achieved through the temperature of the plasma environment and particle density. ρ_0 parameter behaves similarly to other parameters except the ground case. a parameter is not included in Figure 1 because it has a monotonous effect. However, as seen in Figure 1, a parameter can be an alternative to the dominant effect of c_1 parameter in reducing energies.

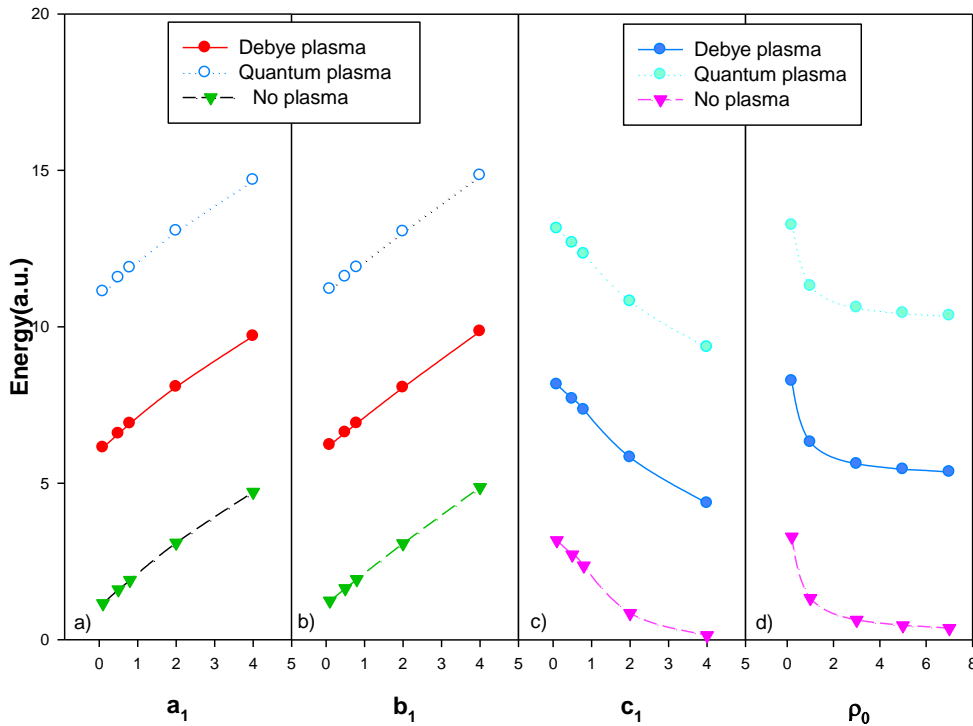


Figure 2: Comparison of the ground state energies, in atomic units, of a) TECQD ($a_1=0.1-4$, $b_1=1$, $c_1=1$) immersed in Debye plasma environment ($a=0$, $b=5$, $\lambda=350$), quantum plasma environment ($a=1$, $b=10$, $\lambda=350$), and free-plasma environment, when $\rho_0=0.5$, b) TECQD ($a_1=1$, $b_1=0.1-4$, $c_1=1$) immersed in Debye plasma environment ($a=0$, $b=5$, $\lambda=350$), quantum plasma environment ($a=1$, $b=10$, $\lambda=350$), and free-plasma environment, when $\rho_0=0.5$, c) TECQD ($a_1=1$, $b_1=1$, $c_1=0.1-4$) immersed in Debye plasma environment ($a=0$, $b=5$, $\lambda=350$), quantum plasma environment ($a=1$, $b=10$, $\lambda=350$), and free-plasma environment, when $\rho_0=0.5$, d) TECQD ($a_1=1$, $b_1=1$, $c_1=1$) immersed in Debye plasma environment ($a=0$, $b=5$, $\lambda=350$), quantum plasma environment ($a=1$, $b=10$, $\lambda=350$), and free-plasma environment, when $\rho_0=0.2-7$.

In Figure 2, the effect of Debye plasma environment modeled by the potential with $a = 0$, $b = 5$, $\lambda = 350$ parameter set, quantum plasma environment modeled by the MGECSG potential with $a = 1$, $b = 10$, $\lambda = 350$ parameter set and a plasma-free environment on TECQD is shown. As can be seen, energy levels are the highest due to the strong shielding effect of the quantum plasma environment. In addition, the energies in the Debye plasma environment are higher than in the free-plasma environment. The main point here is that the localizations of energy levels can be adjusted by means of plasma screening parameters.

The important findings regarding the effects of the VDP on the energies of TECQD in the Debye and quantum plasma environment can be summarized as follows: **i)** b and λ plasma shielding parameters increase the energies while the a parameter decreases. The most dominant plasma shielding parameter on energies is b . All three parameters do not have a significant effect on energy gaps. **ii)** Cornell quantum dot parameters, as a_1 and b_1 , exhibit a similar effect by increasing energies, while c_1 decreases the energies.

Quantum dot parameters also do not have a significant effect on energy gaps. **iii)** The intensity (ρ_0) of the isotropic dependence of VDP (in other words, the form factor) decreases the ground state energies while increasing the other state energies. Therefore, the inclusion of VDP into the system causes an asymmetry in the total interaction potential. ρ_0 parameter is the most effective parameter on the system, and the increase of ρ_0 increases both the energies and energy gaps of the quantum dot. **iv)** The plasma environment provides an important control possibility for the localization of energy levels.

In this study, the VDP effect on the energies of TECQD in the plasma medium has been investigated. Various methods such as the use of plasma in parallel with the development of nanofabrication technology make possible to produce such quantum dots. Increasing the intensity of the harmonic form factor reduces the localization of the ground state in Cornell quantum dot while enhancing the localization of other states. So, it can be said that VDP transforms an asymmetric case the total interaction potential.

However, in the Cornell quantum dot, it has been determined for ρ_0 that it has an increasing effect on the frequencies of possible radiations. It is also an important result that frequency control in the Cornell quantum dot can only be done through ρ_0 . In the light of all these findings, it is clear that uncovering the function of quantum dot parameters will play a very important role for experimental designs.

Conflicts of interest

The authors state that did not have conflict of interests.

References

- [1] Xie W. F., Two interacting electrons in a Gaussian confining potential quantum dot, *Solid State Communications*, 127 (2003) 401-405.
- [2] Kortshagen U., Nonthermal plasma synthesis of semiconductor nanocrystals, *Journal of Physics D: Applied Physics*, 42 (2009) 113001-113023.
- [3] Pi, X. D., Kortshagen, U., Nonthermal plasma synthesized freestanding silicon-germanium alloy nanocrystals, *Nanotechnology*, 20 (2009) 295602-295608.
- [4] Ellenberger, C., Ihn, T., Yannouleas, C., Landman, U., Ensslin, K., Driscall, D., Gassard, A. C., Excitation spectrum of two correlated electrons in a lateral quantum dot with negligible Zeeman splitting, *Physical Review Letters*, 96 (2006) 126806-126900.
- [5] Gutierrez, F. A., Diaz-Valdes, J., Effects of non-spherical screening for inelastic electron-ion scattering, *Journal of Physics B: Atomic, Molecular and Optical Physics*, 27 (1994) 593-600.
- [6] Hong, W., Jung, Y. D., Plasma screening effects on direct $1s \rightarrow 2p$ electron-ion collisional excitation rates in dense plasmas, *Physics of Plasmas*, 3 (1996) 2547-2460.
- [7] Brandenburg, R., Schweinzer, J., Fiedler, S., Aumayr, F., Winter, H. P., Modelling of fast neutral Li beams for fusion edge plasma diagnostics, *Plasma Physics Controlled Fusion*, 41 (1999) 471-484.
- [8] Nakai, S., Mima, K., Laser driven inertial fusion energy: present and prospective, *Reports on Progress in Physics*, 67 (2004) 321-349.
- [9] Saha, J. K., Bhattacharyya, S., Mukherjee, T. K., Mukherjee, P. K., $2pnp$ ($^{1,3}\text{Pe}$) states of neutral He and Li^+ ions under Debye plasma screening, *Journal of Physics B: Atomic, Molecular and Optical Physics*, 42 (2009) 245701-245711.
- [10] Robinson, M. P., Laburthe Torla, B., Noel, W., M., Gallagher, T. F., Pillet, P., Spontaneous Evolution of Rydberg Atoms into an Ultracold Plasma, *Physical Review Letters*, 85 (2000) 4466-4469.
- [11] Kisslinger, L. S., Scattering of mesons by light nuclei, *Physical Review*, 98 (1955) 761-765.
- [12] Razavy, M., Field, G., Levinger, J. S. 1962. Analytical solutions for velocity-dependent nuclear potentials, *Physical Review*, 125 (1962) 269-272.
- [13] Green, A. E. S., Darewych, G., Berezdivin, R., Morse function and velocity-dependent nuclear potentials, *Physical Review*, 157 (1967) 929-932.
- [14] Green, A. E. S., Rio, D. E., Ueda, T., Analytic velocity-dependent potential for bound and scattering states of electrons and atoms, *Physical Review A*, 24 (1981) 3010-3018.
- [15] Soylu, A., Bayrak, O., Boztosun, I., Effect of the velocity-dependent potentials on the energy eigenvalues of the Morse potential, *Central European Journal of Physics*, 10 (2012) 953-959.
- [16] Bayrak, O., Soylu, A., Boztosun, I., Effect of the velocity-dependent potentials on the bound state energy eigenvalues, *Chinese Physics Letters*, 28 (2011) 40304-40307.
- [17] Jaghoub, M. I., Perturbation theory for velocity-dependent potentials, *European Physical Journal A*, 15 (2002) 443-448.
- [18] Eed, H., A variation iteration method for isotropic velocity-dependent potentials: Scattering case, *European Physical Journal A*, 50 (2014) 185-192.
- [19] Bahar, M. K., Plasma screening effects on the energies of hydrogen atom under the influence of velocity-dependent potential, *Physics of Plasmas*, 21 (2014) 072706-072716.
- [20] Serrano, L. I., Lipparini, E., Spin response of unpolarized quantum dots, *Europhysics Letter*, 40 (1997) 667-672.
- [21] Barranca, M., Pi, M., Gatica, S. M., Hernandez, E. S., Navarro, J., Structure and energetics of mixed ^4He - ^3He drops, *Physical Review B*, 56 (1997) 8997-9003.
- [22] Geller, M. R., Khan, W., Quantum mechanics of electrons in crystals with graded composition, *Physical Review Letter*, 70 (1993) 3103-3106.

- [23] Lin, C. Y., Ho, Y. K., Effects of screened Coulomb (Yukawa) and exponential-cosine-screened Coulomb potentials on photoionization of H and He⁺, *European Physical Journal D*, 57 (2010) 21-26.
- [24] Shukla, P. K., Eliasson, B., Screening and wake potentials of a test charge in quantum plasmas, *Physics Letters A*, 372 (2008) 2897-2899.
- [25] Soylu, A., Plasma screening effects on the energies of hydrogen atom, *Physics of Plasmas*, 19 (2012) 072701-072709.
- [26] Jaghoub, M. I., s-wave bound and scattering state wave functions for a velocity-dependent Kisslinger potential, *European Physical Journal A*, 11 (2001) 175-183.
- [27] Jaghoub, M. I., Bound and scattering wave functions for a velocity-dependent Kisslinger potential for $l > 0$, *European Physical Journal A*, 13 (2002) 349-354.
- [28] Jaghoub, M. I., Effect of ordering ambiguity in constructing the Schrödinger equation on perturbation theory, *European Physical Journal A*, 28 (2006) 253-257.
- [29] Jaghoub, M. I., Perturbation theory for isotropic velocity-dependent potentials: Bound-states case, *European Physical Journal A*, 27 (2006) 99-103.
- [30] Jaghoub, M. I., Perturbation theory for isotropic velocity-dependent potentials: Scattering case, *Physical Review A*, 74 (2006) 032702-032709.
- [31] Ciftci, H., Hall, R. L., Saad, N., Asymptotic iteration method for eigenvalue problems, *Journal of Physics A: Mathematical and General*, 36 (2003) 11807-11816.
- [32] Ciftci, H., Hall, R. L., Saad, N., Construction of exact solutions to eigenvalue problems by the asymptotic iteration method, *Journal of Physics A: Mathematical and General*, 38 (2005) 1147-1155.
- [33] Saad, N., Ciftci, H., Hall, R. L., Criterion for polynomial solutions to a class of linear differential equations of second order, *Journal of Physics A: Mathematical and General*, 39 (2005) 13445-13454.
- [34] Bahar M. K., Soylu A., Two-electron quantum dot in plasmas under the external fields, *Physics of Plasmas*, 25 (2018) 022106-022118.
- [35] Bahar M. K., Soylu A., Confinement control mechanism for two-electron Hulthen quantum dots in plasmas, *Journal of Physics B: Atomic, Molecular and Optical Physics*, 51 (2018) 105701-105715.
- [36] Bahar M. K., Soylu A., Laser-driven two-electron quantum dot in plasmas, *Physics of Plasmas*, 25 (2018) 062113-062125.



Examination of ^{99m}Tc -mdp radioactivity after injection according to time and distance

Arzu COŞKUN¹ , Melek GÖKBULUT^{2,*} , Fadime DEMİR³ , İbrahim YİĞİTOĞLU⁴

Betül ÇETİN⁵

¹Toros University, Department of Medical Services and Techniques, Mersin/ TURKEY

²Tokat Gaziosmanpaşa University, Erbaa Vocational School of Health Services, Department of Medical Services and Techniques Tokat/TURKEY

³Tokat Gaziosmanpaşa University, Faculty of Medicine, Department of Nuclear Medicine, Tokat/TURKEY

⁴Tokat Gaziosmanpaşa University, Department of Physics, Faculty of Arts and Sciences, Tokat/TURKEY

⁵Amasya University, Department of Physics, Faculty of Arts and Sciences, Amasya/TURKEY

Abstract

In nuclear medicine, the imaging process used to diagnose diseases and to examine the functions of organs is carried out with radiopharmaceuticals containing radioisotope. In this study, the amount of external radiation emitted from bone scintigraphy patients who were given ^{99m}Tc -MDP kit was examined. The measurements have been performed using FLUKE Victoreen ASM 990 portable detector at Nuclear Medicine Department Medicine Faculty in Tokat Gaziosmanpaşa University. The external dose rate values have been measured at 0.50 m, 1.0 m, 2.0 m and 3.0 m away from the patient considered as the source of radiation. All measurements have been taken within approximately one hour and 10 minutes at 10 minutes intervals after injection of the pharmaceutical. In this study, the highest external dose rate value is measured $13.81 \mu\text{Sv h}^{-1}$ from 0.50 m distance after 30 minutes from the radiopharmaceutical injection and the lowest external dose rate value $1.53 \mu\text{Sv h}^{-1}$ is obtained from 3.0 m distance after 60 minutes. Then, dose rate values per unit activity were calculated and the highest value was found as $20.57 \mu\text{Sv h}^{-1} \text{GBq}^{-1}$ 30 minutes after injection at 0.50 m. The results obtained were compared with other studies in the literature.

Article info

History:

Received: 21.10.2020

Accepted: 04.04.2021

Keywords:

Radiopharmaceutical

Bone Scintigraphy

^{99m}Tc -MDP

Single Photon

Emission

Tomography

1. Introduction

Radiopharmaceuticals are medicinal drugs that contained radioactive compound. The usefulness of radiopharmaceutical, which has two components, radionuclide and pharmaceutical, is determined by the properties of these two components. When designing a radiopharmaceutical, a pharmaceutical is first selected according to its localization in a given organ or its participation in the physiological function of the organ. In nuclear medicine nearly 95% of the radiopharmaceuticals are used in nuclear imaging to evaluate organ functions and organ physiology, while the rest are used for treatment [1,2].

In nuclear medicine, the radiation-based medical imaging techniques that are made using radiopharmaceuticals are single photon emission computed tomography (SPECT) and positron emission tomography (PET). The image is created by detecting

the radiation emitted by the applied radiopharmaceuticals. These radiation-based imaging techniques are provided information not only for diagnostic purposes but also for early diagnosis of cancer and organ functions. They are complementary to the conventional anatomic imaging modalities of computed tomography (CT) and magnetic resonance (MR) imaging [3,4].

Besides the fundamental differences in the design and properties of SPECT and PET, the most important difference between the two imaging systems is based on the properties of the radioisotopes used. For SPECT, single photon emitting radionuclides are used, while in the PET are used radionuclides that make β^+ decay realized with a positron release. SPECT radiopharmaceuticals are medium to long half-life radionuclide containing agents that allow biological processes to be observed longer than PET radiopharmaceuticals. Generally, in SPECT

*Corresponding author. e-mail address: melek.kgb@gmail.com.

applications are used Technetium-99m (half-life, 6 hours), Samarium-153 (half-life, 1.9 days), Indium-111 (half-life, 2.8 days), Iodine-123 (half-life 13.3 hours), Iodine-131 (half-life, 8 days), Thallium-201 (half-life, 73 hours) and Gallium-67 (half-life 78 hours). For PET applications, Fluorine-18 (half-life, 110 minute), Carbon-11 (half-life, 20 minute), Nitrogen-13 (half-life, 10 minute), Oxygen-15 (half-life, 2 minute) and Gallium-68 (half-life, 68 minute) are used [5].

Some of these radionuclides are produced in particle accelerators, such as cyclotrons, where the target material is bombarded with charged particles, while others are produced by radionuclide generator systems. In radionuclide generator systems, radionuclides of short half-life are produced from long half-life radionuclides by chemical or physical separation methods [1]. Technetium-99m, which has a wide range of uses such as thyroid, liver, bone, kidney imaging and myocardial perfusion is supplied from molybdenum-99 (half-life, 66 hours) generator and emits gamma radiation with an energy of 140 keV [3].

Technetium-99m methylene diphosphonate (^{99m}Tc -MDP) introduced by Subramanian et al. [6] is an excellent bone imaging agent used to detect bone metastasis associated with many forms of cancer. The most important feature of ^{99m}Tc -MDP is that it contains phosphate. Thus, it can be attached to the bone tissue. Thus, it allows us to detect bone tissue abnormalities. ^{99m}Tc -MDP injection is done intravenously. The dose given in adult patients varies between 20-30 mCi, while the dose given in children is 2 mCi. The image is taken approximately two to three hours after the injection since it is cleared of soft tissues and peaked in bone tissue approximately two to three hours after the radiopharmaceutical injection. Also another important feature of ^{99m}Tc -MDP is that it is excreted from the kidney. In this way, it gives additional contribution related to urinary system pathologies from time to time. Kidney function affects both bone and organ involvement in Bone Scintigraphy (BS) [7,8].

After scintigraphy application, the patient emits radiation to the environment. The effect of the emitted radiation decreases depending on time and distance. Following the radionuclide application, all the hospital staff, as well as the radiation worker, will be at risk from the radiation released from the patient. At the same time, family members and street people will be exposed to radiation, as the patient will emit rays even after leaving the hospital. Therefore, informing patients and their relatives about radiation exposure is essential. The current system of radiation protection that is internationally accepted provides no dose limits

for patients. However, dose limits are prescribed for staff and members of the public. Furthermore, there are dose constraints for carers, and some countries also provide dose constraints for staff [9-11]. According to TAEK data, the dose taken at a distance of 1.0 m from the patient should not be discharged until $30 \mu\text{Sv h}^{-1}$ [12,13].

The first aim of this current study is to determine the external dose rates with respect to distance from patient for radiation security. Another purpose of this study is to examine how the external radiation dose rate changes over time, taking into account the radiopharmaceutical clearance effect due to physical decay of ^{99m}Tc -MDP. For this, the measurements were taken on a patient and the distance at which the measurement was taken and the time after injection were recorded.

2. Materials and Methods

In this study, the external dose rate measurements have been performed at Nuclear Medicine Department, Medicine Faculty in Tokat Gaziosmanpaşa University by taking the patient as the source of radiation. The measurements were made with FLUKE Victoreen ASM 990 portable detector which had been calibrated using a Cs-137 source. The ASM-990 series are designed to be detected alpha, beta, gamma, neutron, or x-ray radiation within a range of $1 \mu\text{R h}^{-1}$ to 1R h^{-1} , depending on the selected probe, such as Geiger-Muller, neutron, proportional counter, scintillation. These detectors are used as a general survey meter with the proper probe combination. The ASM-990 is a portable, battery operated general-purpose survey meter for use with all Victoreen Geiger-Mueller (GM) and scintillation probes, proportional counting probes and neutron probes. The ASM-992 is identical to the ASM-990 with the addition of a second, internal GM tube and supporting circuitry. The ASM-993 contains both an internal GM tube, as well as an internal pancake probe. The measurements taken before and after the mechanical shocks will not be in variance by more than $\pm 15\%$ [14].

In this study firstly, the background measurement was made in the room where the measurement will be made. The measurements were taken as cps (count per second) and then were converted to $\mu\text{Sv h}^{-1}$ in such a way that 5 cps equals $1 \mu\text{Sv h}^{-1}$ [15]. The background dose rate value was measured as $0.09 \mu\text{Sv h}^{-1}$. The

patient who was given 18.15 mCi (671.55 MBq) ^{99m}Tc -MDP for bone scintigraphy was taken to the room where the measurement will be made four minutes after the injection. Dose rates were measured at 0.50 m, 1.0 m, 2.0 m and 3.0 m perpendicular to the middle of the trunk with the patient in the sitting position 10 minutes after injection. The other measurements were made 10 minutes after the first measurement and with an interval of 10 minutes. The correct distance has been determined by making markings on the floor. All measurements taken at each distance were determined

by taking the average of ten data taken every 10 seconds.

3. Results and Discussion

In our study, measurements were taken as cps and values were converted to $\mu\text{Sv h}^{-1}$. All measurements are performed 10 minutes after injection, 10 minutes apart, within 1 hour and 10 minutes. The measured of the dose rates values at distance of 0.50, 1.0, 2.0 and 3.0 m are presented in Table 1.

Table 1. Dose rate ($\mu\text{Sv h}^{-1}$) depending on distance and time.

Time	Distance (meter)			
	0.50 m	1.0 m	2.0 m	3.0 m
10.min	11.72	7.81	3.49	2.36
20.min	13.31	9.17	4.31	2.91
30.min.	13.81	9.82	3.89	2.46
40.min	12.70	9.49	3.81	2.02
50.min	11.42	7.71	3.70	1.96
60.min.	8.08	5.88	2.82	1.53
70.min	8.15	6.04	2.84	1.66

As seen in Table 1, the highest external dose rate value is measured as $13.81 \mu\text{Sv h}^{-1}$ at a distance of 0.50 meter 30 minutes after the radiopharmaceutical injection, and the lowest dose rate value is measured as $1.53 \mu\text{Sv h}^{-1}$ from 3.0 meter distance 60 minutes after injection. The

measured dose rate values per unit activity for each distance and time after administration are listed in Table 2. As can be seen in Table 2, the greatest value is found as $20.57 \mu\text{Sv h}^{-1} \text{GBq}^{-1}$ at 0.50 m in 30 minutes after administration.

Table 2. Dose rate per unit activity ($\mu\text{Sv h}^{-1} \text{GBq}^{-1}$) for each distance and time after administration.

Time (min.)	Distance (meter)			
	0.50 m	1.0 m	2.0 m	3.0 m
10. min.	17.45	11.63	5.20	3.51
20. min.	19.82	13.65	6.43	4.33
30. min	20.57	14.62	5.79	3.66
40. min	18,91	14.14	5.68	3.00
50. min	17.00	11.47	5.52	2.92
60. min.	12.04	8.75	4.20	2.28
70. min	12.14	8.99	4.23	2.47

The change of measured dose rate values over time at certain distances is given in figures 1-4. In figures 1 and 2, it is observed that the external dose rate values are taken from the patient at 0.50 m and 1.0 m distances increase within 30 minutes and decrease within the

next 30 minutes. Figures 3 and 4 show that external dose rate values measured at 2.0 m and 3.0 m from the patient peak within 20 minutes and decrease over time. From figures 1-4, it is seen that the external dose rate values increase a little at the 60th and 70th minutes

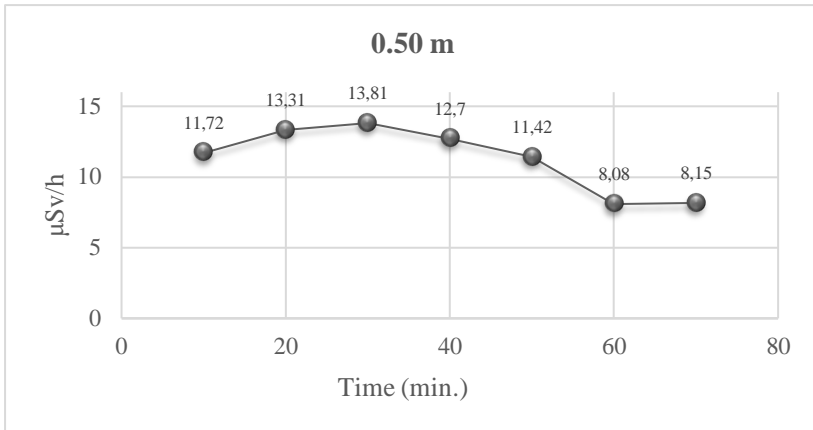


Figure 1. Change of dose rates in time at 0.50 m after the pharmaceutical injection.

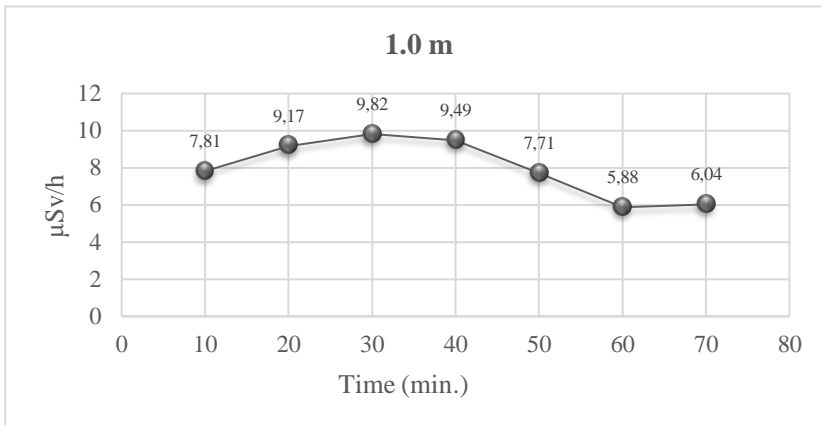


Figure 2. Change of dose rates in time at 1.0 m after the pharmaceutical injection.

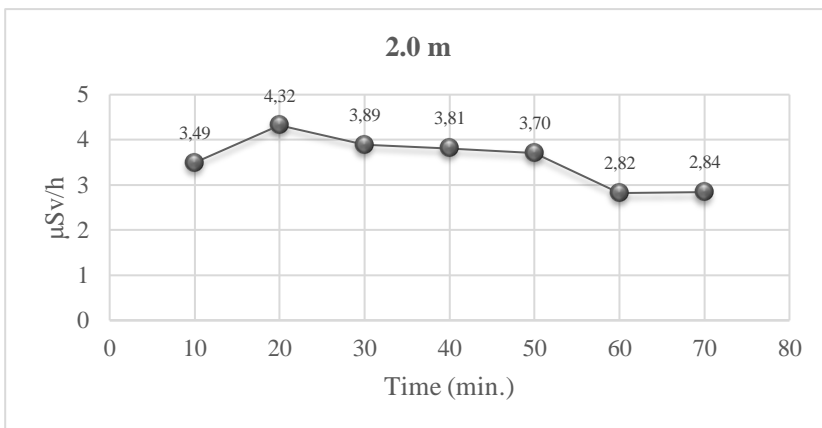


Figure 3. Change of dose rates in time at 2.0 m after the pharmaceutical injection.

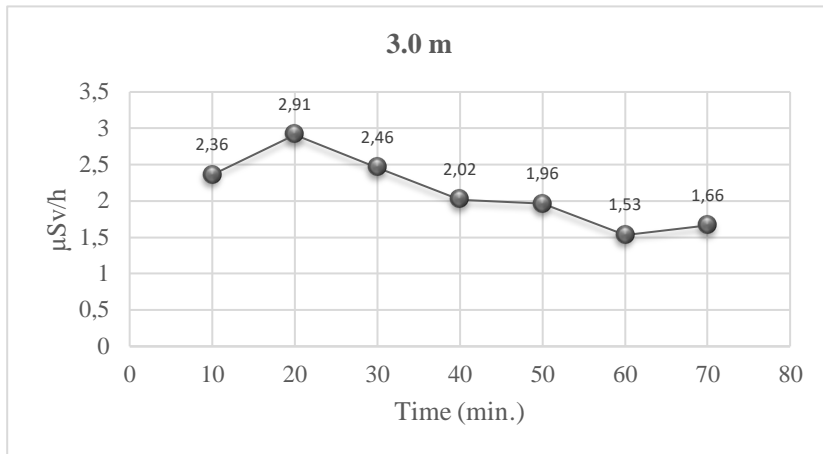


Figure 4. Change of dose rates in time at 3.0 m after the pharmaceutical injection.

The main uptake of radiopharmaceuticals containing phosphates such as pyrophosphate and polyphosphate used for bone scintigraphy happens in the bones, with a very small proportion in the kidneys, and the excretion is via the renal system. The rate of the biological process, such as uptake, metabolism, and excretion, is usually given as the half-life of the corresponding exponential function [16]. Biological clearance for each radiopharmaceutical is specified as the fraction of administered activity assigned to each half-life. In this context, it is reported that a fraction of 0.3 of the administered activity for $^{99m}\text{Tc-MDP}$ is taken up by bone with a half-time of 30 min, and retained there with halftimes of 2 h (0.3) and 72 h (0.4) [16,17]. In addition, the dose rate varies depending on the varying distribution of radiopharmaceuticals within the body and the amount of accumulation in certain organs in the body. For Tc-99 bone scans, the activity is more uniformly distributed throughout the skeleton [18].

This situation is clearly seen from Table 1 and Figures 1-2. It was predicted that the increase in the external dose rate values obtained within the first 30 minutes and the decrease within the next 30 minutes may be due to the biological clearance effect. Considering the time intervals of approximately 10 seconds for each distance, it was thought that the external dose rate values taken at 2 m and 3 m were taken within 25-30 minutes. In this context, it was forecasted in Figures 2 and 3 that the decrease in external dose values after 20 minutes may be originated due to biological clearance effect.

The graphic representation of the measurements within 10, 30, 50 and 60 minutes after administration respect to distance are given in Figures 5, 6, 7 and 8. From figures 5-8, the external dose rate values are seen to decrease as the distance from the patient increases. Also, it is observed that the sharpest decreasing trend is between 0.50 m and 2.0 m and the lowest decreasing trend is between 2.0 and 3.0 meters from figures 5 and 7. In figures 6 and 8, the sharpest decreasing trend is observed between 1.0 and 2.0 meters. It is calculated that the measured within 10, 20 and 50 minutes external dose rate values at 0.50 m decreased by an average factor of $0.32 \mu\text{Sv h}^{-1}$ at 1.0 m. In addition, it is calculated that the measured within 30, 40, 60 and 70 minutes external dose rate values at 0.50 m decreased by an average factor of $0.27 \mu\text{Sv h}^{-1}$ at 1.0 m.

The variation in the dose rate with respect to distance from an adult patient depends on the anatomical distribution of the radiopharmaceutical [19] and the reduction of the radiation intensity with the square of the distance [20]. Here, it was estimated that the decrease factor of the external dose rate values measured at different time intervals according to the distance changes depending on the anatomical distribution of the radiopharmaceutical in the body. It was also seen that the external dose rate values decreased with the distance as related to the inverse square law.

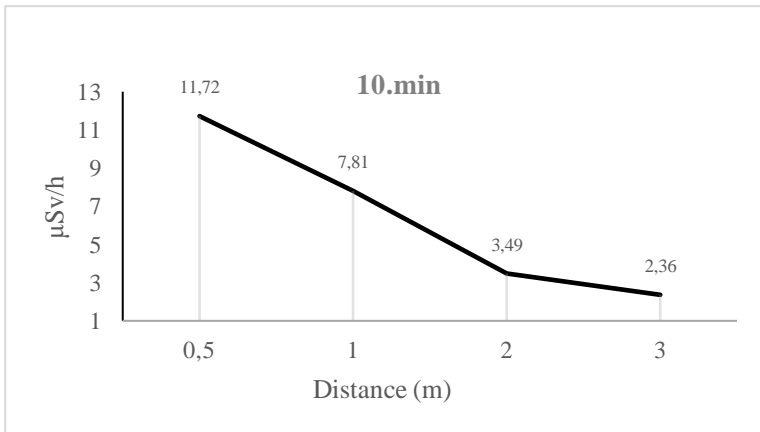


Figure 5. The change of dose rates by distance 10 minutes after the pharmaceutical injection.

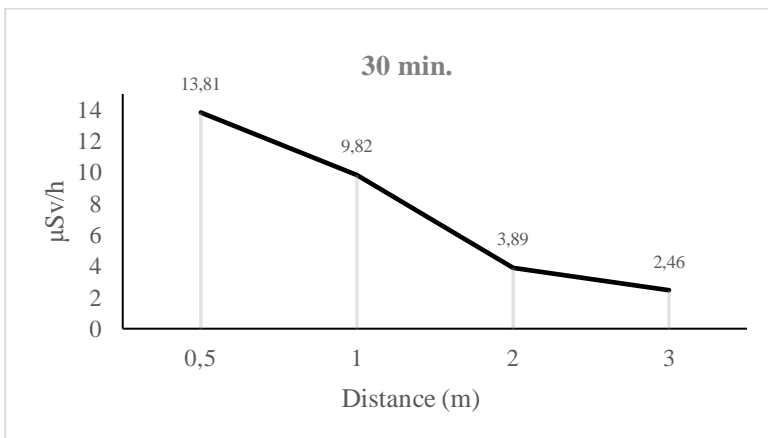


Figure 6. The change of dose rates by distance 30 minutes after the pharmaceutical injection.

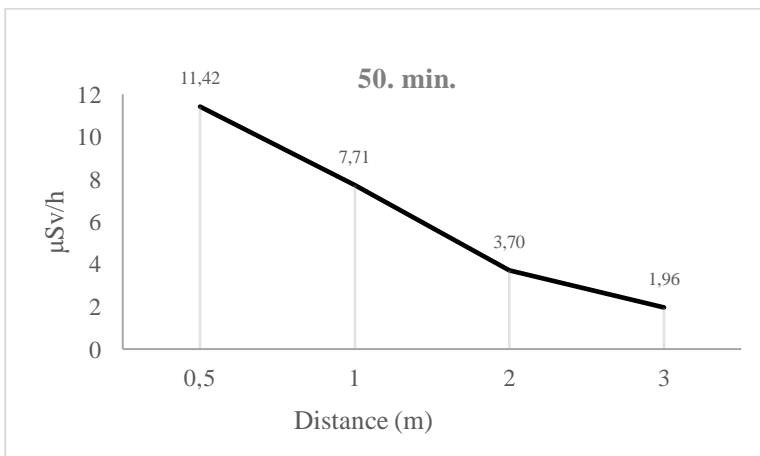


Figure 7. The change of dose rates by distance 50 minutes after the pharmaceutical injection.

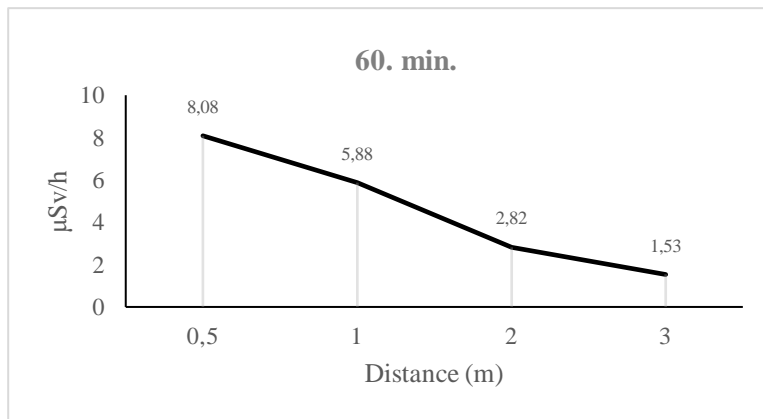


Figure 8. The change of dose rates by distance 60 minutes after the pharmaceutical injection.

The measured dose rate values and the dose rate per unit injected activity found by the other studies are presented in Table 3.

Table 3. A list of dose rates values and dose rate per unit injected activity for Tc-99m MDP in literature.

References	Activity (MBq)	Distance (meter)			
		Dose rate ($\mu\text{Sv h}^{-1}$)		Dose rate per activity ($\mu\text{Sv h}^{-1} \text{GBq}^{-1}$)	
		0.50 m	1.0 m	0.50 m	1.0 m
Harding et al.	500	12.10	3.10	24.20	6.20
Mountford et al.	550	11.30	3.50	20.55	6.36
Gomez-Palacios et al.	814	15.9	5.7	19.53	7.00
Bayram et al.	740	5.6 ± 2.0	3.3 ± 1.2	7.58 ± 2.70	4.46 ± 1.62
Barlett et al.	864	-	4.0	-	4.62
Stenstad et al.	-	20 ± 7	10 ± 3	-	-

In general, the external dose rates measured in the present study are consistent with one or the other previous studies, but not all studies. When compared with the studies of Harding et al. [18] and Mountford et al. [19], it is seen that the results obtained at 0.50 m within 40 and 50 minutes are consistent, but the values obtained at all time intervals at 1.0 m are higher. The value obtained at 1.0 m in 60 minutes is closer to the result obtained in the study conducted by Stenstad et al. [21]. However, the dose rate values per unit activity taken within 20 and 30 minutes at 0.50 m are consistent with the results obtained by Gomez-Palacios et al. [22] and Mountford et al. [19]. The dose rate value per unit activity taken within 60 minutes at 1.0 m is closer with the result obtained by Gomez-Palacios et al. [22]. In these studies, the measurement time after injection is not exactly specified. In these studies, involving multiple patients and different scan types, the average time after administration was specified.

4. Conclusion

In this study, it was concluded that the external dose rate values vary depending on the anatomical distribution of the radiopharmaceutical in the body and the time of administration. In addition, it was concluded that the increase and decrease of the external dose rate values at a certain time interval after administration may be due to the biological clearance effect of $^{99\text{m}}\text{Tc-MDP}$. The obtained results show that the dose rate decreases respect to distance. It was concluded that this situation is related to the inverse square law, which shows that the radiation intensity decreases with the square of the distance. The lowest value obtained in these measurements can be taken as a safe distance to avoid exposure to high radiation from the patient, who is the radiation source. This provides healthcare staff to protect themselves better. The high amount of radiation emitted from the injected patient can pose a risk for both employees and individuals with whom the patient may be in contact or remain in the same environment. In addition, considering that all patients are waiting in the same room, the external dose rate is estimated to be higher. According to the results, close contact with the patient for a while should be

avoided in order to be protected from environmental radiation. Thus, the amount of activity will decrease according to the half-life and will not pose an environmental risk.

Conflicts of interest

The authors state that there is no conflict of interests.

References

- [1] Saha G. B., Fundamentals of Nuclear Pharmacy, 6nd ed. London: Springer, (2010) 83-100.
- [2] Lee Y. S., Radiopharmaceuticals for Molecular Imaging, *The Open Nuclear Medicine Journal*, 2 (2010) 178-185.
- [3] Grupen C., Buvat I., Handbook of Particle Detection and Imaging, New York: Springer, (2012) 859-881.
- [4] Teksöz S., Müftüler F. Z., Nükleer Tıpta Kullanılan Radyoizotoplar ve Biyomedikal Uygulamaları, *Nuclear Medicine Seminar*, 5 (2019) 10-14.
- [5] Gündoğdu E. A., Özgenç E., Ekinçi M., Özdemir D. İ., Aşıkoglu M., Nükleer Tıpta Görüntüleme ve Tedavide Kullanılan Radyofarmasötikler, *Journal of Literature Pharmacy Sciences*, 7 (1) (2018) 24-34.
- [6] Subramanian G., McAfee J. G., Blair R. J., Kallfelz F. A., Thomas, F. D., Technetium-99m-Methylene Diphosphonate a Superior Agent for Skeletal Imaging: Comparison with other Technetium Complexes, *Journal of Nuclear Medicine*, 16 (1975) 744-755.
- [7] Önsel Ç., Kantarcı F., Görüntüleme Yöntemleri Sempozyumu, İstanbul Üniversitesi Cerrahpaşa Tıp Fakültesi Sürekli Tıp Eğitimi Etkinlikleri. Birinci Basım, İstanbul, 2010.
- [8] Salmanoğlu E., Peksoy İ., Tc-99m MDP'nin intraarteryal enjeksiyonu, *Cukurova Medical Journal*, 41(1) (2016) 75-78.
- [9] IAEA., International basic safety standards for protection against ionizing radiation and for the safety of radiation sources, International Atomic Energy Agency. Safety Series No. 115. Vienna, (1996) 20-30.
- [10] Valantin J., Radiological Protection in Medicine. ICRP Publication 105. Ann. ICRP 3 (2008) 17-22.
- [11] Eckerman K., Harrison J., Menzel H. G., Clement C. H., Compendium of Dose Coefficients based on ICRP Publication 60. ICRP Publication 119, *Ann. ICRP*, 41(1) (2011) 13-22.
- [12] IAEA., Release of Patients After Radionuclide Therapy, International Atomic Energy Agency. Safety Report Series No. 63. Vienna, (2009) 3-15.
- [13] TAEK., Radyonüklit Tedavisi Gören Hastaların Taburcu Edilmesine İlişkin Kılavuz. Ankara: RSGD-KLV-009 (Rev.2), Türkiye Atom Enerji Kurumu, (2016) 7-22.
- [14] ASM 990 Series, Advanced Survey Meter, Available at: <https://www.flukebiomedical.com/products/radiation-measurement>. Retrieved March 25, 2020.
- [15] Chabot G., Instrumentation and Measurements Surveys and Measurements (SM), Health Physics Society, Available at: <http://hps.org/publicinformation/ate/q4148.html>. Retrieved May 25, 2020.
- [16] Vennart J., Radiation Dose to Patients from Radiopharmaceuticals, ICRP Publication 53. Ann. ICRP, 18 (1-4) (1998) 213-217.
- [17] Bartlett M. L., Estimated Dose From Diagnostic Nuclear Medicine Patients to People Outside The Nuclear Medicine Department, *Radiation Protection Dosimetry*, 157 (1) (2013) 44-52.
- [18] Harding L. K., Mostafa A. B., Roden L., Williams N., Dose rates from patients having nuclear medicine investigations, *Nuclear Medicine Communications*, 6 (1985) 191-194.
- [19] Mountford P. J., Odoherly M. J., Forge N. I., Jeffries A., Coakley A. J., Radiation Dose Rates From Adult Patients Undergoing Nuclear Medicine Investigations, *Nuclear Medicine Communications*, 12 (1991) 767-777.
- [20] Martin J. E., Physics for Radiation Protection. 2nd ed. Weinheim: Wiley-Vch, (2006) 305-310.
- [21] Stenstad L. I., Pedersen G. A., Landmark A. D., Bratthheim B., Nuclear Radiation Dose to the Surroundings From Patients Who are Undergoing Nuclear Medicine Examinations, *Peer Reviewed Article*, 1 (2014) 11-18.
- [22] Gomez-Palacios M., Terron J. A., Dominguez P., Vera D. R., Osuna R. F., Radiation Doses in the Surroundings of Patients Undergoing Nuclear Medicine Diagnostic Studies, *The Radiation Safety Journal*, 89 (2) (2005) 27-34.
- [23] Bayram T., Yilmaz A. H., Demir M., Sonmez B., Radiation Dose to Technologists per Nuclear Medicine Examination and Estimation of Annual Dose, *Journal of Nuclear Medicine Technology*, 39 (2011) 55-59.



Investigation of physical and structural properties of cs doped $\text{YBa}_2\text{Cu}_3\text{O}_{7-\delta}$ superconductors

Öznur BAĞ^{1,*} , Saffet NEZİR² 

¹ Gaziosmanpaşa University, Department of Physics, Faculty of Arts and Science, Tokat/TURKEY

² Kırıkkale University, Department of Physics, Faculty of Arts and Science, Kırıkkale/TURKEY

Abstract

In this work, $\text{YBa}_{2-x}\text{Cs}_x\text{Cu}_3\text{O}_{7-\delta}$ ($x = 0.05, 0.1, 0.2$ and 0.3 wt. %) samples were prepared by using solid state reaction method. Some electrical, physical and structural properties of these compounds were examined by using SEM (scanning electron microscopy), XRD (X-ray diffraction), electrical resistivity, critical current density and AC susceptibility measurements, respectively. On the basis of the SEM measurements, it would seem that increasing the amount of Cs doping, the porous structures decrease and the grain size increases up to approximately $50 \mu\text{m}$. Unit cell parameters were calculated by employing XRD measurements. On the basis of the data obtained from X-ray diffraction, Cs atoms displaced Ba atoms in the crystal structure. From the measurements of electrical resistivity at 80 K - 120 K temperature, it was determined that the highest transition temperature was 91.5 K after addition of 0.05 wt. % Cs. The critical transition temperature was decreased by increasing the amount of Cs doping. Critical current density measurements on the same samples showed that as the amount of Cs doping increases, the values of J_c decrease. AC magnetic susceptibility measurements showed a sharper transition to the superconducting state in $\text{YBa}_{2-x}\text{Cs}_x\text{Cu}_3\text{O}_{7-\delta}$ ($x = 0.05, 0.1, 0.2$ and 0.3 wt.%) samples with the increase in the additive amount.

Article info

History:

Received: 09.09.2020

Accepted: 12.04.2021

Keywords:

Cs doping,
Superconductor,
YBCO

1. Introduction

The discovery of high-temperature superconductor Y–Ba–Cu–O in 1987 has stimulated the intensity of scientists in development of the superconducting application theoretically [1]. $\text{YBa}_2\text{Cu}_3\text{O}_{7-\delta}$ (YBCO) superconducting oxides are expected to be used in many technological applications such as magnetic levitation, high-field magnets, magnetic shields, motors and generators, because of their high critical current density (J_c) at 77 K and a high magnetic field [2]. There has been a considerable interest [3-4] in the preparation of good quality Y-Ba-Cu-O superconductors [5]. By adding different elements, such as Nb [6], Pr [7], Au [8], to the Y-Ba-Cu-O superconductor, the material is tried to be made more suitable for use in technological fields [9-10-11-12].

The synthesis of new ceramic materials with improved superconducting properties is one of the major concerns of today's researchers. Since the discovery of high temperature superconductors, many have tried to obtain compounds with better physical and morphological properties using simpler methods. The most commonly used chemical synthesis methods are solid state [13], sol-gel [14], automatic combustion [15], metal organic

chemical vapor deposition (MOCVD) [16] and microwave-based methods [17]. The most commonly used methods can be considered as a solid state reaction method, melting-casting method and sol-gel (nitrate), thin-film method. A solid-state method is the most widely preferred by superconductivity research groups due to the ease of use and cheapness [10].

The aim of this study was to synthesize and characterize the YBCO high temperature superconductor doped with different Cs element percentages and to investigate the effects of Cs doping on the properties of these superconducting compounds. A solid state reaction method was used to prepare $\text{YBa}_{2-x}\text{Cs}_x\text{Cu}_3\text{O}_{7-\delta}$ ($x = 0.05, 0.1, 0.2$ and 0.3 wt. %) superconducting compounds. We have studied the physical, structural and electrical properties of produced samples with XRD (X-ray powder diffraction), SEM (scanning electrical microscope), electrical resistivity, critical current density and AC susceptibility measurements.

2. Materials and Methods

The starting composition of $\text{YBa}_{2-x}\text{Cs}_x\text{Cu}_3\text{O}_{7-\delta}$ ($x = 0.05, 0.1, 0.2$ and 0.3 wt. %) samples were prepared by using high purity nitrate compounds ($\text{Y}(\text{NO}_3)_3 \cdot 6\text{H}_2\text{O}$,

*Corresponding author. e-mail address: oznurbag@gmail.com

$\text{Ba}(\text{NO}_3)_2$, $\text{Cu}(\text{NO}_3)_3 \cdot 3\text{H}_2\text{O}$ and $\text{Cs}(\text{NO}_3)$). The samples were subjected to calcination process for 4 h at 650 °C. After cooling to room temperature, the samples were ground for 2 h and pressed under a pressure of 440 MPa into pellets. The samples were put into a furnace at room temperature. The samples were sintered at 935 °C and attended under flowing oxygen atmosphere for 40 h, and then cooled to room temperature. The heating and cooling temperature rates were chosen to be 5 °C/min⁻¹ and 1 °C/min⁻¹, respectively. A schematic representation of sintering process is shown in Figure 1.

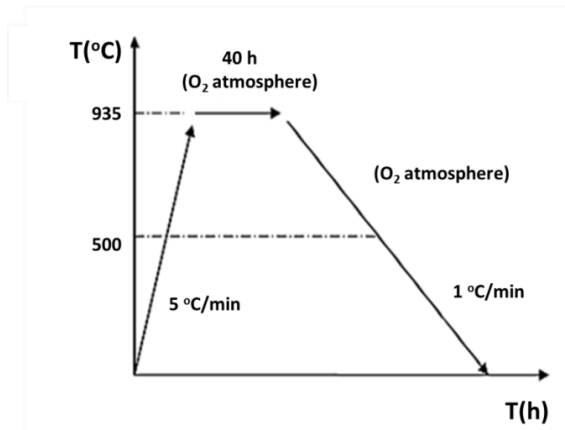


Figure 1. Schematic drawing of sintering process for the samples preparation.

The morphology of all superconducting samples are examined by using scanning electron microscope (Model Jeol JSM 5600). X-ray diffraction data were recorded using a Rigaku diffractometer with $\text{Cu-K}\alpha$ radiation over the range $2\theta = 10^\circ - 60^\circ$. The lattice parameters of superconducting samples were estimated by utilizing X-ray diffraction measurements. The superconducting transition temperature (T_c) and critical current density of samples was determined by a standart four-probe method [18]. Magnetic measurements were performed using a 7130 AC susceptometer of Lake Shore at temperature range of 40 K-100 K with a fixed magnetic field (80 m/A) and fixed frequency (111 Hz).

3. Results and Discussion

SEM images of the samples are shown in Figure 2. In the light of SEM analysis, it has been detected that the average particle size boosts as the amount of the addition grows [19, 20, 21]. The particles in the sample with 0.05 Cs addition are by and large circular and have 10 – 15 μm while the particles in the sample with 0.1 Cs addition are in the shape of a rectangular prism and their particle height can extend up to 30 μm . As illustrated in the Fig. 2, the particle height can reach up

to 50 μm in the samples which assume 0.2 and 0.3 addition rate and their width is about 10 μm on average. Furthermore, it can be inferred that the gaps among the particles have vanished to a great extent unlike first two samples, which leads to better contact among the particles [22]. As a result, it is contemplated that it will end in higher values of critical current density compared those of others. It is believed that to be increased the formation of liquid phase in the YBaCuO with Cs addition and it has also lead to remarkable growth in the grains.

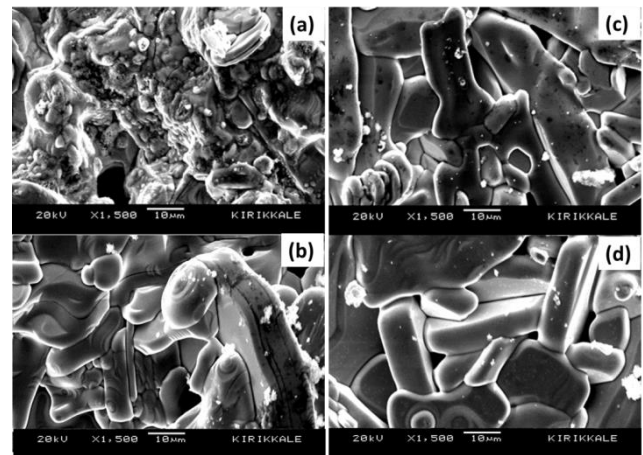


Figure 2. SEM micrographs of $\text{YBa}_{2-x}\text{Cs}_x\text{Cu}_3\text{O}_{7-\delta}$ ($x = 0.05, 0.1, 0.2$ and 0.3 wt. %) a) 0.05 Cs b) 0.1 Cs c) 0.2 Cs d) 0.3 Cs.

The XRD patterns of $\text{YBa}_{2-x}\text{Cs}_x\text{Cu}_3\text{O}_{7-\delta}$ ($x = 0, 0.05, 0.1, 0.2$ and 0.3 wt. %) are shown in Figure 3. All samples have the $\text{YBa}_{2-x}\text{Cs}_x\text{Cu}_3\text{O}_{7-\delta}$ ($x = 0.05, 0.1, 0.2$ and 0.3 wt. %) phase which is responsible of the superconducting state. As seen in Figure 3, it is understood that the samples completed the structural phase formation as a result of annealing and all the peaks obtained are compatible with the literature [23, 24, 25]. As can inferred from the figure, there appeared no superconductor phase and peaks belonging to tetragonal phase with low oxygen level. The (103), (113) and (123) peaks are seemed to decrease with increasing of Cs addition. Peaks such as (003), (004), (005) and (006) at the direction of c axis appear noticeably. That demonstrates that particles on the samples acquire acceleration throughout c axis as the amount of the addition increases. On the basis of ASTM data, no characteristic Cs peak has been observed as a result of comparison and contrast of characteristic peaks belonging to Cs with sample peaks. Such a portrait proves the fact that all Cs atoms replacing Ba atoms have largely occupied the spaces of Ba atoms bearing a crystal structure.

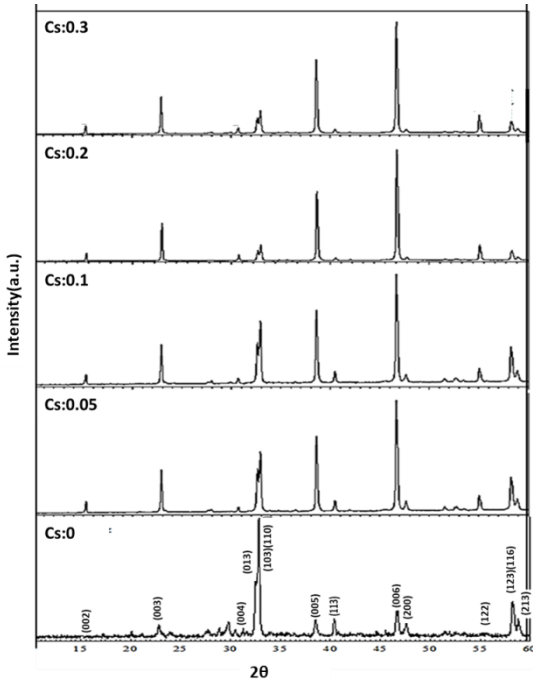


Figure 3. The X-ray diffraction patterns of $\text{YBa}_{2-x}\text{Cs}_x\text{Cu}_3\text{O}_{7-\delta}$ ($x = 0, 0.05, 0.1, 0.2$ and 0.3 wt. %).

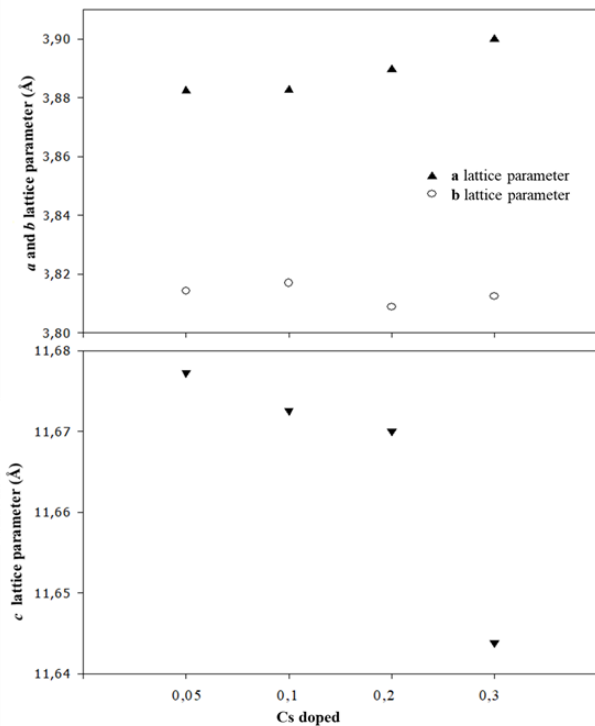


Figure 4. The lattice parameters of $\text{YBa}_{2-x}\text{Cs}_x\text{Cu}_3\text{O}_{7-\delta}$ ($x = 0.05, 0.1, 0.2$ and 0.3 wt. %).

The lattice parameters obtained from X-ray diffraction of the samples and are plotted in Figure 4. The a parameter is found to increase continuously and the c parameter decrease with increasing of Cs concentration. It is estimated that this is caused by the fact that the ionic radius of Cs entering instead of Ba is larger, due to the O (5) gaps, the a axis expands a little

and thus the c axis is slightly contracted [26]. It is thought that there is not much change in the b parameter due to the O (1) ions located in the b axis.

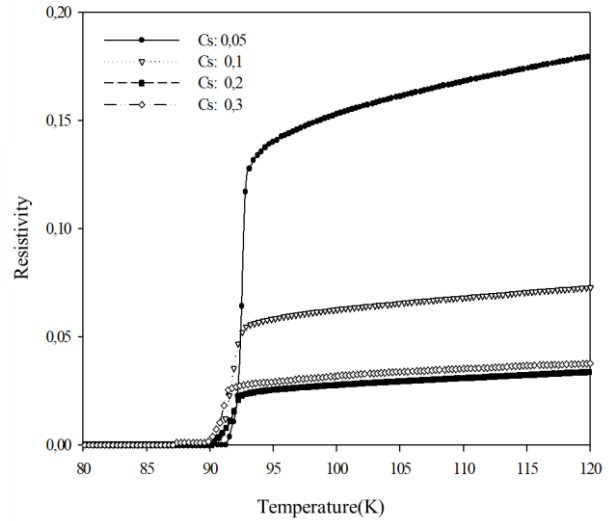


Figure 5. The electrical resistivity measurements of $\text{YBa}_{2-x}\text{Cs}_x\text{Cu}_3\text{O}_{7-\delta}$ ($x = 0.05, 0.1, 0.2$ and 0.3 wt. %).

Figure 5 is shown that electrical resistivity measurement of $\text{YBa}_{2-x}\text{Cs}_x\text{Cu}_3\text{O}_{7-\delta}$ ($x = 0, 0.05, 0.1, 0.2$ and 0.3 wt. %). As can be deduced from the figure, there happens a slight decrease in the resistance values in the normal zone the amount of the addition increases. It has been observed that superconductor transition (ΔT_c) is too sharp (app. 1.5 K). On the other hand, in the sample with 0.05 Cs addition its 91.5 K value decreases to 90 K in the sample in which the addition amount grows up to 0.3 in terms of weight. That effect may be traced from the graphic of the change of normalized impedance by heat illustrated in the Fig. 5. The study by M. Ausloos and his colleagues in which they replaced Ba with 0.05 Cs reported the critical transition heat as 80 K [27]. Whereas, 91.5 K heat was measured in the sample which we manufactured using the same addition.

Critical current density measurements were conducted applying 5 μA current through standard four-probe method. Figure 6 shows the measurement results. On the basis of measurements, it has been perceived that J_c values increase as the amount of the addition increases. While J_c is about 40-55 A/cm^2 in the samples with low addition, it moves to its maximum value, that is 160 A/cm^2 , in the sample with 0.3 Cs addition. It is estimated that the increase in the contact among the particles due to the decrease in the porosity and the increase in the particle size lead to such a change as can be inferred upon the analysis of SEM images.

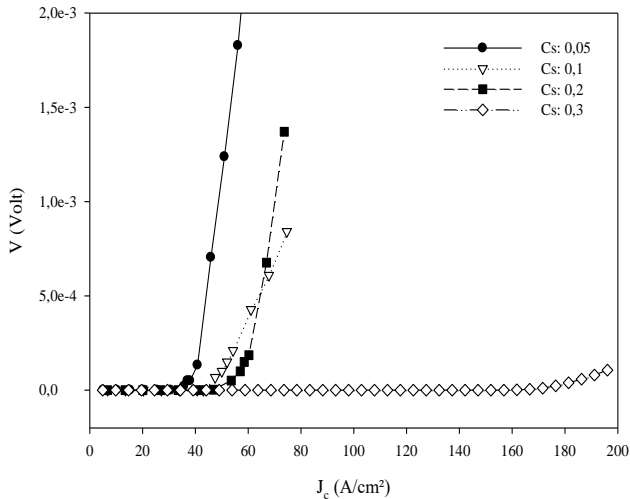


Figure 6. The critical current density J_c of $\text{YBa}_{2-x}\text{Cs}_x\text{Cu}_3\text{O}_{7-\delta}$ ($x = 0.05, 0.1, 0.2$ and 0.3 wt. %).

Figure 7 shows the AC magnetic measurements at the temperature range of 40-100 K. As mentioned in the literature [28, 29, 30], coupling diamagnetic shielding seems clearly in relatively more granular the samples. In the samples where the Cs additive ratio is 0.2 and 0.3, the grain effect decreases considerably and the material passes into superconductivity more sharply.

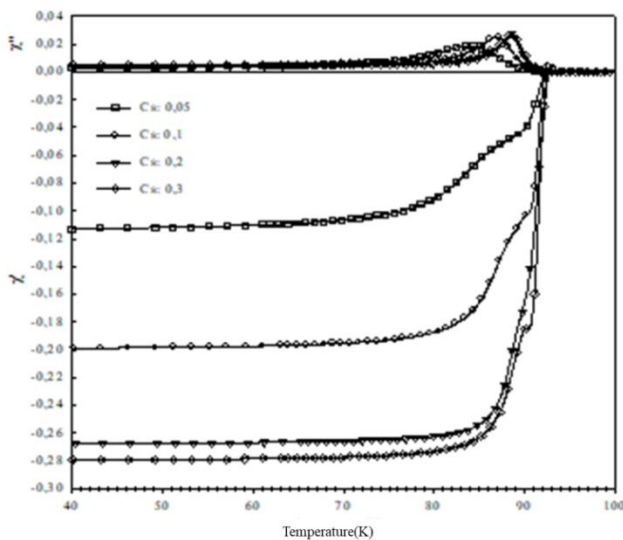


Figure 7. AC magnetic susceptibility of $\text{YBa}_{2-x}\text{Cs}_x\text{Cu}_3\text{O}_{7-\delta}$ ($x = 0.05, 0.1, 0.2$ and 0.3 wt. %).

4. Conclusions

In summary, Cs-added YBCO compounds were produced using the compounds of nitrated unlike conventional samples and we have identified some electrical, physical and structural properties of Cs-added YBaCuO superconducting samples. Scanning electron microscopy (SEM) images were obtained for annealed (at 935°C for 40 h) samples. It can be seen

that the porous structure in the samples has decreased with the increasing of the amount of the additive.

According to XRD measurements, (001) peak in the grains of all superconducting samples was observed to be significantly with the increasing of the amount of the additive. There appeared no superconductor phase and peaks belonging to tetragonal phase with low oxygen level. So it is appeared that the samples were completed the structural phase formation. By calculating the lattice parameters, it is observed a significant decrease in the lattice parameter c . This is estimated to cause the Cs atoms settle in the place of Ba atoms. The electrical resistivity measurement shows the resistivity of the samples and it is observed to occur in a slight decrease with increasing the amount of contribution. The study by M. Ausloos and his colleagues in which they replaced Ba with 0.05 Cs reported the critical transition heat as 80 K [26]. Whereas, 91.5 K heat was measured in the sample which we manufactured using the same addition. According to the results of the AC magnetic susceptibility measurements, as the amount of additive increased, it was seen that there was a visible decrease towards the ideal value of -1 in the real part of magnetic susceptibility. Cs addition enhances the formation of liquid phase in the YBCO superconducting compounds and as a consequence, it is believed that the coarse-grained structure emerged.

Conflicts of interest

The authors state that did not have conflict of interests.

References

- [1] Wu M.K., Ashbourn J., Torng C. J., Hor P.H., Meng R.L., Gao L., Huang Z.J., Wang Y.Q. and Chu C.W., Superconductivity at 93 K in a new mixed-phase Y-Ba-Cu-O compound system at ambient pressure, *Phys. Rev. Lett.*, 58 (1987) 908.
- [2] Zhang R.X., Yang H.X., Tian H.F., Chen G.F., Wu S.L., Wei L.L., Li J.Q., Superconductivity in the orthorhombic phase of thermoelectric $\text{CsPb}_x\text{Bi}_{4-x}\text{Te}_6$ with $0.3 \leq x \leq 1.0$, *Journal of Solid State Chemistry*, 232 (2015) 50–55.
- [3] Mumkani M., Melt processing of YBaCuO superconductors and critical currents, *Modern Physica Lett. B* 4(3) (1990) 163.
- [4] Yanmaz E., Drake A., Harris I.R. and Abell J.S., Melt processing of powdered arc-cast $\text{YBa}_2\text{Cu}_3\text{O}_y$ materials, *J. Alloys Compounds*, 195 (1993) 23.

- [5] Gencer A., Ateğ A., Aksu E., Nezir S., Çelebi S. And Yanmaz E., Microstructural and physical properties of $\text{YBa}_2\text{Cu}_3\text{O}_{7-\delta}$ superconductors prepared by the flame-quench-melt-growth (FQMG) method, *Physica C*, 279 (1997) 165-172.
- [6] Naik S.P.K., Raju P.M.S., Seshubai V., Role of Sm and Nb on the preform optimized infiltration growth processed YBCO superconductors, *Materials Chemistry and Physics*, 182 (2016) 503-507.
- [7] Vovk R.V., Khadzhai G.Y., Dobrovolskiy O.V., Resistive measurements of the pseudogap in lightly Pr-doped $\text{Y}_{1-x}\text{Pr}_x\text{Ba}_2\text{Cu}_3\text{O}_{7-x}$ single crystals under high hydrostatic pressure, *Solid State Communications*, 204 (2015) 64–66.
- [8] Dadras S., Gharehgasloo Z., Effect of Au nanoparticles doping on polycrystalline YBCO high temperature superconductor, *Physica B*, 492 (2016) 45–49.
- [9] Guo N.N., Leu M.C., Additive manufacturing: technology, applications and research needs, *Front. Mech. Eng.*, 8 (2013) 215–243.
- [10] Wei X., Nagarajan R.S., Peng E., Xue J., Wang J., Ding J., Fabrication of $\text{YBa}_2\text{Cu}_3\text{O}_{7-x}$ (YBCO) superconductor bulk structures by extrusion freeforming, *Ceramics International*, 42 (2016) 15836–15842.
- [11] Volochova D., et al., YBCO bulk superconductors doped with gadolinium and samarium, *Physica C-Superconductivity and Its Applications*, (2013) 494.
- [12] Volochova D., et al., Contamination of YBCO bulk superconductors by samarium and ytterbium, *Physica C-Superconductivity and Its Applications*, (2014) 496.
- [13] Grigoryan S., et al., A new way of preparing the Y–Ba–Cu–O high-temperature superconductor using the sol–gel method, *Supercond. Sci. Technol.*, (2003), 16 (10) 1202.
- [14] Tang X., Zhao Y. and Grivel J.C., Influence of initial pH on the microstructure of $\text{YBa}_2\text{Cu}_3\text{O}_{7-x}$ superconducting thin films derived from DEA-aqueous sol-gel method, *Ceramics International*, (2013) 39.
- [15] Suan M.S.M. and Johan M.R., Synthesis of Al_2O_3 nanoparticles highly distributed in $\text{YBa}_2\text{Cu}_3\text{O}_7$ superconductor by citrate-nitrate auto-combustion reaction, *Physica C-Superconductivity and Its Applications*, 492 (2013) 49.
- [16] Li S.W., et al.. Morphology and superconducting properties of photo-assisted MOCVD processed YBCO film by variation of sublimation temperature of the Cu-based precursor, *Physica C-Superconductivity and Its Applications*, (2012) 478.
- [17] Baghurst D.R., Chippindale A.M., and Mingos D.M.P., Microwave syntheses for superconducting ceramics, *Nature*, (1988) 332.
- [18] Schildermans I., Van Bael M.K., Knaepen E., Yperman J., Mullens J. and Poucke L.V., *Physica C*, (1997) 4848278, 55.
- [19] Cheng C.W., Innes A.C.R., McN Alford N., Harmer M.A. and Birchall J., The effect of porosity on the superconducting properties of $\text{YBa}_2\text{Cu}_3\text{O}_x$ ceramic, *Supercond. Sci. Technol.* 1, 113 (1988).
- [20] Murakami M., Supercond. Processing of bulk YBaCuO , *Sci. Technol.* 5, 185 (1992).
- [21] LaGraff J.R. and Payne D.A., Chemical diffusion of oxygen in single-crystal and polycrystalline $\text{YBa}_2\text{Cu}_3\text{O}_{6+x}$ determined by electrical-resistance measurements, The American Physical Society, *Phys. Rev. B.* 47 (1993) 3380.
- [22] Dadras S., Dehghani S., Davoudiniya M., Falahati S., Improving superconducting properties of YBCO high temperature superconductor by Graphene Oxide doping, *Materials Chemistry and Physics*, 193 (2017) 496-500.
- [23] Yvon K. and François M., Crystal structures of high-Tc oxides, *Z. Phys. B - Condensed Matter*, 76(1989) 413.
- [24] Alecu G., Crystal Structures of Some High-Temperature Superconductors, *Romanian Reports Of Physics*, 56 (2004) 404.
- [25] Cava R.J., Batlogg B., van Dover R.B., Murphy D.V., Sunshine S., Siegrist T., Remeika J.P., Rietman E.A., Zahurak S. and Espinosa G.P., Bulk superconductivity at 91 K in single-phase oxygen-deficient perovskite $\text{Ba}_2\text{YCu}_3\text{O}_{9-6}$, *Physical Review Letter*, 59 (1987) 1676.
- [26] Kikuchi M., Syono Y., Tokiwa A., Oh-Ishi K., Arai H., Hiraga K., Kobayashi N., Sasaoka T. and Muto Y., *Japanese journal of Applied Physics*, 26 (1987) L1066.
- [27] Ausloos M., Superconductivity in $\text{YBa}_{1.95}\text{Cs}_{0.05}\text{Cu}_3\text{O}_{7-y}$ granular ceramics, *Physical Review B*, 39 (1989) 2729.
- [28] Goldford R.B., Lelental M. and Thompson C.A., *Alternating-Field Susceptometry and Magnetic Susceptibility of Superconductors*, NISTIR. 3977 (1991) 1.

- [29] Nikola M. and Goldfarb R.B., Flux creep and activation energies at the grain boundaries of Y-Ba-Cu-O superconductors, *Physical Review B.*, 39 (1989) 6615.
- [30] Calzona V., Cimberle M.R., Ferdeghini C., Putti M., Sırı A.S., Vaccarone R., Supercurrent lengthscale in sintered YBCO and critical state model, *Physica C.*, 157 (1989) 425.



Effect of pressure, temperature, and magnetic field on the binding energy of the electron-hole system in III-V group semiconductors

Pınar BAŞER^{1,*}

¹Sivas Cumhuriyet University, Department of Physics, Sivas/ TURKEY

Abstract

In this study, ground state binding energy of heavy hole magneto exciton in GaAs/In_{0.47}Ga_{0.53}As cylindrical quantum well wires (CQWWs) were calculated using variational technique depending on wire size and external parameters. We can briefly state the change of binding energy with hydrostatic pressure, temperature, wire radius and external magnetic field strength as follows. With increasing temperature for constant pressure and magnetic field strength the exciton binding energy decreases slightly. On the other hand, increasing magnetic field strength and pressure increase the binding energy as the particle's quantum confinement effects increase. To interpret these results, we examined pressure and temperature changes of barrier heights, effective masses, wire radius, dielectric constant, and band offsets. Conduction and valence band offset increase by 37% with pressure, while band offsets decrease by -1.55% with temperature. These differences in values are directly due to the difference in pressure and temperature coefficients of the prohibited band gaps of GaInAs and InAs. These variations in binding energy, as well as in electron and hole energies, depending on structure parameters and external parameters provide a prediction to produce adjustable semiconductor devices.

Article info

History:

Received: 01.02.2021

Accepted: 26.04.2021

Keywords:

Quantum Wires;
Exciton Binding
Energy; III-IV
Semiconductor

1. Introduction

Studying electron behavior trapped in one-dimensional structures is interesting in terms of solid-state physics and device applications. It is known that quantum well wires (QWWs) structures are used to improve the performance of lasers and nonlinear devices and in new optoelectronic device designs. Advances in crystal growth techniques have allowed the physical realization of semiconductor one dimensional (1D) QWWs structures on nanometer scale. The determination of the Coulombic interaction term, which consists of a confinement of electrons and holes in one-dimensional quantum wires, is very important since it gives information about the optical properties of the structure. Since the particle motion in QWWs structures is free in one dimension, the exciton binding energy and exciton oscillator size increase considerably compared to quantum well (QW) structures where particle since the QWWs particle is confined in two dimensions, it can be said that the exciton binding energy increases significantly compared to QW structures where the particle motion is restricted in one dimension [1]. These semiconductor materials have an important place in device applications. For this reason, both exciton and

impurity levels have an important place in determining their optical properties.

The electron hole pair connected to each other by the Coulomb interaction is called an exciton. Numerous experimental and theoretical studies have been carried out showing that the confinement effects of excitonic levels in low-dimensional structures change with applied external fields, hydrostatic pressure, and temperature, and excitonic levels in low-dimensional structures have contributed to optoelectronic device designs [2-6].

Since the symmetry of the system in an external electric and magnetic field decreases, level divisions and new transitions are seen in the spectrum of the exciton. In addition, the ionization and stabilization of exciton states originating from new fields, the formation of diamagnetic bands and the like are observed in the energy spectrum. The effects of external fields on low dimensional structures have been studied extensively [7-12].

Similar to the external magnetic field, hydrostatic pressure and temperature applied to nano structures are external parameters that change the properties of low-dimensional systems. For example, depending on the

*Corresponding author. e-mail address: pbaser@cumhuriyet.edu.tr

<http://dergipark.gov.tr/csj> ©2021 Faculty of Science, Sivas Cumhuriyet University

direction of the magnetic field, another electronic confinement occurs in addition to the spatial confinement. Therefore, new electronic properties arise depending on the magnetic field. Since the band gap of the material can be changed by changing these external parameters applied to optoelectronic devices, the semiconductor properties are also changed.

It is an important effect that changes the electronic properties of semiconductors at hydrostatic pressure, such as external fields. Since the pressure changes the lattice parameters and therefore the average distance between electrons and holes, the forbidden band gap and the periodic potential of the structure change with the applied pressure. Similarly, it alters the electronic structure of the semiconductor with temperature. For these reasons, pressure and temperature effects have been studied. The observed temperature-dependent energy range is consistent with the empirical Varshni equation [13]. For these reasons, it has been the focus of attention to examine the properties of GaAs/GaAlAs and GaAs/ InGaAs semiconductors to these external parameters [14].

Structures consisting of $\text{In}_x\text{Ga}_{1-x}\text{As}$ ternary compound grown on GaAs substrate are of great interest due to their applications in micro and optoelectronics. $\text{In}_x\text{Ga}_{1-x}\text{As}$ is a ternary semiconductor compound with direct bandwidths ranging from 0.36 eV to 1.42 eV [15-18]. Some application areas of this semiconductor compound are light emitting diodes (LEDs), laser diodes (LDs) [19-22], quantum well infrared photo detectors (QWIP) [23, 24], high electron mobility transistor (HEMT) devices [25], as well as medium to mid-infrared light sources [26]. Characterization studies for these materials date back to 1978 [27, 28].

Since the lattice constants of GaAs, InP and d InAs are 5.65, 5.86, and 6.05 Å, respectively, the ability to grow thick, high-quality epitaxial layers of $\text{In}_x\text{Ga}_{1-x}\text{As}$ on a GaAs, InP, or InAs substrate is very limited due to Where $|\vec{r}| = |\vec{r}_e - \vec{r}_h|$ the relative is coordinate, \vec{P}_e and $m_e^*(P, T)$ define the momentum operator and the effective mass of the electron, respectively, while \vec{P}_h and $m_h^*(P, T)$ are the momentum operator and the

$$V_{e(h)}(\rho_{e(h)}, P, T) = \begin{cases} V_{0e(h)}(P, T) & \rho_{e(h)} \geq R(P) \\ 0, & \rho_{e(h)} < R(P) \end{cases} \quad (2)$$

Where $R(P)$ is the wire radius of CQWWs, $V_{0e}(P, T)$ is the conduction band offset, $V_{0h}(P, T)$ is the valans band offset. Band offsets of the GaAs/ $\text{In}_{0.47}\text{Ga}_{0.53}\text{As}$ heterostructure for the conduction and valence band,

lattice mismatch except for a specific composition. For example, only $\text{In}_{0.53}\text{Ga}_{0.47}\text{As}$ lattice matches to InP, and thus very good quality thick films of this composition can be grown on InP [29-31].

One-dimensional nanostructures have great potential not only for basic research materials due to their unique structural and physical properties relative to their ingot structures, but also for future technological applications. The one-dimensional motion of the particle in CQWWs lasers results in improved static and dynamic laser performance. The very low threshold current seen in these lasers will be useful for optoelectronic device and signal applications. With this motivation, the aim of this study is to investigate the effect of magnetic field, hydrostatic pressure, temperature, and wire radius on the binding energy of exciton levels in GaAs/ $\text{In}_{0.47}\text{Ga}_{0.53}\text{As}$ one dimensional QWWs. Variational method and effective mass approach were used in these calculations.

2. Materials and Methods

The Hamilton equation of the exciton under the magnetic field applied in the z direction, which is the growth direction of the hetero structure, is defined as in Eq. 1. The solution is made under the variational technique and effective mass approach, considering the changes under pressure and temperature [32]. Theoretical calculations also use cylindrical gauge $\vec{A}_{e(h)}(\vec{r}) = (\vec{B} \times \vec{r})/2$, and parabolic band approaches. Here the symbol e represents the electron, and the symbol h indicates the hole.

$$H = \frac{1}{2m_e^*(P, T)} \left(\vec{P}_e + \frac{e}{c} \vec{A}_e \right)^2 + \frac{1}{2m_h^*(P, T)} \left(\vec{P}_h - \frac{e}{c} \vec{A}_h \right)^2 + V_e(\rho_e, P, T) + V_h(\rho_h, P, T) - \frac{e^2}{\varepsilon(P, T)|\vec{r}|} \quad (1)$$

effective mass of the hole depending on pressure and temperature, respectively. $\varepsilon(P, T)$ is the dielectric constant and $V_{e(h)}(\rho_{e(h)}, P, T)$ is the confining potentials, defined as [33]

70% (30%) of the total band gap difference is taken as [34]. Schematic representation of the cylindrical quantum wire in Fig. 1 (a), in Fig.1 (b), the potential profile consisting of the sum of the parabolic confinement caused by the magnetic field and the spatial confinement is shown.

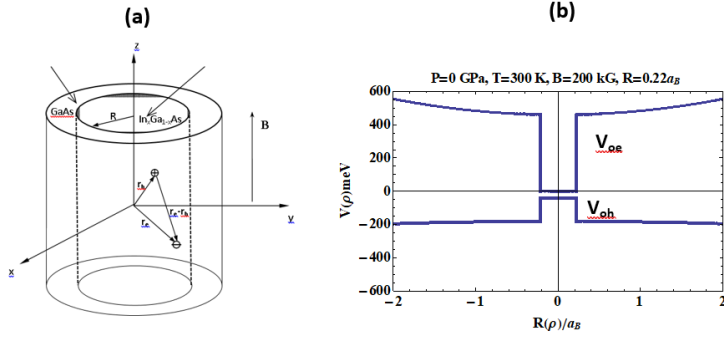


Figure 1. (a) Schematic representation of a cylindrical quantum wire (b) Spatial and parabolic confinement potential for $P=0$ GPa, $T=300$ K, $B=200$ kG.

Pressure dependence of wire radius it can be derived from fractional change in volume

$(\Delta V/V_0 = (-3P(S_{11} + S_{12})))$ due to change in hydrostatic pressure is given by [35],

$$R(P) = R(0)[1 - 3P(S_{11} + 2S_{12})]^{1/2} \quad (3)$$

$R(0)$ is the original wire radius at $P = 0$ GPa. Here, S_{11} and S_{12} are elastic constants. It can be defined as $|\vec{r}|$ in the Hamiltonian equation.

$$|\vec{r}| = |\vec{r}_e - \vec{r}_h| = \sqrt{\rho_e^2 + \rho_h^2 - 2\rho_e\rho_h \cos(\phi_e - \phi_h) + (z_e - z_h)^2} \quad (4)$$

Since the difference between the effective mass and dielectric constants, which are among the parameters changing due to temperature and pressure, is very small, the values of GaAs semiconductor were used in the calculations of GaAs and GaInAs. Parameter values of GaAs were used in calculations [$m_e^* = 0.0665 m_0$, $m_h^* = 0.134 m_0$, m_0 is the free electron mass, and $\epsilon = 12.4$] [36]. It is given as the electron mass depending on external parameters.

$$m_e^*(P, T) = \left[1 + E_p^\Gamma \left(\frac{2}{E_g^\Gamma(P, T)} + \frac{1}{E_g^\Gamma(P, T) + 0.341} \right) \right]^{-1} m_0 \quad (5)$$

Where $E_p^\Gamma = 7.51$ eV. We used the isotropic heavy hole mass here. For a heavy hole, the effective mass depends solely on hydrostatic pressure and is given by

$$m_h^*(P) = [0.134 + (a_2 P + a_3 P^2)] m_0 \quad (6)$$

where $a_2 = -0.1 \times 10^{-2}$ GPa $^{-1}$ and $a_3 = 5.5 \times 10^{-4}$ GPa $^{-2}$. The heavy hole isotropic hole mass is calculated from

$$(m_h^*)^{-1} = \left(\frac{2}{3}\right) (m_h^*(x, y))^{-1} + \left(\frac{1}{3}\right) (m_h^*(z))^{-1} \quad (7)$$

$\varepsilon(P, T)$ is defined by [36]

$$\varepsilon(P, T) = \begin{cases} 12.74 e^{-1.67 \cdot 10^{-2} P} e^{9.4 \cdot 10^{-5} (T - 75.6)}, & T \leq 200 K \\ 13.18 e^{-1.73 \cdot 10^{-2} P} e^{20.4 \cdot 10^{-5} (T - 300)}, & T > 200 K \end{cases} \quad (8)$$

$E_g^\Gamma(P, T)$, temperature, pressure dependent band gap at Γ points is given by

$$E_g^\Gamma(P, T) = E_g^0 + \alpha P - \beta T^2 (T + c)^{-1} \quad (9)$$

Where E_g^0 is the forbidden band gap at room temperature without pressure, $E_g^0(GaAs) = 1.52$ eV, $E_g^0(InAs) = 0.42$ eV, α is the pressure coefficient $\alpha(GaAs) = 10.8 \times 10^{-2}$ eV/GPa, $\alpha(InAs) = 7.7 \times 10^{-2}$ eV/GPa, β and c are temperature coefficients, $\beta(GaAs) = 5.405 \times 10^{-4}$ eV/K, $\beta(InAs) = 4.19 \times 10^{-4}$ eV/K) and $c(GaAs) = 204$ K, $c(InAs) = 271$ K [37, 38].

The band gap $E_g(P, T)$ equation for the $In_xGa_{1-x}As$ compound can be written as follows [39].

$$E_g^{GaInAs}(P, T) = E_g^{GaAs}(P, T) + [E_g^{InAs}(P, T) - E_g^{GaAs}(P, T)]x - 0.475x(1 - x) \quad (10)$$

The Hamiltonian eigenfunctions in the absence of the interaction term are defined by confluent hypergeometric functions. In the wave function equation, while N is the normalization constant, $({}_1F_1(-a_{01}, 1, \xi))$ and $U(-a'_{01}, 1, \xi)$ are hypergeometric functions that describe the particle in the InGaAs material within the GaAs material, respectively.

$$\Psi_1(\vec{r}_e, \vec{r}_h)$$

$$= \begin{cases} N \exp\left(-\frac{\xi_e + \xi_h}{2}\right) {}_1F_1(-a_{o1(e)}, 1, \xi_{R(e)}) {}_1F_1(-a_{o1(h)}, 1, \xi_{R(h)}) & \rho_{e(h)} \leq R(P) \\ N \frac{{}_1F_1(-a_{o1(e)}, 1, \xi_{R(e)})}{U(-a'_{o1(e)}, 1, \xi_{R(e)})} \exp\left(-\frac{\xi_e + \xi_h}{2}\right) U(-a'_{o1(e)}, 1, \xi_e) {}_1F_1(-a_{o1(h)}, 1, \xi_h) & \rho_e > R(P) \text{ and } \rho_h \leq R(P) \\ N \frac{{}_1F_1(-a_{o1(h)}, 1, \xi_{R(h)})}{U(-a'_{o1(h)}, 1, \xi_{R(h)})} \exp\left(-\frac{\xi_e + \xi_h}{2}\right) {}_1F_1(-a'_{o1(e)}, 1, \xi_e) {}_1F_1(-a_{o1(h)}, 1, \xi_h) & \rho_e \leq R(P) \text{ and } \rho_h > R(P) \\ N \frac{{}_1F_1(-a_{o1(e)}, 1, \xi_{R(e)})}{U(-a'_{o1(e)}, 1, \xi_{R(e)})} \frac{{}_1F_1(-a_{o1(h)}, 1, \xi_{R(h)})}{U(-a'_{o1(h)}, 1, \xi_{R(h)})} \exp\left(-\frac{\xi_e + \xi_h}{2}\right) U(-a'_{o1(e)}, 1, \xi_e) {}_1F_1(-a_{o1(h)}, 1, \xi_h) & \rho_{e(h)} > R(P) \end{cases} \quad (11)$$

Here the cyclotron radius $\alpha_{c[e(h)]}$ is defined by $\alpha_{c[e(h)]} = \left(\sqrt{\rho_{e(h)}^2 / \mu_{e(h)} \omega_{c[e(h)]}}\right)$ while the variable $\xi_{e(h)}$ is defined by $\xi_{e(h)} = (\rho_{e(h)}^2 / 2\alpha_{c[e(h)]}^2)$. Where $\omega_{c[e(h)]}$ is the cyclotron frequency, μ defines the reduced mass, $\omega_{c[e(h)]}$ is defined by $\omega_{c[e(h)]} = (eB/m_e^*(h))$ and μ is defined by $\mu = (m_e^* m_h^* / m_e^* + m_h^*)$. Here a_{o1} and a'_{o1} are eigenvalues inside and outside the wire radius, respectively, and these eigenvalues can be found by applying the boundary condition $\rho_{e(h)} = R$ to wave functions and their derivatives in the Eq. 11. The Hamiltonian's solution in Eq. 1 is given as the product of the term containing the variational function and the radial solutions, considering the exciton term [40]. N_1 is the normalization constant

$$\psi(\vec{r}_e, \vec{r}_h) = N_1 \psi_1(\vec{r}_e, \vec{r}_h) \exp(-\lambda|\vec{r}_e - \vec{r}_h|) \quad (12)$$

We can calculate the exciton binding energy in CQWWs from the difference in energy between the state where there is no columbic term and the state of interaction. The energies are scaled to the Rydberg constant, the Bohr radius in lengths (scaled with Rydberg constant for $P=0$, $R_B = (\mu e^4 / \epsilon_0^2 \hbar^2)$ (3.5 meV in GaAs) and Bohr radius, $a_B = (\epsilon_0 \hbar^2 / \mu e^2)$ (155Å in GaAs)). Binding energy is given by $E_b(R, B, P, T)$ [40],

$$E_b(R, B, P, T) = E_{e1} + E_{hh1} - \min_{\lambda} \langle \psi | \hat{H} | \psi \rangle \quad (13)$$

Where E_{e1} and E_{hh1} are magnetoelectric band energies. $\min_{\lambda} \langle \psi | \hat{H} | \psi \rangle$ is the minimized value of $\langle \psi | \hat{H} | \psi \rangle$ with respect to λ .

3. Results and Discussion

The change of the heavy hole exciton binding energy in CQWWs consisting of GaAs-InGaAs heterostructure for different pressure values at room temperature and in the absence of magnetic field, depending on the wire size is given by Fig. 2. In numerical calculations, in concentration is $x = 0.47$, $V_{oe}=124.13$, $V_{oh}=53.19$ meV and $\mu=0.0447m_o$ [40]. For all pressure values, we see that the binding energy decreases as the wire radius increases. This is in line with our expectations, because as the wire radius increases the spatial limitation on the particle decreases. In this case, we find the probability density of the particle at any value of the large wire radius. It is clearly seen in Fig. 3 (a). Since the electron and the hole move closer together as the wire radius decreases, with decreasing wire radius the binding energy increases until a certain maximum value is reached. Particles of maximum value are closest to each other. As can be seen from the Fig. 3 (b). With the wire radius decreasing after this maximum value, the binding energy rapidly decreases to the characteristic bulk value of the GaAs. The correctness of this statement is shown in Fig. 3 (c).

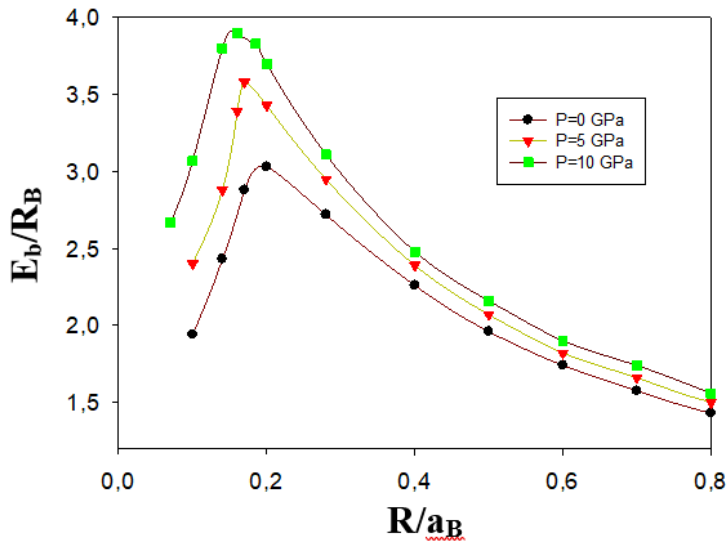


Figure 2. Exciton ground state binding energy for various hydrostatic pressure values

In addition, another point that draws attention is that the pressure value increases, and the maximum binding energy occurs at smaller wire radii. This is in line with our expectation, as the exciton Bohr radius decreases with increasing pressure. The changes in Fig. 2, where

we interpret the increase and decrease of the binding energies depending on the size of CQWWs, can be corrected by the exciton probability distributions plotted at room temperature $P = 10$ GPa for a certain wire size in Fig. 3 (a), Fig. 3 (b) and Fig. 3 (c), respectively.

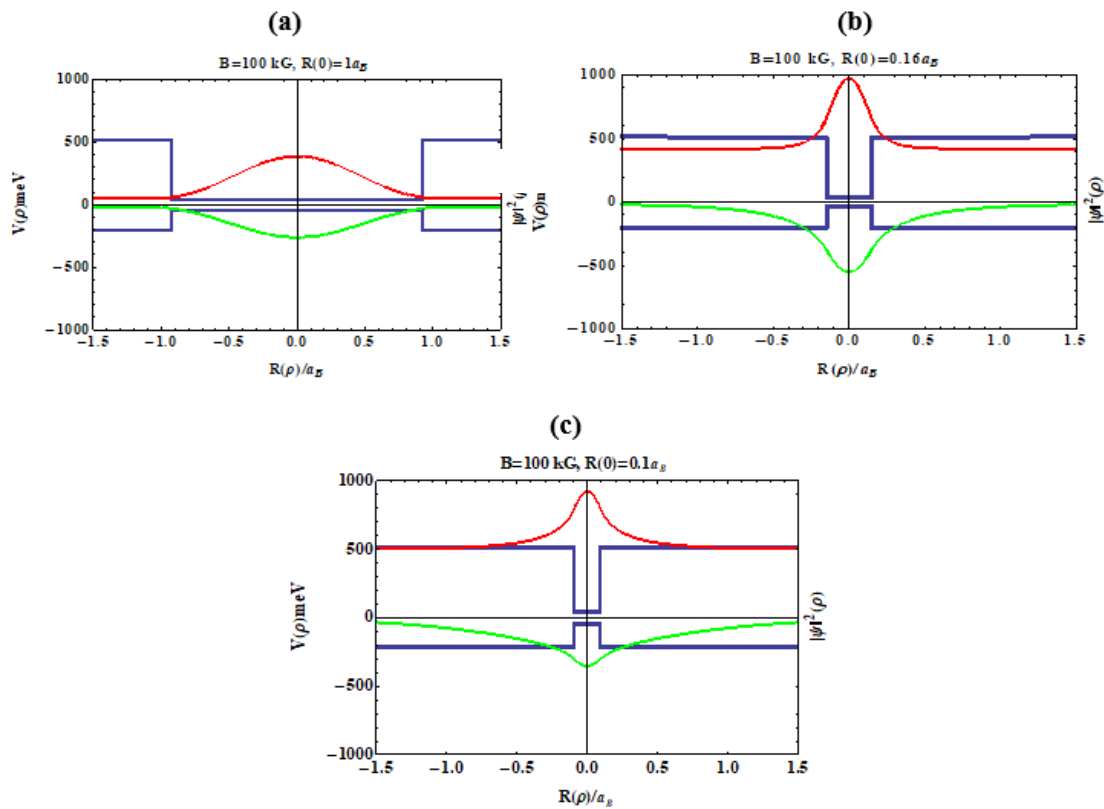


Figure 3. Probability distribution of the heavy hole exciton in the CQWWs on the wire size for (a) $R=1 a_B$ (b) $R=0.16 a_B$ (c) $R=0.1 a_B$.

For the wire radius for $R = 1 a_B$, the electron and the hole may not be close to each other as the spatial confinement is weakened. For this reason, the binding energy is expected to decrease in large wire radii. (Fig. 3 (a)). In the case of $R = 0.16 a_B$, the spatial confinement effect is strong, and the particles are closest to each other, so the binding energy is highest (Fig. 3 (b)). Particles from the wire size of $R = 0.1 a_B$ are very energetic and the quantum encirclement effect is very reduced, so the particles appear to leak out of the wire and the binding energy decreases again (Fig. 3 (c)).

In addition, as can be seen from Fig. 2, as the pressure increases at all wire radius values, the binding energy also increases. To illustrate this situation better, we

have given the parameter change of the structure according to the pressure for $T = 300$ K, $B=0$ kG and $R=0.2 a_B$ in Table 1. This can be understood from the fact that as the pressure increases, the values of $R(P)$ and $\epsilon(P, T)$ decrease, while the confinement potential, electron effective mass and hole effective mass increase. When the pressure is changed from 0 GPa to 10 GPa, the increase in potential heights is 0.37%, while the decrease in the wire radius is -0.10%.

In this case, as the encircling effects on the particles increase, it is seen that the magnetoelectronic binding energy increases depending on the pressure. Table 2 shows the change of parameters with temperature for $P = 0$ GPa, $B = 0$ kG and $R = 0.2 a_B$. In this table, potential heights are given in meV.

Table 1. Change of CQWWs parameters with hydrostatic pressure

P(GPa)	ϵ	$\frac{\epsilon}{\%}$	R(P)/ a_B	$\frac{R(P)}{a_B}$ %	m_e/m_0	$\frac{m_e}{m_0}$ %	m_{hh}/m_0	$\frac{m_h}{m_0}$ %	V_{oe}	$\frac{V_{oe}}{\%}$	V_{oh}	$\frac{V_{oh}}{\%}$
0	13.18	0.00%	0.20	0.00%	0.067	0.00%	0.134	0.00%	124.13	0.00%	53.19	0.00%
5	12.08	-0.22%	0.19	-0.05%	0.087	-1.49%	0.143	0.067%	146.98	0.18%	62.99	0.18%
10	11.08	-0.44%	0.18	-0.10%	0.110	-1.49%	0.180	0.34%	169.83	0.37%	72.78	0.37%

Table 2. Change of CQWWs parameters with temperature

T(K)	ϵ	$\frac{\epsilon}{\%}$	m_e/m_0	$\frac{m_e}{m_0}$ %	V_{oe}	$\frac{V_{oe}}{\%}$	V_{oh}	$\frac{V_{oh}}{\%}$
0	12.39	0.00%	0.067	0.00%	126.08	0.00%	54.03	0.00%
50	12.52	0.22%	0.066	-1.49%	126.00	-0.06%	54.00	-0.06%
100	12.65	0.44%	0.066	-1.49%	125.77	-0.24%	53.90	-0.24%
150	12.78	0.67%	0.066	-1.49%	125.47	-0.48%	53.77	-0.48%
200	12.91	1.04%	0.065	-2.98%	125.07	-0.80%	53.60	-0.78%
250	13.04	1.55%	0.064	-4.47%	124.62	-1.15%	53.41	-1.15%
300	13.18	2.07%	0.063	-5.97%	124.13	-1.55%	53.19	-1.55%

With increasing temperature, we would expect the binding energy to decrease because with temperature, the effective mass and confinement potential decrease while the dielectric constant increases. However, as

can be seen from Table 2, these change percentages are very low. So, the temperature changes do not affect the binding energy. However, increasing dielectric constant (weaker coulombic interaction) and

decreasing potential height (less confinement) and effective mass (higher mobility) all contribute to a decrease in binding energy show that the temperature effect is negligible, we plotted the variation of the bond energy with temperature at the wire radius $R = 0.3 a_B$.

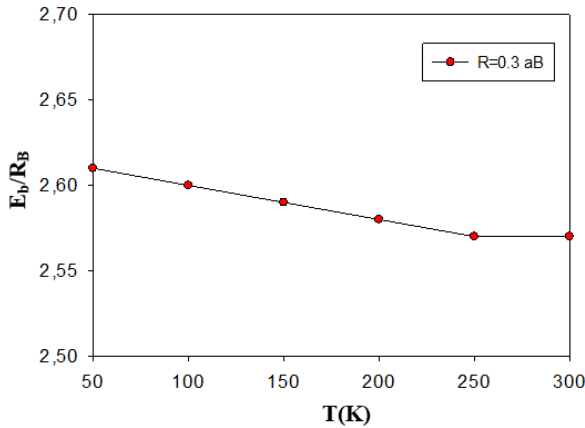


Figure 4. Change of binding energy with temperature at wire radius $R(0) = 0.3 a_B$

As can be seen from Fig. 4, the percentage change in binding energy in this temperature range is even less than 1.15 percent. To see the percentage changes in Table 1 and Table 2 more clearly, in Fig. 5 (a) and Fig. 5 (b), the effective masses, potential heights for the electron and hole, the wire radius and dielectric constant versus P and T versus the total we showed the percentage changes.

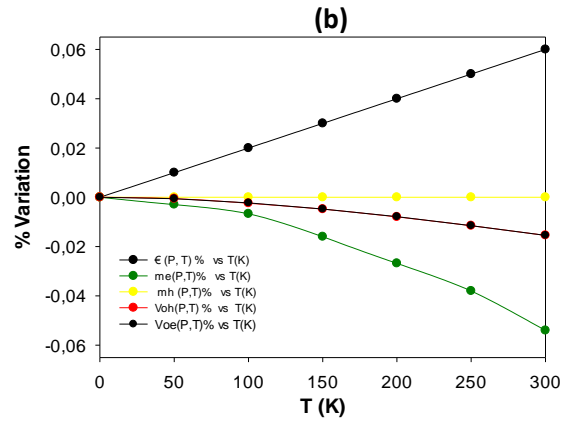
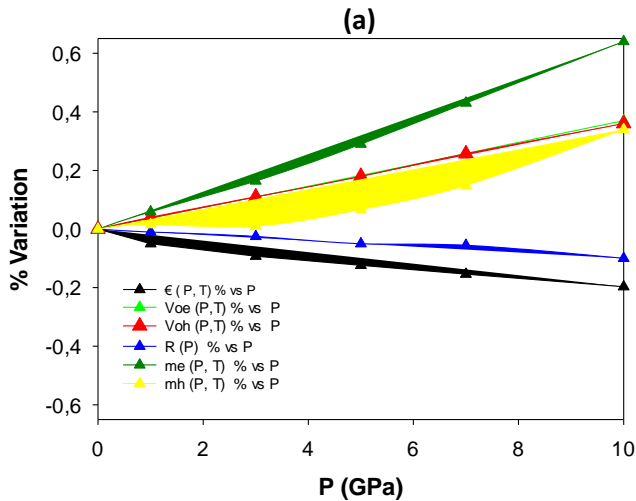


Figure 5. Percentage change of changing parameters with pressure and temperature in GaAs / InGaAs CQWWs (a) vs P (b) vs T

Lines with triangle symbols show the percentage change with pressure (Fig. 5 (a)), while the lines with circle symbols show the percentage changes of parameters (Fig. 5 (b)) depending on the temperature. It is seen that the change with temperature is much less than the change with pressure. It can be seen from Fig. 5 (b) that the system is very stable under temperature changes. However, Fig. 5 (a) shows that the change of the parameters of the system with pressure is much more than the temperature. Fig. 6 shows how binding energy is affected by the magnetic field at $P = 0$ GPa and $T = 300$ K.

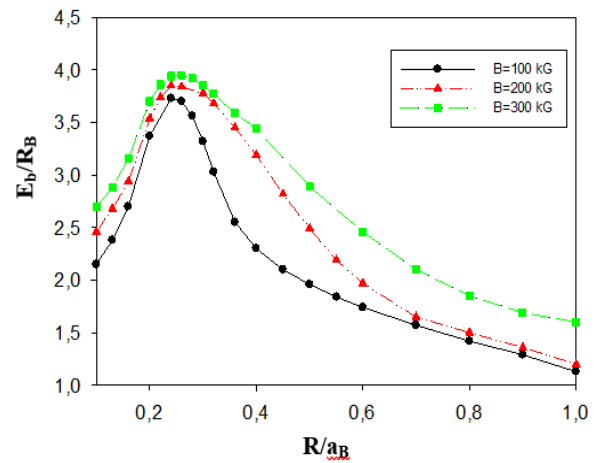


Figure 6. Radius variation of binding energy for different magnetic field sizes

In general, it is seen that the binding energy increases with the increase of magnetic field strength. As the wire radius increases ($R \geq 0.5 a_B$) the spatial envelope decreases and the magnetic envelope is effective on the exciton. In the range of $0.22 a_B < R < 0.5 a_B$ for any magnetic field strength, the exciton binding energy begins to increase with decreasing wire radius from the bulk value of InGaAs until it reaches a maximum

value. In this radius range spatial confinement dominates the binding energy. Finally, the bulk value of (GaAs) drops sharply after reaching a maximum point. This value is approximately $2.23 R_B$ [38].

Conclusions

In this study, we calculated the change of exciton binding energy in GaAs / $\text{In}_{0.47}\text{Ga}_{0.53}\text{As}$ CQWWs depending on external parameters such as magnetic field, temperature and hydrostatic pressure and wire size. As the wire radius decreases, the bonding energy starts to increase and after reaching a maximum value, it decreases until the ingot GaAs value. The variation of the ground state binding energy depending on external parameters can be summarized as follows. Heavy hole exciton binding energy, depending on hydrostatic pressure and magnetic field. We have seen that due to the increasing hydrostatic pressure and magnetic field, the heavy hole exciton binding energy increases in accordance with the literature. The hydrostatic pressure effect is weaker at large wire radius values. With the increasing temperature under constant pressure and magnetic field, the bonding energy decreases, albeit a little. However, since the temperature-related decrease in the 0-300 K range is below 1.15 percent, we can say that the bonding energy almost does not change with temperature.

Acknowledgment

The author would like to thank Sivas Cumhuriyet University for its opportunities.

Conflicts of interest

The author state that did not have conflict of interests.

References

- [1] Ando H., Nojima, S., Kanbe, H., Band- edge optical absorption spectra of GaAs quantum wires calculated by multiband effective mass theory, *Journal of Applied Physics* 74 (1993) 6383-6390.
- [2] Gurmessa A., Mengesha M., *International Journal of Physical Sciences*, 14 (7) (2019) 55-61.
- [3] Duque C. A., Oliveira L. E., de Dios-Leyva M., correlated electron-hole transitions in bulk GaAs and GaAs-(Ga, Al) As quantum wells: effects of applied electric and inplane magnetic fields, *Brazilian Journal of Physics*, 36 (2006) 1038-1041.
- [4] Pokutnyi S. I., Tyc M. H., Salejda W., Misiewicz J., Two-dimensional WannierMott exciton in a uniform electric field, *Physics of the Solid State.*, 43 (2001) 923- 926.
- [5] Raigoza N., Duque C.A., Reyes-Go'mez E., Oliveira L.E., Effects of hydrostatic pressure and applied electric fields on the exciton states in GaAs-(Ga, Al) As quantum wells, *Physica B*, 367 (2005) 267–274.
- [6] Venkateswaran U., Chandrasekhar M., Chandrasekhar H. R., Bojak B. A., Chambers F.A., Meese J. M., *Phys. Rev. B*, 33 (1986) 8416-8423.
- [7] Saravanan S., John Peter A., Binding Energy of a Magneto-exciton in an InAsP Quantum Well Wire for the Potential Application of Telecommunication Networks, *Materials Today: Proceedings*, 2 (2015) 4373- 4377.
- [8] Vurgaftman I. and Meyer J. R., Ram-Mohan L. R., Band parameters for III–V compound semiconductors and their alloys, *Journal of Applied Physics*, 89 (2001) 5815 -5875.
- [9] Morales A. L., Raigoza N., Duque C. A. and Oliveira L. E., Effects of growthdirection electric and magnetic fields on excitons in GaAs– $\text{Ga}_{1-x}\text{Al}_x\text{As}$ coupled double quantum wells, *Phys. Rev. B*, 77 (2008) 113309-1-113309-4.
- [10] Butov L. V., Shashkin A. A., Dolgoplov V. T., Campman K. L., and Gossard A. C., Magneto-optics of the spatially separated electron and hole layers in GaAs/ $\text{Al}_x\text{Ga}_{1-x}\text{As}$ coupled quantum wells, *Phys. Rev. B*, 60 (1999) 8753-8758.
- [11] Kavokin A. V. Kokhanovski S. I. Nesvizhki A. I. Sasin M. E. Sesyan R. P. Ustinov V. M. Yu. Egorov A. Zhukov A. E. and Gupalov S. V. *Semiconductors*, 31 (1997) 950-960.
- [12] Agekyan V. T., Spectroscopic properties of semiconductor crystals with direct forbidden energy gap, *Phys. Stat. Sol. (a)*, 43 (1977) 11-42.
- [13] Varshni Y. P., Temperature dependence of the energy gap in semiconductors, *Physica*, 34 (1967) 149-154.
- [14] Peter A. J., Gnanasekar K., Navaneethakrishnan K., Binding energy of impurity states in a parabolic quantum dot in a strong magnetic field, *Phys. Stat. Sol. (b)*, 242 (2005) 2480-2488.
- [15] Di Dio M., Lomascolo M., Passaseo A., Gerardi C., Giannini C., Quirini A., Tapfer L., Giugno P.V., De Vittorio M., Greco D., Convertino A. L.,

- Vasanelli L., Rinaldi R., Cingolani R., *J. Appl. Phys.*, 80 (1996) 482-489.
- [16] Martini S., Quivy A. A., da Silva E. C. F., Leite J. R., Real-time determination of the segregation strength of indium atoms in InGaAs layers grown by molecular-beam epitaxy, *Appl. Phys. Lett.*, 81 (2002) 2863-2865.
- [17] Martini S., Quivy A. A., Tabata A., Leite J. R., Influence of the temperature and excitation power on the optical properties of InGaAs/GaAs quantum wells grown on vicinal GaAs (001) surfaces (2001), *Journal of Applied Physics*, 90 (2001) 2280- 2289.
- [18] Bratkovski A. and Kamins T. I., Nanowire-Based Light-Emitting Diodes and Light-Detection Devices with Nanocrystalline Outer Surface, Google Patents, (2010)
- [19] Baba T., Yogo Y., Suzuki K., Koyama F., Iga K., Near room temperature continuous wave lasing characteristics of GaInAsP/InP surface emitting laser, *Electron. Lett.*, 29 (1993) 913-914.
- [20] Uchida T., Koyama F., and Iga K., Control of GaInAs/InP layer thickness for surface-emitting lasers by chemical beam epitaxy, *Electron. Communi. in Japan Part II*, 75 (1992) 101-107.
- [21] Pyun S. H., Jeong W. G., Korean J., *Phys. Soc J. Korean Phys. Soc.*, 56 (2010) 586- 590.
- [22] Soulby M. R., Revin D. G., Commin J. P., Krysa A. B., Roberts J. S., Cockburn J. W., Probing diagonal laser transitions in InGaAs/AlInAs/InP quantum cascade lasers, *J. Appl. Phys.*, 106 (2009) 123106-123109.
- [23] Matthews M. R., Steed R. J., Frogley M. D., Phillips C. C., Attaluri R. S. and Krishna S., Transient photoconductivity measurements of carrier lifetimes in an InAs/In_{0.15}Ga_{0.85}As dots-in-a-well detector, *Appl. Phys. Lett.*, 90 (2007) 103519-1- 103519-4.
- [24] Tsao S., Lim H., Zhang W., and Razeghi M., High operating temperature 320×256320×256 middle-wavelength infrared focal plane array imaging based on an InAs/InGaAs/InAlAs/InP/InAs/InGaAs/InAlAs/InP quantum dot infrared photodetector, *Appl. Phys. Lett.*, 90 (2007) 201109-1-201109-3.
- [25] Zekentes K., Halkias G., Dimoulas A., Tabata A., Benyattou T., Guillot G., Morante J. R., Peiró F., Cornet A., Georgakilas A., Christou A., Materials problems for the development of InGaAs/InAlAs HEMT technology, *Mater. Sci. Eng. B*, 20 (1993) 21-25.
- [26] Connolly J. P. and Rohr C., Quantum well cells for thermophotovoltaics, *Semicond. Sci. Technol*, 18 (2003) 216-220.
- [27] Nahory R. E., Pollack M. A., Johnston W. D., and Barns R. L., Band gap versus composition and demonstration of Vegard's law for In_{1-x}Ga_xAsP_{1-y} lattice matched to InP, *Appl. Phys. Lett.*, 33 (1978) 659-661.
- [28] Fritz I. J., Klem J. F., Schirber J. E., Olsen J. A., and Bonner W. A., InGaAs/GaAs multiple strained-layer structure grown on a lattice-matched InGaAs substrate wafer, *Appl. Phys. Lett.* 66 (1995) 1957-1959.
- [29] Adachi S., Oe K., Internal strain and photoelastic effects in Ga_{1-x}Al_xAs/GaAs and In_{1-x}Ga_xAs_yP_{1-y}/InP crystals, *J. Appl. Phys.* 54, (1983)6620-6627.
- [30] Guldner Y., Vieren J. P., Voos M., Delahaye F., Dominguez D., Hirtz J. P., Razeghi M., Quantum Hall effect in In_{0.53}Ga_{0.47}As-InP heterojunctions with two populated electric subbands, *Phys. Rev. B*, 33 (1986) 3990-3993.
- [31] Lamberti C., Bordiga S., Structural and optical investigation of InAs_xP_{1-x}/InP strained superlattices, *J. Appl. Phys.*, 83 (1998) 1058-1077.
- [32] Elagoz S., Karki H. D., Baser P., Sokmen I., The magnetoexciton binding energy dependency on aluminium concentration in cylindrical quantum wires, *Superlatt. and Microstruct.*, 45 (2009) 506-513.
- [33] Karki H. D., Elagoz S., Baser P., Amca R., Sokmen I., Barrier height effect on binding energies of shallow hydrogenic impurities in coaxial GaAs/Al_xGa_{1-x}As quantum well wires under a uniform magnetic field, *Superlatt. Microstruct.*, (4) (2007) 227-236.
- [34] Ji G., Huang D., Reddy U. K., Henderson T. S., Houdre R., and Morkoç H., Optical investigation of highly strained InGaAs/GaAs multiple quantum wells, *Journal of Applied Physics*, 62 (8) (1987) 3366-3373.
- [35] Peter, Y. Yu., Cardona M., Fundamentals of Semiconductors, Berlin: Springer, (1996) 276-290.
- [36] Baser P., Karki H. D., Demir I., Elagoz S., The hydrostatic pressure, and temperature effects on the binding energy of magnetoexcitons in

cylindrical quantum well wires, *Superlatt. Microstruct.*, 63 (2013) 100-109.

- [37] Beltran Rios C. L., Porrás-Montenegro N., Pressure, and magnetic field effects on the binding energy of excitonic states in single and coupled GaAs-AlGaAs quantum wells, *Microelectronics Journal*, 36 (2005) 369-373.
- [38] Baser P., Pressure, and temperature effects on magnetoelectric band energies in GaAs / In_xGa_{1-x}As cylindrical quantum wires, *Cumhuriyet Science Journal*, 41(3) (2020) 699-705.
- [39] Başer P, Altuntas I, Elagoz S, The hydrostatic pressure, and temperature effects on hydrogenic impurity binding energies in GaAs/In_xGa_{1-x}As/GaAs square quantum well, *Superlattice Microst.*, 92 (2016) 210-216.
- [40] Baser P., Electronic properties of low dimensional systems: the hydrogenic impurities and excitonic binding energies in cylindrical Ga_{1-x}Al_xAs /GaAs quantum wires under an externally applied magnetic field, Marmara University, Institute of science PhD. Thesis, (2007).

A study on Freeman-Tukey test statistic under the symmetry model for square contingency tables

Gökçen ALTUN¹ 

¹ Bartın University, Department of Computer Technology and Information Systems, 74100, Bartın / TURKEY

Abstract

The symmetry model is the basic model in the analysis of square contingency tables. Multiple test statistics have been developed for the goodness of fit test. Freeman-Tukey test statistics is appropriate to be used in large samples. However, the required sample size to use the Freeman-Tukey test statistics is not clear. In this paper, the asymptotic properties of Freeman-Tukey test statistic are discussed via extensive Monte-Carlo simulation study. The Freeman-Tukey test statistic is compared with members of power-divergence family test statistic under the symmetry model. The results of simulation study are evaluated based on the Type-I error and power of a test. The results of simulation study and artificial data study show that Freeman-Tukey's T^2 test statistic does not converge to chi-squared distribution for both sparse and non-sparse square contingency tables.

Article info

History:
Received: 02.12.2020
Accepted: 31.03.2021

Keywords:
Freeman-Tukey test statistic, Power-divergence family, Goodness-of-fit test statistics, Square contingency tables, Symmetry model.

1. Introduction

Square contingency tables that arise independent samples where the row and column variables have the same level. Let n_{ij} be the observed frequency in the cell (i,j) and p_{ij} denotes the probability of the same cell. The representation of the $R \times R$ dimensional square contingency table can be found in [1]. Some specific models used in the analysis of these kinds of tables. These models are mostly in the symmetrical pattern. Then, the complete symmetry model (S) is defined by;

$$p_{ij} = p_{ji}, \quad i, j = 1, 2, \dots, R, \quad (\text{for } i \neq j) \quad (1)$$

and is based on $R(R-1)/2$ degree of freedom, where R is the dimension of the square table [2]. The likelihood estimates of expected values e_{ij} under the S model is $e_{ij} = (n_{ij} + n_{ji})/2$. This model indicates that the probability that an observation will fall in cell (i,j) is equal to probability that it falls in symmetric cell (j,i).

Goodness-of-fit tests summarize the discrepancy between the observed values and the expected values under the corresponding model. Cressie and Read (1984) introduced a class of goodness-of-fit test statistics named as power-divergence (PD) family of statistics. The PD statistic includes Pearson's χ^2 and the likelihood ratio statistic G^2 as well as other

statistics such as Freeman-Tukey's T^2 , the modified likelihood ratio statistics GM^2 , and Neyman's modified χ^2 statistics. All of these statistics are asymptotically chi-squared distributed with appropriate degrees of freedom [3,4,5].

The researchers have shown a great interest to compare goodness of test statistics for analyzing the sparse contingency tables. Cochran et. al. showed that Pearson statistic does not follow the chi-squared distribution well for small expected values [6-8]. Cochran et. al. discussed which approximation is "reasonable" for the Pearson chi-squared statistic [6-10]. "Standard rules" specify that the minimum cell expectation should be five, with a few cells possibly smaller. The true sampling distributions converge to chi-squared as $n \rightarrow \infty$, for a fixed number of cells N . The adequacy of the chi-squared approximation depends both on n and N [11]. Cochran suggested that to test independence with $df > 1$, a minimum expected value $e_{ij} \approx 1$ is permissible as long as no more than about 20% of $e_{ij} < 5$ [6]. Koehler et al. showed that it is more appropriate to use χ^2 test statistics instead of G^2 for sparse tables and small sample sizes [12-14]. When n/N (sparseness index) is less than 5 the distribution of G^2 is usually poorly approximated by chi-squared. Depending on the sparseness, p values can be either too large or too

small. As N increases, the approximation to the chi-square distribution decreases [13]. However, Haberman showed that the approximation tends to be poor for sparse tables containing both small and moderately large e_{ij} (see, Cressie and Read (1989) and Lawal (1984) for detailed information) [15-17]. Larntz compared Pearson's χ^2 , likelihood ratio statistic G^2 and Freeman-Tukey's T^2 statistics based on the five models [14]. Larntz stated that Pearson's χ^2 demonstrates the best approximation to the chi-squared distribution for small samples and the other two statistics are not approximate well [14]. Fienberg emphasized that the behavior of G^2 in large sparse multinomial structures requires serious attention [3]. Baglivo et al. stated that each statistic in the power-divergence family can be regarded as a different measure of goodness of fit and these differences make the tests useful in different situations [18]. Many authors including Bishop et al., Aitchinson et al., Simonoff and Burman concerned with smoothing such tables in order to avoid the problems associated with sparseness [19-23]. Kim et al. studied on Zelterman's D^2 statistic and compared the efficiency of Zelterman's D^2 statistic with other well-known statistics via simulation study [24,25]. Aktaş compared the power-divergence statistics based on the power values under the Quasi-Independence model in square contingency tables [26].

In this paper, we compare the PD statistics for various λ values concerning their power values and Type-I

$$I(\lambda) = \frac{2}{\lambda(\lambda + 1)} \sum_{i=1}^R \sum_{j=1}^R n_{ij} \left[\left(\frac{n_{ij}}{e_{ij}} \right)^\lambda - 1 \right], \quad i, j = 1, 2, \dots, R, \quad \lambda \in \mathfrak{R} \tag{2}$$

The PD family of statistics, given in (2), is not valid of $\lambda = 0$ and $\lambda = -1$. Therefore, the following equations are obtained by using limit for the cases $\lambda = 0$ and $\lambda = -1$.

$$\lim_{\lambda \rightarrow 0} \frac{2}{\lambda(\lambda + 1)} \sum_{i=1}^R \sum_{j=1}^R n_{ij} \left[\left(\frac{n_{ij}}{e_{ij}} \right)^\lambda - 1 \right] = 2 \sum_{i=1}^R \sum_{j=1}^R n_{ij} \left(\log \frac{n_{ij}}{e_{ij}} \right) \tag{3}$$

$$\lim_{\lambda \rightarrow -1} \frac{2}{\lambda(\lambda + 1)} \sum_{i=1}^R \sum_{j=1}^R n_{ij} \left[\left(\frac{n_{ij}}{e_{ij}} \right)^\lambda - 1 \right] = 2 \sum_{i=1}^R \sum_{j=1}^R e_{ij} \left(\log \frac{e_{ij}}{n_{ij}} \right) \tag{4}$$

It is straightforward to verify that the statistic $I(\lambda)$ reduces to Pearson's χ^2 when $\lambda = 1$, likelihood ratio G^2 when $\lambda = 0$, Freeman Tukey's T^2 when $\lambda = -1/2$

2.2. Simulation study

In the simulation study, the Type-I errors of the power-divergence statistics are obtained for $\lambda = 0.1, 0.2, 0.3, 0.4, 0.5, 0.6, 0.7, 0.8, 0.9, 1(\chi^2), 0(G^2), -1/2(T^2), 2/3(C^2)$.

The powers of the tests are calculated under the S model. $N = 50,000$ sample of sizes $n =$

errors under the S model in the square contingency table where the observations are cross-classified by two variables with the same categories. The goal of this paper is to show that Freeman-Tukey's T^2 test statistic does not converge to the chi-squared distribution not only in sparse square contingency tables but also in non-sparse square contingency tables. To achieve this goal, an extensive simulation study is conducted to show the relative efficiencies of PD test statistics under the symmetry model with various dimensions of tables and different sample sizes.

The remaining part of the paper is organized as follows: In Section 2, PD family of statistics are presented with its theoretical background. Section 2 also contains the simulation study and application to the artificial data set. Some concluding remarks are given in Section 3.

2. Materials and Methods

2.1. Power-Divergence family

Cressie and Read introduced a class of goodness-of-fit test statistics that can be expressed based on a family of power-divergence statistics. All members of the statistics are members of the power-divergence family. Let n_{ij} and e_{ij} represent the observed and expected frequencies. The PD family of statistics, $I(\lambda)$, is given by [27]

and Cressie Read test statistic C^2 when $\lambda = 2/3$. All of these statistics are asymptotically chi-squared distributed with appropriate degrees of freedom.

10,15, ...,200 for $R = 3$, $n = 20,25, \dots,300$ for $R = 4$, $n = 30,35, \dots,600$ for $R = 5$ and $n =$

40,45, ...,900 for $R = 6$ are generated by means of multinomial distribution under the S model using the probability matrices given below. The results of the

study are obtained by using the R programming language.

Table 1. Probability matrices for generating random frequencies from the S model.

R	Type I error	Power of a test
3	$\begin{bmatrix} 0,05 & 0,13 & 0,17 \\ 0,13 & 0,05 & 0,125 \\ 0,17 & 0,125 & 0,05 \end{bmatrix}$	$\begin{bmatrix} 0,05 & 0,10 & 0,15 \\ 0,30 & 0,05 & 0,19 \\ 0,05 & 0,06 & 0,05 \end{bmatrix}$
4	$\begin{bmatrix} 0,02 & 0,08 & 0,10 & 0,06 \\ 0,08 & 0,02 & 0,05 & 0,11 \\ 0,10 & 0,05 & 0,02 & 0,06 \\ 0,06 & 0,11 & 0,06 & 0,02 \end{bmatrix}$	$\begin{bmatrix} 0,02 & 0,04 & 0,15 & 0,03 \\ 0,12 & 0,02 & 0,085 & 0,055 \\ 0,05 & 0,035 & 0,02 & 0,09 \\ 0,09 & 0,145 & 0,03 & 0,02 \end{bmatrix}$
5	$\begin{bmatrix} 0,01 & 0,05 & 0,08 & 0,04 & 0,045 \\ 0,05 & 0,01 & 0,03 & 0,09 & 0,01 \\ 0,08 & 0,03 & 0,01 & 0,02 & 0,06 \\ 0,04 & 0,09 & 0,02 & 0,01 & 0,05 \\ 0,045 & 0,01 & 0,06 & 0,05 & 0,01 \end{bmatrix}$	$\begin{bmatrix} 0,01 & 0,075 & 0,04 & 0,04 & 0,0225 \\ 0,025 & 0,01 & 0,045 & 0,045 & 0,015 \\ 0,12 & 0,015 & 0,01 & 0,01 & 0,09 \\ 0,02 & 0,135 & 0,03 & 0,01 & 0,025 \\ 0,0675 & 0,005 & 0,03 & 0,075 & 0,01 \end{bmatrix}$
6	$\begin{bmatrix} 0,001 & 0,017 & 0,02 & 0,03 & 0,012 & 0,014 \\ 0,017 & 0,001 & 0,07 & 0,05 & 0,02 & 0,013 \\ 0,02 & 0,07 & 0,001 & 0,09 & 0,009 & 0,06 \\ 0,03 & 0,05 & 0,09 & 0,001 & 0,044 & 0,008 \\ 0,012 & 0,02 & 0,009 & 0,044 & 0,001 & 0,04 \\ 0,014 & 0,013 & 0,06 & 0,008 & 0,04 & 0,001 \end{bmatrix}$	$\begin{bmatrix} 0,001 & 0,0255 & 0,01 & 0,045 & 0,018 & 0,007 \\ 0,0085 & 0,001 & 0,105 & 0,025 & 0,03 & 0,0065 \\ 0,03 & 0,035 & 0,001 & 0,045 & 0,0135 & 0,09 \\ 0,015 & 0,075 & 0,135 & 0,001 & 0,066 & 0,012 \\ 0,006 & 0,01 & 0,0045 & 0,022 & 0,001 & 0,02 \\ 0,021 & 0,0195 & 0,03 & 0,004 & 0,06 & 0,001 \end{bmatrix}$

Since the type 1 error is calculated under the accuracy of the H_0 hypothesis, the matrices generated for the type 1 error are symmetrical. For the strength of the test, the deterioration in the symmetrical structure of the matrix is made on the condition that the symmetrical cells with respect to the diagonal are approximately 1 to 3. The convergences of test statistics to chi-squared distribution are evaluated based on the critical point, 0.06, for the Type-I error. When the obtained Type-I error is lower than 0.06 value, the corresponding test statistic is asymptotically distributed as chi-squared distribution. Figures 1.a and 1.b display the simulation results for $R=3$.

As seen from Figure 1.a, when the sample size is lower than 50, all test statistics, except G^2 , T^2 , $I(0.1)$ and $I(0.2)$, converge to the chi-squared distribution. When the sample size is higher than 50, all test statistics, except for T^2 converge to the chi-squared distribution. It is clear that the test statistic with the highest power of a test is T^2 (Figure 1.b). However, the T^2 test statistic converges to the chi-squared distribution after the sample size is approximately 80. This issue can be expressed based on the sparseness index. It is easy to see that T^2 test statistic converges to chi-squared distribution when the sparseness index is higher than 9 for $R=3$.

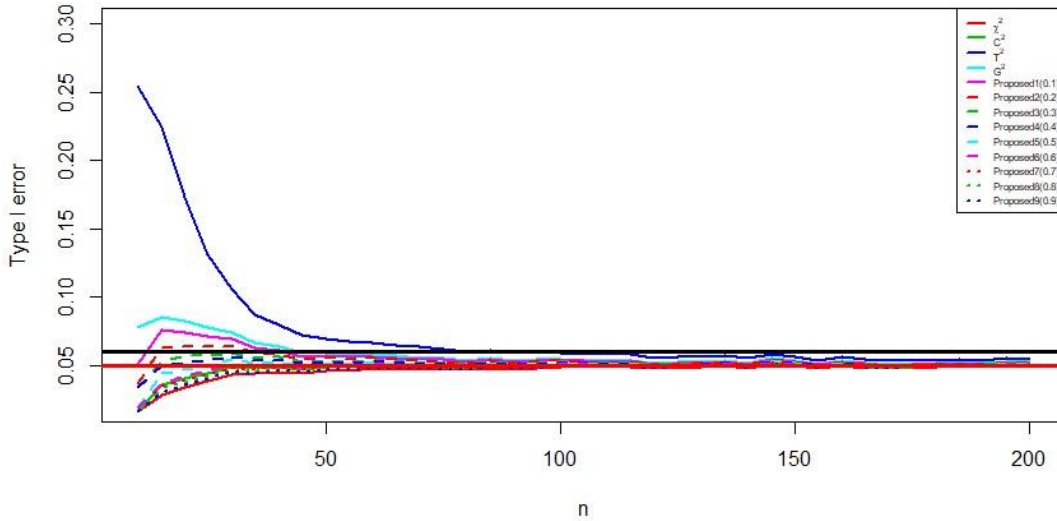


Figure 1a. The Type-I errors of the corresponding test statistics for 3×3 square contingency tables.

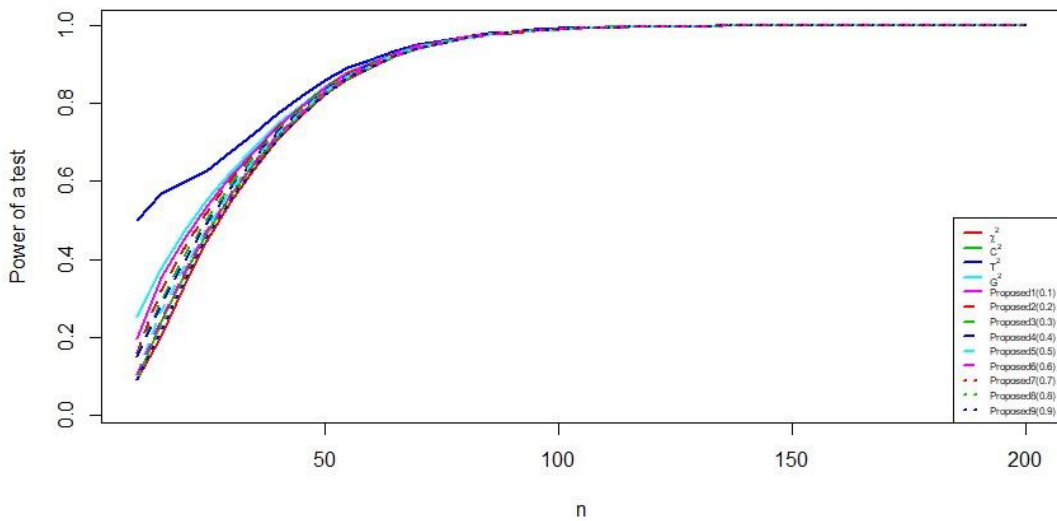


Figure 1b. The power of a test results of the corresponding test statistics for 3×3 square contingency tables.

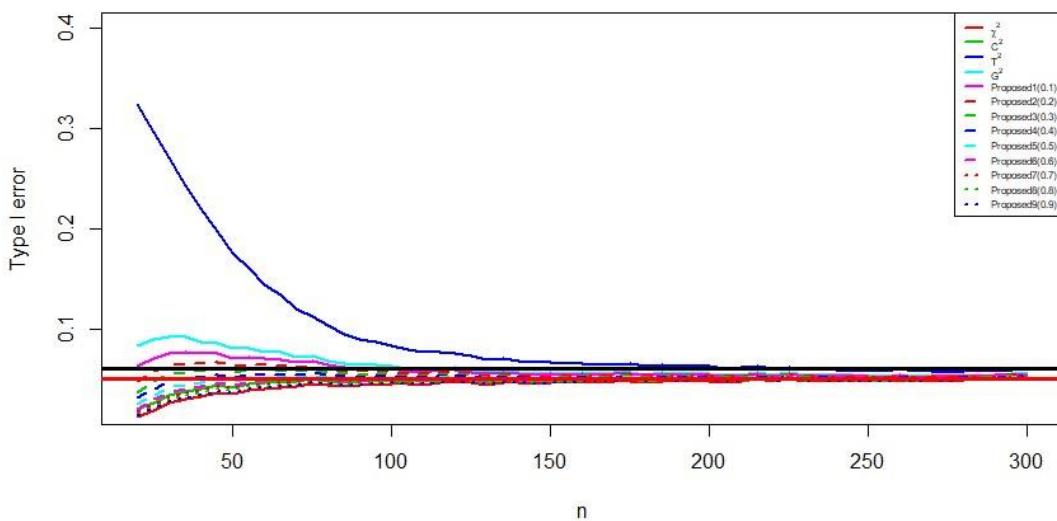


Figure 2a. The Type-I errors of the corresponding test statistics for 4×4 square contingency tables.

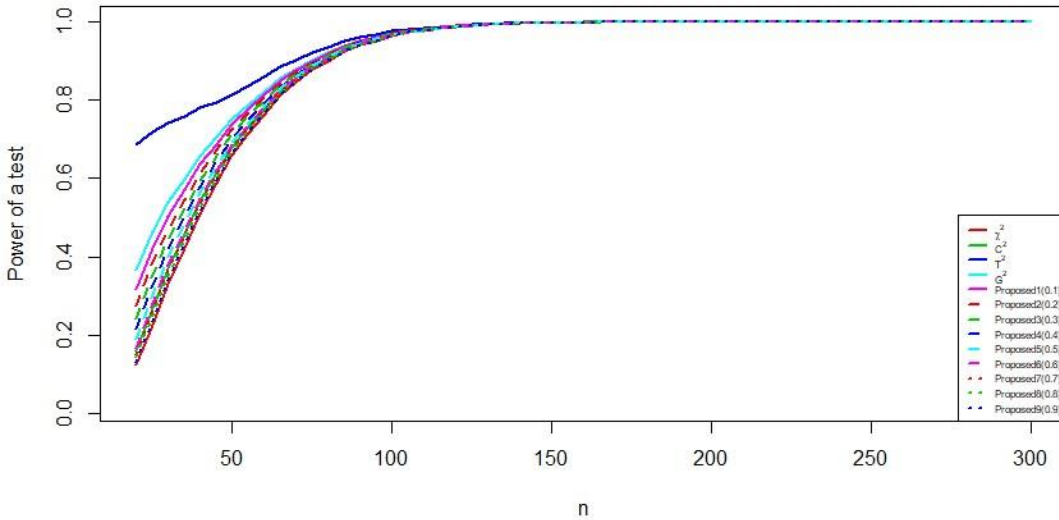


Figure 2b. The power of a test results of the corresponding test statistics for 4×4 square contingency tables.

Figures 2.a and 2.b displays the simulation results for $R=4$. As seen from the Figure 2.a, all test statistics, except $G^2, T^2, I(0.1)$ and $I(0.2)$, converge to the chi-squared distribution when the sample size is lower than 100. When the sample size is higher than 100, all test statistics except for T^2 converge to the chi-squared distribution. From Figure 2.b, it is clear that the test statistic with the highest power of a test is Freeman Tukey's T^2 . However, the T^2 test statistic converges to the chi-squared distribution when the sample size is approximately 200. It can be expressed based on the sparseness index. Freeman Tukey's T^2 converges to chi-squared distribution when the sparseness index is higher than 12 for $R=4$. Figures 3.a and 3.b display the simulation results for $R=5$. From the Figure 3.a, all test

statistics, except $G^2, T^2, I(0.1)$ and $I(0.2)$ converge to the chi-squared distribution when the sample size is approximately 200. When the sample size is higher than 200, all test statistics except for G^2 and T^2 approximate to the chi-squared distribution. Likelihood ratio test statistic G^2 converges to the chi-squared distribution after the sample size is approximately 300. From Figure 3.b, it is clear that the test statistic with the highest power of a test is Freeman Tukey's T^2 .

However, the T^2 test statistic converges to the chi-squared distribution after the sample size is approximately 600. In other words, Freeman Tukey's T^2 converges to chi-squared distribution when the sparseness index is higher than 24 for $R=5$.

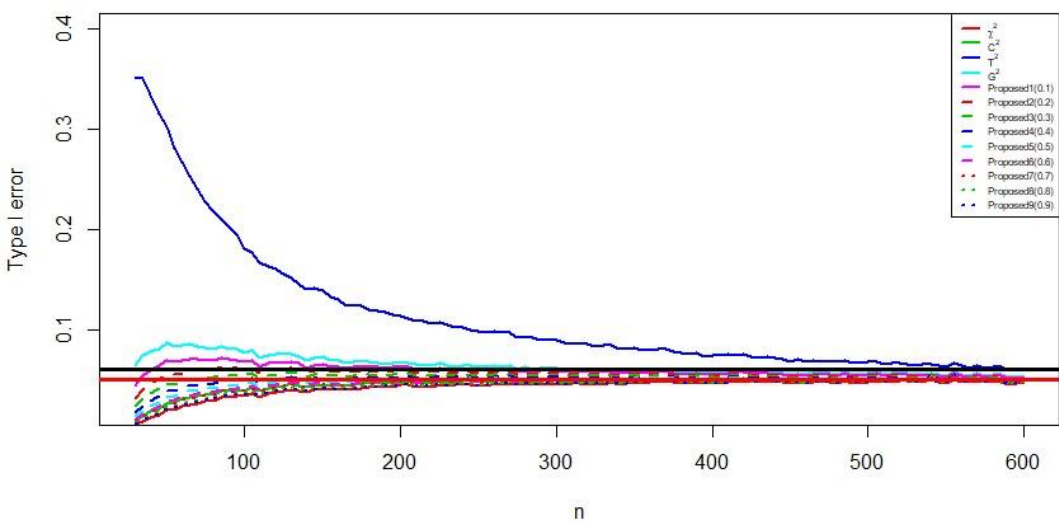


Figure 3a. The Type-I errors of the corresponding test statistics for 5×5 square contingency tables.

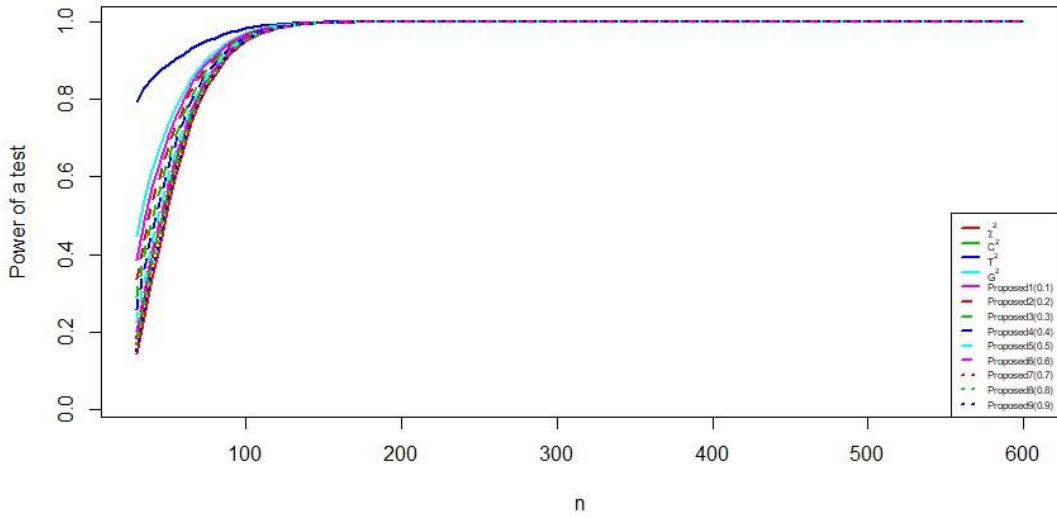


Figure 3b. The power of a test results of the corresponding test statistics for 5×5 square contingency tables

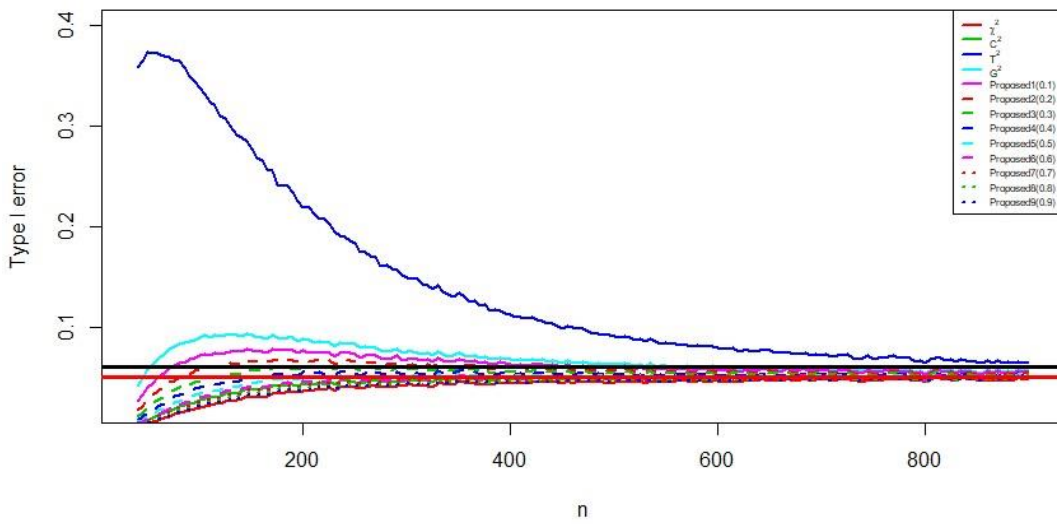


Figure 4a. The Type-I errors of the corresponding test statistics for 6×6 square contingency tables.

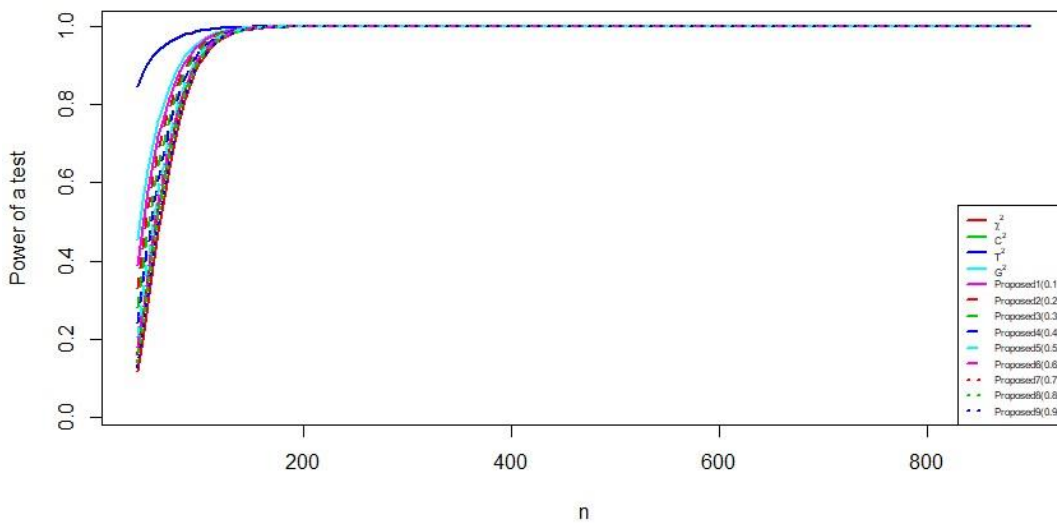


Figure 4b. The power of a test results of the corresponding test statistics for 6×6 square contingency tables.

Figures 4.a and 4.b display the simulation results for R=6. From the Figure 4.a, all test statistics, except $G^2, T^2, I(0.1)$ and $I(0.2)$ converge to the chi-squared distribution when the sample size is lower than 400. When the sample size is higher than 400, all test statistics except for $G^2, I(0.1)$ and T^2 converge to the chi-squared distribution. Likelihood ratio G^2 and $I(0.1)$ test statistic converges to the chi-squared distribution when the sample size is approximately 500. From Figure 3.b, it is clear that the test statistic with the highest power of a test is Freeman Tukey's T^2 . However, the T^2 test statistic converges to the chi-squared distribution when the sample size is approximately 900. Based on the sparseness index, Freeman Tukey's T^2 converges to chi-squared distribution when the sparseness index is higher than 25 for R=6.

As seen from simulation results, the goodness-of-fit test statistics and test statistics corresponding to different λ values introduced from the PD family of statistics do not converge to the chi-squared distribution in very small or sparse samples. When the sample size increases, it is clear that all of the test statistics converge to the chi-squared distribution. However, the key point here is that the Freeman

Tukey's T^2 test statistic does not converge to the chi-squared distribution in large samples. It is also possible to say the same comment for Likelihood ratio G^2 test statistic up to a certain sample size. The sample size should be very large to use the Freeman Tukey's T^2 test statistic in analysis of square contingency tables. In other words, if the sparseness index is lower than 5, all test statistics do not show well-convergence to the chi-squared distribution. When the sparseness index is higher than 5, some of the test statistics show well-convergence to the chi-squared distribution. However, the sparseness index should be very large for the convergence of Freeman Tukey's T^2 test statistic to the chi-squared distribution. Therefore, the use of Freeman Tukey's T^2 in the analysis of square contingency tables requires a very large sparseness index or frequencies.

2.3. Artificial data study

Here, an artificial data set is generated under the S model for n=200 and R=5 to demonstrate the efficiencies of test statistics. Since the data set is generated under the S model, the expectation is that the S model holds for the generated data. Table 2 shows the simulated data set.

Table 2. Artificial data for 5 X 5 square contingency table

	[1]	[2]	[3]	[4]	[5]	Total
[1]	9 (9)	1 (7.5)	10 (10)	7 (7.5)	8 (8)	35
[2]	14 (7.5)	8 (8)	10 (9.5)	12 (9)	10 (8.5)	54
[3]	10 (10)	9 (9.5)	5 (5)	5 (6.5)	10 (9)	39
[4]	8 (7.5)	6 (9)	8 (6.5)	9 (9)	7 (6)	38
[5]	8 (8)	7 (8.5)	8 (9)	5 (6)	6 (6)	34
Total	49	31	41	38	41	200

The artificial data set is fitted to the S model by using the test statistics given in Section 2. Table 3 lists the estimated test values and corresponding p-values. As seen from Table 3, all test statistics, except T^2 , reveal that the corresponding data is well-fitted with the S model. The T^2 test statistic rejects the H_0 hypothesis with p-value=0.0282. Here, H_0 represents that the S model holds for the corresponding data set. Since the

T^2 test statistic does not converge to chi-squared distribution not only small samples but also large samples, the T^2 test statistic causes the false decision in hypothesis testing which is called a Type-I error.

Table 3. Results for artificial data set under the S model

Test statistics and λ values	values	p-value
$\chi^2(1)$	15.1632	0.1262
$G^2(0)$	17.3930	0.0660
$T^2(-1/2)$	20.1069	0.0282
$C^2(2/3)$	15.5816	0.1123
0.1	17.0151	0.0740
0.2	16.6800	0.0818
0.3	16.3841	0.0892
0.4	16.1237	0.0961
0.5	15.8959	0.1027
0.6	15.6980	0.1086
0.7	15.5277	0.1140
0.8	15.3830	0.1187
0.9	15.2620	0.1228

3. Results and Discussion

In this paper, the goodness-of-fit test statistics which are commonly used in the literature such as χ^2 , G^2 , T^2 and power-divergence statistics for various λ values are compared in terms of their Type-I error and powers under the S model in square contingency table. The square contingency table analyses in the literature are mostly for large sample sizes. In small samples, there is not enough square contingency table study. It is stated in the studies conducted that T^2 test statistics should be used in large samples. However, how large the sample should be is not included. As a result of the simulation study, it is concluded that all test statistics in large samples asymptotically converge to the chi-square distribution, but the sample size should be very large for T^2 test statistics converge to the chi-square distribution. As a result of the study, it is stated that how much the sample size should be. A simulation study is conducted to demonstrate the converge of these statistics to chi-squared distribution for small and large samples. It is concluded that Freeman-Tukey's T^2 test statistics are not well in convergency to chi-squared distribution not only in sparse square contingency tables but also in non-sparse square contingency tables. We hope that the results given in the paper will be very useful to practitioners and academicians studying in this field.

Conflicts of interest

The authors state that did not have a conflict of interests.

References

- [1] Altun G., Karesel Olumsuzluk Tablolarında Model Uyumunun Sapma Ölçüsü ile Belirlenmesi, PD Thesis, Hacettepe Üniversitesi, Fen Bilimleri Enstitüsü, (2018).
- [2] Goodman L. A., Multiplicative models for square contingency tables with ordered categories, *Biometrika.*, 66(3) (1979) 413-418.
- [3] Fienberg S. E., The use of chi-squared statistics for categorical data problems, *Journal of the Royal Statistical Society. Series B (Methodological.)*, 41(1) (1979) 54-64.
- [4] Horn S. D., Goodness-of-fit tests for discrete data: a review and an application to a health impairment scale, *Biometrics.*, 33(1) (1977) 237-247.
- [5] Watson G. S., Some recent results in chi-square goodness-of-fit tests, *Biometrics.*, 15(3) (1959) 440-468.
- [6] Cochran W. G., The χ^2 test of goodness of fit, *The Annals of Mathematical Statistics.*, 23(3) (1952) 315-345.
- [7] Tate M. W., Hyer L. A., Inaccuracy of the X^2 test of goodness of fit when expected frequencies are small, *Journal of the American Statistical Association.*, 68(344) (1973) 836-841.
- [8] Yarnold J. K., The minimum expectation in X^2 goodness of fit tests and the accuracy of approximations for the null distribution, *Journal of the American Statistical Association.*, 65 (330) (1970) 864-886.
- [9] Fisher R. A., Statistical methods for research workers, 13th ed. New York: Hafner Publishing Co, (1958) 356.
- [10] Roscoe J. T., Byars J. A., An investigation of the restraints with respect to sample size commonly imposed on the use of the chi-square statistic, *Journal of the American Statistical Association.*, 66(336) (1971) 755-759.
- [11] Agresti A, Categorical data analysis, 2nd ed. New Jersey: John Wiley & Sons, (2003) 482.
- [12] Koehler K. J., Goodness-of-fit tests for log-linear models in sparse contingency tables, *Journal of the American Statistical Association.*, 81 (394) (1986) 483-493.

- [13] Koehler, K. J., Larntz, K., An empirical investigation of goodness-of-fit statistics for sparse multinomials, *Journal of the American Statistical Association.*, 75(370) (1980) 336-344.
- [14] Larntz K., Small-sample comparisons of exact levels for chi-squared goodness-of-fit statistics, *Journal of the American Statistical Association.*, 73(362) (1978) 253-263.
- [15] Haberman S. J., A warning on the use of chi-squared statistics with frequency tables with small expected cell counts, *Journal of the American Statistical Association.*, 83(402) (1988) 555-560.
- [16] Cressie N., Read T. R., Pearson's X^2 and the loglikelihood ratio statistic G^2 : a comparative review, *International Statistical Review/Revue Internationale de Statistique.*, 57(1) (1989) 19-43.
- [17] Lawal H. B., Comparisons of the X^2 , Y^2 , Freeman-Tukey and Williams's improved G^2 test statistics in small samples of one-way multinomials, *Biometrika*, 71(2) (1984) 415-418.
- [18] Baglivo J., Olivier D., Pagano M., Methods for exact goodness-of-fit tests, *Journal of the American Statistical Association.*, 87(418) (1992) 464-469.
- [19] Bishop Y. M. M., Fienberg S. E., Holland P. W., Discrete multivariate analysis: Theory and practice, Cambridge: The Massachusetts Institute of Technology Press Google Scholar., (1975).
- [20] Aitchison J., Aitken C. G., Multivariate binary discrimination by the kernel method, *Biometrika.*, 63(3) (1976) 413-420.
- [21] Simonoff J. S., A penalty function approach to smoothing large sparse contingency tables, *The Annals of Statistics.*, 11(1) (1983) 208-218
- [22] Simonoff J. S., Probability estimation via smoothing in sparse contingency tables with ordered categories, *Statistics & Probability Letters.*, 5(1) (1987) 55-63.
- [23] Burman P., Central limit theorem for quadratic forms for sparse tables, *Journal of Multivariate Analysis.*, 22(2) (1987) 258-277.
- [24] Kim S. H., Choi H., Lee S., Estimate-based goodness-of-fit test for large sparse multinomial distributions, *Computational Statistics & Data Analysis.*, 53(4) (2009) 1122-1131.
- [25] Zelterman D., Goodness-of-fit tests for large sparse multinomial distributions, *Journal of the American Statistical Association.*, 82(398) (1987) 624-629.
- [26] AKTAŞ S., Power Divergence Statistics under Quasi Independence Model for Square Contingency Tables, *Sains Malaysiana.*, 45(10) (2016) 1573-1578.
- [27] Cressie N., Read T. R., Multinomial goodness-of-fit tests, *Journal of the Royal Statistical Society, Series B (Methodological).*, 46(3) (1984) 440-464.

The Nakagami–Weibull distribution in modeling real-life data

Ibrahim ABDULLAH^{1,*} , Obalowu JOB² 

¹Yobe State University, Department of Mathematics and Statistics, Damaturu/ NIGERIA

²University of Ilorin, Department of Statistics, Ilorin/ NIGERIA

Abstract

In this article, a four-parameter Nakagami Weibull distributions (NW) is proposed. We study a few statistical properties such as quantile function, moments, moment generating function, entropy, and order statistics have been derived. The maximum likelihood estimate is used to estimate the parameter of the NW distribution. We fit the proposed NW distribution to a real-life data set to examine its potential and flexibility. Our findings showed that the NW distribution performs much better than its competitors, with favorable comparisons to existing distributions in terms of goodness-of-fit.

Article info

History:
Received: 21.11.2020
Accepted: 28.04.2021

Keywords:
Nakagami Weibull,
Moment,
Entropy,
Quantile function

1. Introduction

The continuous probabilities distribution has some essential problems and limitations in modeling real-life data set, has led statistician by adding at least one shape parameter to the baseline distribution to developed new flexible distributions. Methods for generating new families of distributions have been developed by many mathematical statisticians. The beta-generalized family of distribution was developed by [1], the exponentiated generalized class of distributions by [2], Exponentiated Weibull distribution: statistical properties and applications by [3], Beta-Nakagami distribution by [4], Weibull generalized family of distributions by [5], On the exponentiated generalized inverse exponential distribution by [6], Beta generated Kumaraswamy and many compound families of distribution by [7], Exponentiated half-logistic family of distributions by [8], additive Weibull generated distributions by [9], Kummer beta generalized family of distributions by [10], The generalized odd inverted exponential-G family of distributions by [11], the Marshall-Olkin odd Burr III-G family of distributions by [12] and the generalized odd Gamma-G family of distributions by [13].

The Nakagami distribution is a continuous probability distribution with applications in measuring alternation of wireless signal traversing multiple paths, and Weibull distribution is one of the continuous probability distributions used to model a variety of life behaviors.

2. Theoretical Framework of Nakagami Weibull (NW) Distribution

If X is a continuous random variable from the Nakagami distribution with two parameter λ and β , then the *cdf* Eq. (1) and *pdf* Eq. (2) of the Nakagami generalized family of distribution (OGNak-G) due to [14] is given by:

$$F(x, \lambda, \beta, \eta) = \frac{1}{\Gamma(\lambda)} \gamma \left\{ \lambda, \frac{\lambda}{\beta} \left[\frac{G(x; \eta)}{(1 - G(x; \eta))} \right]^2 \right\} \quad (1)$$

The probability density function of the OGNak-G is given by:

$$f(x; \lambda, \beta, \eta) = \frac{2\lambda^\lambda}{\Gamma(\lambda)\beta^\lambda} g(x; \eta) \frac{[G(x; \eta)]^{2\lambda-1}}{[1 - G(x; \eta)]^{2\lambda+1}} e^{-\frac{\lambda}{\beta} \left[\frac{G(x; \eta)}{1 - G(x; \eta)} \right]^2}; x \in \mathfrak{R}, \quad (2)$$

2.1. The proposed NW Distribution

The Weibull distribution is our parent distribution, with two parameters. δ is the scale parameter and α is the shape parameter that has its cdf and pdf given by:

$$g(x; \delta, \alpha) = \delta \alpha x^{\alpha-1} e^{-\delta x^\alpha}; x \geq 0, \delta, \alpha > 0 \tag{3}$$

$$G(x; \delta) = 1 - e^{-\delta x^\alpha} \tag{4}$$

$$f(x; \lambda, \beta, \eta) = \frac{2\lambda^\lambda}{\Gamma(\lambda)\beta^\lambda} \delta \alpha x^{\alpha-1} e^{-\delta x^\alpha} \frac{(1 - e^{-\delta x^\alpha})^{2\lambda-1}}{(e^{-\delta x^\alpha})^{2\lambda+1}} e^{-\frac{\lambda}{\beta}(e^{\delta x^\alpha} - 1)^2}; x \in \mathfrak{R} \tag{6}$$

Using the generator propose by [14] in Eq. (1), the *cdf* of the proposed Nakagami Weibull distribution is given by:

$$F(x, \lambda, \beta, \eta) = \gamma_* \left\{ \lambda, \frac{\lambda}{\beta} \left[\frac{1 - e^{-\delta x^\alpha}}{e^{-\delta x^\alpha}} \right]^2 \right\} \tag{5}$$

where $\eta = (\delta, \alpha)$

and its corresponding pdf is given by:

2.2. Investigation of the proposed NW distribution for a PDF

$$\int_0^\infty f(x) dx = 1$$

To demonstrate that the NW distribution is a pdf, we proceed as follows:

$$\int_0^\infty \frac{2\lambda^\lambda}{\Gamma(\lambda)\beta^\lambda} \delta \alpha x^{\alpha-1} e^{-\delta x^\alpha} \frac{(1 - e^{-\delta x^\alpha})^{2\lambda-1}}{(e^{-\delta x^\alpha})^{2\lambda+1}} e^{-\frac{\lambda}{\beta}(e^{\delta x^\alpha} - 1)^2} dx = 1 \tag{7}$$

let $y = \frac{\lambda}{\beta}(e^{\delta x^\alpha} - 1)^2$

Therefore, $\frac{1}{\Gamma(\lambda)} \int_0^\infty y^{\lambda-1} e^{-y} dy = 1$

Nakagami Weibull Distribution is a pdf

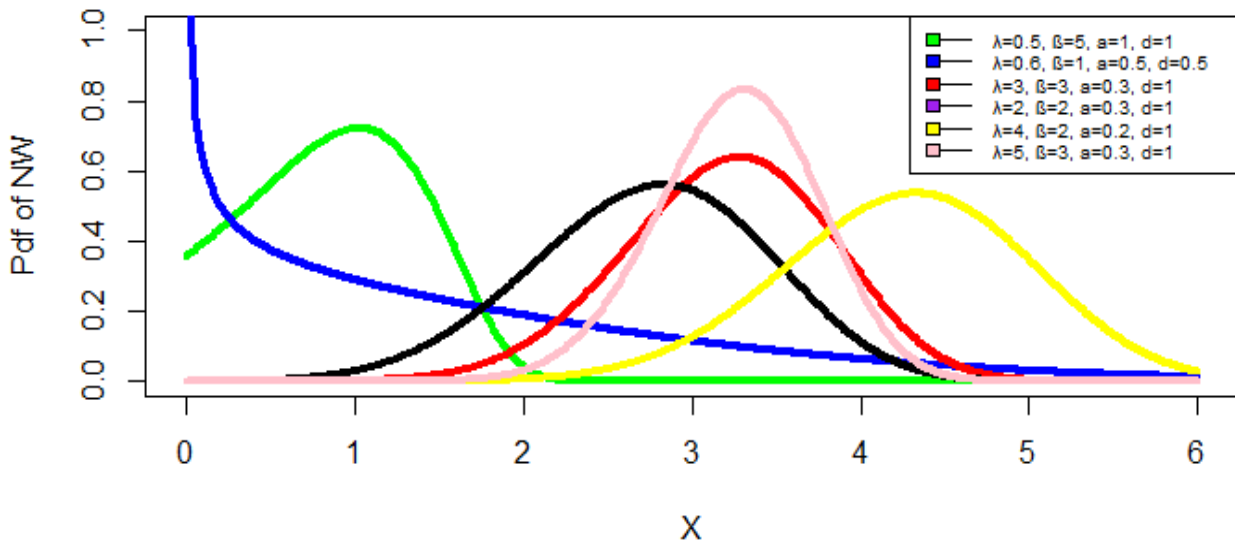


Figure 1. The pdf of the NW distribution for different set of values of the parameters.

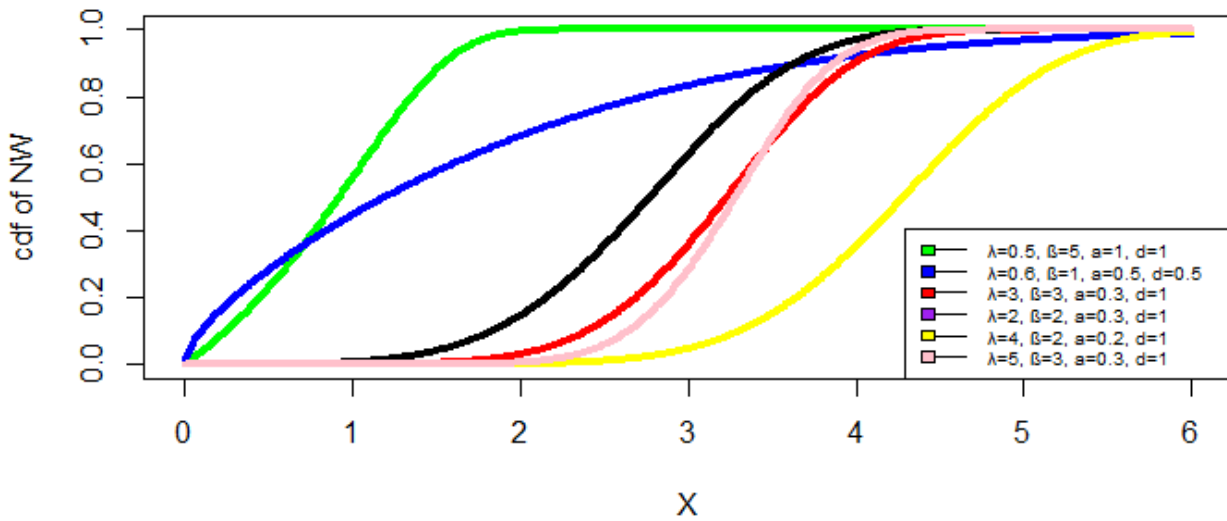


Figure 2. The cdf of the NW distribution for different set of values of the parameters.

2.3. Linear representation

Using generalized binomial and Taylor expansion in Eq. (6) one can obtain

$$f(x; \lambda, \beta, \eta) = \frac{2}{\Gamma(\lambda)} \delta \alpha \sum_{i,k,j=0}^{\infty} \left(\frac{\lambda}{\beta}\right)^{\lambda+i} \omega_{i,k,j} x^{\alpha-1} e^{-j\delta x^\alpha} \tag{8}$$

where $\omega_{i,k,j} = \frac{(-1)^{i+j}}{i!} \binom{2(\lambda+i)+k-1}{k} \binom{2(\lambda+i)+k-1}{j}$

2.4. Reliability analysis for the new Nakagami Weibull Distribution

We proposed new survival function and the hazard function of the Nakagami Weibull distribution are provided as follows:

Survival function is given by:

$$S(x) = 1 - \gamma_* \left\{ \lambda, \frac{\lambda}{\beta} \left[\frac{1 - e^{-\delta x^\alpha}}{e^{-\delta x^\alpha}} \right]^2 \right\} \tag{9}$$

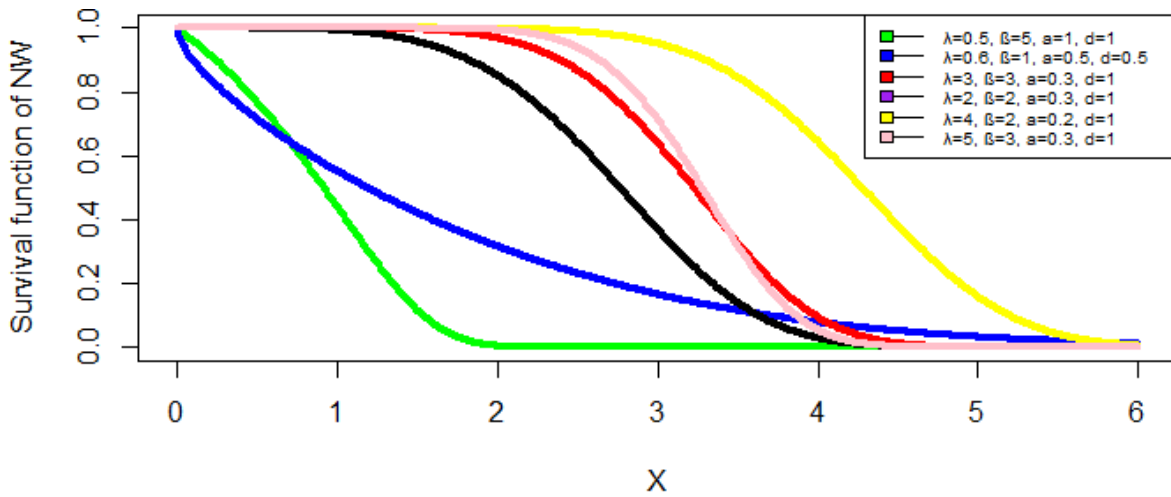


Figure 3. The survival function of the NW distribution for different set of values of the parameters.

Hazard function is given by:

$$h(x) = \frac{\frac{2\lambda^\lambda}{\Gamma(\lambda)\beta^\lambda} \delta \alpha x^{\alpha-1} e^{-\delta x^\alpha} \frac{(1-e^{-\delta x^\alpha})^{2\lambda-1}}{(e^{-\delta x^\alpha})^{2\lambda+1}} e^{-\frac{\lambda}{\beta}(e^{\delta x^\alpha}-1)^2}}{1 - \gamma_* \left\{ \lambda, \frac{\lambda}{\beta} \left[\frac{1-e^{-\delta x^\alpha}}{e^{-\delta x^\alpha}} \right]^2 \right\}} \tag{10}$$

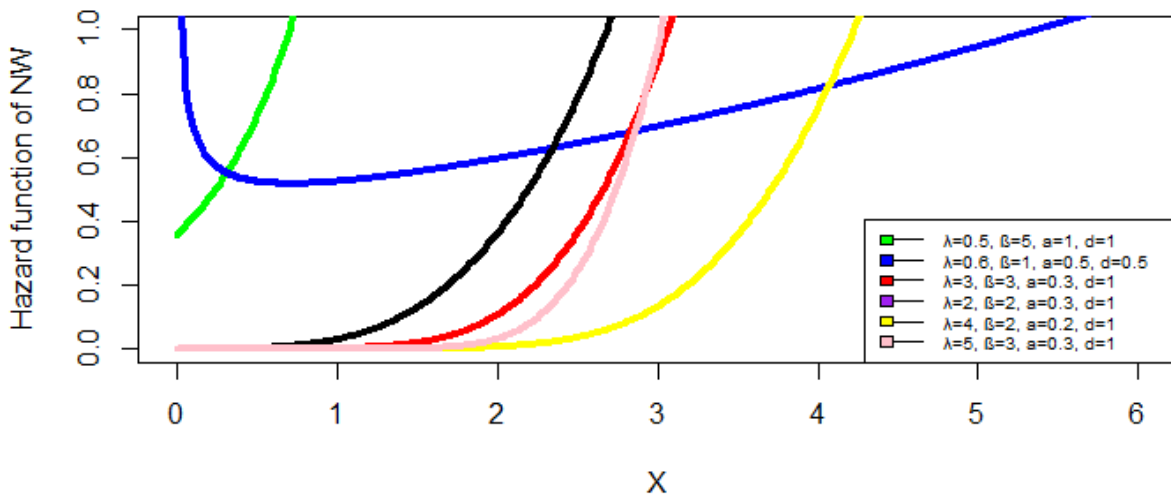


Figure 4. The hazard function of the NW distribution for different set of values of the parameters.

2.5. Mathematical and statistical properties

Moment play an important role in statistical analysis when a new probability distribution is developed. Using Eq. (8), we obtain the following:

$$E(X^r) = \int_0^\infty \frac{2}{\Gamma(\lambda)} \delta \alpha \sum_{i,k,j=0}^\infty \left(\frac{\lambda}{\beta}\right)^{\lambda+i} \omega_{i,k,j} x^{r+\alpha-1} e^{-j\delta x^\alpha} dx \tag{11}$$

$$\mu'_r = \frac{2}{\Gamma(\lambda)} \sum_{i,k,j=0}^{\infty} \left(\frac{\lambda}{\beta}\right)^{\lambda+i} \omega_{i,k,j} \frac{\Gamma\left(\frac{r}{\alpha}+1\right)}{\delta^\alpha j^{\frac{r}{\alpha}+1}}; \quad r=1,2,3\dots \tag{12}$$

The mean and variance of NW distribution are obtained, respectively as follows

$$E(X) = \frac{2}{\Gamma(\lambda)} \sum_{i,k,j=0}^{\infty} \left(\frac{\lambda}{\beta}\right)^{\lambda+i} \omega_{i,k,j} \frac{\Gamma\left(\frac{1}{\alpha}+1\right)}{\delta^\alpha j^{\frac{1}{\alpha}+1}} \tag{13}$$

$$Var(X) = \frac{2}{\Gamma(\lambda)} \sum_{i,k,j=0}^{\infty} \left(\frac{\lambda}{\beta}\right)^{\lambda+i} \omega_{i,k,j} \frac{\Gamma\left(\frac{2}{\alpha}+1\right)}{\delta^\alpha j^{\frac{2}{\alpha}+1}} - \left\{ \frac{2}{\Gamma(\lambda)} \sum_{i,k,j=0}^{\infty} \left(\frac{\lambda}{\beta}\right)^{\lambda+i} \omega_{i,k,j} \frac{\Gamma\left(\frac{1}{\alpha}+1\right)}{\delta^\alpha j^{\frac{1}{\alpha}+1}} \right\}^2 \tag{14}$$

Moment generating function of NW will take this form:

$$M_X(t) = E(e^{tX}) = \sum_{r=0}^{\infty} \frac{t^r \mu'_r}{r!}$$

$$M_X(t) = \frac{2}{\Gamma(\lambda)} \sum_{i,k,j,r=0}^{\infty} \frac{t^r}{r!} \left(\frac{\lambda}{\beta}\right)^{\lambda+i} \omega_{i,k,j} \frac{\Gamma\left(\frac{r}{\alpha}+1\right)}{\delta^\alpha j^{\frac{r}{\alpha}+1}} \tag{15}$$

2.5.1. Incomplete moments of NW distribution

The main applications of the first incomplete moment refer to the mean deviations and the Bonferroni and Lorenz curves. These curves are very useful in reliability, medicine, economics, insurance and demography (see [15]). Considering the NW distribution discussed in Eq. (8) the r^{th} incomplete moment for NW is derived by using Eq. (16) as follows:

$$M_r^q = \int_0^t x^r f(x) dx \tag{16}$$

$$= \frac{2}{\Gamma(\lambda)} \delta^\alpha \sum_{i,k,j=0}^{\infty} \left(\frac{\lambda}{\beta}\right)^{\lambda+i} \omega_{i,k,j} \int_0^t x^{r+\alpha-1} e^{-j\delta x^\alpha} dx$$

$$M_r^q = \frac{2}{\Gamma(\lambda)} \sum_{i,k,j=0}^{\infty} \left(\frac{\lambda}{\beta}\right)^{\lambda+i} \omega_{i,k,j} \frac{1}{j^{\frac{r}{\alpha}+1} \delta^\alpha} \gamma\left(\frac{r}{\alpha}+1, j\delta x^\alpha\right) \tag{17}$$

2.5.2. Entropy

The entropy of a random variable X is a measure of variation of the uncertainly. The Renyi entropy is defined as

$I_R(\sigma) = \frac{1}{1-\sigma} \log \left[\int_0^\infty f^\sigma(x) dx \right]$, Where $\sigma > 0$ and $\sigma \neq 1$. Based on $f(x)$ of any distribution from Eq. (6).

$$f^\sigma(x) = \left(\frac{2\delta\alpha}{\Gamma(\lambda)} \right)^\sigma \left(\frac{\lambda}{\beta} \right)^{\lambda\sigma} x^{\sigma(\alpha-1)} e^{-\sigma\delta x^\alpha} \frac{(1 - e^{-\delta x^\alpha})^{\sigma(2\lambda-1)}}{(e^{-\delta x^\alpha})^{\sigma(2\lambda+1)}} e^{-\frac{\sigma\lambda}{\beta}(e^{\delta x^\alpha} - 1)^2} \tag{18}$$

Using generalized binomial and Taylor expansion in Eq. (18), one can obtain

$$f^\sigma(x) = \sum_{q,i,j=0}^\infty \pi_{q,i,j} x^{\sigma(\alpha-1)} e^{-j\delta x^\alpha} \tag{19}$$

where

$$\pi_{q,i,j} = \frac{(-1)^{q+j}}{q!} \binom{2\lambda\sigma + 2q - 1 + i}{i} \binom{\sigma(2\lambda - 1) + 2q + i}{j} \sigma^q \left(\frac{\lambda}{\beta} \right)^{\lambda\sigma + q} \left(\frac{2\delta\alpha}{\Gamma(\lambda)} \right)^\sigma$$

$$\int_0^\infty f^\sigma(x) dx = \int_0^\infty \sum_{q,i,j=0}^\infty \pi_{q,i,j} x^{\sigma(\alpha-1)} e^{-j\delta x^\alpha} dx \tag{20}$$

$$I_R(\sigma) = \frac{1}{1-\sigma} \log \left[\int_0^\infty \sum_{q,i,j=0}^\infty \pi_{q,i,j} x^{\sigma(\alpha-1)} e^{-j\delta x^\alpha} dx \right] \tag{21}$$

2.5.3. The mode

The mode of the NW density function can be derived by differentiating the natural logarithm of Eq. (6) with respect to x as follows:

$$\frac{\alpha - 1}{x} - \delta\alpha x^{\alpha-1} + \frac{(2\lambda - 1)\delta\alpha x^{\alpha-1} e^{-\delta x^\alpha}}{(1 - e^{-\delta x^\alpha})} + (2\lambda + 1)\delta\alpha x^{\alpha-1} - \frac{2\lambda}{\beta} (e^{\delta x^\alpha} - 1)\delta\alpha x^{\alpha-1} e^{\delta x^\alpha} = 0 \tag{22}$$

Solving the Eq. (22) numerically we can find the mode(s).

If x_0 is a root of the Eq.(22), then it must be $\frac{d^2}{dx^2} \log f(x_0) < 0$,

$$= -\frac{\alpha - 1}{x} - \delta\alpha(\alpha - 1)x^{\alpha-2} - \frac{(2\lambda - 1)\delta\alpha x^{\alpha-2} e^{-\delta x^\alpha} \left[(\alpha - 1)e^{-\delta x^\alpha} + \delta\alpha x^\alpha - \alpha + 1 \right]}{(1 - e^{-\delta x^\alpha})^2} + (2\lambda + 1)\delta\alpha(\alpha - 1)x^{\alpha-2} - \frac{2\lambda}{\beta} \delta\alpha x^{\alpha-2} e^{\delta x^\alpha} (2\delta\alpha x^\alpha e^{\delta x^\alpha} - \delta\alpha x^\alpha + \alpha e^{\delta x^\alpha} - e^{\delta x^\alpha} - \alpha + 1) \tag{23}$$

The Eq. (23) is a nonlinear and does not have an analytic solution with respect to x therefore we have to solve it numerically.

2.5.4. Order statistics

Let $X_{(1)}, X_{(2)}, \dots, X_{(n)}$. represent random sample for the order statistic, X_1, X_2, \dots, X_n from a continuous population with *cdf* $F_X(x)$ and *pdf* $f_X(x)$. Then the pdf of $X_{(j)}$ is

$$f_{X_{(j)}}(x) = \frac{n!}{(j-1)!(n-j)!} f_X(x) [F_X(x)]^{j-1} [1 - F_X(x)]^{n-j}, \text{ for } -\infty < x < \infty$$

By using binomial expansion

$$[1 - F_X(x)]^{n-j} = \sum_{z=0}^{n-j} {}^{n-j}C_z [F_X(x)]^z$$

Therefore,

$$f_{X_{(j)}}(x) = \sum_{z=0}^{n-j} {}^{n-j}C_z f_X(x) [F_X(x)]^{z+j-1}, \text{ for } -\infty < x < \infty \tag{24}$$

(See [16]).

Hence, the j^{th} order statistic for the NW distribution is given by using Eq. (5) and Eq. (6), we obtain

$$f_{X_{(j)}}(x) = \sum_{z=0}^{n-j} {}^{n-j}C_z \frac{2\lambda^\lambda}{\Gamma(\lambda)\beta^\lambda} \delta \alpha x^{\alpha-1} e^{-\delta x^\alpha} \frac{(1 - e^{-\delta x^\alpha})^{2\lambda-1}}{(e^{-\delta x^\alpha})^{2\lambda+1}} e^{-\frac{\lambda}{\beta}(e^{\delta x^\alpha} - 1)^2} \gamma_* \left\{ \lambda, \frac{\lambda}{\beta}(e^{\delta x^\alpha} - 1)^2 \right\}^{z+j-1} \tag{25}$$

2.5.5. Quantile Function

The quantile function of the NW distribution is obtained by inverting the distribution function defined in Eq. (5) as follows:

$$u = \gamma_* \left\{ \lambda, \frac{\lambda}{\beta} \left[\frac{G(x;\eta)}{(1-G(x;\eta))} \right]^2 \right\}$$

$$x = \left\langle \frac{-1}{\delta} \ln \left\langle 1 - \left[\frac{\left[\frac{\beta}{\lambda} \gamma^{-1}(\lambda, u\Gamma(\lambda)) \right]}{1 + \left[\frac{\beta}{\lambda} \gamma^{-1}(\lambda, u\Gamma(\lambda)) \right]} \right]^{1/2} \right\rangle \right\rangle^{\frac{1}{\alpha}} \tag{26}$$

2.6. Maximum likelihood estimates of the parameters of Nakagami Weibull Distribution

Many approaches of estimating parameter were introduced in the literature. In this section, we deal with the estimation of the unknown parameters for the NW distributions based on complete samples only by maximum likelihood. Let X_1, X_2, \dots, X_n be observed values from the NW distribution with set of parameters $\Theta = (\lambda, \beta, \delta, \alpha)^T$. The log-likelihood function for parameter vector $\Theta = (\lambda, \beta, \delta, \alpha)^T$ is obtained from (6) as follows:

$$L(x; \Theta) = \prod_{i=1}^n f(x_i; \Theta) \tag{27}$$

$$= \prod_{i=1}^n \frac{2\lambda^\lambda}{\Gamma(\lambda)\beta^\lambda} \delta \alpha x^{\alpha-1} e^{-\delta x^\alpha} \frac{(1 - e^{-\delta x^\alpha})^{2\lambda-1}}{(e^{-\delta x^\alpha})^{2\lambda+1}} e^{-\frac{\lambda}{\beta}(e^{\delta x^\alpha} - 1)^2} \tag{28}$$

$$\ell(x; \Theta) = n \log 2 + n \lambda \log \lambda - n \log \Gamma(\lambda) - n \lambda \log \beta + n \log \delta + n \log \alpha -$$

$$\delta \sum x^\alpha + (2\lambda - 1) \log \sum (1 - e^{-\delta x^\alpha}) - (2\lambda + 1) \log \sum (e^{-\delta x^\alpha}) - \frac{\lambda}{\beta} \sum (e^{\delta x^\alpha} - 1)^2$$

$$\frac{\partial \ell(x; \Theta)}{\partial \lambda} = n \log \lambda n + -n\Psi(\lambda) - n \log \beta - \frac{1}{\beta} (e^{\delta x^\alpha} - 1) \tag{29}$$

$$\frac{\partial \ell(x; \Theta)}{\partial \beta} = \frac{\lambda}{\beta^2} (e^{\delta x^\alpha} - 1)^2 - \frac{n\lambda}{\beta} \tag{30}$$

$$\frac{\partial \ell(x; \Theta)}{\partial \delta} = \frac{n}{\delta} - \sum x^\alpha + (2\lambda - 1) \frac{\sum x^\alpha e^{-\delta x^\alpha}}{\sum (1 - e^{-\delta x^\alpha})} + (2\lambda + 1) \frac{\sum x^\alpha e^{-\delta x^\alpha}}{\sum e^{-\delta x^\alpha}} - \frac{2\lambda}{\beta} \sum (e^{\delta x^\alpha} - 1) x^\alpha e^{-\delta x^\alpha} \tag{31}$$

$$\frac{\partial \ell(x; \Theta)}{\partial \alpha} = \frac{n}{\alpha} - \delta \alpha \sum x^{\alpha-1} + (2\lambda - 1) \frac{\sum \delta \alpha x^{\alpha-1} e^{-\delta x^\alpha}}{\sum (1 - e^{-\delta x^\alpha})} + (2\lambda + 1) \frac{\sum \delta \alpha x^{\alpha-1} e^{-\delta x^\alpha}}{\sum (e^{-\delta x^\alpha})} - \frac{2\lambda}{\beta} \sum \delta \alpha x^{\alpha-1} (1 - e^{\delta x^\alpha}) \tag{32}$$

These estimates can't be solved algebraically, and statistical software can be used to solve them numerically via iterative technique in the AdequacyModel package available in the R.

3. Results and Discussion

In this section, fitting NW distribution. We provide two applications to real life data set to demonstrate the potentiality of the NW distribution and compare its performance, to other generated models. The Akaike information criterion (AIC), Consistent Akaike Information Criterion (CAIC), Bayesian information criterion (BIC), Anderson-Darling (A), Kolmogorov Smirnov test (K.S), and the P-Value of K.S test, have been chosen for the comparison of the models. The distributions: Odd Generalize Gamma Frechet (OGGFr) [117], Odd Generalized Gamma Weibull (OGGW) [17], the generalized odd inverted exponential-G family of distributions [11], Exponentiated Weibull Weibull (EWW) [3], Weibull-Exponential (WE) [18] have been selected for comparison. The parameters of models have been estimated by the MLE method.

The first data, we used the breaking stress of carbon fibers of 50 mm length (GPa) from [19], [20] and [14]. The data is as follows: 0.39, 0.85, 1.08, 1.25, 1.47, 1.57, 1.61, 1.61, 1.69, 1.80, 1.84, 1.87, 1.89, 2.03, 2.03, 2.05, 2.12, 2.35, 2.41, 2.43, 2.48, 2.50, 2.53, 2.55, 2.55, 2.56, 2.59, 2.67, 2.73, 2.74, 2.79, 2.81, 2.82, 2.85, 2.87, 2.88, 2.93, 2.95, 2.96, 2.97, 3.09, 3.11, 3.11, 3.15, 3.15, 3.19, 3.22, 3.22, 3.27, 3.28, 3.31, 3.31, 3.33, 3.39, 3.39, 3.56, 3.60, 3.65, 3.68, 3.70, 3.75, 4.20, 4.38, 4.42, 4.70, 4.90.

Table 1 displays a summary of goodness-of-fit measures for the stress of carbon fibers of 50 mm length (GPa) and MLEs for this data with different models, respectively. The NW with the smallest AIC criteria is selected as the best model with all other criteria. As you see, the P-Value for NW is also more than all other distributions.

Table 1: Summary of MLEs and goodness-of-fit statistics for the first data set

Models	MLE	$-\ell$	AIC	CAIC	BIC	A.D	K.S	P Value
NW	$\lambda = 1.6103057$ $\beta = 1.1390558$ $\delta = 0.2809454$ $\alpha = 0.8761429$	86.190	180.381	181.037	189.140	0.528	0.109	0.413
OGGFr	$\lambda = 1.9147482$ $\beta = 1.2807083$ $\delta = 1.7515636$ $\alpha = 0.9275479$	91.388	190.776	191.432	199.534	1.249	0.166	0.052
OGGW	$\lambda = 1.5477753$ $\beta = 1.5594958$ $\delta = 0.2641594$ $\alpha = 1.0745220$	86.277	180.555	181.210	189.313	0.511	0.11583	0.339

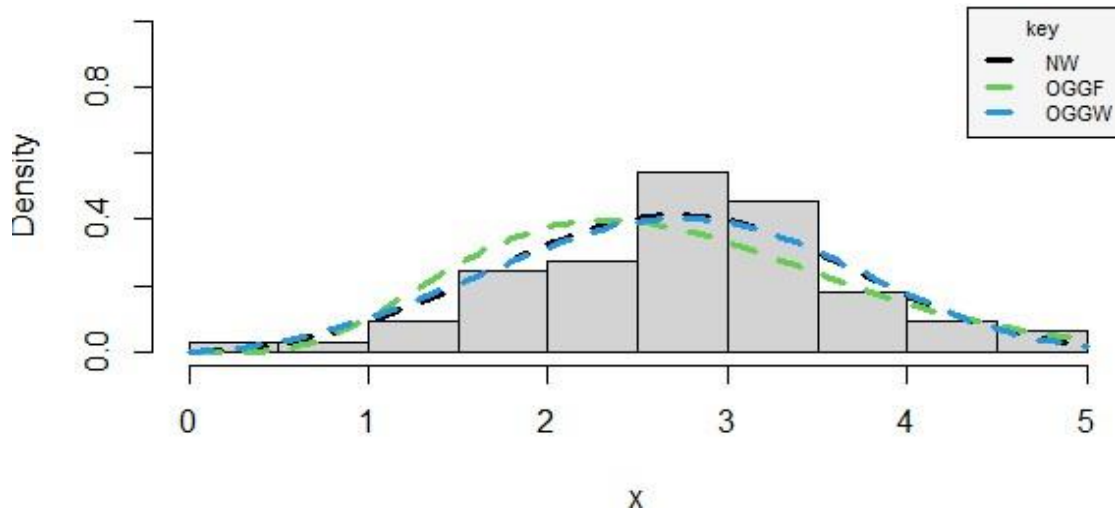


Figure 5. Histogram and estimated pdfs for data sets 1.

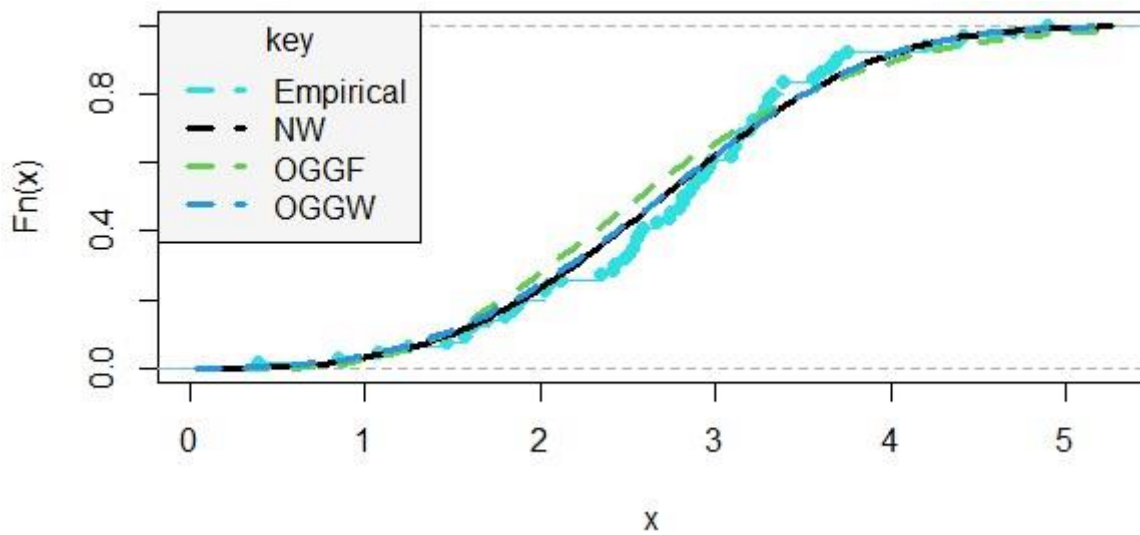


Figure 6. Plots of estimated cdf for data Sets 1.

The second data, we used thirty successive values of March precipitation in Minneapolis/St Paul from [21] and [22]. The data set are as follows:

0.77, 1.74, 0.81, 1.20, 1.95, 1.20, 0.47, 1.43, 3.37, 2.20, 3.00, 3.09, 1.51, 2.10, 0.52, 1.62, 1.31, 0.32, 0.59, 0.81, 2.81, 1.87, 1.18, 1.35, 4.75, 2.48, 0.96, 1.89, 0.90, 2.05.

Table 2 displays a summary of the goodness-of-fit measures for the March precipitation in Minneapolis/St Paul and MLEs for this data with different models, respectively. The NW with the smallest AIC criteria is selected as the best model with all other criteria. As you see, the P-Value for NW is also more than all other distributions.

Table 2: Summary of MLEs and goodness-of-fit statistics for the second data set

Models	MLE	$-\ell$	AIC	CAIC	BIC	A.D	K.S	P Value
NW	$\lambda=1.5347926$ $\beta=0.5178431$ $\delta=0.3999663$ $\alpha=0.5250054$	38.747	85.493	87.093	91.098	0.170	0.066	0.999
EWG	$\lambda=1.5264454$ $\beta=0.6836198$ $\delta=1.3895067$ $\alpha=0.6091976$ $\theta=0.6701214$	39.206	88.412	90.912	95.418	0.235	0.1023	0.911
OGGW	$\lambda=1.3057645$ $\beta=1.5374857$ $\delta=0.5881135$ $\alpha=0.6735570$	39.335	86.670	88.270	92.275	0.237	0.081	0.989

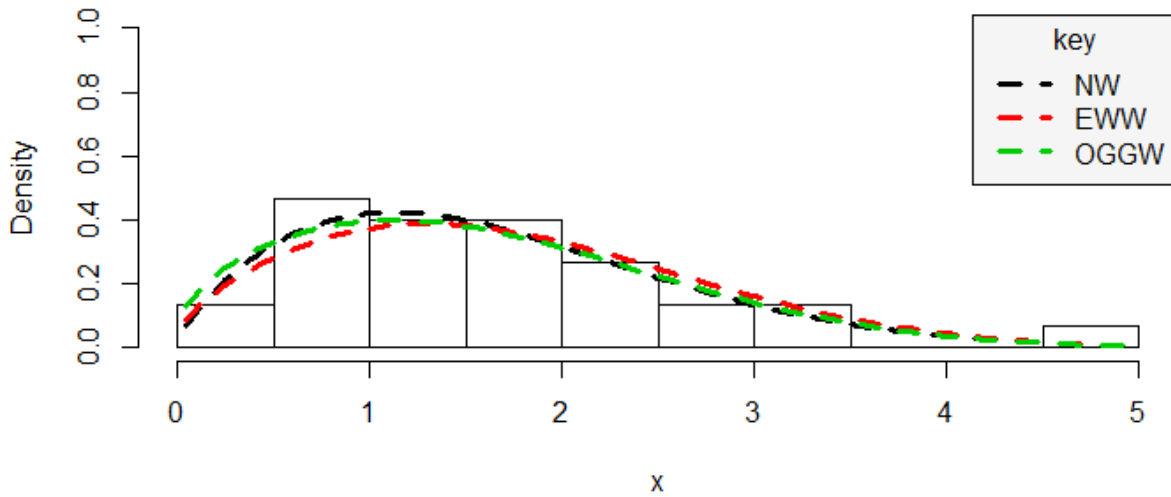


Figure 7. Histogram and estimated pdfs for data Sets 2.

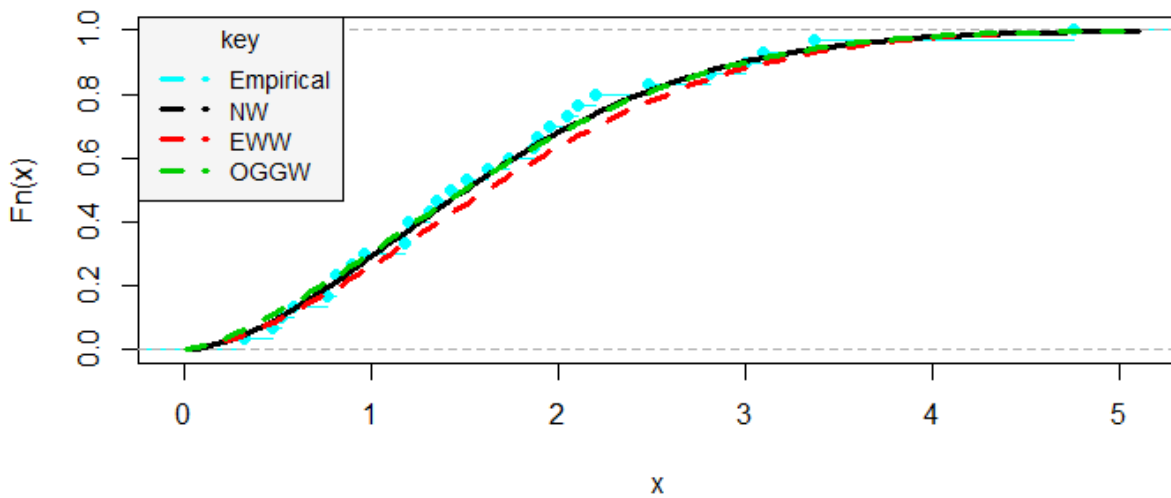


Figure 8. Plots of estimated cdf for data sets 2.

Conclusions

We introduce a new four-parameter, the so called Nakagami Weibull distribution. The main statistical properties are provided. The model parameters estimation is approached by maximum likelihood. We prove empirically the usefulness of the NW distribution is demonstrated in two applications to show its superiority compared to other competitive distributions in terms of minimum AIC criteria is selected as the best model. It seems that the result is consistent with other criteria. We hope that the NW may attract wider applications in many applied areas.

Acknowledgment

The authors would love to express gratitude to anonymous referees and the Editor, for their productive comments, which have improved the contents of the article paper.

Conflicts of interest

There are no conflicts of interest disclosed by the authors in relation to the publication of this work.

References

- [1] Nicholas E, Carl L, and Felix F. Beta-normal distribution and its applications, *Communications in Statistics-Theory and methods*, 31(4) (2002) 497-512.
- [2] Gauss MC, Edwin MMO, and Daniel CC da C. The exponentiated generalized class of distributions, *Journal of Data Science*, 11(1) (2013) 1-27.
- [3] Mohammed E and Amal H. Exponentiated weibull weibull distribution: Statistical properties and applications, *Gazi University Journal of Science*, 32(2) (2019) 616-635.
- [4] Olanrewaju IS and Kazeem AA. On the beta-nakagami distribution, *Progress in Applied Mathematics*, 5(1) (2013) 49-58.
- [5] Marcelo B., Rodrigo B.S., Gauss M.C., The weibull-g family of probability distributions, *Journal of Data Science*, 12(1) (2014) 53-68.
- [6] Oguntunde PE, Adejumo AO, and Owoloko EA. Exponential Inverse Exponential (EIE) Distribution with Applications to Lifetime Data, *Asian Journal of Scientific Research*, 10 (2017) 169-177.
- [7] Laba H and Subrata C. Beta generated kumaraswamy-g and other new families of distributions. *arXiv preprint arXiv* (2016) 1603.00634.
- [8] Gauss MC, Morad A, and Edwin MMO. The Exponentiated Half-Logistic Family of Distributions: Properties and Applications, *Journal of Probability and Statistics*, vol. 2014 (2014) ID 864396, 21. Available at: <https://doi.org/10.1155/2014/864396>.
- [9] Amal SH and Saeed EH. A new family of additive weibull-generated distributions, *International Journal of Mathematics And its Applications*, 4(2) (2016) 151-164.
- [10] Rodrigo RP, Gauss MC, Clarice GBD, Edwin MMO, and Saralees N. The new class of kummer beta generalized distributions, *SORT-Statistics and Operations Research Transactions*, 36(2) (2012) 153-180.
- [11] Saliou D and Christophe C. The generalized odd inverted exponential-g family of distributions: properties and applications, *Eurasian Bulletin of Mathematics (ISSN: 2687-5632)*, 2(3) (2019) 86-110.
- [12] Ahmed Z.A., Gauss C., Farrukh J, Mohamed E, and Mohamed N. The marshall-olkin odd burr iii-g family of distributions: *Theory, estimation and applications*, Available at: <https://hal.archives-ouvertes.fr/hal-02376067>. Retrieved November 22, 2019.
- [13] Bistoon H, Mahmoud A, and Morad A. The generalized odd gamma-g family of distributions: properties and applications, *Austrian Journal of Statistics*, 47(2) (2018) 69-89.
- [14] Abdullahi, I, Job, O. A new family of odd generalized Nakagami (Nak-G) distributions, *Turkish Journal of Science*, 5 (2) (2020) 85-101.
- [15] Zenga, M. Inequality curve and inequality index based on the ratios between lower and upper arithmetic means, *Statistica e Applicazioni* 4, (2007) 3-27.
- [16] George C., Roger L.B., *Statistical inference*, 2nd ed. Australia ; Pacific Grove, CA : Thomson Learning, (2002).
- [17] Arslan MN, Muhammad HT, Christophe C, Farrukh J, and Akbar MAS. The odds generalized gamma-g family of distributions: Properties, regressions and applications, *Statistica*, 80(1) (2020) 3-38.

- [18] Oguntunde PE, Balogun OS, Okagbue HI, and Bishop SA. The weibull exponential distribution: Its properties and applications, *Journal of Applied Sciences*, 15(11) (2015) 1305-1311.
- [19] Michele DN and Padgett WJ. A bootstrap control chart for weibull percentiles, *Quality and reliability engineering international*, 22(2) (2006) 141-151.
- [20] Gauss MC and Artur JL. The β -birnbaum-saunders distribution: an improved distribution for fatigue life modeling, *Computational Statistics & Data Analysis*, 55(3) (2011) 1445-1461.
- [21] Amal HS, Mohammed AE, and Mohammed S. Type ii half logistic family of distributions with applications, *Pakistan Journal of Statistics and Operation Research*, (2017) 245-264.
- [22] Amal SH, Abd-Elfattah AM, and Asmaa HM. The complementary exponentiated inverted weibull power series family of distributions and its applications, *Journal of Advances in Mathematics and Computer Science*, (2016) 1-20.



Examination of effects of radiation awareness on protection from radiation via structural equation modeling

Sinan SARAÇLI^{1,*}  Olcay ULUCAN² 

¹Afyon Kocatepe University, Faculty of Science, Afyonkarahisar/ TURKEY

²Afyonkarahisar Health Science University, Faculty of Medicine, Afyonkarahisar/ TURKEY

Abstract

This study aims to determine the radiation awareness levels and radiation protection information of university students and to model the effects of radiation awareness levels on radiation protection information. For this purpose, a questionnaire both including the demographic features and the scale is applied to 580 university students to obtain the data set. The data set is analyzed by Explanatory Factor Analysis (EFA), Confirmatory Factor Analysis (CFA), Structural Equation Modeling (SEM). As the results of EFA, while four dimensions for Radiation awareness are determined and they are named; Physics Knowledge, Technical Device Knowledge, Professional Knowledge and Radiation Security Knowledge respectively, Radiation protection knowledge determined in a single dimension. As well as the Physics Knowledge has the greatest effect, Radiation Security Knowledge and Technical Device Knowledge have statistically significant effects on radiation protection information of the students. Improving Physics Knowledge, Radiation Security Knowledge and Technical Device Knowledge via some extra seminars, giving theoretical and applied educations should improve radiation protection information of these students. Even if the results indicate that Professional Knowledge does not have statistically significant effect on radiation protection information, it has an indirect effect. Some improvements about this sub-factor may also improve the radiation protection information. As "entering to radiation areas needs attention" has a direct and significant effect on radiation protection information, the importance of this situation must keep its priority and theoretical and applied educations must be in progress.

Article info

History:

Received: 13.01.2021

Accepted: 05.05.2021

Keywords:

Radiation awareness, Radiation protection information, Structural equation modeling.

1. Introduction

The term radiation refers to energy that is emitted from a source. Although the term is normally reserved for wave phenomena (like electromagnetic radiation) it can also be used to describe emitted particles (like alpha and beta radiation) [1]. Radiation is a very general term, used to describe any process that transmits energy through space or a material away from a source. Light, sound, and radio waves are all examples of radiation.

Studies on occupational exposures, especially large-scale cohort studies, can provide useful information in this regard. The main challenge is to find a sufficiently large cohort for which accurate dose information is available, with a sufficiently period of follow-up to evaluate cancer risk. The National Dose Registry is well suited for this purpose [2]. In the studies conducted, it was stated that the physicians' knowledge about radiation safety was insufficient and hundreds of

unnecessary examinations were carried out every year [3]. Awareness is an understanding of the activities of others, which provides a context for your own activity. This context is used to ensure that individual contributions are relevant to the group's activity as a whole, and to evaluate individual actions with respect to group goals and progress [4].

This study aims to determine the radiation awareness levels and radiation protection information of university students and to determine the effect of radiation awareness levels on radiation protection information with SEM.

2. Materials and Methods

2.1. Population and sample

By the purpose of determining the university students' knowledge levels and the effects of radiation awareness levels on their radiation protection knowledge, the population of this study is determined

*Corresponding author. e-mail address: ssaracli@aku.edu.tr

as the total 3400 students at health occupation high school and health services occupation high school of the University. Because of time, money and etc. restrictions, a sample is chosen among these students via stratified sampling, considering the departments and the classes of these students. The sample size is calculated as 550 according to $n = s^2 \cdot z^2 / d^2$ formulation where s: standard deviation z: critical value and d: precision.

2.2. Data collection

In this study, a questionnaire is used to collect the data set. The questionnaire is developed by the authors of this study by examining the related literature and considering the ideas of the experts in this field. It is composed of three parts. First part includes 8 items related to the socio-demographic features of the students while second part which measures the radiation awareness of students, includes 16 items with four dimensions named as: Physics Knowledge, Technical Device Knowledge, Professional Knowledge, Radiation Security Knowledge and the third part which measures the radiation protection knowledge of students includes 4 items. Second and the third sections of the questionnaire are prepared as a Likert scale type questionnaire, ranging from 1 'strongly disagree' to 5 'strongly agree'. The data set is collected by applying this questionnaire to 600 university students between the dates 1-30 September 2017. Statistical analyses are conducted over 585 questionnaires due to some unfilled forms. Scale of this study in the questionnaire form is also approved by research ethics review committee by protocol number: 2011-KAEK-2.

2.3. Data analysis

As the data analysis, first off all descriptive statistics of the socio-demographic features of the students are given. Then, EFA, CFA and SEM are applied to find out the dimensions of Radiation awareness scale, to confirm them and to model the relations between the sub-factors of radiation awareness and protection Knowledge. The results are given in related tables and figures. SPSS and LISREL softwares are used to perform the statistical analysis.

EFA attempts to bring intercorrelated variables together under more general, underlying variables. More specifically, the goal of factor analysis is to reduce "the dimensionality of the original space and to give an interpretation to the new space, spanned by a reduced number of new dimensions which are supposed to underlie the old ones" [5]. CFA is generally used as a deductive approach to testing whether some a priori formulated theoretical model

adequately explains covariances among observed variables [6]. SEM is a comprehensive statistical method used in testing hypotheses about causal relationships among observed and unobserved (latent) variables and has proved useful in solving the problems in formulating theoretical constructions [7].

3. Results and Discussion

3.1. Demographic features of the participants

Descriptive statistics of the participants are; as their gender, while 71,1% of the participants are female, 28,9% of them are male. Related with their departments; 14,2% of them are at Nursing, 6,2% of them are at Health Management, 11,3% of them are at Physiotherapy and Rehabilitation, 0,5% of them are at Nourishment and Dietetic, 6% of them are at Elderly Care, 19,3% of them are at Medical Laboratory Techniques, 13,2% of them are at Medical Screening, 8% of them are at Electroneurophysiology, 12,3% of them are at Medical Documentation and Secretarial and 9,1% of them are at Orthopedic Prosthesis and Orthosis. The percentages of the students attending to first, second third and fourth classes are 55,4%, 40%, 2,1% and 2,6% respectively. According to their age category, 45,1% of them are at the ages between 18-19, 43,1% of them are at the ages between 20-21, 8% of them are at the ages between 22-23 and 3,8% of them are at the ages 24 and more. While mother education level percentages of these students are 7% Literate, 51,8% Primary School, 19,5% Secondary School, 17,3% High School and 4,4% University, the percentages of their father education levels are 1,5% Literate, 36,2% Primary School, 18,5% Secondary School, 28,43% High School and 15,4% University. Related to their monthly income, while 18,6% of them get 1400 TL and less, the percentages for 1401-2500 TL, 2501-4000 TL and 4001 TL and more are, 48,4%, 26,7% and 6,3% respectively. They also mentioned that as their residence, 14% of them live in Village, 33,8% of them live in County, 26,3% of them live in Province and 25,8% of them live in Metropolis.

3.2. EFA results of radiation awareness and protection knowledge

Results of EFA for Radiation awareness and protection knowledge scales are given in Table 1 and Table 2. Table 1 indicates that, the total variance explanation ratio for the Radiation awareness scale is 54,8% the variance explanation ratios of the sub-factors which are named; Physics Knowledge, Technical Device Knowledge, Professional Knowledge and Radiation Security Knowledge are 18,132%, 13,601%, 13,614% and 9,479% respectively.

Table 1.EFA Results and Cronbach's α values for Radiation awareness scale

Factors/Items	Factor Loading	Eigen value	Explained Variance (%)	α
FB. Physics Knowledge				
ted dose amount of human body decreases by moving away from the radiation source.	0.736	4.179	18.132	0.780
FB2. There may be some precautions to protect against exposure to radiation.	0.741			
FB3. The damage of radiation is related to the exposure time.	0.740			
FB4. The amount of the radiation changes the damage level	0.675			
TCB. Technical Device Knowledge				
TCB1.Koroner Angio devices work with radiation	0.661	2.126	13.601	0.669
TCB2.Bonedensitometry includes radiation	0.651			
TCB3.Magnetic Rezones (MR) do not include radiation.	0.596			
TCB4.Torax computer-based tomography includes much radiation compared with lung roentgen.	0.537			
TCB5.Mamografy includes radiation.	0.489			
MB. Professional Knowledge				
MB1. I have information about X-rays.	0.803	1.237	13.614	0.697
MB2. I know when the radiation is first used in medicine.	0.677			
MB3. I have information about school levels of radiology education	0.631			
MB4. I was aware of the effects of radiation on human health when I preferred this profession.	0.612			
RGB. Radiation Security Knowledge				
RGB1. I think that the education that I will get is enough to work on my professional.	0.800	1.211	9.479	0.513
RGB2. I believe in my knowledge about protection from radiation and patient dose.	0.734			
RGB3. I don't have any information about the apparatus protecting from radiation.	0.519			

According to the factor loadings, the item " There may be some precaution to protect exposure to radiation (FB2) has the greatest loading (0.741) on factor *Physics Knowledge*. For the factor *Technical Device Knowledge*, it can be seen that the loading of the item "Koroner Angio devices work with radiation" (TCB1) is the greatest (0.661). for the factor *Professional Knowledge*, the item having the greatest factor loading

is "I have information about X rays" (MB1) with the loading 0.803 and for the last factor named as *Radiation Security Knowledge*, the factor loading of the item "I think that the education that I will get is enough to work on my professional" (RGB1) is the greatest among other loadings (0.800). The Eigenvalues and the Cronbach's alpha values of each factor is also given in Table 1.

Table 2. EFA Results and Cronbach's α values for Radiation protection scale

Factors/Items	Factor Loading	Eigen value	Explained Variance (%)	α
RKB. Radiation Protection Knowledge				
RKB1. There is a relation between Cancer and Radiation	0.742	1.211	50.683	0.675
RKB2. Radiation is harmful for the living beings.	0.776			
RKB3. Radiation has no side effect	0.560			
RKB4. Entering to radiation areas needs attention	0.749			

Table 2 indicates that the factor named Radiation Protection Knowledge, explains the 50.683% of total variance and the most important item on this factor is

"Radiation is harmful to the living beings" (RKB2) with the factor loading of 0.776. Besides the Cronbach's alpha value is calculated as 0.675.

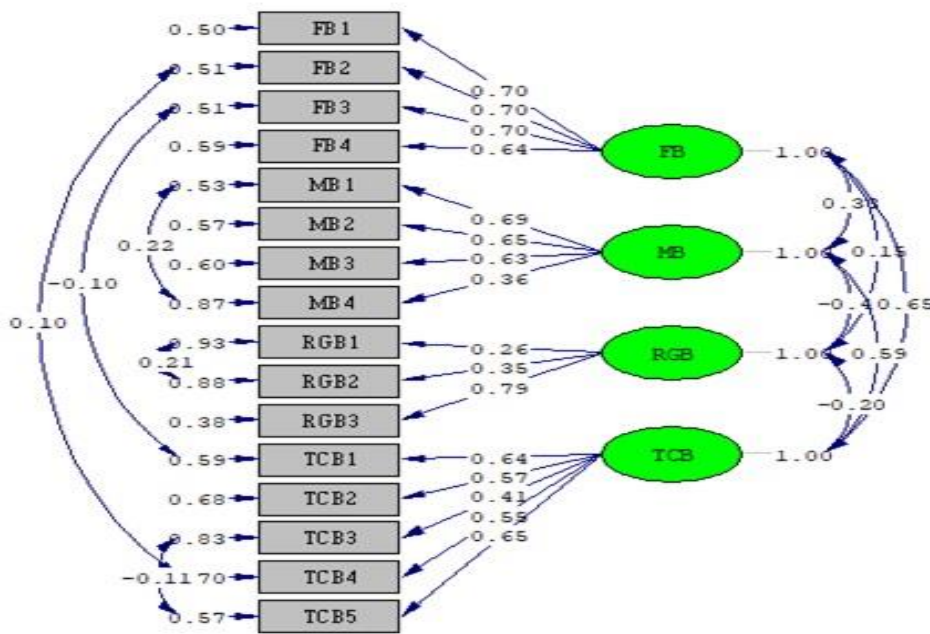
3.3. Confirmatory factor analysis results of radiation awareness scale

Results of Confirmatory Factor Analysis for the sub-factors (Physics Knowledge (FB), Technical Device Knowledge (TCB), Professional Knowledge (MB), and Radiation Security Knowledge (RGB)) of Radiation awareness Scale is given in Figure 1. As it can be seen from Figure 1. some modifications related to the suggestions of the software are applied by setting the error covariances between the variables free to obtain statistically the best and the most significant model.

According to model given in Figure 1. it can be seen that the most important items on Physics Knowledge (FB) are FB1 "Effected dose amount of human body decreases by moving away from the radiation source", FB2 "There may be some precautions to protect against exposure to radiation", and FB3 "The damage of radiation is related with the exposure time" with the coefficients of 0.70. Besides MB1, "I have information about X rays" found the most effective item on

Professional Knowledge (MB) with the coefficient of 0.69, TCB5, "Mamografy includes radiation" found the most effective item on Technical Device Knowledge (TCB) with the coefficient of 0.65 and RGB3, "I don't have any information about the apparatus protecting from radiation" found the most effective item on Radiation Security Knowledge (RGB) with the coefficient of 0.79.

Figure 1. also indicates that the highest correlation among all the latent variables (factors) is between FB and TCB with the coefficient of 0.65. While between FB and MB, FB and RGB and MB and TCB have positive correlations with the coefficients of 0.38, 0.15 and 0.59 respectively, there is a negative correlation between MB and RGB and RGB and TCB with the coefficients of -0.40 and -0.20 respectively. Goodness of fit statistics for the CFA is given in Figure 2. is also given in table 3. On the other hand, the $\chi^2/df=2.41$ is also one of the other indicators of acceptable model criteria.



Chi-Square=224.40, df=93, P-value=0.00000, RMSEA=0.049

Figure 1. CFA results of radiation awareness scale

3.4. SEM results for radiation awareness and radiation protection knowledge.

Results of SEM is given in Figure 2. For this model Alternative Study Hypotheses are generated as below.

- **H₁**: Radiation Protection Knowledge of the students increases as their Physics Knowledge increases.
- **H₂**: Radiation Protection Knowledge of the students increases as their Professional Knowledge increases.
- **H₃**: Radiation Protection Knowledge of the students increases as their Radiation Security Knowledge increases.
- **H₄**: Radiation Protection Knowledge of the students increases as their Technical Device Knowledge increases.

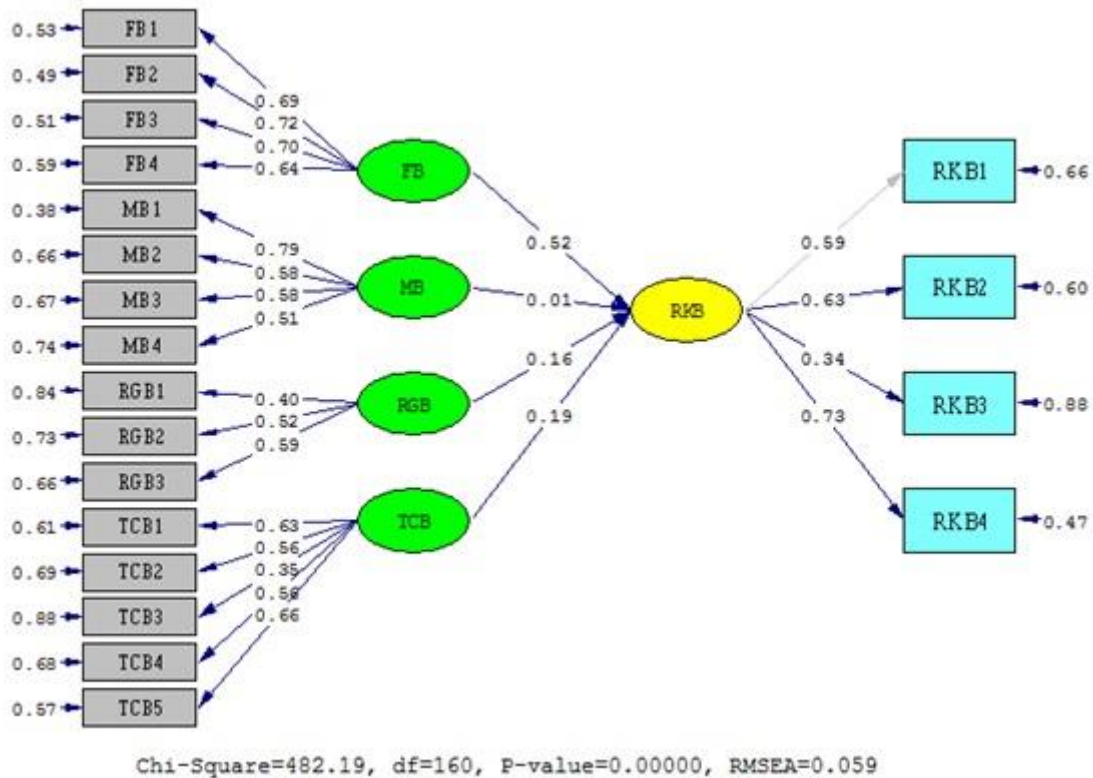


Figure 2. SEM results of radiation awareness and protection knowledge

Similar to the findings of CFA, Figure. 2. indicates that, on Physics Knowledge, FB2 "There may be some precautions to protect against exposure to radiation", on Professional Knowledge MB1, "I have information about X rays", on Radiation Security Knowledge RGB3, "I don't have any information about the apparatus protecting from radiation", on Technical Device Knowledge TCB5, "Mamografy includes radiation" and on Radiation Protection Knowledge, RKB4 "Entering to Radiation areas needs attention" found most effective items. The partial correlation coefficients between these items and factors can be seen in the Figure 2.

As a result of SEM, it can be said that if there will be one unit increase on the Physics Knowledge of students, there will be 0.52 unit increase on their

Radiation Protection Knowledge. Similarly, if there will be one unit increase on the Radiation Security Knowledge of students, there will be 0.16 unit increase on their Radiation Protection Knowledge and if there will be one unit increase on the Technical Device Knowledge of students, there will be 0.19 unit increase on their Radiation Protection Knowledge. As it can be seen from Figure 2, there is almost no effect of Professional Knowledge on these students Radiation Protection Knowledge. The correlation coefficient between these latent variables (factors) also statistically not significant. Goodness of fit statistics for the structural model given in Figure 2. is also given in Table 3. On the other hand, the $\chi^2/df=3.01$ is also one of the other indicators of acceptable model criteria.

Table 3. Limits and the results for CFA and SEM.

Fitness Criterion	Perfect Fitness	Acceptable Fitness	CFA	SEM
RMSEA	$0 < RMSEA < 0.05$	$0.05 \leq RMSEA < 0.10$	0.049	0.059
NFI	$0.95 \leq NFI \leq 1$	$0.90 < NFI < 0.95$	0.94	0.92
NNFI	$0.97 \leq NNFI \leq 1$	$0.95 \leq NNFI < 0.97$	0.96	0.94
CFI	$0.97 \leq CFI \leq 1$	$0.95 \leq CFI < 0.97$	0.97	0.95
SRMR	$0 \leq SRMR < 0.05$	$0.05 \leq SRMR < 0.10$	0.060	0.063
GFI	$0.95 \leq GFI \leq 1$	$0.90 \leq GFI < 0.95$	0.95	0.92
AGFI	$0.90 \leq AGFI \leq 1$	$0.85 \leq AGFI < 0.90$	0.93	0.90

Source: [8] (RMSEA: Root Mean Square Error of Approximation, NFI: Normed Fit Index, NNFI: Non-Normed Fit Index, CFI: Comparative Fit Index, SRMR: Standardized Root Mean Square Residual, GFI: Goodness of Fit Index, AGFI: Adjusted Goodness of Fit Index).

As it can be seen from Table 3; all criteria of the goodness of fit statistics obtained from CFA and SEM are within the acceptable and perfect fitness bounds. These results also confirm that the models given in Figure 1 and Figure 2 are statistically significant.

The results of the hypotheses testing related to the structural model given in Figure 2, standardized parameter estimates and *t* values are given in table 4.

Table 4. Standardized parameter estimates, *t* values and results of the hypotheses testing.

Hypotheses	Paths	Standardized parameter estimates	<i>t</i> values	Results
H ₁	(FB)→(RKB)	0.52	5.14	Confirmed
H ₂	(MB)→(RKB)	0.01	0.20	<i>Not Confirmed</i>
H ₃	(RGB)→(RKB)	0.16	2.04	Confirmed
H ₄	(TCB)→(RKB)	0.19	1.96	Confirmed

Table 4 shows that the paths, which also indicate the relations, from Physics Knowledge to Radiation Protection Knowledge, from Radiation Security Knowledge to Radiation Protection Knowledge and Technical Device Knowledge to Radiation Protection Knowledge are all statistically significant. Only the relation between Professional Knowledge and Radiation Protection Knowledge is statistically not significant.

3.5. Discussion

In this study, which is aimed to statistically model the effect of radiation awareness levels on radiation protection information, the results indicate that, within the four sub-factors of radiation awareness, three of them have a significant effect on radiation protection information. As well as the Physics Knowledge has the greatest effect, improving this knowledge via some extra seminars, theoretical and applied educations and should improve radiation protection information of these students. On the other hand, the same improvements in Radiation Security Knowledge and Technical Device Knowledge may also improve the radiation protection information. We believe that even if the results indicate that Professional Knowledge does not have statistically significant effect on radiation protection information, it has an indirect affect. Some improvements about this sub-factor may also improve the radiation protection information. As entering to radiation areas needs attention has a direct and significant effect on radiation protection information, importance of this situation must keep its priority and theoretical and applied educations must be in progress.

This research has also some limitations. First, even if the scale in the questionnaire is prepared with the help of earlier studies and the professionals on radiology, reliability of this scale may change according to different samples. However, this could be a first step in developing further research to test the causal

hypotheses on the various dimensions of university students' radiation protection knowledge. Upcoming studies should increase the reliability and importance of this study. Secondly, the data here are collected from the students at the specific date interval at the University. Even if the sample size is enough for this study, the results may differ for different samples.

4. Conclusion

It's a known fact that radiology experts are at some risk at their work because of the harmful effects of radiation. Considering this fact, awareness of radiation may have much positive effect on protection from radiation. This study emphasizes the importance of radiology awareness on protection from radiation for radiology experts. Related to the results of this study, radiation awareness of the radiology experts can be measured by Physics Knowledge, Technical Device Knowledge, Professional Knowledge and Radiation Security Knowledge. Within this awareness, Physics Knowledge has the greatest effect on Radiation Protection Knowledge. As a conclusion; importance of well-educated staff will affect obtaining both correct and well results and help to medical improvements in radiology. At that point; educational improvement about radiology may give better rollback on radiology.

Conflicts of interest

The authors declared no conflicts of interest.

Authorship Contributions

This study is a part of Olcay Ulucan's MS thesis supervised by Sinan Saraçlı at Afyon Kocatepe University Institute of Science.

References

- [1] ThePhysicsHypertextbook, Radiobiology.

Available at: <https://physics.info/radiobiology/>. Retrieved December 21, 2019.

- [2] Sont W.N., Zielinski J.M. and Ashmore J.P., First analysis of cancer incidence and occupational radiation exposure based on the National Dose Registry of Canada, *Am J Epidemiol.*, 153 (2001) 309–318.
- [3] Jacob K., Vivian G. and Steel J.R., X-ray Dose Training: Are We Exposed to Enough?, *Clinical Radiology.*, 59 (2004) 928-934.
- [4] Dourish P., Bellotti V., Awareness and Coordination in Shared Workspaces, CSCW '92 Proceedings of the 1992 ACM Conference on Computer-Supported Cooperative Work., (1992) 107-114
- [5] Rietveld T., Van Hout R., Statistical Techniques for the Study of Language and Language Behaviour, Berlin, New York: Mouton de Gruyter, (1993).
- [6] Lance C.E., Vandenberg R.J., Confirmatory factor analysis, In F. Drasgow & N. Schmitt (Eds.), The Jossey-Bass business & management series, Measuring and analyzing behavior in organizations: Advances in measurement and data analysis, *Jossey-Bass.*, (2002) 221–254.
- [7] Reisinger Y., Turner L., Structural equation modeling with LISREL: Application in tourism, *Tourism Management.*, 20 (1999) 71-88.
- [8] Schermelleh-Engel K., Moosbrugger H., Evaluating the Fit of Structural Equation Models: Tests of Significance and Descriptive Goodness-of-Fit Measures, *Methods of Psychological Research Online.*, 8 (2003) 23-74.



Estimation of organic matter dependent on different variables in drinking water network using artificial neural network and multiple regression methods

Sayiter YILDIZ^{1,*} , Can Bülent KARAKUŞ² 

¹Sivas Cumhuriyet University, Faculty of Engineering, Department of Environmental, Sivas/TURKEY

²Sivas Cumhuriyet University, Faculty of Architecture, Fine Arts and Design, Department of Urban And Regional Planning, Sivas/TURKEY

Abstract

The aim of this study is to estimate of organic matter values based on chlorine and turbidity values with the help of ANN and multiple regression (MR) methods. Three different models were done with ANN, and the statistical performance of these models was evaluated with statistical parameters like; μ , SE, σ , R^2 , RMSE and MAPE. The R^2 value of the selected best model was found to be quite high with 0.94. The relationship between the evaluation results of the ANN model and the empirical data ($R^2 = 0.92$) showed that the model was quite successful. In the MR analysis, R^2 was determined as 0.63, and a middling significant ($p < 0.05$) relationship was found. Since the calculated F value was greater than the tabulated F value, it was concluded that there is a clear relationship between dependent and independent variables. In addition, spatial distribution maps of chlorine, turbidity, organic matter values were created with the help of the GIS. With these maps, the estimated distribution of the measured parameters in the whole city network was accomplished. This study revealed that turbidity and chlorine parameters are related to organic matter value, and by establishing this relationship, organic matter can be estimated by ANN.

Article info

History:
Received: 15.03.2021
Accepted: 04.06.2021

Keywords:
Drinking water network,
Organic matter,
Artificial neural network,
Multiple regression methods.

1. Introduction

Water quality is a term describes the physical, chemical, and biological properties of water according to the suitability of water for a particular use. Water quality is influenced by natural and anthropogenic influences [1].

Natural organic matter is defined as a mixture of complex and diversified organic compounds resulted from natural processes occurring in the environment. Dead and live plants, animals, microorganisms, and their decomposition products can be precursors of natural organic matter [2]. Therefore, natural organic matter emerges as a result of contact between water present in the hydrological cycle and dead or living organic matter [3]. Natural organic matter in aquatic environments originates of both natural and human origin. However, the main source of natural organic matter is terrestrial vegetation and soils [4]. It is found widely in both surface and groundwater as a result of biological, geological, and hydrological interactions [5].

Organic matter in water is one of the most significant parameters affecting water quality. Organic substances found naturally in surface and underground water sources cause undesirable problems in many cases. The most important of these problems is that chlorine added to water for disinfection purposes creates trihalomethane (THM) compounds and other halogenated organic compounds as a result of the reaction with humic substances or other anthropogenic compounds in water [6, 7]. Since natural organic materials can cause problems with color and taste as well as forming disinfection by-products, the presence of natural organic matter in drinking water has attracted much interest in recent years [8].

Chlorine and chlorine compounds are the materials most commonly used in water treatment facilities. The most important feature of chlorine is that it has residual disinfection potential that prevents both the growth of microorganisms in drinking water networks and the entry of contaminants due to pipe breaks, maintenance of the network, negative pressure problems [9].

*Corresponding author. e-mail address: sayildiz@cumhuriyet.edu.tr.

The suspended particles or colloidal substances in the water cause turbidity that prevents the transmission of light in the water. Turbidity can be caused by organic or inorganic substances, or a combination of the two. Usually microorganisms (viruses, bacteria and protozoa) are added to the particles to remove turbidity by filtration, which greatly reduces the microbial pollution in the treated water [10].

Turbidity is a measure of the refractibility of light for water, and it has been used traditionally to indicate the quality of drinking water. Although microbiological contamination is usually joined by increased turbidity, other factors such as organic matter and silt also impact the turbidity levels in the water exiting the treatment plant [11]. Acceptable turbidity limits for water exiting from the treatment plant may vary between countries, but are generally less than 1 or 2 NTU [12]. However, to ensure the efficacy of disinfection, the turbidity must not be higher than NTU and Much less is preferred [10].

High levels of turbidity can stimulate bacterial growth by protecting microorganisms from the impacts of disinfection, which causes a great demand for chlorine. It is imperative to implement a comprehensive management strategy whereby multiple barriers are used in conjugation with disinfection to block or eliminate bacterial pollution, including water source protection and suitable treatment processes, in addition to protection during storage and distribution [10].

Water quality data are generally required to define the efficiency of water pollution control measures and the compliance level with determined standards of quality [13]. There is also a need for evaluating general water quality conditions and modeling water quality processes over a wide area. Therefore, water quality monitoring programs help to illuminate various processes that affect water quality and provide necessary information to water managers in decision-making [14].

In recent years, various studies have been carried out on water quality prediction models [15, 16]. However, traditional methods of data processing are no longer good enough to solve the trouble, as many factors that affect water quality have a complex nonlinear relationship [17]. On the other hand, ANN has been widely adopted for system identification, model definition, design optimization, and analysis, and

prediction, which can mimic the basic features of the human brain like self-adaptation, self-regulation, and fault tolerance [18, 19]. ANN networks can map the non-linear relationships that form the properties of aquatic ecosystems, and this distinguishes them from other statistical-based water quality models that suppose a linear relationship among response and prediction variables and their natural distribution [20]. In the last two decades, ANNs have made significant progress in practice in nearly all research areas [21-26].

In this study; Depending on the chlorine and turbidity amounts in the drinking water network of Sivas city, the amount of organic matter in the water was estimated by ANN and multiple regression (MR) methods. The predictability of this parameter, which is very important in terms of drinking water quality, depending on its varying values in different parts of the network was investigated. In addition, spatial distribution maps of chlorine, turbidity, organic matter measured in the drinking water network with the help of GIS and organic matter estimated by ANN were created. With these maps, the estimated distribution of the measured and predicted parameters in the whole city network was revealed. This study will contribute to different environmental studies where ANN, multiple regression analysis and spatial distribution maps will be evaluated together.

2. Materials and Methods

In this study, the results of turbidity, chlorine and organic matter analysis performed on samples taken from Sivas city drinking water distribution network by Sivas Municipality were used. The results of samples taken from 43 different points (Figure 1) that will represent the network starting from near the tank feeding the city network to the end point of the network were used in ANN and MR modeling. During the study, computer aided software program MATLAB R2013 was used for ANN calculations while Excel 2010 was utilized for regression analysis.

Using the IDW (Inverse Distance Weighted) interpolation method in the Spatial Analyst Module of the ArcGIS 10.2 software, spatial distribution maps were created for the measured turbidity, chlorine, organic matter values and the estimated organic matter values in the drinking water line in the study area.

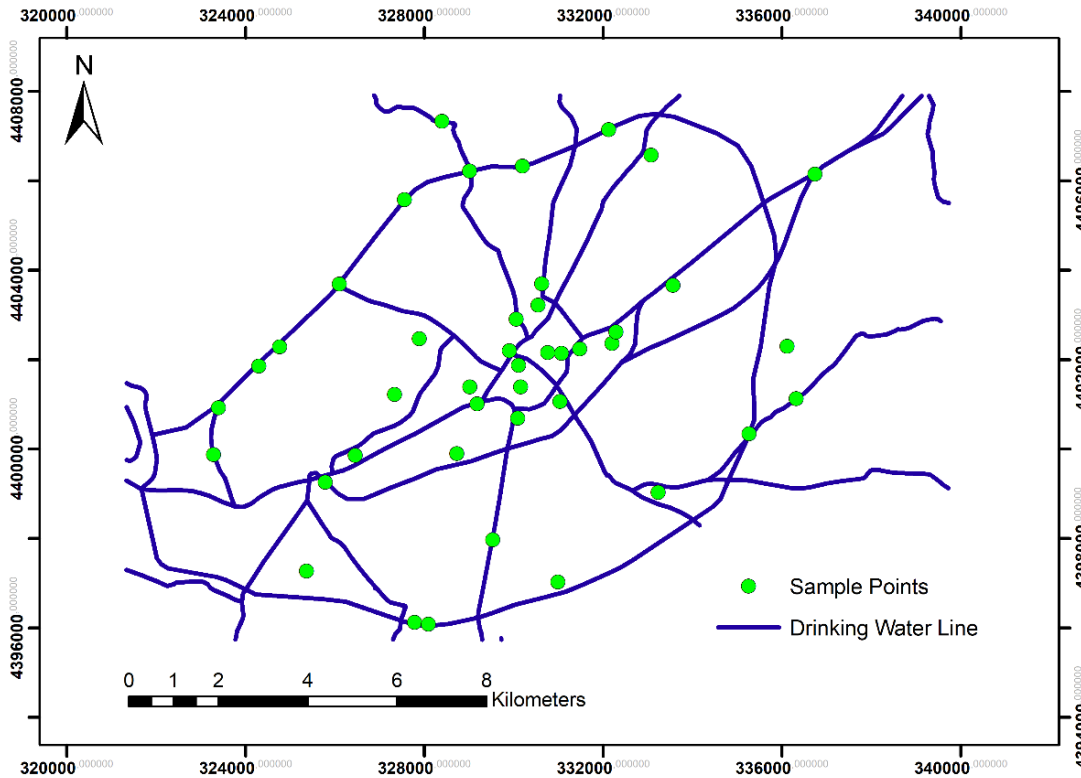


Figure 1. Sampled points on the network

2.1. Artificial Neural Network (ANN) Model

ANN was used to model the relationship between different data obtained by empirical methods and the estimation of a variable accordingly. In Figure 2, a simple ANN architecture was presented where the inputs are x_1, x_2, \dots, x_n and the weight coefficients of each input are $W_{k1}, W_{k2}, \dots, W_{kn}$. Here, x_n represents the input signals and W_{kn} represents the weight coefficients of these signals. The results from the thresholding function of the Y network are shown [25].

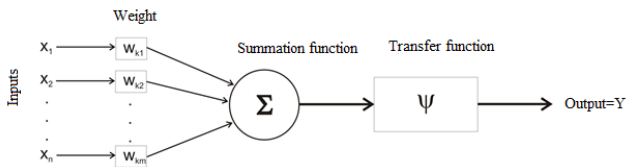


Figure 2. ANN cell model

The back propagation algorithm is a training algorithm and is widely used especially in engineering applications. The number of hidden layers in ANN can be augmented depending on nature of the problem [27]. The simple architecture of ANN's back propagation algorithm is given in Figure 3.

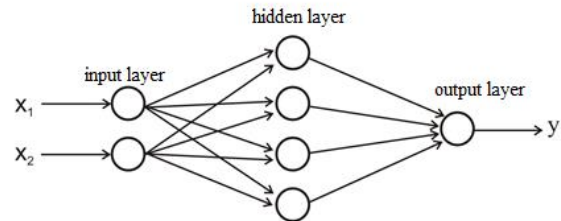


Figure 3. Simple architecture of ANN's back propagation algorithm

3. Results and Discussion

3.1. Organic matter estimation with ANN

The artificial neural network uses a modular neural network structure, which is a very strong computational technique, to model complex nonlinear relationships, especially when the relationship between variables is unknown in detail [28]. The basic structure of an ANN model generally consists of three various layers; The input layer, the hidden layer or layers and the output layer. The data is entered into the model and the weighted sum of the input is calculated in the input layer, The data is processed in the hidden layer or layers, while in the output layer the ANN results are produced. Each layer is made up of one or more fundamental components called a neuron or node [29].

The foundations of a neural network are the neurons that make up the hidden and output layers of the network (Fig.4).

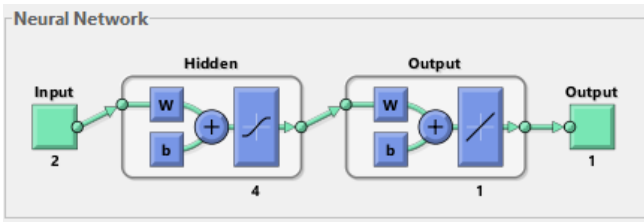


Figure 4. ANN structure

When designing an ANN, determining the number of neurons in the hidden layer is important. Too many hidden nodes can lead to over-compliance issues. Too few nodes in the hidden layer can cause non-compliance problems [30]. The number of hidden layers is chosen depending on the intricacy of the problem, yet one hidden layer is usually adequate to model most problems [31].

The training, validation and testing data of the ANN model that provides the best estimation are given in Figure 5. The statistical performance of the models was estimated depending on the statistical parameters μ , σ , R^2 .

In addition, RMSE and MAPE were used to evaluate the quality of models developed between the data estimated with ANN and the actual data [32]. RMSE is a measure of the quality of fit, and best describes the mean of the measurement error in predicting the dependent variable [33]. The statistical performance of the study is given in Table 1.

RMSE, MAPE and R2 are often used as a criterion to estimate network performance by comparing the error and measured data obtained from conjoint neural network studies [34]. RMSE and MAPE are calculated according to Equation 1-2.

$$RMSE = \sqrt{\frac{1}{n} \sum_{t=1}^n (t_i - z_i)^2} \tag{1}$$

$$MAPE = \frac{1}{n} \sum_{t=1}^n \frac{|(t_i - z_i)|}{z_i} \times 100 \tag{2}$$

Here; "t_i" and "z_i" are the estimated and actual outputs, while "n" represents the number of points in the data

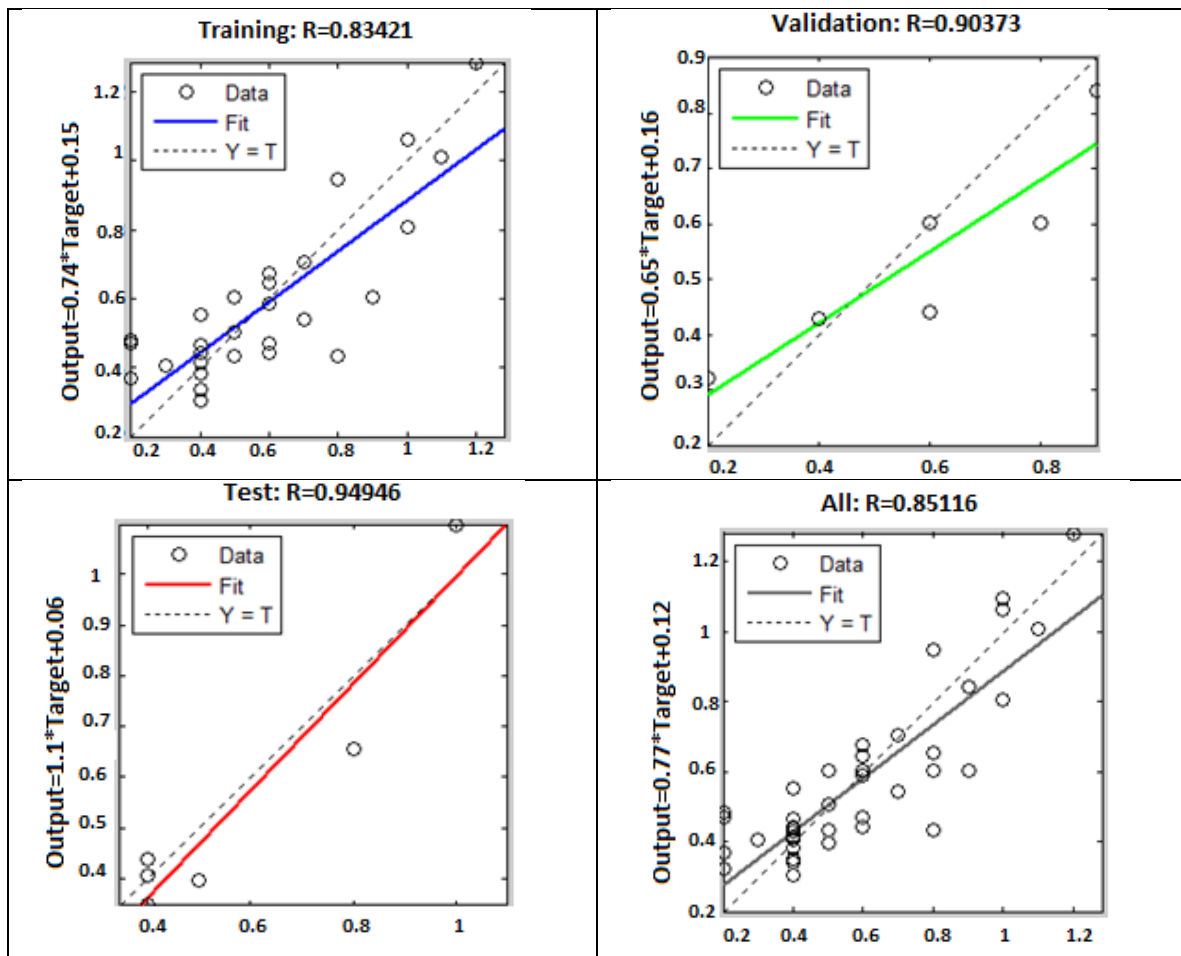


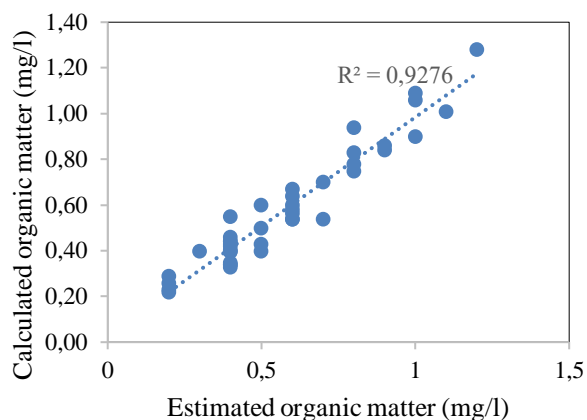
Figure 5. Training, validation and testing data obtained in ANN

Table 1. Statistical performance of ANN models

Model	Yapı	R ²	σ	SE	μ	RMSE	MAPE
I	2-2-1-1	0.82	0.22	0.10	1.01	0.61	19.42
II	2-3-1-1	0.90	0.14	0.07	0.96	0.62	13.10
III	2-4-1-1	0.92	0.13	0.06	0.99	0.62	11.61

As can be seen in Table 5, the results show that there is a considerable relationship between the values observed in the models created. However, the 2-4-1-1 model is seen as the best model in respect of R² and SE. RMSE values are very close to each other in all three models. The MAPE value is also an impartial statistic for measuring the predictive ability of a model. Low MAPE value indicates the best model performance [35].

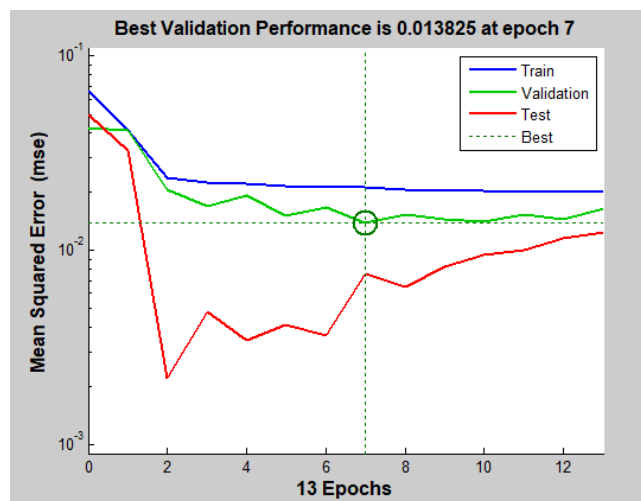
The relationship between the results of estimating the designed ANN model and the empirical data was arranged in order to assess the success of the ANN modeling used as an efficient tool. The diagram of the estimated organic matter values with ANN is shown in Figure 6.

**Figure 6.** Comparison of calculated and estimated organic matter results.

As seen in Figure 6, the estimated results and calculated data of the designed ANN model were compared, and it was found that they were in good harmony (R² 0.92).

ANN proved to be an efficient method for modeling organic materials with high R² values. The efficiency of the ANN model was settled based on maximizing R² and lowering the MSE value of the test set (1–13 neurons corresponding to the hidden layer). According to the graph of the lowest mean of squares error (MSE), and the number of epochs for the optimized ANN models (Fig.7), there was no significant change in the performance of the method after 7 stages. As seen in

Figure 6; the network was trained successfully with the algorithm of flexible back propagation.

**Figure 7.** Number of epochs for optimal ANN models according to MSE

3.2 Multiple regression analysis

The purpose of MR analysis is to define two or more independent variables at the same time to explain the variations of a dependent variable. In this study, turbidity and chlorine were accepted as independent variables, while organic matter was accepted as dependent variable. MR analysis was carried out to determine the relationship between organic matter and two independent variables. The studied statistical variables studied are given in Table 2.

Table 2. Statistical data of the variables

	Turbidity	Chlorine	Organic matter
Mean	0.57	0.29	0.57
Maximum	1.75	0.40	1.20
Minimum	0.30	0.15	0.20
Median	0.44	0.30	0.50
Variation	0.10	0.002	0.06
Standard Deviation	0.32	0.05	0.25
Skewness	2.23	-0.05	0.63
Kurtosis	4.68	0.19	-0.30

The approval of the model was made by considering the F test, t test and correlation coefficients. The statistical results of the model are given in Table 7. The importance of the R² value can be determined by means of the T-test, supposing that there is normal distribution of the variables and random selection of observations. The test compares the t value calculated using the null hypothesis to the tabulated t value. The

confidence level was chosen as 95% in this test, and the critical t value was obtained as ± 1.66. If the calculated t value is higher than the tabulated t value, the null hypothesis is inadmissible. This indicates R is important. If the calculated t value is lower than the tabulated t value, the null hypothesis is admissible. Thus, R is not important [24, 36]. Statistical results of the variables are given in Table 3.

Table 3. Statistical results

Independent Value	Dependent Value	R ²	Adjusted R ²	Unstandardized Coefficients	Standard Error	Calculated F value	Tabulated F value	Sign .
Turbidity	Organic matter	0.63	0.61	0.63	0.07	33.59	0.29	0.00
Chlorine				-0.20				
Independent Value	Calculated t		Tabulated t value		Sign .			
Turbidity	8.04		± 1.66		0.05			
Chlorine	-0.43				0.66			

As seen in Table 3, calculated t values are larger than tabulated t values. In this case, R is important. It was determined as R² = 0.63 and there is a middling significant (p<0.05) relationship. In addition, the calculated F value was higher than the tabulated F value. In this case, the null hypothesis is rejected. There is a real relationship between dependent and independent variables.

3.3. Spatial distribution maps

The Inverse Distance Weighted (IDW) Interpolation Method was used while creating spatial distribution maps of chlorine, turbidity, organic matter measured from the network and organic matter estimated by ANN.

Inverse Distance Weighted (IDW) Interpolation Method

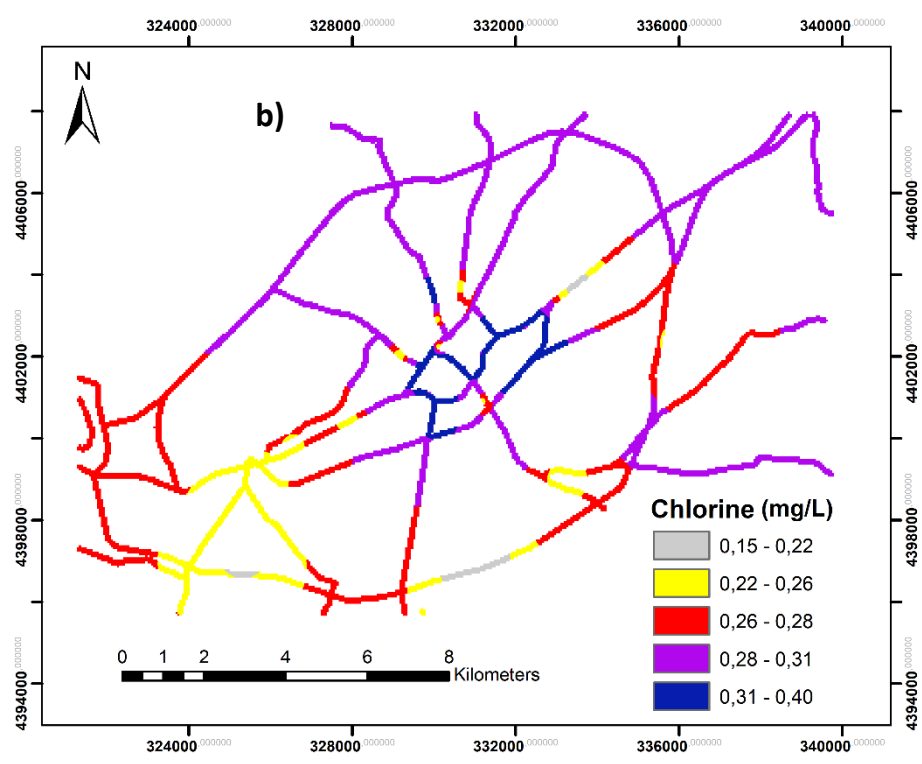
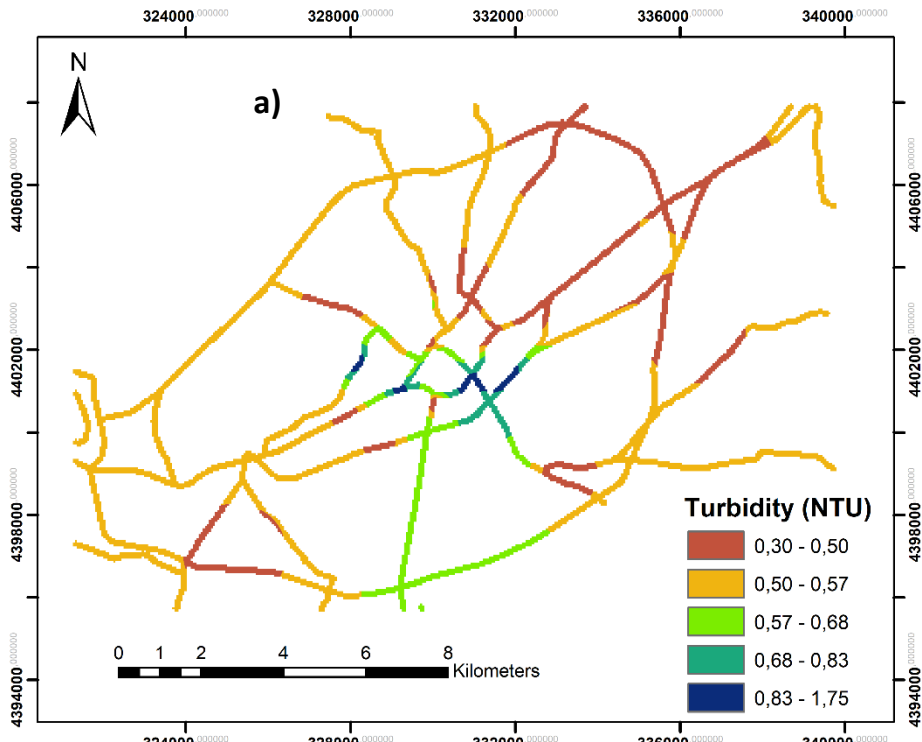
This method is an interpolation method that predicts values of cell by means of average values of sample data points in the vicinity of each cell. The sample points closest to the cell are given a high weight value. The further away from the estimation location, the effects of the points decrease. If any point is located in an area that is quite different from the estimation location, it may not be appropriate to consider a very distant point in this method. This problem can be solved provided that a sufficient number of points is taken into account and a surface is created for small areas. The number of points varies depending on the amount, distribution, and surface character of the

sample points [37]. The basis of this method is the calculation of distances from the desired point to data points, and the linear weighting of the effect of data points on the value at the desired point using an inverse function [38].

$$Z(X_0) = \frac{\sum_{i=1}^n Z(X_i) \cdot d_{i0}^{-r}}{\sum_{i=1}^n d_{i0}^{-r}} \tag{3}$$

Here; X₀ is the position where the predictions are made, and this position is a function of adjacent measurements, n [Z (X_i) and i = 1, 2, ..., n]. r is the exponential number determining the assigned weight of each observation, and d is the distance between the observation position (X_i) and the estimated position (X₀).

The larger the exponent, the smaller the assigned weight of observations at a given distance from the estimation location. The increase in exponents shows that the estimations are very similar to the closest observations [39]. Spatial distribution maps created for each parameter are given in Figure 8.



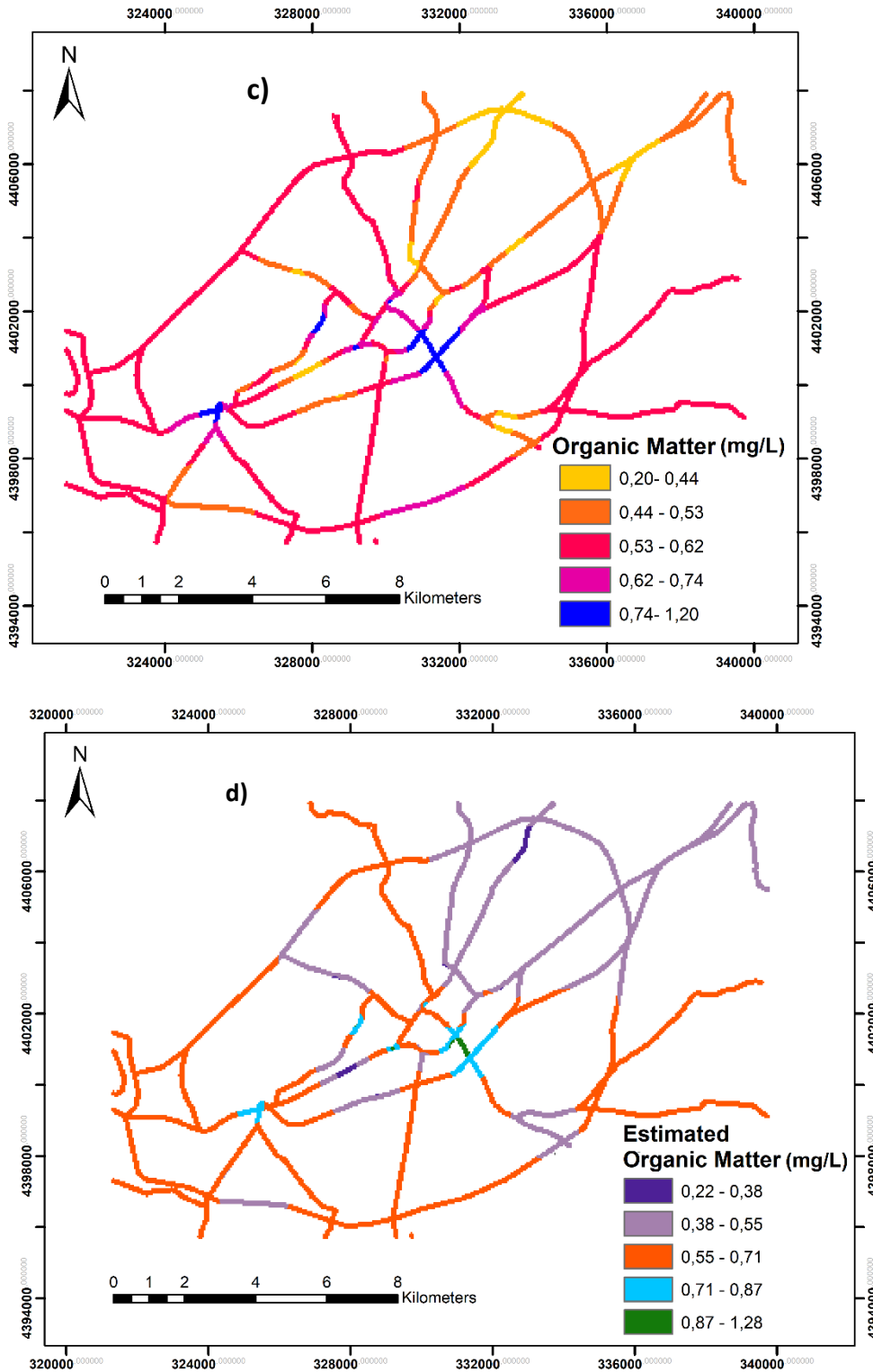


Figure 8. Spatial distribution maps for turbidity (a), chlorine (b), measured organic matter (c), estimated organic matter (d)

The measured turbidity values in the drinking water network vary between 0.30-1.75 NTU. The lowest values of turbidity in the drinking water network were observed in the north-east parts of the network, while the greatest values were seen in the middle parts of the network (Figure 8a). It was observed that chlorine and organic matter values were high in the middle parts of the city network (Figures 8b, 8c). When a general

evaluation is made in terms of measured and estimated organic matter in the city network; The measured and estimated organic matter amounts were approximately close to each other, and the max and min values of these amounts were observed in similar parts of the network (Figures 8c, 8d).

4. Conclusions

In this study, organic matter values were estimated by ANN and MR depending on the chlorine and turbidity measured in the drinking water network. Three different modelling were conducted with ANN, and the statistical performance of the models was evaluated with μ , SE, σ , R^2 , RMSE and MAPE parameters. The R^2 value of the graph of the empirical data and of the estimation results of the ANN model was 0.92 and showed that the model was quite successful. In the MR analysis, R^2 was determined as 0.63, and a middling significant ($p < 0.05$) relationship was found. Since the

calculated F value is higher than the tabulated F one, it is inferred that there is an actual relationship between dependent and independent variables. In addition, the estimated distributions of the measured parameters at 43 points representing the whole network gave an important prediction about the water quality in the network. In this study, it was revealed that the turbidity and chlorine parameters are related to the organic matter value and that the organic matter can be estimated by ANN by establishing this relationship.

Conflicts of interest

The author states no conflict of interests.

References

- [1] Khalil B., Ouarda T.B.M.J., St-Hilaire A., Estimation of water quality characteristics at ungauged sites using artificial neural networks and canonical correlation analysis, *Journal of Hydrology*, 405 (2011) 277–287.
- [2] Chow C.W.K., Van Leeuwen J.A., Drikas M., Fabris R., Spark K.M., Page D.W., The impact of the character of natural organic matter in conventional treatment with alum, *Water Science and Tech.*, 40(9) (1999) 97–104.
- [3] Bridgeman J., Bierzoza M., Baker A., The application of fluorescence spectroscopy to organic matter characterisation in drinking water treatment, *Reviews in Environmental Science and Bio/Tech.*, 10(3) (2011) 277–290.
- [4] Matilainen A., Removal of the natural organic matter in the different stage of the drinking water treatment process, Thesis for the degree of PD, University of technology, (2007).
- [5] Sillanpää M., Ncibi M.C. Matilainen A., Vepsäläinen M., Removal of natural organic matter in drinking water treatment by coagulation: a comprehensive review, *Chemosphere*, 190 (2018) 54-71.
- [6] Fallahizadeh S., Neamati B., Fadaei A., Mengelizadeh N., Removal of Natural Organic Matter (NOM), Turbidity, and Color of surface water by integration of enhanced coagulation process and direct filtration, *Journal of Advances in Environmental Health Res.*, 5(2) (2017) 108-113.
- [7] Gümüş D., Akbal F., Removal of Natural Organic Matter In Drinking Waters And Prevention Of Trihalomethanes Formation, *Sigma: Journal of Engineering & Natural Sci.*, 31(4) (2013).
- [8] Trinh T.K., Kang L.S., Response surface methodological approach to optimize the coagulation-flocculation process in drinking water treatment, *Chem. Eng. Res. Des.*, 89(7) (2011) 1126-1135.
- [9] Ramos H. M., Loureiro D., Lopes A., Fernandes C., Covas D., Reis L.F., Cunha M.C., Evaluation of chlorine decay in drinking water systems for different flow conditions: from theory to practice, *Water Resources Managment*, 24(4) (2010) 815-834.
- [10] WHO, Guidelines for drinking water quality: training pack, 4nd ed. Geneva Switzerland, (2017) 564.
- [11] Mann A.G., Tam C.C., Higgins C.D., Rodrigues L.C., The association between drinking water turbidity and gastrointestinal illness: a systematic review, *BMC Public Health.*, 7(1) (2007) 256.
- [12] Rouse R., New Drinking Water Regulations in the UK. London, Drinking Water Inspectorate, (2001).
- [13] Whitfield P., Goals and data collection designs for water quality monitoring, *Water Resour. Bull.*, 24 (4) (1988) 775–780.
- [14] Khalil B., Ouarda T.B.M.J., Statistical approaches used to assess and redesign surface water quality monitoring networks, *J. Environ. Monit.*, 11 (2009) 1915–1929.
- [15] Chen J.C., Chang N.B. Shieh W.K., Assessing wastewater reclamation potential by neural network model, *Eng. Appl. Artif. Intell.*, 16 (2003) 149–157.
- [16] Li R.Z., Advanced and trend analysis of theoretical methodology for water quality

- forecast, *J. Hefei Univ. Technol.*, 29 (2006) 26–30.
- [17] Xiang S.L., Liu Z.M., Ma L.P., Study of multivariate linear regression analysis model for ground water quality prediction, *Guizhou Sci.*, 24 (2006) 60–62.
- [18] Niu Z.G., Zhang H.W., Liu H.B., Application of neural network to prediction of coastal water quality, *J. Tianjin Polytechnic Univ.*, 25 (2006) 89–92.
- [19] Shu J., Using neural network model to predict water quality, *North Environ.*, 31 (2006) 44–46.
- [20] Lek S., Delacoste M., Baran P., Dimopoulos I., Lauga J., Aulagnier S., Application of neural networks to modelling nonlinear relationships in ecology, *Ecol. Model.*, 90 (1996) 39–52.
- [21] Chu W.C., Bose N.K., Speech signal prediction using feedforward neural network, *Electro. Lett.*, 34 (1998) 999–1001.
- [22] Messikh N., Samar M.H., Messikh L., Neural network analysis of liquid–liquid extraction of phenol from wastewater using TBP solvent, *Desalination.*, 208 (2007) 42–48.
- [23] Hanbay D., Turkoglu I., Demir Y., Prediction of wastewater treatment plant performance based on wavelet packet decomposition and neural networks, *Expert Syst. Appl.*, 34 (2008) 1038–1043.
- [24] Yıldız S., Değirmenci M., Estimation of oxygen exchange during treatment sludge composting through multiple regression and artificial neural networks, *International J. of Environmental Res.*, 9(4), (2015) 1173–1182.
- [25] Yıldız S., Artificial neural network (ANN) approach for modeling Zn (II) adsorption in batch process, *Korean J. of Chemical Eng.*, 34(9) (2017) 2423-2434.
- [26] Yıldız S., Artificial neural network (ANN) approach For modeling of Ni(II) adsorption from aqueous solution by peanut shell, *Ecol. Chem. Eng. S.*, 25(4) (2018) 581-604.
- [27] Demuth H., Beale M., Neural network toolbox for use with MATLAB, The MathWorks Inc. Natick, (2001) 840.
- [28] Smith M., Neural Networks for Statistical Modelling, Van Nostrand Reinhold, NY., (1994) 235.
- [29] Dreyfus G., Martinez J.M., Samuelides M., Gordon M.B., Badran F., Thiria S., Herault, Drinking Water and Health, Vol. 2., National Academy of Sciences, Washington, DC., (1980).
- [30] Shu C., Ouarda T.B.M.J., Flood frequency analysis at ungauged sites using artificial neural networks in canonical correlation analysis physiographic space, *Water Resour. Res.*, 43 (2007).
- [31] Rezvan K., Fakhri Y., Mehrorang G., Kheibar D., Back propagation artificial neural network and central composite design modeling of operational parameter impact for sunset yellow and azur (II) adsorption onto MWCNT and MWCNT-Pd-NPs: Isotherm and kinetic study, *Chemometrics and Intelligent Laboratory Systems.*, 159 (2016) 127–137.
- [32] Nabavi-Pelesaraei A., Kouchaki-Penchah H., Amid S., Modeling and optimization of CO₂ emissions for tangerine production using artificial neural networks and data envelopment analysis, *International Journal of Biosci.*, 4(7) (2014) 148–158.
- [33] Singh K.P., Basant A., Malik A., Jain G., Artificial neural network modeling of the river water quality-a case study, *Ecological Model.*, 220(6) (2009) 888-895.
- [34] Alves E.M., Rodrigues R.J., Dos Santos Corrêa C., Fidemann T., Rocha J.C., Buzzo J.L.L., et al., Use of ultraviolet–visible spectrophotometry associated with artificial neural networks as an alternative for determining the water quality index, *Env. Monit. and Assess.*, 190(6) (2018) 319.
- [35] Olyaie E., Banejad H., Chau K.W., Melesse A.M., A comparison of various artificial intelligence approaches performance for estimating suspended sediment load of river systems: A case study in United States, *Env. Monit. and Assess.*, 187(4) (2015) 189.
- [36] Yıldız S., Karakuş C.B., Estimation of irrigation water quality index with development of an optimum model: a case study, *Environment, Development and Sustain.*, 22 (2020) 4771–4786.
- [37] Esri., Desktop spatial analysis for ArcGIS, Esri Information Systems Engineering and Education Ltd. Sti. 1st Edition, Ankara, (2014).
- [38] Loyd C.D., Local Models for Spatial Analysis, 2nd ed. ISBN 9780367864934, Temple University, Philadelphia, PA, USA., (2010) 98.

- [39] Aksu H.H., Hepdeniz K., Mapping with the aid of Geographic Information System and analysis of annual and monthly average maximum air temperature distribution in Burdur. *Mehmet Akif Ersoy University Journal of the Graduate School of Natural and Applied Sci.*, 7 (2016) 202-214.



Optimization of operational parameters at laboratory scale membrane bioreactor for treatment of high-strength opium alkaloid wastewater: The effect of pretreatment

İpek ÇELEN-ERDEM^{1,*} , Gülsüm Melike ÜRPER-BAYRAM^{2,3} , Derya Y. KÖSEOĞLU-İMER² , İsmail KOYUNCU^{2,3} , İzzet ÖZTÜRK²

¹Environment and Cleaner Production Institute TUBITAK Marmara Research Center Kocaeli / TURKEY

²Istanbul Technical University, Civil Engineering Faculty, Department of Environmental Engineering, Istanbul Technical University Istanbul, 34469, TURKEY

³Istanbul Technical University, National Research Center on Membrane Technologies, Istanbul, 34469, TURKEY

Abstract

Two different membrane treatment scenarios have been applied for treatment of the high strength dark color alkaloid industry wastewater. A membrane bioreactor (MBR) system having separately UF and MF membranes was operated with raw alkaloid wastewater treatment (scenario-A) and anaerobically pre-treated alkaloid wastewater (scenario-B). NF 270, NF 90 and RO (XLE) membranes were used as a polish-ing step at two different recovery ratios of 50% and 75% for both scenarios. In scenario-A, the COD re-moval efficiencies for MBR-MF and MBR-UF were found as 86±9% and 55±24%, respectively. At the polishing step, RO performance after scenario-A indicated that the 99.6% COD and complete color remov-al was achieved. On the other hand, in the scenario-B, the COD removal efficiencies for MBR-MF and MBR-UF were found as 41±16.4% and 24±18.3%, respectively. RO experiments with raw wastewater indi-cated that the 99.6% COD and complete color removal were achieved. The most crucial problem during direct MBR operation was found as a foaming problem and prevented by anti-foaming agent which caused an increase in effluent COD concentration and chemical cost. For these reasons, it can be concluded that MBR operation with anaerobically pre-treated was more effective than the other scenario.

Article info

History:

Received: 05.10.2020

Accepted: 08.04.2021

Keywords:

Alkaloid wastewater, Pretreatment, Membrane technologies, Membrane bioreactor, Treatment process.

1. Introduction

The opiate is a chemical naturally existing in the opium poppy plant, and it is consumed on a big scale by medical sectors and scientific areas. The significant alkaloids are classified as morphine, codeine, thebaine, narcotine, and papaverine [1]. During the production process, the poppy capsules are ground and treated with lime, and the slurry is pressed to extract the liquid that contains the alkaloids. The liquid's pH is adjusted by adding Na₂CO₃ and a filtration process separates the impurities. In the extraction process, the alkaloids are extracted with specific solvents such as toluene and butanol. The morphine is crystallized by adding NH₄OH and separated from the solution by centrifuges. The used solvents and the water are sent to the distillation column to recover toluene, alcohol groups and the remaining wastewater treated in wastewater treatment plant [2]. The opium is cultivated and processed in a few countries such as India,

Australia, France, Hungary, Spain, Ukraine, Yugoslavia, and Turkey [3]. However, a limited number of researchers have worked on the treatment of alkaloid wastewater until now. Biological and physicochemical treatment studies on the effluent of opium wastewater treatment plant were performed by Kınlı [4], and chemical oxygen demand (COD) removal efficiency reached 70% in anaerobic treatment process. Also, ozone oxidation was used as the pretreatment technology of the aerobically treated effluents, and the color and COD removal efficiencies of the process were found at 87% and 30%, respectively. Ozturk et al. [5] also investigated the anaerobic treatment for composite wastewater generated from the process water (extracting from distillation column section) and domestic wastewater of an alkaloid industry. In this study, a full scale Anaerobic Internal Cycling (AIC) reactor was operated with an organic loading rate (OLR) of 5 kg

*Corresponding author. e-mail address: i_celen@yahoo.com

COD/m³.day. COD and VFA removal efficiencies were found as 85 and 95%, respectively. The biogas production rate was obtained as 0,1-0,35 m³ CH₄/COD_{removed}. The main operational parameters stated in the study were very high salinity and sulphate concentration in composite wastewater. Sakar et al. [6] operated an electro dialysis (EC) process for sulphate removal from the concentrate stream at nanofiltration (NF) membrane process of alkaloid wastewater. They concluded that 99% of sulfate concentration was retained by membrane and found in concentrate streams of NF90 and NF245 membranes.

Aytimur and Atalay [7] worked on reducing the organic matter in Alkaloid Industry raw wastewater and operated a conventional activated sludge system for biological treatment with 88% COD removal and also the catalytic wet air oxidation (WAO) process for extra chemical oxidation with the COD removal efficiency of 35%. They concluded that combining these processes is not very effective, and the biological treatment was sufficient for reaching high COD removal efficiency as a single process. Similarly, Kacar et al. [8] investigated the pretreatment of the alkaloid processing wastewater in Turkey by WAO followed by the pressure and temperature on COD removal. The catalyst types in the experiments were Cu(NO₃)₂, Co(NO₃)₂, Ni(NO₃)₂, FeCl₂. They reported that above 26% of COD removal efficiency was obtained in 2 h of operating time at 150 °C, 0.65 MPa, and an airflow rate of 1.57 x 10⁻⁵ m³s⁻¹. Bural et al. [9] investigated the effect of gamma irradiation as pretreatment step on aerobic biological treatment of opium alkaloid wastewater. Two sequencing batch reactors (SBRs) were used as a biological treatment setup in the experiments, one of the reactors was fed with raw wastewater without any irradiation, and the other one was operated with irradiation of 40 kGy at the same raw wastewater. The reactors were gradually fed with increasing COD concentrations because of biomass acclimatization to opium alkaloid wastewater. At the operation with 5000 mg/L COD concentration, the COD removal efficiencies were 79% and 73% for reactors fed with raw and irradiated wastewater, respectively.

Another anaerobic treatment study of alkaloid processing wastewater was presented by Aydin et al. [10]. The treatment study was conducted at an 11.5 L lab-scale UASB (Upflow Anaerobic Sludge Bed) reactor for 825 days under different hydraulic retention times (HRTs) (0.84-1.62 days) and organic loading rates (OLRs) (3.4-12.25 kg COD/m³day) at 35±2 °C. The COD removal efficiency slightly decreased with the increase of OLR and decreasing HRT. However, the UASB reactor was operated at high COD removal

efficiency varying between 74-88%. They also identified some toxic organic chemicals such as N, N-dimethylaniline, and toluene in the opium wastewaters. These compounds are known to be inhibitory for biological treatment processes. Dereli et al. [11] applied Anaerobic Digestion Model No. 1 (ADM1), developed by the IWA (International Water Association) Task group for Mathematical Modeling on Anaerobic Digestion, for the data obtained by Aydin et al. [10]. The validation results indicated that the calibrated ADM1 could predict the experimental results of effluent COD and pH with reasonable accuracy, whereas some discrepancies were observed for methane gas productions. Cengiz et al [1] worked on the hydrothermal gasification of opium alkaloid wastewater and found 95% COD removal efficiency at 600 °C in the presence of a catalyst at an amount of 0.375–0.625 g. Koyuncu [12] carried out membrane treatability studies, and Koyuncu et al. [13] carried out the membrane process and ozonation experiments on the opium alkaloid industry. Lab-scale membrane and ozonation reactors were performed in the experiments. Low-pressure reverse osmosis membranes were used to remove COD, color, and conductivity from biologically pretreated opium alkaloid industry effluents. The influent COD, color, and conductivity were measured as 1900 mg/L, 1750 Pt-Co, and 3500 µS/cm. The removal efficiency of COD, color, and conductivity were found greater than %99. Moreover, they experienced 41% of COD treatment efficiency with ozonation applied in biologically treated opium alkaloid wastewater in 50 min. The dark-red brownish color of wastewater turned to light yellow after 50 min. of ozonation with 96% of color removal efficiency. Gencsoy [14] investigated the anaerobic treatment of the opium alkaloid industry. A laboratory scale UASBR was operated at different organic loading rates varying from 3.75 to 10 kg COD/ m³-day at mesophilic conditions. It was found that anaerobic treatment's COD removal efficiency reached 87% at UASBR for 5 kg COD/m³-day organic loading rate. Besides, the ratio of CH₄ content in produced biogas was measured as 72%. From all literature studies, it is concluded that the anaerobic pre-treatment is a very feasible process to upgrade the existing full-scale activated sludge system for the industry.

This study aims to apply two different scenarios to treat the opium alkaloid processing industrial wastewater. The first scenario was the direct application of membrane bioreactor (MBR) for raw alkaloid wastewater treatment without any pretreatment process. At the second scenario, the MBR system was operated after anaerobically pretreated alkaloid wastewater. The polishing step was applied for both

scenarios using NF and RO membranes. The study's primary purpose is to investigate the effect and importance of the anaerobic pretreatment of high-strength opium alkaloid wastewater before the application of membrane technologies and to compare the results of two scenarios. Opium alkaloid wastewater is very complex wastewater and has high pollutant concentrations. For this reason, different membrane treatment scenarios were proposed in this study to solve this significant industrial wastewater pollution problem. The study's novelty is to evaluate the different operating scenarios with and without

pretreatment and build an optimum and sustainable treatment process flow-chart.

2. Material and Methods

2.1. Wastewater characteristics

The raw wastewater was taken from the opium alkaloid processing plant which located in Afyon Province in Turkey. The characteristics of raw wastewater and the discharge standards of receiving environment at the effluent stream of the wastewater treatment plant are shown in Table 1. All analyses were carried out according to Standard Methods [15].

Table 1. Characteristics of wastewater streams used in the experimental runs

Parameters	Properties of raw wastewater	Discharge standards ^a
pH	4.7±0.6	6-12
Biochemical Oxygen Demand (BOD) (mg/L)	10151±3908	-
Chemical Oxygen Demand (COD) (mg/L) (as soluble)	32995.±8811	-
Total Suspended Solid (SS) (mg/L)	427.5±235	-
Volatile Suspended Solids (VSS) (mg/L)	426±217.5	-
Total Dissolved Solids (TDS) (mg/L)	41133±6559	500
Inorganic TDS (mg/L)	15910±8584	-
Conductivity (µs/cm)	29750±10111	-
Volatile fatty acids (VFA) (mg/L)	5806±1773	-
Total Kjeldahl Nitrogen (TKN) (mg/L)	561±71	15
Ammonium Nitrogen (NH ₄ -N) (mg/L)	22±5.6	-
SO ₄ ²⁻ (mg/L)	11656±4087	1700
Total Phosphorus (TP) (mg/L)	23.8±6.7	-
Alkalinity (mg/L CaCO ₃)	4504±1866	-
Color (Pt-Co)	2500	-
Particle size, µm	13.18	-

^a Water Pollution Control Regulations of Turkey

2.2. Properties of membranes

Nanofiltration (NF) and reverse osmosis (RO) membranes were provided by Dow/Filmtec and the

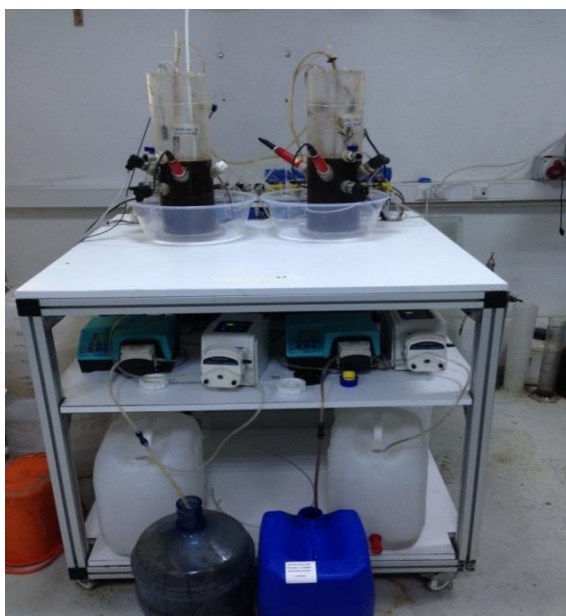
microfiltration membrane (MF) was purchased from Microdyn Nadir. Table 2 provides some information of the membranes given by the manufacturers.

Table 2. The technical characteristics of used membranes

Membrane	Manufacturer	Molecular weight cut-off, (Da) / Pore size (μm)	Material	Flux ($\text{L}/\text{m}^2\cdot\text{h}$)
MP 005	Microdyn Nadir	-/0.05	Polyethersulfone	> 200
NF 270	Dow	~200-400/-	Polyamide	42-58
NF 90	Dow	~200-400/-	Polyamide	27-35
XLE	Dow	~100 /-	Polyamide	19-24

2.3. Experimental set-up

This study examined the treatment of high-strength dark color opium alkaloid processing industry wastewater and anaerobically pretreated opium alkaloid wastewater effluent with membrane technology. In the experimental system, two parallel laboratory scale membrane bioreactors (MBR) with and without anaerobic pretreatment were used and the volume of each cylindrical MBR was 6 L with height and internal diameter of 35 cm and 14 cm, respectively (Fig. 1). MBR was established with microfiltration (MF) and ultrafiltration (UF) membrane modules at submerged mode in the bioreactor in series operation. Monitoring parameters were determined as pH, ORP (Oxidation Reduction Potential), temperature, and dissolved oxygen and were controlled with an online system. Before the treatment, the activated sludge was taken from the return sludge line at the leachate wastewater treatment plant and it was used for inoculation medium.

**Figure 1.** Laboratory scale MBR system

A flow chart of the membrane treatment scenarios is shown in Fig. 2. In the first scenario (Scenario-A) the raw wastewater (Fig 2a) was directly fed to the MBR system and the system was operated at different membrane types (MF and UF, named as Scenario-A1 and Scenario-A2). The MBRs were first operated at step-fed mode with gradually increasing ratios (raw wastewater volume/total volume) in order to acclimatize the biomass to opium alkaloid raw wastewater. After acclimation, the raw wastewater fed to parallel MBR-MF systems for Scenario-A1 and after reaching steady state conditions, UF modules were installed other MBR systems for Scenario-A2. Both MBR systems were tested at the same operating conditions. The effluent streams of MBR-MF and MBR-UF operations were simultaneously filtrated from NF and RO membranes at different recovery ratios for the polishing step. A 300-mL of stirred cell (Sterlitech HP4750, USA) was used for RO and NF filtration. The membrane diameter was 0.049 m and the effective membrane area was $1.46 \times 10^{-3} \text{ m}^2$. The maximum operating pressure for this cell was $69 \times 10^5 \text{ Pa}$.

In the second scenario (Scenario-B), the raw wastewater was first exposed to anaerobic pretreatment and then MBRs having MF and UF were used for second step biological treatment Scenario-B1 and Scenario-B2, respectively (as seen from Fig 2b). In the last scenario, (Scenario-B3) the anaerobic pretreated wastewater was directly filtrated from the UF membrane. For all the treatment strategies, similar to Scenario-A NF and RO membrane operations were used as a polishing treatment step.

Table 3. The properties of the anaerobic digester effluent

Parameters	Value
pH	8.2
Soluble chemical oxygen demand (COD) (mg/L)	2027±6 83
Suspended Solid (SS) (mg/L)	15900
Color (PtCo)	3887
Particle size, µm	0.032

At the anaerobic treatment phase, a laboratory scale anaerobic digester (W8) was used and the system consists two separate reactors (Armfield Ltd, UK). Anaerobic treatment experiments were carried out over a nine-month period. The details of this experiment were published by Çelen-Erdem et al. [16]. The effluent stream of reactor was fed to both MBR systems. The characteristics of the anaerobic digester effluent are shown in Table 3.

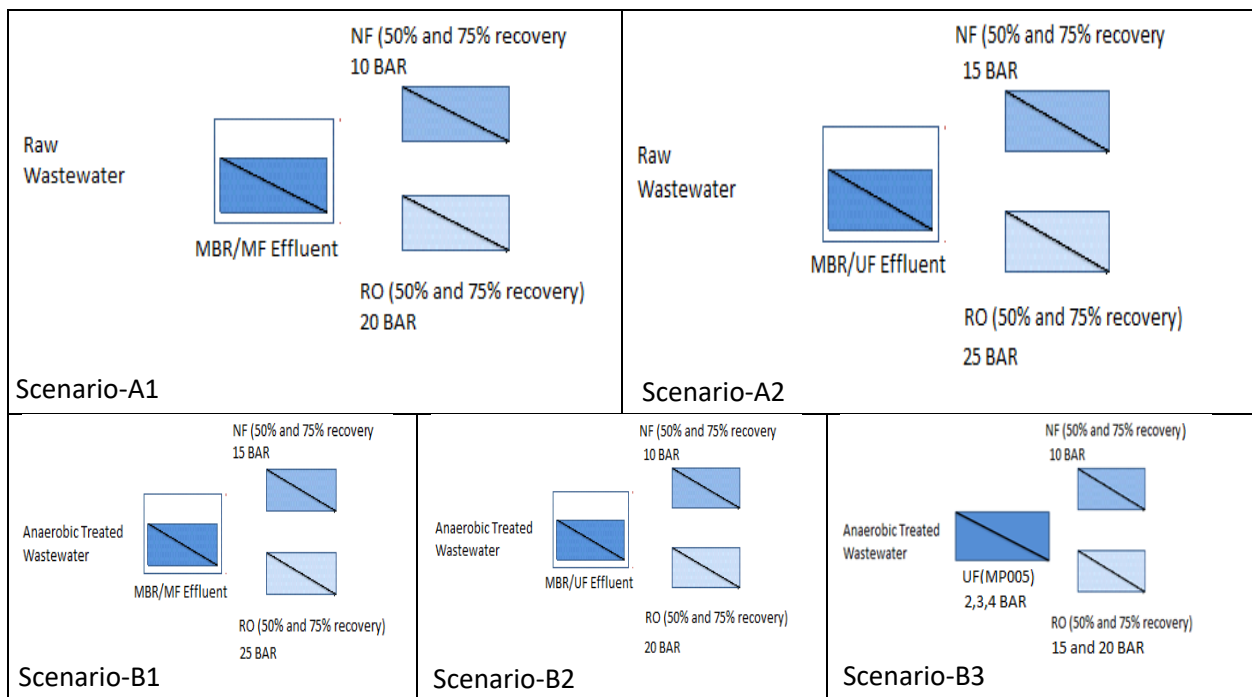


Figure 2. Membrane treatment strategies applied in experimental runs (a) Raw wastewater (b) Anaerobically pretreated wastewater

3. Results and Discussion

3.1. Treatability of raw alkaloid wastewaters with MBR operation (Scenario-A)

3.1.1. MBR operation

In this Scenario-A, the MBR system was fed gradually with raw opium alkaloid wastewater with step-fed mode to acclimatize the biomass. Two different membrane types were used for MBR operation as MF (Scenario-A1) and UF (Scenario-A2). The steady state conditions reached 60 days at MBR-MF and 80 days at MBR-UF, respectively.

The MLSS (Mixed Liquor Suspended Solids) concentration in the MBR reactor was measured at

around 15100 mg/L at the beginning of experiment. After the feeding of raw wastewater with step-fed mode, the MLSS and MLVSS (Mixed Liquor Volatile Suspended Solids) concentrations gradually increased in MBR and the trend is graphically shown in Figure 3a. The average values of MLSS and MLVSS concentrations were measured as 32555±16 mg/L, 40347±16 mg/L for MBR-MF and 25083±12 mg/L, 27164±11 mg/L for MBR-UF operations, respectively. The removal efficiency of organic

matter was evaluated by means of COD concentration removal. The average influent and effluent COD concentrations for MBR-MF were 15136 ± 89 mg/L and 1858 ± 96 mg/L, respectively. However, the average influent and effluent COD concentrations were 35713 ± 99 mg/L and 18529 ± 12 mg/L, respectively for MBR-UF. In this period, the most important operational drawback in MBR was the foaming problem during the experiment. For prevention of this problem, about 0.2-0.5 mL anti-foaming agent was used at everyday but it increased the effluent COD concentration and the COD removal efficiency was affected negatively [17,18]. As can be followed from the Figure 3b, the COD removal efficiencies for MBR-MF and MBR-UF were found as $86 \pm 9\%$ and $55 \pm 24\%$, respectively. Due to the very high load, the sieving effect on the particles improves the turbidity and suspended solids

in a very limited amount of suspended solids in the effluents from both MBRs [19,20].

As shown in Figure 3c, for MBR-MF the permeate flux value and daily treated wastewater flow were about 2 ± 0.9 L/m²h and 3.5 ± 1.6 L/day, respectively. However, when the MBR-UF was used the average the permeate flux value and daily treated wastewater flow were 2 ± 1.16 L/m²h and 3.5 ± 1.96 L/day, respectively. Color removal was not achieved as can be seen in Figure 3d. The approximate pH was 7.9 and ORP was 366 mV during the running time. At MBR operation with raw wastewater, it can be said that the flux and flowrate value of UF membrane were greater than that of MF membrane, although the COD values were increasing step by step. COD removal efficiencies of UF membrane were also higher than MF membrane.

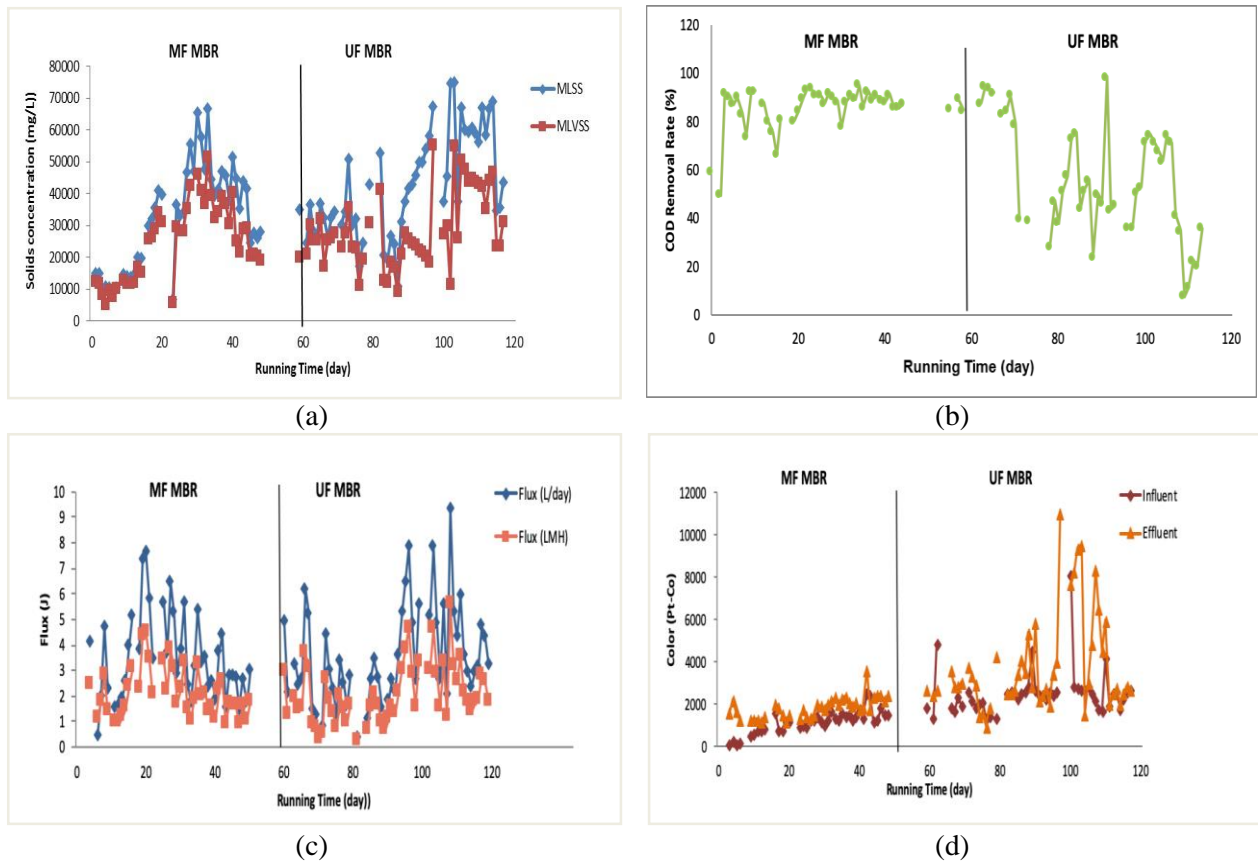


Figure 3. The graph of parameters during MBR operation with raw alkaloid wastewater (a) MLSS and MLVSS, (b) COD (c) Flux and (d) Color results

3.1.2. NF and RO treatment studies

In Scenario-A, the permeate streams from MBR/MF (scenario-A1) and MBR/UF (scenario-A2) were treated separately by NF (NF270 and NF90 membranes) and RO (XLE membrane) systems at two different recovery ratios (75% and 50%). The NF (NF 270 and NF 90) and RO (XLE) membranes were operated at two recovery ratios of 50% and 75%. RO experiments with raw wastewater indicated that the 99.6% COD and complete color removal was

achieved. The performance of RO membrane based on the removal efficiency of conductivity, COD, and color was higher than that of NF membrane (Table 4 and 5). In a study by Fazlioglu et al. [21] used industrial wastewater with MBR process and they investigated NF and RO membrane and their suitability for agricultural irrigation. They also found RO permeate more suitable for most of the parameters especially high conductivity removal efficiency.

Table 4. NF and RO experiment results of MBR-MF with raw alkaloid wastewater

Membrane type	Pressure (bar)	Recovery Ratio (%)	Flux (LMH)	Conductivity (mS/cm)		COD (mg/L)		Color (Pt-Co)	
				Influent	Effluent	Influent	Effluent	Influent	Effluent
NF270	10	75%	7.55	13.3	9.45	1220	300	3975	238.5
NF270	10	50%	10.8	13.3	8.72	1220	402.5	3975	148
XLE	15	50%	6.45	13.3	1.5	1220	61.5	3975	119
XLE	15	75%	2.6	13.3	1.8	1220	82.5	3975	108.5

Table 5. NF and RO experiment results of MBR-UF with raw alkaloid wastewater

Membrane type	Pressure (bar)	Recovery Ratio (%)	Flux (LMH)	Conductivity (mS/cm)		COD (mg/L)		Color (Pt-Co)	
				Influent	Effluent	Influent	Effluent	Influent	Effluent
NF270	15	50%	8.6	40.6	11.5	18500	9500	4625	498
NF270	15	75%	2.7	40.6	19.6	18500	1925	4625	461.5
NF90	30	50%	2.1	40.6	14	18500	1055	4625	629
NF90	30	75%	2.2	40.6	15.8	18500	1400	4625	1000
XLE	25	50%	2.8	40.6	3.8	18500	244	4625	104.5
XLE	25	75%	2.6	40.6	10.6	18500	322	4625	96

3.2. Treatment of anaerobically pretreated wastewater in MBR (Scenario-B)

3.2.1 MBR operation

In Scenario-B, the raw wastewater was firstly exposed to anaerobic treatment and then the effluent stream of anaerobic digester was fed to MBR-MF for 60 days and MBR-UF for 60 days. During the

experiments, two different membrane types were used for MBR operation of anaerobic treated effluent as MF (Scenario-B1) and UF (Scenario-B2). In Fig.4a, the change of MLSS concentration at MBR with anaerobic pretreated wastewater is given and the MLSS concentration was measured about 15900 mg/L at the beginning of the experiment. The average values of the MLSS become 10461±52 mg/L and 16454±76 mg/L in the MBR-MF and MBR-UF

reactors, respectively. The average values of MLSS and MLVSS concentrations were measured as 10461 ± 52 mg/L, 7326 ± 31 for MBR-MF and 16454 ± 76 , 7565 ± 27 mg/L for MBR-UF operations, respectively. The average influent and effluent COD concentrations for MBR-MF were 2120 ± 96 mg/L and 1401 ± 46 mg/L, respectively. However, the average influent and effluent COD concentrations for MBR-UF were 2847 ± 12 mg/L and 2466 ± 99 mg/L, respectively. As can be followed from the Figure 4b, the COD removal efficiencies for MBR-MF and MBR-UF were found as 41 ± 16 % and 24 ± 18 %, respectively.

As shown in Figure 4c, for MBR-MF the permeate flux value and daily treated wastewater flow were about 2.4 ± 0.9 L/m²h and 4 ± 1.7 L/day, respectively. However, when the MBR-UF was used the average the permeate flux value and daily treated wastewater flow were 3 ± 2.2 L/m²h and 5 ± 3.7 L/day, respectively. Color removal was not achieved as can be seen in Figure 4d. During the reactor performance HRT was approximately 1.25 days, pH and ORP were 9.0 and 366 mV respectively. Also, no sludge was discarded from the system.

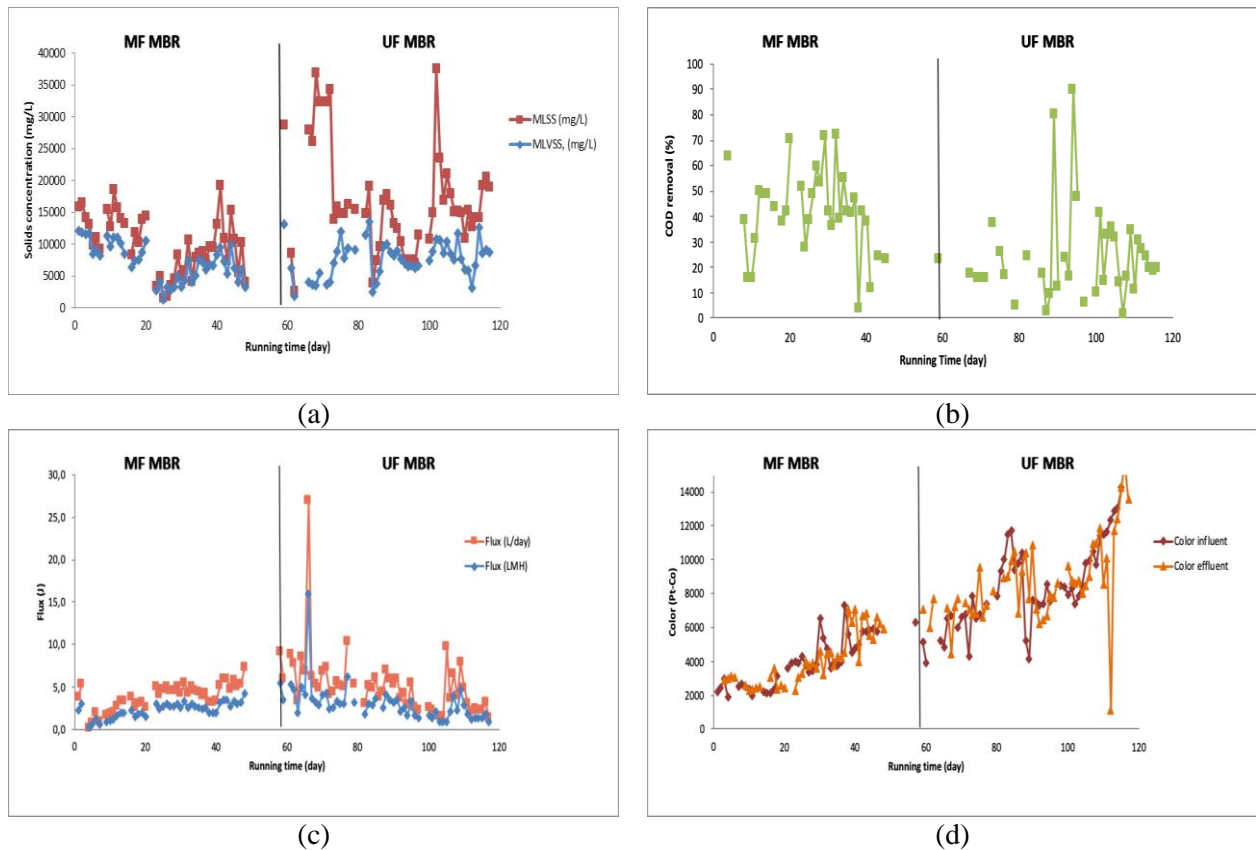


Figure 4. The graph of parameters during MBR operation with anaerobically pretreated alkaloid wastewater (a) MLSS and MLVSS, (b) COD (c) Flux, and (d) Color results.

3.2.2. NF and RO treatment studies

As shown in Figure 2b, two different types of membrane treatment strategies were applied to the anaerobically pretreated opium alkaloid wastewater. The effluents from MBR/MF (scenario-B1) and MBR/UF (scenario-B2) were treated by NF and RO units. Moreover, low COD removal of anaerobically pretreated opium alkaloid wastewater was determined in the MBR. Therefore, the NF and RO

membrane applications with UF pretreatment were used in order to increase the removal rates (Scenario-B3). The NF (NF 270) and the RO (XLE) membranes were operated at the recovery ratio of 50–75%. RO experiments with raw wastewater indicated that the 99.6% COD and complete color removal were achieved. The performance of RO membrane based on the removal efficiency of conductivity, COD, and color was higher than that of NF membrane (Table 6 and 7).

Table 6. NF and RO experiment results of MBR-MF with anaerobically pretreated alkaloid wastewater

Membrane type	Pressure (bar)	Recovery Ratio (%)	Flux (LMH)	Conductivity (mS/cm)		COD (mg/L)		Color (Pt-Co)	
				Influent	Effluent	Influent	Effluent	Influent	Effluent
NF270	10	75	10.4	20.2	17.3	3700	1160	6925	369
NF270	10	50	23.0	20.2	15.6	3700	120	6925	1010
XLE	20	50	3.4	20.2	7.1	3700	40	6925	149
XLE	20	75	3.2	20.2	14.9	3700	98	6925	170

Table 7. NF and RO experiment results of MBR-UF with anaerobically pretreated alkaloid wastewater

Membrane type	Pressure (bar)	Recovery Ratio (%)	Flux (LMH)	Conductivity (mS/cm)		COD (mg/L)		Color (Pt-Co)	
				Influent	Effluent	Influent	Effluent	Influent	Effluent
UF-MP005	2	100	8.6	13.5	13.3	3140	1680	5280	2800
UF-MP005	3	100	8.6	13.5	13.3	3140	1680	5280	2800
UF-MP005	4	100	11.3	13.5	13.3	3140	1680	5280	2800
NF270	10	75	10.5	13.3	10.6	1680	306	2800	336
NF270	10	50	14.7	13.3	9.5	1680	226	2800	364
XLE	15	50	2.9	13.3	2.9	1680	128	2800	107
XLE	20	75	3.5	13.3	2.0	1680	105	2800	84
XLE	20	50	10.4	13.3	1.0	1680	51	2800	70

Table 8. NF and RO experiment results of UF with anaerobically pretreated alkaloid wastewater

Membrane type	Pressure (bar)	Recovery Ratio (%)	Flux (LMH)	Conductivity (mS/cm)		COD (mg/L)		Color (Pt-Co)	
				Influent	Effluent	Influent	Effluent	Influent	Effluent
	2	100	8.6	13.5	13.3	3140	1680	5280	2800
UF-MP005	3	100	8.8	13.5	13.3	3140	1680	5280	2800
	4	100	11.3	13.5	13.3	3140	1680	5280	2800
NF270	10	75	10.5	13.3	10.6	1680	306	2800	336
NF270	10	50	14.7	13.3	9.5	1680	226	2800	364
XLE	15	50	2.9	13.3	2.9	1680	128	2800	107
XLE	20	75	3.5	13.3	2.0	1680	105	2800	84
XLE	20	50	10.4	13.3	1.0	1680	51	2800	70

At the last part of the experiments, UF-MP005 was applied to the effluents of anaerobically treated opium alkaloid processing effluent as pretreatment (Figure 2b). Experimental results indicated that COD, color, and conductivity removals of 46%, 47%, and 0%, respectively, were possible at a pressure of 2, 3, 4 bar as shown in Table 8. The NF (NF 270) and reverse osmosis were applied to the UF pretreated effluent. It demonstrated that the pretreatment before NF and XLE is necessary to obtain high conductivity, COD and color removal.

COD removal of anaerobically pretreated opium alkaloid wastewater was very low in the MBR treatment experiments. However, when NF membrane application with UF pretreatment option was applied, 82% COD and 88% color removal were obtained at 75% recovery. The removal efficiencies

of COD and color were as 94% and 97%, respectively, were achieved for NF runs with UF pretreatment.

3.3 Performance evaluation of all scenarios

To describe results of experiments, performance of all scenarios was compared in terms of flux, COD and conductivity rejections. As shown in Table 9, permeate values for COD, color and conductivity did not change significantly for the XLE-RO membrane with 75% recovery ratio. However, anaerobic pretreatment strongly influenced the solute rejections by NF and RO, probably due to lower contact time to solutes with membrane surface because the flux was nearly doubled than raw waste water system. It was seen that although most of the parameters make RO permeate more suitable than NF except flux.

Table 9. Comparison of permeate qualities all scenarios.

Type	Parameter	Units	Permeates				
			50% Recovery Ratio			75% Recovery Ratio	
			XLE			NF 270	XLE
			NF 270	15 bar	20 bar	NF 270	XLE
Raw Waste Water + MBR MF (Scenario-A1)	Flux	LMH	10.8	6.45		7.55	2.6
	COD	mg/L	402.5	61.5		300	82.5
	Color	Pt-Co	148	119		238,5	108,5
	Conductivity	mS/cm	8.72	1.5		9.45	1.8
Raw Waste Water + MBR UF (Scenario- A2)	Flux	LMH	8.6		2.8	2.7	2.6
	COD	mg/L	9500		244	1925	322
	Color	Pt-Co	498		104,5	461.5	96
	Conductivity	mS/cm	11.5		3.8	19.6	10.6
Anaerobically Pretreated Wastewater + MBR MF (Scenario-B1)	Flux	LMH	23		3.4	10.4	3.2
	COD	mg/L	120		40	1160	98
	Color	Pt-Co	1010		149	369	170
	Conductivity	mS/cm	15.6		7.1	17.3	14.9
Anaerobically Pretreated Wastewater + MBR UF (Scenario-B2)	Flux	LMH	14.7	2.9	3.5	10.5	3.5
	COD	mg/L	226	128	51	306	105
	Color	Pt-Co	364	107	70	336	84
	Conductivity	mS/cm	9.5	2.9	1	10.6	2
Anaerobically Pretreated Wastewater + UF (Scenario-B3)	Flux	LMH	14.7	2.9	10.4	10.5	3.5
	COD	mg/L	226	128	51	206	105
	Color	Pt-Co	364	107	70	336	84
	Conductivity	mS/cm	9.5	2.9	1	10.6	2

4. Results and Discussion

In this study, the treatment of opium alkaloid wastewater was studied with 5 different scenarios. There is a limited number of studies investigating treatment of opium alkaloid wastewater in the literature. Table 10 summarizes the key performance parameters reported in the literature([12] and [22]) for different operations. The usage of NF membrane with MBR system enhanced the NF performance.

The results can be summarized as follows.

(1) The high COD concentration of the wastewater in the MBR experiments caused severe problems such as foaming problem, the chemical usage to prevent foaming. In order to prevent those problems, the wastewater was anaerobically pretreated.

(2) 99.6% COD and complete color removal were achieved with the RO experiments with alkaloid wastewater.

(3) Very low COD removal of anaerobically pretreated opium alkaloid wastewater was obtained in the MBR treatment experiments. The best treatment scenario for the anaerobically pretreated opium alkaloid wastewater was using RO unit following MBR/UF.

(4) COD removal of concentrated opium alkaloid wastewater was 46% in the MBR system. However, when the NF and RO membrane applications were applied, the COD removals were increased to 94% and 99.6%, respectively.

(5) For both concentrated and anaerobically pretreated opium alkaloid wastewater treatment scenarios, permeate flux value was increased with NF application.

Table 10. Comparison of the treatment performance of Opium Alkaloid Wastewater with this study.

Pretreatment	Membrane Systems	Advanced Treatment	Operation Parameter	Flux (LMH)	COD Removal (%)	Conductivity Removal (%)	Color Removal (%)	Scale	References
Anaerobic Treatment	MBR MF	NF 270	10 bar, % 50 RR	23	97	23	85.4	Laboratory	This study
		RO (XLE)	20 bar, % 50 RR	3.4	>98	65	97.5	Laboratory	
	MBR UF	NF 270	10 bar, % 50 RR	14.7	86.5	28.Haz	87	Laboratory	
		RO (XLE)	20 bar, % 50 RR	10.4	97	92.4	97.5	Laboratory	
	UF	RO (XLE)	20 bar, % 50 RR	10.4	97	92.5	97.5	Laboratory	
	-	MBR MF	NF 270	10 bar, % 50 RR	10.8	67	34	96	
RO (XLE)			15 bar, % 50 RR	6.45	93	95	97	Laboratory	
2-stage Aerobic Treatment	MBR	RO (XLE)	25 bar, % 50 RR	2.8	>98	90.6	97.7	Laboratory	
		NF 90 + NF 270	30 bar, % 75 RR	15	95	88	>98	Pilot	[12]
2-stage Aerobic Treatment	UF	NF	24 bar, % 70 RR	70	>97	94	>99	Laboratory	
		NF	18 bar, % 70 RR	12	97	>98	>99	Pilot	
2-stage Aerobic Treatment + Anaerobic Treatment Anaerobic Pretreated	UF	RO	25 bar	16	98	99	>99	Laboratory	
		NF	24 bar	33	95	88	>98	Laboratory	[22]

Acknowledgements

We wish to express our appreciation to the administrative and the technical staff of TMO for the financial support and cooperation during this research project.

Conflicts of Interest

The authors state that did not have conflict of interests

Abbreviations

AIC	Anaerobic Internal Cycling	MLVSS	Mixed Liquor Volatile Suspended Solids
BOD	Biological Oxygen Demand	NF	Nanofiltration
COD	Chemical Oxygen Demand	OLRs	Organic Loading Rates
EC	Electrodialysis	ORP	Oxidation Reduction Potential
HRTs	Hydraulic Retention Times	RO	Reverse Osmosis
IWA	International Water Association	UASB	Upflow Anaerobic Sludge Bed)
MBR	Membrane Bioreactor	UF	Ultrafiltration
MF	Microfiltration	VFA	Volatile Fatty Acids
MLSS	Mixed Liquor Suspended Solids	WAO	Wet Air Oxidation

Conflicts of Interest

The authors state that did not have conflict of interests.

References

- [1] Cengiz N.Ü., Sağlam M., Yüksel M., Ballice L., Treatment of high-strength opium alkaloid wastewater using hydrothermal gasification, *J. Supercrit. Fluids*, 130 (2017) 301–310.
- [2] Sevimli M.F., Aydın A.F., Sarikaya H.Z., Öztürk İ., Characterization and treatment of effluent from opium alkaloid processing wastewater, *Water Sci. Technol.*, 40 (1999) 23–30.
- [3] Yaniv Z., Dudai N., Medicinal and aromatic plants of the middle-east, Netherlands: Springer, (2014).
- [4] Kınılı H., The report of treatability studies of biological wastewater treatment plant effluent of TMO Opium Alkaloids Plant, Marmara Res. Center, TÜBİTAK, Gebze, Türkiye, (1994).
- [5] Ozturk I., Aydın A.F., Koyuncu I., Technical Evaluation Report for Upgrading of Bolvadin Alkaloid Industry Wastewater Treatment Plant, Istanbul Tech. Univ., Istanbul, (2008).
- [6] Sakar H., Balcik Canbolat C., Karagunduz A., Keskinler B., Sulfate removal from nanofiltration concentrate of alkaloid wastewater by electrodialysis, *Desalin. Water Treat.*, 57 (2016) 21003–21014.
- [7] Aytimur G., Atalay S., Treatment of an alkaloid industry wastewater by biological oxidation and/or chemical oxidation, *Energy Sources*, 26 (2004) 661–670.
- [8] Kaçar Y., Alpay E., Ceylan V.K., Pretreatment of Afyon alcaloide factory's wastewater by wet air oxidation (WAO), *Water Res.*, 37 (2003) 1170–1176.
- [9] Bural C.B., Demirer G.N., Kantoglu O., Dilek F.B., Treatment of opium alkaloid containing wastewater in sequencing batch reactor (SBR)—Effect of gamma irradiation, *Radiat. Phys. Chem.*, 79 (2010) 519–526.
- [10] Aydın A.F., Ersahin M.E., Dereli R.K., Sarikaya H.Z., Ozturk I., Long-term anaerobic treatability studies on opium alkaloids industry effluents, *J. Environ. Sci. Heal. Part A.*, 45 (2010) 192–200.
- [11] Dereli R.K., Ersahin M.E., Ozturk H., Ozturk I., Aydın A.F., Applicability of Anaerobic Digestion Model No. 1 (ADM1) for a specific industrial wastewater: Opium alkaloid effluents, *Chem. Eng. J.*, 165 (2010) 89–94.

- [12] Koyuncu I., An advanced treatment of high-strength opium alkaloid processing industry wastewaters with membrane technology: Pretreatment, fouling and retention characteristics of membranes, *Desalination*, 155 (2003) 265–275.
- [13] Koyuncu I., Sevimli M.F., Ozturk I., Aydin A.F., Application of membrane and ozonation technologies to remove color from agro-industry effluents, *Water Sci. Technol.*, 43 (2001) 233–241.
- [14] Gençsoy E.B., Afyon Alkaloidleri Endüstrisi Atıksularının Anaerobik Arıtılması, M.Sc thesis., İstanbul Technical University, (2003).
- [15] A. American Public Health Association, Standard methods for the examination of water and wastewater, American public health association Washington DC, (1995).
- [16] Çelen Erdem İ., Türker M., Çiftçi G., Öztürk İ., Çiftçi T., Afyon Alkaloidleri Endüstrisi Atıksularının Anaerobik Proseslerle Arıtılabilirliği, *Mühendislik Bilim. ve Tasarım Derg.*, 6(3) (2018) 479-486.
- [17] Bouhabila E.H., Ben Aïm R., Buisson H., Microfiltration of activated sludge using submerged membrane with air bubbling (application to wastewater treatment), *Desalination*, 118 (1998) 315–322.
- [18] Benitez J., Rodríguez A., Malaver R., Stabilization and dewatering of wastewater using hollow fiber membranes, *Water Res.*, 29 (1995) 2281–2286.
- [19] Arévalo J., Ruiz L.M., Parada-Albarracín J.A., González-Pérez D.M., Pérez J., Moreno B., Gómez M.A., Wastewater reuse after treatment by MBR. Microfiltration or ultrafiltration?, *Desalination*, 299 (2012) 22–27.
- [20] Domínguez L., Cases V., Birek C., Rodríguez M., Prats D., Influence of organic loading rate on the performance of ultrafiltration and microfiltration membrane bioreactors at high sludge retention time, *Chem. Eng. J.*, 181 (2012) 132–143.
- [21] Hacızafıoğlu M.C., Tomasini H.R., Kabay N., Bertin L., Pek T., Kitiş M., Yiğit N., Yüksel M., Effect of pressure on desalination of MBR effluents with high salinity by using NF and RO processes for reuse in irrigation, *J. Water Process Eng.*, 25 (2018) 22–27.
- [22] Insel G., Karagunduz A., Aksel M., Cokgor E., Kor-Bicakci G., Ozyildiz G., Toroz I., Keskinler B., Membrane integrated process for advances treatment of high strength opium alkaloids wastewaters, *Wat. Sci.Technol.*, 77(7) (2018) 1899-1908.



Investigation of behavior of cooling tower structure under external loads

Asuman Işıl ÇARHOGLU^{1,*}

¹Süleyman Demirel University, Faculty of Engineering,, Department of Civil Engineering, Isparta / TURKEY

Abstract

Cooling towers are high and thin structures which are widely used at the industry and nuclear facilities. These structures are built on column elements as reinforced concrete. Determining the behavior of the buildings affected by the dynamic loads such as wind and earthquake is very important in terms of preventing the loss of life and property. In this study, hyperbolic cooling with 117m height tower was examined and the behaviors of the structure in earthquake and wind effects were investigated. During the application of the wind load, 25m / sec wind velocity was applied and three ground motion records were applied to the structures in the course of the earthquake analysis. The wind load was calculated in accordance with the ASCE 7-10 standard and it was given as angular. As a result of the analysis, the values of the displacement and stress were obtained and examined. According to the results of the wind load analysis; As the height of the tower increases, the values of wind load increase and the displacement values occurring in the building increase. The values of displacement and stress vary angularly depending on angular wind load. It is seen that the highest values of displacement and stress values were obtained in Kobe earthquake. Displacement values were examined depending on the height and the largest displacement values were obtained at the top part.

Article info

History:
Received: 27.04.2020
Accepted: 02.05.2021

Keywords:
Cooling Tower,
Time History Analysis,
Finite Element
Methods,
Wind Load,
Earthquake Load.

1. Introduction

Cooling towers are buildings heights of which are more, thicknesses of which are low, diameters of which are more and they are used at industrial plants such as oil refineries, energy and nuclear power plants. These important facilities can be affected by forces such as earthquakes and wind. Therefore, it is necessary to examine the resistance of these structures in the impact of earthquake and wind. The intended use of cooling towers is to remove the heat taken from the cooling water in the system. Since the heat present in the water is provided to cool under the influence of the atmosphere, these structures are constructed as high in order to benefit from the effect of air. The sliding mold technique is used during the construction of these structures and the construction of these structures is carried out part by part [1].

The cooling tower is designed by the engineer as more slender and thinner for the purpose of increasing the dead load. The relationship between height and shell thickness is of great significance in terms of the stability problem occurring due to the loads such as wind and dead load [2]. It is very important to

determine the situation of stress, durability, elastic stability, vibration values in such big structures because of the interaction of loading condition with the meridian shape of the cooling towers [3]. Three from eight cooling towers located in Ferrybridge power stations in the UK collapsed due to the aerodynamic effects which are about wind velocity 19m/s in 1965. In 1973, the cooling tower situated in Scotland Ardeer Power Plant collapsed because of the strong wind effect [4].

There are many studies related to the behavior of cooling towers under the influence of wind and earthquake. Karakas et al. [5] examined the static and dynamic behavior of cooling tower and wind turbine structures by considering soil-structure interaction in their study. They considered Vlasov soil model in the analysis of the soil-structure interaction. Based on the results of the study performed by Karakaş, it was seen that the frequency values decreased depending on the cooling tower height and wall thickness, according to the results of the structure-soil interaction analysis; the frequency values decrease by the rigid base situation. It was observed that there were large increases in tensile strength and small increases in meridian

*Corresponding author. e-mail address: isilcarhoglu@sdu.edu.tr
<http://dergipark.gov.tr/csj> ©2021 Faculty of Science, Sivas Cumhuriyet University

strength due to the wind effect, and also changes in displacement values occurred as a result of wind and earthquake effects. Karakas et al. [6] examined the behavior of the cooling tower structure under the effect of wind by using the Vlasov soil model. It was seen that shear forces, bending and torsional moments at the columns increased when the structure-soil interaction was taken into consideration. Karakas et al. [7] analyzed the soil structure interaction by modeling the cooling tower using the SAP2000-OAPI program. They dealt with the cooling towers with different H/a ratio and evaluated the results obtained by performing the analysis by using the Vlasov soil model. It was observed that the frequency values decreased when the soil structure interaction was compared in terms of the rigid situation, in addition to when the height of the tower and the slenderness rates increased, the frequency values decreased and the frequency values increased with the increasing of the curvature. Ghomi and Kharrazi [8] examined the behavior of cooling tower which were exposed to the earthquake effect. The big displacements and stresses occurred in the columns and the structure as determined by Ghomi and Kharrazi. Yu et al [9] analyzed the behavior of the tower under the influence of wind by applying angular wind load to a cooling tower. G. Murali et al. [10] examined two cooling towers with 122m and 200 m height. They studied the behavior of these towers under the wind effect. They applied the wind load to the structures angularly and compared the values obtained as a result of the analysis. It was shown that the values of the bending moment and membrane force were different for three towers. Greiner and Derler investigated the behavior of cylinder shell structures under the effect of wind pressure by considering geometric nonlinearity and material plasticity. The results of the test and numerical studies performed by Greiner and Derler were compared [11]. Afshari and Dehghanpour [12] explained the types of cooling tower and its cooling principles. The working principles of the cooling tower were compared in terms of the mechanical and natural draft. In addition to these, A fluent simulation was performed. Asadzadeh et al. [13] performed in the modal and nonlinear time history analysis of the cooling tower structure. The columns supporting the cooling tower were designed as I and Λ type. The effect of the angle of inclination in the columns was investigated. The angle variation of the columns is affected by the analysis results. Dehghanpour et. al. [14] examined the behavior of a cooling tower under the wind load effect in the cases of before and after reinforcement by reinforcing with CFRP (carbon fiber reinforced polymer) material with different thicknesses. The obtained stress and displacement values are compared.

The aim of the study is to examine the behavior of the cooling tower exposed to the external loads such as earthquake and wind effects. For this reason, while the wind loading analysis was performed in accordance with ASCE 7-10 regulation, earthquake analysis was performed by using time history analysis by taking into account of a cooling tower being 117m [15]. The wind loads were angularly applied to the cooling structure and the values obtained from the results obtained angularly. In the earthquake analysis, The earthquakes having different characteristics were applied to the cooling tower. One of the earthquakes applied to the structure is Kobe earthquake whose magnitude, ground acceleration, ground velocity are quite high.

2. Materials and Methods

In our country, many earthquakes causing a number of losses of lives and property occurred. Many buildings were damaged in the August 17, 1999 earthquake. Earthquakes occurred before and after 1999 earthquake show that examination of the industrial buildings is very important in terms of the earthquake engineering. It is necessary to determine the behavior of the structures under earthquake effect in order to be able to prevent these losses.

The wind, earthquake and temperature effects are of great importance when internal forces occurring in cooling tower structures are determined. Hyperbolic design of cooling towers increases the strength of the structure, however fewer material is used [16]. The meridional shape of a hyperbolic cooling tower comprises of lower and upper hyperbola parts and these parts join in throat. The curve varies along the height of the tower because the tower axis with the axis of the hyperbola does not need to match, and the greatest value is usually seen in the throat part [3]. Hyperbolic shell geometry is shown in Figure 1 [16].

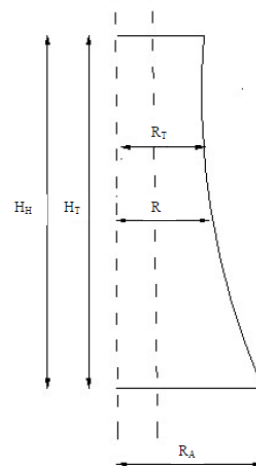


Figure 1. Hyperbolic shell [16]

$$R = c + a \sqrt{1 + \frac{z^2}{b^2}} \quad (1)$$

$$b = \frac{H_T}{\sqrt{\left(\frac{R_A - C}{R_T - C}\right)^2 - 1}} \quad (2)$$

R is determined according to the equation 1-2. Hyperbolic shell design can be performed with the equations [16]. The geometric properties of the cooling tower are presented in Figure 2a. The dimensions of tower designed are as follows; the total height of the cooling towers is 117m, column height is 9m, the base diameter is 103.5m, shell base is 98m, diameter of throat is 54m, diameter of top part is 58.5m.

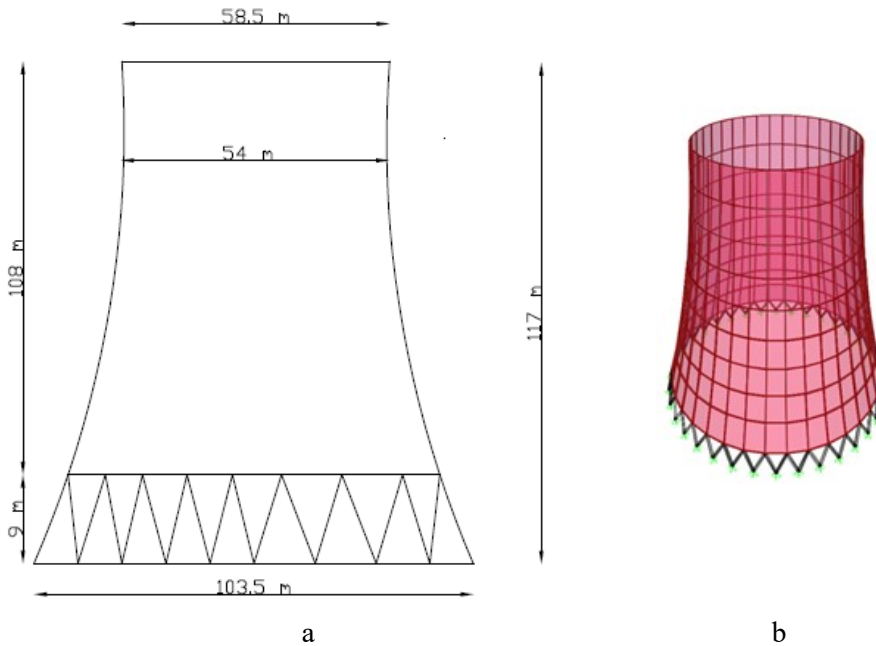


Figure 2. a) The geometric properties b) mesh shape of the cooling tower building

The cooling tower structure was modeled as a shell element with the SAP 2000 finite element program [17]. The finite element model of the cooling tower in Figure 2b. Cooling towers are supported by columns. V shaped columns consisted of line element with 2 noded were designed. Columns gave 6 degrees of freedom at each node. The columns carrying the cooling tower consist of reinforced concrete elements and their diameters are 90 cm. In the structure designed, 32 columns were used and the cooling tower wall was divided into 324 shell elements. The tower is divided into 36 parts in the radial direction. The wall thickness of cooling tower was designed as 700mm in lower parts and 250mm in other parts. C30 concrete was used in the shell walls of the cooling tower structure and supporting columns.

2.1. Wind load analysis

The effect of the angular distribution with the vertical effect of the wind loads formed in symmetrical circular structures such as cooling tower is very important. Wind loads formed in the vertical direction depend on climatic conditions and soil surface roughness, and

wind loads formed angularly depend on the structure surface roughness [5].

Wind loads are determined according to ASCE 7-10 standard in order to examine the behavior of cooling tower structures under the effect of wind. Wind load calculation is made by using equation 3 - equation 6 [15].

$$P(z) = q_z G C_{pe}(\theta) \quad (3)$$

$$q_z = 0.613 \cdot K_z K_{zt} K_d \cdot I \cdot V^2 \quad (4)$$

q_z	Wind pressure
G	Storm effect factor
$C_{pe}(\theta)$	Angular pressure distribution
K_z	Speed pressure effect coefficient
K_{zt}	Topography factor
K_d	Wind direction coefficient
I	Importance factor

$$G = 0.925 \left(\frac{1 + 1.7 I_z \sqrt{g_Q^2 Q^2 + g_R^2 R^2}}{1 + 1.7 g_v I_z} \right) \quad (5)$$

Q; Ground response factor is calculated by equation 6.

$$Q = \frac{1}{\sqrt{1 + 0.63 \left(\frac{B+h}{L} \right) \frac{1}{\bar{z}}}}} \quad (6)$$

I_z	Turbulence density at \bar{z} height
\bar{z}	Equivalent height of the structure ($\bar{z} = 0.6h$)
g_Q	Peak factor for soil response
g_v	Peak factor for wind response
Q	Ground response factor

The value of design wind pressure at any height value is determined by multiplying the values of the wind pressure, storm effect factor and the angular pressure distribution. Wind pressure (q_z) is calculated based on the values of K_z, K_{zt}, K_d, I by using equation 3. K_z, K_{zt}, K_d and I coefficient values are provided in the

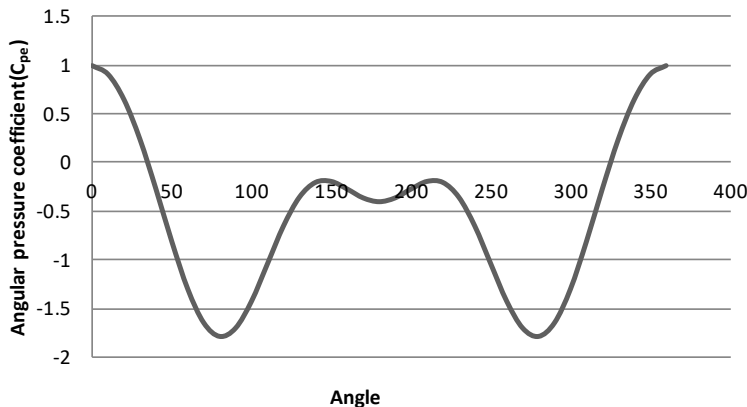


Figure 4. Angular pressure coefficients

In this study, 25m/sec wind speed is applied to the cooling tower building and since these structures are circular cross-section, the values of the wind pressure are calculated as angular according to the equation 3-equation 7. The values of the angular pressure coefficient used in the calculations are shown in Figure 4. The values of wind load applied to the tower were obtained by multiplying with the wind pressure values determined for each z height by establishing values of C_{pe} according to the angles.

regulation. The storm effect factor can be taken as 0.85 in rigid and other structures and it is also obtained by using equation 4 [5, 15, 18, 19].

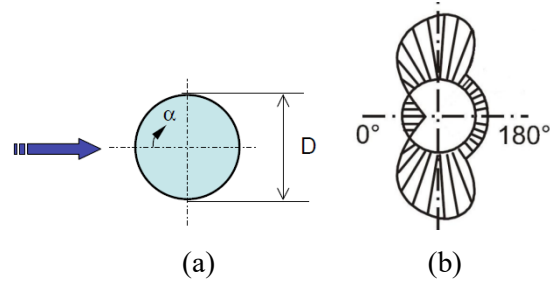
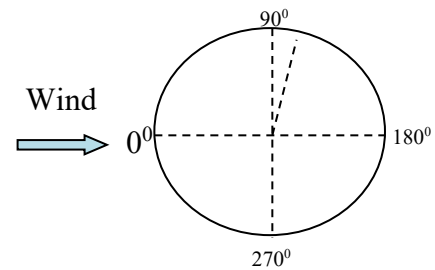


Figure 3. (a) Wind flow in circular sections [20] (b) Pressure distribution in circular structures [18;21]

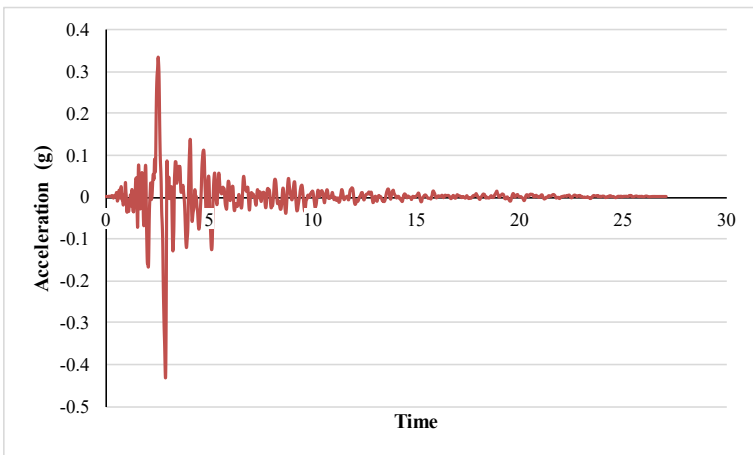
The condition of the effect of wind in one direction to the circular cross-sectional structures is shown in Figure 3a and the pressure distribution resulting is shown in Figure 3b [18; 20; 21]. C_{pe} coefficient for circular cross-section conditions is determined according to the equation 7 which belongs to Greiner. In the Formula 7, α is the angle that the wind load makes with the circular cross section [18; 22].

$$C_{pe} = -0.55 + 0.25 * \cos\alpha + 1.0 * \cos 2\alpha + 0.45 * \cos 3\alpha - 0.15 * \cos 4\alpha \quad (7)$$

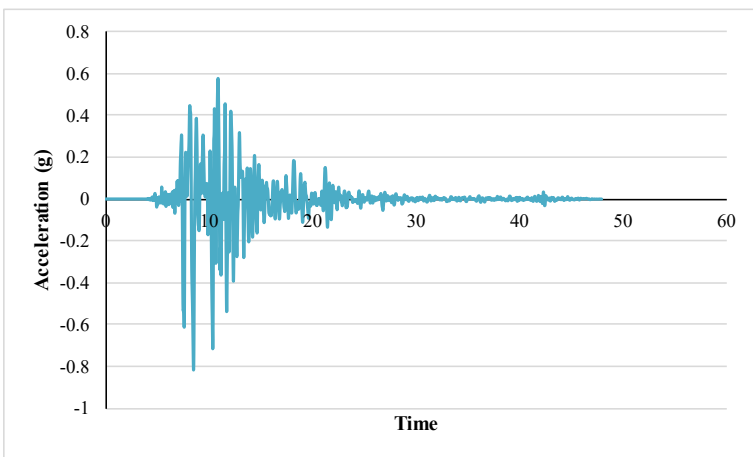


2.2. Earthquake analysis with the time history method

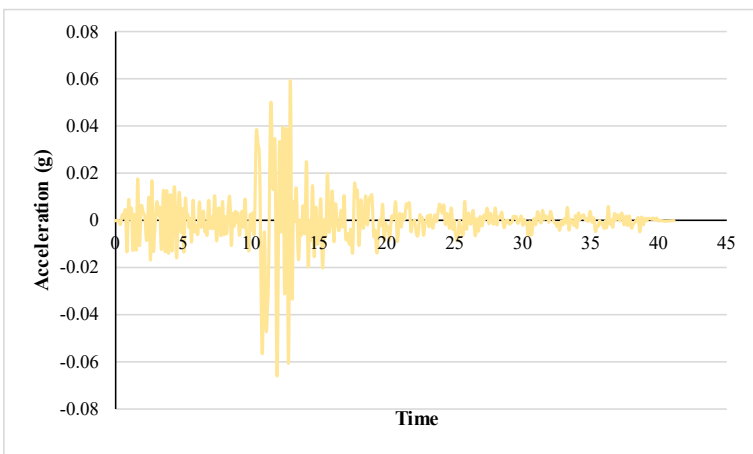
The dynamic analyses were performed with the time history method by applying three ground motion records to the cooling towers. The features of the earthquakes used in the analyzes are presented in Table 1 [23]. Time-dependent acceleration recordings of earthquakes are shown in Figure 5.



a) 1979 Coyote Lake Earthquake



b) 1995 Kobe Earthquake



c) 1980 Anza Earthquake

Figure 5. Time-dependent acceleration records of **(a)** 1979 Coyote Lake, **(b)** 1995 Kobe, **(c)**1980 Anza Earthquake

Table 1. The features of earthquakes used in the analysis [23]

Earthquake	Date	Magnitude (M _w)	Record	Ground Velocity (cm/s)	Ground Acceleration (g)	Focus Depth (km)
Coyote Lake	06/08/1979	5.8	G06230	49.2	0.4339	3.1
Kobe	16/01/1995	6.9	KJM000	79.3	0.8213	6.9
Anza (HorseCany)	25/02/1980	4.9	AZF315	2.6	0.066	12.1

3. Results and Discussion

In this study, cooling tower structure is modelled and analysis are performed under the effect of earthquake and wind. Firstly, The period values of the cooling tower structure were obtained by performing modal analysis. Secondly, The wind analysis was made according to ASCE 7-10 regulation [15]. Then, the ground motion records with different properties were applied to the cooling tower structure.

3.1. Mode shapes and frequency values

Mode shapes and frequency values obtained by using SAP 2000 finite element program. There are mode shapes and the value of frequency in the analysis result of the modal analysis made in Figure 6. The first four frequency values in the cooling tower structure are 1.14Hz., 1.14Hz., 1.30Hz. and 1.30 Hz.

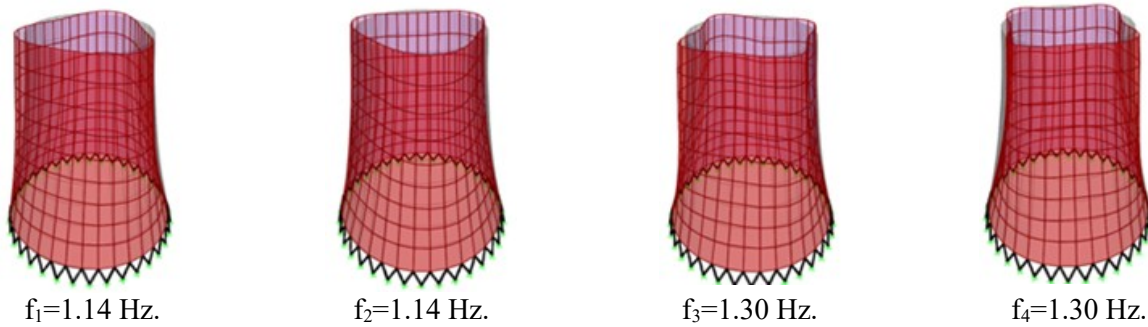


Figure 6. The mode shapes and period values in cooling tower

The math model of the cooling tower structure can be designed as a single degree of freedom system. The first natural frequency value of a single degree system with fixed supported.

The value of first frequency of vibration can be estimated according to Equation 9 [24,25].

$$\omega = \frac{1.875}{H^2} \sqrt{\frac{EI}{m}} \tag{9}$$

$$f = \frac{\omega}{2\pi} \tag{10}$$

Here, H; height of the tower; I; moment of inertia, E; elasticity modulus, f; first natural frequency, m; mass of the tower. The mass, height and weight of, volume

of cooling tower are 117m and 24 KN/m³. The average dimension is taken as 78m.

$$\omega = 7.91 \text{ s}^{-1}$$

$$f = 1.26 \text{ Hz}$$

The frequency value obtained from equation 9 and equation 10 is very close to the value obtained from modal analysis performed with SAP 2000 finite element program.

3.2. The application of wind load to the cooling tower structure

The displacement and stress and their values were examined by considering the angular changes of the structure in case of wind load effect on cooling tower structure.

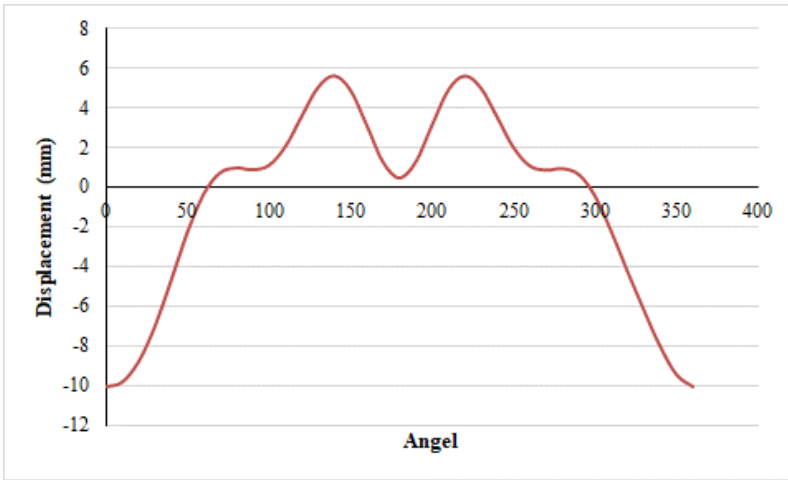


Figure 7. Angular displacement values

There are the graphics of displacement values occurring in the angular direction in Figure 7. The wind load comes to the structure as angular and is applied angularly by multiplying the wind load with the angular pressure coefficient at each height z . It was shown that the wind speeds are gradually decreasing 10mm at 0° , 9.8mm at 10° and 8.8 mm at 20° . While

the largest values occur in the direction of the wind, the values decrease in the other direction.

Displacement values depending on the height are shown in Figure 8. The largest displacement is seen to be obtained at a height of 117 m. Since the wind load increases with the height of the floor, displacement values increase as the height of the structure increases.

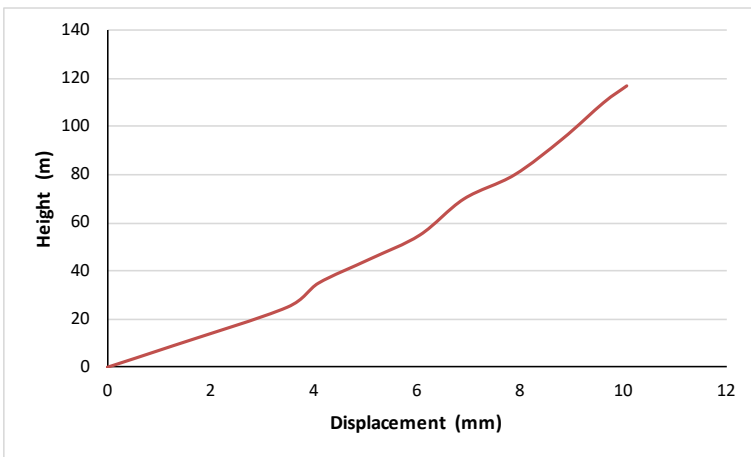


Figure 8. The values of displacement depending on the height

In Figure 9, there are stress shapes in which the pressure and tensile stresses occur in the structure when the speed of the wind is 25m / sec. It is seen that the stresses intensify in the parts close to the base and in the throat in the direction of the wind.

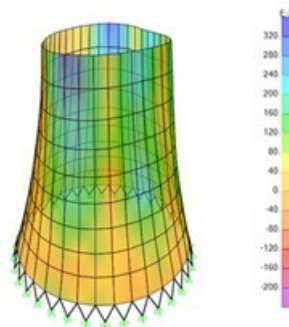


Figure 9. The tensile status of the building in 25 m/s wind speed

3.3. Application of earthquake load to the cooling tower structure

Three time dependent acceleration recordings were applied to the structure and displacement and stress

values were obtained. The displacement and stress values are respectively shown in Figure 10 and 11. The biggest stress and displacement values were obtained in Kobe earthquake.

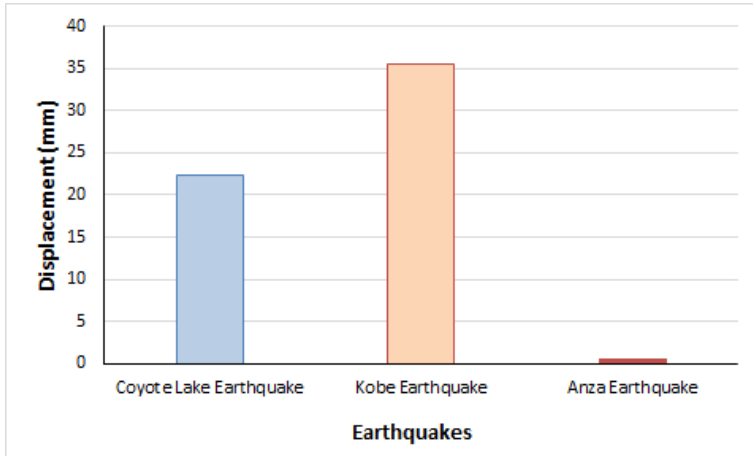


Figure 10. Displacement values found in the earthquake analysis

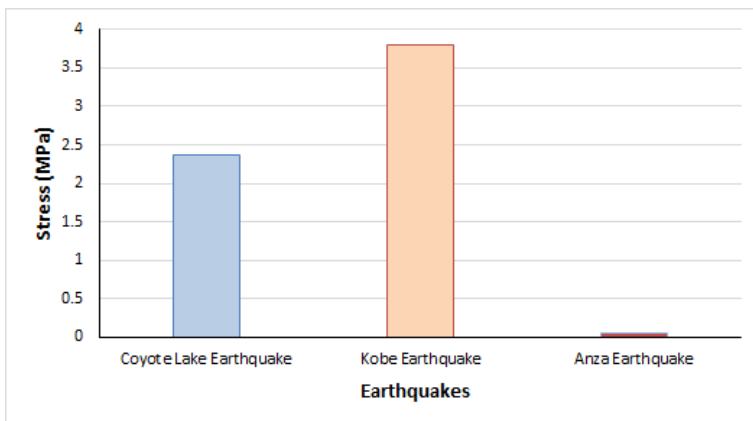
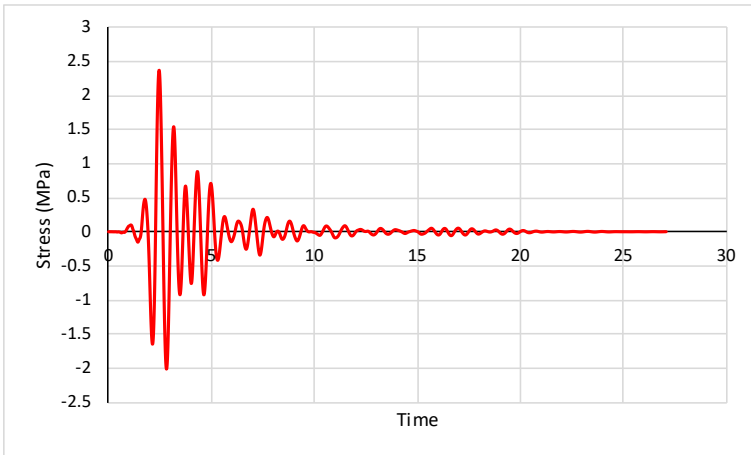


Figure 11. Stress values found in the earthquake analysis

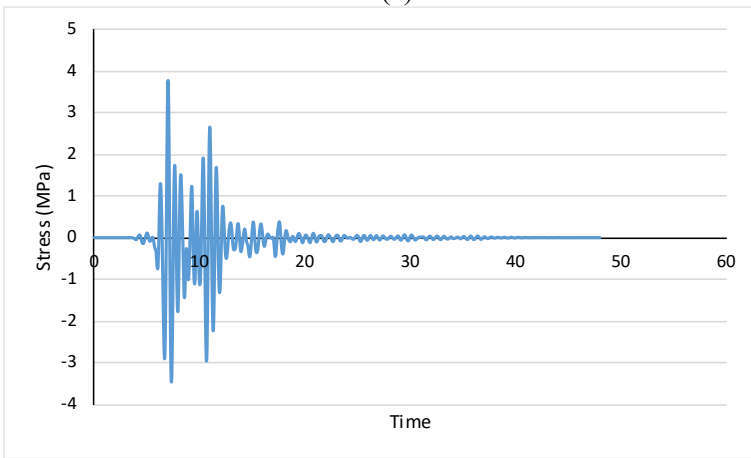
The stress graph dependent to time in the structure in the case of Kobe, Coyote Lake and Anza earthquakes are shown in Figure 12 a,b and c. While the biggest displacement and stress value were obtained in Kobe earthquake, the smallest values were obtained in Anza earthquake.

Displacement and stress values were obtained by applying time-dependent acceleration records of 3 earthquakes. The biggest displacement value was 35.51 mm and the maximum stress value was 3.7 MPa with Kobe earthquake, the smallest displacement value was 0.58mm and the stress value was 0.048 MPa in 1980 Anza earthquake. In 1979 Coyota Lake earthquake, 22.29 mm displacement and 2.3 MPa

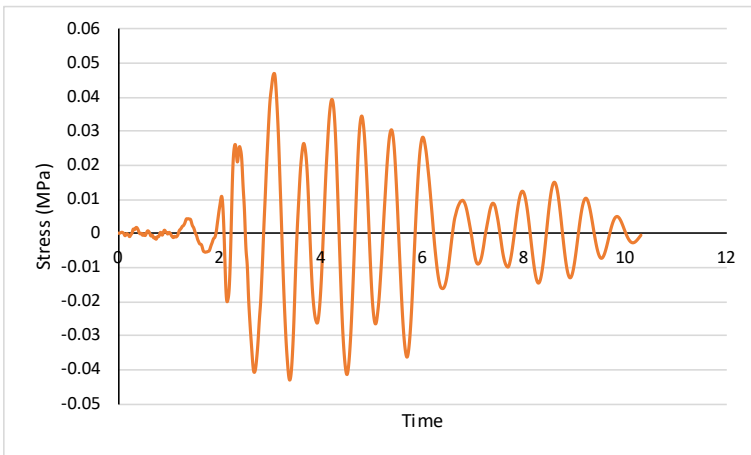
stress value was obtained. The Kobe earthquake is a quite big earthquake and its magnitude is 6.9. The magnitudes of Coyota Lake and Anza earthquakes are 5.8 and 4.9, respectively. Kobe earthquake has a ground velocity of 79.3 m / sec, an effective ground acceleration of 0.82 and a focal depth of 6.9 km. velocity and ground acceleration are quite higher than other earthquakes. The ground velocity and ground acceleration of Anza earthquakes have the smallest value and its depth of focus has the largest value. In Figure 12, It is seen that the values of the biggest stress occurred in the duration when the effective ground acceleration of the earthquakes is greatest.



(a)



(b)



(c)

Figure 12. Maximum stress graph found in the earthquake analysis for **(a)** Coyote Lake Earthquake **(b)** Kobe Earthquake **(c)** Anza Earthquake

4. Conclusion

In this study, the behavior of the cooling tower under the influence of wind and earthquake was examined. ASCE-7-10 regulation was used for wind analysis [15]. Wind loads were determined by using angular coefficient values in circular cross-sectional systems. In earthquake analysis, three ground motion records were applied to the structure according to time history analysis.

As a result of the earthquake analysis; while the greatest displacement and stress values are obtained in Kobe earthquake, the values obtained in Coyota Lake and Anza earthquakes are gradually decreasing. Effective ground acceleration and ground velocity of Kobe earthquake is higher than other earthquakes. The earthquake effective ground acceleration and ground speed of which are the lowest is observed in Anza earthquake. Accordingly, it is seen that the smallest displacement and stress values are obtained from Anza earthquake. The largest displacement values in the structure occur at the top of the tower.

The structure was examined under the effect of wind speed of 25 m / sec and displacement and stress values were obtained. The wind pressure was applied at the maximum value in the wind direction and the wind pressure values changed according to the angle change. Displacement values were determined as angular and dependent on height. According to the values obtained depending on the height, the greatest value is at the top part. It is seen that the values changed according to the angular change in the values of the displacement obtained as angular.

Conflicts of Interest

The authors state that there is no conflict of interests.

References

- [1] Özgan K., Karakaş A. İ., Daloğlu A.T., Hiperbolik soğutma kulelerinin deprem analizi, *Pamukkale Üniversitesi Müh. Bilim Dergisi*, 22(6) (2016) 433-441.
- [2] Sabouri-Ghomi S., Kharrazi M. H. K., Javidan P. Effect of stiffening rings on buckling stability of RC hyperbolic cooling towers, *Thin-walled structures*, 44 (2) (2006) 152-158.
- [3] Busch D., Harte R., Krätzig W.B., Montag U. New Natural Draft Cooling Tower of 200m of height, *J. Engineering Structures*, 24 (2002) 1509-1521.
- [4] Zhao L., Ge Y., Kareem A., Fluctuating wind pressure distribution around full-scale cooling towers, *Journal of Wind Engineering and Industrial Aerodynamics*, 165 (2017) 34-45.
- [5] Karakaş A.İ., Elastik zemine oturan kule tipi yapıların SAP 2000–OAPI kullanılarak yapısal analizi ve optimum tasarımı, PhD Thesis, Karadeniz Technical University, The Graduate School of Natural and Applied Sciences, 2017.
- [6] Karakaş A.İ., Özgan K., Daloğlu A.T., A consistent FEM-Vlasov model for hyperbolic cooling towers on layered soil under unsymmetrical wind load, *Wind and Structures*, 22(6) (2016) 617-633.
- [7] Karakaş A.I., Özgan K., Daloğlu A. T., A Parametric study for free vibration analysis of hyperbolic cooling towers on elastic foundation using consistent FEM-Vlasov model., *Arc Appl. Mech.*, 86 (2015) 869-882.
- [8] Ghomi S.S., Kharrazi M.H.K., Reinforced Concrete Column-Supported Hyperboloid Cooling Tower Stability Assessment for Seismic Loads., *ScientiaIronica*, 12(2) (2005) 241-246.
- [9] Yu Q, Gu X.L., Li Y., Lin F., Collapse Mechanism of Reinforced Concrete Superlarge Cooling Towers Subjected to Strong Winds, *J. Perform Constr. Facil.*, 31(6) (2017) 04017101.
- [10] Murali G, Vardhan C. M. V. and Reddy B.V. P. K., Response of Cooling Towers to Wind Loads, *ARPN Journal of Engineering and Applied Sciences*, 7(1) (2012) 114-120.
- [11] Greiner R., Derler P. Effect of imperfections on wind-loaded cylindrical shells, *Thin-Walled Structures*, 23 (1-4) (1995) 271-281.
- [12] Afshari, F., and Dehghanpour, H., A Review Study On Cooling Towers; Types, Performance and Application, *ALKU J. of Sci.*, Special Issue (2019) 1-10.
- [13] Asadzadeh E., Alam M., Asadzadeh,S., Dynamic response of layered hyperbolic cooling tower considering the effects of support inclinations, *Structural Engineering and Mechanics*, 50(6) (2014) 797-816.
- [14] Dehghanpour H., Afshari F.Yılmaz K., ABAQUS Modeling and Investigation of Nuclear Central Cooling Tower Reinforced by CFRP., *ALKU J. Sci.*, Special Issue (2019) 59-70.

- [15] ASCE 7-10, Minimum design loads for buildings and other structures, Reston, Virginia, American Society of Civil Engineers, (2010).
Lisans Tezi, İstanbul Teknik Üniversitesi, İstanbul, Fen Bilimleri Enstitüsü, 2015.
- [16] Almási J., Approximated determination of cooling tower dimensions, *Periodica Polytechnica Civil Engineering*, 25 (1-2) (1981).
- [17] Habibullah and Wilson, SAP 2000 User Manual, Computer Program, USA, Computers and Structures, Berkeley, (1998).
- [18] Kanbur F.A., 500 Kw Enerji Kapasiteli Bir Rüzgâr Türbinin Çelik Kule Tasarımı, Yüksek Lisans Tezi, İnşaat Mühendisliği Bölümü, İstanbul Teknik Üniversitesi, Fen Bilimleri Enstitüsü, 2014.
- [19] Özlek C., ASCE 7-10, Eurocode 1-4 Ve Ts 498 Yönetmelikleri Kullanılarak Yapılara Etki Eden Rüzgar Yüklerinin Karşılaştırılması. Yüksek Lisans Tezi, İstanbul Teknik Üniversitesi, İstanbul, Fen Bilimleri Enstitüsü, 2015.
- [20] İstanbul Yüksek Binalar Rüzgâr Yönetmeliği, İstanbul Büyükşehir Belediyesi İmar Müdürlüğü, İstanbul, Türkiye, 2009.
- [21] Eurocode 1: Action on structures-General actions, EN 1991-1-4, 2002.
- [22] Brown C.J., Nielsen J., Silos: Fundamentals of Theory, Behaviour and Design, E&FN Spon, London, 1998.
- [23] Pacific Earthquake Engineering Research (PEER) Center, PEER Strong Motion Database. Available at: <http://peer.berkeley.edu>. Retrieved March, 2021.
- [24] Clough, R.W., Penzien, J., Dynamics of Structures, New York: McGraw-Hill, (1975).
- [25] Celep, Z., Yapı dinamiği. Beta Dağıtım, 2014.



Computational analysis of optical trapping of transparent and reflecting micron-sized spherical particles

Ufuk PARALI^{1,*}

¹ KalyonPV Research and Development Center, Kalyon Güneş Teknolojileri Üretim A.Ş., 06909, Ankara / TURKEY

Abstract

In the ray-optics regime, we calculated the radial and axial force field on a micron-sized spherical particle in an optical levitation trap. The momentum change in the photon-stream path of tightly focused incident laser beam causes the calculated force field in the optical trap. The computational results for the force field are compared with the literature and a good agreement is obtained. Utilizing the benchmarked force field, the optical trapping dynamics of (i) a transparent spherical particle with continuous-wave TEM_{00} Gaussian beam and (ii) a reflecting spherical particle with continuous-wave TEM_{01}^* Laguerre-Gaussian beam under various conditions are simulated in Matlab.

Article info

History:

Received: 27.01.2020

Accepted: 20.05.2021

Keywords:

Optical trapping,
Gaussian beam,
Laguerre-Gaussian
beam,
Micron-sized particle.

1. Introduction

Trapping and precisely manipulating micron and sub-micron scale objects without interfering with a physical attachment is an interesting technical challenge. In the early 1970s, Ashkin and colleagues have reported the first applicable observation of acceleration and trapping of particles by radiation forces [1-6]. The technique opened the door to the study of the dynamics of single suspended particles, molecules, biological cells, and water droplets held in an optical levitation trap and to completely isolate these objects from their immediate surroundings [7, 8]. Thus, using radiation forces obtained by tightly focusing laser beams has become a useful tool for trapping and manipulating micrometer-sized particles in many scientific areas such as chemistry, physics and biology [2,3,9-15]. There are three different approaches for deriving the theoretical expressions for radiation forces due to laser beam exposures; (i) the electromagnetic dipole model that calculates the radiation force for particles in the Rayleigh regime where the objects are much smaller than the wavelength of the laser beam, and (ii) the ray-optics approach which has been first studied by Ashkin and applicable to the objects larger than the wavelength of the laser beam used in optical levitation trap [2,7,16-20]. Especially the single-beam gradient trap setups were originally designed for Rayleigh particles [2,5,21]. These setups are also named as optical tweezers which has been experimentally shown that they could be used for trapping and manipulating

micron-sized biological particles such as living cells and organelles within living cells [2,3,6,22]. In 2018, Ashkin won the Nobel Prize for his contributions to the optical tweezers and their application to biological systems. (iii) The third approach for the mathematical definition of the radiation force is the Lorenz-Mie model which has been used for the objects with dimensions close to the wavelength of the tightly focused laser beam utilized in optical trap setup [23]. Recently, the studies on the optical levitation of sub-micron particles are

being focused on trapping by ultrashort laser pulses [24,25] high precision nano-g acceleration sensing [26,27] manipulation of the trapped sub-micron particles and applications in optomechanics [28,29].

There are unique design requirements for an optical levitation trap setup. Especially regarding stability, loading of targets under vacuum and trapping of transparent or reflective targets, a computational tool requirement to help inform further development and experimental considerations motivate the work we present here. In this work, we focused on Ashkin's approach of ray-optics model [1-6] and computationally analysed the optical trapping of transparent and reflecting micron-sized spherical particles. This paper gives the computational results of (i) optical trapping of a transparent spherical particle with continuous-wave TEM_{00} Gaussian beam, and (ii) optical trapping of a reflecting spherical particle with continuous-wave TEM_{01}^* Laguerre-Gaussian beam under various conditions. Both the evolution of axial

*Corresponding author. e-mail address: uparali@kalyonpv.com

<http://dergipark.gov.tr/csj> ©2021 Faculty of Science, Sivas Cumhuriyet University

and radial dynamics are calculated in Matlab utilizing Velocity Verlet integrator algorithm.

The rest of this paper is organised as follows; Section 2 gives the analytical model and the simulation results for optical trapping of transparent spherical particle with TEM_{00} Gaussian beam. The benchmarking process for the developed Matlab code is explained in this part. Section 3 describes the analytical model for optical trapping of reflecting spherical particle with TEM_{01}^* Laguerre-Gaussian beam and gives the simulation results. The conclusion and the proposed future work is explained in Section 4. In Appendix, the Matlab modules developed in this study are given.

2. Optical Trapping of Transparent Micron-sized Spherical Particle with TEM_{00} Gaussian Beam

In this study, the equations for the axial and radial force fields of the ray-optics model have been utilized from Gauthier et al. [7]. We calculated and simulated the force fields on a micron-sized transparent spherical particle due to TEM_{00} Gaussian beam exposure using Matlab. In Section 2.1, the results for the benchmarking of the developed Matlab code is given. Once the force fields are obtained correctly, using Velocity Verlet algorithm in Section 2.2, we simulated the evolution of the axial position, radial position and radial velocity of the particle trapped in TEM_{00} Gaussian beam as shown in Figure 1 below.

Due to the change in the momentum of the photon-stream while passing through the transparent micron-sized spherical particle, a net force occurs on the particle as shown in Figure 1a. Here, particle has an initial radial offset with respect to the center of the Gaussian beam. Under the exposure of this force, particle departs towards the centre of the Gaussian beam. Once it reaches the center of the beam, the transverse force diminishes and only the longitudinal force in the direction of the Gaussian beam remains (see Figure 1b). Here, the transverse direction is on the radial axis and the longitudinal direction is on the propagation direction of the beam which is assumed to be on the z-dimension (see Figure 1c). Due to the viscosity effect, the transparent spherical particle will have damped oscillation in the transverse direction at the vicinity of the center of the beam as depicted in Figure 1c. Here, the comparison for the trapping of transparent and reflecting particles are also shown in Figure 1c. The difference between the trapping dynamics of transparent and reflecting spherical particle is that; while trapping a transparent spherical particle with TEM_{00} mode is possible, for trapping reflecting spherical particle TEM_{01}^* mode is needed. In order to trap a reflecting particle with TEM_{01}^* mode, the particle must be located somewhere in the 2nd and the 3rd regions of the beam. In these regions, reflecting particle will have a damped oscillation just as similar to the transparent particle having a damped oscillation under TEM_{00} mode exposure as shown in Figure 1c.

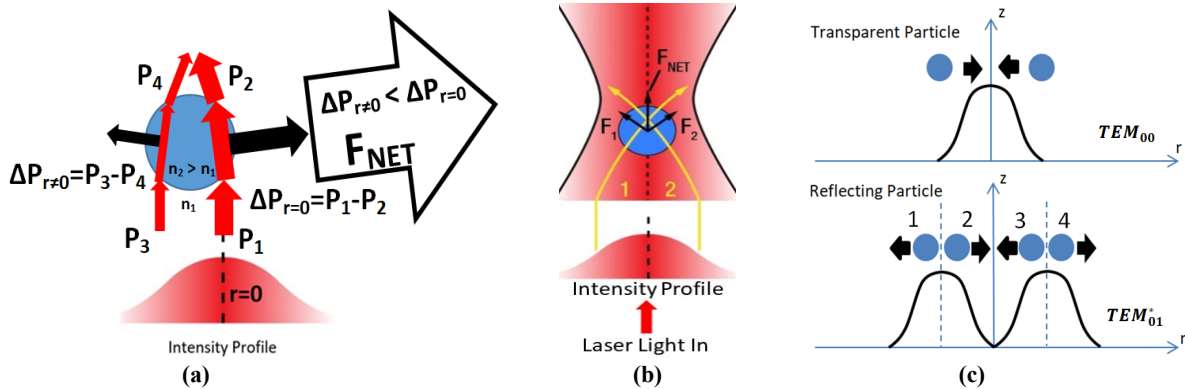


Figure 1. (a) Ray-optics approach of the photon-stream path incident upon the lower side of a transparent spherical particle with an arbitrarily given initial radial offset with respect to the center axis of the Gaussian beam. Here, $\Delta P_{r=0}$, $\Delta P_{r \neq 0}$, n_1 and n_2 denotes for the momentum change at $r=0$, momentum change at $r \neq 0$, ambient refractive index and particle refractive index, respectively. **(b)** Transparent spherical particle located in the center of a Gaussian beam [30]. **(c)** Comparison of trapping transparent spherical particle with TEM_{00} Gaussian beam and trapping reflecting spherical particle with TEM_{01}^* Laguerre-Gaussian beam. It is not possible to trap a reflecting particle with TEM_{00} mode.

For the trapping simulations of the transparent spherical particle, we must explicitly define the intensity of the TEM_{00} Gaussian beam in the numerical model. It is defined as:

$$I(\rho, z) = \frac{2P}{\pi W(z)^2} \exp\left[\frac{-2\rho^2}{W(z)^2}\right] \quad (1)$$

where; **(i)** ρ is the radial displacement of a point on the surface of the spherical particle (not the center of the

particle) (see Figures 2a and 2b). If the center of the spherical particle is displaced from the center of the beam by \bar{a} , then we can write the radial displacement (with respect to the global coordinate system) of a point on the sphere as \bar{d} . Therefore, the magnitude of the radial displacement is defined as ρ . In other words, ρ is the radial distance from the beam's axis. From Figures 2a and 2b, we can write;

$$\bar{d} = \rho \hat{d} \tag{2}$$

where $\rho = |\bar{d}|$. Here, \bar{d} is the position of points on the surface of the spherical particle with respect to the global coordinate system. Thus looking at Figures 2a and 2b, the following can be written;

$$\bar{a} = a_x \hat{a}_x + a_y \hat{a}_y + a_z \hat{a}_z \tag{3}$$

and

$$\bar{b} = x \hat{a}_x + y \hat{a}_y + z \hat{a}_z \tag{4}$$

where \bar{a} is the position of the center of the spherical particle with respect to the global coordinate system. Here, $x = R \sin \theta \cos \phi$ and $y = R \sin \theta \sin \phi$. Using \bar{a} and \bar{b} , we can write

$$\bar{d} = \bar{a} + \bar{b} \tag{5}$$

Assume $a_y = 0$ and $a_z = 0$. Thus,

$$\bar{d} = (a_x + x) \hat{a}_x + y \hat{a}_y \tag{6}$$

and

$$\rho = |\bar{d}| \rightarrow \rho = \sqrt{\bar{d} \cdot \bar{d}}, \tag{7}$$

$$\rho = (a_x^2 + 2a_x x + x^2 + y^2)^{1/2}. \tag{8}$$

Here, we can define ρ as:

$$\rho = [a_x^2 + 2a_x R \sin \theta \cos \phi + (R \sin \theta \cos \phi)^2 + (R \sin \theta \sin \phi)^2]^{1/2} \tag{9}$$

where $\theta \in [0, \pi/2]$ and $\phi \in [0, 2\pi]$.

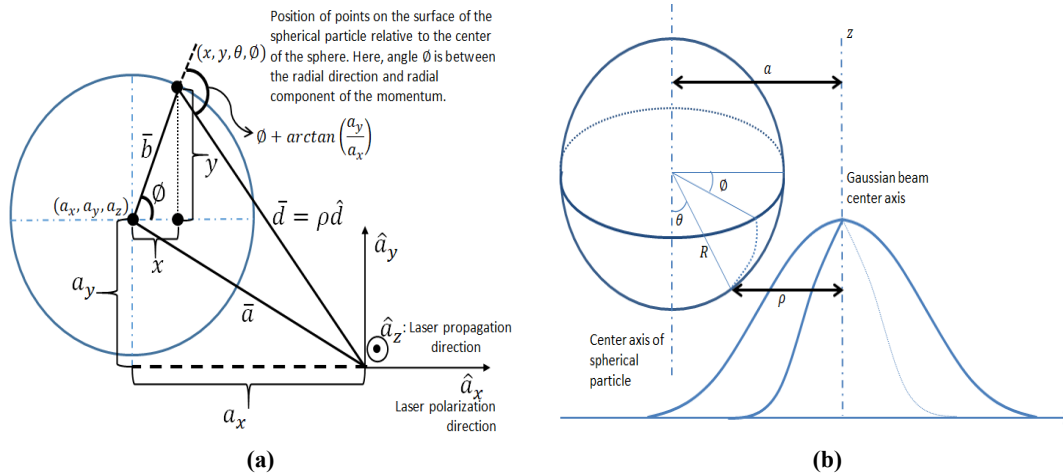


Figure 2. (a) 2-dimensional view of the spherical particle from the above. Here, the propagation of the Gaussian beam is at \hat{a}_z direction. (b) 3-dimensional view of a spherical particle under the exposure of a TEM_{00} Gaussian beam. Particle has an arbitrary initial radial offset with respect to the center axis of the beam. Here, ϕ is the polar angle, θ is the incident angle and $|\bar{a}|$ is the radial distance between the center axis of the beam and center axis of the sphere [8].

(ii) z is the vertical displacement of a point on the surface of the spherical particle (not the center of the particle). In other words, it is the distance measured along the beam's direction of propagation with $z = 0$ located at the minimum waist;

$$z = a_z - R \cos \theta \tag{10}$$

(iii) P is the total power of the laser beam and $w(z)$ is the beam width defined as:

$$w(z) = w_0 \left[1 + \left(\frac{z}{z_0} \right)^2 \right]^{1/2} \tag{11}$$

where w_0 is the beam waist and z_0 is the Rayleigh range defined as $z_0 = \pi w_0^2 / \lambda_0$ where λ_0 is the wavelength of the laser beam.

2.1. Benchmarking the Matlab code by comparing force plots

There is a vast amount of literature on optical trapping codes containing force plots of the optical gradient forces. As mentioned above, in this study, the equations for the axial and radial force fields of the ray-

optics model have been utilized from Gauthier et al. [7]. Thus, in order to validate our optical force modules of the Matlab code are functioning correctly, the Matlab outputs of our code are compared with the results of [7]. In the benchmarking simulations, three cases were tested and compared in which the radius of the spherical particle is (i) smaller than the beam waist,

(ii) equal to the beam waist and (iii) larger than the beam waist as shown in Figure 3 below. For a correct comparison of the results in the benchmarking process, the physical parameters of [7] are utilized as listed in Table 1 below. In the next section, dynamic viscosity, refractive index of the spherical particle, wavelength of the beam and the laser power are changed.

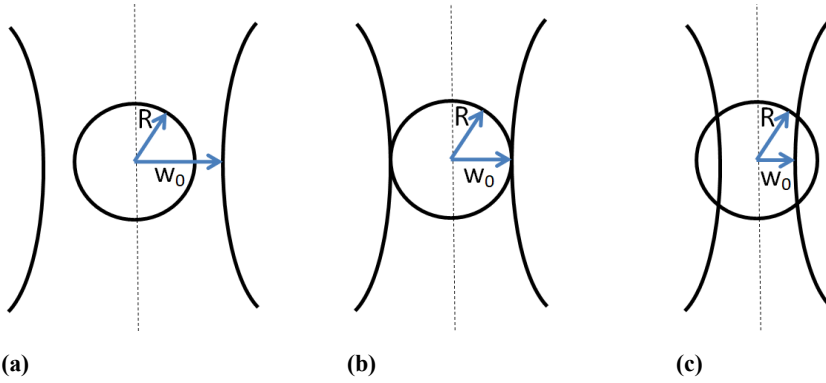


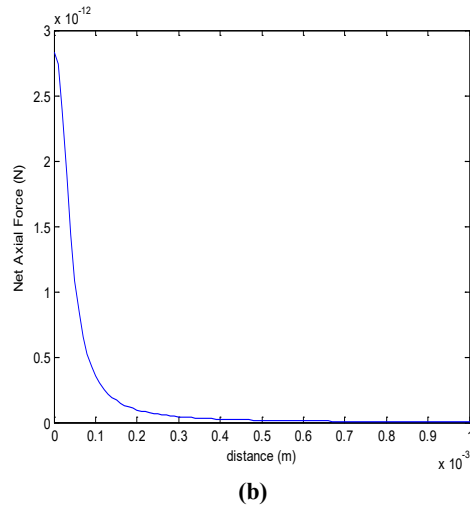
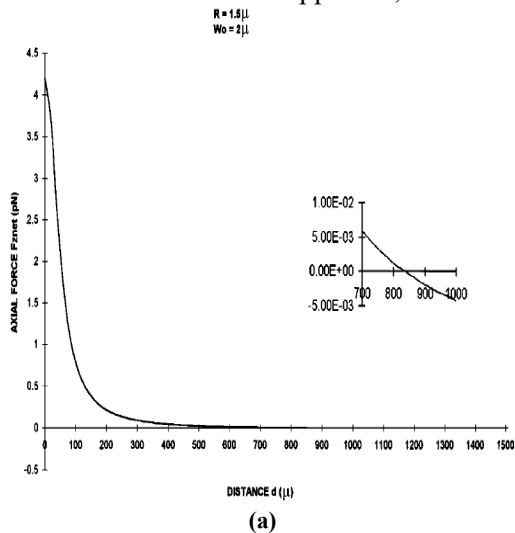
Figure 3. (a) Radius of spherical particle is smaller than laser beam waist ($R < w_0$). (b) Radius of spherical particle is equal to laser beam waist ($R = w_0$). (c) Radius of spherical particle is larger than laser beam waist ($R > w_0$).

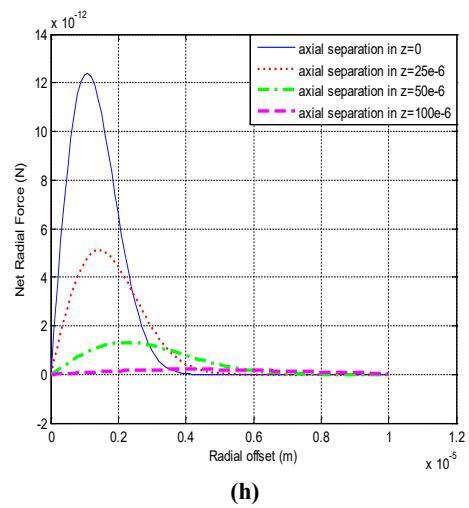
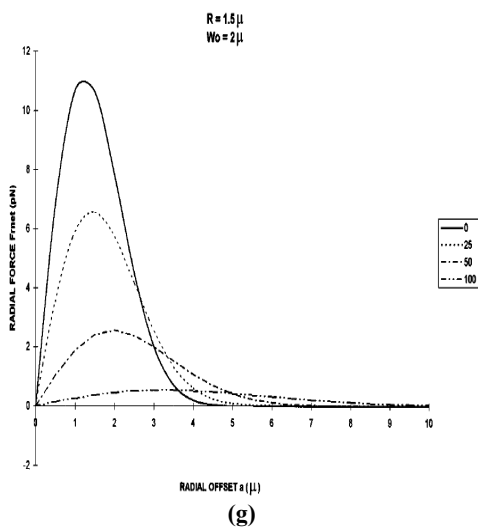
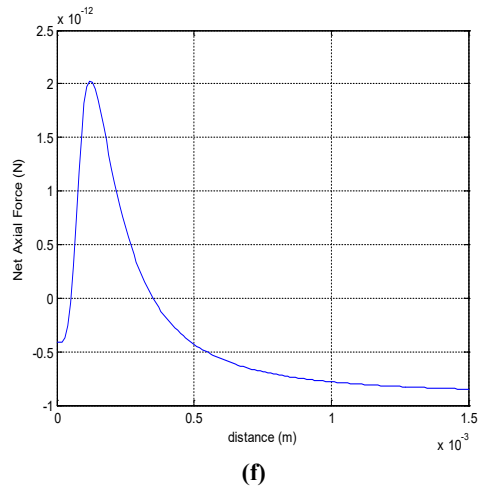
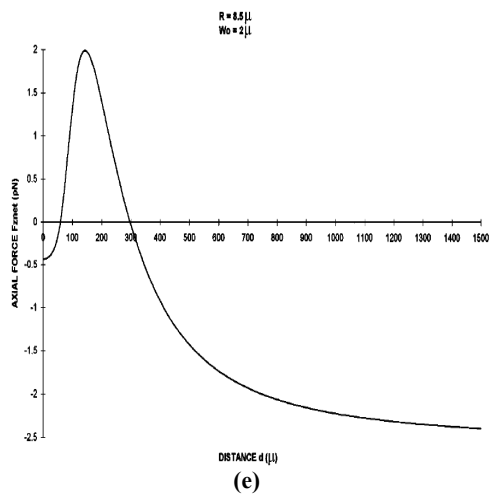
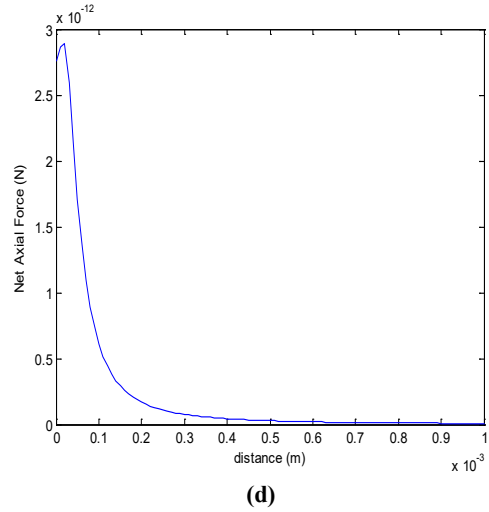
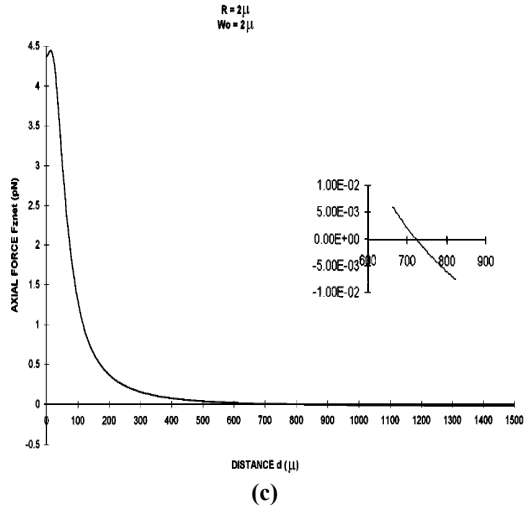
Table 1. Values of the parameters utilized from Gauthier et al. [7] for code benchmarking calculations.

Input Parameters	Value
Initial radial offset (m)	0
Initial axial offset (m)	0 (for Figures 4-b, 4-d and 4-f)
Initial axial offset (m)	(0-25-50-100) $\times 10^{-6}$ (for Figures 4-h and 4-j)
Particle radius (m)	(1.5-2-2.5) $\times 10^{-6}$
Beam waist (m) – FWHM	2×10^{-6}
Laser power (mW)	20
Density of the particle (kg/m^3)	1197.2
Medium dynamic viscosity ($\text{kgm}^{-1}\text{s}^{-1}$)	1.8×10^{-7} (=18 $\mu\text{Pa}\cdot\text{sec}$)
Laser wavelength (nm)	514
Ambient refractive index – n_1	1.333
Particle refractive index – n_2	1.5568

Looking at Figure 4 below, a good agreement is seen between the force curves acting as a sanity check against our Matlab code. In the Appendix, the related

Matlab modules implemented in the benchmarking calculations are provided.





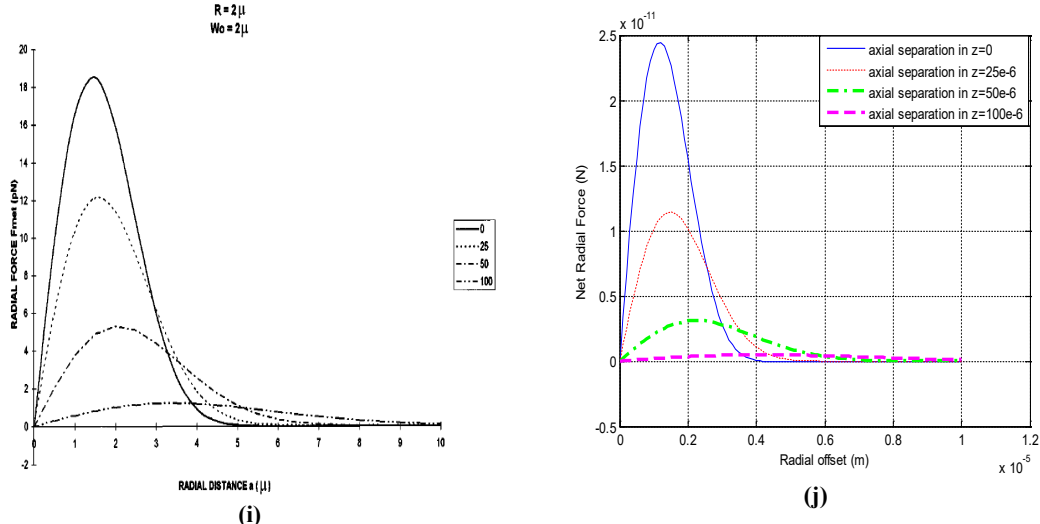


Figure 4. (a) Evolution of axial force with axial distance from beam waist for $R=1.5 \mu m$ (radius of transparent spherical particle) and $w_0=2 \mu m$ (laser beam waist) [7]. (b) Corresponding Matlab output of our code for Fig. 3-a ($R=1.5 \mu m$, $w_0=2 \mu m$). (c) Evolution of axial force with axial distance from beam waist for $R=2 \mu m$ and $w_0=2 \mu m$ [7]. (d) Corresponding Matlab output of our code for Fig. 3-c ($R=2 \mu m$, $w_0=2 \mu m$). (e) Evolution of axial force with axial distance from beam waist for $R=8.5 \mu m$ and $w_0=2 \mu m$ [7]. (f) Corresponding Matlab output of our code for Fig. 3-e ($R=8.5 \mu m$, $w_0=2 \mu m$). (g) Evolution of radial force with radial distance from beam axis for $R=1.5 \mu m$ and $w_0=2 \mu m$ [7]. (h) Corresponding Matlab output of our code for Fig. 3-g ($R=1.5 \mu m$, $w_0=2 \mu m$). (i) Evolution of radial force with radial distance from beam axis for $R=2 \mu m$ and $w_0=2 \mu m$ [7]. (j) Corresponding Matlab output of our code for Fig. 3-i ($R=2 \mu m$, $w_0=2 \mu m$).

2.2. Simulation results for optical trapping of transparent spherical micro-particle

Once the credibility of the code was established proving the force fields are being calculated properly, as the next step we move forward to investigate the dynamics of the transparent spherical particle under TEM_{00} Gaussian beam exposure. Thus, in order to understand the evolution of the axial and radial dynamics of the particle in the optical trap, we utilized the Velocity Verlet (VV) algorithm in side the code. It is a popular integrator giving precisely the velocity and the position of the particle at the same time t in a three-stage calculation [31]:

$$V\left(t_0 + \frac{\Delta t}{2}\right) = V(t_0) + \frac{\Delta t}{2} \frac{F(r(t_0), t_0)}{m} \quad (12)$$

$$r(t_0 + \Delta t) = r(t_0) + \Delta t V\left(t_0 + \frac{\Delta t}{2}\right) \quad (13)$$

$$V(t_0 + \Delta t) = V\left(t_0 + \frac{\Delta t}{2}\right) + \frac{\Delta t}{2} \frac{F(r(t_0 + \Delta t), t_0 + \Delta t)}{m} \quad (14)$$

Here, F is the force field (Lorentz force) on the particle. It must be noted that F is being calculated twice in the VV algorithm. The first evaluation of F is at the initial time and position of the particle (see Eq. 12). The second evaluation of F is at the next position of the particle after the time-step Δt (see Eq. 14) [31].

In the simulations, we utilized the following values for the given parameters in Table 2 below:

Table 2. Values of the parameters used in the simulations of optical trapping dynamics of transparent spherical particle.

Input Parameters	Value
Initial radial offset (m)	1×10^{-6}
Initial axial offset (m)	-5×10^{-3}
Initial axial velocity (ms^{-1})	5.0
Particle radius (m)	5×10^{-6}
Beam waist (m) – FWHM	4×10^{-6}
Laser power (mW)	200
Density of the particle (kg/m^3)	2500
Medium dynamic viscosity ($kgm^{-1}s^{-1}$)	1.82×10^{-6}
Laser wavelength (nm)	532
Simulation step size (sec) – Δt	5×10^{-5}
Ambient refractive index – n_1	1.0
Particle refractive index – n_2	1.52

The simulation results for the evolution of the axial and radial trajectories of the transparent spherical particle in the optical trap are given in Figure 5 below. In the Appendix, the related Matlab modules implemented for these simulations are provided. For a proper experimental design of an optical trap, it is vital to understand the axial and radial dynamics of a particle located in the optical trap. Thus having a computational tool providing the evolution of particle trajectory is extremely beneficial for the experimentalists working in this research field.

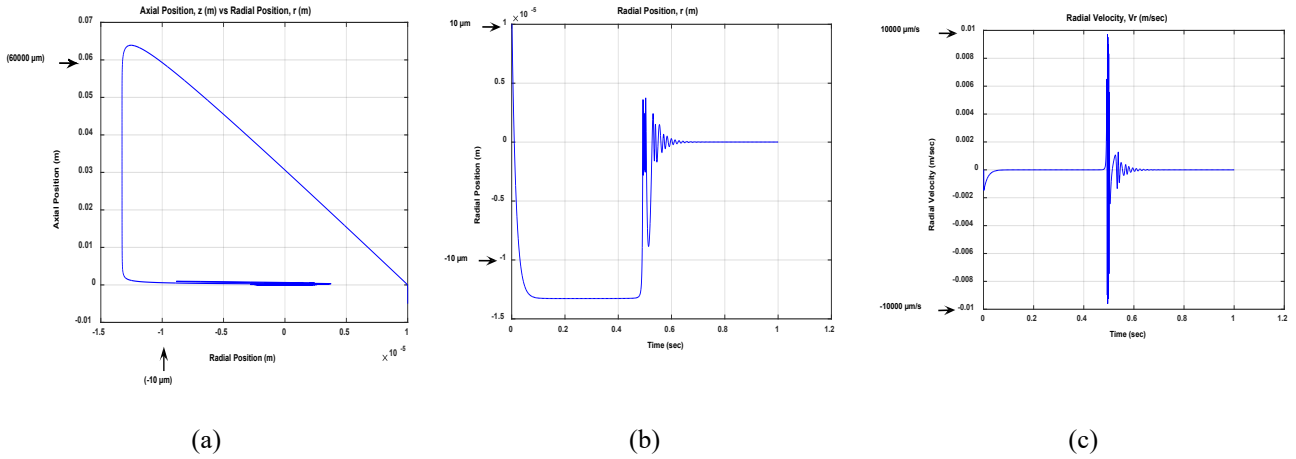


Figure 5. (a) Radial vs axial trajectory of the particle under TEM_{00} beam exposure in the optical trap. (b) Temporal evolution of the damped oscillation of the particle at the vicinity of the center axis of the TEM_{00} laser beam. (c) Temporal evolution of the radial velocity of the particle in the optical trap.

3. Optical Trapping Of A Reflecting Particle Under TEM_{01}^* Laguerre-Gaussian Beam

As explained in Section 2, different than trapping a transparent particle with a TEM_{00} beam, we need TEM_{01}^* Laguerre-Gaussian beam for trapping a

reflecting spherical particle. In this section, first the derivation of the intensity expression of Laguerre-Gaussian donut beam in terms of total beam power is discussed. Laguerre-Gaussian beams are the higher-order Gaussian beams in cylindrical coordinates [32,33]:

$$E_{p,l}(\rho, \theta, z) = \frac{A_{p,l}}{w(z)} \left(\frac{\sqrt{2}\rho}{w(z)}\right)^l L_p^l \left(\frac{2\rho^2}{w(z)}\right) \exp\left(\frac{-\rho^2}{w(z)^2}\right) \exp\left(\frac{ik\rho^2}{2R(z)}\right) \exp(i[l\theta - \varphi(z)]) \quad (15)$$

where $\rho = (x^2 + y^2)^{1/2}$, $\theta = \tan^{-1}(y/x)$, $w(z)$ is the beam width defined same as the Gaussian beam width, L_p^l is the associated Laguerre polynomial of radial order p and azimuthal order l and $A_{p,l}$ is the constant term for normalizing the beam equation [34]:

$$A_{p=0,l=1} = \sqrt{\frac{2}{\pi}}, \quad (21)$$

and

$$L_0^1 \left(\frac{2\rho^2}{w(z)}\right) = 1 \text{ where } L_0^l(x)=1. \quad (22)$$

$$A_{p,l} = p! \left(\frac{2}{\pi p!(|l|+p)!}\right)^{1/2}. \quad (16)$$

Using Eqs. 21 and 22 in Eq. 19, we can get:

Here, if $l \neq 0$ and $p = 0$, then the beams have a characteristic single-ringed donut. The radius of donut is proportional to $l^{1/2}$. Thus, $LG_0^1|_{(p=0,l=1)} = TEM_{01}^*$ [33-35]. For LG_p^l mode, the amplitude expression can be defined from Eq. 15 as below [32,33,35]:

$$I_{LG_0^1} = \frac{c\varepsilon_0}{2} \left[\frac{\sqrt{2/\pi}}{w(z)} \left(\frac{\sqrt{2}\rho}{w(z)}\right) \exp\left(\frac{-\rho^2}{w(z)^2}\right) \right]^2, \quad (23)$$

$$E_{o,p,l}(\rho, \theta, z) = \frac{A_{p,l}}{w(z)} \left(\frac{\sqrt{2}\rho}{w(z)}\right)^l L_p^l \left(\frac{2\rho^2}{w(z)}\right) \exp\left(\frac{-\rho^2}{w(z)^2}\right) \quad (17)$$

$$I_{LG_0^1} = (2c\varepsilon_0) \left[\frac{1}{\pi w(z)^4} \rho^2 \exp\left(\frac{-2\rho^2}{w(z)^2}\right) \right]. \quad (24)$$

Using Eq. 17, the intensity expression of the donut mode can be derived [35]:

The total optical power carried by the beam is the integral of the optical intensity over a transverse plane as $P = \int_0^\infty I(\rho, z) 2\pi\rho d\rho$ [34,35].

$$I_{LG_0^1} = \frac{c\varepsilon_0}{2} (E_{o,p=0,l=1})^2, \quad (18)$$

Thus using Eq. 24, the total power can be written as [33-35]:

$$I_{LG_0^1} = \frac{c\varepsilon_0}{2} \left[\frac{A_{p=0,l=1}}{w(z)} \left(\frac{\sqrt{2}\rho}{w(z)}\right) L_0^1 \left(\frac{2\rho^2}{w(z)}\right) \exp\left(\frac{-\rho^2}{w(z)^2}\right) \right]^2 \quad (19)$$

where

$$A_{p=0,l=1} = \left[p! \left(\frac{2}{\pi p!(|l|+p)!}\right)^{1/2} \right]_{p=0,l=1}, \quad (20)$$

$$P = \frac{2c\varepsilon_0}{\pi w(z)^4} \int_0^\infty \rho^2 \exp\left(\frac{-2\rho^2}{w(z)^2}\right) 2\pi\rho d\rho, \quad (25)$$

$$P = \frac{4c\varepsilon_0}{w(z)^4} \int_0^\infty \rho^3 \exp\left(\frac{-2\rho^2}{w(z)^2}\right) d\rho. \quad (26)$$

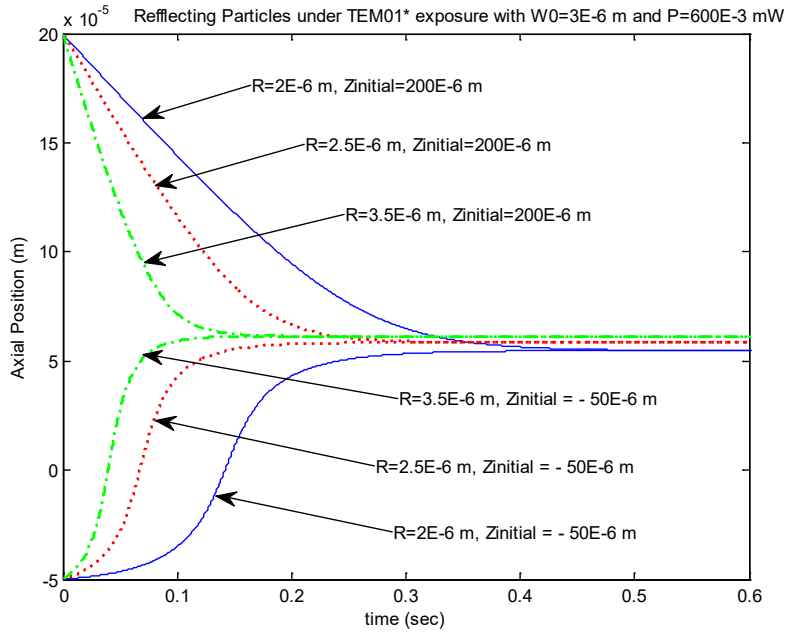


Figure 6. The axial stabilization of the particles with different radius (R) values and initial axial positions (Zinitial).

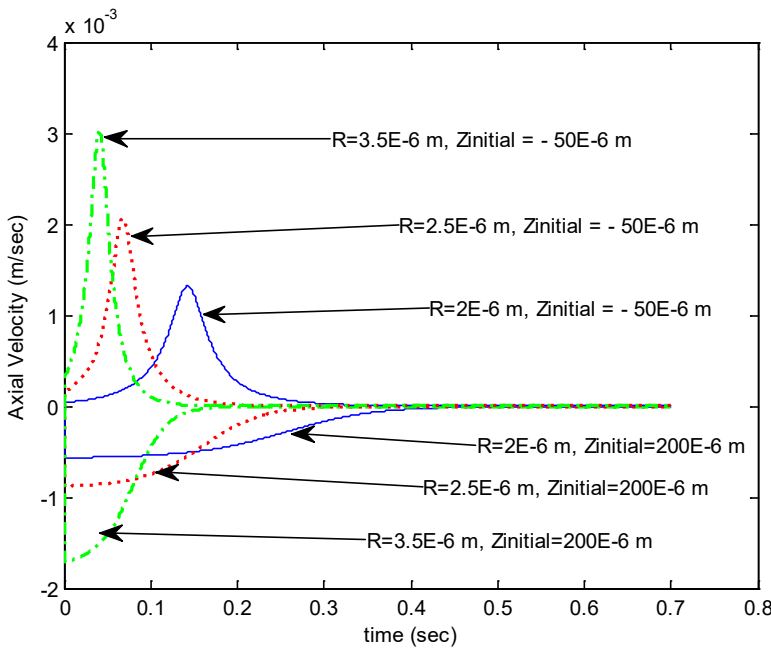


Figure 7. The axial velocity of the particles with different radius (R) values and initial axial positions (Zinitial).

4. Conclusion and Future Work

The momentum change in the photon-stream path of incident laser beam causes radiation force field. Using this radiation force field for trapping and manipulating micron-sized particles by tightly focusing laser beams in an optical trap has become a useful tool for many recent research areas. Due to the unique design requirements in an optical trap experiment, a computational tool is required for a better setup development. In this work, using Ashkin’s approach of

ray-optics model, we computationally analysed the optical levitation trapping of transparent and reflecting micron-sized spherical particles. We calculated the radiation force field using continuous-wave TEM_{00} Gaussian and TEM_{01}^* Laguerre-Gaussian laser beams for the optical trapping of transparent and reflecting particles, respectively. Utilizing Velocity Verlet algorithm, evolution of optical levitation trap dynamics are analysed in Matlab. As a future challenging work,

we aim to focus on analytical modelling and simulation of optical trapping of micron-sized metamaterials having negative index of refraction.

Appendix

A.1. Matlab code for the benchmarking process and optical trapping simulations of the transparent spherical micro-particle

This section gives the Matlab functions developed for both benchmarking process and optical trap

simulations. Figure 8 below gives the geometric model of the photon-stream path of the incident beam on a transparent spherical particle where the refractive index of the particle is greater than the refractive index of the ambient. During calculating the force field on the particle, we took into consideration the momentum change due to the 1st reflected & transmitted beams and 2nd reflected & transmitted beams in this ray-optics model.

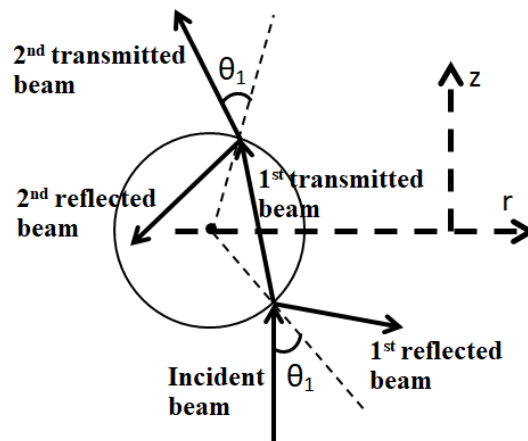


Figure 8. Reflected and transmitted ray-optics model of a transparent spherical particle under the exposure of a laser beam. The force due to the momentum change with respect to the 1st reflected & transmitted beams and 2nd reflected & transmitted beams are calculated in the given Matlab modules below. Using the calculated force-fields, the trap dynamics of the particle is simulated.

```
function f=forceAxial()
% Written by Ufuk Paralı
% This function calculates (within the geometrical
optics regime) the total axial force
% on a transparent spherical particle in the optical trap
due to the 1st reflected and
% 1st transmitted photon-stream paths and 2nd
reflected and 2nd transmitted photon-
% stream paths of a continuous-wave TEM00
Gaussian laser beam.
global az
global ax
global R
global W0
global P
global n0
global ns
global lambda0
ax=0; % Initial radial offset of particle from center axis
of laser beam
R=2e-6; % Radius of spherical particle
W0=1.5e-6; % Beam waist
P=20e-3; % Laser power
n0=1.333; % Refractive index of ambient
ns=1.5468; % Refractive index of transparent spherical
particle
lambda0=514e-9; % Laser wavelength - m
density=1000; % Particle density - kg/m^3
m=density*(4/3)*pi*R^3; % mass of the spherical
particle - kg
g=9.8; % m/s^2
ForceWeight=m*g;
counter=1; % counter initialization

for az=0:1e-5:5e-3
    posAxial(counter)=az; % Axial position of the
particle in the trap
    % Axial force due to the 1st reflected photon-stream
path

    ForceOneRZ=dblquad(@forceOneReflectedZ,0,2*pi,
0,pi/2);

    % Axial force due to the 1st transmitted photon-
stream path

    ForceOneTZ=dblquad(@forceOneTransmittedZ,0,2*pi,
0,pi/2);

    % Axial force due to the 2nd reflected photon-
stream path
```

```

ForceTwoRZ=dblquad(@forceTwoReflectedZ,0,2*pi
,0,pi/2);

    % Axial force due to 2nd transmitted photon-stream
path

ForceTwoTZ=dblquad(@forceTwoTransmittedZ,0,2*
pi,0,pi/2);

    % Total axial force on the particle

ForceAxial(counter)=ForceOneRZ+ForceOneTZ+For
ceTwoRZ+ForceTwoTZ-
    ForceWeight;
    counter=counter+1;
end
plot(posAxial,ForceAxial)
grid on
return

function f=forceRadial()
% Written by Ufuk Paralı
% This function calculates (within the geometrical
optics regime) the total radial force
% on a transparent spherical particle in the optical trap
due to the 1st reflected and
% 1st transmitted photon-stream paths and 2nd
reflected and 2nd transmitted photon-
% stream paths of a continuous-wave TEM00
Gaussian laser beam.
global az
global ax
global R
global W0
global P
global n0
global ns
global lambda0
az=0; % Initial axial offset of the particle in the trap
R=2e-6; % Radius of spherical particle
W0=1.5e-6; % Beam waist
P=20e-3; % Laser power
n0=1.333; % Refractive index of ambient
ns=1.5468; % Refractive index of transparent spherical
particle
lambda0=514e-9; % Laser wavelength - m
counter=1; % counter initialization
for ax=0:1e-7:10e-6;
    posRadial(counter)=ax; % Radial position of the
particle in the trap
    % Radial force due to the 1st reflected photon-
stream path
    ForceOneRR=-
dblquad(@forceOneReflectedR,0,2*pi,0,pi/2);

    % Radial force due to the 1st transmitted photon-
stream path
    ForceOneTR=-
dblquad(@forceOneTransmittedR,0,2*pi,0,pi/2);

    % Radial force due to the 2nd reflected photon-
stream path
    ForceTwoRR=-
dblquad(@forceTwoReflectedR,0,2*pi,0,pi/2);

    % Radial force due to the 2nd transmitted photon-
stream path
    ForceTwoTR=-
dblquad(@forceTwoTransmittedR,0,2*pi,0,pi/2);

    % Total radial force on the particle

ForceRadial(counter)=ForceOneRR+ForceOneTR+F
orceTwoRR+ForceTwoTR;
    counter=counter+1;
end
plot(posRadial,ForceRadial)
grid on
return
function f=opticalTrapDynamics()
% Written by Ufuk Paralı
% This function calculates (within the geometrical
optics regime) the optical trap
% dynamics of a transparent spherical particle due to
the 1st reflected and
% 1st transmitted photon-stream paths and 2nd
reflected and 2nd transmitted photon-
% stream paths of a continuous-wave TEM00
Gaussian laser beam.
% (see Figure 5 in the text)
global az
global ax
global R
global W0
global P
global n0
global ns
global lambda0
az=-5e-3; % Initial axial position of particle
ax=1e-6; % Initial radial offset of particle from center
axis of laser beam
R=5e-6; % Radius of transparent spherical particle
W0=4e-6; % Beam waist
P=200e-3; % Laser power
n0=1.0; % Refractive index of ambient
ns=1.52; % Refractive index of transparent spherical
particle
lambda0=532e-9; % Laser wavelength - m
velAxialinit=5; % Initial axial velocity - m/sec

```

```

velRadialinit=0; % Initial radial velocity - m/sec
finaltime=0.0005; % Simulation duration - sec
dt=0.00005; % Simulation time step
density=2500; % Particle density - kg/m^3
m=density*(4/3)*pi*R^3; % mass of the spherical
particle - kg
g=9.8; % m/s^2
ForceWeight=m*g;
eta=1.82e-6; % Medium dynamic viscosity – kg/m.sec
drag=6*3.14*eta; % drag due to viscosity
k=drag*R; % Spring constant due to drag
timeArrayCommon=zeros(1,(finaltime/dt)+2);
accelerationArrayAxial=zeros(1,(finaltime/dt)+2);
positionArrayAxial=zeros(1,(finaltime/dt)+2);
velocityArrayAxial=zeros(1,(finaltime/dt)+2);
accelerationArrayRadial=zeros(1,(finaltime/dt)+2);
positionArrayRadial=zeros(1,(finaltime/dt)+2);
velocityArrayRadial=zeros(1,(finaltime/dt)+2);
counterCommon=1; % counter initialization
positionArrayAxial(counterCommon)=az;
positionArrayRadial(counterCommon)=ax;
velocityArrayAxial(counterCommon)=velAxialinit;
velocityArrayRadial(counterCommon)=velRadialinit;
tic; % Simulation start time
for timeCommon=0:dt:finaltime
    timeCommon

    ForceOneRZ=dblquad(@forceOneReflectedZ,0,2*pi,
0,pi/2);

    ForceOneTZ=dblquad(@forceOneTransmittedZ,0,2*
pi,0,pi/2);

    ForceTwoRZ=dblquad(@forceTwoReflectedZ,0,2*pi
,0,pi/2);

    ForceTwoTZ=dblquad(@forceTwoTransmittedZ,0,2*
pi,0,pi/2);

    ForceOneRR=dblquad(@forceOneReflectedR,0,2*pi,
0,pi/2);

    ForceOneTR=dblquad(@forceOneTransmittedR,0,2*
pi,0,pi/2);

    ForceTwoRR=dblquad(@forceTwoReflectedR,0,2*pi
,0,pi/2);

    ForceTwoTR=dblquad(@forceTwoTransmittedR,0,2
*pi,0,pi/2);
    ForceDragAxial=-
k*velocityArrayAxial(counterCommon); %Dragforce
in axial direction

    ForceDragRadial=-
k*velocityArrayRadial(counterCommon);%Dragforce
radial direction

    ForceAxialNet=ForceOneRZ+ForceOneTZ+ForceTw
oRZ+ForceTwoTZ+ForceDragAxial-
    ForceWeight;

    if (positionArrayRadial(counterCommon)==0)
        ForceRadialNet=ForceDragRadial;
    else

    ForceRadialNet=ForceOneRR+ForceOneTR+ForceT
woRR+ForceTwoTR+
        ForceDragRadial;
    end
    % Beginning of Velocity Verlet Algorithm

    accelerationArrayAxial(counterCommon)=ForceAxia
lNet/m;

    accelerationArrayRadial(counterCommon)=ForceRad
ialNet/m;

    VelAxialHalfTimeStep=velocityArrayAxial(counte
rCommon)+0.5*
        accelerationArrayAxial(counterCommon)*dt;

    positionArrayAxial(counterCommon+1)=positionArr
ayAxial(counterCommon)+
        VelAxialHalfTimeStep*dt;

    VelRadialHalfTimeStep=velocityArrayRadial(counte
rCommon)+0.5*
        accelerationArrayRadial(counterCommon)*dt;

    positionArrayRadial(counterCommon+1)=positionAr
rayRadial(counterCommon)+
        1*VelRadialHalfTimeStep*dt;

    az=positionArrayAxial(counterCommon+1);
    ax=positionArrayRadial(counterCommon+1);

    ForceOneRZ=dblquad(@forceOneReflectedZ,0,2*pi,
0,pi/2);

    ForceOneTZ=dblquad(@forceOneTransmittedZ,0,2*
pi,0,pi/2);

    ForceTwoRZ=dblquad(@forceTwoReflectedZ,0,2*pi
,0,pi/2);

```

```

ForceTwoTZ=dblquad(@forceTwoTransmittedZ,0,2*
pi,0,pi/2);

ForceOneRR=dblquad(@forceOneReflectedR,0,2*pi,
0,pi/2);

ForceOneTR=dblquad(@forceOneTransmittedR,0,2*
pi,0,pi/2);

ForceTwoRR=dblquad(@forceTwoReflectedR,0,2*pi
,0,pi/2);

ForceTwoTR=dblquad(@forceTwoTransmittedR,0,2
*pi,0,pi/2);
    ForceDragAxial=-k*VelAxialHalfTimeStep;
    ForceDragRadial=-k*VelRadialHalfTimeStep;

ForceAxialNet=ForceOneRZ+ForceOneTZ+ForceTw
oRZ+ForceTwoTZ+
    ForceDragAxial-ForceWeight;

    if (positionArrayRadial(counterCommon+1)==0)
        ForceRadialNet=ForceDragRadial;
    else

ForceRadialNet=ForceOneRR+ForceOneTR+ForceT
woRR+ForceTwoTR+
    ForceDragRadial;
    end

accelerationArrayAxial(counterCommon+1)=ForceA
xialNet/m;

accelerationArrayRadial(counterCommon+1)=ForceR
adialNet/m;

velocityArrayAxial(counterCommon+1)=VelAxialHa
lfTimeStep+0.5*
    accelerationArrayAxial(counterCommon+1)*dt;

velocityArrayRadial(counterCommon+1)=VelRadial
HalfTimeStep+0.5*
    accelerationArrayRadial(counterCommon+1)*dt;
    % End of Velocity Verlet Algorithm
    counterCommon=counterCommon+1;
end
toc; % Simulation end time
timeArrayCommon(counterCommon)=timeCommon
+dt;

figure,plot(positionArrayRadial,positionArrayAxial),
xlabel('Radial Position (m)'),
ylabel('Axial Position (m)'),title('Axial Position, z (m)
vs Radial Position, r (m)');

figure,plot(timeArrayCommon,positionArrayRadial),
xlabel('Time (sec)'),
ylabel('Radial Position (m)'),title('Radial Position, r
(m)');

figure,plot(timeArrayCommon,velocityArrayRadial),
xlabel('Time (sec)'),
ylabel('Radial Velocity (m/sec)'),title('Radial Velocity,
Vr (m/sec)');
return

function Ints=Intensity(ro,z)
% Written by Ufuk Paralı
% This function calculates the intensity of TEM00
Gaussian beam.
global W0
global P
global lambda0
z0=(pi*W0*W0)/lambda0; % Rayleigh range
Wz2=(W0^2)*(1+((z)/z0).^2); % Square of beam
width – (square of Eq. 11 in the text)
Ints=(2*P./(pi*(Wz2))).*exp(-2*(ro.^2)./(Wz2)); %
Intensity – see Eq. 1 in the text
return

function r1square=refCoefSquare(theta1,theta2)
% Written by Ufuk Paralı
% This function calculates the power reflectance
coefficient
% See Eq. 9 of Gauthier et al. [7].
global n0
global ns
global lambda0
r1square=((n0*ns)^2*((cos(theta1)).^2-
(cos(theta2)).^2).^2)/((n0*ns)*((cos(theta1)).^2+
(cos(theta2)).^2)+((n0^2)+(ns^2))*(cos(theta1).*cos(t
heta2))).^2;
return

function ro2=rho2(phi,theta1,ax)
% Written by Ufuk Paralı
% This function calculates the radial distance ( $\rho$ ) of a
point
% on the surface of the spherical particle from the
beam's axis.
global R
% Radial distance – see Eq. 9 in the text
ro2=((ax)^2+(2*(ax)*R*sin(theta1).*cos(phi))+(R*si
n(theta1)).^2+(R*sin(theta1)).^2).^0.5);
return

```

```

function s=Snell(T1)
% Written by Ufuk Paralı
% Snell function
global n0
global ns
s=asin((n0/ns)*sin(T1));
return

function F1rz=forceOneReflectedZ(phi,theta1)
% Written by Ufuk Paralı
% This function calculates the axial force due to the 1st
reflected
% photon-stream path (see Figure 8) given by Eq. 22
of Gauthier et al. [7].
global az
global ax
global R
global n0
global ns
global lambda0
c=3e8;
theta2=Snell(theta1);
rhoTheta1Phi=rho2(phi,theta1,ax);
z=az-R*cos(theta1);
F1rz=(0.5/c)*n0*(1+cos(2*theta1)).*Intensity(rhoTheta1Phi,z).*refCoefSquare(theta1,theta2)*(R^2).*sin(2*theta1);
return

function F1tz=forceOneTransmittedZ(phi,theta1)
% Written by Ufuk Paralı
% This function calculates the axial force due to the 1st
transmitted
% photon-stream path (see Figure 8) given by Eq. 23
of Gauthier et al. [7].
global az
global ax
global R
global n0
global ns
global lambda0
c=3e8;
theta2=Snell(theta1);
rhoTheta1Phi=rho2(phi,theta1,ax);
z=az-R*cos(theta1);
F1tz=(0.5/c)*(n0-ns*cos(theta1-theta2)).*Intensity(rhoTheta1Phi,z).*(1-refCoefSquare(theta1,theta2))*(R^2).*sin(2*theta1);
return

function F2rz=forceTwoReflectedZ(phi,theta1)
% Written by Ufuk Paralı
% This function calculates the axial force due to the 2nd
reflected
% photon-stream path (see Figure 8) given by Eq. 24
of Gauthier et al. [7].
global az
global ax
global R
global n0
global ns
global lambda0
c=3e8;
theta2=Snell(theta1);
rhoTheta1Phi=rho2(phi,theta1,ax);
z=az-R*cos(theta1);
F2rz=(0.5/c)*ns*(cos(theta1-theta2)+cos(3*theta2-theta1)).*Intensity(rhoTheta1Phi,z).*(1-refCoefSquare(theta1,theta2)).*refCoefSquare(theta1,theta2)*(R^2).*sin(2*theta1);
return

function F2tz=forceTwoTransmittedZ(phi,theta1)
% Written by Ufuk Paralı
% This function calculates the axial force due to the 2nd
transmitted
% photon-stream path (see Figure 8) given by Eq. 25
of Gauthier et al. [7].
global az
global ax
global R
global n0
global ns
global lambda0
c=3e8;
theta2=Snell(theta1);
rhoTheta1Phi=rho2(phi,theta1,ax);
z=az-R*cos(theta1);
F2tz=(0.5/c)*(ns*cos(theta1-theta2)-n0*cos(2*(theta1-theta2))).*Intensity(rhoTheta1Phi,z).*(1-refCoefSquare(theta1,theta2)).*(1-refCoefSquare(theta1,theta2))*(R^2).*sin(2*theta1);
return

function F1rr=forceOneReflectedR(phi,theta1)
% Written by Ufuk Paralı
% This function calculates the radial force due to the 1st
reflected
% photon-stream path (see Figure 8) given by Eq. 34
of Gauthier et al. [7].
global ax
global az
global R
global n0
global ns

```

```

global lambda0
c=3e8; % Speed of light - m/sec
z=az-R*cos(theta1); % Vertical displacement of a
point – see Eq. 10 in the text
theta2=Snell(theta1);
rhoTheta1Phi=rho2(phi,theta1,ax);
F1rr=-
(n0*0.5/c)*Intensity(rhoTheta1Phi,z).*sin(2*theta1).*
refCoefSquare(theta1,theta2)*(R^2).*cos(phi).*sin(2*
theta1);
return

```

```

function F1tr=forceOneTransmittedR(phi,theta1)
% Written by Ufuk Paralı
% This function calculates the radial force due to the
1st transmitted
% photon-stream path (see Figure 8) given by Eq. 35
of Gauthier et al. [7].

```

```

global ax
global az
global R
global n0
global ns
global lambda0
c=3e8;
z=az-R*cos(theta1);
theta2=Snell(theta1);
rhoTheta1Phi=rho2(phi,theta1,ax);
F1tr=(ns*0.5/c)*Intensity(rhoTheta1Phi,z).*sin(theta1
-theta2).*
(1-
refCoefSquare(theta1,theta2))*(R^2).*cos(phi).*sin(2
*theta1);
return

```

```

function F2rr=forceTwoReflectedR(phi,theta1)
% Written by Ufuk Paralı
% This function calculates the radial force due to the
2nd reflected
% photon-stream path (see Figure 8) given by Eq. 36
of Gauthier et al. [7].

```

```

global ax
global az
global R
global n0
global ns
global lambda0
c=3e8;
z=az-R*cos(theta1);
theta2=Snell(theta1);
rhoTheta1Phi=rho2(phi,theta1,ax);

```

```

F2rr=(ns*0.5/c)*Intensity(rhoTheta1Phi,z).*sin(3*th
eta2-theta1)-sin(theta1-theta2))*
(1-
refCoefSquare(theta1,theta2))*refCoefSquare(theta1,t
heta2)*
(R^2).*cos(phi).*sin(2*theta1);
return

```

```

function F2tr=forceTwoTransmittedR(phi,theta1)
% Written by Ufuk Paralı
% This function calculates the radial force due to the
2nd transmitted
% photon-stream path (see Figure 8) given by Eq. 37
of Gauthier et al. [7].

```

```

global ax
global az
global R
global n0
global ns
global lambda0
c=3e8;
z=az-R*cos(theta1);
theta2=Snell(theta1);
rhoTheta1Phi=rho2(phi,theta1,ax);
F2tr=(0.5/c)*Intensity(rhoTheta1Phi,z).*n0*sin(2*(t
heta1-theta2))-ns*
sin(theta1-theta2)).*(1-
refCoefSquare(theta1,theta2)).*
(1-
refCoefSquare(theta1,theta2))*(R^2).*cos(phi).*sin(2
*theta1);
return

```

Acknowledgements

U.P. would like to acknowledge support from TÜBİTAK 1059B191401929 (The Scientific and Technological Research Council of Turkey) for his visit to Physics Department of Imperial College London. We would like to gratefully thank Prof. Roland A. Smith, Dr. Samuel Giltrap and Dr. Chris J. Price for their many helpful comments and suggestions for the numerical modeling and simulation of the optical levitation trap.

Conflicts of Interest

The authors state that they did not have conflict of interests.

References

- [1] Ashkin A., Acceleration and trapping of particles by radiation pressure, *Phys. Rev.*, 24(4) (1970) 156-159.
- [2] Ashkin A., Dziedzic J. M., Stability of optical levitation by radiation pressure, *Applied Physics Letters*, 24(12) (1974) 586-588.
- [3] Ashkin A., Dziedzic J.M., Optical levitation in high vacuum, *Applied Physics Letters*, 28(6) (1976) 333-335.
- [4] Ashkin A., Dziedzic J.M., Optical Trapping and Manipulation of Viruses and Bacteria, *Science*, 235-4795 (1987) 1517-1520.
- [5] Ashkin A., Dziedzic J.M., Yamane T., Optical trapping and manipulation of single cells using infrared laser beams, *Nature*, 330-6150 (1987) 769-771.
- [6] Ashkin A., Forces of a single-beam gradient laser trap on a dielectric sphere in the ray optics regime, *Biophysical Journal*, 61(2) (1992) 569-582.
- [7] Gauthier R.C., Wallace S., Optical levitation of spheres: analytical development and numerical computations of the force equations, *J. Opt. Soc. Am. B.*, 12(9) (1995) 1680-1686.
- [8] Kim S.B., Kim S.S., Radiation forces on spheres in loosely focused Gaussian beam: ray-optics regime, *J. Opt. Soc. Am. B.*, 23(5) (2006) 897-903.
- [9] Ganic D., Gan X., Gu M., Optical trapping force with annular and doughnut laser beams based on vectorial diffraction, *Optics Express*, 13(4) (2005) 1260-1265.
- [10] Price C.J., Donnelly T.D., Giltrap S., Stuart N.H., Parker S., Patankar S., Lowe H.F., Drew D., Gumbrell E.T. and Smith R.A., An in-vacuo optical levitation trap for high-intensity laser interaction experiments with isolated microtargets, *Review of Scientific Instruments*, 86(3) (2015) 033502.
- [11] Sakai K. and Noda S., Optical trapping of metal particles in doughnut-shaped beam emitted by photonic-crystal laser, *Electronics Letters*, 43(2) (2007) 107-108.
- [12] Zhang Y., Li Y., Qi J., Cui G., Liu H., Chen J., Zhao L., Xu J., Sun Q., Influence of absorption on optical trapping force of spherical particles in a focused Gaussian beam, *J. Opt. A: Pure Appl. Opt.*, 10(8) (2008) 085001.
- [13] Shahabadi, V., Ebrahim M., Daryoush A., Optimized anti-reflection core-shell microspheres for enhanced optical trapping by structured light beams, *Scientific Reports*, 11(1) (2021) 1-10.
- [14] Kalume, A., Chuji W., Yong-Le P., Optical-Trapping Laser Techniques for Characterizing Airborne Aerosol Particles and Its Application in Chemical Aerosol Study, *Micromachines*, 12(4) (2021) 466.
- [15] Komoto S. et al., Optical Trapping of Polystyrene Nanoparticles on Black Silicon: Implications for Trapping and Studying Bacteria and Viruses, *ACS Applied Nano Materials*, 3(10) (2020) 9831-9841.
- [16] Barton J.P., Alexander D., Schaub S.A., Theoretical determination of net radiation force and torque for a spherical particle illuminated by a focused laser beam, *J. Appl. Phys.*, 66(10) (1989) 4594-4602.
- [17] Kim J.S., Lee S.S., Scattering of laser beams and the optical potential well for a homogeneous sphere, *J. Opt. Soc. Am.*, 73(3) (1983) 303-312.
- [18] Barton J.P., Alexander D., S. A. Schaub, Internal and near-surface electromagnetic fields for a spherical particle irradiated by a focused laser beam, *J. Appl. Phys.*, 64(4) (1988) 1632-1639.
- [19] Ashkin A., Forces of a single-beam gradient laser trap on a dielectric sphere in the ray optics regime, *Biophys. J.*, 61(2) (1992) 569-582.
- [20] Chang S., Lee S.S., Optical torque exerted on a homogeneous sphere levitated in circularly polarized fundamental-mode laser beam, *J. Opt. Soc. Am. B.*, 2(11) (1985) 1853-1860.
- [21] Ashkin A., Trapping of atoms by resonance radiation pressure, *Phys. Rev. Lett.*, 40(12) (1978) 729-732.
- [22] Ashkin A, Dziedzic J.M., Bjorkholm J.E., Chu S., Observation of a single-beam gradient force optical trap for dielectric particles, *Optics Lett.*, 11(5) (1986) 288-290.
- [23] Zhang Y., Li Y., Cui G., Liu H., Chen J., Xu J., Sun Q., Transverse optical trapping of spherical particle with strong absorption in a focused Gaussian beam, *Proc. of SPIE*, 6832-68320K-1 (2008).
- [24] Usman A., Ching W., Masuhara H., Optical trapping of nanoparticles by ultrashort laser pulse, *Science Progress*, 96(1) (2013) 1-18.
- [25] Choudhary D., Mossa A., Jadhav M., Cecconi C., Bio-molecular Applications of Recent

- Developments in Optical Tweezers, *Biomolecules*, 9(1) (2019) 23.
- [26] Hempston D., Vovrosh J., Winstone G., Rashid M., Ulbricht H., Force sensing with an optically levitated charged nanoparticle, *Appl. Phys. Lett.*, 111(13) (2017) 133111.
- [27] Monteiro F., Ghosh S., Fine A.G., Moore D.C., Optical levitation of 10 nanogram spheres with nano-g acceleration sensitivity, *Phys. Rev. A.*, 96(6) (2017) 063841.
- [28] Kim J., Shin J.H., Stable, Free-space Optical Trapping and Manipulation of Sub-micron Particles in an Integrated Microfluidic Chip, *Scientific Reports*, 6 (2016) 33842.
- [29] Vovrosh J., Rashid M., Hempston D., Bateman J., Paternostro M., H. Ulbricht, Parametric Feedback Cooling of Levitated Optomechanics in a Parabolic Mirror Trap, *J. Opt. Soc. Am. B.*, 34(7) (2017) 1421-1428.
- [30] Thorlabs Optical Tweezers Microscope System, Trapping Theory & Force Analysis. Available at: https://www.thorlabs.com/newgrouppage9.cfm?objectgroup_id=12442. Retrieved 2020.
- [31] Wilson K.R., Swope W, Andersen H., Berens P., A computer simulation method for the calculation of equilibrium constants for the formation of physical clusters of molecules: Application to small water clusters, *J. Chem. Phys.*, 76(1) (1982) 637-649.
- [32] Saleh B.E.A., Teich M.C., Fundamentals of Photonics, 2nd ed., New Jersey: John Wiley & Sons, (2007)
- [33] Galvez E.J., Gaussian beams in the optics course, *Am. J. Phys.*, 74(4) (2006) 355-361.
- [34] Beijersbergen M.W., Allen L., Veen H.O., Woerdman J.P., Astigmatic laser mode converters and transfer of orbital angular momentum, *Optics Communications*, 96(3) (1993) 123-132.
- [35] Zauderer E., Complex argument Hermite-Gaussian and Laguerre-Gaussian beams, *J. Opt. Soc. Am. A.*, 3(4) (1986) 465-469.
- [36] Gradshteyn I.S., Ryzhik I.M., Table of Integrals, Series and Products, 8th ed., California: Elsevier, (2015)



Optimization of process parameters in coagulation of landfill leachate by $Al_2(SO_4)_3$ and PACI

Emine CAN-GÜVEN^{1,*} 

¹Yıldız Technical University, Department of Environmental Engineering, İstanbul/ TURKEY

Abstract

In this study, landfill leachate treatment by coagulation and optimization of process parameters were aimed. Alum ($Al_2(SO_4)_3$) and Poly Aluminum Chloride (PACI) were used as coagulants to remove total suspended solids (TSS) from landfill leachate, and coagulant dose, reaction time, and pH were optimized as process variables. The Box-Behnken, one of the response surface methodology designs, was used in modeling the coagulation process. The R^2 values were very high (>95%) for TSS removal and the models were sufficiently in good agreement with experimental results. The TSS removal efficiencies in coagulation processes with alum and PACI under optimum process conditions determined by the model were 62.1% and 76.4%, respectively while the experimental values under optimum operating conditions were 60.8% and 75.1% in alum and PACI coagulation processes, respectively. According to the results of the study, both coagulation processes were effective in TSS removal from landfill leachate, and response surface methodology is a useful tool for optimizing the treatment parameters. The removal efficiency of the coagulation process conducted with PACI is higher than that of the alum process. Thus, it can be inferred that PACI is more effective under optimized conditions in this study.

Article info

History:

Received: 26.01.2021

Accepted: 20.05.2021

Keywords:

Alum,
Box Behnken design,
Chemical coagulation
Optimization,
Poly Aluminum,
Chloride.

1. Introduction

Landfilling is the most widely used method in the disposal of solid wastes all over the world. Leachate, which has a high pollution load, occurs through rainwater in landfill storage areas [1]. The content of the leachate has a highly variable structure in terms of pollutant types and concentrations. Leachate contains a high quantity of organic matter, ammonia, heavy metals, and a wide variety of toxic contaminants [2]. Factors affecting the leachate characteristics are the type and compression ratio of the waste, amount of precipitation, hydrology, design, and operating conditions of the site. Besides, the age of the landfill is one of the most affecting parameters of leachate content. Leachate that occurred approximately 10 years after storage has a stable characteristic and is characterized by very strong organic content, high ammonia concentration, and low biodegradability [3]. This leachate is stated as mature leachate and its biological treatment is almost impossible and poses a risk to the environment [3–5]. Efficient treatment of leachate should be conducted to lower the high concentrations of pollutants to acceptable levels for final discharge. Physicochemical methods are

preferred for leachate with a low biochemical oxygen demand/chemical oxygen demand (BOD/COD) ratio and high concentrations of toxic components [6, 7].

Landfill leachate treatment is one of the most important issues in solid waste landfilling. Treatment of leachate with a complex structure is very difficult with a single method. Besides, an appropriate treatment method should be applied to the leachate, which has varying characteristics depending on the stored waste, compression degree, age, and design of storage area, season, and climate conditions. In the selection of the leachate treatment system, parameters such as the characteristics of the leachate, the storage age, discharge criteria, the efficiency of the treatment system, the leachate flow rate, investment and operating costs, the need for qualified personnel, and the land requirement should be considered [8]. Biological methods (aerobic, anaerobic), physicochemical methods (chemical treatment, oxidation, adsorption, reverse osmosis, ammonia stripping) and combined systems are among the processes applied in the treatment of leachate. The biological treatment process is usually the first step of this combination and is followed by physicochemical methods [9].

*Corresponding author. e-mail address: ecguven@yildiz.edu.tr

<http://dergipark.gov.tr/csj> ©2021 Faculty of Science, Sivas Cumhuriyet University

Coagulation and flocculation are some of the most preferred physicochemical methods in leachate treatment [10–12]. Coagulation is a comparatively simple and controllable pre-treatment or post-treatment method in leachate treatment to provide more biodegradability [13]. However, optimization of process parameters such as pH, optimum coagulant dosage, reaction time, and selection of appropriate coagulant is essential in the design of a coagulation process in leachate treatment [14]. The traditional one factor at a time optimization method is both time and energy-consuming approach. It is also a lack of the evaluation of interactions between variables. Thus, a better alternative such as response surface methodology (RSM) comes into prominence. Box-Behnken experimental design is one of the RSM designs and it provides to determine the interactive effects of variables and their impact factor [15]. Among the RSM designs, the minimum number of experimental sets is provided by applying the Box-Behnken design [16, 17].

The purpose of this study was to investigate total suspended solids (TSS) removal from landfill leachate by chemical coagulation. In this study, the efficiency of two different coagulants, namely, Alum and Poly Aluminum Chloride were investigated. The effects of independent variables on the coagulation processes were optimized by the Box-Behnken experimental design, which provides optimum process conditions with a minimum number of the experimental run. In the coagulation processes conducted with Alum and Poly Aluminum Chloride, optimum values of initial pH, coagulant dose, and treatment time were determined for TSS removal from landfill leachate.

2. Materials and Methods

2.1. Landfill leachate

The landfill leachate samples used in the study were obtained in October 2020 from Odayeri Landfill Leachate Treatment Plant, İstanbul, Turkey. Wastewater samples were stored at + 4 °C to prevent biological activity.

Table 1. Characteristics of landfill leachate used in this study

Parameter	Value
pH	8.09±0.015
COD, mg/L	13100±26.7
Conductivity, mS/cm	37.4±0.15
TSS, mg/L	1110±47.5

The wastewater characterization before and after treatment was carried out using methods recommended by APHA [18]. The characteristics of landfill leachate used in this study are given in Table 1.

2.2. Experimental design and analytical methods

The solutions (10 g/L) of alum ($\text{Al}_2(\text{SO}_4)_3$) and poly aluminum chloride (PACl) were prepared and used in the experiments. After pH adjustment with 6 N H_2SO_4 and 6 N NaOH solutions, 100 ml of wastewater sample was put into a 250 ml beaker and placed in the Jar-test apparatus. Then the coagulant dosage determined by the model was added to the wastewater. The samples were rapidly mixed at 200 rpm for 2 minutes. Slow mixing was conducted at the desired value of the model at 45 rpm. The samples were settled for 30 minutes after the reaction time ended. The supernatant was separated for TSS analysis. TSS analysis was carried out according to standard methods and the removal efficiency was calculated according to Equation 1.

$$RE = \frac{C_0 - C}{C_0} \times 100 \quad (1)$$

where C_0 and C (mg/L) were the TSS of the samples before and after the treatments, respectively.

Response surface methodology provides the optimization of process variables with a minimum number of experiments. In this study, the Box-Behnken design of RSM was applied for the modeling of the coagulation process for TSS removal in landfill leachate using alum and PACl coagulants. Design Expert 11.1.0.1 software was used for modeling process variables. The levels and ranges of the independent variables are given in Table 2.

15 experimental sets for each coagulant were conducted with three levels of RSM and three independent variables. The ranges for pH, dosage, and reaction time were 6-10, 1-5 g/L, and 15-45 minutes, respectively. The ranges and coded values were determined from the results of the preliminary studies.

Table 2. The levels and ranges of the variables of the experimental design matrix

Coagulant	Factor	Levels and ranges		
		-1	0	1
Alum	A-pH	6	8	10
	B-Dosage, g/L	1	3	5
	C-Reaction Time, min.	15	30	45
Coagulant	Factor	Levels and ranges		
		-1	0	1
PACl	A-pH	6	8	10
	B-Dosage, mg/L	1	3	5
	C-Reaction Time, min.	15	30	45

Equation 2 shows the interaction among the independent variables (pH, dosage, and reaction time) and the response (TSS removal). In this equation, Y is the response (TSS removal); b_0 is the constant; b_i , b_{ii} , and b_{ij} are the coefficients of the linear, quadratic, and interaction effects respectively; X_i and X_j are the independent variables; n is the number of independent variables, and e is the prediction error.

$$Y = b_0 + \sum_{j=1}^n b_j x_j + \sum_{j=1}^n b_{jj} x_j^2 + \sum_i \sum_{<j=2}^n b_{ij} x_i x_j + e_i \tag{2}$$

3. Results and Discussion

The regression equations for TSS removal by coagulation using alum and PACl are presented in Equations 3 and 4, respectively. The signs of the coefficients can be used to identify the synergistic (positive sign) and antagonistic (negative sign) effects

of the variables. In the coagulation process conducted with alum, TSS removal efficiency increases with the increase in dosage and reaction time while it decreases with increasing pH value. Besides, in the coagulation process conducted with PACl, TSS removal efficiency increases with the increased pH, dosage, and reaction time.

Alum;

$$\begin{aligned} \text{TSS removal, \%} &= +43.87 - 3.90 \cdot A + 17.76 \cdot B + 3.50 \cdot C - 0.47 \cdot A \cdot B - 0.8869 \cdot A \cdot C + 1.55 \cdot B \\ &\cdot C + 5.86 \cdot A^2 - 13.1 \cdot B + 2.39 \cdot C^2 \end{aligned} \tag{3}$$

PACl;

$$\begin{aligned} \text{TSS removal, \%} &= +65.69 + 3.58 \cdot A + 11.22 \cdot B + 6.99 \cdot C + 1.71 \cdot A \cdot B + 1.22 \cdot A \cdot C - 1.05 \cdot B \\ &\cdot C - 5.73 \cdot A^2 - 3.50 \cdot B^2 - 5.19 \cdot C^2 \end{aligned} \tag{4}$$

In the coagulation process applied for TSS removal from leachate, 15 sets of analyzes were performed for each coagulant. Experimental design matrix obtained

for coagulation processes, removal efficiencies estimated using the model, and obtained from the experiments are given in Table 3. The TSS removal

efficiencies from landfill leachate vary between 13.6-60.6% in the alum coagulation process while it ranged from 35.7 % to 76.2% in the PACl coagulation process.

Normal probability plots drawn to check the normality of the data are given in Figure 1a and Figure 1c for alum and PACl, respectively.

Table 3. Box-Behnken Design matrix with predicted and actual TSS removal ratios in coagulation process with alum and PACl coagulants

Run	Factors			TSS removal with Alum, %		TSS removal with PACl, %	
	pH	Alum or PACl dosage, g/l	Reaction time, min	Actual	Predicted	Actual	Predicted
1	6	1	30	19.8	22.3	45.0	43.4
2	10	1	30	13.6	15.5	47.7	47.1
3	6	5	30	60.6	58.8	61.8	62.4
4	10	5	30	52.5	50.0	71.3	72.9
5	6	3	15	52.3	51.6	45.8	45.4
6	10	3	15	45.6	45.6	51.6	50.2
7	6	3	45	60.4	60.4	55.5	56.9
8	10	3	45	50.2	50.8	66.2	66.6
9	8	1	15	15.3	13.5	35.7	37.7
10	8	5	15	43.4	45.9	62.5	62.3
11	8	1	45	19.8	17.4	53.6	53.8
12	8	5	45	54.1	55.9	76.2	74.2
13	8	3	30	46.7	43.9	64.2	65.7
14	8	3	30	43.4	43.9	68.5	65.7
15	8	3	30	41.5	43.9	64.4	65.7

Whether the residuals show a normal distribution can be interpreted according to the straightness of the line on the plot [19–21]. The data show the normal distribution and the normality assumption was confirmed as can be seen from the figures. The removal efficiencies obtained from the experimental studies

under the conditions determined by the model versus (vs.) the removal efficiencies estimated by the model are shown in Figures 1b and 1d for alum and PACl, respectively. The obtained lines and high R² values show the agreement between the experimental and estimated removal efficiencies.

Table 4. ANOVA results for TSS removal by alum coagulant

	Sum of Squares	Df	Mean Square	f	p
Model	3595.51	9	399.50	37.81	0.0005
A-pH	121.46	1	121.46	11.50	0.0194
B-Dosage, g/L	2522.64	1	2522.64	238.78	< 0.0001
C-Reaction time, min	97.77	1	97.77	9.25	0.0287
AB	0.8838	1	0.8838	0.0837	0.7840
AC	3.15	1	3.15	0.2978	0.6087
BC	9.55	1	9.55	0.9038	0.3854
A ²	126.82	1	126.82	12.00	0.0180
B ²	633.39	1	633.39	59.95	0.0006
C ²	21.01	1	21.01	1.99	0.2175
Residual	52.82	5	10.56		
Lack of Fit	38.98	3	12.99	1.88	0.3662
Pure error	13.85	2	6.92		
Cor Total	3648.33	14			
Std. Dev.	3.25				
Mean	41.28				
C.V. %	7.87				
R ²	0.9855				
Adjusted R ²	0.9595				
Adeq Precision	17.6895				

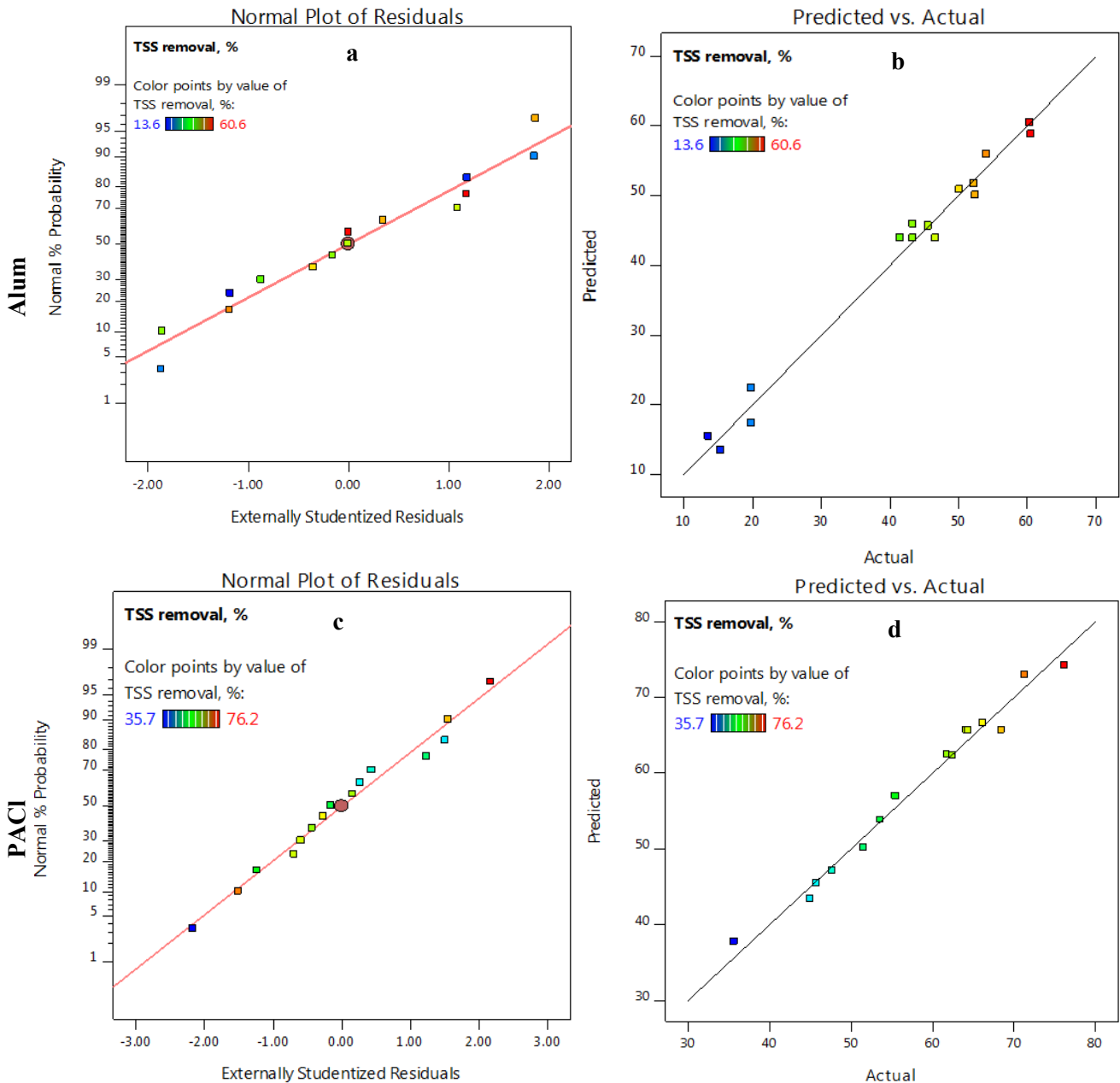


Figure 1. Normal probability plots and predicted versus actual values plottings for alum and PACl coagulants

The model was statistically evaluated by conducting the Analysis of Variance (ANOVA) analysis. The ANOVA results of the coagulation process conducted with alum and PACl are shown in Table 4 and Table 5, respectively. Various coefficients are calculated and evaluated to check the model suitability. The coefficients used for this purpose are coefficient of determination (R^2), adjusted R^2 , the coefficient of variance (CV), and adequate precision (AP). The conformity of the model is checked by R^2 values and closeness to 1 indicates stronger and better predictive models. The R^2 values obtained for TSS removals indicate that most data variations can be explained by the model. Besides, the Adjusted R^2 values close to the

R^2 indicate the significance of the model. Adjusted R^2 values in this study were found close to R^2 for both coagulants (Table 4 and Table 5). The CV value is an effective parameter used in evaluating the reproducibility feature of the model, and the CV value is required to be lower than 10 to interpret the model reproducible [22, 23]. Adequate precision value, which is used to measure the signal-to-noise ratio, is required to be 4 and above [24, 25]. As a result of the variance analysis, CV values obtained for TSS removal with both coagulants were found to be lower than 10 and adequate precision values were higher than four. These ratios also show that the models are reproducible for both processes.

Table 5. ANOVA results for TSS removal by PACl coagulant

	Sum of Squares	Df	Mean Square	f	p
Model	1754.97	9	195.00	31.62	0.0007
A-pH	102.67	1	102.67	16.65	0.0095
B-Dosage, g/L	1007.11	1	1007.11	163.31	< 0.0001
C-Reaction time, min	390.60	1	390.60	63.34	0.0005
AB	11.70	1	11.70	1.90	0.2269
AC	6.00	1	6.00	0.9733	0.3692
BC	4.41	1	4.41	0.7151	0.4363
A ²	121.11	1	121.11	19.64	0.0068
B ²	45.29	1	45.29	7.34	0.0423
C ²	99.35	1	99.35	16.11	0.0102
Residual	30.83	5	6.17		
Lack of Fit	19.23	3	6.41	1.10	0.5075
Pure error	11.60	2	5.80		
Cor Total	1785.80	14			
Std. Dev.	2.48				
Mean	58.00				
C.V. %	4.28				
R ²	0.9827				
Adjusted R ²	0.9517				
Adeq Precision	17.9593				

The effect of process variables on TSS removal by coagulation process is shown on 3-D plots in Figure 2. The pH value was selected between 6 and 10 in both alum and PACl coagulation processes. It was observed that the removal efficiency decreased as the pH value increased in the coagulation process carried out with alum. On the other hand, the removal efficiency increased as the pH value increased in the coagulation process conducted with PACl. The TSS removal efficiency increased with increasing coagulant dosage in both processes. The removal of pollutants in the coagulation process is explained by the charge neutralization mechanism, and the negative charges in the particles are neutralized by the addition of cationic coagulants [26]. As the age of landfill increases, the amount of negatively charged particles in the leachate increases, thus the amount of coagulant required to neutralize these particles increase [27]. The increase in TSS removal efficiency from landfill leachate in this study can be explained by this condition. In the coagulation process reaction time between 15 and 45 minutes was modeled. In both processes conducted using alum and PACl, the TSS removal efficiency was increased depending on the increase of treatment time.

The optimum values of process variables for alum and PACl coagulation processes to obtain maximum TSS removal efficiencies were determined by the models. Maximum TSS removal efficiencies were selected to

determine the optimum conditions of the independent variables. The target values of three independent variables of both processes were selected within the range and the optimum conditions are given in Table 6. For the coagulation process conducted with alum, the optimum pH was 6.47, the dosage was 4.29 g/L and the reaction time was 41.83 minutes. The optimum conditions for the PACl coagulation process were as follows: pH 9.12, dosage 4.89 g/L, and the reaction time 37.9 minutes. Under optimum conditions, the TSS removal efficiencies estimated by the model were 62.1 % and 76.4 % for alum and PACl processes, respectively. The removal efficiencies obtained from the experimental studies conducted under optimum conditions to verify the model suitability and the accuracy of the optimization method were found to be 60.8 % and 75.1 % for TSS removal in alum and PACl processes, respectively. The proximity of the removal efficiencies estimated by the model to the obtained results of experimental studies confirms the suitability and accuracy of the approach in the models. The flow rate of landfill leachate in landfilling sites is closely related to precipitation, surface run-off, and infiltration of groundwater percolating through the landfill [5]. The fluctuation in the flow rate of landfill leachate may affect the coagulation process in terms of the amount of used coagulant. Thus, the changes in flow rate should be considered in the operation of the coagulation process.

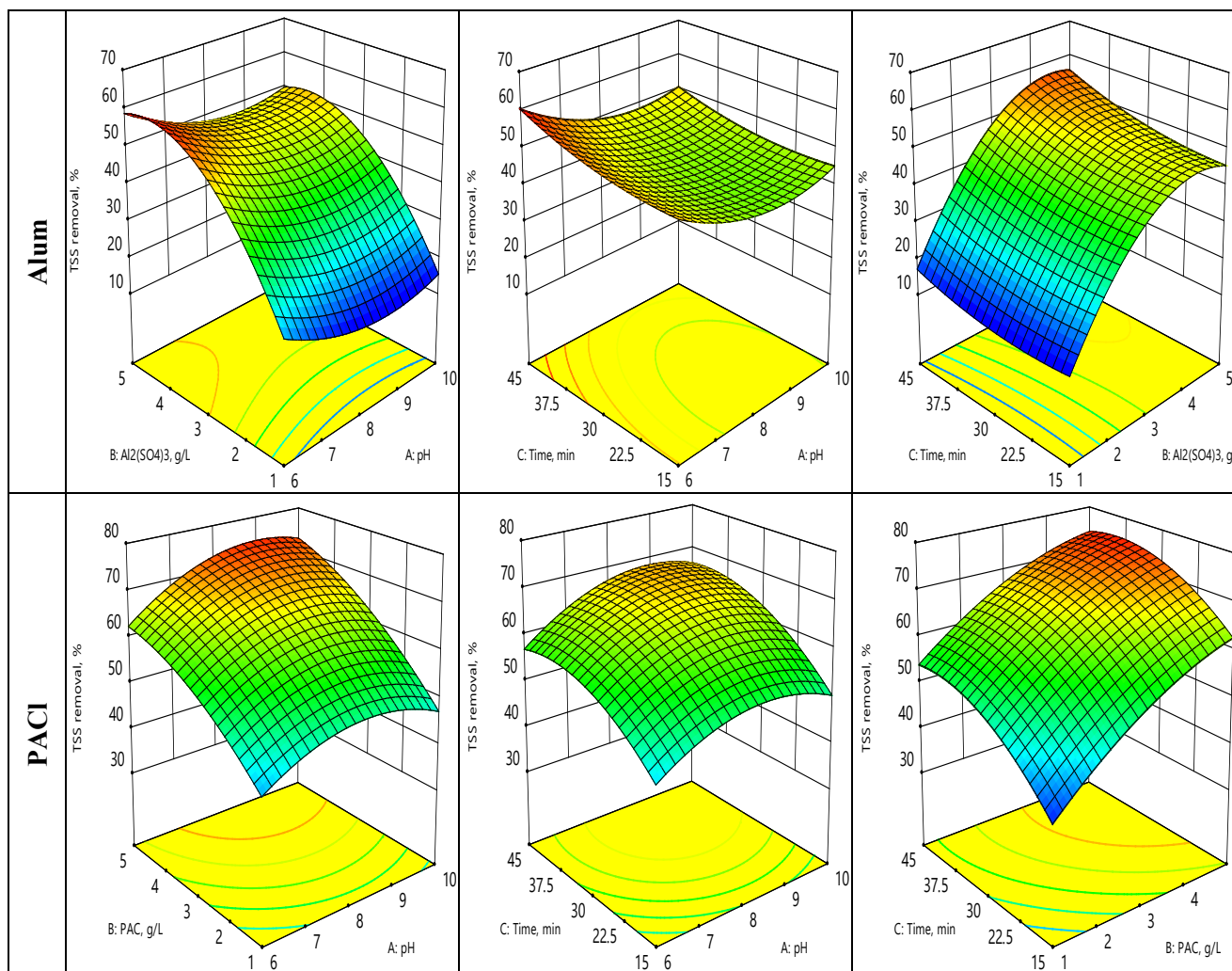


Figure 2. 3-D plots of the effects of independent variables on TSS removal with alum and PACl coagulants

Table 6. Optimum operating conditions and TSS removal efficiencies of alum and PACl

Factor	Optimum Conditions	
	Alum	PACl
pH	6.47	9.12
Reaction time, min	41.83	37.9
Dosage, g/L	4.29	4.89
Predicted removal efficiency, %	62.1	76.4
Experimental Removal Efficiency, %	60.8	75.1

3. Conclusions

This study investigated the optimization of process variables for TSS removal from landfill leachate by chemical coagulation. The Box-Behnken design was applied for modeling and optimization of the performance of the coagulation with alum and PACl coagulants. The optimum pH, reaction time, and coagulant dosage were determined to provide maximum TSS removal from leachate. The high correlation coefficient values show that the models were in good agreement with the experimental data for

both coagulation processes. According to optimum conditions, optimum pH was 6.47, the dosage was 4.29 g/L and the required reaction time was 41.83 min for the coagulation process conducted with alum. Besides, the optimum conditions in the coagulation process conducted with PACl were pH 9.12, dosage 4.89 g/L, and reaction time 37.9 minutes. The experimental TSS removal efficiencies of coagulation with alum and PACl were 60.8 % and 75.1 %, respectively. The removal efficiencies showed that both coagulation processes were effective in TSS removal from landfill leachate. Besides, the results showed that under

optimum conditions in this study PACl is more effective than alum in TSS removal from landfill leachate. As a result, coagulation can be applied as a pretreatment method for TSS removal from landfill leachate, and the response surface methodology is a useful tool for optimizing the process variables.

Acknowledgment

I would like to thank Assoc. Prof. Dr. Gamze Varank and Assoc. Prof. Dr. Senem Yazıcı Güvenç for their support and infrastructure provided.

Conflicts of interest

The author states no conflict of interests

References

- [1] Luo H., Zeng Y., Cheng Y., He D., Pan X., Recent advances in municipal landfill leachate: A review focusing on its characteristics, treatment and toxicity assessment., *Sci. Total Environ.*, 703 (2020) 135468.
- [2] Bakhshoodeh R., Alavi N., Oldham C., Santos R.M., Babaei A.A., Vymazal J., Paydary P., Constructed wetlands for landfill leachate treatment: A review, *Ecological Engineering*, 146 (2020) 105725.
- [3] Hilles A.H., Amr S.S.A., Hussein R.A., Arafa A.I., El-Sebaie O.D., Effect of persulfate and persulfate/H₂O₂ on biodegradability of an anaerobic stabilized landfill leachate, *Waste Manag.*, 44 (2015) 172-177.
- [4] Schiopu A-M., Gavrilesco M., Options for the treatment and management of municipal landfill leachate: common and specific issues, *Clean-Soil, Air, Water*, 38 (2010) 1101-1110.
- [5] Renou S., Givaudan J.G., Poulain S., Dirassouyan F., Moulin P., Landfill leachate treatment: review and opportunity, *J Hazard. Mater.*, 150(3) (2008) 468-493.
- [6] Deng Y., Englehardt J.D., Treatment of landfill leachate by the Fenton process, *Water Res.*, 40(20) (2006) 3683-3694.
- [7] Goi A., Veressinina Y., Trapido M., Fenton process for landfill leachate treatment: evaluation of biodegradability and toxicity, *J Environ. Eng.*, 136(1) (2010) 46-53.
- [8] Akkaya E., Sızıntı sularının havasız çamur yataklı reaktör ve mikrofiltrasyonlu biyoreaktör sistemi ile arıtılabilirliğinin araştırılması, PhD Thesis, Yıldız Tech University, Graduate School of Sciences, 2009.
- [9] Bohdziewicz J., Kwarciak A., The application of hybrid system UASB reactor-RO in landfill leachate treatment, *Desalination*, 222(1-3) (2008) 128-134.
- [10] Rui M.L., Daud Z., Latif A.A.A., Coagulation-flocculation in leachate treatment by using ferric chloride and alum as coagulant, *Int. J. Eng.*, 2(4) (2012) 1929-1934.
- [11] Maleki A., Zazouli M.A., Izanloo H., Rezaee R. Composting plant leachate treatment by coagulation-flocculation process, *Am. J. Agric. Environ. Sci.*, 5(5) (2009) 638-643.
- [12] Tatsi A.A., Zouboulis A.I., Matis K.A., Samaras P., Coagulation--flocculation pretreatment of sanitary landfill leachates, *Chemosphere*, 53(7) (2003) 737-744.
- [13] Liu X., Li X.M., Yang Q., Yue X., Shen T.T., Zheng W., Luo K., Sun Y.H., Zeng G.M., Landfill leachate pretreatment by coagulation-flocculation process using iron-based coagulants: Optimization by response surface methodology, *Chem Eng. J.*, 200 (2012) 39-51.
- [14] Amor C., De Torres-Socias E., Peres J.A., Maldonado M.I., Oller I., Malato S., Lucas M.S., Mature landfill leachate treatment by coagulation/flocculation combined with Fenton and solar photo-Fenton processes, *J Hazard. Mater.*, 286 (2015) 261-268.
- [15] Kaur P., Sangal V.K., Kushwaha J.P., Parametric study of electro-Fenton treatment for real textile wastewater, disposal study and its cost analysis, *Int. J Environ. Sci. Technol.*, 16(2) (2019) 801-810.
- [16] Ahmadi M., Rahmani K., Rahmani A., Rahmani H., Removal of benzotriazole by Photo-Fenton like process using nano zero-valent iron: response surface methodology with a Box-Behnken design, *Polish J Chem. Technol.*, 19(1) (2017) 104-112.
- [17] Mohadesi M., Shokri A., Treatment of oil refinery wastewater by photo-Fenton process using Box--Behnken design method: kinetic study and energy consumption, *Int. J Environ. Sci. Technol.*, 16(11) (2019) 7349-7356.
- [18] APHA, Standard Methods for Examination of Water and Wastewater, 21st ed., American Public Health Association, (2005).
- [19] Almomani F., Rahul R.B., Optimizing nutrient removal of moving bed biofilm reactor process using response surface methodology, *Bioresource technology*, 305 (2020) 123059.

- [20] Sultana N., Hossain S.Z., Alam M.S., Hashish M.M.A., Islam M.S., An experimental investigation and modeling approach of response surface methodology coupled with crow search algorithm for optimizing the properties of jute fiber reinforced concrete, *Construction and Building Materials*, 243 (2020) 118216.
- [21] Mohajeri S., Aziz H.A., Isa M.H., Zahed M.A., Adlan M.N., Statistical optimization of process parameters for landfill leachate treatment using electro-Fenton technique, *J Hazard. Mater.*, 176(1-3) (2010) 749-758.
- [22] Ciric A., Krajnc B., Heath D., Ogrinc N., Response surface methodology and artificial neural network approach for the optimization of ultrasound-assisted extraction of polyphenols from garlic, *Food and Chemical Toxicology*, 135 (2020) 110976.
- [23] Ahmadi M., Ghanbari F., Madihi-Bidgoli S., Photoperoxi-coagulation using activated carbon fiber cathode as an efficient method for benzotriazole removal from aqueous solutions: Modeling, optimization and mechanism, *J. Photochem. Photobiol. A Chem.*, 322 (2016) 85-94.
- [24] Ghafari S., Aziz H.A., Isa M.H., Zinatizadeh A.A., Application of response surface methodology (RSM) to optimize coagulation-flocculation treatment of leachate using poly-aluminum chloride (PAC) and alum, *J. Hazard. Mater.*, 163(2-3) (2009) 650-656.
- [25] Zhang H., Ran X., Wu X., Zhang D., Evaluation of electro-oxidation of biologically treated landfill leachate using response surface methodology, *J. Hazard. Mater.*, 188(1-3) (2011) 261-268.
- [26] Al-Hamadani Y.A., Yusoff M.S., Umar M., Bashir M.J., Adlan M.N., Application of psyllium husk as coagulant and coagulant aid in semi-aerobic landfill leachate treatment, *J. Hazard. Mater.*, 190(1-3) (2011) 582-587.
- [27] Zainol N.A., Aziz H.A., Ibrahim N., Treatment of kulim and kuala sepetang landfills leachates in Malaysia using poly-aluminium chloride (PACl), *Res. J. Chem. Sci.*, 3 (2013) 606X.



Investigation of deformation and element diffusion in joint interface of mild carbon steel and HCrWCI welded by friction welding

Tanju TEKER ¹ , Mustafa ÖZASLAN ^{2,*} 

¹Sivas Cumhuriyet University, Faculty of Technology, Department of Manufacturing Engineering, 58140, Sivas / TURKEY.

²Körfez Vocational and Technical Anatolian High School, 41780, Körfez, Kocaeli / TURKEY.

Abstract

In this study, continuous drive friction welding process is selected for joint dissimilar high chromium white cast iron and mild carbon steel. The microstructure, presence and diffusion of elements, deformation in interface of weld metal were analyzed by scanning electron microscopy (SEM), optical microscopy (OM), energy dispersive spectroscopy (EDS), elemental mapping and X-Ray diffraction (XRD). Elemental analysis was applied to the fractured surface after the tensile test. The rotational speed from the friction welding process parameters had a significant impact on the quality of the welded joint. Due to element diffusion at the weld interface, carbides consisting of Cr_7C_3 and $Cr_{23}C_6$ were occurred. Carbon, which is the dominant element of the diffusion process, was decisive in the emergence of the carbide layer.

Article info

History:

Received: 09.03.2021

Accepted: 15.06.2021

Keywords:

HCrWCI,
Mild carbon steel,
Friction welding,
Elemental mapping,
EDS.

1. Introduction

Basically, welding processes are divided into two groups as solid-state welding and fusion welding. In the fusion welding technique, there is a full melting in the weld interface while there is a partial melting in the solid-state welding technique. Due to metallurgical and thermal incompatibility and differences in their melting temperature, melting welding methods may be possible to join alloys by welding [1-3]. Friction welding (FW) is more preferred than other methods in combining different alloys with solid state technique. In this method, the welding interface is heated by the combined effects of the pressure and relative motion of the alloy rods to be joined. The combination of materials is achieved by the plastic deformation of the material [4-6]. It is widely used in the automotive and aerospace industrial.

FW consists of several stages. In the first stage, after the two parts touch each other, friction begins to occur on the opposite interfaces of the parts to be joined. At this stage, the peripheral speed of the moving part is kept constant and friction force is applied to form a metallurgical bond between the parts during friction. Thus, it is allowed to establish a connection by providing element transitions between the contacting parts. In the meantime, local connections occur between the contact surfaces of the parts. These local associations and separations continue as long as the

friction movement continues. At this stage, the torque value reaches its maximum value [7-9].

With the advancing engineering technology, material groups that do not have circular symmetry and rotational symmetry, hollow or solid tubular materials can be easily welded with the FW method. Ma et al. reported that the different metal connection between AISI 304 and 1045 grade can be achieved by FW. The joining conditions changed the tensile features of the joint by affecting the density of the carbides at the weld interface and the heterogeneous microstructure in the thermo-mechanically affected zone on the AISI 1040 side [10].

High chromium white cast iron (HCrWCI) has been used in various mineral drilling, leveling, processing spindles, brick molds and processing hard rocks [11, 12]. Since the carbon steels are difficult to weld with fusion welding due to their low weldability [13].

In this study, mild carbon steel and high chrome white cast iron are joined by friction welding method using various rotational speeds. The microstructure, presence and diffusion of elements, deformation in interface of weld metal were analyzed.

2. Materials and Methods

In this study, 75 mm long and 10 mm diameter, HCrWCI (3.2% C, 1.16% Si, 2.3% Mn, 27.4% Cr, 0.5% Ni, 2.3% Mo and Bal.% Fe) and mild carbon steel

*Corresponding author. e-mail address: mustafa_044@yahoo.com

(0.41%C, 0.2%Si, 0.8%Mn and Bal.%Fe) were used. The parameters used in the friction welding tests are given in Table 1.

To examine the phases formed in the samples after FW; mild carbon steel side using Nital (2% HNO₃ + 98% Ethanol) solution, HCrWCI side with Vilella solution was etched for 15-20 s. Microstructural properties and deformation, fracture surface

morphology, elemental distributions throughout the interface of weld metal were detected through scanning electron microscopy (SEM: ZEISS EVO LS10), energy dispersive spectroscopy (EDS), optical microscope (OM) and elemental mapping. Phase determinations were carried out by Rigaku X-ray diffractometer (XRD) device with CuK α radiation. After the tensile test, fracture surface elemental mapping analysis was performed.

Table 1. Parameters of the joining process made by friction welding method.

Sample	Rotational Speed (rpm/min.)	Friction Time (s)	Friction Pressure (MPa)	Forging Pressure (MPa)	Forging Time (s)
S1	1600	12	80	150	12
S2	1700	12	80	150	12
S3	1800	12	80	150	12

3. Experimental Results

3.1. Macrograph of the welded joints

The surface macro photographs of S1-S3 welded joints combined using different friction speeds (1600, 1700, 1800 rpm) are shown in Fig. 1. Welded joints without pores and cracks were obtained due to the extreme cooling rate after FW. Significant differences were detected in the quantities of flanges formed with increasing rotational speed [14]. In addition, the flashes formed in the welded joints were in the form of a bowl as stated in the literature. The high rotation speed caused a rapid warming up to high temperatures

at the interface. Due to the temperature gradient, the axial shortening and the proportion of viscous material pushed out of the interface increased. Thermal features were effective in determining which material deforms preferentially in dissimilar metal joint. If the thermal dissipation of one metal was less than the other, then the temperature would increase within a shorter distance of that part of the joint. Even if the strength of the metal with lower thermal dissipation is very high, it will show more deformation. Although a base material has almost the same properties at room temperature, it begins to lose strength faster as the temperature rises, resulting in a higher rate of flash. As the period of cycles increased, the sample lengths shortened.

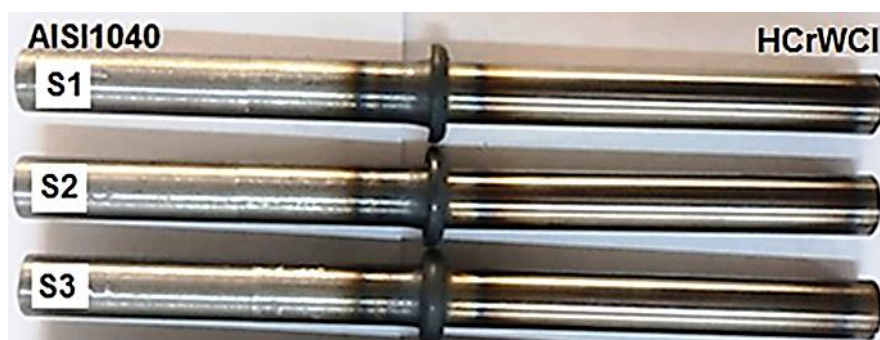


Figure 1. The surface macro photographs of S3 sample.

The view of the regions under thermomechanical interaction is given in Fig. 2. On the HCrWCI side of the welded samples, a narrower thermo-mechanically heat-affected zone was formed compared to the AISI 1040 side. During friction welding, the heat increase caused by friction started from the weld interface and progressed to the base metals. Since the HCrWCI side had a lower thermal conduction coefficient compared to the AISI 1040 side, the heat increase on the HCrWCI

side spreads less per unit time. Therefore, the thermo-mechanically heat affected zone on the AISI1040 side was larger.

3.2. Microstructure of joint interface

Optical and SEM photograph of S3 sample is given in Fig. 3. The microstructure of the joint interface generally displayed a similar appearance.

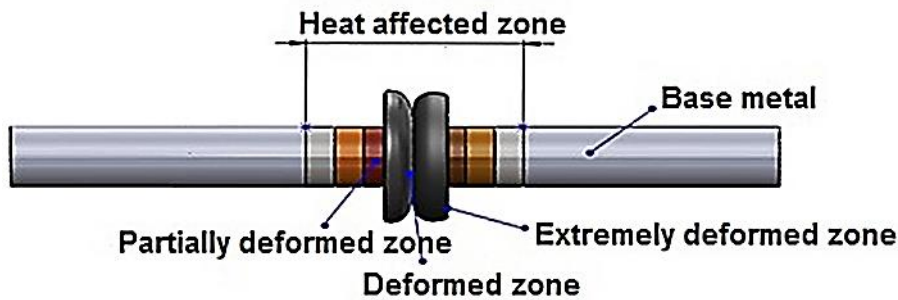


Figure 2. The view of the regions under thermomechanical interaction.

As stated in the literature, it was determined that four different regions were formed in welded joints. These regions are the extremely deformed zone (EDZ), deformed zone (DZ), partially deformed zone (PDZ) and the base metal (BM), respectively [15-17]. The grains of weld zone were thinner than the PDZ. The joint zone reached the highest temperature, which was below the solidus temperature. This led to the growth of ferrite grains. Due to the fully dissolution of austenite in heating, ferrite increased the austenite ratio. The distinction between the maximum temperature obtained at the weld pool and the room

temperature at the period of cooling caused in the rise of the cooling amount. Diffusional conversion to the austenite phase was limited by the cooling leading to the dominant ferrite structure in the weld seam [18]. A thin layer of proeutectoid ferrite consisted and was adjacent to the weld interface on AISI 1040 sides both in the central zone and in the peripheral zone. Lesser ferrite and rough pearlite grains accumulated in the pearlite grain boundaries. Frictional temperature and plastic distortion provided thinning and recrystallization of milled austenite grains induced by mechanical friction at the weld interface.

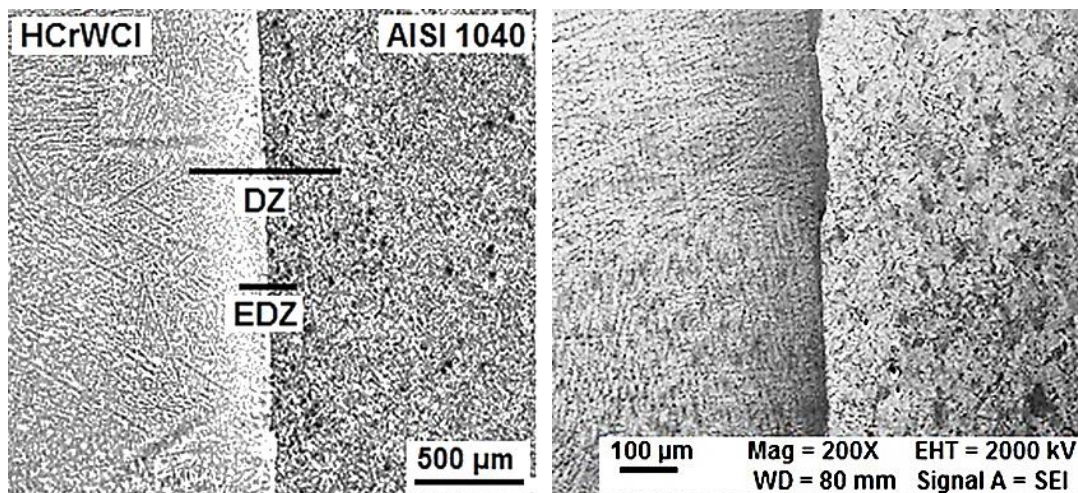


Figure 3. Optical and SEM photograph of S3 sample.

3.3. Phase analysis and weld metal chemical composition

The X-Ray analysis of the S3 welded sample is shown in Fig. 4. Phase and compounds such as Fe, Cr_{23}C_6 , Cr_7C_3 , CrC, Fe_3C were determined in the analyses. These metal carbides formed had a hard and brittle structure due to their ceramic character. Carbon, which is the dominant element of the diffusion process, was decisive in the emergence of the carbide layer. The carbide layer contained Cr_{23}C_6 and a metastable Cr_7C_3 phase. Because, C and Cr reacted easily in FW of HCrWCI to AISI 1040 and formed carbides in the weld

metal. EDS analysis of S3 sample is given in Fig. 5. The temperature at the welding interfaces was higher in S2 and S3 samples due to the increasing rotational speed. Since temperature was a driving force for diffusion, increased heat input with high friction time and rotational rate raised diffusion of Cr, C, Mn, Mo, Si and Ni elements in the weld zone.

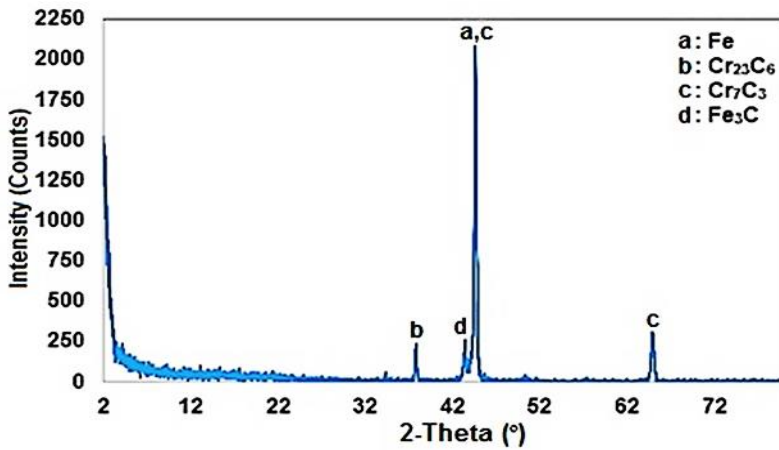


Figure 4. X-Ray analysis of S1 sample.

However, as we moved towards the base metal, the element diffusion decreased. It was determined that the original elemental percentages of the main materials were approached. Due to the differences in the chemical composition of the parent materials and the high heat during the joint operation, elemental

diffusion formed. The more pronounced changes of C and Cr at the joint interface are presented in Fig. 5. Since the diffusion coefficient of Cr is much lower than C, there is no visible Cr content at the weld interface. Carbon was effective in the element diffusion process [19].

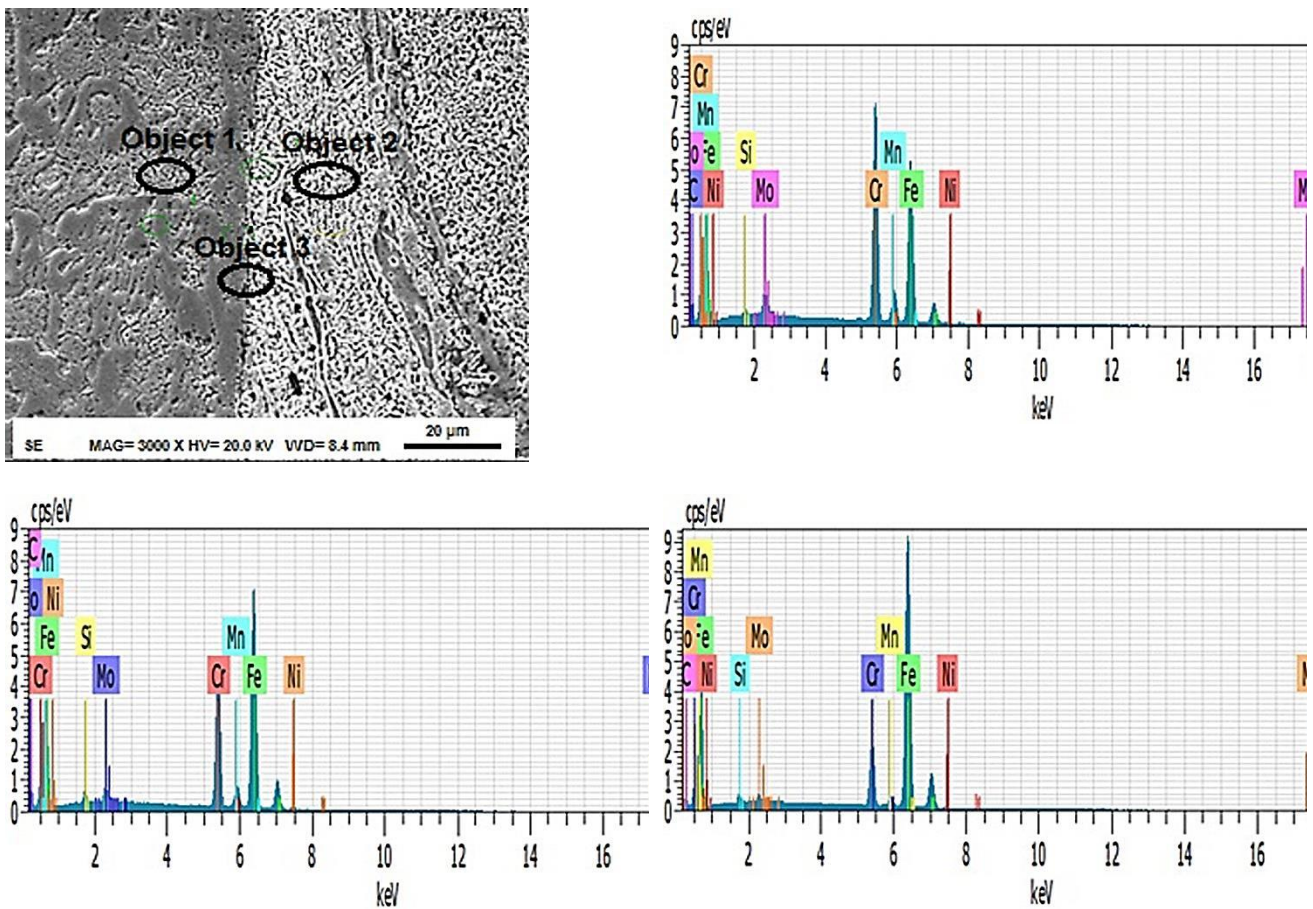


Figure 5. EDS analysis results of S3 sample.

Broken surface elemental mapping analysis of joint interface of S3 sample is given in Fig. 6. The transition of Cr, C, Mo, Ni, Si and Mn elements towards AISI1040 steel by HCrWCI occurred with plastic deformation and diffusion due to mechanical mixture. The iron element dominated the microstructure on the AISI1040 side as the main phase. It was determined that Cr, C, Mo, Si, Ni and Mn elements on the HCrWCI side diffused to the AISI 1040 side. The distribution of alloying elements such as Fe, Cr, C, Mo, Si, Ni and Mn in the weld area differend from place to place. The

carbide layer composed of CrC and Cr₂₃C₆ formed at the weld interface due to element dispersal. Since the Cr is the most important active element in the chemical composition of HCrWCI, formation of chromium carbides in the microstructure was predictable. The major active element in the chemical content of HCrWCI was chromium. Therefore, chromium carbide formation was expected in the microstructure. The brittle cleavage fracture morphology was exhibited in the samples.

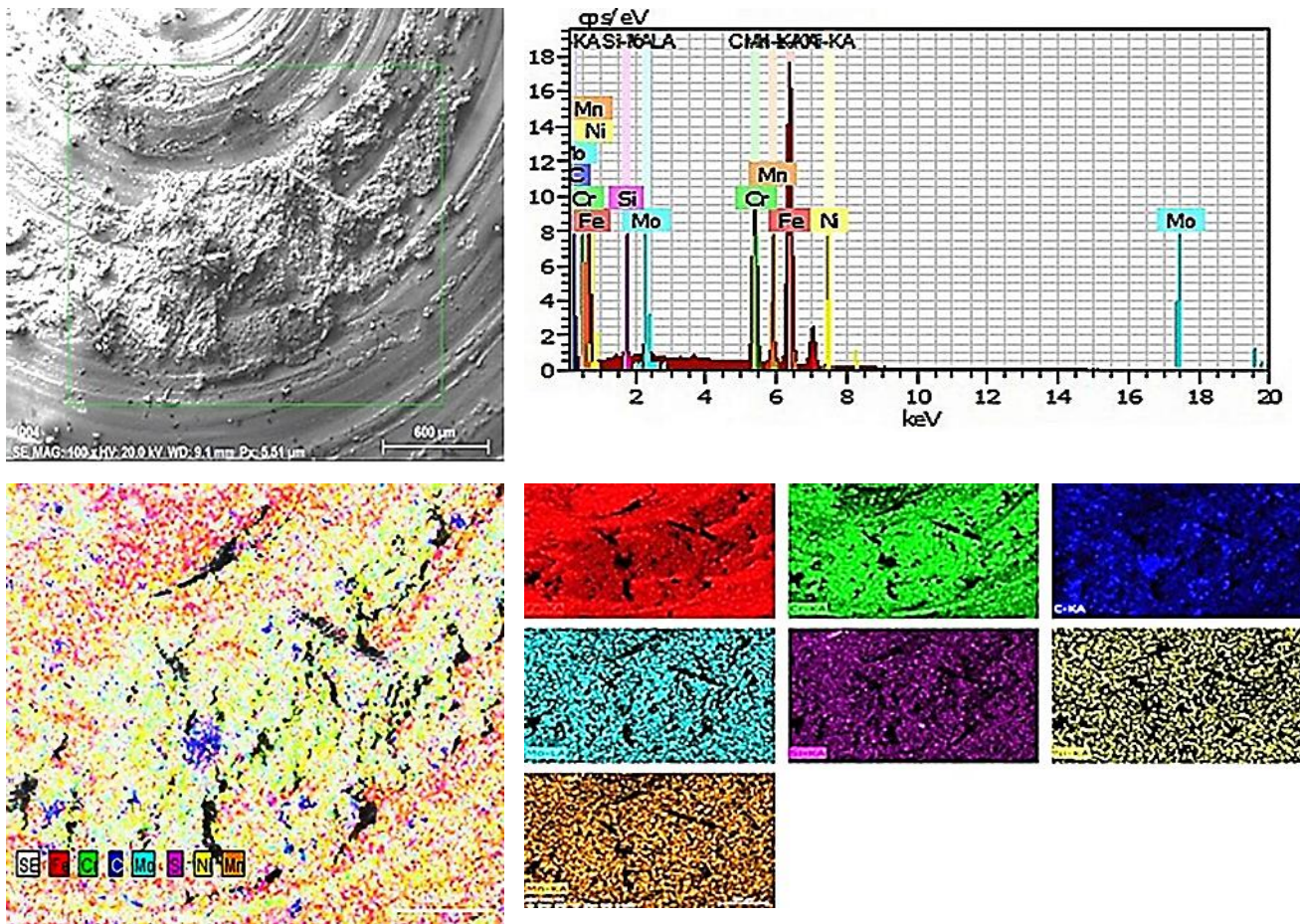


Figure 6. Broken surface elemental mapping analysis of S3 sample.

4. Conclusions

Mild carbon steel and HCrWCI are joined by friction welding under different joint conditions. The microstructures analysis of the weld interfaces, fracture morphology, presence and distribution of elements on joint zone were analyzed. The main conclusions are summarized as follows.

A rotation speed of 1600 rpm was not exactly sufficient for joining AISI 1040-HCrWCI alloys, but a rotation speed of 1800 rpm was adequate.

The rotational speed from the FW process parameters had a significant impact on the quality of the welded joint.

As stated in the literature, it was determined that four different regions were formed in welded joints.

Significant differences were detected in the quantities of flanges formed with increasing rotational period.

Due to the differences in the chemical composition of the parent materials and the high heat during the joint operation, elemental diffusion formed.

The carbides composed of Cr₇C₃ and Cr₂₃C₆ formed at the weld interface due to element dispersal.

Carbon was effective in the element diffusion leading to the formation of the carbides.

The brittle cleavage fracture morphology was exhibited in the samples.

Acknowledgment

This work, ADYU was supported by the Scientific Research Project Unit under the project number (MÜFYL/2018-001).

Conflicts of interest

The authors state that did not have conflict of interests

References

- [1] Paventhan R., Lakshminarayanan P., Fatigue behaviour of friction welded medium carbon steel and austenitic stainless steel dissimilar joint, *Mater. Des.*, 32(4) (2011) 1888–1894.
- [2] Arivazhagan N., Senthilkumaran K., Narayanan S., Devendranath Ramkumar K., Surendra S., Prakash S., Hot corrosion behavior of friction welded AISI4140 and AISI 304 in K₂SO₄–60% NaCl mixture, *J. Mater. Sci. Tech.*, 28(10) (2012) 895–904.
- [3] Muralimohan C.H., Muthupandi V., Sivaprasad K., Properties of friction welding titanium stainless steel joints with a nickel interlayer, *Procedia Mater. Sci.*, 5 (2014) 1120–1129.
- [4] Madhusudhan R.G., Role of nickel as an interlayer in dissimilar metal friction welding of maraging steel to low alloy steel, *J. Mater. Proces. Tech.*, 212(1) (2012) 66–77.
- [5] Çelik S., Ersözlü İ., Investigation of the mechanical properties and microstructure of friction welded joints between AISI4140 and AISI1050 steels, *Mater. Des.*, 30(4) (2008) 970–976.
- [6] Damodaram R., Raman S., Rao P.K., Microstructure and mechanical properties of friction welded alloy 718, *Mater. Sci. Eng.*, 560 (2013) 781–786.
- [7] Lippold J.C., Kotecki D.J., *Welding metallurgy and weldability of stainless steels*, New Jersey: John Wiley, (2005).
- [8] Yin Y., Yang X., Cui L., Cao J., Xu W., Microstructure and mechanical properties of underwater friction taper plug weld on X65 steel with carbon and stainless steel plugs, *Sci. Technol. Weld. Join.*, 21 (4) (2016) 259–266.
- [9] Li W., Vairis A., Preuss M., Ma T., Linear and rotary friction welding review, *Int. Mater. Rev.*, 61(2) (2016) 71–100.
- [10] Ma H., Qin G., Geng P., Li F., Fu B., Meng X., Microstructure characterization and properties of carbon steel to stainless steel dissimilar metal joint made by friction welding, *Mater. Des.*, 86 (2015) 587–597.
- [11] Suresh D., Meshram G., Madhusudhan R., Friction welding of AA6061 to AISI4340 using silver interlayer, *Defence Tech.*, 11(3) (2015) 292–298.
- [12] Kumar R., Alasubramanian M., Experimental investigation of Ti6Al4V titanium alloy and 304L stainless steel friction welded with copper interlayer, *Defence Tech.*, 11(1) (2015) 65–75.
- [13] Soysal T., Effect of solidification models on predicting susceptibility of carbon steels to solidification cracking, *Weld. World.*, (2021) 1-12. <https://doi.org/10.1007/s40194-021-01132-0>
- [14] Azizieh M., Khamisi M., Lee D.J., Yoon E.Y., Kim H.S., Characterizations of dissimilar friction welding of ST37 and CK60 steels, *Int. J. Adv. Manuf. Technol.* 85 (2016) 2773–2781.
- [15] Winiczenko R., Effect of friction welding parameters on the tensile strength and microstructural properties of dissimilar AISI 1020-ASTM A536 joints, *Int. J. Adv. Manuf. Technol.*, 84 (2016) 941–955.
- [16] Mortensen K. S., Jensen C.G., Conrad L.C., Losee F., Mechanical properties and microstructures of inertia friction welded 416 stainless steel, *Weld. J.*, 80 11, (2001) 268–273.
- [17] Kalsi N.S., Sharma V.S., A statistical analysis of rotary friction welding of steel with varying carbon in workpieces, *Int. J. Adv. Manuf. Technol.*, 57 (2011) 957–967.
- [18] Kimura M., Kasuya K., Kusaka M., Kaizu K., Fuji A., Effect of friction welding condition on joining phenomena and joint strength of friction welded joint between brass and low carbon steel, *Sci. Technol. Weld. Join.*, 14(5) (2009) 404–412.
- [19] Teker T., Karakurt E.M., Ozabacı M., Güleriyüz Y., Investigation of weldability of AISI 304 and AISI 1030 steels welded by friction welding, *Metal. Res. Tech.*, 117(6) (2020) 601–609.



Detection of epileptic seizures from EEG signals with Hilbert Huang Transformation

Muzaffer ASLAN^{1,*} , Zeynep Mine ALÇİN² 

¹Bingöl University, Faculty of Engineering and Architecture, Department of Electrical and Electronics Engineering, Bingöl/TURKEY

²Vedat Topçuoğlu Anatolian Vocational High School, Electrical and Electronics Department, Gaziantep/TURKEY

Abstract

Epilepsy is a significant neurological disease that occurs due to abnormal activities of a particular portion of brain neurons. Electroencephalography (EEG) signals are mainly used to detect this disease. Epilepsy can be diagnosed automatically by measuring and analyzing the non-linearity and non-stationary properties of EEG signals. In this study, the Hilbert Huang Transformation (HHT) is proposed to extract the distinctive features from EEG signals for epileptic seizure detection. Research work, firstly, the mean Instantaneous Amplitude (IA) and mean Instantaneous Frequency (IF) data were extracted from EEG signals with Hilbert Huang Transformation (HHT) as a feature. Then, these features were classified with Extreme Learning Machine (ELM). Classification results indicated that epileptic seizures are detected with high accuracy. In addition, the performance evaluation of the proposed method was compared with some other techniques studied by using the same dataset recently. According to the experimental results, HHT based approach has 0.5-1% better classification accuracy than current studies and higher accuracy in detecting epileptic seizures than similar studies.

Article info

History:
Received: 05.02.2020
Accepted: 17.06.2021

Keywords:
Electroencephalogram (EEG) signal, Hilbert–Huang Transform (HHT), Feature extraction, Classification.

1. Introduction

Biomedical signals are crucial for both diagnosis and treatment of diseases and for displaying health conditions. Although biomedical signals are examined in two groups as electrical and non-electrical signals, electrical biomedical signals are widely used in scientific studies. One of the electrical biomedical signals commonly used in biomedical studies is the Electroencephalography (EEG) signal. EEG is a method that can measure and record the electrical activities of the brain and capture temporary events that cause recurrent functional disorders in the human brain [1]. EEG signals are obtained through electrodes placed at specific points on the head. These signals can be defined as voltage changes caused by ionic current occurring in neurons in the brain. Observing these changes is very significant in disease diagnosis. One of the essential purposes of using EEG signals is to be preferred for the detection of epilepsy disease [2]. Epilepsy is a clinical condition caused by the disruption of abnormal electrical activities that occur temporarily in part of the brain cells. It is a neurological disease known as a temporary recurrent

and unpredictable epileptic seizure that can be seen in approximately 50 million people worldwide [3]. Physiological effects such as changes in mental state, lack of attention, empty gaze and inability to remember are primarily observed in patients [4]. In addition, during sudden and unpredictable seizures, due to the loss of consciousness, the person is unable to protect himself at that moment so that the person may be exposed to the risks of injury, suffocation and death [2, 4]. These seizures can be detected and diagnosed by monitoring long-term EEG recordings. Monitoring of EEG signals requires a lot of attention. Although the expert does the monitoring and interpretation of the EEG recordings, sometimes reading error may occur. Systems that can automatically detect epilepsy disorders have been developed to assist specialists in the diagnosis and treatment process. Recently, many EEG signal processing analysis methods have been studied for automated epilepsy detection systems. These methods generally aimed to obtain specific features from the EEG signal and classifying these features [3]. Feature extraction from EEG signals is usually located in the time, frequency, or time-frequency domain (TFD). In the time domain, methods

*Corresponding author. e-mail address: muzaffer.aslan@bingol.edu.tr
<http://dergipark.gov.tr/csj> ©2021 Faculty of Science, Sivas Cumhuriyet University

such as basic component analysis-based radial-based artificial neural networks (ANN) are used [5].

In the studies carried out in the frequency domain, with the assumption that EEG signals are stationary signals, attributes extracted using the Fourier Transform (FT) and Wavelet Transform (WT) are classified by using classification methods such as decision trees, ANN and support vector machines (SVM) [6]. In addition to all these studies, non-stationary EEG signals have been widely used in many scientific studies in this field. Epileptic seizures detections were performed by using the properties of non-stationary EEG signals in the time-frequency region. Siuly et al. [7] calculated the permutation entropy, histogram and statistical properties with the transformation of Hermite transformation EEG signals into a new form. Afterwards, they identified these features by least squares and SVM to classify EEG signals to detect epileptic seizures. Recent studies have benefited from the HHT conversion, a new method proposed by Norden E. Huang in 1998 to analyze both non-linear and non-stationary high-dimensional EEG signals [8]. For detecting epileptic seizures, Hilbert Vibration Decomposition (HVD) was performed by extracting single component attributes of momentary amplitude and frequency changes of EEG signals [9]. Fu et al. [10] detected epileptic seizures with the SVM classifier using features such as mean, variance, skewness and pixel density in the HHT-segmented grayscale time-frequency image histogram. Matris et al. [11] used spectral entropy and spectral energy properties of spectral peaks calculated from the Intrinsic Mode Functions (IMF) for epileptic seizure detection. Shuren ve Zhong have performed epileptic seizure detection using different threshold levels of IMF signals again for their properties obtained by Empirical Mode Decomposition (EMD) to separate EEG signals into several IMFs [12]. Feldman detected epileptic seizures by decomposing HVD, a newer signal decomposition technique, by separating non-stationary time series and suggesting harmonic extraction with reduced energy content [13]. Ghayab et al. [14] sequential feature selection (SFS) features were reduced in size after feature extraction from multi-channel EEG signals with simple random sampling (SRS). Later, these features were classified with the least-square support vector machine (LS_SVM) classifier. In experimental studies, they achieved an accuracy rate of 99.90%. Zhu et al. [15] proposed feature extraction with the Fast Weighted Horizontal Visibility (FWHV) algorithm for seizure detection of EEG signals. They obtained by comparing the extracted features with fast FT and sample entropy. Supriya et al. [16] used statistical methods for feature extraction after converting the

weight visibility graph and EEG signals into a complex network. These features were classified with k-NN and SVM and detected seizures. Kumar et al. [17] proposed feature extraction by dividing WT and EEG signals into different sub-bands for seizure detection. Afterwards, they classified these features with the SVM classifier types. Demir et al. [18] Convolution Neural Network (CNN) based efficient approach was proposed for emotion recognition with EEG. After EEG signals were converted to EEG rhythm images with Continuous Wavelet Transform (CWT), feature extraction was performed with CNN. Deep features are classified with SVM.

In this research, average instantaneous amplitude and mean instantaneous frequency values were obtained as features by the HHT method from stationary and non-linear EEG signals. Epileptic seizures are detected automatically by classifying these features with ELM. In experimental studies, 10-fold cross-validation was performed to evaluate the validity of the method. Results present that the proposed method appears to have achieved a classification accuracy of 0.5-1% better than current studies. The rest of the research work, HHT method and feature extraction are introduced in EEG dataset part 2. In chapter 3, experimental studies are mentioned. Finally, in section 4, evaluations regarding the results of the study are presented.

2. Material and Method

In this section, the methods used for the dataset, feature extraction, and classification are described in detail.

2.1. EEG dataset

EEG is a recording of the electrical activity of the brain from the scalp. These electrical activities have variable frequencies and magnitudes. The magnitude of the EEG signals is in the microvolt levels. EEG signals are divided into four groups according to their frequency: delta (1-4 Hz), theta (4-8 Hz), alpha (8-13 Hz), beta (13-30 Hz), and gamma (30- 80 Hz) [18], [19].

Bonn EEG dataset is utilized to test the method proposed in this research work [20]. The dataset contains five separate EEG sub-datasets, Set A, Set B, Set C, Set D, Set E. Each subset includes 100 EEG signals recorded for 23.6 seconds, and each signal consists of 4097 samples. Datasets A and B are recorded EEG signals from five healthy participants with eyes open and eyes closed, respectively. The C and D dataset contains EEG signals from opposite episodes of the head, respectively, from processes without seizures from five epileptic patients.

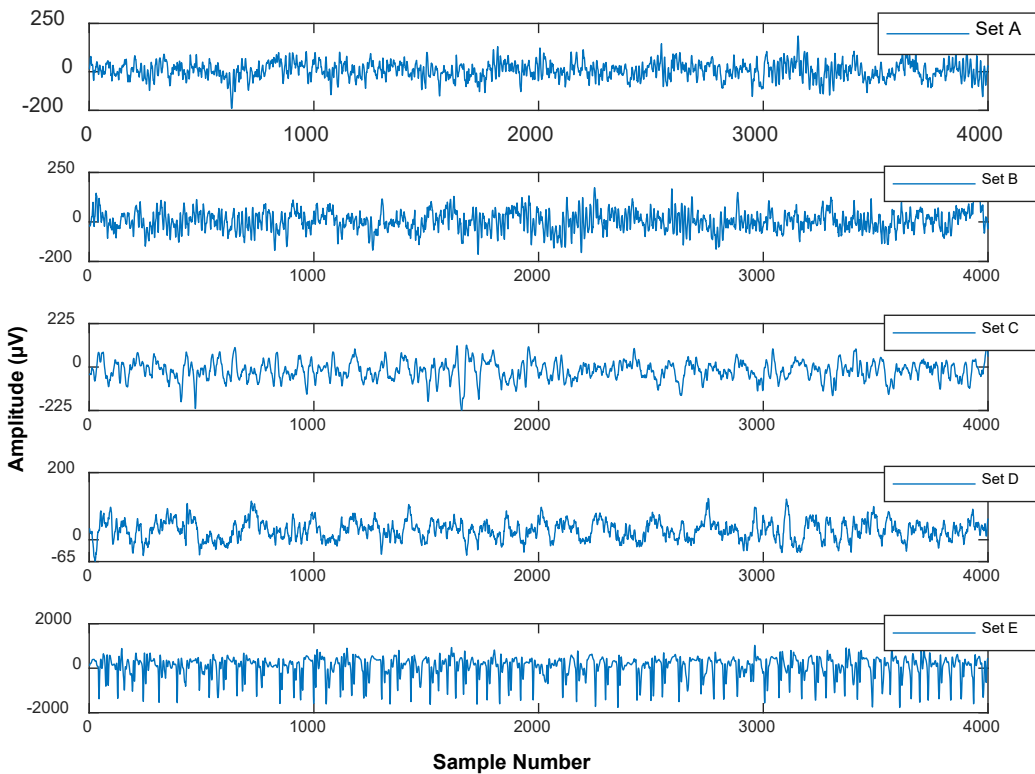


Figure 1. Sample EEG signals of the five subsets A, B, C, D and E.

The E dataset contains EEG signals taken at the time of seizures from five epileptic patients. Figure 1 shows sample EEG signals of the five subsets in the Bonn Dataset.

2.2. Method

In this study, a new time frequency-based method is presented to detect epileptic seizures from EEG signals. The technique, the block diagram of which is given in Figure 2, consists of two separate sections: obtaining attributes and classification. For feature extraction, instantaneous amplitude and instantaneous frequency variations of stationary and non-linear EEG

signals were obtained with HHT. Averages of instantaneous amplitude and frequency changes were taken separately, and their attributes dataset was created.

At the last stage, epileptic seizures were detected automatically by classifying these attribute data with the ELM classifier. ELM was preferred as the classifier due to its successful classification and high performance in classification and regression applications. More detailed information for ELM can be viewed from Huang's [8] article.

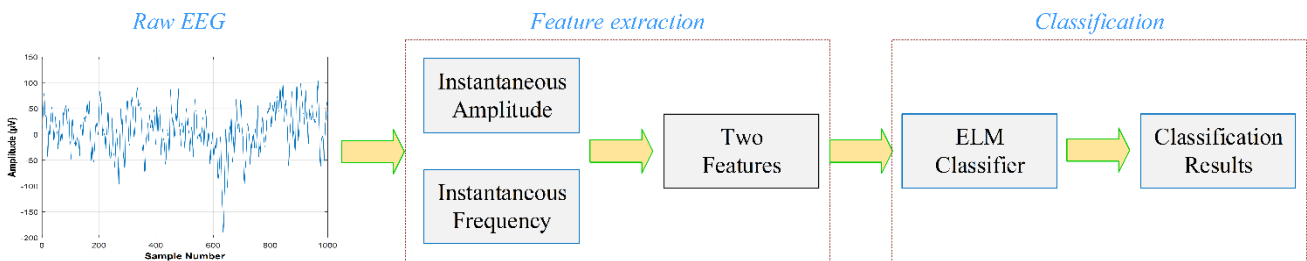


Figure 2. Block diagram of the proposed method.

2.2.1. Hilbert Huang transformation

Norden E. Huang proposed the HHT method in 1998 for the time-frequency analysis of both non linearity and non-stationary signals, in particular. Unlike traditional time frequency analysis methods such as

Fast Fourier Transformation (FFT) and WT, it is used to analyze non-stationary and non-linear signals. HHT consists of two essential components; EMD and IMF [21]. It is particularly suitable for the display of time-frequency-energy systems. The most meaningful way

to physically define such a system is instantaneous frequency information that reveals in-wave frequency modulation. The easiest way to calculate the instantaneous frequency is to use HDD. HHT is a method mainly used to express one-dimensional time series to analytical form in biomedical signal processing and power systems applications [22],[23].

HHT process for a sample $x(t)$ signal could be defined as in (1):

$$H[x(t)] = F^{-1}\{F\{x(t)\}u(t)\} \quad (1)$$

where $F\{\cdot\}$ and $F^{-1}\{\cdot\}$ is FFT and Inverse FFT, respectively, here $u(t)$ expression in equation (1) is presented in equation (2):

$$u(t) = \begin{cases} 1 & n = 0, (N/2) \\ 2 & n = 1, 2, \dots, (N/2) - 1 \\ 0 & n = (N/2) + 1, \dots, N - 1 \end{cases} \quad (2)$$

Here N is the sample length of $x(t)$. HHT uses both FFT and inverse FFT processes. Moreover, using a time series, it is possible to define an analytical signal generated by the imaginary part of the HHT. The HHT result of the time series is an analytical time series, a complex value signal. The amplitude and phase of the signal are time-dependent. This signal contains instantaneous amplitude, instantaneous phase and instantaneous frequency information. In this context, an analytic signal of a real-time $x(t)$ signal $z(t)$ could be defined as in equation (3). The instantaneous amplitude $a(t)$ and instantaneous phase $\varphi(t)$ defined in equation 3 could be found with equation (4).

$$z(t) = x(t) + iy(t) = a(t)e^{i\varphi t} \quad (3)$$

$$a(t) = \sqrt{[x^2(t) + y^2(t)]}, \varphi(t) = \arctan \frac{y(t)}{x(t)} \quad (4)$$

Moreover, the instantaneous frequency could be calculated with the help of $\omega(t) = \frac{d\varphi(t)}{dt}$ relation.

3. Experimental Studies

Feature extraction from raw EEG data is crucial in detecting epileptic seizures. The extracted features should both provide maximum discrimination from raw EEG data and have low computational complexity. In this respect, the method suggested in Fig. 2 was used to extract the features from the raw EEG signals. In the experimental studies, the EEG data from healthy, disease-diagnosed but non-epileptic seizure participants and EEG data for participants who had

seizures in the Bonn EEG dataset were classified as such (A-E, B-E, C-E, D-E and ABCD-E).

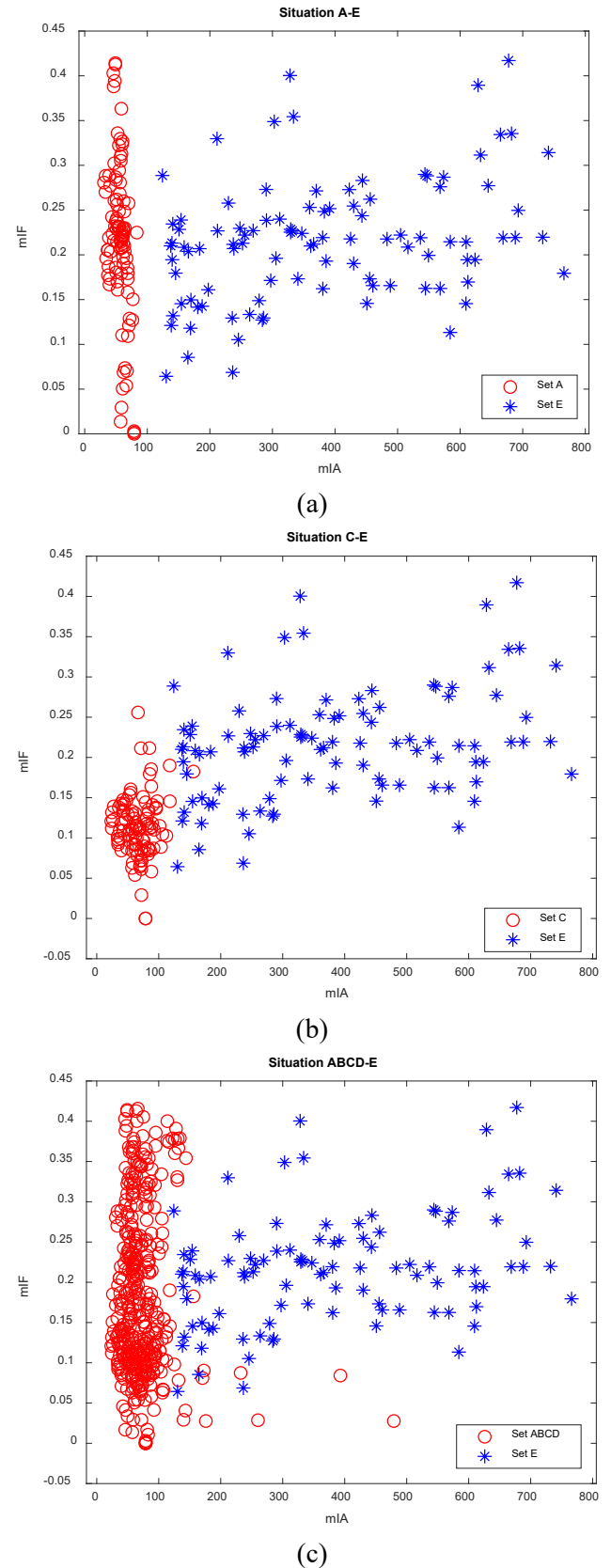


Figure 2. Scattering curves of (a) A-E, (b) C-E and (c) ABCD-E.

Instantaneous amplitude and instantaneous frequency values of EEG signals in each group were obtained with HDD. Then, the average of each signal's instantaneous amplitude and frequency changes was used as an attribute. The scatter curves shown in Figure 3 a-c are created for A-E, C-E and ABCD-E situations better to understand the efficiency of mean IA (mIA) and mean IA (mIF) attributes after they are obtained with HHT. As can be seen in the scatter curves in Fig. 3 (a-c), it shows that it has the potential to extract distinctive features from the attributes obtained from the EEG signals of different datasets.

The obtained attributes are applied to the input of the ELM. The number of hidden layer neurons 1000 in ELM was determined empirically as activation function sigmoid. In the performance evaluation of the proposed method, 10-fold cross-validation is taken into consideration. As the classification criteria, as shown in equations 5, 6 and 7, the accuracy (ACC), sensitivity (SEN) and specificity (SPC) criteria are respectively taken as reference.

$$ACC = \frac{TP+TN}{TP+TN+FP+FN} \times 100 \quad (5)$$

$$SEN = \frac{TP}{TP+FN} \times 100 \quad (6)$$

$$SPC = \frac{TN}{TN+FP} \times 100 \quad (7)$$

Where TP represents the total number of true positive, TN represents the total number of true negative, FP represents the total number of false positive, and FN represents the total number of false negative.

Table 1. HHT method and ELM Classification Performance

Situation	Accuracy (%)	Sensitivity (%)	Specificity (%)
A-E	100	100	100
B-E	99.50	100	99.09
C-E	99.50	99.09	100
D-E	96.50	98.18	99.75
ABCD-E	98.2	93.94	99.50

Table 1 shows the classification results of the proposed method for five different conditions to detect epileptic seizures from EEG signals. The table contains the evaluations of accuracy, sensitivity and specificity performances. As can be seen in Table 1, A-E and B-E appear to achieve 100% and 99.5% accuracy in distinguishing healthy individuals and individuals with epileptic seizures, respectively. Similarly, C-E and D-E achieved 99.5% and 96.5% accuracy in detecting

individuals with epileptic seizures, respectively. In another experimental study (case ABCD-E), a success rate of 98.2% was achieved in distinguishing between healthy (A, B) and disease-diagnosed (C, D) participants and patients with seizures (E).

In addition, the results are shown in Table 2, where the same dataset was used to evaluate better the proposed HHT-based feature extraction and the classification performance with ELM, and some other recent studies and general accuracy rates were compared.

According to our findings in Table 2, for B-E situation, Siuly et al. [7] 0.5% higher accuracy was achieved. In addition, 1% and 0.6% higher accuracy scores were obtained for the C-E and ABCD-E situation, respectively. In the D-E situation, the highest performance is 97.5% accuracy. Our method lagged behind the higher performance with a 1% score. To summarize, it can be seen that the HHT method proposed in four of the experimental studies for 5 different situations has a higher accuracy rate than the other methods.

4. Conclusion and Suggestions

In this research work, a new method based on HHT-based feature extraction is proposed for the detection of epileptic seizures from EEG signals. In this study, the epileptic seizure detection Bonn EEG dataset is used. mIA and mIF attributes obtained from the dataset with HHT are classified with ELM. According to experimental results, 100% accuracy for A-E case, 99.5% for B-E and C-E, 96.5% for D-E and 98.2% for ABCD-E case are achieved. Our proposed method has a more straightforward distinctive feature extraction than the existing methods in the literature; in addition, its better performance in detecting epileptic seizures indicates the superiority of our approach. As a result, it has been put forward that the HHT-based ELM method will contribute to the establishment of a computer-aided medical diagnosis system that enables medical professionals and technicians to make the right decision on patients.

The proposed HHT and ELM based feature extraction method has low computational complexity compared to the state art methods. so the proposed epilepsy detection approach is appropriate for offline real-time and embedded applications.

Table 2. Comparison of the proposed method with the existing methods

Situation	Authors	Methods	Accuracy (%)
A-E	Siuly et al. (2018) [7]	Hermite Transformation LS-SVM	99.5
	Ghayab et al. (2016) [14]	Simple Random Sampling+ Sequential Feature Selection LS-SVM	99.9
	Zhu et al. (2014) [15]	Fast Weighted Horizontal Visibility Graph Constructing Algorithm K-NN	99
	Proposed Method	HHT+ ELM	100
B-E	Siuly et al. (2018) [7]	Hermite Transformation LS-SVM	99
	Zhu et al. (2014) [15]	Fast Weighted Horizontal Visibility Graph Constructing Algorithm K-NN	97
	Supriya et al.(2016) [15]	Complex Network, Modularity and Average weight degree SVM	97.25
	Proposed Method	HHT+ ELM	99.5
C-E	Siuly et al. (2018) [6]	Hermite Transformation LS-SVM	98.5
	Zhu et al. (2014) [15]	Fast Weighted Horizontal Visibility Graph Constructing Algorithm K-NN	98
	Supriya et al.(2016) [15]	Complex Network, Modularity and Average weight degree SVM	98.25
	Proposed Method	HHT+ELM	99.5
D-E	Siuly et al. (2018) [6]	Hermite Transformation LS-SVM	97.5
	Zhu et al. (2014) [15]	Fast Weighted Horizontal Visibility Graph Constructing Algorithm K-NN	93
	Supriya et al.(2016) [15]	Complex Network, Modularity and Average weight degree SVM	93.25
	Proposed Method	HHT+ELM	96.5
ABCD-E	Siuly et al. (2018) [7]	Hermite Transformation LS-SVM	97.6
	Kumar et al. (2014) [20]	DWT-based fuzzy entropy and SVM	92.4
	Proposed Method	HHT+ELM	98.2

Conflicts of interest

The authors state that did not have conflict of interests

References

- [1] Andrzejak R. G., Lehnertz K., Mormann F., Rieke C., David, P., Elger C. E., Indications of nonlinear deterministic and finite-dimensional structures in time series of brain electrical activity: Dependence on recording region and brain state, *Physical Review E.*, 64(6) (2001) 061907
- [2] Çakil D., Inanir S., Baykan H., Aygün, H., Kozan R., Epilepsi ayırıcı tanısında psikojenik non-epileptik nöbetler, *Göztepe Tıp Dergisi.*, 28(1) (2013) 41–47.
- [3] World Health Organization, Epilepsy: a public health imperative. Available at: <https://www.who.int/publications/i/item/epilepsy-a-public-health-imperative>. Retrieved February, 2021.
- [4] Bajaj V., Guo Y., Sengur A., Siuly S., Alcin O. F., A hybrid method based on time–frequency images for classification of alcohol and control EEG signals, *Neural Computing and Applications.*, 28(12) (2017) 3717–3723.
- [5] A. Jaiswal A. K., Banka H., Local pattern transformation based feature extraction techniques for classification of epileptic EEG signals, *Biomedical Signal Processing and Control.*, 34 (2017) 81–92.
- [6] V. Joshi V., Pachori R. B., Vijesh A., Classification of ictal and seizure-free EEG signals using fractional linear prediction, *Biomedical Signal Processing and Control.*, 9(1) (2014) 1–5.
- [7] S. Siuly S., Alcin O. F., Bajaj V., Sengur A., Zhang Y., Exploring Hermite transformation in brain signal analysis for the detection of epileptic seizure, *IET Science Measurement and Technology.*, 13(1) (2019) 35–41.
- [8] Huang N. E., Shen Z., Long S. R., Wu M. C., Snin H. H., Zheng Q., Yen N. C., Tung C. C., Liu H. H., The empirical mode decomposition and the Hubert spectrum for nonlinear and non-stationary

time series analysis, *Proceedings of the Royal Society A: Mathematical, Physical and Engineering Sciences.*, 454(1971) (1998) 903–995.

- [9] Mutlu A. Y., Detection of epileptic dysfunctions in EEG signals using Hilbert vibration decomposition, *Biomedical Signal Processing and Control.*, 40 (2018) 33–40.
- [10] Fu K., Qu J., Chai Y., Dong Y., Classification of seizure based on the time-frequency image of EEG signals using HHT and SVM, *Biomedical Signal Processing and Control.*, 13(1) (2014) 15–22.
- [11] Martis R. J., Acharya U. R., Tan J. H., Petznick A., Yanti R., Chua C. K., Ng E. Y. K., Tong L., Application of empirical mode decomposition (EMD) for automated detection of epilepsy using EEG signals, *International Journal of Neural Systems.*, 22(6) (2012) 1250027 1-16.
- [12] Shuren Q, Zhong J, Extraction of features in EEG signals with the non-stationary signal analysis technology, *The 26th Annual International Conference of the IEEE Engineering in Medicine and Biology Society.*, San Francisco, (2004) 349–352.
- [13] Feldman, M., Time-varying vibration decomposition and analysis based on the Hilbert transform, *Journal of Sound and Vibration.*, 295(3–5) (2006) 518–530.
- [14] Al Ghayab H. R., Li Y., Abdulla S., Diykh M., Wan X., Classification of epileptic EEG signals based on simple random sampling and sequential feature selection, *Brain Informatics.*, 3(2) (2016) 85–91.
- [15] Andrzejak R. G., Lehnertz K., Mormann F., Rieke C., David, P., Elger C. E., Indications of nonlinear deterministic and finite-dimensional structures in time series of brain electrical activity, *Dependence on recording region and brain state*, *Physical Review E.*, 64(6) (2001) 061907 1-8.
- [16] Supriya S., Siuly S., Wang H., Cao J., Zhang Y., Weighted Visibility Graph with Complex Network Features in the Detection of Epilepsy, *IEEE Access.*, 4 (2016) 6554–6566.
- [17] Kumar Y., Dewal M. L., Anand R. S., Epileptic seizure detection using DWT based fuzzy approximate entropy and support vector machine, *Neurocomputing.*, 133 (2014) 271–279.
- [18] Demir F., Sobahi N., Siuly S., Sengur A., Exploring Deep Learning Features For Automatic Classification Of Human Emotion Using EEG Rhythms, *IEEE Sensors Journal.*, (2021) 1–8.
- [19] Turkoglu M., Alcin O. F., Aslan M., Al-Zebari, A., Sengur A., Deep rhythm and long short term memory-based drowsiness detection, *Biomedical Signal Processing and Control.*, 65 (2020) 102364.
- [20] Andrzejak R. G., Lehnertz K., Mormann F., Rieke C., David, P., Elger C. E., Indications of nonlinear deterministic and finite-dimensional structures in time series of brain electrical activity, *Dependence on recording region and brain state*, *Physical Review E.*, 64(6) (2001) 061907 1-8
- [21] Oweis R. J., Abdulhay E. W., Seizure classification in EEG signals utilizing Hilbert-Huang transform, *BioMedical Engineering Online.*, 10(1) (2011) 1-15.
- [22] Wei B., Xie B., Li H., Zhong Z., You Y., An improved Hilbert–Huang transform method for modal parameter identification of a high arch dam, *Applied Mathematical Modelling.*, 91 (2021) 297–310.
- [23] Aydın F., Aslan Z., Recognizing Parkinson’s disease gait patterns by vibes algorithm and Hilbert-Huang transform, *Engineering Science and Technology, an International Journal.*, 24(1) (2021) 112–125.

AUTHOR GUIDELINES

Thank you for choosing to submit your paper to Cumhuriyet Science Journal. The following instructions will ensure we have everything required so your paper can move through pre-evaluating, peer review, production and publication smoothly. Please take the time to read and follow them as closely as possible, as doing so will ensure your paper matches the journal's requirements.

Submission

Cumhuriyet Science Journal is an international, peer-reviewed, free of charge journal covering the full scope of both natural and engineering sciences. Manuscripts should be submitted by one of the authors of the manuscript as online submission after registration to the Cumhuriyet Sciences Journal. Microsoft Word (.doc, .docx, .rtf), files can be submitted. There is no page limit. If there is a problem while uploading the files of manuscript, please try to reduce their file size, especially manuscripts including embedded figures. Submissions by anyone other than one of the authors will not be accepted. The submitting author takes responsibility for the paper during submission and peer review. If for some technical reason submission through the online submission system is not possible, the author can contact csj@cumhuriyet.edu.tr for support.

Submission or processing charges

Cumhuriyet Science Journal does not charge any article submission, processing charges, and printing charge from the authors.

Terms of Submission

Papers must be submitted on the understanding that they have not been published elsewhere (except in the form of an abstract or as part of a published lecture, review, or thesis) and are not currently under consideration by another journal. The submitting author is responsible for ensuring that the article's publication has been approved by all the other coauthors. It is also the authors' responsibility to ensure that the articles emanating from a particular institution are submitted with the approval of the necessary institution. Only an acknowledgment from the editorial office officially establishes the date of receipt. Further correspondence and proofs will be sent to the author(s) before publication unless otherwise indicated. It is a condition of submission of a paper that the corresponding author permit editing of the paper for readability. All enquiries concerning the publication of accepted papers should be addressed to csj@cumhuriyet.edu.tr. Please note that Cumhuriyet Science Journal uses iThenticate software to screen papers for unoriginal material. By submitting your paper to Cumhuriyet Science Journal are agreeing to any necessary originality checks your paper may have to undergo during the peer review and production processes. Upon receiving a new manuscript, the Editorial office conducts initial pre-refereeing checks to ensure the article is legible, complete, correctly formatted, original, within the scope of the journal in question, in the style of a scientific article and written in clear English. Any article that has problems with any of the journal criteria may be rejected at this stage.

Peer Review

This journal operates a single blind review process. All contributions will be initially assessed by the editor for suitability for the journal. Papers deemed suitable are then typically sent to a minimum of two independent expert reviewer to assess the scientific quality of the paper. The author is required to upload the revised article to the system within 15 days by making the corrections suggested by the referee. The article will be rejected if there are no fixes in it. The Editor is responsible for the final decision regarding acceptance or rejection of articles. The Editor's decision is final

Title and Authorship Information

The following information should be included

Paper title

Full author names

Full institutional mailing addresses

Corresponding address

Email address

Abstract

The manuscript should contain an abstract. The researchers who are native speakers of Turkish have to add Turkish title and abstract as well. The abstract should be self-contained and citation-free and should be 250-300 words.

Keywords

Keywords of the scientific articles should be selected from the web address of www.bilimadresleri.com

Introduction

This section should be succinct, with no subheadings.

Materials and Methods

This part should contain sufficient detail so that all procedures can be repeated. It can be divided into subsections if required.

Conflicts of interest

Sample sentence if there is no conflict of interest: The authors stated that did not have conflict of interests.

Acknowledgements

Sample sentences for acknowledgements: The work was supported by grants from CUBAP (T-1111). We would like to acknowledge Prof. Mehmet Sözer, MD, for his precious technical and editorial assistance. We would like to thank

References

References to cited literature should be identified by number in the text in square brackets and grouped at the end of the paper in numerical order of appearance. Each reference must be cited in the text. Always give inclusive page numbers for references to journal articles and a page range or chapter number for books. References should be styled and punctuated according to the following examples

- [1] Karaca E., Ulusoy S., Morgül Ü., Ulusoy H.I., Development of Analytical Method for Sensitive Determination of Streptozotocin based on Solid Phase Extraction, Cumhuriyet Sci. J., 41 (4) (2020) 826-831. (sample reference for journals)
- [2] Keskin B., Ozkan A.S., Inverse Spectral Problems for Dirac Operator with Eigenvalue Dependent Boundary and Jump Conditions, Acta Math. Hungar., 130 (2011) 150-159(sample reference for journals)
- [3] Mazur M.T., Kurman R.J., Dysfunctional Uterine Bleeding. In: Mazur M.T., Kurman R.J., (Eds). Diagnosis of endometrial biopsies and curettings, A practical approach. 2nd ed. Berlin: Springer, (2005) 100-120. (sample reference for book chapters)
- [4] Mazur M.T., Kurman R.J.,Diagnosis of endometrial biopsies and curettings, A practical approach. 2nd ed. Berlin, (2005) 100-120. (sample reference for book)
- [5] National Cancer Institute, Surveillance Epidemiology and End Results. Cancer of the Corpus and Uterus, NOS. Available at: http://seer.cancer.gov/statfacts/html/corp.html?statfacts_page=corp. Retrieved March 2, 2008. (sample reference for websites)
- [6] Surname N., Title of thesis, PD or master thesis, Name of university, name of institue, year. (sample reference for thesis)
- [7] Surname N., Title of fulltext conference paper, name of conference, city, year, pages. (sample reference for Abstratcs in conferences are not accepted as a valid reference except full text)

Preparation of Figures

Each figure can be integrated in the paper body or separately uploaded and should be cited in a consecutive order. Figure widths can be 4-6 inch as 300 dpi. The labels of the figures should be clear and informative. The name and the subtitles of the figures must be 9-point font.

Preparation of Tables

Tables should be cited consecutively in the text. Every table must have a descriptive title and if numerical measurements are given, the units should be included in the column heading. Tables should be simple with simple borders and text written as left text. The name and the subtitle of the tables must be 9-point font

Proofs

Corrected proofs must be returned to the publisher within 2 weeks of receipt. The publisher will do everything possible to ensure prompt publication. It will therefore be appreciated if the manuscripts and figures conform from the outset to the style of the journal.

Copyright

Open Access authors retain the copyrights of their papers, and all open access articles are distributed under the terms of the Creative Commons Attribution license, which permits unrestricted use, distribution and reproduction in any medium, provided that the original work is properly cited.

The use of general descriptive names, trade names, trademarks, and so forth in this publication, even if not specifically identified, does not imply that these names are not protected by the relevant laws and regulations.

While the advice and information in this journal are believed to be true and accurate on the date of its going to press, neither the authors, the editors, nor the publisher can accept any legal responsibility for any errors or omissions that may be made. The publisher makes no warranty, express or implied, with respect to the material contained herein.

Ethical Guidelines

New methods and ethically relevant aspects must be described in detail, bearing in mind the following:

Human Experiments. All work must be conducted in accordance with the Declaration of Helsinki (1964). Papers describing experimental work on human subjects who carry a risk of harm must include:

A statement that the experiment was conducted with the understanding and the consent of the human subject.

A statement that the responsible Ethical Committee has approved the experiments.

Animal Experiments. Papers describing experiments on living animals should provide:

A full description of any anaesthetic and surgical procedure used.

Evidence that all possible steps were taken to avoid animal suffering at each stage of the experiment. Papers describing experiments on isolated tissues must indicate precisely how the donor tissues were obtained.

Submission Preparation Checklist

As part of the submission process, authors are required to check off their submission's compliance with all of the following items, and submissions may be rejected that do not adhere to these guidelines.

The submission has not been previously published, nor is it before another journal for consideration (or an explanation has been provided in Comments to the Editor).

The submission file is in Microsoft Word document file (Times New Roman) format.

Where available, URLs for the references have been provided.

The text is single-spaced; uses a 11-point font; employs italics, rather than underlining (except with URL addresses); and all illustrations, figures, and tables are placed within the text at the appropriate points, rather than at the end.

The text adheres to the stylistic and bibliographic requirements outlined in the Author Guidelines, which is found in About the Journal.

If submitting to a peer-reviewed section of the journal, the instructions in Ensuring a Double-Blind Review have been followed.